

## Habilitation à Diriger des Recherches

# Diving into the Complexities of Multi-Scale Wall-Bounded Turbulence Dynamics

**Lionel Agostini** Chargé de Recherche – CNRS

Date de soutenance envisagée : Septembre 2024

### Composition du jury :

**Jacques Borée**, Professeur

ENSMA, Laboratoire Pprime, Université de Poitiers

**Sergei I Chernyshenko**, Professor of Aerodynamics  
Department of Aeronautics, Imperial College London

**Laurent Cordier**, Directeur de Recherche CNRS  
Laboratoire Pprime, Université de Poitiers

**Nicholas Hutchins**, Professor

Department of Mechanical Engineering, University of Melbourne

**Bérengère Podvin**, Directrice de Recherche CNRS  
Laboratoire EM2C, CentraleSupélec

**Jean-Christophe Robinet**, Professeur

Laboratoire DynFluid, Arts et Métiers Institute of Technology

**Michael Leschziner**, Professor of Aerodynamics

Department of Aeronautics, Imperial College London



# Contents

<b>1</b>	<b>Introduction</b>	<b>3</b>
1.1	Zoologie of a turbulent boundary layer . . . . .	3
1.2	Scales' interconnections . . . . .	6
1.3	Puzzle of wall-bounded flow dynamic . . . . .	9
<b>2</b>	<b>Drag reduction</b>	<b>13</b>
2.1	Control of near-wall structures . . . . .	13
2.1.1	Motivation . . . . .	13
2.1.2	Scientific context . . . . .	13
2.2	Computational conditions . . . . .	16
2.3	Mean-flow characteristics . . . . .	17
2.4	Phase-averaged properties . . . . .	20
2.4.1	Investigating the Connection Between Transient Drag Reduction and Drag Oscillations Around Low-Drag State . . . . .	20
2.4.2	Interactions in the Upper Part of Viscous Sublayer . . . . .	22
2.4.3	Interactions in the Lower Part of the Viscous Sublayer: Hysteresis and Skewness . . . . .	22
2.4.4	Dissipation and Enstrophy . . . . .	27
2.4.5	Enstrophy Components: Interactions with Strain and Skewness . . . . .	31
2.5	Hysteresis and Skewness: New Insights into Drag Reduction . . . . .	35
2.6	Turbulence Vorticity Fluctuations . . . . .	38
2.6.1	The Shear Stress and Vorticity Transport . . . . .	38
2.6.2	Wall-Normal-Enstrophy Component . . . . .	42
2.6.3	Spanwise-Enstrophy Component . . . . .	44
2.7	Simplified View of Drag Reduction mechanisms . . . . .	46
2.8	Concluding remarks . . . . .	49
2.9	effects of the Reynolds number . . . . .	50
<b>3</b>	<b>Reynolds-Number Impact on Drag Reduction</b>	<b>53</b>
3.1	Streaks-Manipulation Limits for Drag Reduction . . . . .	53
3.2	The database . . . . .	55
3.3	Scale Separation . . . . .	56
3.3.1	Outline of Empirical Mode Decomposition Method . . . . .	57
3.3.2	Channel-Flow Scale Separation via Bi-dimensional Empirical Mode Decomposition . . . . .	59
3.4	Coherent Motion-Skin Friction Interaction . . . . .	65
3.5	Large-Scale Influences on Near-Wall Streaks . . . . .	72
3.5.1	Conditional statistics . . . . .	72
3.5.2	Characterising Skin-Friction Fluctuations in Large-Scale Footprints . . . . .	74
3.6	The Multivariate Joint PDF Analysis . . . . .	77
3.6.1	Leveraging Multivariate Joint PDF for In-depth Statistical and Conditional Analysis . . . . .	77
3.6.2	Relating Large-Scale Wall Events to Local Shear Strain Behaviours . . . . .	79
3.6.3	$C_{fLS}$ -distribution of Stress Components . . . . .	81
3.6.4	$C_{fLS}$ -distribution of Stress production . . . . .	84
3.6.5	Small-scale and Large-scale Properties . . . . .	86
3.6.6	Assessing Direct and Indirect Impact of Outer-Flow Structures on Skin Friction . . . . .	93
3.7	Reynolds-Number Impact on Drag Reduction: Summary . . . . .	95

<b>4 Reynolds Effects on Wall-Bounded Flows</b>	<b>99</b>
4.1 Introduction . . . . .	99
4.2 Processing Methodology – Scale Separation using BEMD . . . . .	100
4.3 Small-Scale Response . . . . .	103
4.3.1 Asymmetry in Large-Scale Positive and Negative Influences: A Detailed Investigation	103
4.3.2 Universal SS motions — the $u^*$ field . . . . .	107
4.3.3 Towards a More Comprehensive Predictive Description of Near-Wall Turbulence Universality . . . . .	107
4.4 Compressible Boundary Layer . . . . .	110
4.5 Scale Modulation: Model Limitations and Alternatives . . . . .	114
4.6 Large-Scale Vortices vs Streak Modulation: Routes to Enhanced Drag . . . . .	115
4.7 Analysing Scale Contributions to Turbulent Stress . . . . .	117
4.8 Characteristics of Large-Scale Motions . . . . .	120
4.9 Impact of Large Scales on Small Scales . . . . .	123
4.10 Scale Contributions to Skin Friction . . . . .	127
4.10.1 Analysis of the FIK Relationship . . . . .	127
4.10.2 Analysis of the RD Relationship . . . . .	129
4.11 Final Thoughts on The Reynolds Number Effects . . . . .	134
<b>5 Quasi-steady hypothesis</b>	<b>137</b>
5.1 How Do They Talk? . . . . .	137
5.2 How Auto-encoders learn large-scale structures . . . . .	140
5.3 Statistical characterisation . . . . .	142
5.3.1 Amplitude modulation . . . . .	142
5.3.2 Length-Scale Modulation . . . . .	142
5.3.3 Quasi-steady hypothesis . . . . .	148
5.4 Amplitude Modulation . . . . .	149
5.5 Length-Scale Modulation . . . . .	153
5.6 The Quasi-Steady Hypothesis: Extent of Applicability in Near-Wall Turbulence . . . . .	157
<b>6 Revised Model of Attached Eddies</b>	<b>159</b>
6.1 Introduction: Attached Eddies' Paradigm . . . . .	159
6.2 Introduction: The Application and Limitations of the Attached Eddy Hypothesis . . . . .	161
6.3 Statistical Properties of Eddy-length-scale Sub-ranges . . . . .	163
6.3.1 Inertial Range - Detached Eddies . . . . .	164
6.3.2 Anisotropic Range – Attached Eddies and Large-Scale Motions . . . . .	165
6.3.3 Anisotropic Range – Small-Scale Motions . . . . .	165
6.3.4 Summary of Sub-Ranges . . . . .	168
6.4 The Attached Eddy Hypothesis . . . . .	168
6.4.1 Structure-Function Analysis . . . . .	168
6.4.2 The Regime of Attached Eddies . . . . .	172
6.5 Attached Eddies Hypothesis revisited . . . . .	178
<b>7 Summary</b>	<b>181</b>
<b>8 Research Horizons</b>	<b>185</b>
8.1 Rationale and Purpose Behind my Research Activities . . . . .	185
8.2 novelty and originality . . . . .	186
8.2.1 Momentum and thermal boundary layers . . . . .	186
8.2.2 An introduction to near-wall turbulence dynamics . . . . .	187
8.2.3 Harnessing the power of machine learning for unravelling the complexities of near-wall turbulence . . . . .	189
8.2.4 Machine learning: switch of paradigm . . . . .	190
8.3 Active research activities . . . . .	194
8.3.1 Project: Influence of Near-Wall Turbulence on Heat Transfer & Modelling the Influence of Reynolds Number . . . . .	195

8.3.2 Project : Enhancing Convective heat Transfer by active control of secondary-flow instabilities . . . . .	202
8.4 The ultimate objective of my research activities . . . . .	206



## Acknowledgements

First and foremost, I would like to express my deepest gratitude to the esteemed members of my jury for graciously accepting the roles. I am truly appreciative of the time and effort you have dedicated to reviewing my manuscript, a task that was undoubtedly challenging yet vital to the completion of this work.

I extend my heartfelt thanks to the exceptional team at the supersonic group, including Lionel Larcheveque, Pierre Dupont, Jean-François Debieve, and Jean-Paul Dussauge. Not only did they provide me with the invaluable opportunity to pursue my PhD, but they also ignited within me a passion for research that has been the guiding light throughout my career. I am equally indebted to my incredible supervisors, Michael Leschziner, Georges Papadakis, Datta Gaitonde, and Peter Vincent, who welcomed me into their teams as a research associate. Their wisdom, guidance, and unwavering support have been instrumental in my growth and development as a researcher.

I would also like to recognize and thank my exceptional colleagues from the various laboratories I had the privilege of working in. A special mention goes to Olivier Blesbois, Arvind Mohan, and Sacha Ghebali for their collaboration, camaraderie, and the unforgettable experiences we shared. I am also grateful to the members of the Curiosity team for their warm welcome, particularly Laurent Cordier, whose steadfast support during the CNRS competition was truly appreciated and will never be forgotten.

In these acknowledgements, I must reserve a special place for Michael Leschziner, to whom I owe an immense debt of gratitude for our fruitful and enriching collaboration over the years. His unwavering passion for research has been a constant source of inspiration, and our work together has been pivotal in my growth and progress along my research path. Michael's guidance, profound insights, and dedication have left an indelible mark on my academic journey, shaping me into the researcher I am today.

Last but certainly not least, I would like to express my heartfelt appreciation to my family, especially my wife, whose endless support, patience, and understanding have been my anchor throughout this challenging yet immensely rewarding journey. Your encouragement has been the driving force behind my perseverance, and I am truly blessed to have you all by my side.



# Chapter 1

## Introduction

Wall-bounded turbulent flows are prevalent in numerous engineering applications and natural phenomena, ranging from flows in pipes to atmospheric boundary layers. A unique privilege of fluid mechanics among scientific disciplines is the possession of the Navier-Stokes equations, which provide a comprehensive mathematical framework for describing these flows. However, the inherent nonlinearity of these equations renders direct numerical simulation of turbulence computationally intractable at high Reynolds numbers. In the vicinity of walls, the velocity decreases to zero, resulting in the formation of a shear layer that generates chaotic structures covering a wide range of scales. Despite the apparent disorder, wall-bounded turbulence features coherent and organised structures. As the intensity of the shear increases, the dynamics between the near-wall and outer regions become increasingly complex and rich. This multi-scale nature of near-wall turbulence poses significant challenges for its study, while simultaneously making it a fascinating area of research. Since the seminal work of Prandtl, advancements in our understanding have been incremental, despite extensive research efforts, particularly at higher Reynolds numbers where outer-flow structures become more prevalent. By leveraging high-fidelity simulations, the present work aims to further our fundamental understanding of the physics governing near-wall turbulence through the investigation of both baseline and actively controlled flows. The objective is to uncover novel insights into the dynamics and underlying mechanisms of these complex systems.

### 1.1 Evolution of the Channel Flow Dynamic as the Reynolds Increases

Figure 1.1 illustrates the evolution of structural topology in wall-bounded flows as the Reynolds number increases. At low Reynolds numbers, viscous stress dominates a substantial portion of the boundary layer, enabling local entrainment as the primary momentum-propagation mode. The first coherent structures to appear as turbulence develops are elongated “streaks” aligned with the flow direction. These streaks occur at the edge of the viscous sublayer and generate adjacent regions of high and low velocity in the spanwise direction. The resulting vortical motions transport particles such that low-speed regions ( $u' < 0$ ) are lifted away from the wall ( $v' > 0$ ), while high-speed regions ( $u' > 0$ ) are pushed towards it ( $v' < 0$ ), enabling more effective momentum mixing. The scale of these structures is dependent on the viscous length scale ( $\delta_\nu$ ).

As the Reynolds number increases, the viscous sublayer ( $\delta_\nu$ ) becomes progressively thinner relative to the boundary layer thickness ( $\delta$ ). As a result, the viscous stress is confined to an increasingly smaller region in the immediate vicinity of the wall, while the Reynolds shear stress ( $\overline{u'v'}$ ) strengthens. The viscous stress is observed to be at its maximum at the wall, whereas the Reynolds shear stress is found to reach its maximum at the edge of the viscous sublayer. As the Reynolds number increases, the near-wall streaks are observed to move closer to the wall and decrease in size. Concurrently, new families of structures emerge in the outer region for  $y^+ = yu_\tau/\nu > 100$ , where  $u_\tau$  represents the friction velocity. These families encompass: (i) large-scale motions, which exhibit a remarkable degree of regularity in the spanwise direction and are depicted by the red ovals in Figure 1.1. These large-scale structures are associated with vortical motions similar to streaks but at significantly larger scales, and are thus frequently termed “super-streaks”; and (ii) wall-attached eddies, symbolised by the green triangles, which are generated within the region delimited by  $\delta_\nu$  and  $\delta$ . The concept of attached eddies was originally postulated by Townsend 1980, but initially

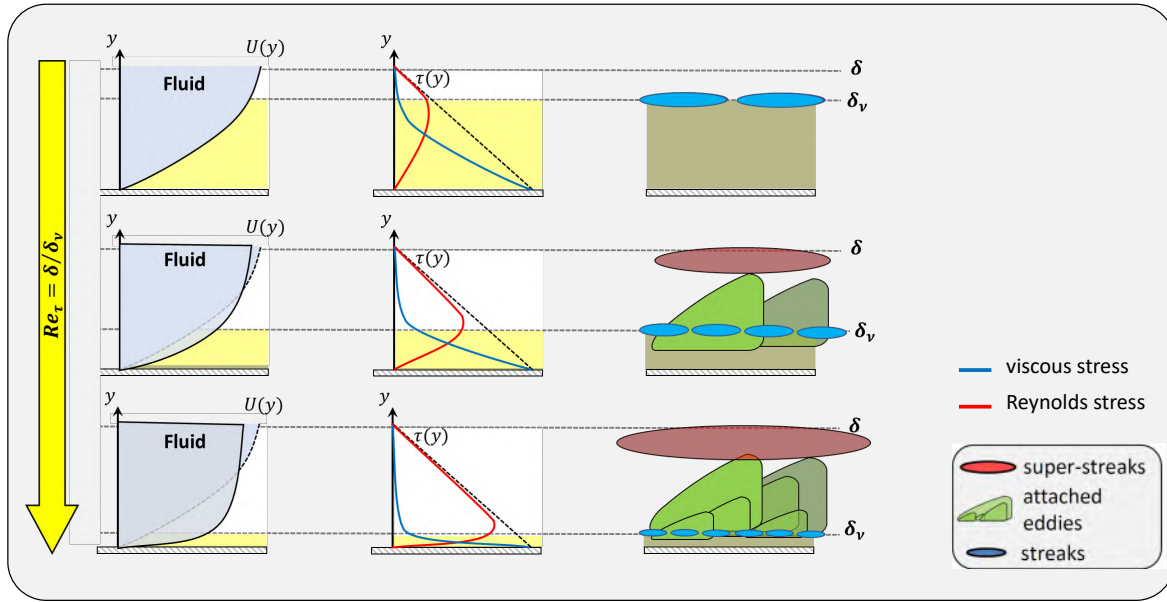


Figure 1.1: Illustration of wall turbulence “zoology” changes as shear layer strengthens.

remained a theoretical construct. However, with the advent of increasingly robust computational techniques and advanced measurement methodologies, which had led to a growing body of evidence now supports their existence.

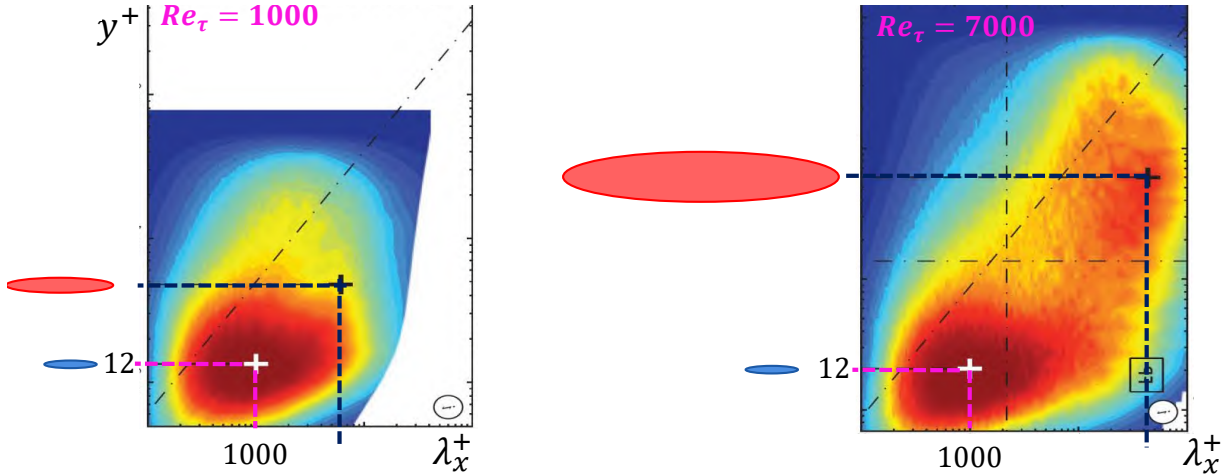


Figure 1.2: Pre-multiplied energy spectra of the streamwise velocity fluctuations ( $k_x \Phi_{uu}$ ) as a function of the streamwise wavelength ( $\lambda_x^+$ ) and the wall-normal distance ( $y^+$ ) for (a)  $Re_\tau = 1000$  and (b)  $Re_\tau = 7000$ . Data extracted from experimental work carried out by Smits, McKeon, and Marusic 2011

The analysis of the energy distribution in wall-bounded turbulent flows, as shown in Figure 1.2, reveals important features of the turbulent structures at two relatively low Reynolds numbers,  $Re_\tau \approx 1000$  and  $Re_\tau \approx 7000$ , compared to flow conditions encountered in practical applications. The spectra were obtained from hot-wire measurements within a turbulent boundary layer (Smits, McKeon, and Marusic 2011). The wall-normal/streamwise wavelength distribution of the streamwise energy, represented by the pre-multiplied power spectrum  $k_x \Phi_{uu}(\lambda_x)$ , provides insights into the scale-dependent energy distribution and the connections between near-wall and outer-flow structures.

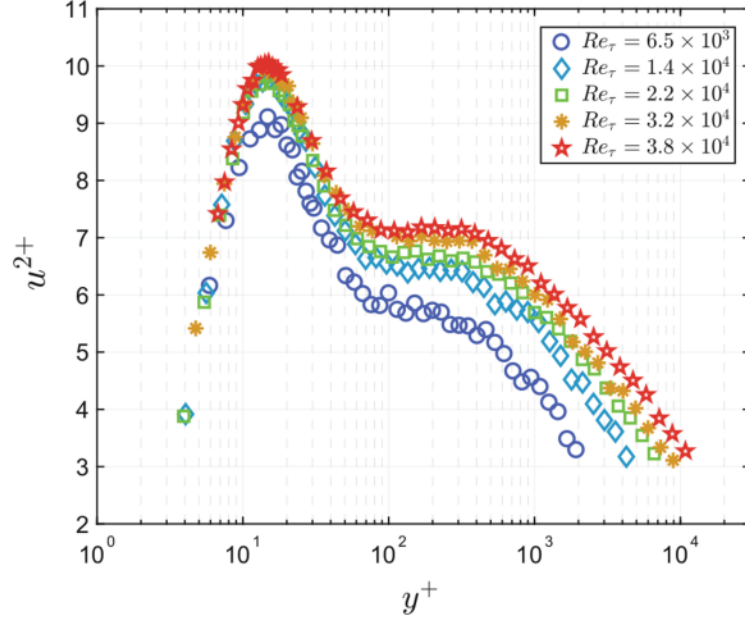


Figure 1.3: Profiles of  $\overline{u'u'}^+$  measured in the installation called CICLoPE (Center for International Cooperation in Long Pipe Experiments) (Fiorini et al. 2017).

At both Reynolds numbers, a distinct peak is observed at  $y^+ \approx 12$  and  $\lambda_x^+ \approx 1000$ , which is associated with the energetic near-wall streaks. The ‘‘collapse’’ of these peaks when quantities are normalised by the friction velocity ( $u_\tau$ ) suggests a degree of universality in the near-wall region, with the streaks’ features being largely independent of the Reynolds number, at least in terms of their streamwise wavelength and wall-normal location. However, the most striking difference between the two Reynolds numbers lies in the outer region of the boundary layer. At  $Re_\tau \approx 1000$ , there is a hint of a second peak emerging at larger wall-normal distances and longer wavelengths, which becomes much more pronounced at  $Re_\tau \approx 7000$ , confirming the strengthening and growth of outer-flow structures as the Reynolds number increases, as evident from Figure 1.2. Interestingly, the influence of the outer-flow structures is not confined to the outer region of the boundary layer. Indeed, the energy spectra reveal that these structures have a footprint that extends down to the wall, as indicated by the appreciable energy levels at large wavelengths across the entire wall-normal range. Furthermore, the energy distribution between the inner and outer peaks suggests that additional energy production occurs in this intermediate region, and this is likely attributed to the presence of attached eddies. The analysis of the pre-multiplied energy spectra provides valuable insights into the scale-dependent energy distribution and the connection between near-wall and outer-flow structures in wall-bounded turbulent flows. The results highlight the universality of near-wall streaks, the strengthening and growth of outer-flow structures with increasing Reynolds number, and the potential role in energy production, and provide an overview of the complex multi-scale dynamics in turbulent boundary layers.

The wall-normal distributions of the streamwise velocity variance,  $\overline{u'u'}(y)$ , for different Reynolds numbers are conveyed by Figure 1.3, which can be obtained by integrating the power spectrum,  $\Phi_{uu}(\lambda_x)$ , along the streamwise wavelength  $\lambda_x$  at each wall-normal location  $y$ . These distributions were obtained from measurements acquired within the CICLoPE facility for Reynolds numbers ranging from  $Re_\tau = U_\infty u_\tau / \nu = 6.5 \times 10^3$  to  $3.8 \times 10^4$ , they reveal three distinct regions in the  $\overline{u'u'}(y)$  profile.

The first region is characterised by a prominent peak located around  $y^+ \approx 12$ , which is attributed to the energy production associated with near-wall streaks. As the Reynolds number increases, the magnitude of this inner peak also grows, suggesting that the outer-flow structures have a significant impact on the near-wall region. This observation underscores the importance of the interaction between outer-flow structures and near-wall dynamics in the overall turbulence production mechanism. The second region in the  $\overline{u'u'}(y)$  profile is a plateau, followed by a third region : the logarithmic decrease. These wall-normal distribution

can be understood by considering the connection between the Reynolds number and the scale separation in wall-bounded turbulence. The Reynolds number,  $Re_\tau$ , can be defined as the ratio between the outer length scale  $\delta$  and the viscous lengthscale  $\delta_\nu$  ( $Re_\tau = \delta/\delta_\nu$ ). As  $Re_\tau$  increases, the spectral space between these two scales expands, allowing for the emergence of new hierarchies of attached eddies, as conceptually represented in Figure 1.1. The growth of the spectral space with increasing Reynolds number leads to a thicker logarithmic region in the mean-velocity profile, which corresponds to the plateau and logarithmic decay observed in the  $\overline{u'u}(y)$  profiles. Moreover, the amplitude of the plateau grows with Reynolds number, indicating an intensification of the outer-layer structures. This behaviour is consistent with the identification of a diagonally stretched region of elevated energy density in the outer layer, extending to  $y^+ \approx 300 - 500$  and over a significant range of wavelengths. The examination of the wall-normal distribution of the streamwise velocity variance offers a deeper understanding of the interactions between scales and the energy distribution in wall-bounded turbulent flows. The amplification of the inner peak as the Reynolds number increases demonstrates the increasing influence of outer-flow structures on the near-wall region. The emergence of the plateau and the logarithmic decay in the  $\overline{u'u}(y)$  profile is a direct consequence of the increasing spectral gap between the outer and viscous length scales. This gap facilitates the formation of new hierarchies of attached eddies. These observations emphasise the inherently multi-scale nature of wall-bounded turbulence and the importance of the role played by the connection between near-wall and outer-flow dynamics in shaping the flow behaviour.

The evolution of the boundary layer structural topology as shear stress intensifies is summarised by the conceptual illustration conveyed in Figure 1.4. With increasing Reynolds number, measuring or simulating the full spectrum of structures populating the flow becomes increasingly challenging, as the smallest eddies diminish in scale while the largest coherent structures—the super streaks—expand in magnitude. When direct numerical simulation (DNS) is applied under such conditions, it is straightforward to demonstrate that the resulting disparity in scales necessitates numerical grids growing in proportion to  $Re_\tau^3$  to capture all motions. Hence, simulations at high Reynolds numbers incur extremely high costs. The maximum  $Re_\tau$  simulated by DNS for channel flow is around 5200, which is relatively low compared to industrial and atmospheric boundary layer applications where  $Re_\tau$  magnitudes approach 100000. While specialised experimental facilities exist to probe high Reynolds number boundary layer flows, escalating Reynolds numbers impose challenges in resolving small-scale flow structures. Specifically, the decreasing scale and wall-proximity of these eddies, paired with their intensifying frequencies, progressively obstruct detection and quantification. Even cutting-edge metrological techniques falter in capturing diminutive scales, with motions falling below requisite measurement resolutions. Although tremendous progress has been made in metrological techniques, limitations persist in experimentally resolving the complete spectrum of turbulent motions, particularly near-wall structures. Accessing the full range of scales, from large coherent motions to Kolmogorov scales, remains an outstanding challenge for enabling comprehensive characterisation of high Reynolds number wall-bounded turbulence across all relevant length scales. Advanced numerical simulations can provide insights, but surrogate models are essential to reduce problem complexity and enable lower-cost solutions. These models offer conceptual frameworks to deepen our physical understanding and predict flow dynamics. Figure 1.4 summarises the previous observations by providing a conceptual representation of the structural topology evolution as shear stress intensifies.

## 1.2 Scales' interconnections

The evolution of large-scale motions with increasing Reynolds number and their influence on near-wall structures is a crucial aspect of turbulent boundary layer dynamics. Figure 1.5(a) presents the wall-normal distribution of streamwise velocity variance for a channel flow at  $Re_\tau \approx 4200$ , decomposed into contributions from large scales (LS) and small scales (SS) (database from Lozano-Durán and Jiménez 2014b). The SS exhibit a distinct energy peak near  $y^+ \approx 12$ , associated with near-wall streaks, while the LS energy reaches a maximum around  $y^+ \approx 280$  for this Reynolds number. This outer peak is a manifestation of the intensification of large-scale structures in the outer region as the Reynolds number increases. Mathis, Hutchins, and Marusic (2009) proposed that these energetic structures move away from the wall as Reynolds number increases, following the relation  $y^+ \approx 3.9\sqrt{Re_\tau}$ , typically at  $y \approx 0.1 - 0.2h$ , which agrees with the value  $y^+ \approx 280$  determined from Figure 1.5(a).

Streamwise velocity fields parallel to the wall at  $y^+ \approx 280$  and  $y^+ \approx 12$  are shown in Figures 1.5(b) and 1.5(c), respectively. The outer-flow velocity field reveals the presence of approximately three large-scale structures in the spanwise direction, corresponding to a separation of order  $1h$ , consistent with previous find-

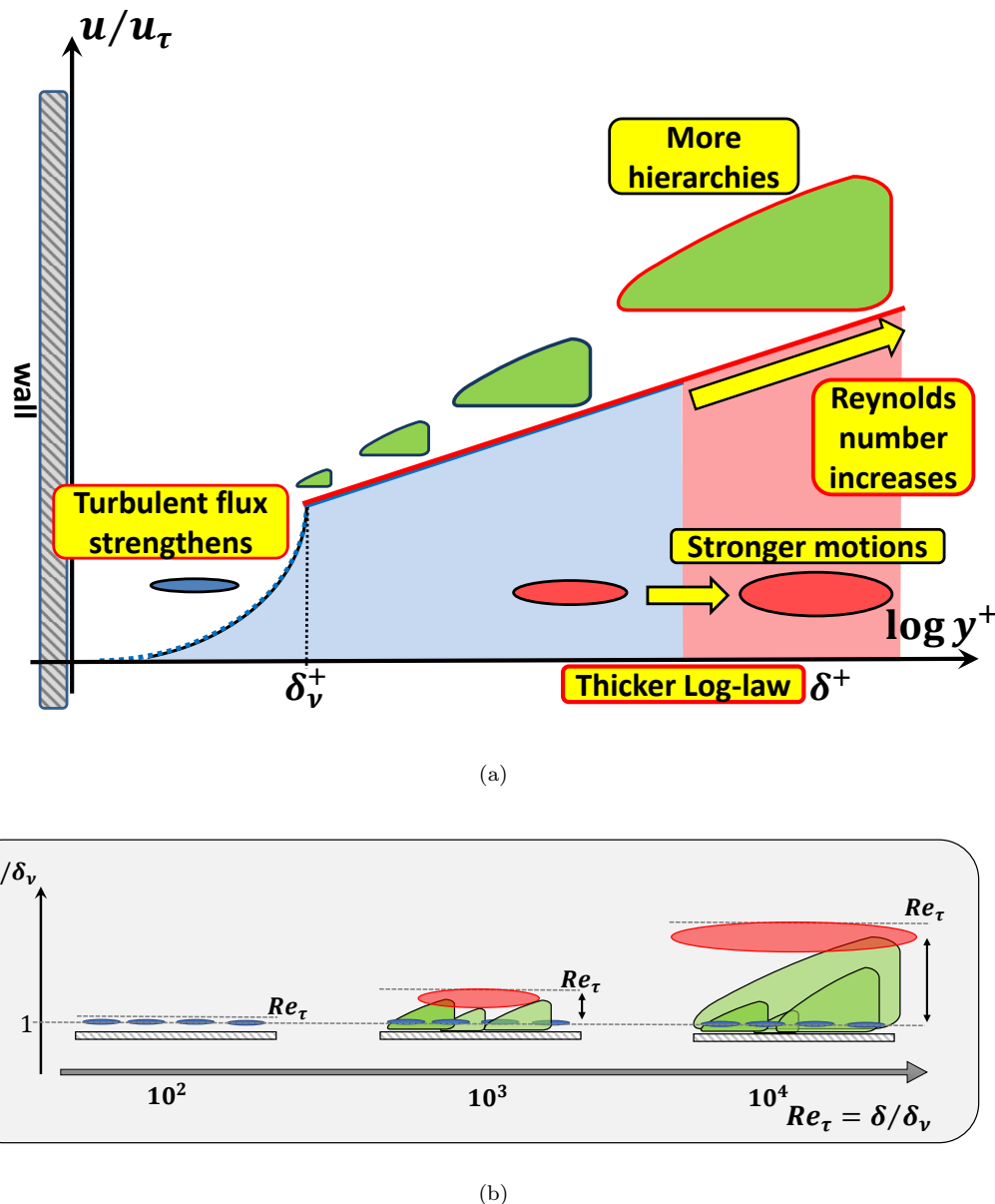


Figure 1.4: Conceptual representation of structures populating wall-bounded flow

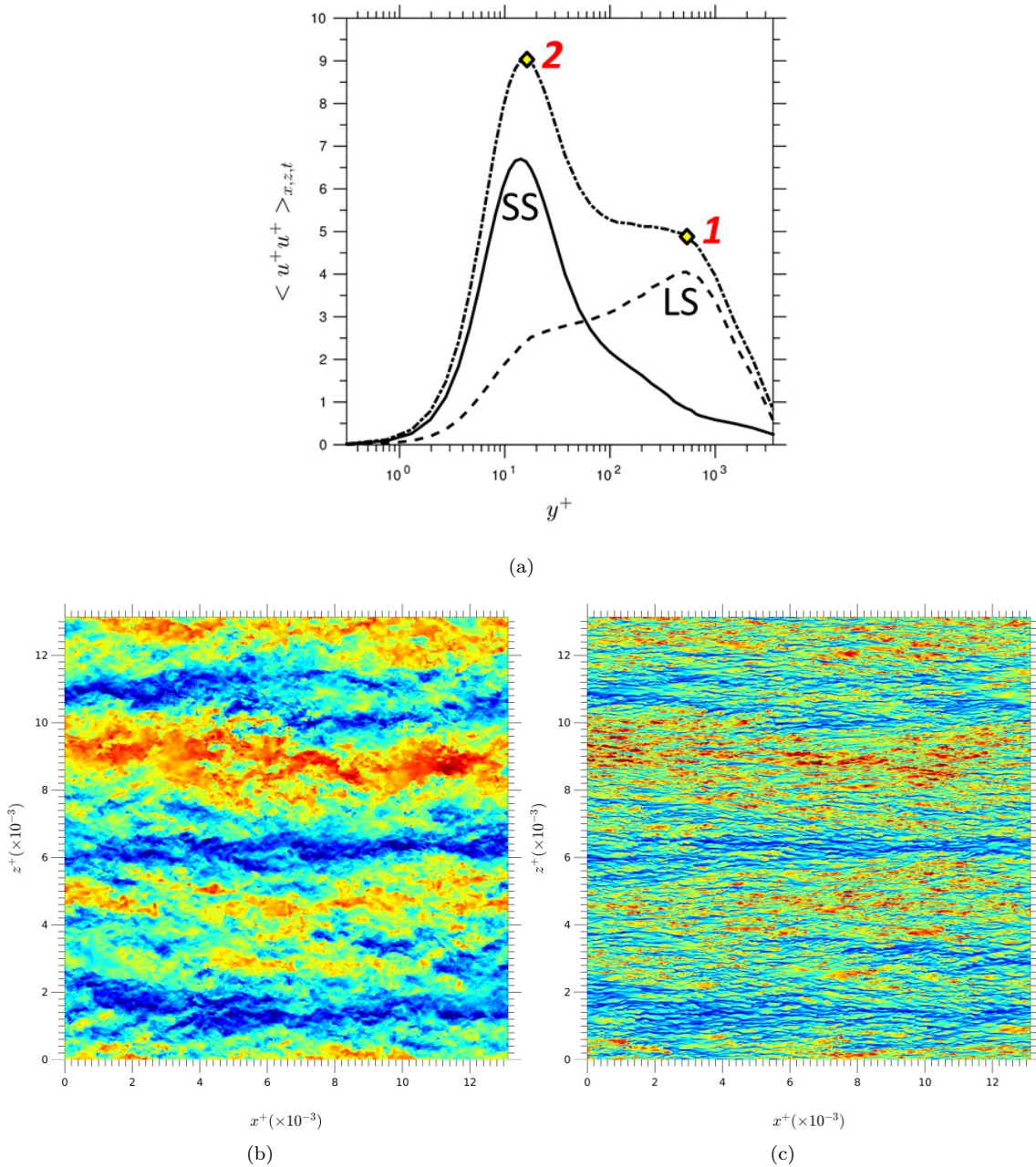


Figure 1.5: (a) Profiles of  $\overline{u'' u''}^+$  produced by the small scales (SS) and the large scales (LS). Longitudinal velocity fields at: (b)  $y^+ \approx 280$  - 1, (c)  $y^+ \approx 12.5$  - 2. Data extracted from a channel flow at a  $Re_\tau \approx 4200$  Lozano-Durán and Jiménez 2014a.

ings (Mathis, Hutchins, and Marusic 2009). Closer to the wall, at  $y^+ \approx 12$ , the velocity fluctuations highlight the coexistence of small-scale motions ( $\lambda_z^+ \approx 100$  and  $\lambda_x^+ \approx 1000$ ) alongside the footprints of the large-scale structures ( $\lambda_z^+ \approx 1000$  and  $\lambda_x^+ \approx 12000$ ). These footprints originate from coherent outer flow structures extending across the entire boundary layer, leaving their signature on the near-wall region through positive and negative large-scale fluctuations corresponding to sweep and ejection motions, respectively. While a strict interpretation of footprinting associates this process only with positive large-scale near-wall fluctuations induced by sweeping motions, positive and negative large-scale events are intimately connected via the association of sweeps to ejections (Lozano-Durán, Bae, and Encinar 2020). Thus, footprints arguably encompass both positive and negative large-scale fluctuations induced by the outer-flow motions. The co-existence between small and large scales is not independent, as evident from Figure 1.5(c). In areas where the footprint is negative, the streaks appear more elongated and of weaker amplitudes compared to those in areas of positive footprints. As the Reynolds number increases, the outer motions become progressively stronger, along with their influence on the near-wall structures. This influence is characterized by the direct alteration of near-wall turbulence through the "footprint" effect and the indirect strengthening of streaks, known as "modulation". The observation of large-scale motions modulating near-wall turbulence has been the focus of several studies by Marusic and collaborators (Mathis, Hutchins, and Marusic 2009; Marusic, Mathis, and Hutchins 2010b; Talluru et al. 2014), aiming to predict near-wall turbulence. These studies have led to the development of an empirical relationship that allows the prediction of near-wall turbulence statistics at any Reynolds number from a "universal" small-scale signal unaffected by large-scale motions. However, this empirical relationship has limitations, and understanding the evolution of large structure characteristics and their interaction with small scales is crucial for accurately predicting near-wall turbulence properties across Reynolds numbers. Moreover, the increasing contribution of outer structures with Reynolds number highlights the reduced effectiveness of low Reynolds number control strategies at higher Reynolds numbers.

The growing influence of large-scale structures on near-wall turbulence at higher Reynolds numbers has significant implications for turbulence modelling and flow control. Many turbulence models rely on near-wall scaling assumptions, which may become less accurate as the large-scale motions increasingly dominate the near-wall dynamics. This calls for the development of advanced turbulence models that can capture the multi-scale interactions and the evolving structural topology of high Reynolds number turbulent boundary layers.

Furthermore, the design of effective flow control strategies at high Reynolds numbers must consider the dominant role of large-scale structures. Control methods that are successful at low Reynolds numbers, such as those targeting near-wall structures, may become less effective as the outer structures increasingly dictate the near-wall turbulence features. Novel control strategies should aim to manipulate or disrupt the large-scale structures in the outer region, thereby indirectly influencing the near-wall turbulence.

To gain a deeper understanding of the scale interactions and their Reynolds number dependence, further research could focus on the quantitative analysis of the modulation effect, the spectral energy distribution across scales, and the comparison of these phenomena in various canonical wall-bounded turbulent flows. Such investigations will provide valuable insights into the fundamental mechanisms governing the complex dynamics of high Reynolds number turbulent boundary layers, ultimately facilitating the development of more accurate predictive models and effective flow control strategies.

### 1.3 Simplified Representation of Near-Wall Turbulence Dynamic as an Incomplete Puzzle

Figure 1.6 presents a simplified conceptual representation of wall-bounded turbulence, illustrating three distinct families of structures and their potential interactions. This schematic provides a framework to guide focused research efforts in investigating the complexities of near-wall turbulence. The primary objective is to elucidate the features of each structural component and the nature of their interactions, both of which are crucial to constructing a comprehensive wall-bounded turbulence paradigm. Unraveling wall turbulence can be likened to solving a puzzle, with each family of structures representing a piece with unique features and dynamics that require detailed examination. Large-scale motions, near-wall streaks, and attached eddies are the main pieces demanding dedicated research efforts. However, understanding the individual components alone is insufficient; it is equally essential to study how these structures interact and influence each other, as depicted by the arrows in Figure 1.6. To complete the puzzle and develop a unified understanding of wall-bounded turbulence, a comprehensive approach is necessary, involving targeted studies of individual

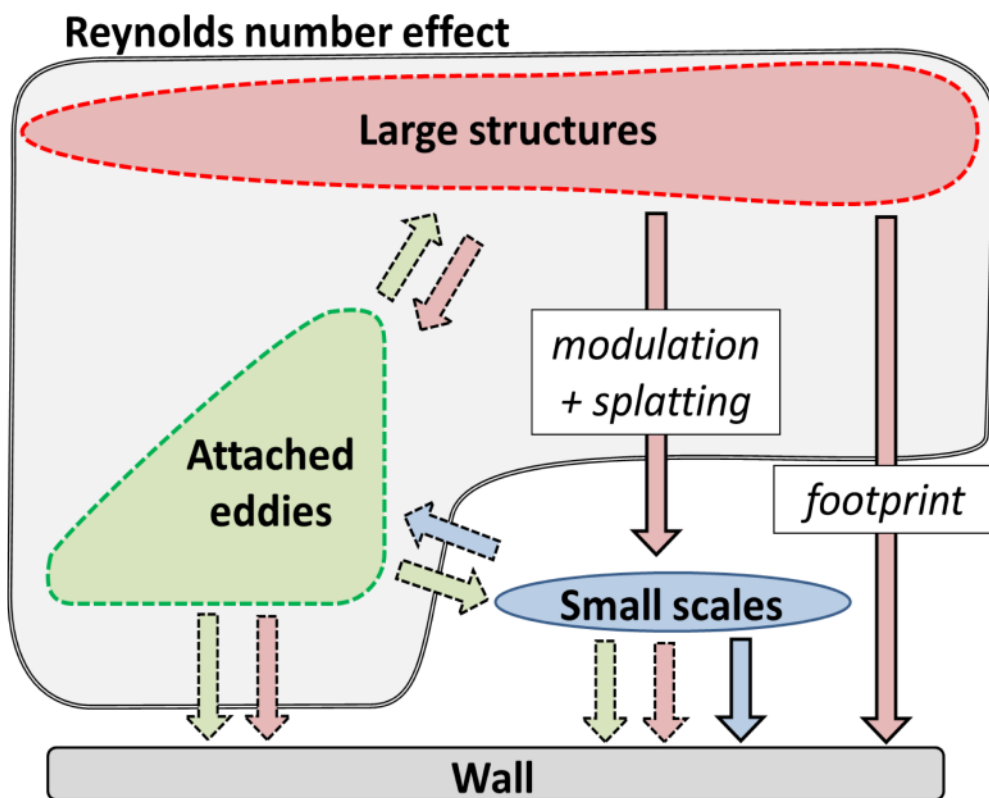


Figure 1.6: Simplified conceptual representation of the eddies families populating wall-bounded flow and their potential interactions. Elucidating the characteristics of each family and the nature of their interconnections is necessary for constructing an integrated theory of wall turbulence.

components and their interactions. By identifying the nature of these interactions, one can ascertain how the elements relate to each other and contribute to the dynamics of wall-bounded turbulence. The ultimate goal is to formulate an integrated theory, a comprehensive conceptual framework that synthesizes the understanding of individual structural components and their interactions to provide a holistic representation of wall turbulence.

Despite extensive prior research, comprehension of these structures, their interactions, and their momentum-mixing impacts at the wall remains incomplete. This manuscript presents research seeking to advance understanding of the features and physics of structures governing wall-turbulence dynamics and their interactions. Employing high-fidelity simulations, the current work scrutinizes large-scale motions, near-wall streaks, and attached eddies, with particular emphasis on elucidating the interactions between eddies and their impacts on near-wall activity. This effort is motivated by the need to piece together how wall turbulence maintains itself through the couplings of its fundamental components. Elucidating eddy features, dynamics, and connections remains critical for constructing predictive models across varying conditions and designing efficient control strategies.

By adopting a puzzle-solving approach and conducting targeted research, this manuscript presents a comprehensive investigation into the complex dynamics of wall-bounded flow. The research is meticulously structured into individual chapters, each focusing on a specific aspect of wall-bounded turbulence:

- Chapter 2 The second chapter focuses on the influence of actuated flow generated by oscillating spanwise wall motion on the formation of streaks and its subsequent impact on drag reduction. This study sheds light on the intricate relationship between the Stokes layer and streak formation, contributing to the development of effective drag reduction strategies.
- Chapter 3 The third chapter investigates the reasons behind the diminishing efficiency of drag reduction strategies designed for lower Reynolds numbers as the Reynolds number increases. Understanding this phenomenon is crucial for developing robust and scalable drag reduction techniques that can be applied across a wide range of flow conditions.
- Chapter 4 The fourth chapter explores the effects of the Reynolds number on wall-bounded flow, particularly the interaction between outer structures and near-wall structures and their impact on momentum mixing. By refining existing predictive models, this study aims to enhance the accuracy of flow predictions and further our understanding of the complex interactions within wall-bounded turbulence.
- Chapter 5 The fifth chapter examines the adaptability of small-scale structures in the near-wall region to the shear-stress fluctuations imposed by large-scale outer-flow structures within a canonical boundary layer flow. This study reveals the quasi-steady nature of the flow dynamics resulting from this adaptation, providing valuable insights into the interplay between different scales of turbulent structures.
- Chapter 6 The sixth chapter examines the phenomenon of attached eddies and proposes modifications to existing theory to improve the accuracy of flow statistics predictions. By refining these models, the study aims to enhance our predictive capabilities and deepen our understanding of the role of attached eddies in wall-bounded turbulence.

Through these focused studies, the manuscript offers a comprehensive exploration of the complexities of flow dynamics, significantly advancing our understanding and predictive capabilities in the field of wall-bounded turbulence. By adopting a puzzle-solving approach and conducting targeted research, this work lays the foundation for the development of a comprehensive theory of wall-bounded turbulence, which will have far-reaching implications for various applications, such as drag reduction, flow control, and the design of more efficient fluid systems.



## Chapter 2

# Reducing Drag by Manipulating Near-Wall Turbulence

### 2.1 Introduction : Active flow control by wall oscillations

#### 2.1.1 Motivation

Turbulent flows dictate the performance characteristics of numerous industrial equipment and environmental applications. One important consequence of Turbulence is high friction drag on surfaces, the increase relative to laminar conditions easily reaching factors of 10-100, depending on the Reynolds number of the flow. In many applications, the friction drag is extremely influential to the operational effectiveness of the device or process. This applies especially to transport, involving either self-propelling bodies moving in a fluid or fluids being transported in ducts and pipes. Considering only the civil aviation, the United Nations' International Civil Aviation Organization (ICAO) expects its emissions to roughly triple by 2050, at which time aircraft might account for 25% of the global carbon budget ([ICCT](#)). There is, therefore, significant pressure to reduce transport-related emissions, of which friction drag is a major constituent. Therefor there is considerable interest, both from fundamental and long-term practical perspectives, in active-control methods that aim to reduce the friction drag of turbulent boundary layers on walls.

#### 2.1.2 Scientific context

##### Why spanwise wall oscillation?

For flow at relatively low Reynolds number, it is generally accepted that the effectiveness of any control method targeting turbulent skin friction must be rooted in its ability to disrupt and suppress the mechanisms responsible for sustaining the transport of momentum across the viscosity-affected near-wall layer – a process that is associated with quasi-organised streamwise vortices. There are very few control options that are demonstrably effective at reducing friction drag over large surfaces, and it must be acknowledged that all involve formidable engineering challenges. Passive devices, such as riblets and super-hydrophobic surfaces, either offer modest drag-reduction margins and degrade rapidly, or are only realisable in very special circumstances - e.g. in liquids. Active methods, most of the time involve wall-based actuation. At low Reynolds number, all target the processes in the viscosity-affected near-wall layer, and all are designed to disrupt the near-wall streaky structure and associated regeneration mechanism that sustains the streaks and vortical motions. Leaving aside rather tentative attempts to use synthetic jets, active dimples/pimples and plasma actuators, mostly applied locally and at very low Reynolds number, one of tenable approach – at least in a laboratory setting ([Auteri et al. 2010](#); [Marusic et al. 2021](#)) – is to impose unsteady transverse shear onto the thin viscous sublayer by oscillatory wall motion. The oscillatory flow patterns that are most effective involve streamwise waves of spanwise motion, where the spanwise velocity of the wall is given by :

$$W = W_m \sin(2\pi x/\lambda_x - 2\pi t/T) \quad (2.1)$$

Here,  $W_m$  is the maximum spanwise velocity,  $\lambda_x$  is the wavelength of the streamwise waves, and  $T$  is the period of the oscillation, and are the control parameters. With a careful choice of actuation parameters, gross

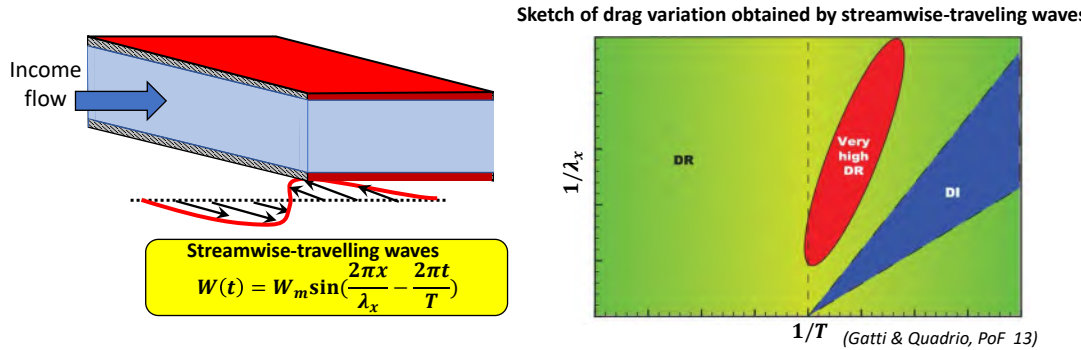


Figure 2.1: Left-hand side plot: schematic of the system for turbulent channel flow with travelling-wave actuation. Right-hand side plot: map of the drag variation in the plane spanned by  $\lambda_x-T$ , DR: Drag reduction and DI: Drag increase. (Gatti and Quadrio 2013)

drag-reduction level in excess of 45% has been demonstrated in direct numerical simulations of low Reynolds number channel flows, the drag can be also substantially enhanced, depending on the choice of actuation parameters (see Figure 2.1) (Quadrio and Ricco 2004; Quadrio, Ricco, and Viotti 2009).

The study of the effects of spanwise wall motion on streamwise wall-bounded turbulent flows can be traced back to the pioneering work of Furuya, Nakamura, and Kawachi 1966. In this study, a turbulent flow was observed moving along the axial direction of a cylinder while the cylinder simultaneously rotated. Later studies by Bissonnette and Mellor 1974 and Lohmann 1976 investigated the effect of transverse wall motion on a boundary layer undergoing transition. These studies revealed a strong correlation between the axial and transverse components of the mean velocity.

When a transverse strain rate was applied to an initially axial boundary layer, the intensity of all components of the Reynolds stress tensor increased substantially. Initially, these increases were confined to regions near the wall, but over time, they became more uniformly distributed. During the early stages of the adjustment process, which occurs over approximately ten initial boundary layer thicknesses, the amplified Reynolds stress led to a decrease in the velocity of the inner part of the boundary layer, resulting in drag reduction.

As the flow moves downstream, the spanwise strain gradually penetrates the buffer and log-layer, and its streamwise variation diminishes. This leads to an enhancement of the shear strain, which in turn strengthens the small-scale structures and consequently increases the drag. Thus, to attain substantial and consistent reductions in drag, a spanwise wall motion that varies periodically and/or exhibits a streamwise wave-like pattern has to be implemented. Later Bradshaw and Pontikos 1985 by investigating turbulent boundary layer on an ‘infinite’ swept wing found that spatial variation in spanwise shear played an important role for sustaining drag reduction. This was the first confirmation of the importance of the rate of change of spanwise strain and their insights greatly influenced later work on spanwise-wall motion forcing.

### Is wall oscillation effective?

Several recent computational and experimental studies, both for channel flow (e.g. Quadrio and Ricco 2004, Ricco and Quadrio 2008, Quadrio, Ricco, and Viotti 2009, Touber and Leschziner 2012, Agostini, Touber, and Leschziner 2014) and for spatially evolving boundary layers (e.g. Choi 2002, Di Cicca et al. 2002, Ricco 2004, Skote 2011, Skote 2013, Lardeau and Leschziner 2013) demonstrate that oscillatory spanwise wall motion, either spatially homogeneous or in the form of in-plane waves, results in a substantial decline in skin friction, if the actuation period and wave length are chosen judiciously. One particularly important constraint to respect is that the unsteady layer generated by the wall motion remains confined to the viscous sublayer – that is, the actuation has to result in an unsteady *Stokes* layer. In the case of streamwise-homogeneous wall motion, the skin friction is observed to drop by a maximum of around 35% at the friction Reynolds number  $Re_\tau \approx \mathcal{O}(200)$ , a wall-velocity amplitude  $W_m^+ = W_m/u_\tau = 12$  and oscillation period  $T^+ = Tu_\tau^2/\nu \approx 100$ , although this maximum margin appears to decrease roughly in proportion to  $Re_\tau^{-0.2}$ , a rate based on simulations in the range  $Re_\tau \approx 200-1500$  (Quadrio and Ricco 2004; Ricco and Quadrio 2008; Touber and Leschziner 2012; Chung and Hurst 2014). Quadrio, Ricco, and Viotti 2009 show that even higher gross margins – around 45% at  $Re_\tau \approx \mathcal{O}(200)$  – can be achieved if the wall motion is imposed in the form of streamwise stationary or

travelling waves.

### What is the optimal oscillation and why?

One broadly consistent observation that emerges from most channel-flow studies is that the optimum oscillation period is  $T^+ \approx 100$  – although in the case of spatially-evolving boundary layers, there is some evidence that the optimum value is somewhat lower, closer to 70 (Ricco 2004; Skote 2011; Skote 2012; Lardeau and Leschziner 2013). At the optimum period, the drag reduces, following a transient phase observed to be around three oscillation periods, to a low-drag state (in a time-averaged sense), which is characterised by insignificant periodic fluctuations associated with the actuation time scale. At this condition, the Stokes layer – the unsteady transverse shear layer generated by the wall motion – is confined to the viscous sublayer ( $y^+ \lesssim 15$ ), and the quasi-organised near-wall streaks, primarily associated with the turbulent skin friction, are observed to be especially weak and to be almost oblivious to the unsteady motion. Linear analysis by Blesbois et al. 2013, based on the General Optimum Perturbation (GOP) theory, suggests that this insensitivity is associated with the fact that streak amplification, following their destruction through effects of the unsteady Stokes strain (the wall-normal gradient of the spanwise velocity) at  $T^+ = 100 - 200$ , is subject to a time scale  $t^+ = \mathcal{O}(80)$ . Hence, it may be inferred that if the proportion of the actuation period during which the strain field allows the streaks to re-establish is too short, the streaks never fully recover and the drag remains low. As the oscillation period increases, the Stokes layer penetrates into the turbulent buffer layer, and the Stokes strain in the viscous sublayer declines. This, in combination with the increased actuation time scale, relative to the streak-generation time scale, degrades the drag-reduction effectiveness, and one feature accompanying this degradation is the appearance of distinct oscillatory variations of the skin friction and turbulence properties around the low-drag state. Studying drag-reduction mechanisms from the perspective of non-optimal actuation provides a unique lens to examine the fundamental interactions at play. This is achieved by scrutinizing phase-averaged turbulence properties during periods of both drag increase and decrease within an actuation period. Touber and Leschziner 2012 were first in showing that at a Reynolds number of  $Re_\tau \approx 500$  and a non-dimensional time of  $T^+ = 200$ , there are distinctive oscillations in the structure of the streaks near the wall. These streaks undergo a cycle of attenuation and intensification twice during each actuation period. The attenuation phase correlates with low and rapidly fluctuating Stokes strain and its direction, while the intensification phase is associated with high Stokes strain values and a slow, phase-wise change in the strain. The orientation of the streaks is almost bimodal, influenced by the direction of the shear-strain vector in the viscous sublayer when the Stokes strain is high and remains consistent in both strength and direction. However, when the strain vector undergoes rapid changes, the streaks are neither pronounced nor have a clear direction. These observations, coupled with the analysis of data averaged based on streak conditions by Touber and Leschziner 2012, and the linear analysis by Blesbois et al. 2013, provide some understanding of the physical mechanisms that underpin the drag reduction phenomenon. Despite these insights, the fundamental nature of the interactions by which unsteady Stokes motion decreases turbulence and drag is not fully explained, and the exact mechanisms involved is a topic of active debate in the scientific community.

In the quest to understand the mechanisms that guide drag towards a low time-averaged level, researchers have examined the transient behaviour of flow properties when spanwise oscillations are applied to the baseline flow. Channel-flow investigations by Quadrio and Ricco 2003 and Xu and Huang 2005 have unveiled a non-monotonic reduction in drag and turbulence intensity. Interestingly, turbulence production experiences surges, predominantly during the initial part of the transient journey towards the low-drag state, which is generally achieved within approximately three oscillation periods. Later, the relationship between enstrophy and dissipation during this transient phase was specifically investigated by Ricco and colleagues (Ricco et al. 2012). The authors of the DNS studies of the transient drag response at a Reynolds number of approximately 200 suggest that the primary mechanism is an upsurge in enstrophy, instigated by the Stokes strain. This subsequently results in a related increase in turbulence dissipation, which ultimately leads to a reduction in both turbulence and drag.

### How can drag-reduction mechanisms be revealed?

The starting point of the work presented in this manuscript is to scrutinise whether the paradigm proposed by Ricco et al. 2012 is validated by a comprehensive analysis of the phase variation of turbulent quantities. This is achieved through an examination of data derived from direct numerical simulations at a Reynolds number of  $Re_\tau \approx 1000$  (for the baseline flow) and in contrast to earlier studies, the emphasis here is on the

phase-averaged fields of stochastic properties, which exhibit periodic time variations as a result of actuation at the non-optimal period  $T^+ = 200$ . This methodology is preferred over the analysis of the transient phase for several reasons: (i) it enables a distinct separation of stochastic turbulence from transient motions, (ii) it mitigates uncertainties that arise from the incomplete penetration of the Stokes motion through the viscous sublayer during the transient period, and (iii) it allows the findings and conclusions to be based on a substantially larger statistical sample. The results also presents a parallel comparison of analogous variations for the streamwise Reynolds stress, dissipation, and enstrophy. These comparisons provide strong evidence that the processes linking the phase-averaged drag decline to the stochastic turbulence fields during the periodic drag oscillations around the low-drag state are identical to those operating during the transient phase.

## 2.2 Computational conditions

All simulations reported herein have been performed with a variant of the general non-orthogonal-grid, block-structured, finite-volume method based on a fully co-located storage and realised in the in-house code STREAM-LES, initially developed by Temmerman et al. 2003 for incompressible flows. The algorithm advances the velocity field in time by means of a fractional-step method incorporating fourth-order approximations for the convective and diffusive fluxes and a third-order Gear-like scheme documented in Fishpool and Leschziner 2009, shown to possess advantageous stability and accuracy properties, relative to a corresponding second-order time-advancement scheme. Zero divergence is secured by solving the pressure-Poisson equation with second-order accuracy, combining the application of an implicit successive over-relaxation (SOR) method with a multigrid scheme. Pressure-velocity decoupling, arising from the fully-collocated storage of velocity and pressure, is counteracted by employing the so-called Rhee & Chow interpolation scheme (Rhee and Chow 1983). Fishpool and Leschziner 2009 demonstrate that the loss of energy due to artificial dissipation arising from the Rhee & Chow interpolation is low. The code is fully parallelised using MPI, with pre-determined grid blocks or sub-domains assigned to individual processors.

The actuation under consideration is restricted to a purely sinusoidal spanwise oscillation of the wall, namely  $W(t) = W_m \sin(2\pi t/T)$  and in the present study,  $W_m^+ = 12$  and  $T^+ = 100$  or  $200$ . These values are the same as those used by Touber and Leschziner 2012 at  $Re_\tau \approx 500$  as well as others reporting DNS studies investigating drag-reduction phenomena in channel flow at lower  $Re_\tau$  values. As previously indicated,  $T^+ = 100$  is close to the optimum actuation period in channel flow within the range of Reynolds number investigated so far. However, given this  $T^+$  value, the maximum drag-reduction margin is materially sensitive to  $W_m^+$ , varying between 22% and 39% within the range  $W_m^+ = 6 - 18$  at  $Re_\tau \approx 200$  (Quadrio and Ricco 2004). This dependence is of sub-ordinate importance, however, in the context of the present primary objective of studying the periodic fluctuations of drag and turbulence properties in non-optimal conditions.

All simulations were performed over the same box of length, height and depth  $4\pi h \times 2h \times 2\pi h$ , respectively, corresponding to approximately  $12 \times 2 \times 6 \cdot 10^3$  wall units. The box was covered by  $1056 \times 528 \times 1056$  ( $= 589 \cdot 10^6$ ) nodes. The corresponding cell dimensions were  $\Delta x^+, \Delta y^+_{min}, \Delta y^+_{max}, \Delta z^+ = 12.2, 0.4, 7.2, 6.1$ . These normalised values arise upon the use of the actual (rather than the nominal) friction Reynolds number for the unactuated flow, namely  $Re_\tau \approx 1025$ . All simulations are performed at a constant time-marching step  $\Delta t^+ = 0.125$ , chosen such that the CFL number, based on the maximum streamwise velocity, did not exceed 0.25. In the actuated flows, data were collected over a period  $t^+ = 4600$  (about 7 flow-through times), corresponding to 46 and 23 actuation periods  $T^+ = 100$  and  $200$ , respectively. The statistical averaging exploited both spanwise and streamwise homogeneity, as well as the symmetry about the channel centre-plane. Given the relatively low number of actuation cycles covered at  $T^+ = 200$ , the statistical convergence of phase-averaged quantities requires clarification. This will be done ahead of the presentation of phase-averaged results in Section 2.4.4.

The adequacy of the resolution was investigated in various ways, including a simulation of the unactuated flow over a grid of 1.2bn cells, an examination of the resolved dissipation, relative to the imbalance of other terms in the turbulence-energy budget, and an evaluation of the ratio of cell distances to the Kolmogorov length scale. Figure 2.2 compares the present turbulence-energy budget for the baseline flow with two published sets of DNS data: one by Moser, Kim, and Mansour 1999 at  $Re_\tau \approx 590$  and the other by Hoyas and Jiménez 2008 at  $Re_\tau \approx 950$ . Figure 2.2(a) shows that the cell length scale, identified by the cubic root of the cell dimensions, is around twice the Kolmogorov scale across the entire channel. This resolution is comparable to that in many other published DNS studies.

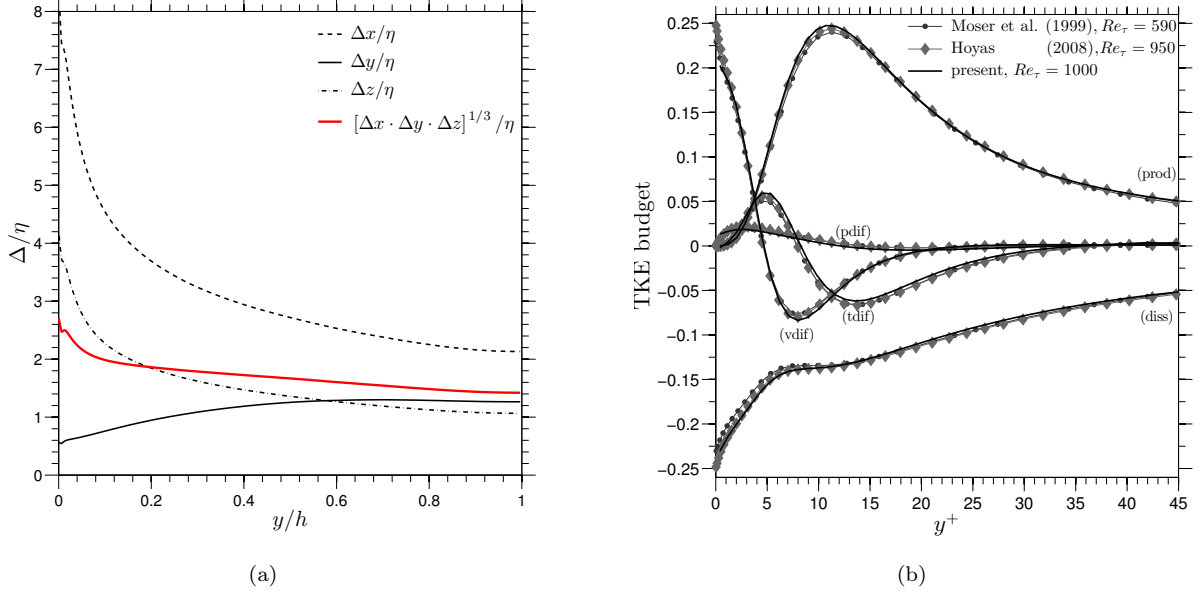


Figure 2.2: Resolution indicators: (a) comparison of cell dimensions relative to the Kolmogorov length scale; (b) turbulence-energy budget at  $Re_\tau \approx 1000$  relative to that of Moser, Kim, and Mansour 1999 at  $Re_\tau \approx 590$  and Hoyas and Jiménez 2008 at  $Re_\tau \approx 950$  for the baseline channel flow (“prod”=production, “diss”=dissipation, “tdiff”=turbulent diffusion, “vdif”=viscous diffusion, “pdif”=pressure diffusion).

## 2.3 Mean-flow characteristics

The emphasis of this investigation is on the phase-averaged properties and related interpretations. However, it is informative to first consider a narrow selection of time-averaged data that conveys an overall picture of the actuated flows, relative to the baseline state. Results derived for  $Re_\tau \approx 1000$  relate to a wide variety of properties and include full second-moment budgets for all stress components. The budgets, in particular, show characteristics that follow, certainly in qualitative terms, those discussed extensively by Touber and Leschziner 2012 at  $Re_\tau \approx 500$ , and are therefore not included here. On the other hand, phase-averaged budgets for  $T^+ = 200$  are included in Section 2.4. These also provide a good impression of the time-averaged behaviour at that actuation period, as the phase-averaged variations around the mean are not large.

Figure 2.3 shows time-averaged logarithmic velocity profiles, scaled with the *actual* wall-shear stress, and profiles of the normal Reynolds stresses, scaled with the *nominal* wall-shear stress (i.e. that of the unactuated flow). In the latter, and in other figures to follow, the double-primes indicate that the turbulence correlations are formed with the stochastic fluctuations. These arise from the decomposition:

$$U = \tilde{U} + u'' = \overline{U} + \hat{u} + u'' \quad (2.2)$$

where  $\overline{U}$  is the time-averaged value,  $\tilde{U}$  is the phase-averaged value, evaluated from

$$\tilde{U}|_\varphi = \frac{1}{N} \sum_{n=1}^N \left( \frac{1}{IK} \sum_{i,k=1,1}^{I,K} U_{i,k}|_{\varphi+(n-1)T} \right) \quad (2.3)$$

with  $\varphi \in \{0, T\}$ ,  $i, k$  are  $x, z$  grid indices,  $N$  is the number of cycles over which averaging is performed,  $\hat{u}$  is the periodic fluctuation and  $u''$  is the stochastic (purely turbulent) contribution. The use of nominal scaling for the Reynolds stresses is deliberate, because it brings out, essentially, the absolute response of the turbulence to the actuation for the given bulk Reynolds number. In contrast, scaling with the actual friction velocity would be indicative of the degree of universality of the wall-scaled stresses; although this is an important issue, it is not one that is of principal interest in the present considerations.

Qualitatively, the response of the mean velocity and the stresses is similar to that reported and discussed extensively by Touber and Leschziner 2012 for  $Re_\tau \approx 500$ , but the *magnitude* of the response to the actuation is somewhat lower, reflecting the lower drag-reduction margins. Major points deserving highlight are:

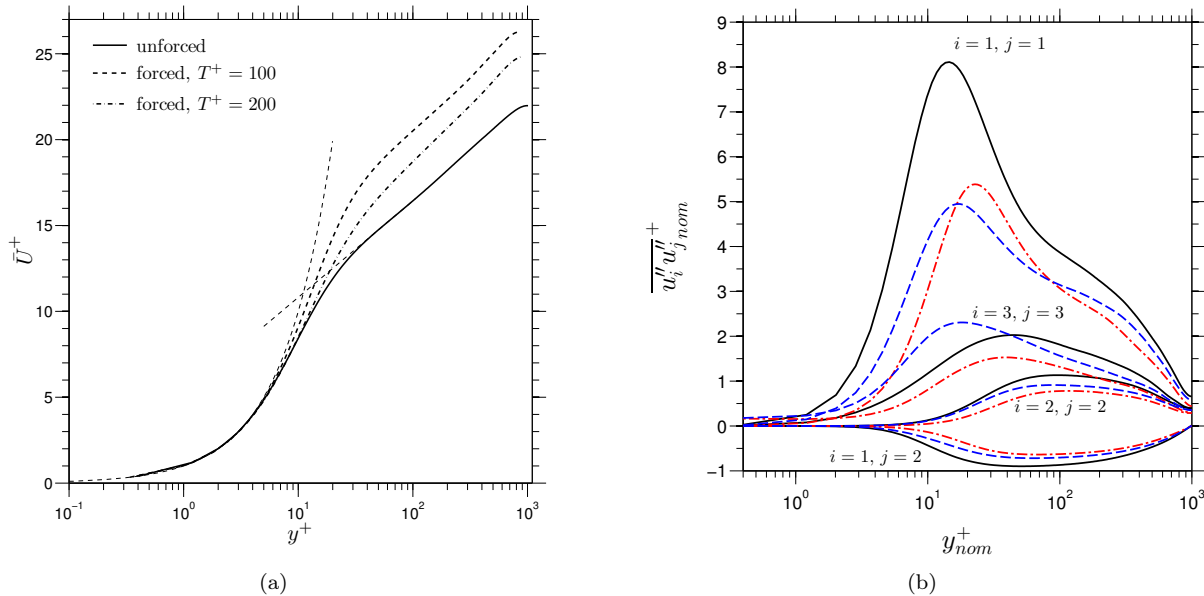


Figure 2.3: Profiles of (a) time-averaged logarithmic velocity profiles, scaled with the actual wall-shear stress; (b) time-averaged Reynolds stresses, scaled with baseline (nominal) wall-shear stress. Dashed (blue) lines identify  $T^+ = 200$ ; chain (red) lines identify  $T^+ = 100$ ; solid (black) lines identify baseline flow; double-primes indicate stochastic fluctuations, as defined in equation 2.2.

1. The elevation of the log-law caused by a thickening of the viscous sublayer by approximately 5 wall units at  $T^+ = 100$ ;
2. The large reduction in the streamwise stress (up to 40% at the peak), especially in the lower parts of the viscous sublayer – indicative of the strong reduction in streak intensity;
3. The decrease in the maximum wall-normal stress and shear stress by around 30% – this level scaling closely with the decrease in skin friction, and anticipated in view of the role played by the wall-normal stress in the shear-stress production rate;
4. The elevated value of the spanwise stress at  $T^+ = 200$ , exceeding the baseline level, and reflecting the consequences of the penetration of the Stokes layer into the turbulent region above the viscous sublayer and thus increasing the Stokes-strain-driven production  $P_{\widetilde{w''} \widetilde{w''}^+} = -2\widetilde{w''} \widetilde{v''} \partial_y \widetilde{W}^+$ , where the tilde identifies phase-averaging and the double-prime identifies stochastic fluctuations (see equation 2.2); and
5. The *lower* peak of the streamwise stress at  $T^+ = 200$  relative to that at  $T^+ = 100$ , associated with the periodic tilting of the streaks and their amplification at the phase in which tilting is strongest (see discussion by Touber and Leschziner 2012).

An additional point deserving emphasis is that the spanwise stress at  $T^+ = 100$  is lower than the baseline level, despite the additional production term  $P_{\widetilde{w''} \widetilde{w''}^+}$  that drives the spanwise normal stress. At the near-optimum actuation period, this term is very small, and the stress level is dictated by the pressure-strain process that transfers energy from the streamwise normal stress to the spanwise component. In contrast, at  $T^+ = 200$ , this extra generation is significant. As will be shown in Section 2.4.4, the phase-averaged production  $P_{\widetilde{w''} \widetilde{w''}^+}$  varies substantially during the actuation cycle, between a mildly negative value to a maximum of around 65% of the maximum streamwise-stress production ( $P_{\widetilde{u''} \widetilde{u''}^+} = -2\widetilde{u''} \widetilde{v''} \partial_y \widetilde{U}^+$ ). As a consequence, the time-averaged magnitude of the spanwise-stress production is around 30% of that of the streamwise stress.

Figure 2.4 compares joint  $u'' - v''$  PDFs for  $T^+ = 100$  and the baseline flow, both at  $y^+ \approx 13.5$ . The choice of this particular value of the wall distance is rooted in the fact, as conveyed in Figure 2.3, that this is

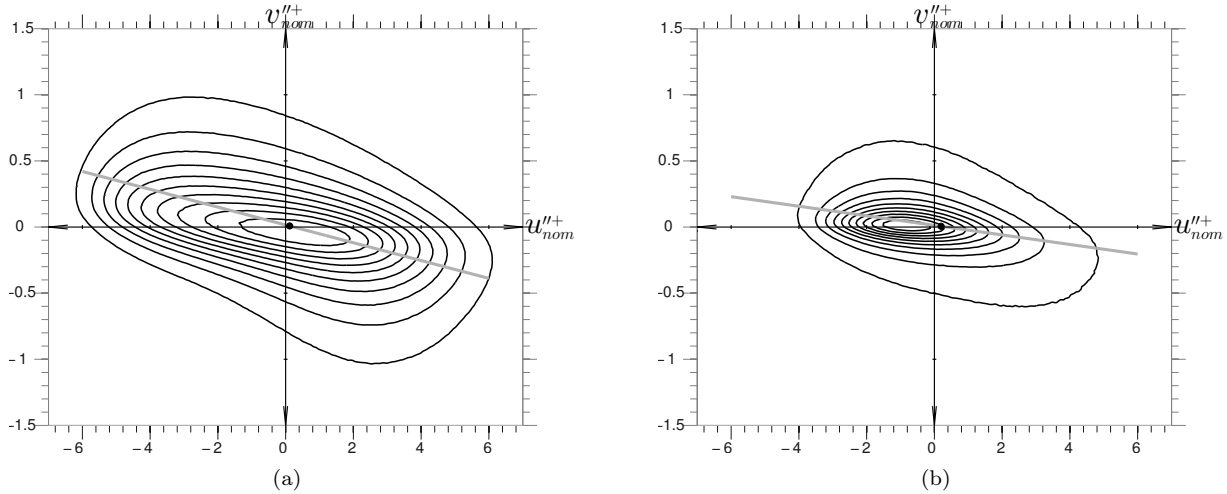


Figure 2.4: Joint  $u'' - v''$  PDFs at  $y^+ = 13.5$  (a) for the baseline flow and (b) for the actuated flow at  $T^+ = 100$ .

the location around which the streamwise turbulence intensity (i.e. the streak strength) reaches its maximum value in the unactuated flow, and at which the actuation has the most pronounced effect on that intensity. The straight lines in the plots identify the principal axes of the PDFs, in a least-squares sense, determined from a scatter plot of all  $u'' - v''$  realisations recorded. The comparison reveals three main differences provoked by the actuation. First, as expected, there is a strong narrowing when actuation is imposed. Second, the reduction is more pronounced in the  $Q_2$  quadrant ( $u'' < 0, v'' > 0$ ) than in the  $Q_4$  quadrant ( $u'' > 0, v'' < 0$ ), indicating that the diminution of ejection intensity is more influential than that of sweeps. Third, there is a marked anti-clock-wise tilt in the PDF's axis, indicative of a reduced level of cross-correlation between  $u''$  and  $v''$  fluctuations.

Finally, in this section, Figure 2.5 shows the response of wall-normal and spanwise components of the enstrophy,  $\omega_y'' = \frac{\partial u''}{\partial z} - \frac{\partial w''}{\partial x} \approx \frac{\partial u''}{\partial z}$  and  $\omega_z'' = \frac{\partial w''}{\partial x} - \frac{\partial v''}{\partial y}$  respectively, to the actuation at  $T^+ = 100$ . The streamwise component ( $\omega_x'' = \frac{\partial w''}{\partial y} - \frac{\partial v''}{\partial z}$ ) is relatively weak, and is also observed to be rather insensitive to the actuation, due to the fact that gradients of the streak strength – the intensity of the streamwise fluctuations – do not contribute directly to the streamwise component ( $\widetilde{\omega_x'' \omega_x''}$ ). The actuation is seen to result in a dramatic reduction in the other two components, reflecting the weakening of the streaks and their spanwise and wall-normal gradients. The reduction in the wall-normal component ( $\widetilde{\omega_y'' \omega_y''}$ ) is accentuated by the decline, albeit modest, in the spanwise-velocity fluctuations, reflected by the reduced level of the spanwise stress, as shown in Figure 2.3. The spanwise enstrophy component ( $\widetilde{\omega_z'' \omega_z''}$ ) is also very sensitive to the streak strength, being dependent on wall-normal gradients of the streamwise fluctuations. Hence, its decline also reflects the weakening of the streaks. Clearly, however, the detailed response of the two enstrophy components to the actuation differs greatly from each other. The wall-normal component has a maximum at around  $y^+ \approx 13.5$ , and this signifies the major contribution the streaky structures make to the wall-normal vorticity fluctuations. Its low magnitude, relative to the spanwise component, reflects the relatively large spanwise distances separating neighbouring streaks. In contrast, the strong near-wall maximum of the spanwise enstrophy component, in the baseline flow, is qualitatively consistent with the maximum of turbulence-dissipation rate observed at the wall, and is associated with the rise in the wall-normal derivative of the wall-parallel velocity fluctuations as the eddies “flatten” in consonance with the approach to the two-component state at the wall. Its severe reduction by the actuation is partly a consequence of the strong damping in the streamwise fluctuations and their production across the lower part of the viscous sublayer, where the Stokes-strain-induced skewness is large and especially disruptive. As observed from the turbulence-energy budget (not included), this reduction is further enhanced by the decline in viscous diffusion of turbulence towards the wall, and thus in the balancing dissipation, in response to the actuation-induced depression of production in the upper region of the viscous sublayer. The intimate link between dissipation and enstrophy will be pursued further in the discussion of phase-averaged properties in Section 2.4.4.

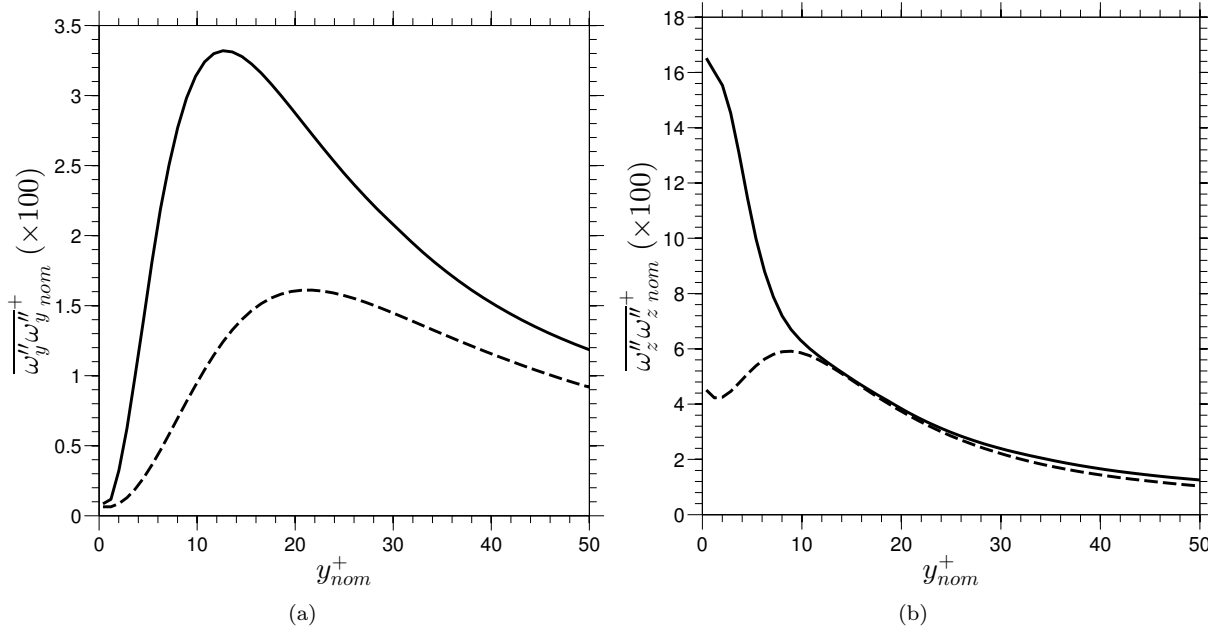


Figure 2.5: Components of the enstrophy in (a) wall-normal direction and (b) in spanwise direction, at  $T^+ = 100$  (dashed lines), relative to the baseline flow (solid lines).

## 2.4 Phase-averaged properties

This section deals with the phase-wise variations of the turbulence properties during the actuation cycle around the low-drag state. With few exceptions, the considerations are restricted to  $T^+ = 200$ , because it is only at this value that significant periodic fluctuations arise around the low-drag state.

In Touber and Leschziner 2012, an argument is presented that links the phase-wise damping and amplification of the streaks and their orientations to the shear-strain magnitude and the phase-wise rate of change in that strain during the actuation cycle around the location where the streaks are most vigorous, i.e.  $y^+ \approx 12 - 15$ . This argument is revisited, scrutinised and augmented in the following discussion. To this end, phase-wise variations of various phase-averaged turbulence properties, including second moments and their respective production rates, are examined over the actuation period, juxtaposed with phase-wise variations of the skin friction and/or properties of the unsteady strain rate. It will be shown, by reference to properties in the lower regions of the viscous sublayer, that the inter-dependence identified by Touber and Leschziner 2012 is part of a more complex scenario than that derived previously from observations of interactions in the upper portion of the viscous sublayer.

Specifically, localised regions of high velocity skewness in the lower part of the viscous sublayer are identified as promoting the drag-reduction process and as causing a distinctive hysteresis in all turbulence properties within any one cycle, wherein the drag-reduction and drag-increase phases do not follow the same path. The role of the skewness in promoting drag reduction is examined by reference to its effects on the enstrophy and its components, with particular emphasis placed on the transfer of enstrophy from the wall-normal component to the spanwise component during the drag-reduction phase. It will finally be argued, on the basis of stress budgets and comparisons between enstrophy and turbulence dissipation, that the latter does not play a decisive role in the drag-reduction process, but that this process is driven by the response of the streaks and turbulence production to temporal variations in the Stokes-strain and spatial variations in the velocity skewness.

### 2.4.1 Investigating the Connection Between Transient Drag Reduction and Drag Oscillations Around Low-Drag State

Prior to this analysis, it is appropriate to address two preliminary questions. First, are the periodic interactions around the low-drag state compatible with those in the transient process, where drag decays towards

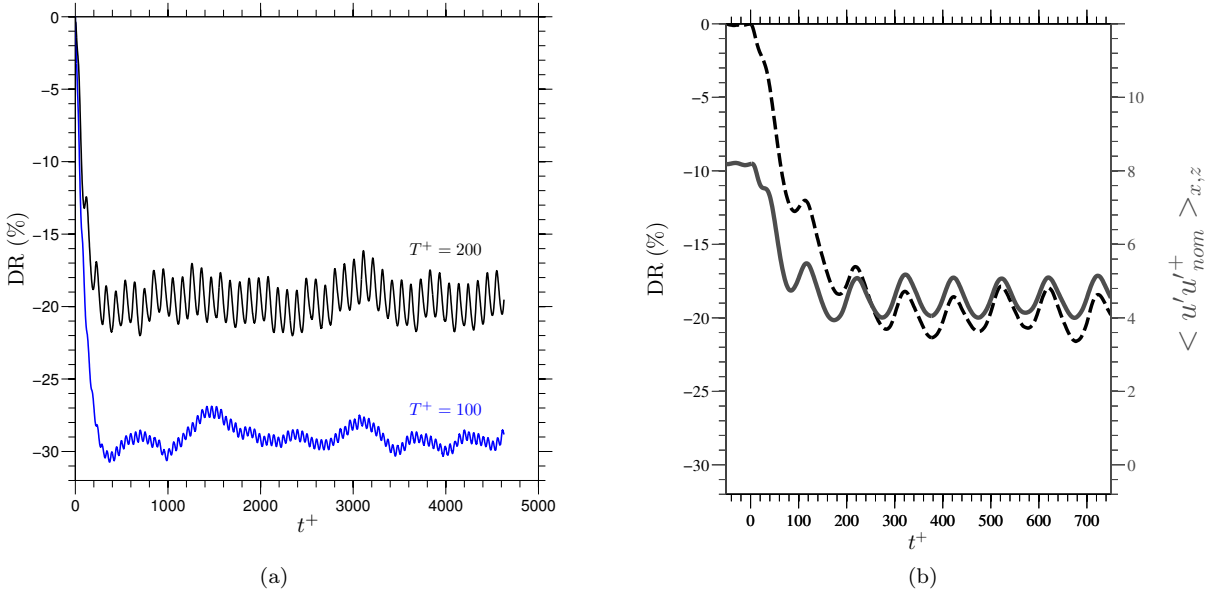


Figure 2.6: Temporal variation of (a) the wall-integrated skin-friction reduction, and (b) the skin-friction reduction (dashed line) and the  $x-z$ -plane-averaged streamwise stress at  $y^+ \approx 13.5$  (solid line) at  $T^+ = 200$ , (...) indicates  $x-z$  averaging.

its equilibrium low-drag level after the actuation onset? Second, are the phase-averaged statistics converged? The relevance of these questions arises from Figure 2.6(a), which shows skin friction variations following actuation onset over 46 and 23 cycles for  $T^+ = 100$  and 200, respectively. This figure reveals the following key features:

1. At  $T^+ = 100$ , the skin friction hardly responds to the actuation. Hence, no useful information can be extracted on the drag-reduction mechanisms at the low-drag state.
2. The low-drag state is reached within 2-3 actuation cycles, for both actuation periods. In both cases, this state is attained around  $t^+ \approx 300$ . The decline must be linked to the wall-normal penetration, mainly by viscous diffusion, of the Stokes motion across the sublayer. In non-turbulent conditions, it can be readily shown that the time scale for perturbations to propagate from the wall is  $t^+ = y^{+2}$ . Hence, subject to purely viscous transport, the time for the Stokes motion to reach  $y^+ \approx 12$ , where streaks are most vigorous, is  $t^+ = 170$ . In reality, turbulence in the upper viscous layer will reduce this period by around 30%, as the turbulent shear stress rises cubically with  $y$  and surpasses the viscous stress at  $y^+ = 10$ . However, the drag clearly begins dropping almost immediately after actuation onset. This implies near-wall processes are influential, pointing to another mechanism besides interactions at  $y^+ \approx 12$ .
3. The transient path, especially at  $T^+ = 200$ , has oscillatory features similar to those around the low-drag state.
4. At  $T^+ = 200$ , skin-friction fluctuations have a peak-to-trough magnitude about 20% of the mean drag-reduction margin.
5. Both skin-friction variations feature, like the baseline case distributions, long-time-scale components identifying large-scale structure “footprinting”. These outer “super-streaks” reside in the outer flow.

The correspondence between transient and periodic fluctuations is addressed in Figure 2.6(b). This shows the relationship between skin friction variations and the  $x-z$ -averaged streamwise turbulence intensity at  $y^+ \approx 13.5$ , where streaks are very sensitive to actuation. Reductions/increases in drag and turbulence intensity are closely correlated over the entire period, transient and low-drag state. This indicates the transient phase is not exceptional, and focusing on the low-drag state is appropriate. This is strengthened by analogous dissipation and enstrophy observations in the following discussion.

### 2.4.2 Interactions in the Upper Part of Viscous Sublayer

The cycle-averaged skin-friction distribution is shown in Figure 2.7, together with the phase-wise variation of the Stokes strain and its phase-wise derivative. The reason for including the latter is that Touber and Leschziner 2012 link the streak damping and amplification during an actuation phase to the phase-wise *rate of change* in the strain vector in the upper portion of the viscous sublayer. The horizontal-dashed line in the Stokes-strain plots is at  $y^+ = 13.5$ , the level around which several of the turbulence quantities reach their maximum values, including the streamwise and spanwise turbulence intensities. Consistent with observations made in Touber and Leschziner 2012, Figure 2.7 shows that the skin friction rises when the Stokes strain in the upper portion of the viscous sublayer is high and ‘‘lingers’’, while it declines when the strain is low and changes rapidly with the phase. Thus, the maximum skin friction is attained after a sustained period of high Stokes strain, while the minimum is reached following a sustained period of low and rapidly changing strain. It is emphasized, however, that these interactions are specific to the level at which the streaks are strongest.

Next, Figure 2.8 demonstrates that the streamwise and spanwise stresses, Figures 2.8(a) and 2.8(b), and their respective production rates, Figures 2.8(c) and 2.8(d), all reach maxima at  $y^+ \approx 13 - 15$ , and that these peaks are well correlated, in phase, with skin-friction maxima, the productions leading the respective stresses by a small phase margin. The peak spanwise stress is substantial, reaching about 50% of the peak streamwise stress, and this reflects the high rate of Stokes-strain-driven production in the upper portion of the viscous sublayer at the non-optimum actuation period considered. This production is positive almost throughout the phase-space domain, but closer examination reveals it to be marginally negative around the locus at which the Stokes strain vanishes, and hence where it changes most rapidly in phase. Corresponding to the above correlation of maxima, the lowest values in the stresses and their productions, again at  $y^+ \approx 13 - 15$ , correlate well with the skin-friction minima.

The behaviour described above accords well with observations by Touber and Leschziner 2012 on the response of the streaks to the Stokes strain at  $Re_\tau = 500$ . Thus, the streaks are observed to be well established when the skin friction reaches a maximum, while they are weak, disorganized and ill-defined when the skin-friction is at its minimum. Moreover, when the streaks are well defined, their orientation in the wall-parallel plane is dictated by the magnitude and direction of the total strain in the upper portion of the viscous sublayer. Shortly after the Stokes strain at this position peaks – the lag being around  $0.1T^+$  – the streaks are re-established in a direction that is in harmony with the sign of the Stokes strain. Hence, as demonstrated by Figures 2.9(a) and 2.9(c), the streaks assume two orientations within any one cycle, corresponding to the two lobes of the Stokes strain shown in Figure 2.7.

While the above scenario explains the interactions linking variations in streak strength to the Stokes strain, the explanation for the downward trend in the drag towards a reduced time-averaged level relies on the validity of the streak-amplification time scale as derived from the GOP theory by Blesbois et al. 2013. Thus, following a reduction phase, the subsequent recovery is constrained by this time scale, which is  $t^+ \approx 80$ . If the actuation period is too short, the recovery phase is insufficiently long for a complete recovery, and the average drag is thus lowered.

### 2.4.3 Interactions in the Lower Part of the Viscous Sublayer: Hysteresis and Skewness

Two features that Touber and Leschziner 2012’s paradigm cannot explain are the observed drag reduction immediately after actuation starts (Figure 2.6), and a striking hysteresis in all properties during the action cycle. In this hysteresis, the drag-reduction phase is longer than the drag-recovery phase. The skin-friction variation in Figure 2.7(a) clearly shows this hysteresis. Quantitatively, the maximum skin friction rate of change in the two phases corresponds to sinusoidal variations with periods  $T^+ = 120$  and  $80$ , respectively.

Phase-wise asymmetries in all turbulence properties and statistics are associated with the skin-friction hysteresis. This hysteresis can only be explained by a process that is asymmetric in the cycle midpoint, favouring the drag-reduction over drag-recovery phase. It is argued the hysteresis links to phase-wise asymmetric behaviour of the *flow skewness* – the wall-normal velocity-vector direction gradient. Although hysteresis in flows undergoing spanwise oscillation has been observed before (e.g. Skote 2012), connections to drag reduction mechanisms have received little attention. Figures 2.10 and 2.11 exemplify hysteresis in important turbulence quantities.

Figure 2.10 shows phase-averaged shear stress profiles at different actuation cycle positions. Figure 2.10(a) is for the drag drop from maximum to minimum, while 2.10(b) is for the subsequent rise. In the reduction phase, shear stress in the viscous sublayer falls progressively and uniformly within  $y^+ \approx 30$ , with the maximum

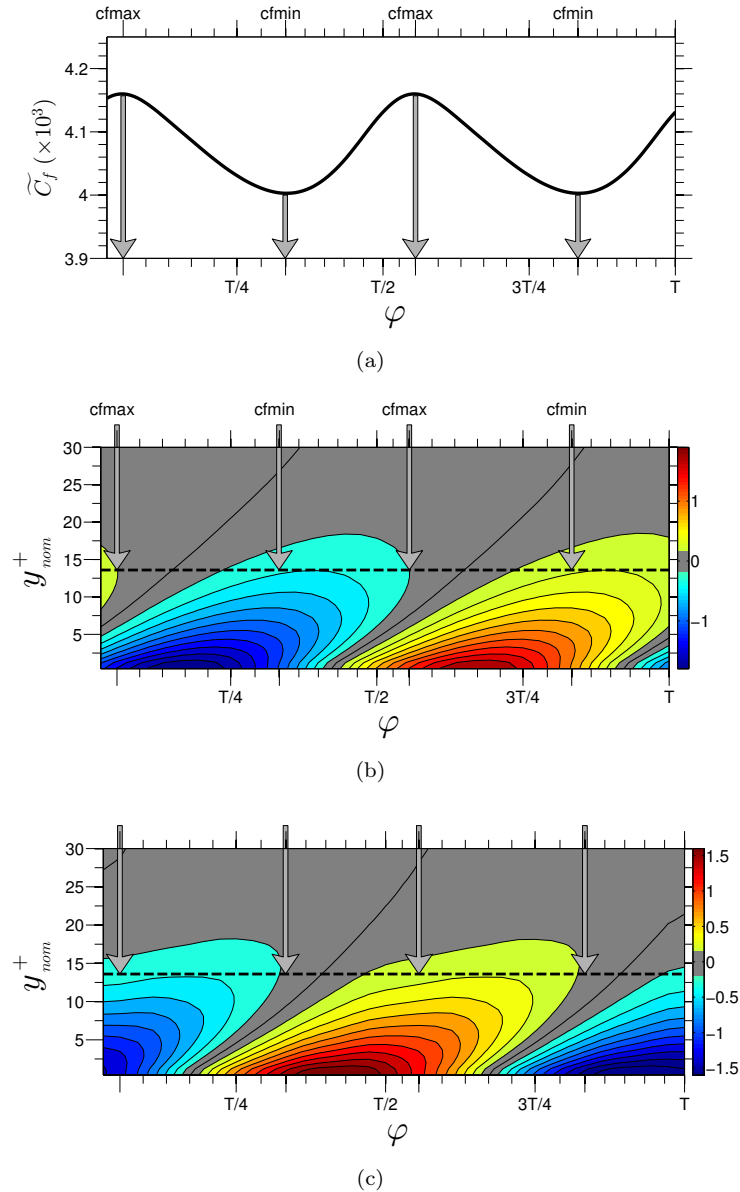


Figure 2.7: Comparison between (a) phase-wise cycle-averaged skin-friction fluctuations, (b) contours of the Stokes strain ( $\partial \tilde{W} / \partial y$ ) and (c) contours of the phase-wise derivative of the Stokes strain, all at  $T^+ = 200$

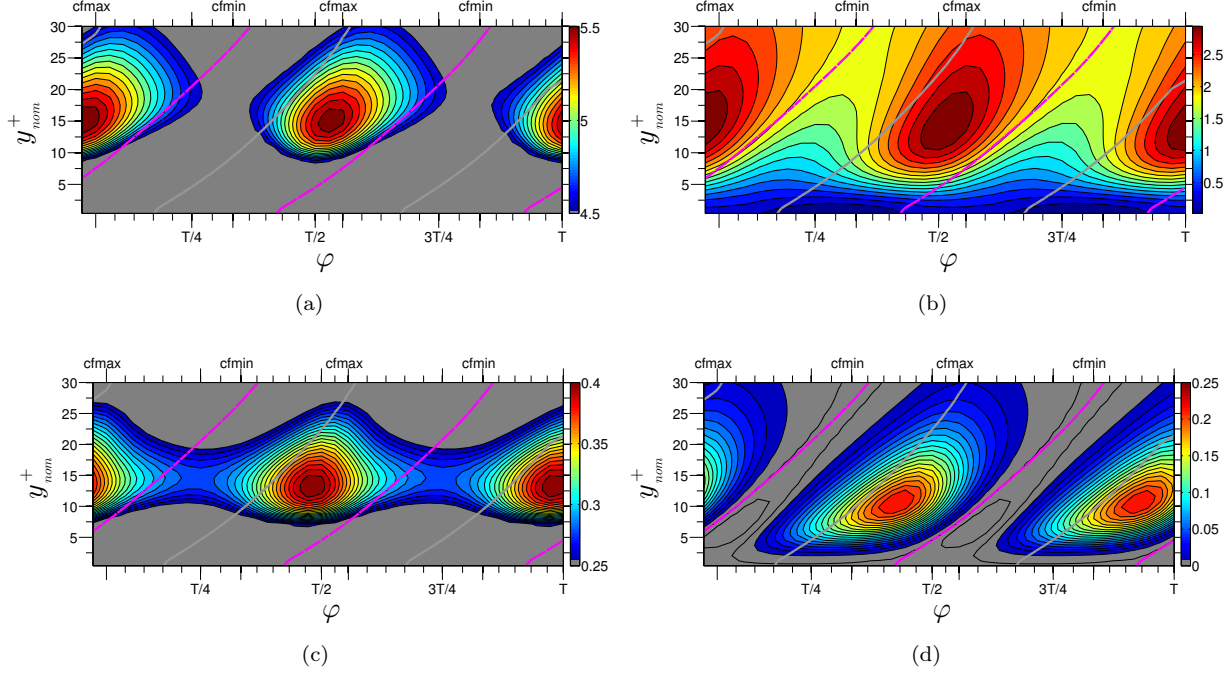


Figure 2.8: Phase-wise variations of (a) the streamwise Reynolds stress ( $\widetilde{u''u''}$ ), (b) the spanwise Reynolds stress ( $\widetilde{w''w''}$ ), (c) the production of the streamwise Reynolds stress ( $\widetilde{P_{u''u''}}$ ) and (d) the production of the spanwise Reynolds stress ( $\widetilde{P_{w''w''}}$ ), all at  $T^+ = 200$ . All quantities are normalised with the nominal friction velocity (grey and magenta curves identify, respectively, the loci of maximum and zero Stokes strain).

shifting outwards about 30 units. During drag rise, the increase does not follow the same path - the process is hysteretic. Specifically, the shear stress rise occurs preferentially near-wall, with an increase close to the wall propagating outwards. The maximum at  $y^+ \approx 25$  re-establishes much faster than it declined in the preceding phase.

The hysteresis is clearly shown in Figure 2.11, which has phase-wise contour plots of fluctuations in the streamwise normal stress, ( $\widetilde{u''u''}^+ - \overline{u''u''}^+$ ), the spanwise normal stress, ( $\widetilde{w''w''}^+ - \overline{w''w''}^+$ ) and the shear stress ( $\widetilde{u''v''}^+ - \overline{u''v''}^+$ ). The dashed black contour lines indicate 75%, 50%, 25% and 0% of the maximum Stokes-strain magnitude. The relevance of the magenta contours will be explained later. All plots (and those not included for other stresses and production rates) reveal the stress magnitude decline progresses over a longer period portion than the increase. Note that red-coloured contours always signify positive perturbations, corresponding to a *reduction* in the shear stress magnitude.

The question that is addressed next is what causes the hysteresis. It is observed first that the causal relationship between the Stokes strain and the stresses at  $y^+ \approx 13 - 15$  (Figure 2.7) does not hold close to the wall. Specifically, as the wall is approached, the phase-lag between the region of lingering, high Stokes strain and the region of high turbulent-stress levels is increasing, to the extent that the region of high Stokes strain progressively coincides with regions of *low* turbulent stresses. One explanation might be that the increasing lag reflects an increasing time scale over which turbulence is amplified. However, this neither accords with the accepted view that the time scale of turbulence events in the viscous sublayer is some weighted combination of the eddy-turnover time scale  $k/\varepsilon$  and the Kolmogorov time scale  $(\nu/\varepsilon)^{1/2}$ , nor with statements derived from the GOP theory. The above two limiting time scales suggest that the weighted combination will reduce towards the wall, because  $k$  declines in proportion to  $y^2$ , and will reach some finite plateau governed by the finite wall value of the dissipation. The GOP predicts, likewise, that the amplification time scale reduces towards the wall, although by a modest amount, based on computations for the range  $y^+ = 6 - 16$ .

Another possible source is a property of the Stokes strain that is likely to disrupt the streak-formation process *and* has a distinct phase-wise asymmetric character. Such a property is the flow *skewness*,  $\partial\theta/\partial y$ , where  $\theta$  is the velocity-vector orientation. Contours of the skewness are shown in Figure 2.12, relative to Stokes-strain contours, and these are also included, in the form of dashed magenta lines, in Figure 2.11. The

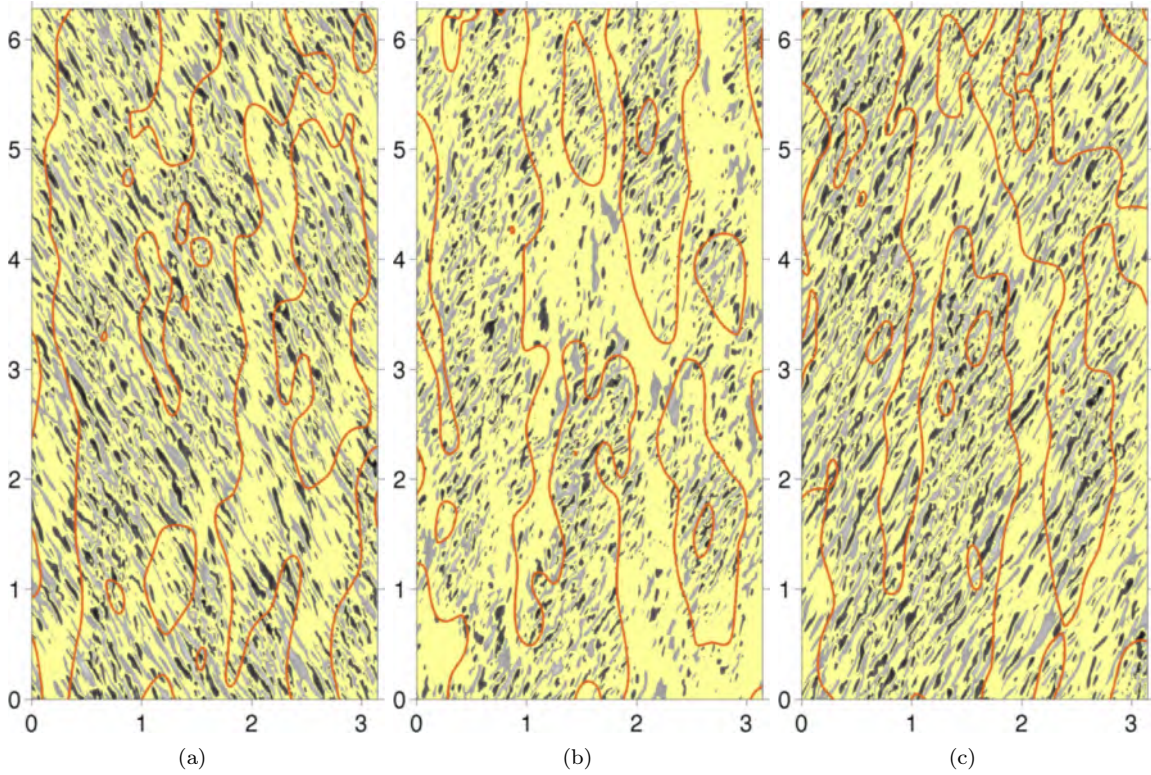


Figure 2.9: Streaky near-wall structure at  $y^+ = 13.5$ , identified by streamwise-velocity fluctuations; (a) at maximum  $C_f$  and negative Stokes strain; (b) at minimum  $C_f$ ; at (c) maximum  $C_f$  and positive Stokes strain. Red contours identify large-scale motions. For contour details, refer to Figure 2.34.

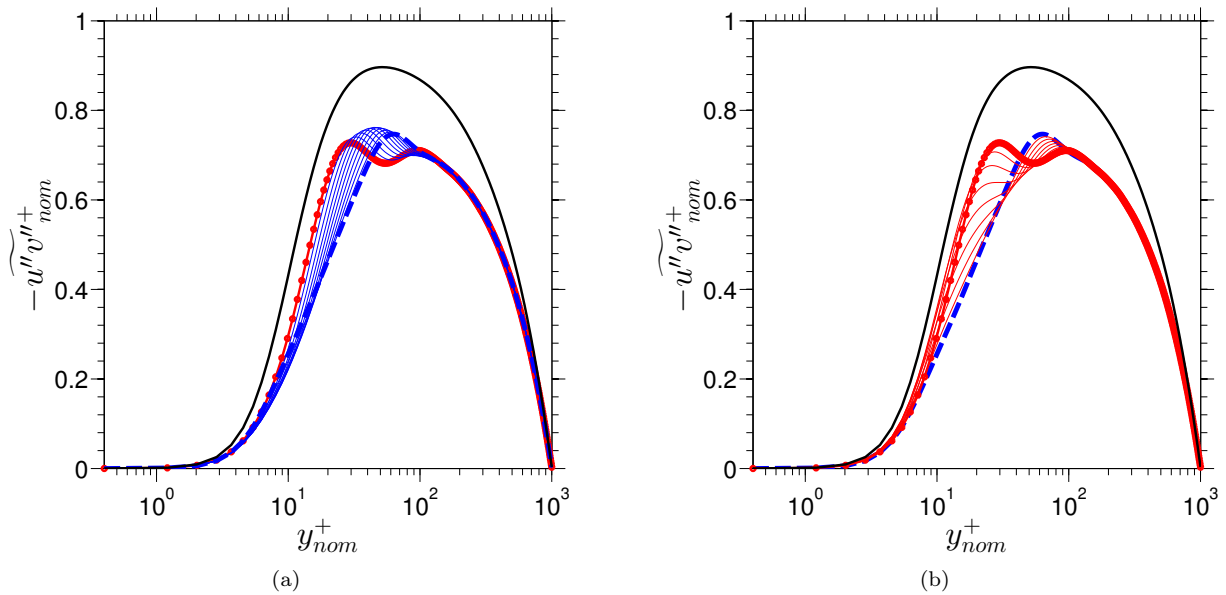


Figure 2.10: Phase-wise variations of profiles of the shear stress during (a) the drag-reduction phase and (b) the drag-increase phase, at  $T^+ = 200$ . Thick solid (red) lines with solid circles correspond to the maximum skin-friction phase value; thick dashed (blue) lines correspond to minimum skin-friction phase value; thick solid (black) lines correspond to the shear-stress profile obtained in the unactuated flow; thin solid (black) lines relate to different phases.

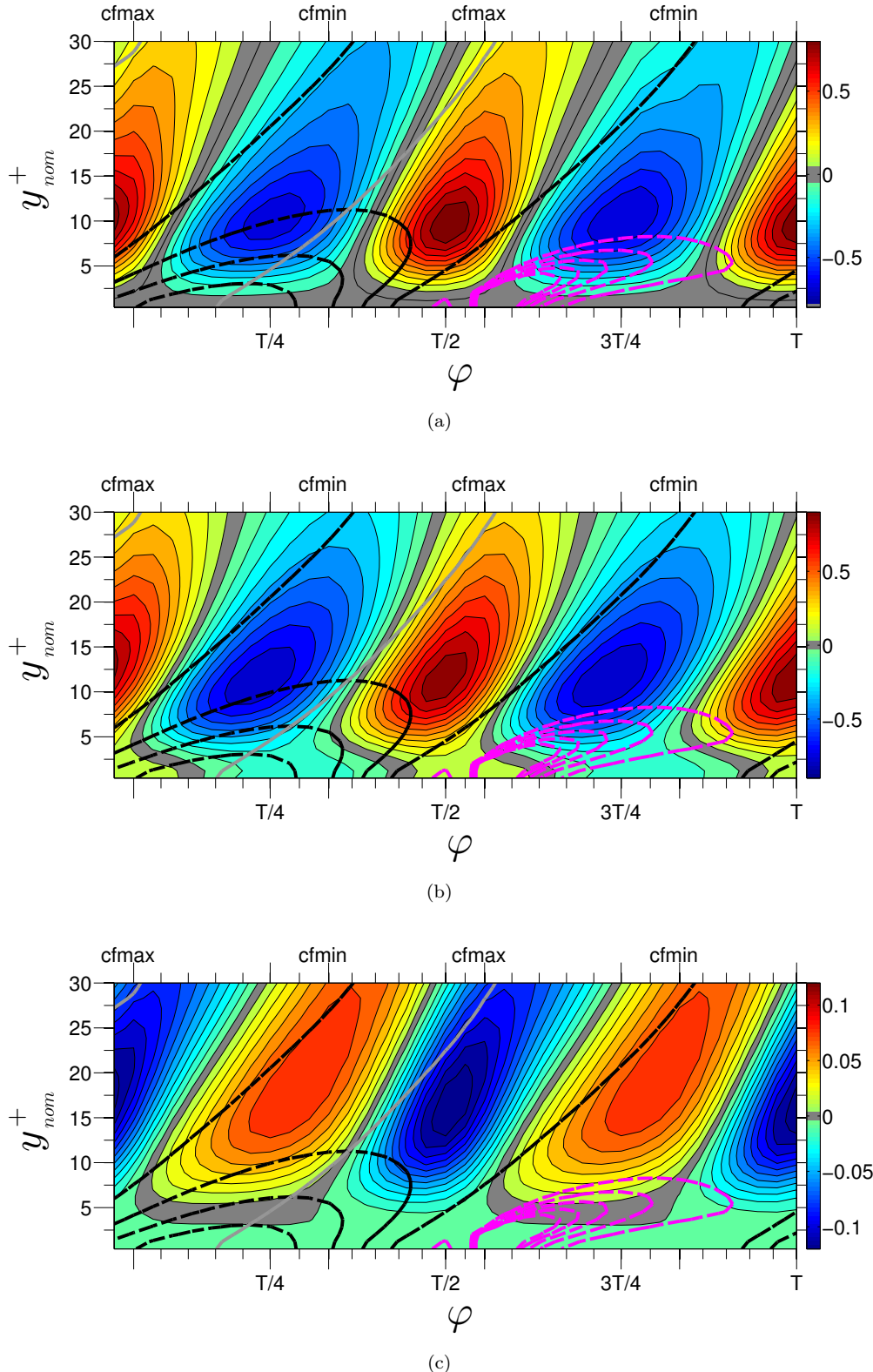


Figure 2.11: Phase-wise variations of fluctuations in (a) the streamwise stress ( $\widetilde{u''u''}^+ - \overline{u''u''}^+$ ), (b) the spanwise stress ( $\widetilde{w''w''}^+ - \overline{w''w''}^+$ ), and (c) the shear-stress ( $\widetilde{u''v''}^+ - \overline{u''v''}^+$ ). Dashed contours represent loci of 75%, 50%, 25% and 0% of the maximum absolute value of the Stokes strain.

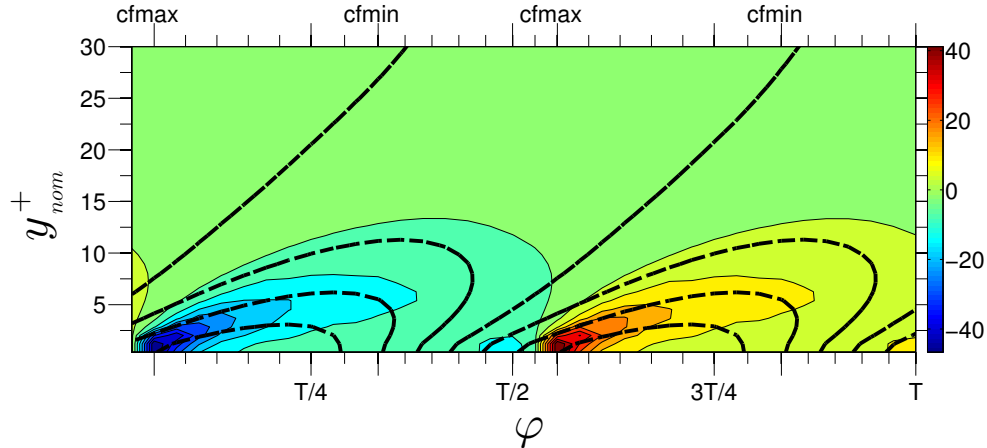


Figure 2.12: Skewness map (wall-normal derivative of velocity angle). Dashed contours represent loci of 75%, 50%, 25% and 0% of the maximum absolute value of the Stokes strain.

skewness is observed to be very high within a tongue that originates at the location  $C_{f,max}$  and traverses the lower portion of the viscous sublayer in which the stresses are depressed. Importantly, the high-skewness region only covers the phase-portion during which the drag declines. Moreover, Figure 2.13 shows that high levels of skewness, again identified by the dashed magenta contours, coincide with near-wall regions in which the production of the streamwise and shear stresses are depressed, despite the high level of the Stokes strain. The exception is the production of the spanwise stress  $P_{w''w''+}$  which is linearly dependent on the Stokes strain and thus directly driven by it. While this is not claimed to be a proof of the origin of the hysteresis and the near-wall suppression of turbulence, the distinct asymmetry of this property and its coincidence with areas of turbulence suppression is striking, and provides credible evidence that skewness is the source of the hysteresis. It causes a prolongation of the drag-reduction phase, relative to the phase of drag increase, and shortens the period over which the streaks are allowed to re-establish against the GOP-predicted streak-amplification time scale  $t^+ \approx 80$ . Thus, at  $T^+ = 200$ , the streak-regeneration time interval is  $t^+ \approx 40$ , while at  $T^+ = 100$ , this value declines to about 20, effectively preventing the re-generation of the streaks and resulting in the insensitivity to the oscillatory actuation around the low-drag state (see Figure 2.6(a)). The fact that the skewness depresses the turbulent level very close to the wall also suggests that it plays an important role in the initial decay of the drag immediately after the onset of the actuation. In fact, at this early stage, skewness is exceptionally high, as the Stokes layer is very thin, so that its effect is likely to be more pronounced than the mechanism in the upper portion of the viscous sublayer, when the Stokes motion has spread across the layer after approximately one half of the actuation period. The fact that the turbulence intensity in the upper portion of the viscous sublayer also begins to decline very shortly after the actuation starts – as is seen from Figure 2.6 – reflect a coupling, via pressure fluctuations, between the near-wall reduction in ejections very close to the wall and the wall-normal fluctuations at higher elevations. Results obtained (but not included herein) for the time-evolution of the budget  $\langle v''v'' \rangle_{x,z}$  in the transient period have revealed a rapid decline in the pressure-velocity interaction across the near-wall layer very shortly after the start of the actuation, within  $t^+ = 10 - 20$ . As this interaction is the principal source driving  $\langle v''v'' \rangle_{x,z}$ , its decline leads to a deduction in that stress and consequently a reduction in the shear stress, the production of which is proportional to  $\langle v''v'' \rangle_{x,z}$ .

#### 2.4.4 Dissipation and Enstrophy

An important issue to address, in view of previous studies (e.g. Ricco et al. 2012), is whether the dissipation and enstrophy play critical roles in driving the drag-reduction process. This is considered next, by reference to stress budgets and enstrophy plots.

First, Figures 2.14 and 2.15 show phase-wise variations of the budgets for the streamwise and the shear stress components, respectively. In the present case of channel flow, the budgets can be expressed by the following equations, which also define the terms plotted in the figures,

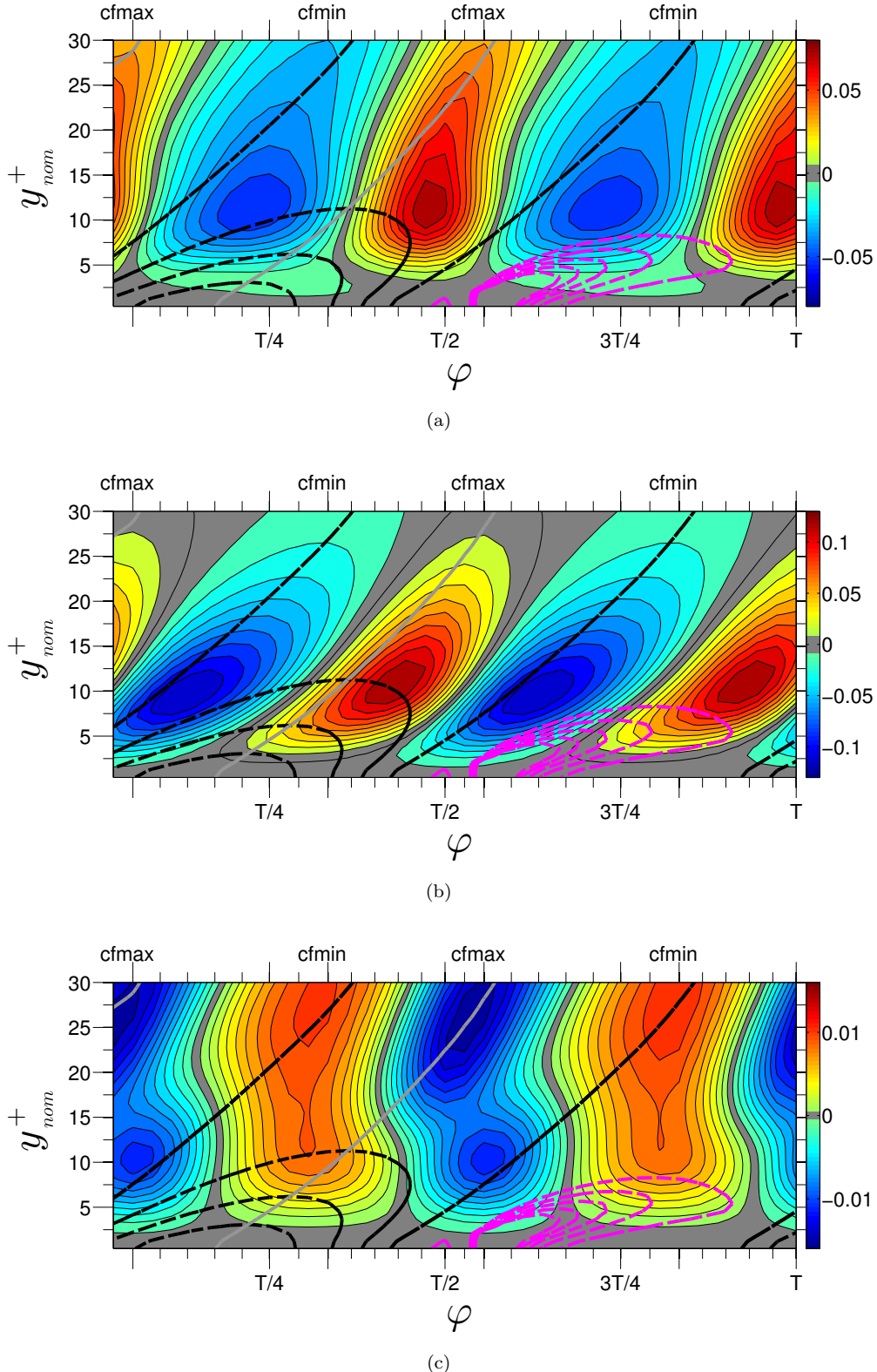


Figure 2.13: Phase-wise variations in the production fluctuations in (a) the streamwise stress ( $P_{\widetilde{u''u''+}} - P_{\widetilde{u''u''-}}$ ), (b) the spanwisestress ( $P_{\widetilde{w''w''+}} - P_{\widetilde{w''w''-}}$ ), and (c) the shear stress ( $P_{\widetilde{v''v''+}} - P_{\widetilde{v''v''-}}$ ). The grey line is the locus of maximum Stokes strain. The dashed magenta contours indicate skewness levels.

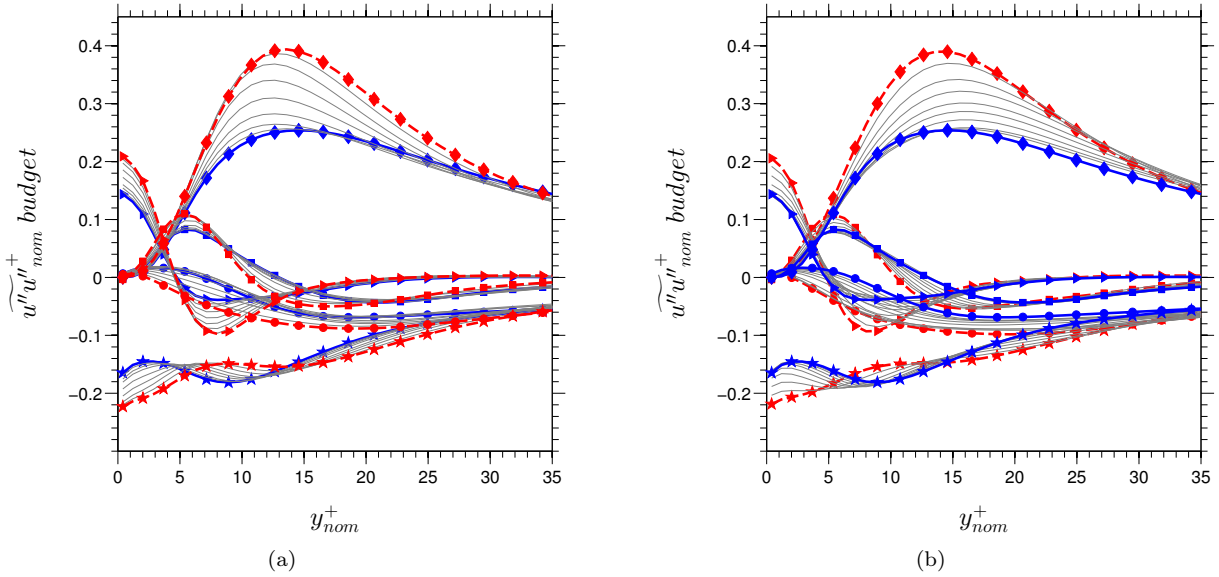


Figure 2.14: Phase-wise fluctuations of the budget contributions for the streamwise normal stress during (a) the drag-increase phase and (b) the drag-decrease phase. Thick dashed (red) lines with symbols correspond to the maximum skin-friction phase value; thick solid (blue) lines with symbols correspond to minimum skin-friction phase value; thin lines identify intermediate phases; budget terms are defined by:  $\blacklozenge$  production,  $\blacksquare$  turbulent diffusion,  $\blacktriangle$  viscous diffusion,  $\bullet$  pressure-velocity interaction,  $\star$  dissipation.

$$\frac{\partial \widetilde{u''u''}}{\partial t} = -\underbrace{\frac{\partial \widetilde{u''u''v''}}{\partial y}}_{\text{tdiff}} + \underbrace{-2\widetilde{u''}\frac{\partial p''}{\partial x}}_{\text{pvel}} - \underbrace{-2\widetilde{u''v''}\frac{\partial \widetilde{U}}{\partial y}}_{\text{prod}} - \underbrace{\frac{2}{Re} \sum_{i=1}^3 \left( \frac{\partial \widetilde{u''}}{\partial x_i} \right)^2}_{\text{diss}} + \underbrace{\frac{1}{Re} \frac{\partial^2 \widetilde{u''u''}}{\partial y^2}}_{\text{vdiff}} \quad (2.4)$$

$$\frac{\partial \widetilde{u''v''}}{\partial t} = -\underbrace{\frac{\partial \widetilde{u''v''v''}}{\partial y}}_{\text{tdiff}} + \underbrace{-\widetilde{u''}\frac{\partial p''}{\partial y} - \widetilde{v''}\frac{\partial p''}{\partial x}}_{\text{pvel}} - \underbrace{-2\widetilde{v''v''}\frac{\partial \widetilde{U}}{\partial y}}_{\text{prod}} - \underbrace{\frac{2}{Re} \sum_{i=1}^3 \left( \frac{\partial \widetilde{u''v''}}{\partial x_i} \right)^2}_{\text{diss}} + \underbrace{\frac{1}{Re} \frac{\partial^2 \widetilde{u''v''}}{\partial y^2}}_{\text{vdiff}} \quad (2.5)$$

For each stress, two sets of plots are presented: the left-hand side plot in each set relates to the drag-rise phase, while the right-hand side one relates to the drag-decrease phase, the phase values at which  $C_f$  reaches its maximum and minimum being indicated by the thicker solid lines with symbols. The imbalance in the budgets presented in Figures 2.14 and 2.15 is shown in Figure 2.16. The three curves in each of the two plots relate, respectively, to the minimum- and maximum- $C_f$  phase positions and to the phase-average. The last should be zero, and the modest imbalance – a maximum of 0.02 in the case of the streamwise stress and much lower in the case of the shear stress – is indicative of the error margin arising from the complex process of determining the budget for the stochastic correlations. However, the phase-wise departure of the imbalance from the phase average was found to agree well with distributions obtained from the phase-wise gradient of the stresses, i.e. the left-hand sides of equations 2.4 and 2.5. Clearly, this unsteady contribution is a small difference between large contributions, and its determination from the imbalance – the right-hand side of equations 2.4 and 2.5 – is difficult and prone to some error. The most important point to highlight in the  $\widetilde{u''u''}^+$  budget is that the substantial fluctuations in production over most of the near-wall layer, reflecting variations in the streak strength and driving the normal-stress fluctuations, are balanced mainly by corresponding fluctuations in diffusion and pressure-velocity interaction. In contrast, variations in the dissipation level are fairly small. Moreover, during the drag-reduction phase, the dissipation decreases over almost the entire wall-normal extent, with the reverse occurring during the drag-increase phase. Very close to the wall the behaviour is different. Here, dissipation has to balance viscous diffusion. Both increase during the drag-increase phase and decrease during the drag-decrease phase. However, near-wall diffusion rises and falls, because the high production away from the wall rises and falls, and this leads to diffusion of energy away from the production maximum to either side of this maximum. Hence, at the wall, variations in dissipation

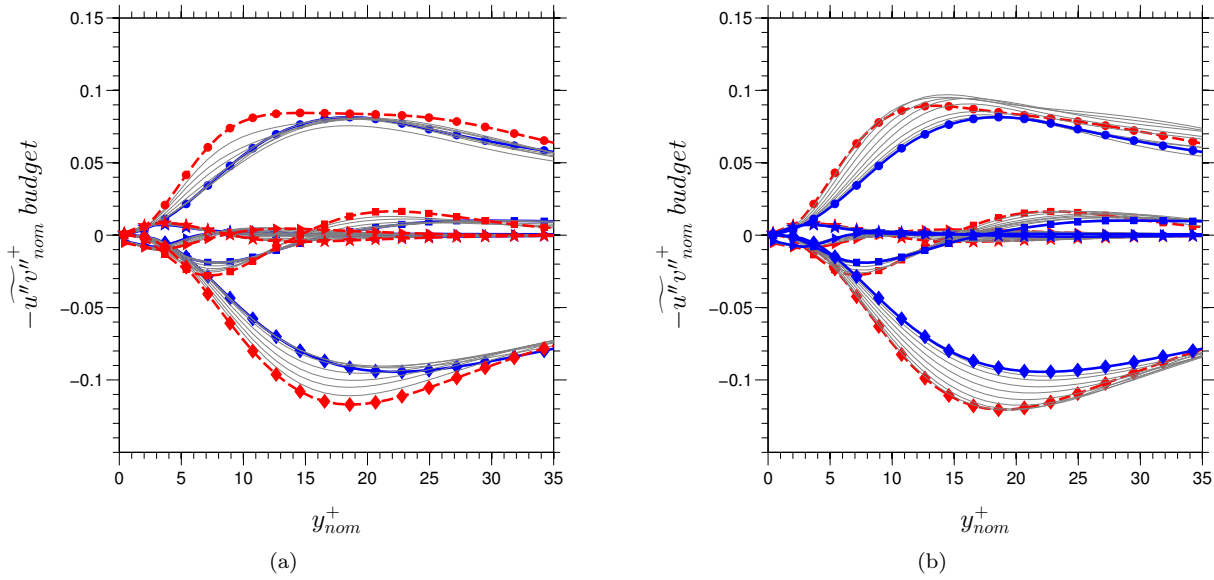


Figure 2.15: Phase-wise fluctuations of the budget contributions for the shear stress during (a) the drag-increase phase and (b) the drag-decrease phase. Lines, symbols and colours have the same meaning as in caption of Figure 2.14.

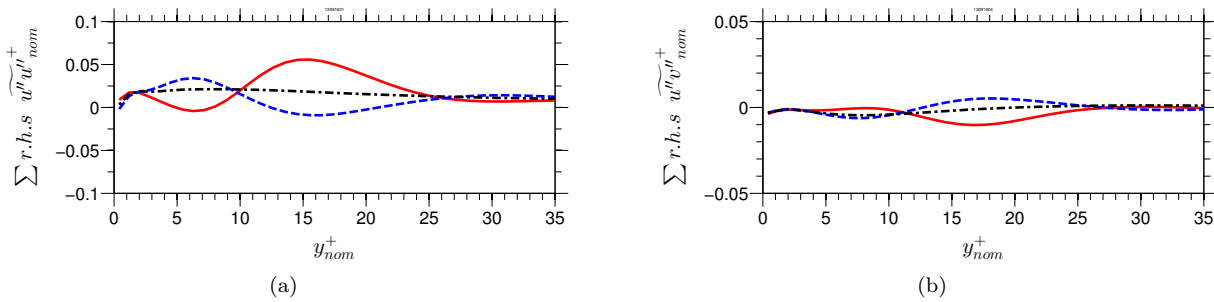


Figure 2.16: Imbalance in the budgets (sum of the right-hand sides of equations 2.4 and 2.5) for (a) the streamwise stress and (b) the shear stress. Solid (red) line corresponds to the maximum  $C_f$  phase; dashed (blue) line corresponds to the minimum  $C_f$  phase; chain (black) line relates to the time average.

are driven by (and are the consequence of) variations in production. A qualitatively similar behaviour is observed in the case of the shear-stress budget, although here, the significant fluctuations in production are balanced by corresponding fluctuations in the pressure-velocity interaction, while the dissipation is almost insignificant, reflecting the near-isotropy of the small-scale dissipative motions. Hence, any influence exercised by the dissipation of the shear stress, and thus drag-reduction process, cannot be direct, but has to proceed via the linkage between turbulence energy and the shear stress.

These observations, especially the harmony between the trends of drag and the dissipation, and the modest phase-wise changes in the dissipation relative to other processes in the budget, are at odds with the mechanism proposed by Ricco et al. 2012, which is based on the argument that the enstrophy is enhanced by the Stokes motion, and thus the increase in enstrophy and dissipation are held responsible for the drag reduction. This contradiction will be reinforced by results for the enstrophy discussed below.

The relationship between dissipation and enstrophy is examined by reference to phase-averaged results for the enstrophy and its components. First, Figure 2.17 compares phase-wise variations of the enstrophy and of the dissipation of turbulence energy. Entirely in accord with expectations, the two are found to be closely correlated. Importantly, both decline during the phase in which the drag decreases, and rise when the drag increases.

At this point, it is opportune to return to the correspondence between the transient phase of the drag-reduction process and the oscillations around the low-drag state, first considered in Figure 2.6. Figure 2.18 compares contours of dissipation and enstrophy, in a manner analogous to that in Figure 2.17. Also included in the figure is a comparison between the  $y$ -wise integrated dissipation rate and the skin-friction during the transient process. The conclusion is, here again, that the transient phase shows no exceptional features, and that the relationship between dissipation and enstrophy does not change, both declining during phases of drag decrease and rising with increasing drag within any one cycle. Moreover, the transient phase of the flow at  $T^+ = 100$  (not included) shows exactly the same correspondence. The overall level of dissipation and enstrophy decline during the initial 2-3 actuation cycles, but this decline is modest, and the fluctuations around the low-drag state give an appearance that is very similar to that in the transient phase. One unusual feature in Figure 2.18 is a thin tongue of elevated dissipation and enstrophy immediately after the onset of the actuation. This is due, entirely, to a minor glitch in the imposition of the plate motion, with the plate velocity having a small finite value at the time the actuation starts, thus causing a temporal discontinuity in the Stokes strain at the wall. The time interval over which this discontinuity affects the flow is  $t^+ \approx 10$ . Reference to Figure 2.6(b) shows that this is a very small portion of the transient period, during which the skin friction hardly changes. The fact that the skin friction begins to drop within this interval reflects the extremely high near-wall skewness associated with the discontinuity. Thus, the increase in dissipation in this interval has no bearing on the drag-reduction scenario. Over the entire remaining part of the transient period, and thereafter, drag reduction is consistently associated with a decrease in dissipation.

#### 2.4.5 Enstrophy Components: Interactions with Strain and Skewness

Figure 2.19 shows phase-wise profiles of the enstrophy component,  $\widetilde{\omega''\omega''_y}$  (any reference to *component* should be understood to relate to one of the three constituents that contribute to the scalar enstrophy). This component is being given preference here, because it reflects the significant phase-dependent variations in streak strength and structure during the actuation cycle – although the increase in spanwise velocity fluctuations, due to Stokes-strain-induced production, also contributes, albeit modestly, to the observed phase sensitivity. The results for  $T^+ = 100$  are included here to convey the fact that the wall-normal enstrophy component for this value varies only weakly with phase, while its time-averaged value is drastically lower than the corresponding level in the baseline case (see Figure 2.5). This also applies to other enstrophy components not included herein. For example, the spanwise enstrophy component reduced by around 50-75 % of its value in the baseline case within  $y^+ \approx 5$ , reflecting the reduction in the near-wall dissipation rate. Consistent with properties already presented, the enstrophy also shows a distinctive hysteresis. Starting from the lowest variation, corresponding to the skin-friction trough in Figure 2.7, the enstrophy increases at the fastest rate in the layer  $y^+ \approx 6 - 15$ , with the maximum moving upwards in the layer  $y^+ \approx 10 - 13$ . In contrast, the decline is more uniform across the viscous sublayer, with the maximum shifting outwards in the range  $y^+ \approx 13 - 20$ . This behaviour is consistent with the inclination of the  $\widetilde{u''u''}^+$  contours in Figure 2.11, the rise following a region of high, lingering Stokes strain, and the fall driven by a concurrence of a rapidly changing Stokes strain in the upper part of the viscous sublayer and high near-wall skewness.

Phase-space contour maps for three components of the enstrophy and their respective productions, all at

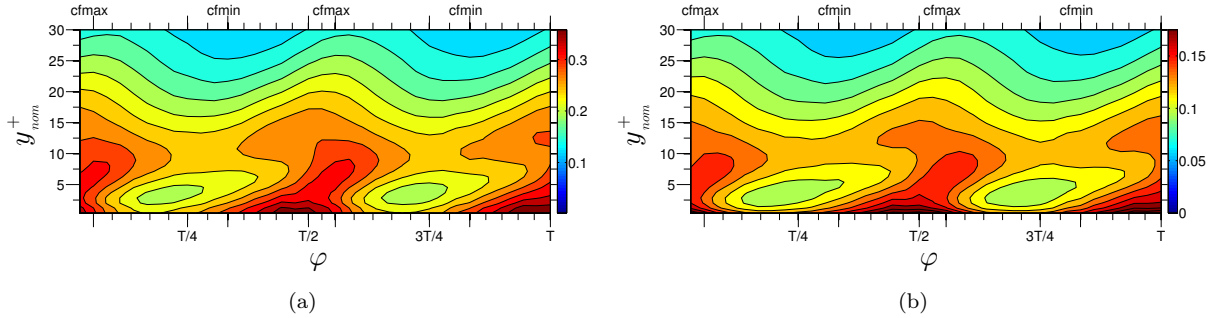


Figure 2.17: Phase variation of : (a) turbulence-energy dissipation ( $\varepsilon_{ii}$ ), (b) enstrophy ( $\widetilde{\omega''_i \omega''_i}$ ).

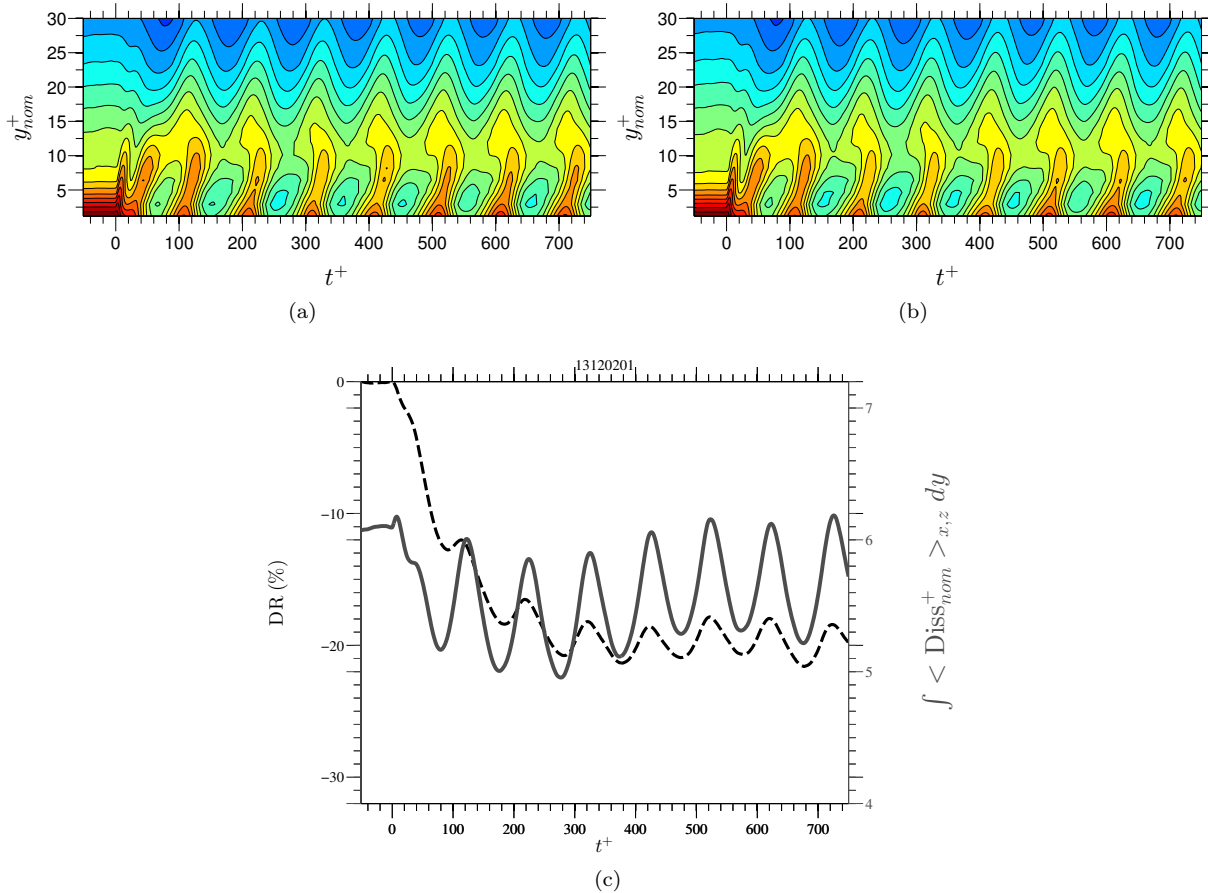


Figure 2.18: Temporal variation of (a) dissipation, (b) enstrophy during the transient phase, at  $T^+ = 200$  and (c) skin friction (dashed line) and y-wise integrated dissipation rate (solid line).

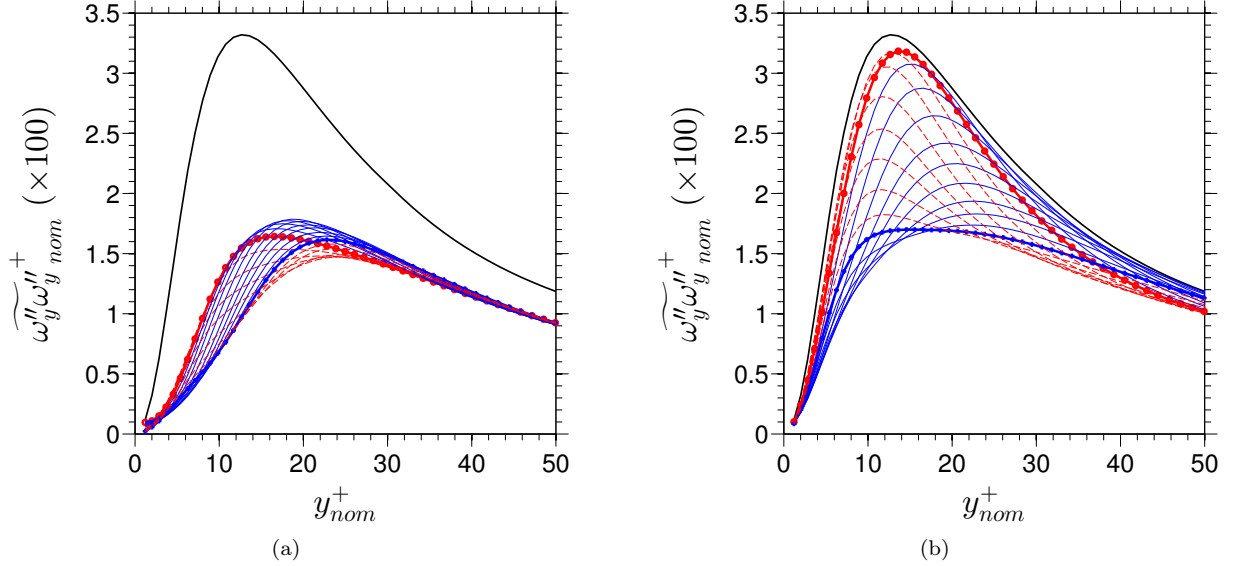


Figure 2.19: Phase-wise variations of the wall-normal component of the enstrophy at (a)  $T^+ = 100$  and (b) at  $T^+ = 200$ . Solid (red) lines with solid symbols correspond to the maximum skin-friction phase value; solid (blue) lines with solid symbols correspond to minimum skin-friction phase value; solid (black) lines relate to the unactuated flow; thin lines identify intermediate phases.

$T^+ = 200$ , are shown in Figure 2.20. To support the discussion to follow, the equation for the enstrophy and simplified forms of the equations for its three components are given below. The simplification amounts to the insertion of the streamwise and Stokes strains into the components of the rotation vector  $\Omega_i$  and the lumping of terms not including the mean-strain into the additive fragments  $T_{xx}$ ,  $T_{yy}$  and  $T_{zz}$ . Thus, the enstrophy equation is governed by:

$$\begin{aligned} \frac{\partial \widetilde{\omega}_i'' \omega_i''}{\partial t} &= -\widetilde{u}_j'' \widetilde{\omega}_i'' \frac{\partial \widetilde{\Omega}_i}{\partial x_j} + \widetilde{\omega}_i'' \widetilde{\omega}_j'' \frac{\partial \widetilde{U}_i}{\partial x_j} + \widetilde{\omega}_i'' \frac{\partial u_i''}{\partial x_j} \widetilde{\Omega}_j \\ &\quad + \widetilde{\omega}_i'' \widetilde{\omega}_j'' \frac{\partial u_i''}{\partial x_j} - \frac{1}{2} \frac{\partial (u_j \widetilde{\omega}_i'' \omega_i'')}{\partial x_j} + \frac{\nu}{2} \frac{\partial^2 \widetilde{\omega}_i'' \omega_i''}{\partial x_j \partial x_j} - \nu \frac{\partial \widetilde{\omega}_i''}{\partial x_j} \frac{\partial \widetilde{\omega}_i''}{\partial x_j} \end{aligned} \quad (2.6)$$

with  $\widetilde{\Omega}_i = [\frac{\partial \widetilde{W}}{\partial y}, 0, -\frac{\partial \widetilde{U}}{\partial y}]$ . The equations for the enstrophy components arise as:

$x$ -component:

$$\begin{aligned} \frac{\partial \widetilde{\omega}_x'' \omega_x''}{\partial t} &= -\widetilde{v}'' \widetilde{\omega}_x'' \frac{\partial^2 \widetilde{W}}{\partial y^2} + \widetilde{\omega}_x'' \widetilde{\omega}_y'' \frac{\partial \widetilde{U}}{\partial y} + \widetilde{\omega}_x'' \frac{\partial u''}{\partial x} \frac{\partial \widetilde{W}}{\partial y} - \widetilde{\omega}_x'' \frac{\partial u}{\partial z} \frac{\partial \widetilde{U}}{\partial y} + T_{xx} \\ &= -\omega_x'' \frac{\partial v'' \frac{\partial \widetilde{W}}{\partial y}}{\partial y} - \omega_x'' \frac{\partial w}{\partial z} \frac{\partial \widetilde{W}}{\partial y} - \omega_x'' \frac{\partial w}{\partial x} \frac{\partial \widetilde{U}}{\partial y} + T_{xx} \end{aligned} \quad (2.7)$$

$y$ -component:

$$\frac{\partial \widetilde{\omega}_y'' \omega_y''}{\partial t} = \widetilde{\omega}_y'' \frac{\partial v''}{\partial x} \frac{\partial \widetilde{W}}{\partial y} - \widetilde{\omega}_y'' \frac{\partial v''}{\partial z} \frac{\partial \widetilde{U}}{\partial y} + T_{yy} \quad (2.8)$$

$z$ -component:

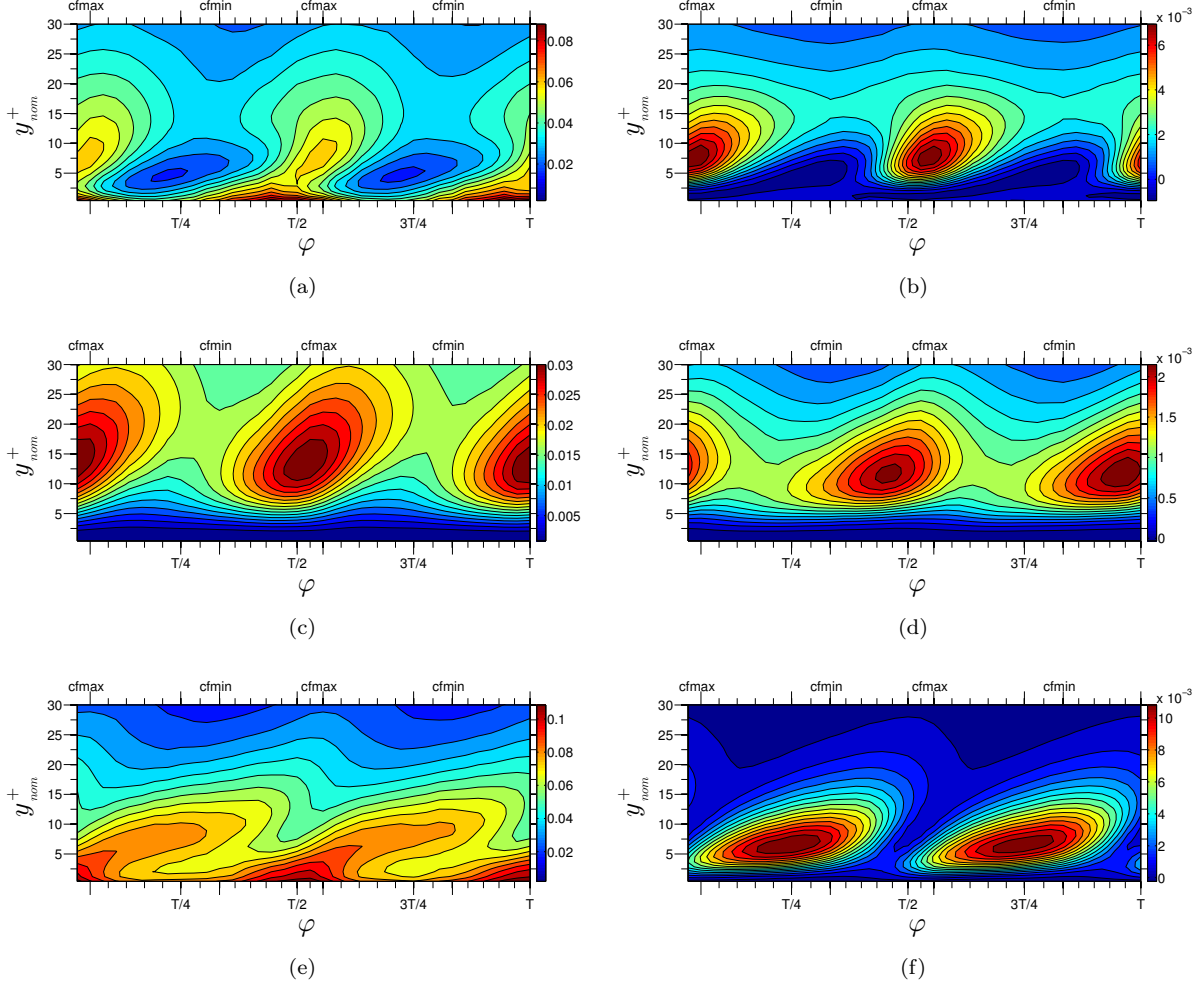


Figure 2.20: Phase variations of the enstrophy components (left columns) and their production rates (right columns): (a) and (b)  $x$ -component; (c) and (d)  $y$ -component; (e) and (f)  $z$ -component.

$$\begin{aligned}
 \frac{\partial \widetilde{\omega_z'' \omega_z''}}{\partial t} &= \widetilde{v'' \omega_z''} \frac{\partial^2 \widetilde{U}}{\partial y^2} + \widetilde{\omega_z'' \omega_y''} \frac{\partial \widetilde{W}}{\partial y} + \widetilde{\omega_z''} \frac{\partial \widetilde{w''}}{\partial x} \frac{\partial \widetilde{W}}{\partial y} - \widetilde{\omega_z''} \frac{\partial \widetilde{w''}}{\partial z} \frac{\partial \widetilde{U}}{\partial y} + T_{zz} \\
 &= \widetilde{\omega_z''} \frac{\partial v''}{\partial y} \frac{\partial \widetilde{U}}{\partial y} + \widetilde{\omega_z''} \frac{\partial u''}{\partial x} \frac{\partial \widetilde{U}}{\partial y} + \widetilde{\omega_z''} \frac{\partial u''}{\partial z} \frac{\partial \widetilde{W}}{\partial y} + T_{zz}
 \end{aligned} \tag{2.9}$$

Phase-averaged budgets (not included), representing equations 2.7, 2.8 and 2.9 and featuring most contributions explicitly, show that the major contributions outside the immediate near-wall region,  $y^+ > 5$ , are mean-strain production and viscous destruction. Hence, production fluctuations are primarily responsible for fluctuations in the enstrophy components.

A first observation derived from Figure 2.20 is that the enstrophy-production rates are well correlated with the respective enstrophy components themselves. Exceptions to this correspondence relate to thin areas very close to the wall in which the link between enstrophy and the high near-wall dissipation governs the former. Second, the streamwise component drops during the drag-reduction phase, while it rises when the drag and streak strength increase. This accords with expectations, as the phases of low streamwise enstrophy go hand-in-hand with low wall-normal (and spanwise) motions, and hence low wall-normal mixing of streamwise momentum. Third, consistent with low/high streamwise enstrophy are corresponding low/high wall-normal enstrophy levels of  $\widetilde{\omega_y'' \omega_y''}$ . As noted earlier, this component is indicative of the decay and regeneration of the streaks during the actuation period. The fact that this component is relatively low (though fluctuating

strongly) is due to the substantial spanwise distances, of order 100 wall units, separating the streak. Here too, the rise and fall of both production and enstrophy are well correlated. Finally, the spanwise component features, unexpectedly at first sight, a rise in the production rate in the region in which the other components show a decline. In order to gain insight into the origins of this “anomalous result”, it is necessary to examine individual terms in equations 2.8 and 2.9 by reference to the strain and skewness map given in Figure 2.12. The gradient,  $\partial\theta/\partial y$ , can be expected to play an important role in the enstrophy equations, because it represents the degree of tilting of vortices by the combined action of the streamwise and Stokes strain. To identify the origin of the unexpected spanwise enstrophy generation, the strain-related production terms are re-written as follows:

$$\begin{aligned} \widetilde{\omega_y''} \frac{\partial v''}{\partial x} \frac{\partial \widetilde{W}}{\partial y} - \widetilde{\omega_y''} \frac{\partial v''}{\partial z} \frac{\partial \widetilde{U}}{\partial y} &= \\ \underbrace{\widetilde{\omega_y''} \frac{\partial v''}{\partial x} \sin \theta \frac{\partial \widetilde{U}_n}{\partial y}}_{-\omega_y'' \frac{\partial v''}{\partial z} \cos \theta \frac{\partial \widetilde{U}_n}{\partial y}} + \underbrace{\widetilde{\omega_y''} \frac{\partial v''}{\partial x} \widetilde{U}_n \cos \theta \frac{\partial \theta}{\partial y}}_{\widetilde{\omega_y''} \frac{\partial v''}{\partial z} \widetilde{U}_n \sin \theta \frac{\partial \theta}{\partial y}} &= \end{aligned} \quad (2.10)$$

Figure 2.21(a)

$$\begin{aligned} \widetilde{\omega_z''} \frac{\partial u''}{\partial z} \frac{\partial \widetilde{W}}{\partial y} + \widetilde{\omega_z''} \frac{\partial u''}{\partial x} \frac{\partial \widetilde{U}}{\partial y} &= \\ \underbrace{\widetilde{\omega_z''} \frac{\partial u''}{\partial z} \sin \theta \frac{\partial \widetilde{U}_n}{\partial y}}_{+\omega_z'' \frac{\partial u''}{\partial x} \cos \theta \frac{\partial \widetilde{U}_n}{\partial y}} + \underbrace{\widetilde{\omega_z''} \frac{\partial u''}{\partial z} \widetilde{U}_n \cos \theta \frac{\partial \theta}{\partial y}}_{\widetilde{\omega_z''} \frac{\partial u''}{\partial x} \widetilde{U}_n \sin \theta \frac{\partial \theta}{\partial y}} &= \end{aligned} \quad (2.11)$$

Figure 2.21(b)

The terms proportional to the strain magnitude,  $\partial \widetilde{U}_n / \partial y$ , may be interpreted as vortex-stretching terms, while the skewness  $\partial \theta / \partial y$  dictates the vortex-tilting process. An examination of all fragments in equations 2.10 and 2.11, not detailed herein, shows that the dominant terms are the third one in equation 2.10 and the second one in equation 2.11. Only these two fragments are given in Figure 2.21. Some other terms make non-negligible contributions too, but the present discussion is intended to focus only on the principal processes. Figure 2.21(a) shows that maxima occur at  $y^+ \approx 15$  at the phase-wise locations at which  $C_f$  peaks; this is in agreement with the total production of  $\widetilde{\omega_y''} \widetilde{\omega_y''}$ , which is dominated by the fragment under consideration. These maxima reflect production by streamwise strain in the virtual absence of skewness. Near the wall, on the other hand, there are regions of very low production, and these are also regions of very high skewness. Here,  $\widetilde{\omega_y''} \widetilde{\omega_y''}$  declines, and this is linked to the high levels of  $\widetilde{\omega_z''} \widetilde{\omega_z''}$  production, seen in Figure 2.21(b), and due to the high level of skewness. In these regions, the Stokes strain is very high, and the tilting associated with this strain transfers enstrophy from the wall-normal component to the spanwise component, which is then amplified by the high skewness. Analogous interactions also occur between  $\widetilde{\omega_x''} \widetilde{\omega_x''}$  and  $\widetilde{\omega_z''} \widetilde{\omega_z''}$ . The transfer and amplification process identified above gives rise to  $\widetilde{\omega_z''} \widetilde{\omega_z''}$  production peaks that coincide with the locations  $C_{f,min}$  rather than  $C_{f,max}$ , which then leads to the field shown in Figure 2.20(f).

## 2.5 Hysteresis and Skewness: New Insights into Drag Reduction

The previous parts were primarily directed towards a clarification of the drag-reduction mechanisms, and thus entailed an examination of the phase-averaged fields of stochastic stresses, their budgets and enstrophy components at  $T^+ = 200$ . Skin-friction fluctuations were found to correlate closely with the streamwise turbulence intensity and its production at the wall-normal region in which the streaks have the highest intensity. This correspondence also applies to the transient phase, ahead of the low-drag state. The present results display features that comply with the scenario described by Touber and Leschziner 2012 – namely,

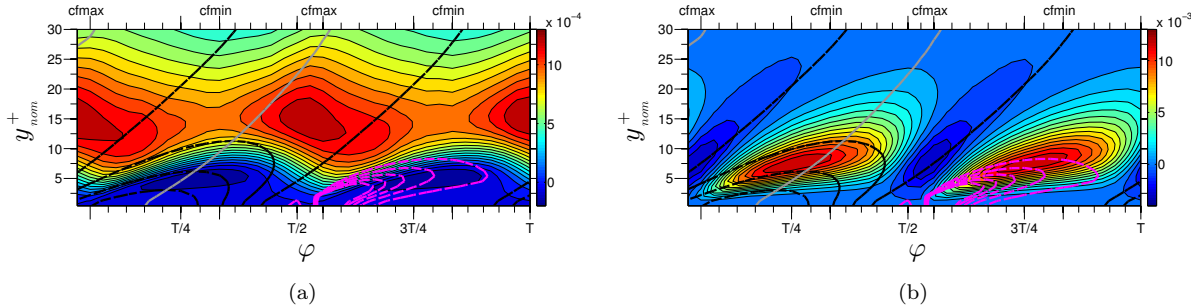


Figure 2.21: Dominant terms in the equations for the  $y$ - and  $z$ -components of the enstrophy: (a) third term in equation 2.10; (b) second term in equation 2.11

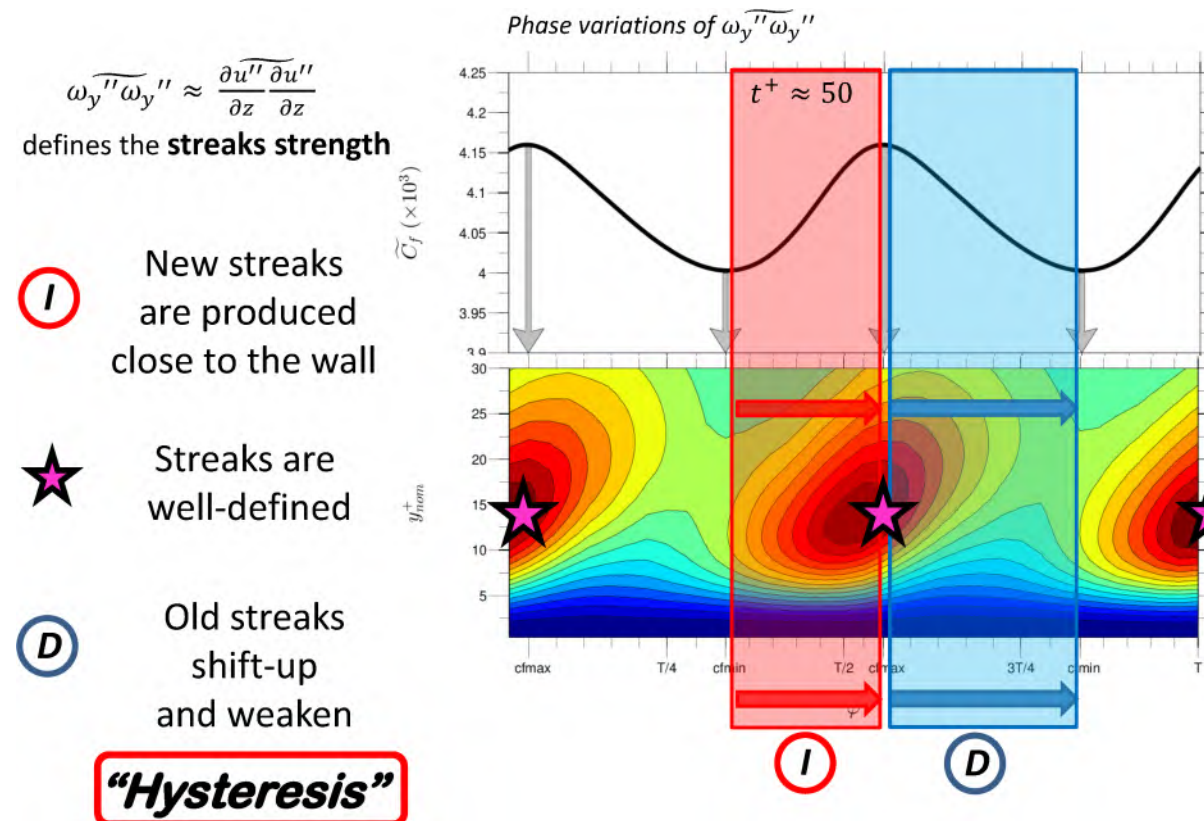


Figure 2.22: Life cycle of a streak exposed to a spanwise oscillating wall motion and associated drag modification.

that phase intervals of high streak strength and skin-friction increase are associated with high, slowly varying Stokes strain at the level at which the streaks reside, while phase intervals of skin-friction decline and low streak strength are associated with rapidly varying, low Stokes strain at the same level. Coupled with results derived from GOP theory, this scenario goes some way towards explaining the drag-reduction process. However, if attention is focused on the region closer to the wall, this turns out to be only one leg of a two-legged set of interactions. Specifically, the examination of turbulence properties in phase/wall-normal-space diagrams reveals the following features, thus leading to the following related conclusions:

1. The phase-wise variations in drag and turbulence within any one actuation cycle display a distinctive hysteresis, wherein the drag-reduction phase extends over a longer proportion of the cycle than the subsequent drag increase. The hysteresis applies to all turbulence properties: their decline and recovery during the actuation cycle proceed along different paths, as illustrated in Figure 2.22.
2. The hysteresis is attributed to the disruptive influence of the near-wall velocity skewness, which dominates only one portion of the actuation cycle, thus introducing a pronounced asymmetry in the structure of the Stokes motion during the cycle. When this skewness is high, the turbulence-generation mechanism near the wall is disrupted, the streaks weaken and this contributes to the decline in drag. When the skewness reduces, turbulence recovers, this recovery occurring predominantly as a consequence of the elevated, lingering Stokes strain in the upper portion of the viscous sublayer. This recovery is inhibited if the period available to this phase is lower than the streak-generation time scale. In this case, the overall effect is a reduction in drag towards an equilibrium low-drag state.
3. The budgets show that the variations in the Reynolds stresses during both drag-decrease and increase phases are driven primarily by fluctuations in production which are balanced mainly by pressure-velocity interaction. In contrast, the dissipation plays a subordinate role. Indeed, in the case of the shear stress, the dissipation is insignificant throughout the actuation cycle. This leads to the conclusion that rising dissipation is not the cause of drag reduction.
4. Fluctuations in dissipation and enstrophy correspond closely. Both are observed to decline when the drag reduces and to rise when the drag increases. This applies not only to fluctuations around the low-drag state, but also to the transient phase.
5. The phase-wise variations in the enstrophy components show that the streamwise and wall-normal components vary in harmony with the skin-friction and turbulent-stress variations. Both decline when turbulence is weakened by the Stokes strain and both increase when the Stokes strain is weak. Peaks in the wall-normal enstrophy components correspond to high streak strength due to streak amplification. The spanwise enstrophy component shows a behaviour that is opposite to that of the other two components. This is explained by the fact that the Stokes strain (or rather skewing) causes tilting in the vortices, which then translates to a transfer of enstrophy between the wall-normal and the spanwise components.

While numerous past computational studies have focused primarily on quantifying drag reduction margins and identifying optimal actuation parameters, a select few have in-depth explored the fundamental drag reduction mechanisms. Notably, studies by Skote 2012, Touber and Leschziner 2012 and Ricco et al. 2012 have shifted attention toward these interactions. The latter two are especially noteworthy for examining unsteady processes to reveal how actuation drives the drag toward a quasi-steady minimum state. However, they reference very different aspects of unsteadiness. Ricco et al. 2012 consider the transient drag decline after suddenly imposing spatially-homogeneous oscillations in a channel at  $Re_\tau \approx 200$ . In contrast, the previous sections studies focused on phase-averaged fluctuations in drag and properties in channel flow with non-optimal wall oscillations. Here, the low-drag state has substantial periodic fluctuations around a reduced time-average.

Both approaches utilise various statistical indicators, especially enstrophy, to identify driving mechanisms. Remarkably, they arrive at very different conclusions: Ricco et al. 2012 argue the drag decline is driven by increased enstrophy and dissipation in the initial transient phase. Our results suggest the opposite - drag decreases and increases with declining and rising enstrophy/dissipation levels, respectively. Instead, our results indicate drag reduction is primarily driven by suppressed strain-induced streak generation from rapid directional changes in strain at the upper viscous sublayer, coupled with high velocity-vector skewness in the lower Stokes layer.

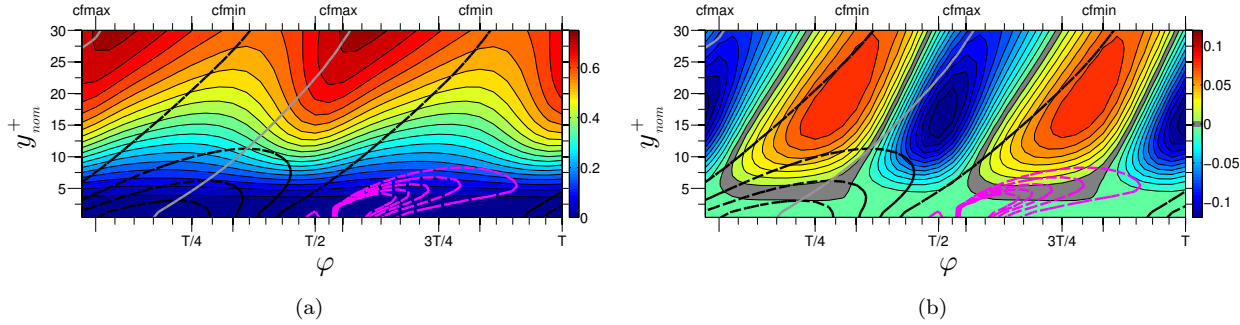


Figure 2.23: Phase-wise and wall-normal variations of (a) the shear stress ( $\widetilde{u''v''}^+$ ), and (b) ( $\widetilde{u''v''}^+ - \widetilde{u''v''}^-$ ). Both wall distance and shear stress are normalised with the friction velocity in the baseline flow. Dashed black lines: loci of 75%, 50%, 25% and 0% of the maximum absolute value of the Stokes strain; grey lines: locus of maximum Stokes strain; continuous black lines: loci of zero Stokes strain; dashed magenta lines: contours of skewness.

To address these “conflicting” results and elucidate the mechanisms involved, the investigation in the next section focuses on the effects of unsteady Stokes strain on the turbulent vorticity field, specifically the phase-averaged stochastic enstrophy components and key terms in the transport equations governing these components.

## 2.6 The Role of Turbulent Vorticity Fluctuations and Their Correlations

### 2.6.1 The Shear Stress and Vorticity Transport

The starting point of the path that links the skin-friction variation to the turbulent vorticity is to express the phase-averaged shear-stress gradient in terms of correlations involving the stochastic vorticity fluctuations. Subject to streamwise and spanwise homogeneity, the relevant relationship is [tennekes\\_first\\_1972](#); [Davidson 2003](#)

$$-\frac{\partial \widetilde{u''v''}^+}{\partial y} = \widetilde{v''\omega_z''}^+ - \widetilde{w''\omega_y''}^+ \quad (2.12)$$

The phase-wise variation of the shear-stress derivative (the left-hand side of equation 2.12), the difference between the two correlations  $\widetilde{v''\omega_z''}^+$  and  $\widetilde{w''\omega_y''}^+$  (the right-hand side of equation 2.12), the two correlations separately, the wall-normal vorticity component  $\widetilde{\omega_y''\omega_y''}^+$  and the auto-correlation  $\widetilde{w''w''}^+$  are given in Figures 2.24 (a)-(f), respectively, the first two of which serving to demonstrate the compatibility between equation 2.12 and the DNS data. The plots include, as in the case of Figure 2.23, contours of the Stokes strain and skewness. In common with the shear-stress itself, its gradient increases with phase, reaching a maximum when the skin-friction peaks (note that the gradient of  $-\widetilde{u''v''}^+$  is positive and only changes sign at  $y^+ \approx 50$ ). At this point, the viscous sublayer is thinnest, and the drag thus highest. Correspondingly, the shear-stress gradient reaches its minimum at the location of minimum skin friction. The phase-wise variation in the gradient is highest at around  $y^+ \approx 10$ , the location around which the curvature of the mean velocity is also highest, and which borders the layer in which the streamwise turbulent intensity associated with the streaks reaches its maximum. This is also roughly the location at which the total shear strain (i.e. the magnitude of the streamwise-strain and Stokes-strain) and its rate of change, associated with the periodic Stokes strain, has the largest effect on the streaks. Very close to the wall, at  $y^+ < 5$ , the steep reduction in shear-stress gradient is due to the asymptotically quadratic decline in this gradient as the wall is approached, in combination with the high levels of skewness during the drag-reduction phases.

Of the two processes in equation 2.12,  $w''\omega_y''^+$  is strongly dominant. A similar observation was made by Xu et al. 2007, although this applies to time-averaged statistics for a channel flow subjected to a drag-reducing steady streamwise body force (*streaming*), which is a very different scenario to the present one. Figures

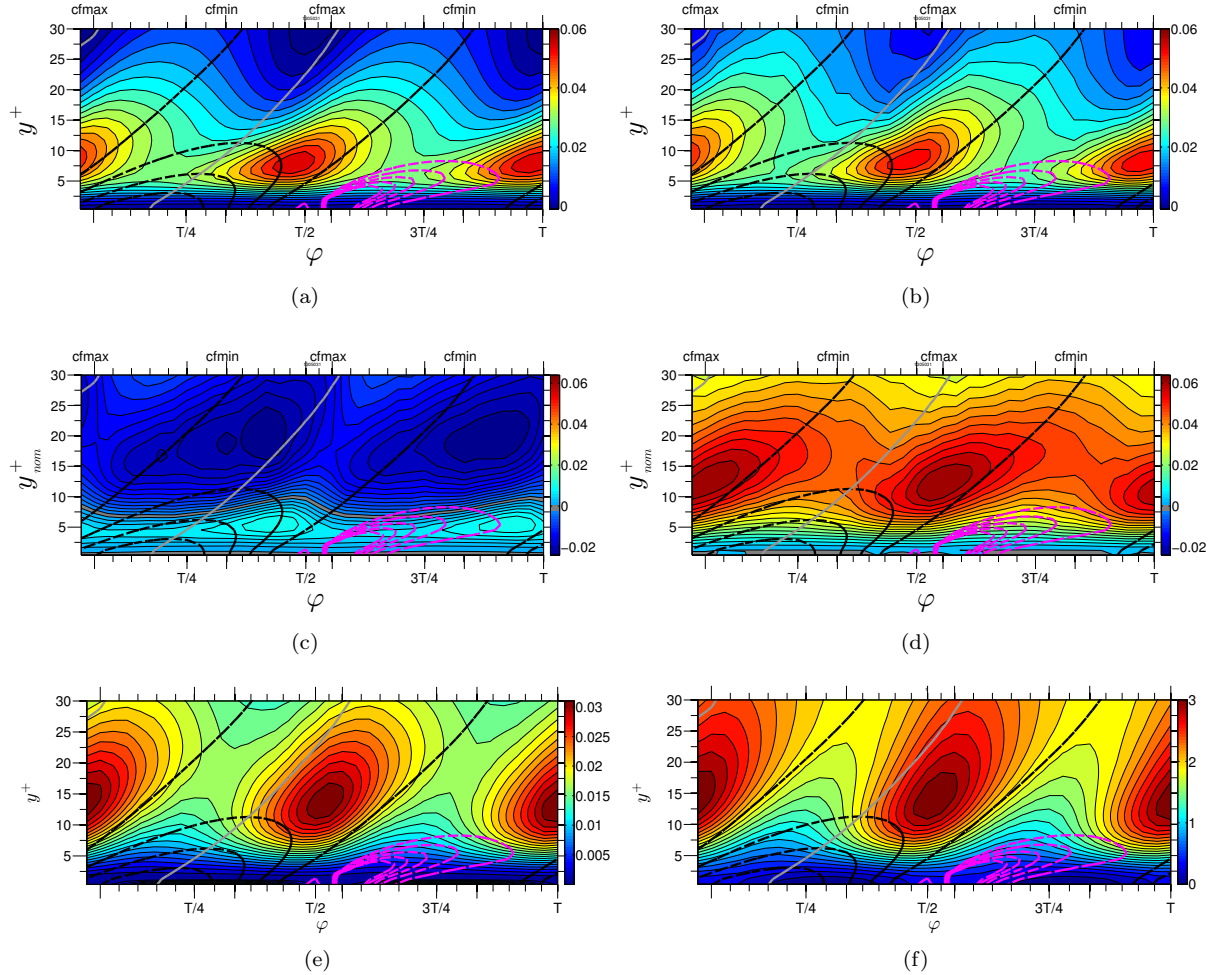


Figure 2.24: Phase-wise variations of (a)  $-\frac{\partial \widetilde{u''v''^+}}{\partial y}$ ; (b) difference of the right-hand terms of equation 2.12 ; (c)  $\widetilde{v''\omega_z''^+}$ ; (d)  $-\widetilde{w''\omega_y''^+}$ , (e)  $\widetilde{\omega_y''\omega_y''^+}$  and (f)  $\widetilde{w''w''^+}$

2.24(e) and 2.24(f) show that the rise and fall in the correlation  $\widetilde{w''\omega_y''^+}$  go hand-in-hand with corresponding variations in  $\widetilde{\omega_y''\omega_y''^+}$  and  $\widetilde{w''w''^+}$ . Correspondingly, the correlation coefficient of  $\widetilde{w''\omega_y''^+}$ , not shown, is found to vary only modestly (around the level 0.3) in the layer  $y^+ = 10 - 15$ , and to peak a little after the  $C_{fmax}$  locations. This behaviour suggests that the phase-wise variations in  $\widetilde{w''\omega_y''^+}$  are driven primarily by the simultaneous increase or decrease in  $\widetilde{w''w''^+}$  and  $\widetilde{\omega_y''\omega_y''^+}$ .

It is readily shown that a combination of equation 2.12 with the  $y$ -wise derivative of the streamwise-momentum equation (with pressure gradient ignored) results in the following equation governing the phase-averaged spanwise vorticity, here being simply the streamwise shear strain:

$$\frac{\partial \widetilde{\Omega_z^+}}{\partial \varphi} = \frac{1}{Re_\tau} \frac{\partial^2 \widetilde{\Omega_z^+}}{\partial y^2} + \frac{\partial \widetilde{w''\omega_y''^+}}{\partial y} - \frac{\partial \widetilde{v''\omega_z''^+}}{\partial y} \quad (2.13)$$

The temporal (phase-wise) variation of the streamwise shear strain is therefore dictated by the response of the gradients of the turbulent correlations  $\widetilde{v''\omega_z''^+}$  and  $\widetilde{w''\omega_y''^+}$  to the unsteady Stokes strain. These gradients may be interpreted, respectively, as a wall-normal turbulent transport of spanwise vorticity and a transfer of wall-normal vorticity to the spanwise component by vortex stretching, caused by the distorting influence of spanwise velocity fluctuations (Jiménez and Pinelli 1999, Xu et al. 2007). A conceptual representation of both processes is given in Figure 2.25.

Figure 2.26 shows the wall-normal gradients of  $-\widetilde{v''\omega_z''^+}$  and  $\widetilde{w''\omega_y''^+}$  – separately, (b) and (c), as well as

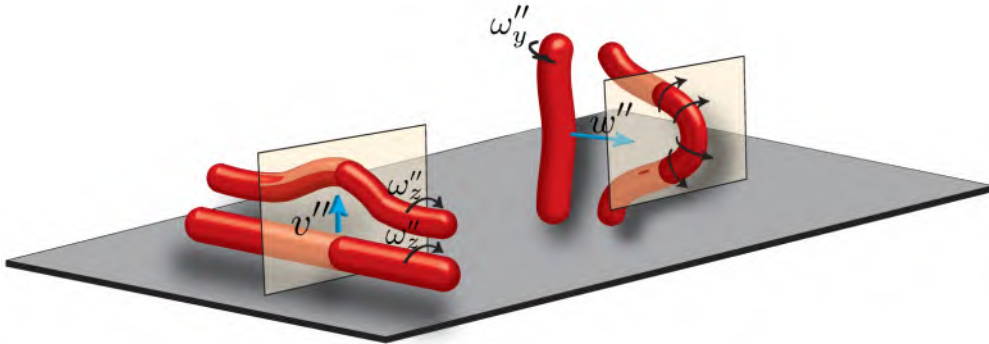


Figure 2.25: Schematic of the wall-normal turbulent transport of spanwise turbulent vorticity and of the transfer of wall-normal vorticity to the spanwise component by vortex stretching, expressed by the two correlations in equation 2.13.

their sum (a) – in equation 2.13, and the sum of all terms on the right-hand-side of the equation relative to the left-hand side, (d) and (e), respectively. As in the case of Figure 2.24, the comparison between plots (d) and (e) serves to demonstrate the compatibility of the DNS data with equation 2.13. In common with equation 2.12, the term containing the vortex-stretching correlation  $\widetilde{w''\omega_y''}^+$ , is seen to dominate in the layer  $y^+ \approx 10 - 15$ . Although the gradient of  $\widetilde{v''\omega_z''}^+$  is also significant, its influence is confined to the near-wall layer  $y^+ = 5 - 10$ , where the skewness is high. Moreover, its phase-wise variation is relatively weak, and this suggests that its role in the rise and fall of the mean streamwise shear strain, and hence in the drag, is subordinate to that of the gradient of  $\widetilde{w''\omega_y''}^+$ . This is also a conclusion derived from Figure 2.26(a).

If attention is directed at the layer  $y^+ \approx 10 - 15$ , within which the turbulent correlations begin to dominate over the viscous term, it is observed in Figure 2.26(d) that  $\partial\widetilde{\Omega_z}^+/\partial\varphi$  is negative during the drag-reduction phase. Hence, the mean spanwise vorticity decreases with phase – i.e., the mean streamwise shear strain increases. Near the wall, however, the position is reversed: during the drag-reduction phase, the spanwise vorticity increases and the strain diminishes, the latter reaching a minimum as  $\frac{\partial\widetilde{\Omega_z}^+}{\partial\varphi} = 0$  at the location  $Cf_{min}$ . The combination of these two responses thus amounts to a thickening of the viscous sublayer and an upward shift in the high velocity-curvature region as the drag decreases. The reverse occurs as the drag increases towards the  $Cf_{max}$  location.

The above observation on the dominant role of vortex-stretching is consistent with the analysis of Jiménez and Pinelli 1999 on the streak-formation mechanisms in simple (uncontrolled) channel flow. They consider the streamwise-averaged form of the equation for the wall-normal enstrophy:

$$\frac{\partial\overline{\Omega_y}^x}{\partial t} = \frac{1}{Re} \left[ \Delta\overline{\Omega_y}^x - Re \frac{\partial}{\partial z} \left( \overline{w'\omega_y'}^x - \overline{v'\omega_z'}^x \right) \right] \quad (2.14)$$

The consequence of performing streamwise averaging only is that the spanwise derivative of the correlations on the right-hand side of equation 2.14 is non-zero, indicating the process by which the wall-normal vorticity is generated, hence how the streak strength evolves. In a sense, this process is akin to streak-conditional averaging, because the streaks are long and thin. Jiménez and Pinelli 1999 argue that the most influential term is  $\partial\overline{v'\omega_z'}^x/\partial z$ , which represents the effects of the vortex-stretching process on  $\overline{\Omega_y}^x$ , analogous to the effect of  $\partial\widetilde{w''\omega_y''}^+/dy$  on  $\widetilde{\Omega_z}^+$  in equation 2.13. In both cases, therefore, vortex stretching is the primary mechanism responsible for elevating the respective vorticity components.

The central role played by the wall-normal-vorticity fluctuations  $\omega_y''$  in the phase-wise drag variations, via the vortex-stretching process  $\widetilde{w''\omega_y''}^+$ , provides motivation for examining the dependence of the wall-normal-enstrophy component on the Stokes strain. As  $\omega_y''$  is dominated by the spanwise derivative of streamwise-velocity fluctuations  $\frac{\partial u''}{\partial z}$ , reflecting the pronounced streaky nature of the near-wall layer, the implication is that a combination of low levels of  $\omega_y''$  (i.e. low streak strength) and low spanwise velocity fluctuations, the latter occurring during phases of low and rapidly changing Stokes strain in the layer around  $y^+ \approx 10 - 15$ , are directly linked to the shear stress and hence drag decrease. Conversely, an amplification of  $\omega_y''$  and

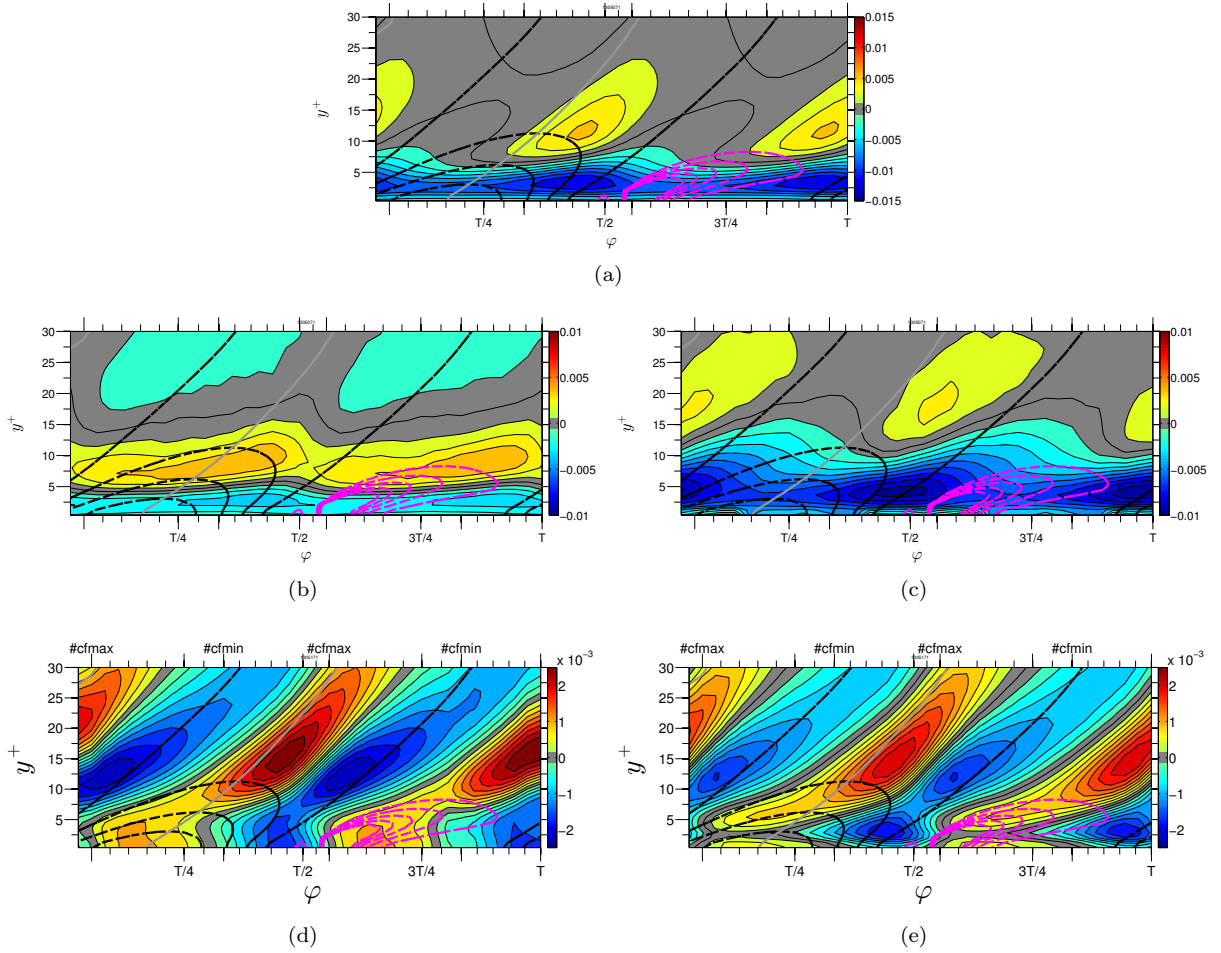


Figure 2.26: Phase-wise variations of (a) the sum  $\frac{\partial \widetilde{w''\omega_y''}^+}{\partial y} - \frac{\partial \widetilde{v''\omega_z''}^+}{\partial y}$  in equation 2.13, (b)  $-\frac{\partial \widetilde{v''\omega_z''}^+}{\partial y}$ , (c)  $+\frac{\partial \widetilde{w''\omega_y''}^+}{\partial y}$ , (d) the left-hand side of equation 2.13 and (e) the sum of all right-hand-side terms in equation 2.13.

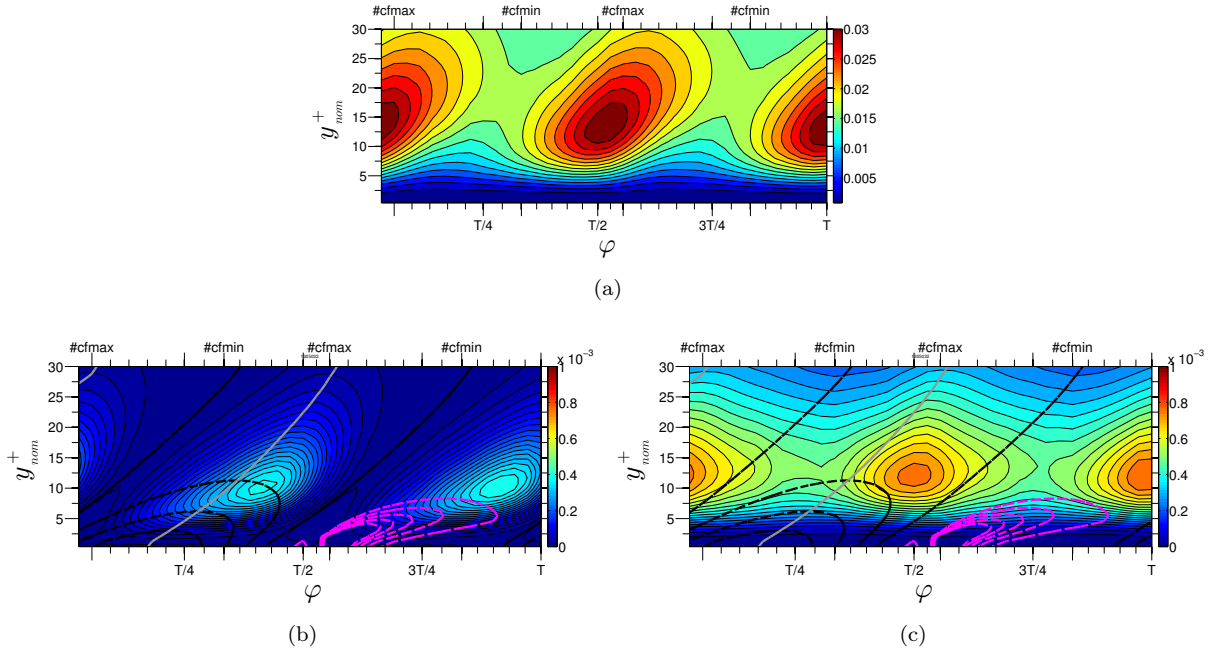


Figure 2.27: Phase-wise variations in (a)  $\widetilde{\omega_y'' \omega_y''}^+$  and (b,c) its two strain-related production terms, as identified in equation 2.15

the streaks, in combination with high spanwise-velocity fluctuations, is associated with drag increase. As regards the spanwise-vorticity fluctuations  $\omega_z''$ , these appear to be particularly important and prominent in the immediate near-wall region, and this suggests the need to also examine the processes affecting the spanwise-enstrophy component. Finally, as the Stokes strain is expected to cause strong periodic spanwise-directed vortex-stretching and tilting, it is reasonable to assume that the Stokes strain will have a major effect on the spanwise-vorticity fluctuations, and that there will be a significant interaction between the wall-normal and spanwise components. These issues are addressed in the following two sections.

## 2.6.2 Wall-Normal-Enstrophy Component

The investigations discussed in the first part highlighted, through phase-averaged Reynolds-stress budgets, that phase variations of turbulence are mainly driven by production fluctuations. This suggests that the discussion of enstrophy variations needs to focus on the role of terms containing the streamwise and spanwise strains. With only such terms given explicitly, the equation for the wall-normal enstrophy component arises as:

$$\frac{\partial \widetilde{\omega_y'' \omega_y''}^+}{\partial \varphi} = \underbrace{\omega_y'' \frac{\partial v''}{\partial x}^+}_{\text{Figure 2.27(b)}} \underbrace{\frac{\partial \widetilde{W}^+}{\partial y}^+}_{\text{Figure 2.27(c)}} - \underbrace{\omega_y'' \frac{\partial v''}{\partial z}^+}_{\text{Figure 2.27(b)}} \underbrace{\frac{\partial \widetilde{U}}{\partial y}^+}_{\text{Figure 2.27(c)}} + T_{yy} \quad (2.15)$$

in which all terms containing purely stochastic fluctuations have been collected in the additive fragment  $T_{yy}$ . This choice is not to be understood as suggesting that  $T_{yy}$  is insignificant, if only because enstrophy dissipation is substantial. Rather, it is motivated by the wish to focus on the phase-wise trends in the enstrophy components in relation to the strain-related productions.

The wall-normal-enstrophy component and the two production terms in equation 2.15 are shown in Figures 2.27(a), 2.27(b) and 2.27(c), respectively. Entirely in accord with expectations, this enstrophy component reaches maxima at locations of skin-friction maxima and at a wall-normal distance  $y^+ \approx 15$  where the streaks are most pronounced. Surprisingly, at first sight, the Stokes-strain-driven production is seen to be small. However, this is due to the fact that the Stokes strain is high only close to the wall, where the wall-normal velocity fluctuations are very low. In fact, as emerges upon comparing Figures 2.28(b) and (d), the

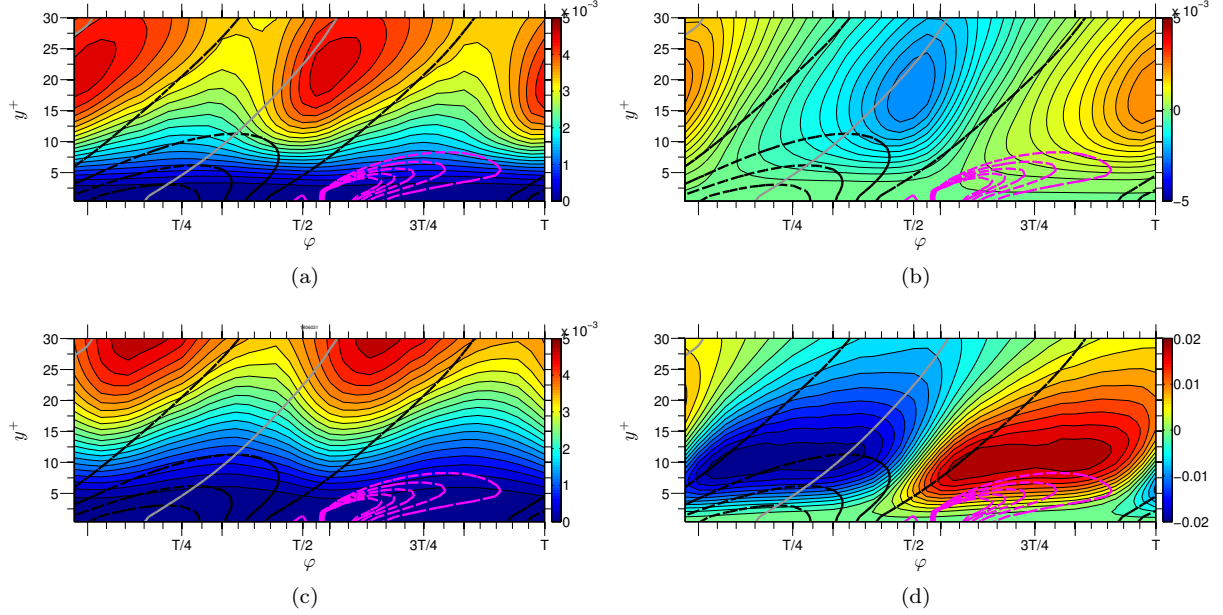


Figure 2.28: Phase-wise variations of (a)  $-\widetilde{\omega_y'' \frac{\partial v''}{\partial z}}^+$  (equation 2.15), (b)  $\widetilde{\omega_y'' \frac{\partial v''}{\partial x}}^+$  (equation 2.15), (c)  $\widetilde{\frac{\partial v''}{\partial z} \frac{\partial v''}{\partial z}}^+$  and (d)  $\widetilde{\omega_z'' \omega_y''}^+$ .

correlation  $\widetilde{\omega_y'' \frac{\partial v''}{\partial x}}^+$  is a small fraction of  $\widetilde{\omega_z'' \omega_y''}^+$ , which signifies that the contribution of  $\frac{\partial v''}{\partial x}$  to  $\omega_z''$  is also insignificant. This was emphatically confirmed by an examination of the auto-correlation of  $\frac{\partial v''}{\partial x}$  relative to  $\frac{\partial u''}{\partial y}$  (not included herein).

In contrast to the lower near-wall layer, the upper portion of the viscosity-affected layer is characterized by a dominance of the streamwise shear strain, low skewness and significantly higher wall-normal velocity fluctuations. Here,  $\partial v''/\partial z$  is significant, its auto-correlation observed (but not shown here) to be around 20% of  $\widetilde{\omega_x'' \omega_x''}^+$  in the layer  $y^+ = 10 - 15$ . Unsurprisingly, therefore,  $\widetilde{\omega_y'' \frac{\partial v''}{\partial z}}^+$  is found to be well correlated with  $\widetilde{\omega_x'' \omega_x''}^+$  (not shown here), although the level of the former is rather low relative to the latter. In addition,  $\widetilde{\omega_y'' \frac{\partial v''}{\partial z}}^+$  is also well correlated with  $\widetilde{\omega_y'' \omega_y''}^+$ , as confirmed upon comparing Figure 2.28(a) with  $\widetilde{\omega_y'' \omega_y''}^+$  in Figure 2.27(a). Hence, all correlations rise in harmony with one another as the drag increases, and all decline as the drag decreases. Finally, the auto-correlation  $\widetilde{\frac{\partial v''}{\partial z} \frac{\partial v''}{\partial z}}^+$ , given in Figure 2.28(c), is also seen to rise and fall together with the other correlations. Consistently, the correlation coefficient of  $\widetilde{\omega_y'' \frac{\partial v''}{\partial z}}^+$  (not included here) varies only weakly with phase. Moreover, the general phase-wise behaviour of  $\widetilde{\omega_y'' \frac{\partial v''}{\partial z}}^+$  accords with the variation of  $\widetilde{\omega_x'' \omega_x''}^+$ , given in Figure 2.20.

The picture thus emerging from the above discussion is that the phase-wise rise and fall in  $\widetilde{\omega_y'' \frac{\partial v''}{\partial z}}^+$ , and hence the generation of  $\widetilde{\omega_y'' \omega_y''}^+$ , is dictated by corresponding – i.e., simultaneous – variations in the two constituents of the correlation. Moreover, the correspondence between  $\widetilde{\omega_y'' \frac{\partial v''}{\partial z}}^+$ ,  $\widetilde{\omega_y'' \omega_y''}^+$  and  $\widetilde{\omega_x'' \omega_x''}^+$  may be argued to reflect the fact that vortex stretching and forward tilting by  $\frac{\partial \tilde{U}}{\partial y}$  tend to intensify  $\omega_x''$  as the streaks strengthen and  $\omega_y''$  increases. Periods in which the drag is declining and is low are characterized by low levels of  $\widetilde{\omega_y'' \omega_y''}^+$ ,  $\widetilde{\omega_y'' \frac{\partial v''}{\partial z}}^+$  and  $\widetilde{\omega_x'' \omega_x''}^+$ . These are phases during which the Stokes strain changes at a rapid rate in the outer layer  $y^+ \approx 10 - 15$ , thus inhibiting streak persistence, and during which near-wall skewness is high in the layer  $y^+ < 8$ , hence intensifying the decline of the near-wall turbulence.

In summary, despite the Stokes strain not appearing explicitly in the primary source term of the wall-normal enstrophy component, it indirectly influences the oscillations in the production term, as illustrated in Figure 2.27(c). This occurs through periodic variations in the correlation that pre-multiplies the high streamwise shear strain, with both fluctuations contributing to the correlation increasing and decreasing in unison. The consequent increase and decrease in the wall-normal enstrophy component within the layer  $y^+ = 10 - 15$  is then directly correlated with fluctuations in the skin friction.

### 2.6.3 Spanwise-Enstrophy Component

To investigate the role of the spanwise vorticity in the correlation  $-\frac{\partial \widetilde{\omega''\omega''_z^+}}{\partial y}$ , shown in Figure 2.26(b), and any relevant interplay between the wall-normal and spanwise-enstrophy components, attention is directed to the equation governing the latter. As in the case of the wall-normal enstrophy equation, that governing  $\widetilde{\omega''\omega''_z^+}$  is written below with only the strain-containing terms given in explicit form:

$$\begin{aligned} \frac{\partial \widetilde{\omega''\omega''_z^+}}{\partial \varphi} &= \widetilde{v''\omega''_z^+} \frac{\partial^2 \widetilde{U}^+}{\partial y^2} + \widetilde{\omega''\omega''_y^+} \frac{\partial \widetilde{W}^+}{\partial y} + \widetilde{\omega''_z \frac{\partial w''^+}{\partial x}} \frac{\partial \widetilde{W}^+}{\partial y} - \widetilde{\omega''_z \frac{\partial w''^+}{\partial z}} \frac{\partial \widetilde{U}^+}{\partial y} + T_{zz} \\ &= \underbrace{\omega''_z \frac{\partial v'' \frac{\partial \widetilde{U}}{\partial y}}{\partial y}}_{\text{Figure 2.29(b)}} + \underbrace{\omega''_z \frac{\partial u''^+}{\partial x} \frac{\partial \widetilde{U}^+}{\partial y}}_{\text{Figure 2.29(c)}} + \underbrace{\omega''_z \frac{\partial u''^+}{\partial z} \frac{\partial \widetilde{W}^+}{\partial y}}_{\text{Figure 2.29(d)}} + T_{zz} \end{aligned} \quad (2.16)$$

Results relating to this equation are shown in Figure 2.29. First, the variation of this enstrophy component itself, as extracted from the DNS data, is conveyed by Figure 2.29(a). The most interesting feature in this plot, when compared to Figure 2.27(a), is that high levels of  $\widetilde{\omega''\omega''_z^+}$  go hand-in-hand with low levels of  $\widetilde{\omega''_y\omega''_y^+}$ , and vice-versa. It is recalled that low levels of wall-normal enstrophy (and drag reduction) coincide with strong Stokes shearing and skewness close to the wall. This is precisely the phase during which the spanwise enstrophy rises in the layer  $y^+ = 5 - 10$ . In fact, regions of elevated  $\widetilde{\omega''\omega''_z^+}$  coincide, broadly, with regions of high skewness. An intuitive concept that might explains this elevation is that the strong vortex tilting and stretching near the wall provoked by the Stokes strain leads to an amplification of the spanwise enstrophy, whilst the wall-normal enstrophy component, and thus streaks, are weakened by reduced streamwise-shear-strain production in equation 2.15.

The two terms associated linearly with the Stokes and streamwise shear strain are given in Figure 2.29(d) and 2.29(c), respectively. This comparison demonstrates the dominance of the term associated with the Stokes strain, its magnitude being of order 5 times higher than the term associated with the streamwise shear strain. In contrast to  $\widetilde{\omega''\omega''_y^+}$ , the spanwise enstrophy component  $\widetilde{\omega''\omega''_z^+}$  is high when the skewness is high. This provides an indication that Stokes-strain-driven stretching and tilting is indeed responsible for the rise in  $\widetilde{\omega''\omega''_z^+}$ .

Additional insight may be gained upon an examination of the correlation  $\widetilde{\omega''_z \frac{\partial u''^+}{\partial z}}$  pre-multiplying the Stokes strain in equation 2.16. This is shown in Figure 2.30, together with a map of the correlation  $\widetilde{\omega''_z \omega''_y^+}$ . The fact that  $\widetilde{\omega''_z \omega''_y^+}$  is very similar to that  $\widetilde{\omega''_z \frac{\partial u''^+}{\partial z}}$  merely confirms that  $\partial u''/\partial z$  is the principal contributor to  $\omega''_y$  (constituting in excess of 90%).

An important observation in Figure 2.30 is that the magnitude of the correlation  $\widetilde{\omega''_z \frac{\partial u''^+}{\partial z}}$  (and thus  $\widetilde{\omega''_z \omega''_y^+}$ ) is high during the drag-reduction phase, and that its maximum coincides with a high level of near-wall skewness and Stokes strain. Moreover, the correlation changes sign within any two sequential drag-decline phases. However, if this correlation is multiplied by the Stokes strain, which also changes sign in any two sequential drag-decline phases, the result is a positive value during all drag-decrease phases, as shown in Figure 2.29(d), and hence an increase in  $\widetilde{\omega''\omega''_z^+}$ . The fact that the correlation  $\widetilde{\omega''_z \frac{\partial u''^+}{\partial z}}$  rises despite a reduction in  $\partial u''/\partial z$  (i.e.  $\omega''_y$ ) as the drag decreases, reflects the high sensitivity and strong response of  $\omega''_z$  to the Stokes strain. Both  $\widetilde{\omega''_z \frac{\partial u''^+}{\partial z}}$  and  $\widetilde{\omega''_z \omega''_y^+}$  change sign in harmony with the sign of the Stokes strain, and this supports the argument that variations in the spanwise vorticity component are driven by near-wall vortex stretching and tilting associated with the Stokes strain.

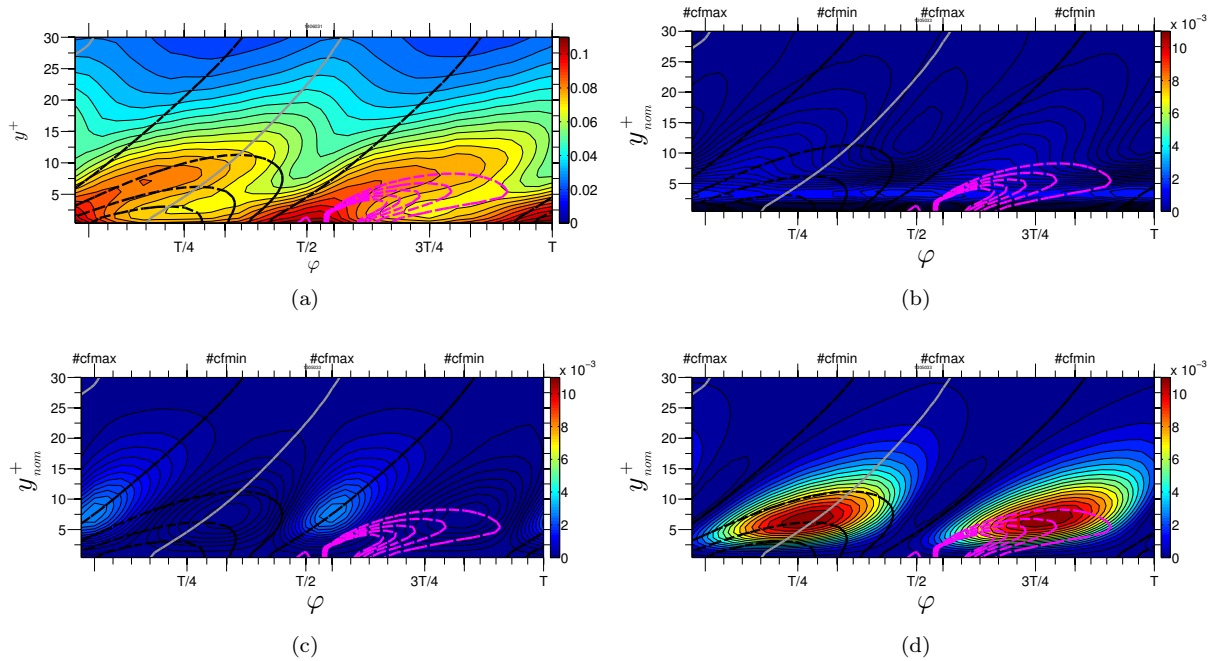


Figure 2.29: Phase-wise variations of (a)  $\widetilde{\omega_z''\omega_z''}^+$  and (b)-(d) its three strain-related production terms, as identified in equation 2.16.

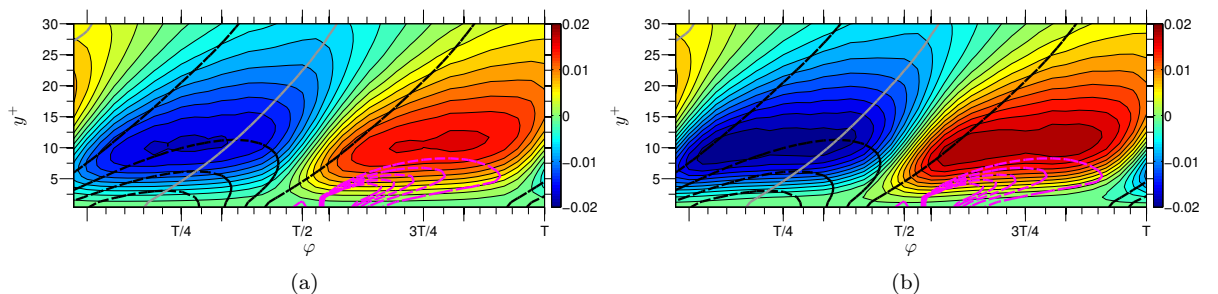


Figure 2.30: Phase-wise variations of (a)  $\widetilde{\omega_z''\frac{\partial u''}{\partial z}}^+$  in equation 2.16, and (b)  $\widetilde{\omega_z''\omega_y''}^+$ .

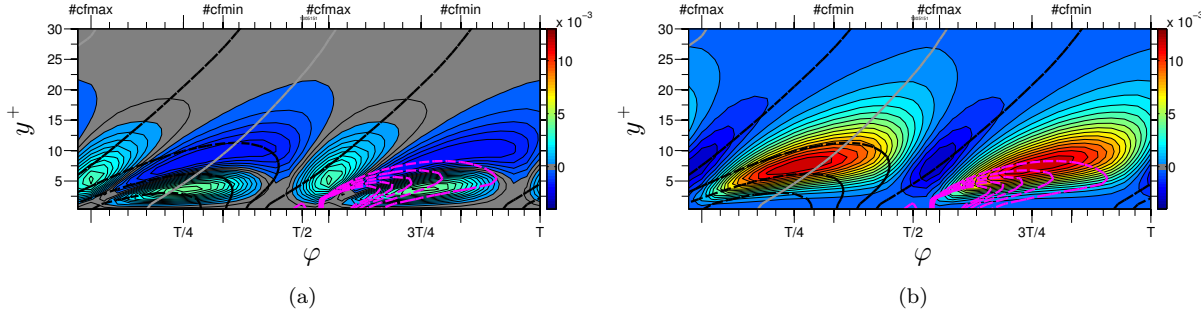


Figure 2.31: Phase-wise variations of the two Stokes-strain-related terms identified in equation 2.17.

A final issue addressed in this section is whether the amplification of the spanwise enstrophy by stretching and tilting can be associated explicitly with the skewness. To answer this question, the strain-related terms in the right-hand-side of equation 2.16 are re-cast in terms of the skewness angle and the wall-normal gradient of the total velocity magnitude  $\tilde{U}_n$ :

$$\widetilde{\omega_z'' \frac{\partial u''}{\partial z}^+ \frac{\partial \tilde{W}}{\partial y}^+} = \underbrace{\omega_z'' \frac{\partial u''}{\partial z}^+ \sin \theta \frac{\partial \tilde{U}_n}{\partial y}^+}_{\text{Fig:2.31(a)}} + \underbrace{\omega_z'' \frac{\partial u''}{\partial z}^+ \tilde{U}_n^+ \cos \theta \frac{\partial \theta}{\partial y}}_{\text{Fig:2.31(b)}} \quad (2.17)$$

The two terms are plotted in Figure 2.31. The only important term is the second, associated with the Stokes strain and the skewness. Within the region of high Stokes strain and skewness, the former causes a periodic realignment of spanwise vorticity fluctuations (Below the low-turbulence layer  $y^+ < 5$ , the transfer is obviously weak). The consequence is that high skewness is associated with an increase in the spanwise-enstrophy component, while the opposite occurs in regions of low skewness and Stokes strain.

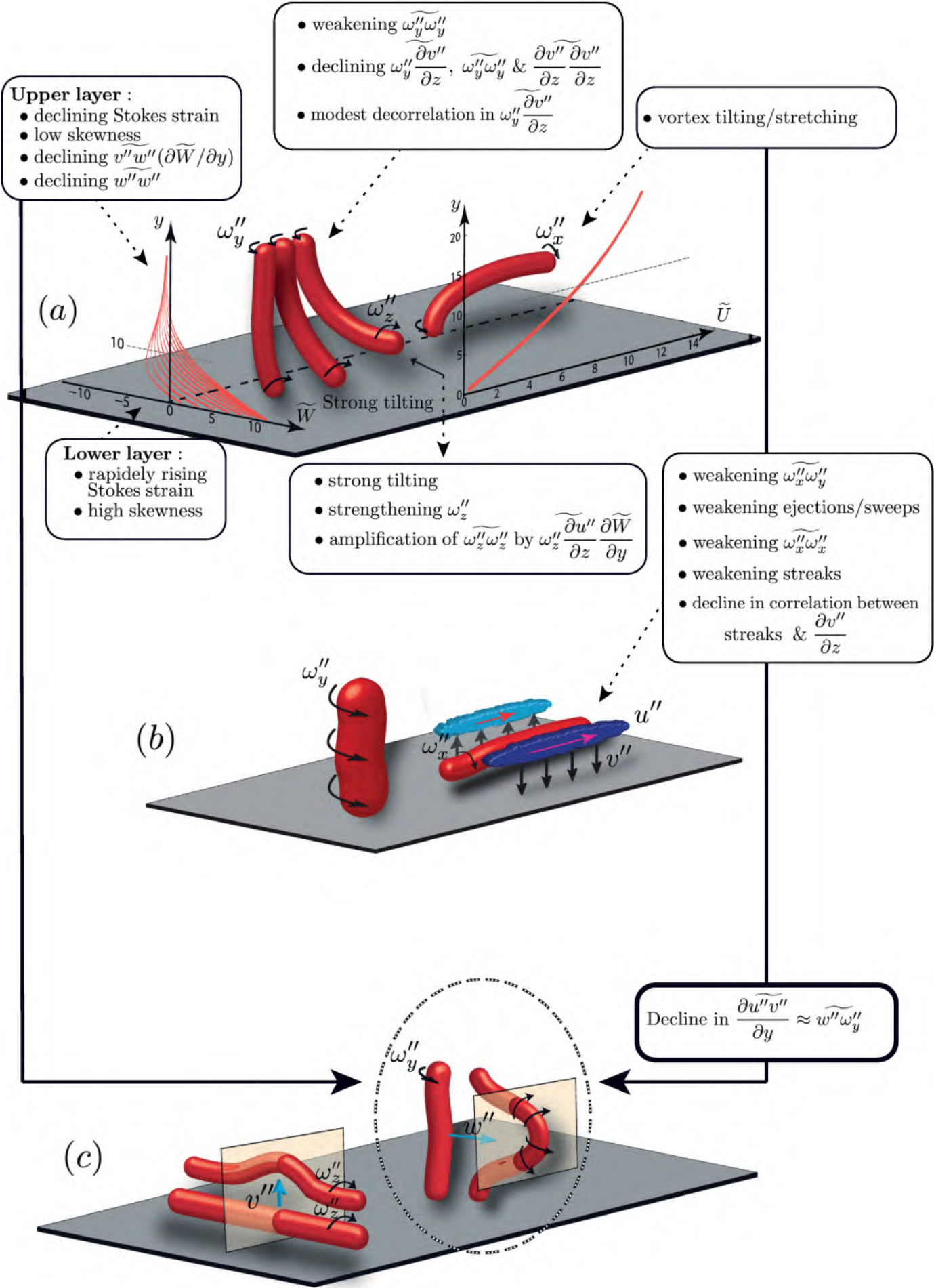
## 2.7 Uncovering the Mechanisms Behind Drag Reduction

The foregoing descriptions and discussion underscore the multi-faceted nature and complexity of the interactions that need to be appreciated in an effort to link them to the drag-reduction scenario. Against this background, the present section provides a summary of the interactions by reference to two sets of *purely conceptual* sketches given in Figures 2.32 and 2.33 for the drag-reduction and drag-rise phase portions, respectively. These must not be interpreted as conveying rigorous statements. Rather, they are intended to support and reiterate, graphically, the arguments and statements derived from the processed DNS data.

Figure 2.32 is intended to clarify, via sketches (a), (b) and (c), the path that leads to a decline in the shear-stress and its gradient, which is at the heart of the drag-reduction process. The end point is sketch (c), which is the same as Figure 2.25. The key processes are those that lead to a reduction in  $\widetilde{w'' w_y''}^+$  to which  $\widetilde{v'' w_z''}^+$  is subordinate.

The starting point is the set of Stokes-strain profiles in sketch (a). As shown in Figures 2.8,  $\widetilde{w'' w''}^+$  declines together with the streak strength  $\widetilde{u'' u''}^+$  within the layer  $y^+ \approx 10 - 15$  in phase intervals of rapidly changing Stokes strain, while both increase when the Stokes strain is high and changes slowly (“lingers”) in phase. The response of the former is closely linked to variations in the rate of production  $-\widetilde{v'' w''} \frac{\partial \tilde{W}}{\partial y}^+$  of  $\widetilde{w'' w''}^+$ . As this production is positive over most of the cycle, the phase-wise variation in  $\widetilde{w'' w''}^+$  is not to be understood as implying that it is the cause of the *time-averaged* drag reduction. Rather, the variation of  $\widetilde{w'' w''}^+$  needs to be seen as linked to the drag fluctuations within the cycle.

The reduction in  $\widetilde{w'' w''}^+$  goes hand-in-hand with a decline in  $\widetilde{\omega_y'' \omega_y''}^+$ , i.e. streak strength. As shown by equation 2.15,  $\widetilde{\omega_y'' \omega_y''}^+$  is driven by  $\widetilde{\omega_y'' \frac{\partial v''}{\partial z}^+ \frac{\partial \tilde{U}}{\partial y}^+}$ . As the streamwise shear strain varies only weakly, the variations in this term are dictated by the correlation between  $\omega_y''$  and  $\frac{\partial v''}{\partial z}$ , both of which (or rather their auto-correlations) decline in harmony with  $\widetilde{\omega_y'' \frac{\partial v''}{\partial z}^+}$ . The correlation coefficient varies only modestly with



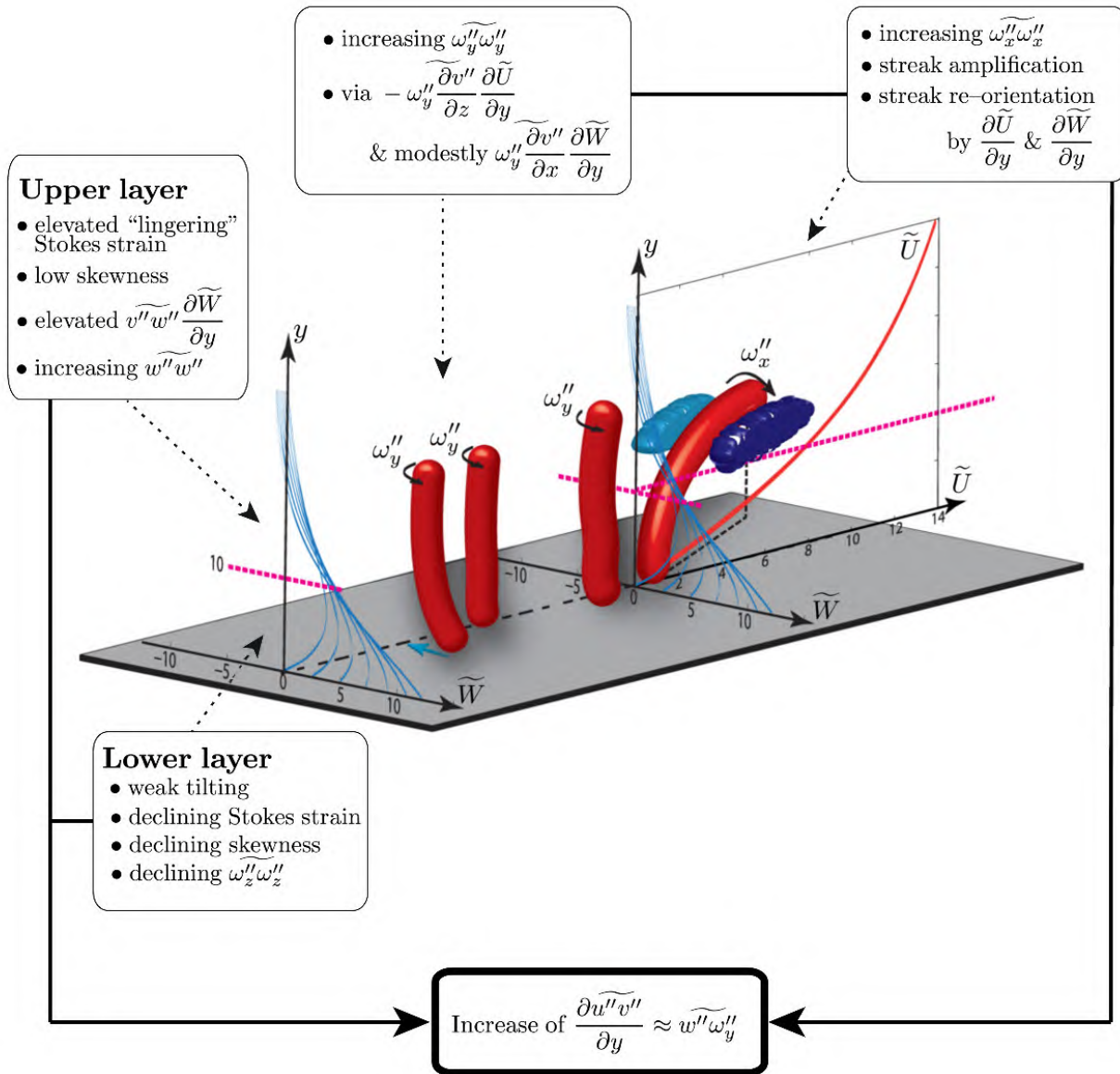


Figure 2.33: Illustration of interactions during the drag-increase interval of the actuation cycle

phase, but does feature a modest decline within the layer  $y^+ = 10 - 15$  during the drag-reduction phase, thus contributing to the decline in the drag.

Because of the link between the streaks and the streamwise vorticity, shown in sketch (b), and the vortex-tilting/stretching process, shown at the right of sketch (a), a reduction in  $\omega_y''$  is expected to be accompanied by a reduction in  $\omega_x''$ , the latter representing quasi-streamwise vortices – or ejections and sweeps – which are associated with the streak formation. Indeed, it is observed that  $\widetilde{\omega_x''\omega_x''}^+$  varies broadly in harmony with  $\widetilde{\omega_y''\omega_y''}^+$ . However, specifically during the drag-reduction phase, there is also a degree of decorrelation between  $\omega_x''$  and  $\omega_y''$ , with consequent decline in the organisation implied by sketch (b). It is primarily the simultaneous decline of  $w''$  and  $\omega_y''$  that leads to a reduction in  $\widetilde{w''\omega_y''}^+$  and hence in the magnitude of the turbulent shear-stress gradient.

With attention returned to the Stokes-strain profiles, an important point to make is that the decline in Stokes strain in the layer  $y^+ \approx 10 - 15$  goes hand-in-hand with a rapid rise in the Stokes strain – and the skewness – in the lower layer, which then provokes the strong tilting and stretching of vortices as shown in the middle of sketch (a), thus leading to a strengthening of  $\omega_z''$ . As shown by equation 2.16, the primary driver of  $\widetilde{\omega_z''\omega_z''}^+$  is  $\omega_z'' \frac{\partial u''}{\partial z} \frac{\partial \widetilde{W}}{\partial y}^+$ . The correlation  $\omega_z'' \frac{\partial u''}{\partial z}$  is almost identical to  $\widetilde{\omega_z''\omega_y''}^+$  (Figure 2.30), and thus expresses the synchronicity of the turbulent vorticity components  $\omega_z''$  and  $\omega_y''$ . While the streak strength (i.e.  $\omega_y''$ ) declines during the drag-reduction interval, the spanwise vorticity fluctuations rise steeply due to the severe tilting effected by  $\frac{\partial \widetilde{W}}{\partial y}^+$ , and the result is the observed increase in  $\widetilde{\omega_z''\omega_z''}^+$ . The fact that the sign of  $\widetilde{\omega_z''\omega_y''}^+$  changes in harmony with that of  $\frac{\partial \widetilde{W}}{\partial y}^+$  clearly implies that the phase-wise variation of  $\widetilde{\omega_z''\omega_y''}^+$  is driven by the periodic switch in spanwise orientation of  $\omega_z''$ .

Figure 2.33 summarizes the interactions that are associated with the drag-increase phase. During this interval, the Stokes strain in the layer  $y^+ \approx 10 - 15$  is relatively high and “lingers” in phase. This elevates the production of  $\widetilde{w''w''}^+$ . In the near-wall region, the Stokes strain decreases and the skewness with it. The spanwise tilting of  $\omega_y''$  vortices is therefore relatively weak. The correlation  $\omega_y'' \frac{\partial v''}{\partial z}^+$  (linked to  $\widetilde{\omega_x''\omega_y''}^+$ ) increases, and with it  $\widetilde{\omega_x''\omega_x''}^+$ . The wall-normal enstrophy  $\widetilde{\omega_y''\omega_y''}^+$  and the streaks are thus amplified and are re-oriented in the  $x - z$  plane by the complementary action of the streamwise shear strain and the Stokes strain, the effect being most pronounced in the layer  $y^+ \approx 10 - 15$ . Hence, the drag-increase interval is driven, primarily, by a simultaneous increase in  $w''$ , and  $\omega_y''$ , supported by a modest increase in the correlation between the two. The result is an increase in the turbulent shear-stress gradient and drag.

## 2.8 Concluding remarks

The aim of this investigation is to supplement previous knowledge on the mechanisms that cause the turbulent friction drag in a boundary layer to decline when the flow is subjected to periodic spanwise wall oscillations. Intentionally, a non-optimal actuation condition was chosen, in which the flow settles down, following a short transient phase, to a low-drag state, relative to which the drag oscillates in harmony with the periodic actuation. Prima facie, this choice does not seem entirely rational, because the maximum drag-reduction margin, at 20%, is about 10% lower than the level at the optimum actuation period. However, the key benefit derived therefrom is that the phase-averaged turbulence statistics, derived from a set of sequential actuation periods, rise and fall together with the drag over the representative actuation cycle. This allows the pertinent processes to be studied based on extensive DNS data collected over many periods. A close equivalence between the phase-averaged mechanisms and those prevailing during the transient phase, in which the drag declines over 2-3 cycles towards its low-drag level has been shown in the first part.

Although it could be argued that the turbulent vorticity field contains no more physical information than that represented by the turbulent velocity fluctuations, new insight can be (and has been) derived from observations of the statistical correlations of the vorticity, relative to an analysis that focuses on correlations of the velocity fluctuations alone, the later undertaken in the first section of the present study. In the second half, the interaction between drag, shear stress, vorticity fluctuations and enstrophy have been examined. This interaction is complex, and it cannot be claimed that all its aspects have been fully exposed. However, the analysis presented herein allows the following main elements associated with the vorticity fluctuations to be summarized as follows:

- The shear stress variation is driven, perhaps counter-intuitively, mainly by distortions of the wall-normal vorticity by spanwise velocity fluctuations – *vortex tilting/stretching* – rather than by wall-normal transport of spanwise vorticity. This represents a direct link between streak strength and the shear stress.
- The wall-normal gradient of the vortex-tilting/stretching correlation is thus the term that drives the streamwise near-wall strain and hence the drag.
- The wall-normal enstrophy component is only weakly linked, directly, to the Stokes strain, as the related generation term in the equation governing this component is insignificant. Rather, this component is governed by variations, in the upper portion of the near-wall layer ( $y^+ \approx 10 - 15$ ), in the correlation between the wall-normal vorticity and the spanwise gradients of ejecting/sweeping motions, the latter associated with streamwise vorticity fluctuations. This term, magnified by the streamwise shear strain, provokes related variations in the wall-normal enstrophy and the drag: when this term is weak, the wall-normal enstrophy declines and the drag reduces.
- Variations of the spanwise enstrophy component, especially strong very close to the wall, are driven primarily by the Stokes strain. This strain magnifies the influence of the correlation that includes the spanwise gradient of the streak strength, which is the major contributor to the wall-normal vorticity fluctuation. The effect is especially prominent in regions of high skewness.
- The fact that the variations in the spanwise enstrophy component lag relative to those in the wall-normal component by a quarter of the actuation period, strongly suggests that the main mechanism is one of spanwise tilting of wall-normal vortices by the Stokes strain.
- The above process occurs simultaneously with a decline in spanwise velocity fluctuations in the upper region of the viscous sublayer, due to declining Stokes strain and increase in the rate of change in that strain in the upper region. This decline contributes to the drag reduction process.
- The subsequent drag increase is a consequence of the increase in streak strength by a high, lingering (slowly varying) Stokes strain in the upper portion of the viscous sublayer, enhanced by weak Stokes strain, weak spanwise tilting/stretching and weak skewness in the lower region of the viscous sublayer. The result is a rise in the correlation between the spanwise streak-intensity gradient and the streamwise vorticity fluctuations – essentially, a strengthening of the quasi-organised streak and streamwise-vortex structure that prevails in an unperturbed boundary layer, except for an in-plate tilting of the streaks in a direction dictated by the strain vector.

## 2.9 Control Effectiveness as Reynolds-Number Increases

The maximum drag reduction at the near-optimum actuation period of  $T^+ = 100$  exhibits a declining trend with increasing Reynolds number, falling from approximately 38% at  $Re_\tau \approx 200$  to 32% at  $Re_\tau \approx 500$ , and further to 29% at the current  $Re_\tau$ . This behaviour suggests a downward trend that is roughly proportional to  $Re_\tau^{-0.2}$ , indicating a decrease in control efficiency as the Reynolds number rises. To investigate the underlying cause of this phenomenon, Figure 2.34(a) presents the streamwise velocity fluctuations on the  $x - z$  plane at  $y^+ \approx 13.5$ , a location where streaks are particularly prominent for the actuated flow. Subsequently, Figures 2.34(b) and 2.34(c) isolate the large-scale and small-scale components, respectively. The large-scale motions are characterised by a length scale of  $\mathcal{O}(10^4)$  units, which corresponds to approximately 10 channel half-heights, and a timescale of  $t_c^+ \approx 600$  in the log layer, consistent with the observations in Figure 2.6(a).

Of particular note is the observation that in regions where strong large-scale sweep events occur, the near-wall streaks are significantly amplified. This leads to an enhancement of momentum mixing and, as a result, an increase in drag. This observation indicates that the emergence of these large-scale outer structures plays a central role in the decline of control efficiency. As the Reynolds number increases, the influence of these outer structures also strengthens, and by locally modifying the nature of the streaks, they counteract the control strategy, thereby providing an explanation for the reduced drag-reduction efficiency observed at higher Reynolds numbers. In the subsequent chapter, this hypothesis will be subjected to further scrutiny to gain a more comprehensive understanding of the mechanisms by which the growing influence of outer structures at higher Reynolds numbers alters the near-wall streaks and, in turn, diminishes the efficacy of the control strategy. This investigation will aim to elucidate the fundamental interactions between the large-scale

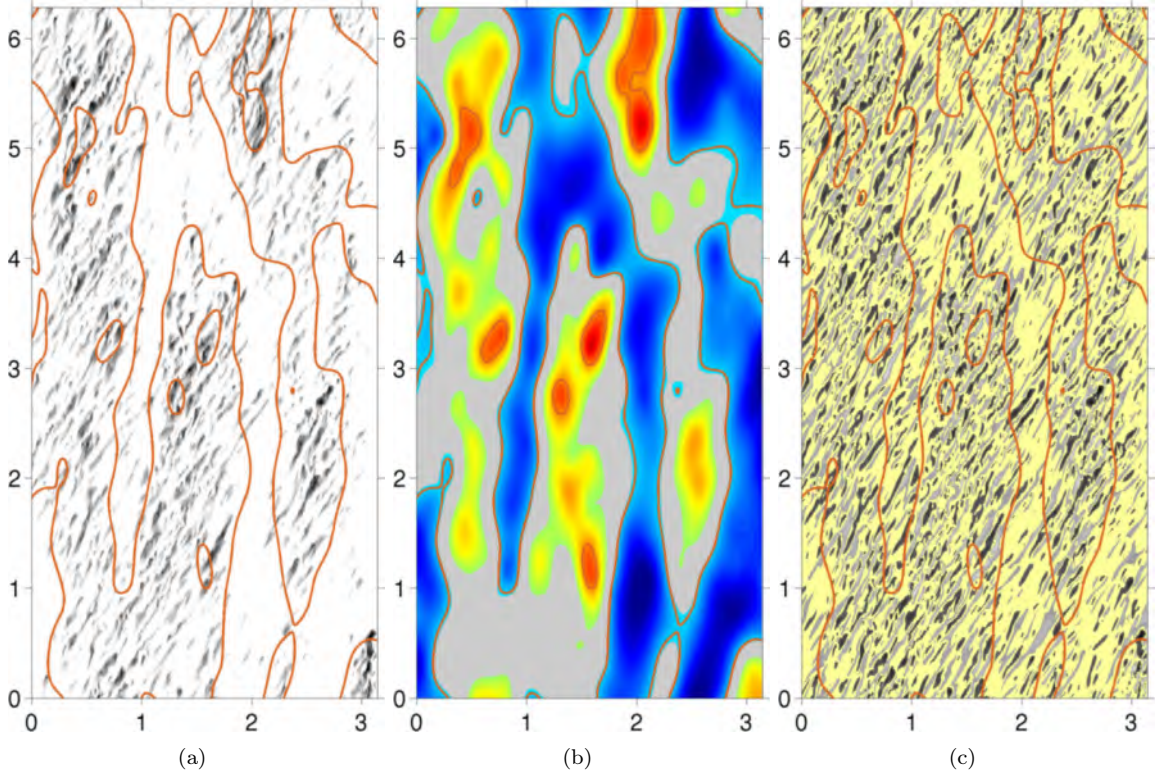


Figure 2.34: Application of the Hilbert-Huang transform to the field of streamwise-velocity fluctuations at  $y^+ = 13.5$ , at the phase-location of maximum skin friction; (a) raw fluctuation field; (b) large-scale velocity fluctuations, red contours: positive fluctuations; blue contours: negative fluctuations. (c) Small-scale velocity fluctuations. Small-scale fluctuations are included only above a magnitude of 7% of the rms velocity at  $y^+ = 13.5$ ; large-scale velocity fluctuations are included above a magnitude of 9%. The scales next to domain length and width are multiples of channel half-height.

outer structures and the near-wall turbulence, with a particular focus on the modulation of the streaks in the presence of drag-reducing spanwise wall motion.



# Chapter 3

## The Effect of Increasing Reynolds Number on Drag-Reduction Control Efficiency

### 3.1 Introduction: Understanding the limitations of turbulence control as Reynolds increases

The present study is motivated by the observed decline in the effectiveness of drag reduction achieved through oscillatory spanwise wall motion as the Reynolds number increases. The central question posed is whether this decline is due to the increasingly strong influence of large-scale outer structures in the log layer on the near-wall turbulence, particularly the streaks' strength in the viscosity-affected layer, a process referred to as *modulation*. To address this question, an extensive statistical analysis is conducted using same DNS data than the previous chapter, -i.e for a channel flow at a friction Reynolds number of 1025, subjected to oscillatory spanwise wall motion with a nominal wall-scaled period of 100. The analysis employs the *Empirical Mode Decomposition* to separate turbulent scales and derive conditional statistics of small-scale motions and skin friction subject to prescribed intensities of large-scale motions, a process known as *footprinting*.

As discussed in the previous chapter (Chapter 2), numerous studies have unequivocally demonstrated that various combinations of oscillatory and spatially-periodic spanwise wall motions, comprising streamwise travelling waves, can lead to substantial reductions in skin friction. Within this subject area, the “Quadrio ma” (Quadrio, Ricco, and Viotti 2009), which illustrates the dependence of the drag-reduction margin on the oscillation frequency and streamwise wavelength of the spanwise motion, has gained significant prominence in the literature on skin-friction control. This map, constructed from extensive DNS computations for the relatively low friction Reynolds number of  $Re_\tau \approx 200$ , reveals that skin friction can be reduced by up to 45%. However, the Reynolds-number dependence of the drag-reduction margin has received comparatively less attention, primarily due to the rapid increase in computational costs associated with DNS as the Reynolds number rises. Consequently, very few DNSs have been performed for  $Re_\tau > 1000$ , particularly those conducted over sufficiently large domains, where streamwise and spanwise periodicity can be considered realistic and credible from an accuracy perspective. This challenge is further exacerbated by the need to accommodate large streamwise wavelengths and/or sufficiently large oscillation periods, the latter being especially relevant when reliable phase-averaged statistics are to be extracted from the data (Agostini, Touber, and Leschziner 2014; Agostini, Touber, and Leschziner 2015). To date, the highest reported Reynolds number is  $Re_\tau \approx 2100$  by Gatti and Quadrio 2013, although this simulation was performed over a very small domain of dimensions  $1.2h \times 2h \times 0.6h$ . Significantly larger domains were employed in simulations by Hurst, Yang, and Chung 2014 for the range  $Re_\tau \approx 200 - 1600$ . In a recent experimental study, Marusic et al. 2021 investigated drag reduction using a novel actuation device in a wind tunnel. The actuation involved generating an upstream travelling wave by synchronizing the motion of sliding surface elements (slats). Their setup enabled the creation of actuation with an amplitude of  $W_m^+ = 12$  and a period of  $T^+ \approx 140$  at  $Re_\tau \approx 6000$  ((2.1)). Using this wave actuation, Marusic et al. achieved drag reduction of up to 25%, which represents a substantial achievement given the challenges associated with implementing the actuation method and accurately

quantifying the drag variation. Although studies reporting simulations at elevated Reynolds numbers (e.g., higher than  $Re_\tau \approx 500$ ) have adopted a variety of actuation scenarii in terms of time-dependence, frequency, and wavelength, the general picture emerging, and confirmed by experiments, is that the drag-reduction margin tends to decline with increasing Reynolds number at a rate of  $Re_\tau^{-\alpha}$ , where  $\alpha$  depends greatly on the actuation parameters and the details of the simulation but typically falls within the range of 0.15-0.3.

Gatti and Quadrio 2016 demonstrate that the classical argument connecting the changes in drag for flow over a rough wall to the vertical shift  $\Delta B$  of the logarithmic part of the mean velocity profile is also applicable to the case of spanwise forcing. They derive a non-linear expression that can be specialized for the Constant Flow Rate (CFR) or Constant Pressure Gradient (CPG) cases, given by:

$$\sqrt{\frac{2}{C_f}} - \sqrt{\frac{2}{C_{f,0}}} = \frac{1}{\kappa} \ln \frac{Re_\tau}{Re_{\tau,0}} + \Delta B \quad (3.1)$$

where  $\Delta B$  is the vertical shift of the logarithmic portion of the mean velocity profile, and the subscript "0" refers to the uncontrolled flow. It is important to note that this equation is derived under the assumption that the von Kármán constant  $\kappa$  is unaffected by the control. The authors also suggest that the upward shift in the velocity log-law, always observed with drag-reducing wall actuation when plotted with the actual, actuation-modified wall shear stress, tends to become constant beyond  $Re_\tau \approx 2000$ , confirming a suggestion made by Luchini 1996 based on a simple analysis linking the thickness of the viscous sublayer to a given drag-reduction level.

This result may be interpreted as suggesting that the physical processes within the viscous sublayer underpinning drag reduction are not adversely affected by distortions arising from the interference of outer structures with the turbulent state near the wall. Although this inference pertains to drag reduction rather than drag itself, its validity, if proven, would be remarkable in light of recent observations on the effects of outer-layer turbulence on the near-wall region. These observations originate from studies on canonical (unforced) boundary layers and channel flows, conducted independently of drag-reduction scenarii (baars\_wall-drag\_2020; Hutchins and Marusic 2007b; Mathis et al. 2011; Smits, McKeon, and Marusic 2011; Hultmark et al. 2012). Such studies, both experimental and computational in nature, unequivocally demonstrate that outer structures in the log-law region, whose energy steadily increases with rising Reynolds number, strongly impact the turbulence properties of the near-wall layer.

As detailed in the introduction, the outer structures are quasi-organized as "super streaks" with streamwise length scales of order  $10h$  and spanwise separations of order  $1h$ . Mathis, Hutchins, and Marusic 2009 proposed, based on hot-wire measurements over a wide range of Reynolds numbers, that these energetic structures are located at  $y^+ \approx 3.9\sqrt{Re_\tau}$ , typically at  $0.1 - 0.2h$ . Extensive experimental work by Marusic, Mathis, Hutchins, and their collaborators (Hutchins et al. 2009; Mathis et al. 2009; Marusic, Mathis, and Hutchins 2010b; Hutchins et al. 2011) has primarily demonstrated, using hot-wire techniques, that the outer structures affect near-wall turbulent fluctuations through two mechanisms: "footprinting" and "modulation". Footprinting is a process by which outer large-scale motions impart correspondingly large translational fluctuations close to the wall, with some streamwise lag between the two, essentially resulting in a near-wall field that is a superposition of large-scale footprints and locally generated small-scale motions. The footprinting process is clearly illustrated in Figure 3.1, which arises from a simulation of an actuated channel flow at  $Re_\tau \approx 1025$ . The images show streamwise-velocity fluctuations across three wall-parallel planes at different wall-normal positions. The essential feature to note in the figure is the correspondence across the near-wall layer of spatially correlated large areas of predominantly elevated and depressed streamwise-velocity fluctuations, separated by roughly  $\Delta z^+ \approx 1000$  and subject to a streamwise lag of approximately  $\Delta x^+ \approx 500$ . Modulation is a more subtle phenomenon, wherein the large-scale motions amplify or attenuate the small-scale turbulence depending on the sign of the large-scale footprints. Footprints arguably encompass both positive and negative large-scale fluctuations induced by the outer-flow motions, which correspond to large-scale sweeps and ejections, respectively.

Figure 3.1(a), which shows the velocity field at  $y^+ \approx 3$ , provides clear indications of modulation. This is evident from the fact that the regions of high velocity and large-scale footprints feature well-established small-scale streaks. – here inclined due to the spanwise Stokes strain induced by a streamwise-homogeneous, oscillatory spanwise wall motion,  $W(t) = W_m \sin(2\pi t/T)$  – while the low-velocity large-scale footprints lack distinct streaky structures or contain very weak streaks.

The relationship between large-scale motion and modulation has been the focus of numerous recent experimental and computational studies, and it will be further explored in Chapter 4.

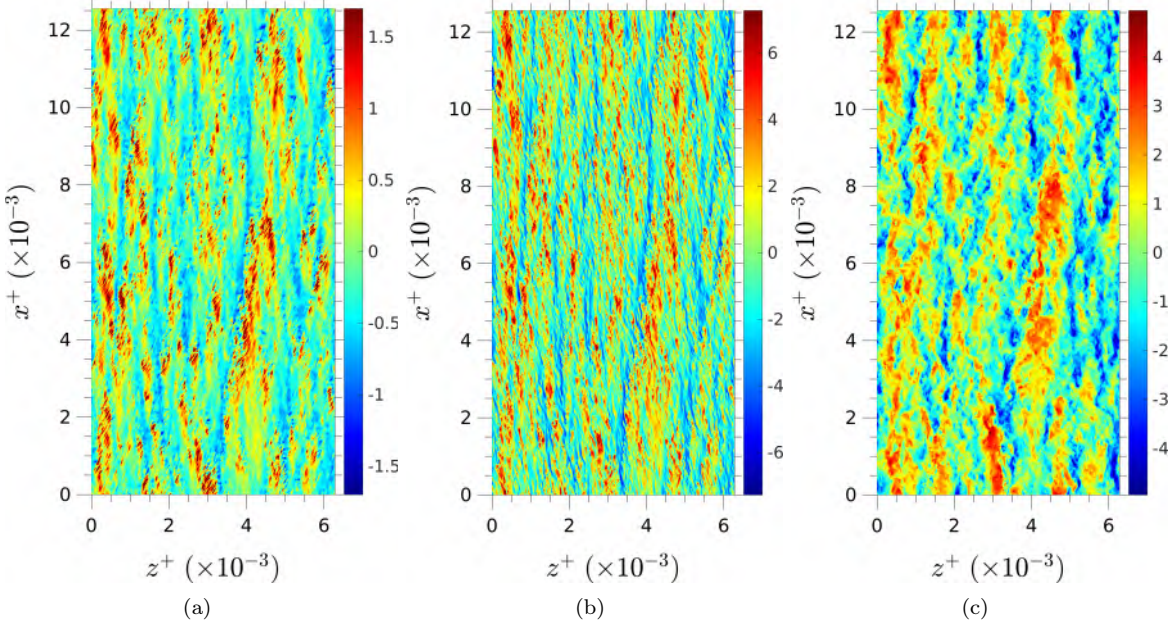


Figure 3.1: Visual representation of the correlation between streamwise velocity fluctuations ( $u^+$ ) at different wall-normal locations : (a)  $y^+ \approx 3$  (surrogate of skin-friction field), (b)  $y^+ \approx 18$  and (c)  $y^+ \approx 200$ . Note correspondence of large-scale regions of predominantly high- and low-velocity fluctuations. Channel flow at  $Re_\tau \approx 1000$  with oscillatory wall motion ( $T^+ = 100$  and  $A^+ = 12$ ).

Few studies have explicitly addressed the impact of large-scale motion, either directly through footprinting or indirectly through modulation, on drag. Giovanetti, Hwang, and Choi 2016 attempted to quantify the contribution of large-scale motion by performing LES for canonical channel flow at  $Re_\tau$  up to 4000 over domains of decreasing size, progressively excluding large-scale motions in the outer region, and estimated the contribution of large-scale motion at around 20%. However, this conclusion must be treated with caution, as any undue restriction in the size of the computational domain can readily lead to significant errors in the predicted drag level, even at very low Reynolds numbers. As detailed in Chapter 2, the drag-reduction level is closely linked to the ability of the spanwise Stokes strain to weaken the near-wall streaks and prevent their re-establishment, strongly suggesting that any mechanism or process hindering the weakening of the streaks, and thus the quasi-streamwise vortices in the near-wall layer, is detrimental to the level of drag reduction achievable under ideal circumstances. Streak modulation arising from outer structures is precisely such a mechanism and must therefore be regarded as a primary candidate for affecting drag-reduction effectiveness. It is this interaction and its consequences that lie at the heart of the present chapter.

## 3.2 Database Characteristics

The DNS data forming the basis of the analysis to follow herein is the same database than the one used in the previous chapter. This study analyses DNS data for a channel flow at Reynolds number based on friction velocity  $Re_\tau \approx 1025$  subjected to a streamwise homogeneous oscillatory spanwise motion, however in this case the focus is on the actuation period  $T^+ = 100$ , as prior results showed that at this  $T^+$ , the mean drag reduction was approximately 30% and fluctuations around the low drag state were minimal (see Figure 2.6(a)), indicating that the time scale of the actuation is low enough to prevent the amplification of the streaks once they are weakened by the unsteady Stokes layer caused by the wall forcing. The characteristics of the simulation and the code are detailed in Chapter 2.2. The simulations were performed over a box of length, height and depth  $4\pi h \times 2h \times 2\pi h$ , respectively, corresponding to approximately  $12 \times 2 \times 6 \times 10^3$  wall units. The question of whether the computational box is large enough to faithfully capture the large scales merits consideration. The large scales of interest here are those at  $y^+ \approx 3.9\sqrt{Re_\tau}$ , the position in the log layer at which the streamwise energy profile is elevated towards an outer plateau. Previous studies

on canonical channel flow at  $Re_\tau = 1000 - 5200$  (Lozano-Durán and Jiménez 2014a; Lee and Moser 2015; Agostini and Leschziner 2017) show (or at least suggest) that the large-scale structures are separated in the spanwise direction by around  $1 - 1.5h$ , so that the present spanwise width of  $6.3h$  can accommodate around 4-5 structures. This may be regarded as sufficient. On the other hand, the streamwise length scale of the structures can exceed  $\lambda_x = 10h$ , and this compares to the length of the computational box  $L_x = 12.6h$ . However, the most energetic structures are argued by Agostini and Leschziner 2016b to have a length scale of around  $\lambda_x \approx 8h$ , and many of the structures have a length scale of 4000 – 6000 wall units. Hoyas and Jiménez (2006) (see also Jiménez 2013) argue that a representative limit of  $\lambda_x \approx 10h$ . Moreover, Lozano-Durán and Jiménez (2014a) show, on the basis of tests with different computational boxes, that the interaction between the large and small scales is correctly represented even if the domain is not large enough to capture the entire range of the large structures. Hence, it appears justifiable to assume that the large-scale structures contained in the computational box constitute a credible basis for quantifying the interactions at issue here.

### 3.3 Scale Separation

The manner in which large scales and small scales are defined and separated is central to the characterisation of the interaction between them. There is no unique approach to this task, and there is, therefore, an inevitable degree of ambiguity in the separation process. The large majority of studies that rely on scale separation are based on Fourier filtering with prescribed cut-off wavelength values, based on features in the pre-multiplied spectra of the streamwise turbulence energy. Baars, Hutchins, and Marusic (2016) proposed an alternative method based on a coherence function in Fourier space between the velocity signals at different wall-normal locations. However, applying this approach to a spatially two-dimensional decomposition would involve significant data storage and processing challenges. In the most elaborate Fourier-based implementation by Zhang and Chernyshenko (2016), the filter cut-off value is determined – or rather chosen – by reference to the Pareto front relating the large-scale-to-large-scale to the small-scale-to-small-scale correlation coefficients. The cut-off is then dictated by the (essentially arbitrary) choice of the large-scale and small-scale correlation coefficients – typically 0.9 and 0.1, respectively. In contrast to the above Fourier-based approach, the route adopted herein entails a spatially two-dimensional extension of Huang et al.’s *Empirical Mode Decomposition* (EMD) (Huang et al. 1998). This method has previously been applied by Agostini and Leschziner (2014) and Agostini and Leschziner (2018) to the analysis of channel-flow data at  $Re_\tau \approx 1025$  and 4200. The EMD has several attractive features that make it well-suited for this task. Each mode represents a relatively narrow range of length scales, which are then collected into two groups of small-scale and large-scale contributions. This process requires judgement, much like the choice of a single Fourier filter to separate small-scale from large-scale components in a temporal signal. Notably, this is the only method that has been applied thus far to the analysis of actuated flows.

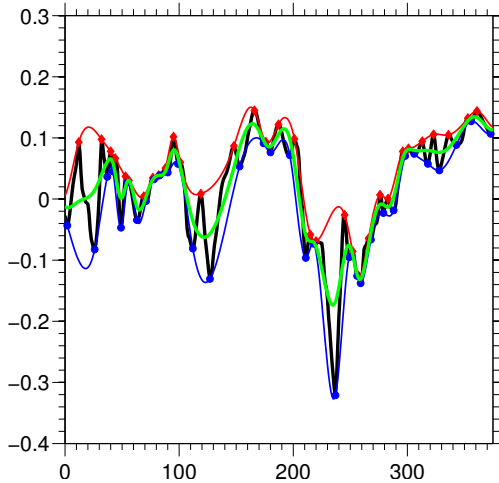


Figure 3.2: Illustration of the principles of Huang et al.’s EMD algorithm, by reference to an arbitrary 1-d signal: upper and lower envelopes are defined by the local maxima and minima, respectively, and the mean value of the envelopes is given in green

### 3.3.1 Outline of Empirical Mode Decomposition Method

The EMD is an algorithm which can produce physically meaningful modal representations of data derived from arbitrary non-stationary or spatially varying processes, including amplitude- and frequency-modulated 1-d signal. The EMD splits any signal into a set of *Intrinsic Mode Functions* (IMFs) based purely on the local characteristic time/space scale of the signal. The method requires no pre-determined functional elements, such as Fourier or wavelet functions. Rather, the IMFs are the EMD-generated basis functions, which arise from the given signal itself.

The method is outlined first by reference to the time-dependent signal shown in Figure 3.2. This signal, denoted by  $f(x)$ , is now subjected to the following iterative process:

1. A residual  $res(x)$  is defined and initialised by  $res(x) = f(x)$ .
2. The local minima and maxima of  $res(x)$  are identified, and upper and lower envelopes,  $E_{up}(x)$  and  $E_{low}(x)$ , respectively, are fitted to the maxima and minima. This is done with the aid of cubic-spline functions.
3. The mean of the two envelopes is computed:  $E_{mn}(x) = (E_{up}(x) + E_{low}(x))/2$
4. The mean envelope is subtracted from the residual:  $res(x) \leftarrow res(x) - E_{mn}(x)$
5. The residual is subjected to a stopping criterion, based on the mean-squares difference between consecutive residuals, normalised by the square of the residual itself. If the criterion is satisfied then the first IMF is obtained as:  $imf_1(x) = res(x)$ ; otherwise  $res(x) \leftarrow res(x) - E_{mn}(x)$  and the above process is repeated until the stopping condition is satisfied.
6. A new signal is generated as  $f(x) \leftarrow f(x) - imf_1$ , and a new residual is initialised,  $res(x) = f(x)$ , and the process is repeated to derive the next IMF.

After this sifting process is completed, the original signal  $f(x)$  can be decomposed as follows:

$$f(x) = \sum_{n=1}^m imf_n(x) + res_m(x) \quad (3.2)$$

Where  $m$  is the number of IMFs and  $res_m$  is the final residual. The first IMF has the smallest time/space scale. As the decomposition proceeds, the time/space scale increases, and hence, the mean frequency of the mode decreases.

Within the scope of this research, snapshots have been leveraged to facilitate the decomposition of velocity fields through the Bi-Empirical Mode Decomposition (BEMD). The BEMD, considered a two-dimensional extension of the traditional EMD, systematically decomposes the original signal into 2D intrinsic mode functions (2D IMFs), progressively extracting frequency information. At each stage of the decomposition, a 2D IMF represents information of higher frequency or smaller scales, while the residual serves as the basis for extracting the subsequent 2D IMF, associated with lower frequency or larger scales. As per equation (3.2), the original data can be recovered. The choice of interpolation function used for constructing the envelopes affects the 2D IMFs, analogous to the case with a 1D signal. In this study, the thin-plate function has been employed for surface fitting (see Bookstein 1989; Nunes et al. 2003), ensuring a globally smooth gradient. The thin-plate function, also known as the thin-plate spline, is a type of radial basis function commonly used for interpolation and smoothing of scattered data points in two or more dimensions. It is named after the physical analogy of minimising the bending energy of a thin metal plate that is constrained to pass through a set of given points. The thin-plate spline provides a smooth interpolation surface that minimizes the total curvature while passing through all the specified data points. Upon completion of the sifting process, the original signal (or image), denoted as  $f(x, y)$ , can be decomposed according to the two-dimensional extension of equation (3.2):  $f(x, y) = \sum_{n=1}^m 2DIMF_n(x, y) + res_m(x, y)$ . The stopping criterion is based on the normalised mean-square difference between two successive residuals.

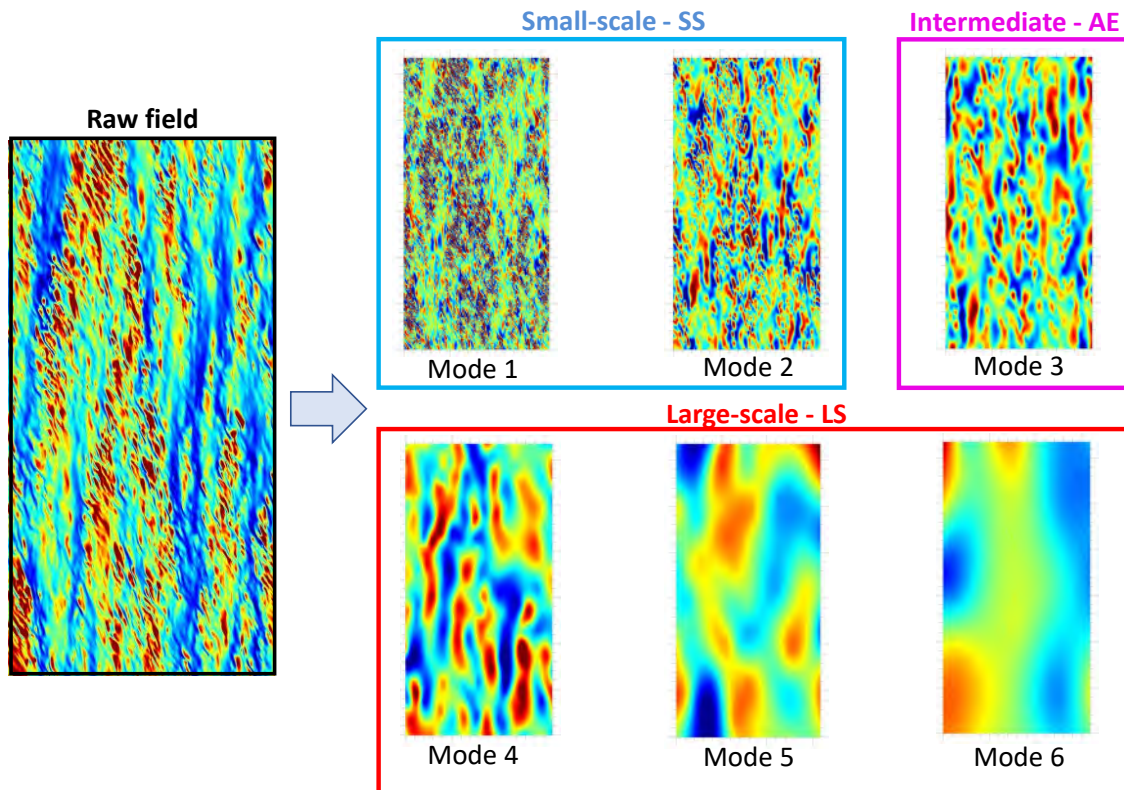


Figure 3.3: BEMD apply to a wall-normal streamwise velocity field, obtained at  $y^+ \approx 12$ . L.h.s plot raw field, r.h.s 2d-imfs modes.

### 3.3.2 Channel-Flow Scale Separation via Bi-dimensional Empirical Mode Decomposition.

An important aspect of studying and quantifying the consequences of footprinting and modulation is the development of a rationally defensible method for separating "large scales" from "small scales." The quotes emphasize that the distinction is not rigorous and depends on how the two scale ranges are defined. Two main approaches have been employed to effect this separation: the imposition of cut-off spectral filters (Bernardini and Pirozzoli 2011; Mathis et al. 2013; Chung et al. 2015; Zhang and Chernyshenko 2016; Hwang and Sung 2017) and the use of Empirical Mode Decomposition (EMD) (Agostini and Leschziner 2014; Cormier, Gatti, and Frohnappel 2016).

The EMD possesses several attractive features that allow it to be used flexibly in the present context. As previously highlighted, the method splits any signal into a set of modes based purely on the local characteristic time/space scales, requiring no pre-determined functional elements such as Fourier or wavelet functions. Instead, the IMFs are the EMD-generated basis functions, arising directly from the given signal itself. Unlike Fourier methods, the EMD does not require filters to separate the scales and does not involve filter-induced loss of energy, as the sum of the modes and the residual is identical to the parent signal (Flandrin, Rilling, and Goncalves 2004; Wu and Huang 2004). In the particular case of white noise, the sum of moments of the modes (e.g., variance) also leads the corresponding moments of the parent signal. Importantly, a mode is not a signal having an unique frequency or length scale but one that has a narrow range of scales and is characterized by a narrow-band spectrum with a mean scale that rises with mode count. An inherent property of the method is that the mean frequency and the bandwidth associated with each mode doubles between two successive modes (see Flandrin, Rilling, and Goncalves 2004).

#### BEMD-mode energy distribution of coherent structures.

Prior to analysing the physical interactions between scales, based on a range of statistical indicators, the characteristics of the BEMD in the present case of  $Re_\tau \approx 1025$  and actuation period  $T^+ = 100$  are illustrated in Figures 3.3 to 3.6.

- Figure 3.3 shows the raw streamwise-velocity fluctuation field containing a wide spectrum of structures (left-hand-side plot). The Empirical Mode Decomposition extracts distinct modes by scale range (right-hand-side plots). The first two modes represent the small-scales, the last three the large scales. Visual inspection reveals a clear correlation between mode 1 and mode 4. This qualitatively demonstrates the connection between near-wall streaks and log layer motions, a key focus of the analysis. The figure illustrates the BEMD's ability to isolate the small from large scales.
- Figure 3.4(a) shows the pre-multiplied spectra across the flow in terms of the spanwise wavelength  $\lambda_z^+$ . The grey contours represent the entire turbulence field, while the coloured contours arise from all BEMD modes  $i = 1 - 6$ , (mode 6 is not visible simply because this mode contains an insignificant proportion of the total energy). Here, it is especially interesting to observe that all modes are highly coherent in the wall-normal direction, with even the largest-scale mode penetrating right down into the viscous sublayer. A quantitative description of the cross-flow correlation will be provided at the end of this section, in Figure 3.7. Figure 3.4(c) illustrates that the energy components, derived from the BEMD modes of the velocity signal, do not sum up to the respective total. The reason is that the total energy,  $\overline{u_{TT}u_{TT}}$ , consists of the mode-specific energy components and cross-mode correlations, ( $\overline{u_i u_j} \neq 0, i \neq j$ ), identified by the magenta line.
- Figure 3.5 provides information on the contribution of the individual BEMD modes to the streamwise energy  $\overline{u'u'}$ . The map in Figure 3.5(b) gives a composite view of the modal energy components in terms of  $y^+$  and the wavelengths of the modes, the latter identified by the vertical black chain lines at wavelength values that correspond to the locations in Figure 3.4(a) at which the spectra of the individual modes reach their respective maxima at  $y^+ = 20$  – again, the location of the streamwise-energy peak. Strictly, the correlation values in Figure 3.5(b) are only relevant at the locations of the modes – i.e., at the discrete modal wave lengths, along the black lines. The continuous contour map thus arises from interpolating between the correlation levels along the lines identifying the modes, and this is done as a visual aid only. The most pertinent feature, in both plots 3.5(a) and 3.5(b), is the rise in mode 4 at  $\lambda_{z,mode}^+ \approx 650$  and  $y^+ \approx 200$ , which signifies most clearly the presence of large-scale outer

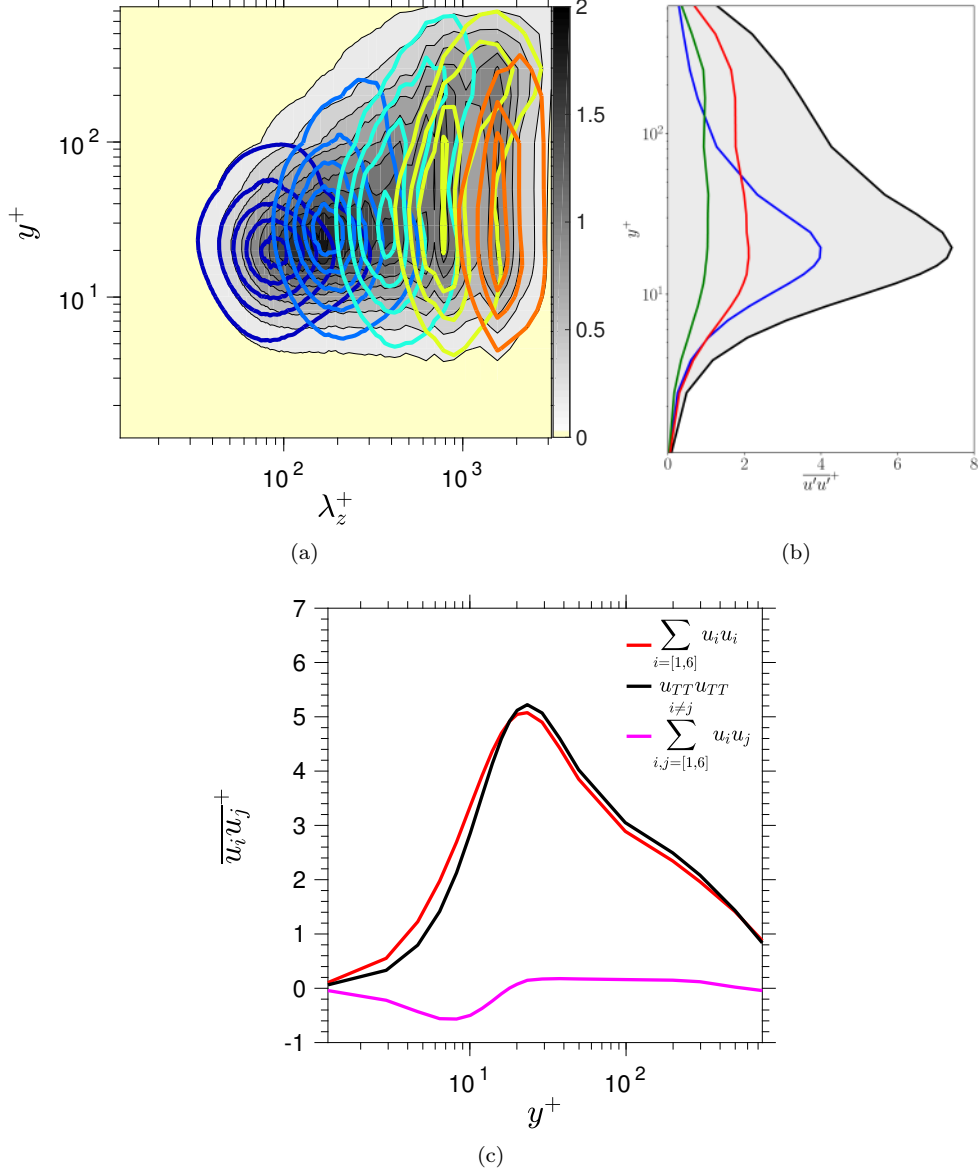


Figure 3.4: Contribution of different scales to streamwise turbulence energy in channel flow at  $Re_\tau \approx 1025$  and  $T^+ = 100$ ; (a) premultiplied spanwise spectral map; grey contours represent the total field; coloured iso-lines represent sub-spectra for the different EMD modes and the residual; (b) scale-wise contributions to streamwise energy: blue line represent small scales (modes 1 and 2 -  $\overline{u_{SS} u_{SS}}^+$ ), red line represents large scales (mode 4, mode 5 and residual-  $\overline{u_{LS} u_{LS}}^+$ ), green line represents intermediate scales (mode 3), black line is the total stress ( $\overline{u'u'}^+$ ), and (c) Wall-normal distributions of the sum of the streamwise energy of EMD modes ( $i = 1 - 6$ ) and cross-mode correlations ( $i, j, i \neq j$ ) relative to the total streamwise energy. and

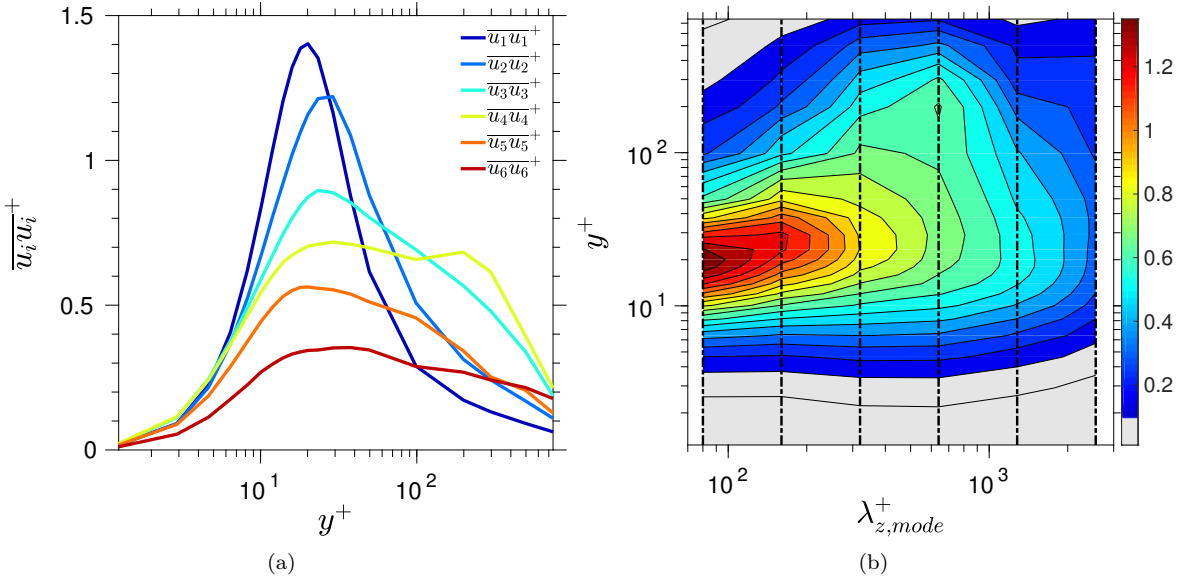


Figure 3.5: Mode-wise contributions to the streamwise energy: (a) profiles of energy contributions from mode 1-6; (b) map of mode-by-mode energy profile, with modes identified by black vertical lines in terms of the wave lengths at which the respective premultiplied spectra of the modes reach their maximum value at  $y^+ = 20$ .

motions. A second informative feature, consistent with comments made in relation to Figure 3.4, is that the energy contribution of large-scale motion is substantial across the entire shear layer, including the buffer layer and the region below it - in effect, justifying the term “footprinting”.

- Modes 1 and 2 are deemed to be “small”, while modes 4, 5 and 6 (which is the residual) are regarded as “large”, the two being separated by the “intermediate” mode 3. Importantly, the sum of the contributions of the scales to any energy component or the shear stress, including components that represent interactions between scales, is identical to the relevant total stress derived directly from the DNS. This is illustrated in Figure 3.4(b), which shows profiles of scale-wise contributions to the streamwise stress, except from a minor scale-interaction component (see Figure 3.4(c)). The profiles demonstrate that the large-scale component persists across the entire near-wall layer, penetrating well into the viscous sublayer, thus representative of footprinting. In the buffer layer,  $y^+ \approx 20$  (rather than 12-15 in the unactuated flow), where the streamwise stress reaches its maximum, the small-scale component dominates. This behaviour is in accord with expectation, as the buffer region is where the small-scale streaks are most pronounced.
- With the decomposition achieved, the effects of the large-scale motions on the properties of the flow as a whole or its small-scale components can be studied. One outcome of the application of the EMD is the PDF of the large-scale skin-friction fluctuations, shown in Figure 3.6(a). This PDF arises from the assumption that the large-scale motion is captured by right-most modes 4, 5 and residual. These structures are seen to cover the spanwise scale within the approximate range  $\lambda_z^+ = 800 - 2000$  - i.e.  $0.8 - 2h$  (as shown in Figure 3.6). They originate at  $y^+ \approx 200$  and persist across almost the entire layer below this position by virtue of the footprinting mechanism. The PDF of the large-scale skin-friction fluctuations (Figure 3.6(a)) is seen to be highly asymmetric. Figure 3.6(c) shows a snapshot of the raw turbulent fluctuation field at  $y^+ \approx 3$ , which is effectively a surrogate of the skin friction. Attention is drawn to the fact that the plots cover one quarter of the extent of the wall-parallel computational domain. An interesting feature to highlight here is the pronounced skewed small-scale patterns within the high-speed red regions. These are the near-wall streaks, tilted by the Stokes strain. When the BEMD is applied to this field, the large-scale fluctuations can be isolated, and these are shown in Figure 3.6(b). The islands identify the extreme +15% and -15% large-scale fluctuation events within the tails of the PDF of the large-scale motions on this plane. The turbulence statistics – e.g. small-scale stresses – conditional on the large-scale motions are determined by sampling the small-scale motions

within islands of the type shown in Figure 3.6(b) and (c). More precisely, the large-scale PDF is divided into 5% bins, and sampling is done within these bins at all  $y^+$  planes for which DNS data were available.

### Spatial extent of influence for different types of coherent structures.

Figure 3.7 contains four maps that convey, in different ways, the level of streamwise variation of the correlation between the skin friction  $Cf$  and velocity modes or combination of modes. Given a velocity-fluctuation mode  $i$ , the two-point correlation coefficient  $R(y^+, \Delta x^+)$  is evaluated from:

$$R(y, \Delta x) = \frac{1}{N_t \times N_z} \sum_{k,l=1}^{N_t, N_z} \left( \frac{r_{12}(y, \Delta x, t_k, z_l)}{\sqrt{r_{11}(y, \Delta x, t_k, z_l)} \cdot \sqrt{r_{22}(\Delta x, t_k, z_l)}} \right) \quad (3.3)$$

where

$$\begin{aligned} r_{12}(y, \Delta x, t_k, z_l) &= \sum_{i=1}^{N_x} [u_i(x_i + \Delta x, t_k, z_l) - \langle u_i(t_k, z_l) \rangle_x] \\ &\quad \times [Cf(x_i + \Delta x, y, t_k, z_l) - \langle Cf(y, t_k, z_l) \rangle_x] \\ r_{11}(\Delta x, t_k, z_l) &= \sum_{i=1}^{N_x} [u_i(x_i + \Delta x, t_k, z_l) - \langle u_i(t_k, z_l) \rangle_x]^2 \\ r_{22}(y, \Delta x, t_k, z_l) &= \sum_{i=1}^{N_t} [Cf(t_i, y, t_k, z_l) - \langle Cf(y, t_k, z_l) \rangle_x]^2, \end{aligned}$$

$\Delta x^+$  is the streamwise separation between the locations at which  $Cf$  and  $u_i$  are sampled.

Figure 3.7(a) shows a mode-by-mode representation of  $R$ , with the black vertical lines retaining the same significance as those in Figure 3.5(b). Figures 3.7(b), (c), and (d) illustrate the correlation coefficients for mode 4, modes 1+2 (representing the small scales), and modes 4+5+6 (representing the large scales), respectively. This classification embodies the perspective that mode 3 cannot be appropriately categorised as either a small-scale or large-scale mode. The justification for this attribution is rooted in the spanwise wave-number location of the modal spectra conveyed by Figure 3.4(a). The grey contours of the total field demonstrate an increase in energy density towards an outer maximum at  $\lambda_z^+ \approx 700$ . In contrast, mode 3 is situated between the inner and outer maxima. Consequently, this mode is considered an intermediate mode, which cannot be ascribed to either the small-scale or large-scale mode sets. Throughout the subsequent presentation and discussion, this mode is designated as the *attached-eddy* (AE) mode. This nomenclature reflects the close association of the intermediate mode with the hierarchy of wall-attached eddies possessing specific statistical properties that align with the attached-eddy hypothesis proposed by Townsend 1980 and Perry and Chong 1982. This connection is further elaborated in Chapter 6 with reference to regions within the spectral maps for streamwise fluctuations in a canonical channel flow at  $Re_\tau \approx 4200$ . Among other characteristics, the connection of the intermediate mode to the set of attached eddies is reflected by the  $y^+$ -wise logarithmic decay of the energy of this mode, as observed in Figure 3.5(a), which constitutes one statistical property that conforms to the attached-eddy hypothesis. Additional details are provided in Chapter 6, dedicated to the Attached Eddy Hypothesis. Figure 3.7 unveils several pertinent facts or features:

- The initial two modes, corresponding to small-scale structures (smaller than  $\lambda_z^+ = 300$ ), exhibit correlation only in close proximity to the wall,  $y^+ < 50$ . The inverse lambda shape reflects a distinct hysteresis in the cycle of streak decay and generation during the periodic actuation cycle and the Stokes layer, an interaction that is discussed in detail in Chapter 2.
- Mode 4, characterised by a spanwise length scale of  $\lambda_z^+ \approx 700$ , is of particular significance as it reflects an enhanced connection between large-scale motions at  $y^+ \approx 200$  and the skin friction. However, the correlation coefficient at this wall-normal distance is approximately 0.25, which is a rather modest value compared to the level observed in canonical (unactuated) channel flow at the same Reynolds number (as will be demonstrated in Chapter 5). A weak maximum, around 0.35, is observed in the correlation coefficient of mode 4 in the lower portion of the buffer layer. Both the modest correlation

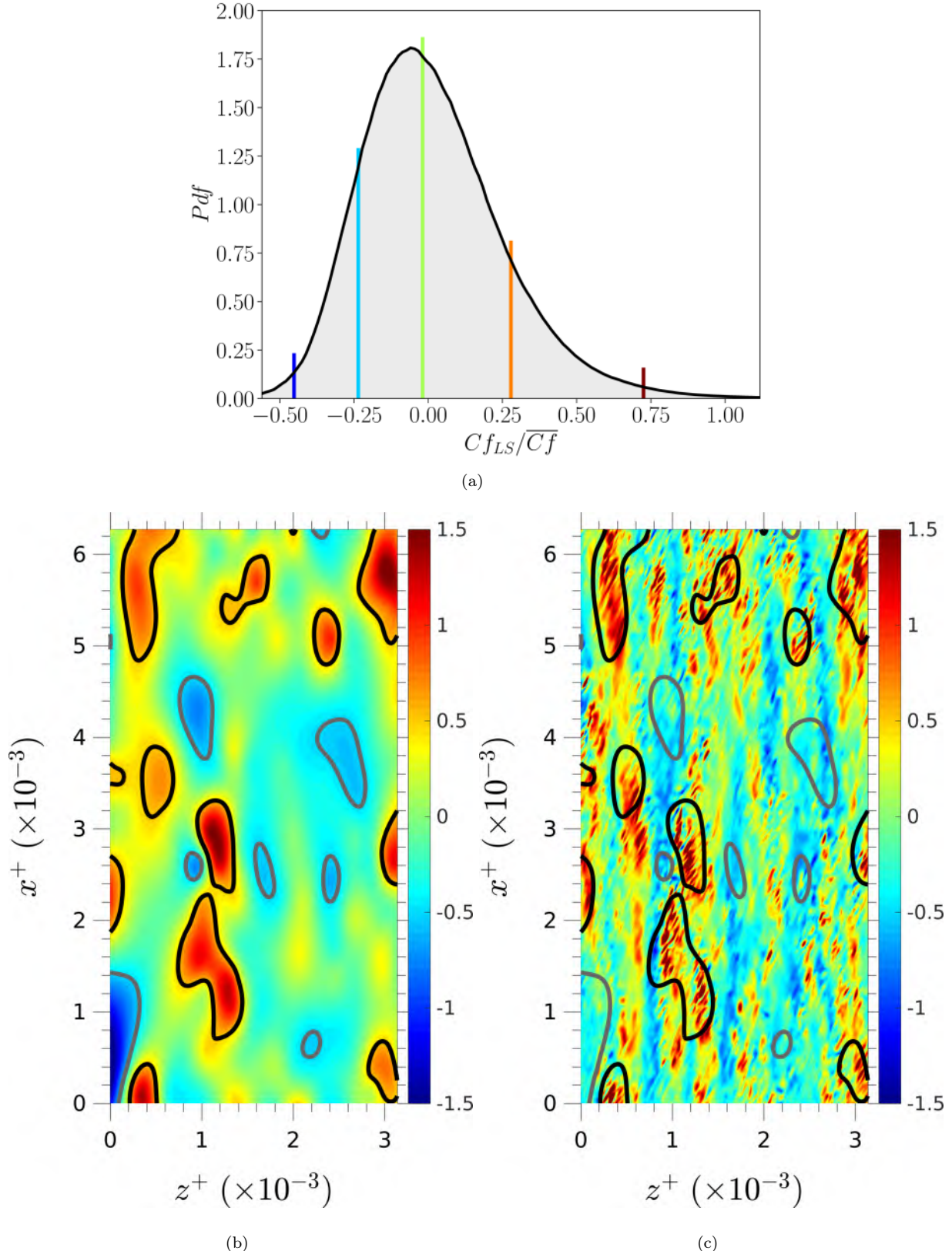


Figure 3.6: Illustration of EMD processing across one wall-parallel plane at  $y^+ \approx 3$ ; (a) PDF of large-scale streamwise-velocity fluctuations derived from EMD, dashed dark blue and red lines correspond to 1% extreme events, light blue and orange lines correspond to 10% and green line to 50% (median of PDF); (b) large-scale fluctuations obtained by summing up all EMD modes (4 and above) across one quarter of the computational box; (c) full field of streamwise fluctuations: black and grey iso-lines correspond to the 15% extreme large-scale positive and negative large-scale fluctuations, respectively. Inclined small-scale streaks within black islands reflect spanwise Stokes strain.

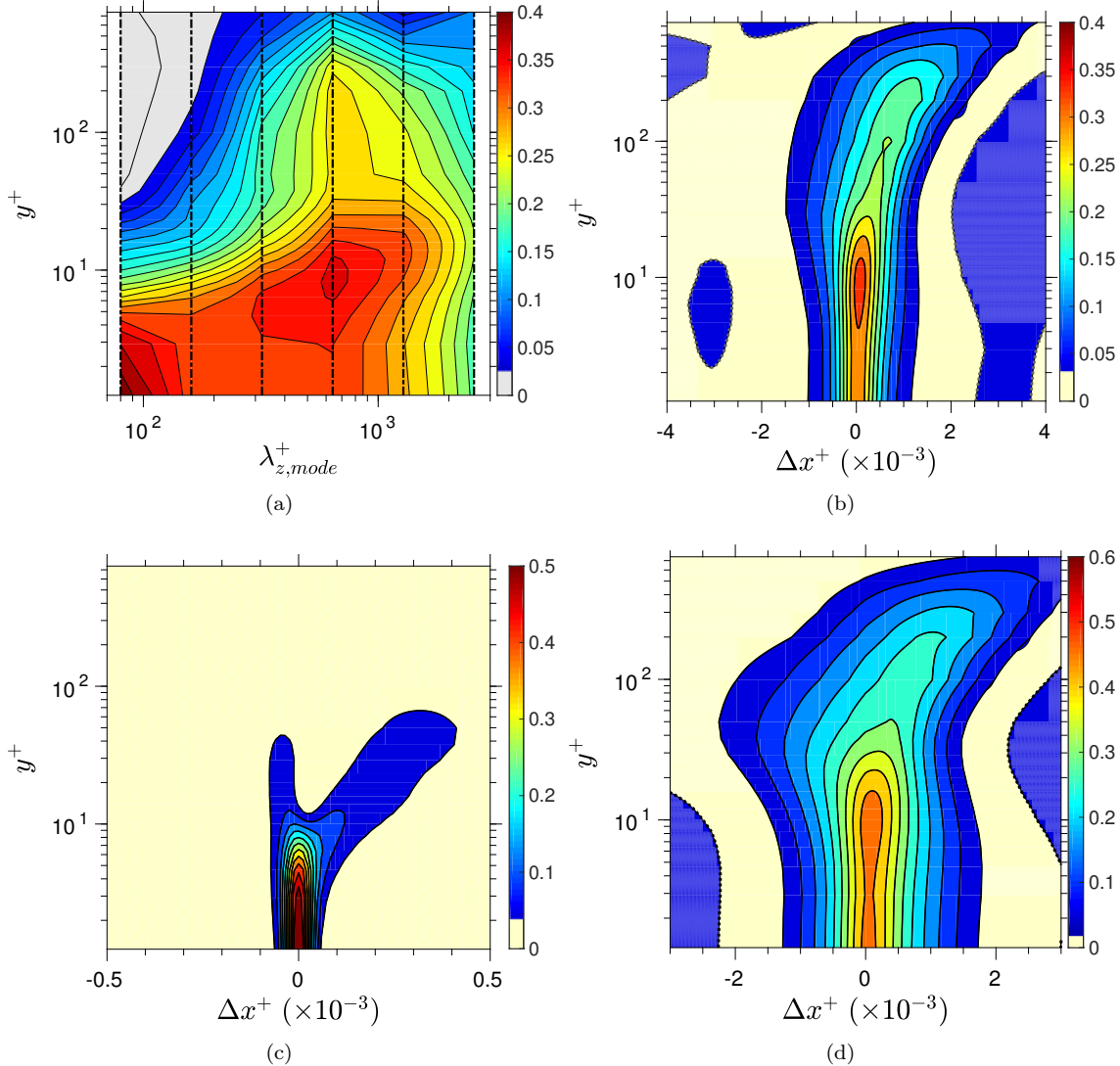


Figure 3.7: Correlation-coefficient maps: (a) map of maximum correlation coefficient  $R_{Cf,mode}(y^+, \Delta x^+)$  at any  $y^+$  position of modes from 1 to 6 with  $Cf$  (black lines have the same meaning as in figure 3); (b) correlation map of  $Cf$  with the mode 4 ; (c) correlation map of  $Cf$  with the small-scale modes (1+2) and (d) correlation map of  $Cf$  with large-scale motions (modes 4+5+6).

beyond the buffer layer and the maximum within it may be attributed to the de-correlating influence of the unsteady transverse Stokes strain in the viscous sublayer. It is also plausible that the peak in correlation is partly due to an asymmetric streak modulation by sweeps and ejections associated with positive and negative large-scale motions, respectively, and additionally to the local generation of mode-4 energy that enhances the impact of scales at the wavelength of mode 4 on near-wall turbulence and skin friction. A degree of support for the last supposition is provided by Figure 3.5(a), which shows the mode-4 energy to be elevated in the buffer layer relative to the energy at  $y^+ > 100$ .

- The composite correlation coefficient of modes 4-6, regarded as large-scale modes, exhibits a maximum correlation coefficient of approximately 0.35 at  $y^+ \approx 200$ , and the  $y$ -wise locus of the maximum features an inclination that characterises a lag of order  $\Delta x^+ \approx 1000$ . This lag was previously highlighted, in qualitative terms, by reference to Figure 3.5(a). The S-shape of the correlation map indirectly indicates that the eddies associated with modes 4-6 are detached, as the shape implies that perturbations are transmitted upwards only in the upper part of the near-wall layer and not from the wall. Here again, it is initially surprising to observe the relatively low magnitude of the correlation coefficient. However, it is informative to note that a map (not included) of the correlation coefficient connecting the large-scale component of  $Cf$  (modes 4-6) with the large-scale velocity fluctuations (modes 4-6) leads to a correlation coefficient of about 0.6 at  $y^+ \approx 200$ .

Finally, it is instructive to refer to Figure 3.14 in Section 3.5, which effectively conveys the effect of large-scale fluctuations on the small scales, where fluctuation fields are reconstructed from modes 1+2 and modes 4+5+6, respectively. The primary conclusion derived from this figure is that regions of elevated and reduced small-scale activity are visually well correlated with the regions of large-scale fluctuations – a relationship that reflects the process of modulation. The fact that streaks are pronounced in regions of positive large-scale fluctuations while being virtually absent in regions of negative large-scale fluctuations provides an initial indication of substantial differences in the level of small-scale modulation within positive and negative large-scale footprints. These differences may be partially connected to the fact that large-scale footprints significantly alter the local level of the friction velocity  $u_\tau$ , causing the wall-scaled period  $T^+$  to depart significantly from the optimum mean value  $T^+ \approx 100$ , thus locally favouring the recovery of streaks during the actuation cycle.

### 3.4 Modal Dissection of the Coherent Motion-Skin Friction Interaction

An subject of particular interest in the context of drag reduction is the origin of the processes that contribute to the generation of drag. One route to investigating this issue is via the Fukagata-Iwamoto-Kasagi (FIK) identity (see Fukagata, Iwamoto, and Kasagi 2002), which derives the friction drag from the cross-flow integrated streamwise momentum equation. In the present channel-flow configuration, the FIK identity takes the simple form:

$$Cf = \frac{6}{Re_b} + 6 \int_0^1 \left(1 - \frac{y}{h}\right) \left(-\frac{\bar{uv}}{U_b^2}\right) d\left(\frac{y}{h}\right) \quad (3.4)$$

With the attribution of modes to the large-, intermediate-, and small-scale fields now established, it becomes possible to quantify the relative contributions of these three groups of modal motions to the skin friction. To accomplish this, the FIK identity can be employed, where the first term represents the viscous contribution,  $Re_b = \frac{U_b h}{\nu}$  is the bulk Reynolds number,  $U_b$  is the bulk velocity, and  $h$  is the channel half-height. The contributions to the shear stress can be represented by the following matrix:

$$\bar{u}_i \bar{v}_j = \begin{vmatrix} \bar{u}_{SS} \bar{v}_{SS} & \bar{u}_{SS} \bar{v}_{AE} & \bar{u}_{SS} \bar{v}_{LS} & \bar{u}_{AE} \bar{v}_{SS} & \bar{u}_{AE} \bar{v}_{AE} & \bar{u}_{AE} \bar{v}_{LS} & \bar{u}_{LS} \bar{v}_{SS} & \bar{u}_{LS} \bar{v}_{AE} & \bar{u}_{LS} \bar{v}_{LS} \end{vmatrix} \quad (3.5)$$

The elements of this matrix can then be inserted into the FIK identity (equation 3.4). In the matrix,  $AE$  represents the attached-eddy mode 3,  $SS$  denotes the sum of modes 1+2, and  $LS$  stands for the combination of modes 4+5+6. Figure 3.8(a) illustrates the profiles of the shear-stress contributions, while Figure (b) conveys the magnitude of the mixed terms  $-\bar{u}_i \bar{v}_j$ , with  $i \neq j$ . These mixed terms express the interactions among the modes contributing to their respective correlations.

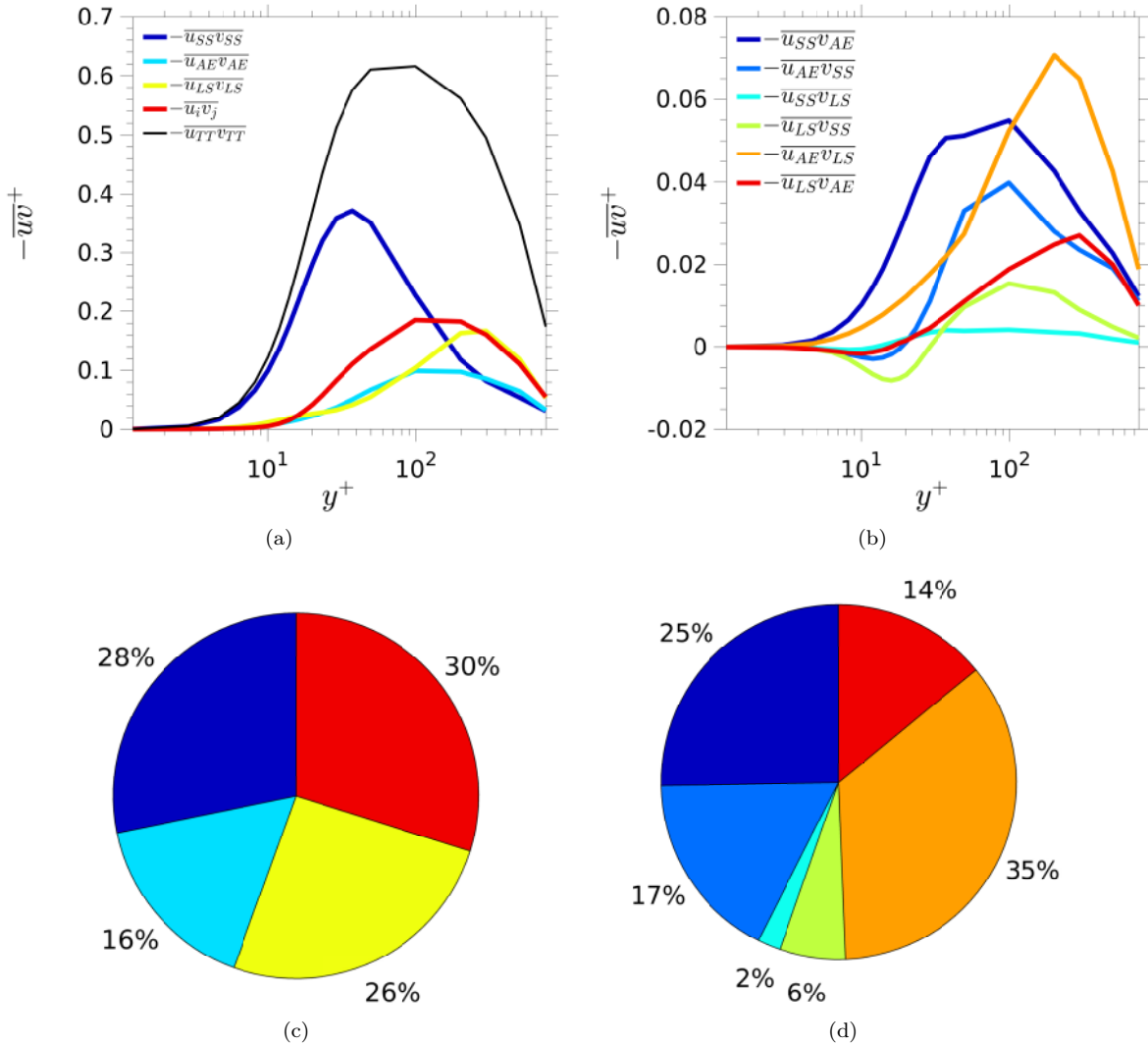


Figure 3.8: Contributions of scales (*SS*-modes 1+2, *LS*-modes 4+5+6 and *AE*-mode 3) to the shear stress and skin friction  $C_f$ ; (a,b) profiles of shear-stress fragments in equation 3.5; (c) contribution of the correlations in figure 5 (a) to the skin friction; (d) contribution of the individual inter-scale fragments  $-u_i u_j$  to the sum of  $-u_i u_j$ .

By decomposing the shear stress into its constituent components, this approach provides a clear and systematic way to assess the relative importance of large-, intermediate-, and small-scale motions in determining the skin friction. The matrix representation, coupled with the FIK identity, offers a concise and effective means of quantifying these contributions, while the accompanying figures provide visual insights into the profiles and interactions of the various terms.

The *LS* contribution to the skin friction is shown to be 26%, but the mixed mode contributions are also substantial, in contrast to the analogous fragments of streamwise energy, as will be shown below. In contrast to the above “direct” contribution of the *LS* modes, their “indirect” effect, via the modulation, cannot be determined by the  $\overline{uv}$  scale decomposition, but the fact that *SS* – *LS* cross-terms are finite suggests that the small-scale modulation is asymmetric. The *AE* mode makes an important contribution too, its direct contribution being 16%. Of the mixed-mode terms, those correlating small-scale and large-scale motions are relatively modest, but the variation of  $\overline{u_{LS}v_{SS}}$  is especially interesting, in so far as this represents the modulating effect of the streamwise *LS* fluctuations on the wall-normal *SS* motions. The correlation is seen to be positive up to about  $y^+ \approx 30$  and negative beyond this distance – i.e., it reduces the magnitude of the shear stress in the near-wall region and increases it outside the buffer layer. A qualitatively similar behaviour

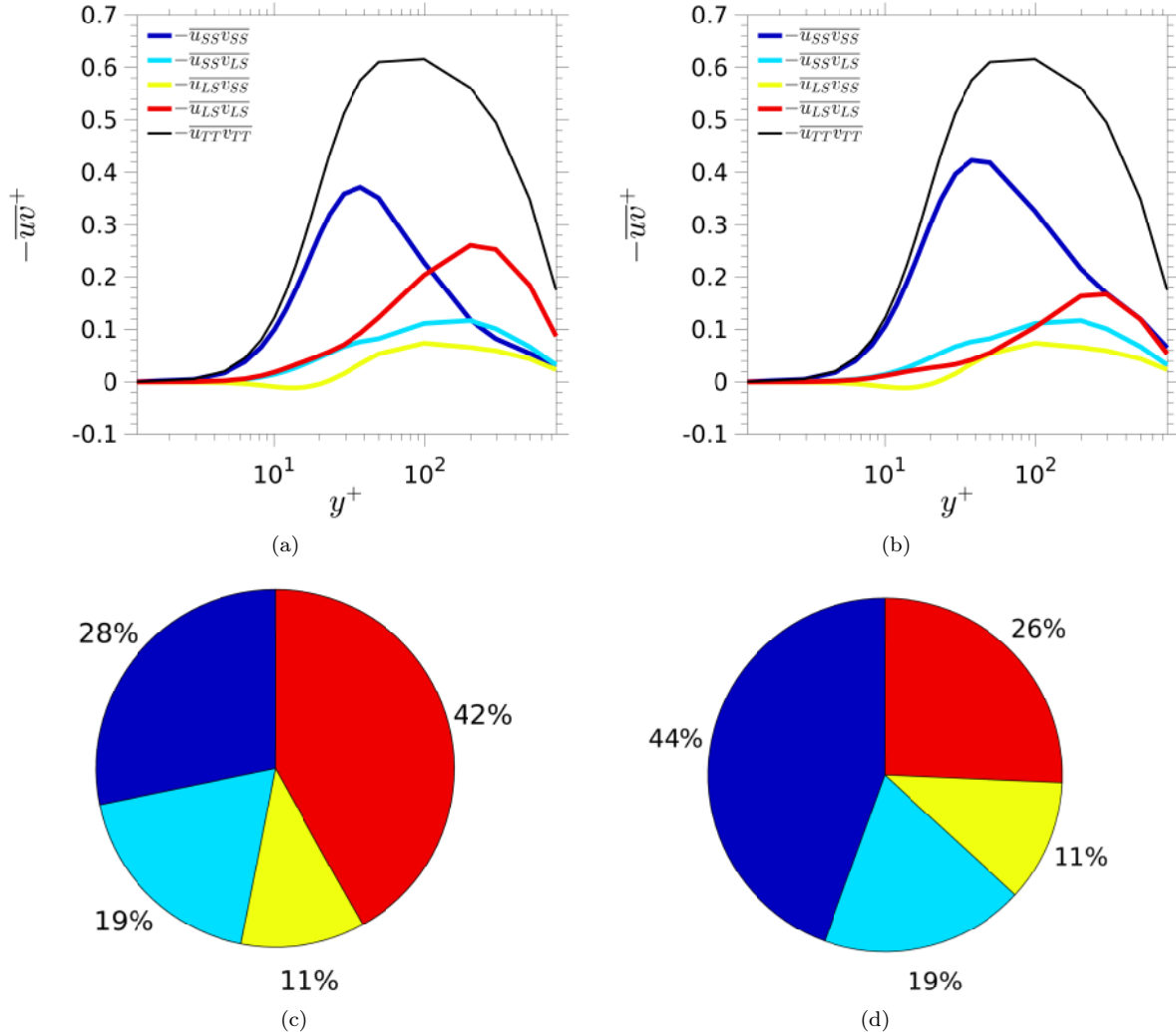


Figure 3.9: Contributions of scales (SS-modes 1+2, LS-modes 4+5+6) to the shear stress and skin friction  $C_f$  subject to the intermediate AE mode 3 being attributed either to the LS set or the SS set; (a,c) profiles of shear-stress fragments and skin-friction contributions with the AE mode included in the LS set; (b,d) profiles of shear-stress fragments and skin-friction contributions with the AE mode included in the SS set.

is also observed in respect of the term  $\overline{u}_{LS}v_{AE}$ .

It is interesting to examine the consequence of including the AE mode either in the LS set or the SS set – that is, to regard the AE mode as being part of the large-scale or part of the small-scale field, respectively. The result of this alternative attributions is shown in Figure 3.9. Thus, the inclusion of the AE mode in the LS set results in the LS contribution to  $C_f$  rising substantially, to 42%, relative to the level of 26% shown in Figure 3.8, while the effect of including the AE mode in the SS field merely causes an increase in the relative contribution of the SS mode to  $C_f$ . In both cases, the contribution of mixed-mode fragments is small, as neither includes explicit correlations involving the AE mode.

The effect of attributing different sets of modes to the SS and LS contributions to the streamwise energy is shown in Figure 3.10. Plots 3.10(a)-(c) correspond, respectively, to the results in Figures 3.8 and 3.9. Thus, in Figure 3.10(a), the AE mode is treated as a separate mode, while in Figures 3.10(b) and (c), the AE mode is included in the LS and SS sets, respectively. In all three cases, the sum of the contributions is equal to the total streamwise energy. Also in all three cases, contributions other than the SS and LS sets are relatively minor, and this includes the relatively modest AE contribution when treated separately. Naturally, the inclusion of the AE mode in the LS set, Figure 3.10(b), elevates the relative importance of the latter, while the inclusion of the AE mode in the SS set, elevates the SS profile.

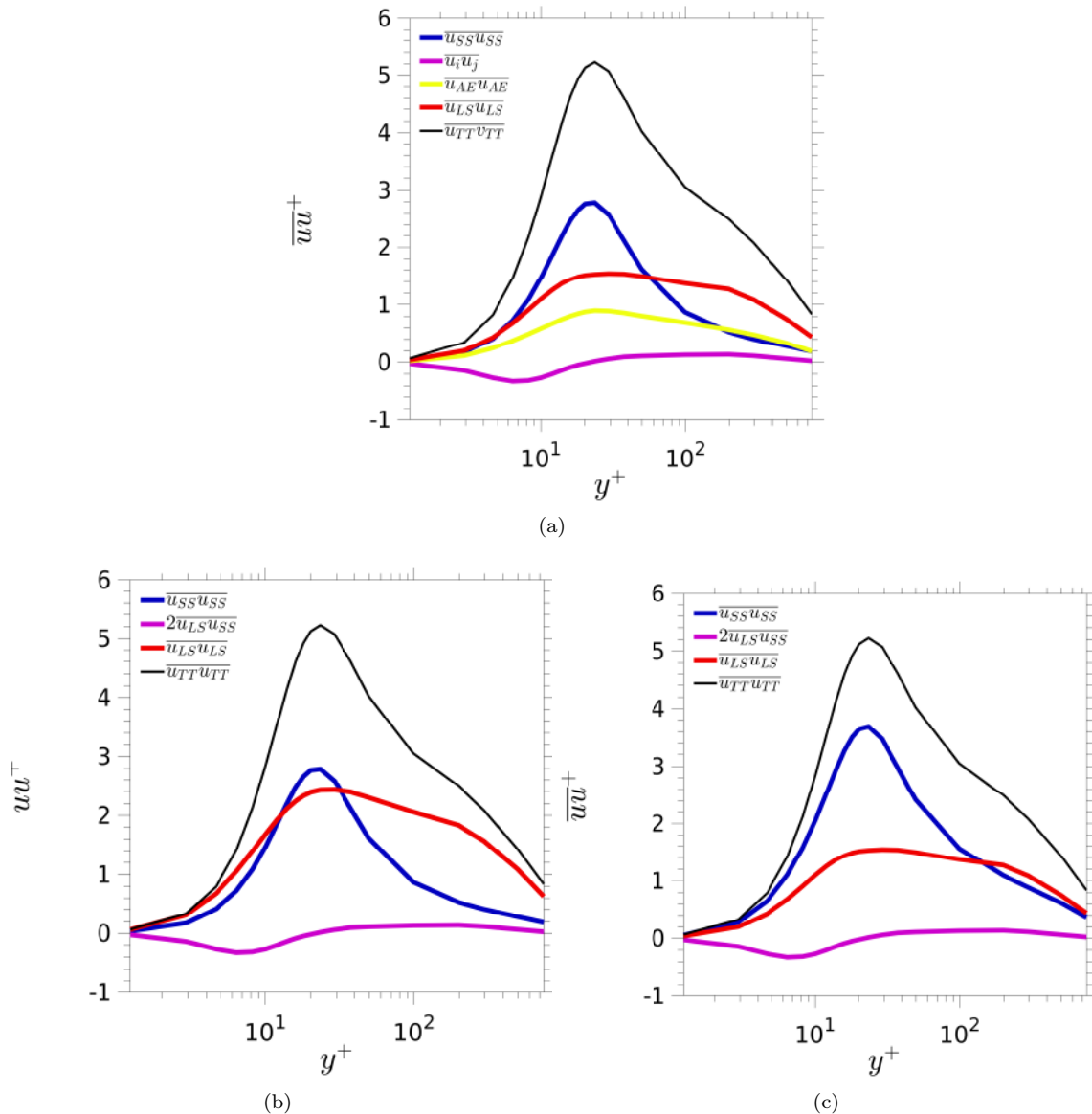


Figure 3.10: Contributions of scales to the streamwise normal stress: (a)  $SS$ ,  $LS$  and  $AE$  modes treated as separate; (b)  $AE$  mode included in the  $LS$  set; (c)  $AE$  mode included in  $SS$  set.

A more differentiated view of the contribution of modes to the skin friction is given in Figure 3.11 by way of streamwise spectra of skin-friction fluctuations. The spectrum of the total (raw) data is given by the black line and features two maxima, namely at  $\lambda_x^+ \approx 150$  and 5000, the former associated with *SS* motions and the latter with *LS* footprints, thus illustrating the importance of the *LS* motions. Figure 3.11(a) shows, separately, the contributions of the *SS*, *LS* and *AE* modes. The sum of these three fragments is also shown by the blue line in Figure 3.11(c), and this demonstrates that this sum is not the total. However, the inclusion of the mixed-mode terms, given by the red line, results in the total being correctly returned. The mixed-mode contributions conveyed by Figure 3.11(b) is seen to be quite influential, and this is analogous to the important contribution made by corresponding mixed-mode terms to the shear-stress profiles in Figure 3.8.

The significance of large-scales to the skin friction and its small-scale field can be further demonstrated using probability density functions (PDFs) of the total (*TT*), large-scale (*LS*), and small-scale (*SS*) fluctuations, normalized by the skin friction of the unactuated flow. These contributions are derived from the EMD decomposition:  $Cf_{TT} = Cf_{SS} + Cf_{AE} + Cf_{LS} + \bar{C}f$ . Figure 3.12 presents these PDFs, with the area underneath all four curves being unity. The mean (centre of gravity) of the PDF of the raw data is 0.7, corresponding to the 30% drag-reduction achieved by the actuation. The *LS* motions cause significant skin-friction fluctuations ranging from approximately -30% to +60% of the mean value, and its PDF is notably skewed, mirroring the skewness of the PDF of the total fluctuations. This skewness signifies a lower incidence of strong positive fluctuations associated with sweeps, relative to a higher incidence of weaker negative fluctuations associated with ejections.

An interesting insight into the effects of the interactions between the *LS* and *SS* motions on the skin friction is provided by the joint  $Cf_{SS} - Cf_{LS}$  PDF, shown in Figure 3.12(d). This plot reveals that *SS* fluctuations are significantly weaker in regions of negative *LS* fluctuations, while they tend to be substantially stronger in regions of positive *LS* fluctuations. This observation indicates a material asymmetry in the modulation of the *SS* fluctuation intensity (or energy) by the *LS* motions – a topic that will be explored in depth in the next section. Furthermore, there exists a non-negligible correlation between *SS* and *LS* fluctuations: large positive *LS* fluctuations are preferentially associated with negative *SS* fluctuations, rather than positive ones. In other words, the "local mean" of the *SS* fluctuations is predominantly negative in the presence of positive *LS* fluctuations. This suggests an increasing level of skewness in the *SS* fluctuations when conditioned on large positive *LS* fluctuations, thus amplifying the asymmetry in the modulation.

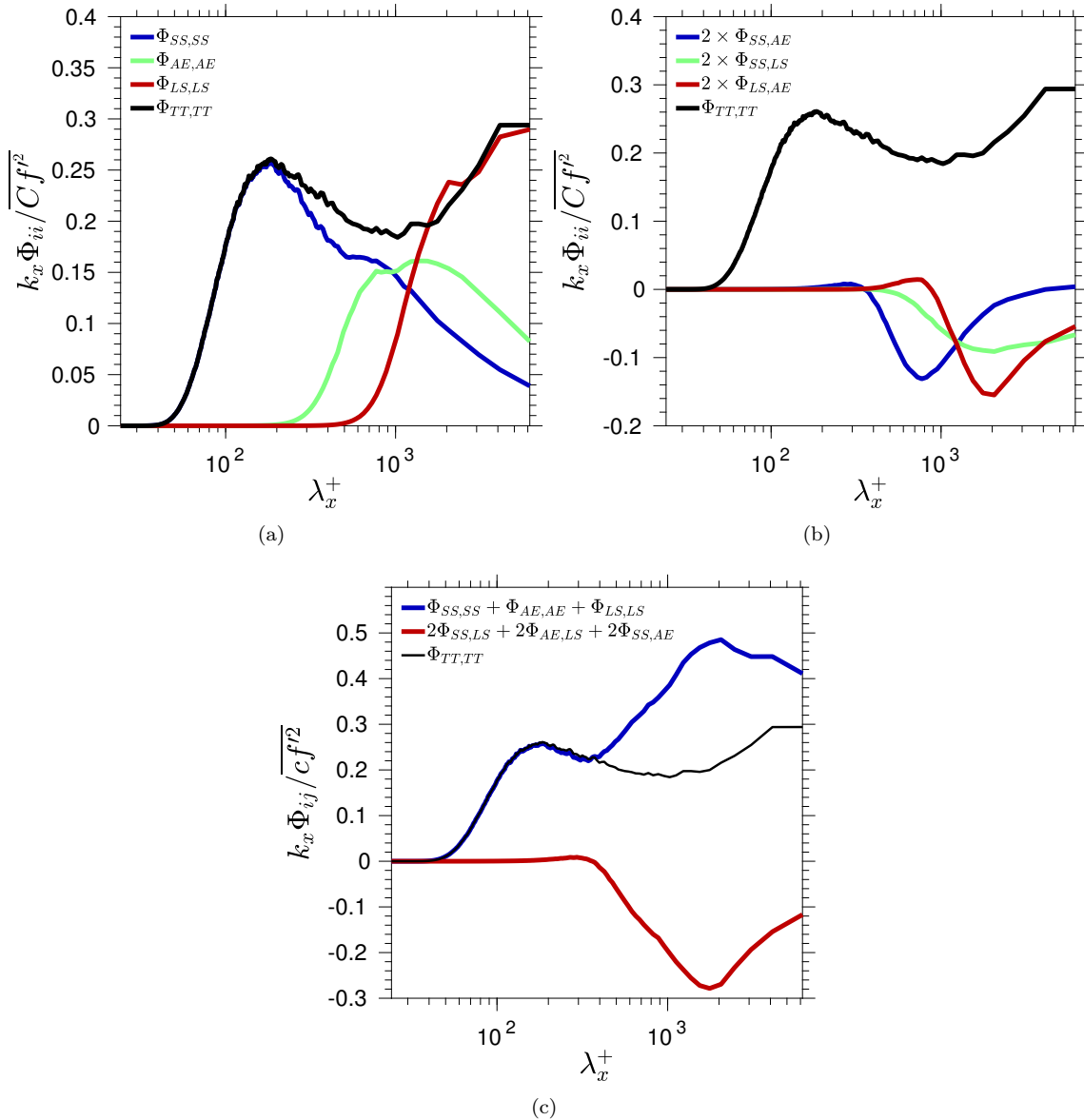


Figure 3.11: Contributions of scales to streamwise skin-friction spectrum: (a) contribution of  $SS, LS$  and  $AE$  modes treated as separate; (b) inter-scales contributions of  $SS, LS$  and  $AE$  modes and (c) sum of principal ( $LS, SS, AE$ ) contributions and mixed-mode contributions

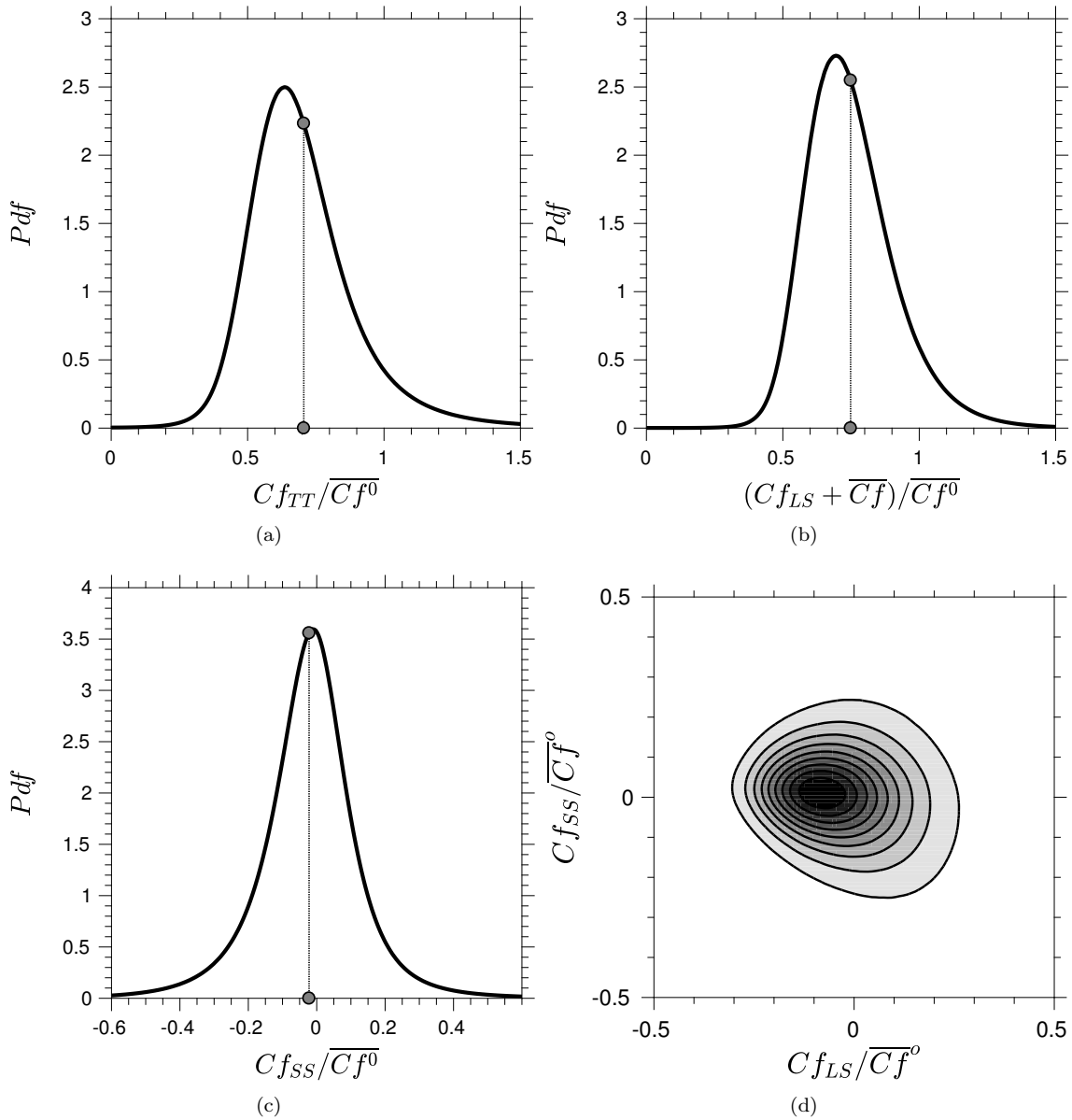


Figure 3.12: PDFs of skin-friction fluctuations: (a) total (raw) data; (b) LS contribution; (c) SS contribution and (d) joint PDF of SS and LS skin-friction fluctuations.

### 3.5 Large-Scale Influences on Near-Wall Streaks

#### 3.5.1 Conditional statistics

##### Methodology

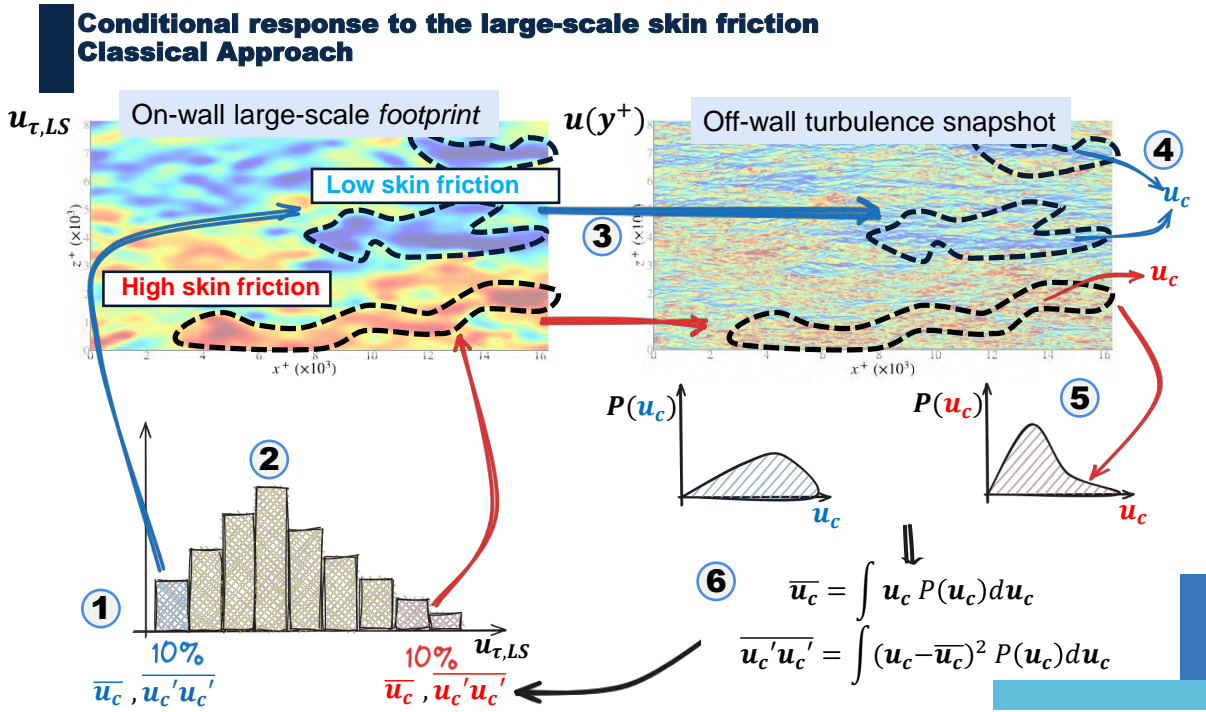


Figure 3.13: Schematic representation of the conditional analysis procedure.

The objective here is to investigate the response of small-scale turbulence to large-scale fluctuation at the wall produced by the outer-flow structures. Conditional analysis provides a powerful approach for investigating this connection by examining the statistical properties of small-scale turbulence conditioned on specific ranges of large-scale skin friction values. This analysis can elucidate the modulation of small-scale turbulence by large-scale structures. To conduct a conditional analysis, the following steps, as illustrated in Figure 3.13, should be undertaken:

1. Define the histogram of the variable upon which the conditional analysis is to be performed. In this instance, the variable of interest is the large-scale friction velocity, denoted as  $u_{\tau,LS}$ .
2. Identify the bins within the histogram of  $u_{\tau,LS}$  that correspond to the events of interest. These bins represent specific ranges of  $u_{\tau,LS}$  values that are to be analysed.
3. Identify the frontiers of patches corresponding to the limit values of the selected bins. These frontiers are then mapped onto the field of the variable for which the analysis is to be performed. In the sketch, this variable is represented by the off-wall streamwise velocity snapshot, denoted as  $u(y^+)$ .
4. Extract the values of  $u(y^+)$  from the patches defined by the frontiers mapped in step 3. These extracted values represent the conditional values of  $u(y^+)$ , given the specific range of  $u_{\tau,LS}$  values in the selected bin, and are noted  $u_c$ .
5. Construct the probability density function (PDF) of the conditional values extracted in step 4. This PDF, denoted as  $P(u_c)$ , represents the distribution of  $u(y^+)$  within the patches corresponding to the selected bin of  $u_{\tau,LS}$  values.
6. Define the conditional statistics using the PDF obtained in step 5. The conditional mean ( $\bar{u}_c$ ) and conditional variance ( $(\bar{u}'_c u'_c)$ ) can be calculated using the following equations:

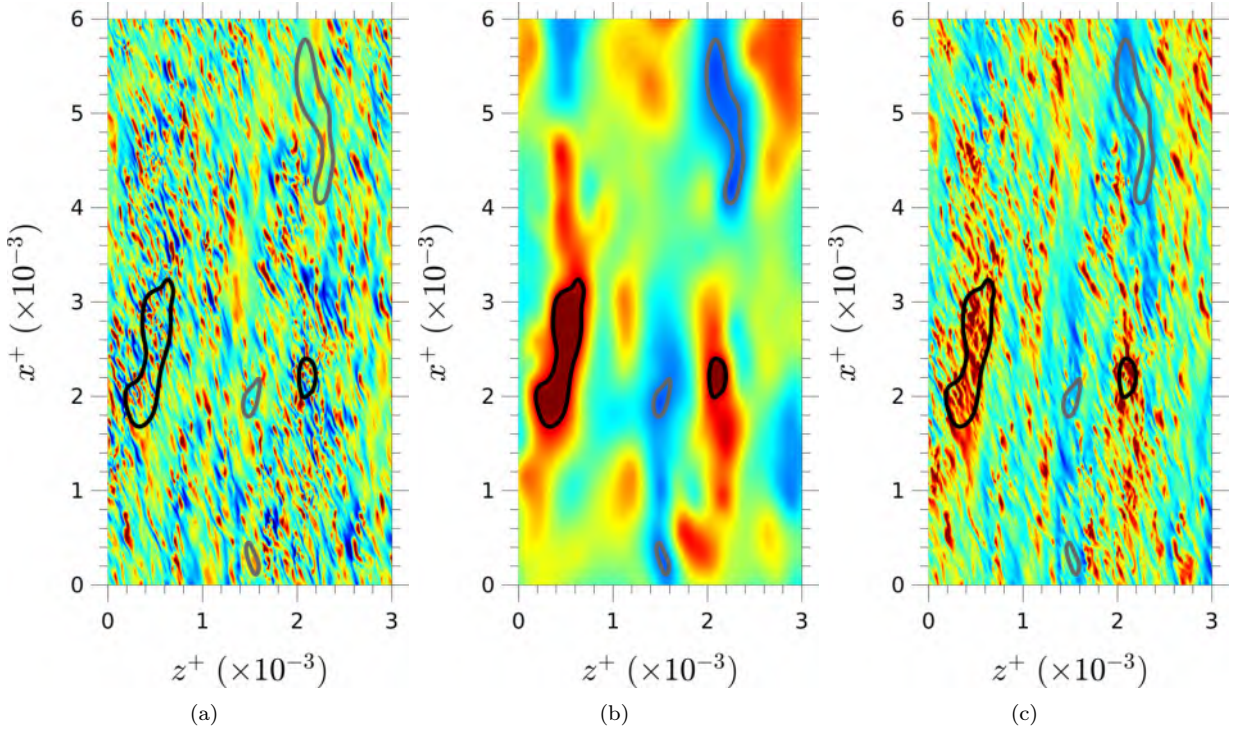


Figure 3.14: Illustration of the conditional sampling and averaging process for small-scale properties within defined portions of large-scale footprints; (a) *SS* field, (b) *LS* field and (c) raw field, at  $y^+ = 13$ .

$$\overline{u_c} = \int u_c P(u_c) du_c \quad (3.6)$$

$$\overline{u'_c u'_c} = \int (u_c - \overline{u_c})^2 P(u_c) du_c \quad (3.7)$$

7. Repeat steps 2-6 for every range of large-scale friction velocity ( $u_{\tau,LS}$ ) values of interest. This allows for the analysis of the conditional response of  $u(y^+)$  to different ranges of  $u_{\tau,LS}$  values.

By adhering to these steps, a comprehensive conditional analysis can be conducted to investigate the manner in which the off-wall turbulence responds to various ranges of large-scale skin friction ( $u_{\tau,LS}$ ) values.

### Application

In order to extract statistical data that provide insight into the interactions between the large outer and small inner scales, statistics are derived from the *SS* velocity fluctuations conditioned on regions of high-velocity, low-velocity, and near-zero *LS* footprints. Regions of high-velocity and low-velocity *LS* motions are defined here as those which fall into a chosen portion (5%, 10%, etc.) of the lowest and highest motions within the PDF of the entire *LS* field, while regions which are, essentially, devoid of *LS* footprints are defined as those which fall into a selected central portion of the PDF. This is illustrated in Figures 3.14(b) and (c), which exemplify, respectively, sampled patches within the fields of *LS* and *SS* motions, subject to a condition level of +5%. It needs to be emphasized that there is no fundamentally profound reason for any particular choice of the bands in the *LS* PDF within which *SS* motions are sampled. A choice of 5% or 10%, say, is motivated by the wish to bring out as clearly as is possible differences in the effects of positive and negative *LS* fluctuations on the *SS* motions. Increasing the conditional limit weakens these differences, but does not change the nature of the message, as will be shown below.

Figure 3.14 conveys the fact that the streaky structure — the inclined densely-spaced lines — are rather weak in regions of low *LS* motions, due to the fact that the near-optimum wall actuation (in the mean)

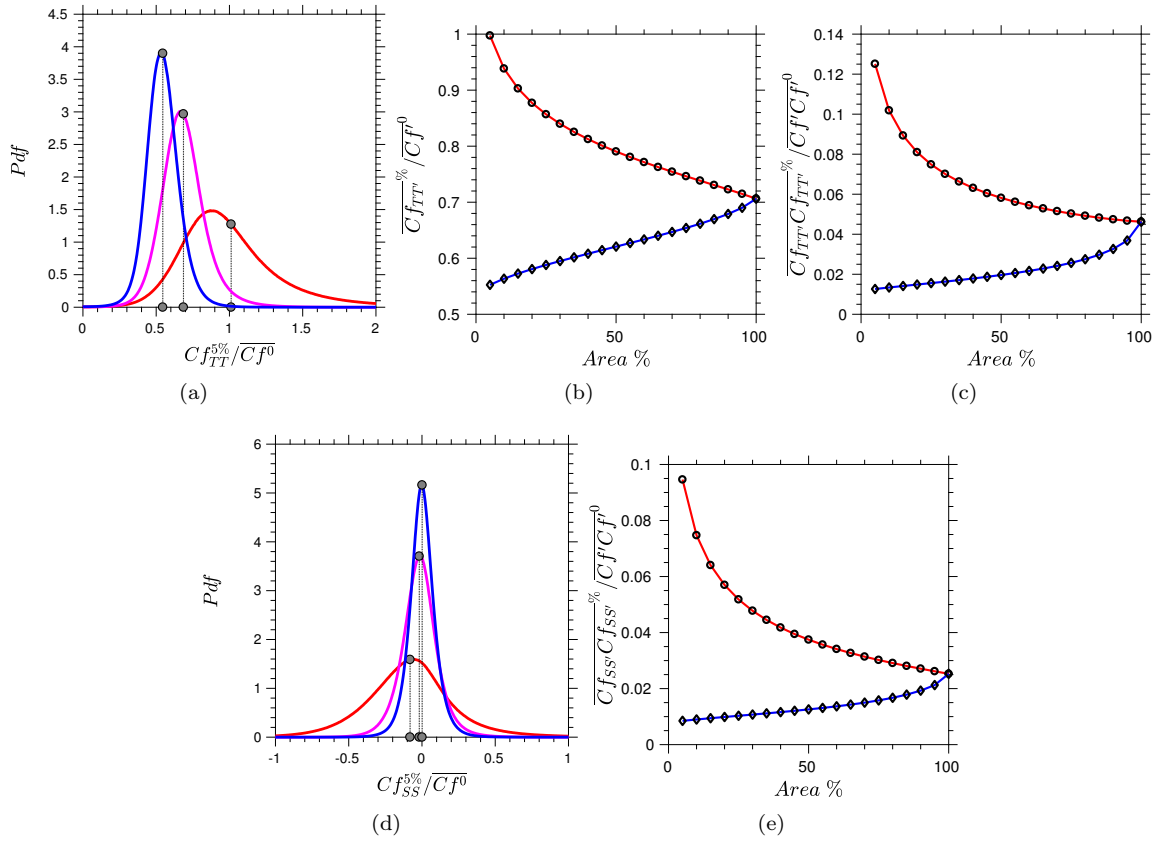


Figure 3.15: PDFs of skin-friction fluctuations: (a) PDFs of total fluctuations conditional on extreme 5% of large-scale fluctuations (red and blue profiles) and on 5% regions of lowest large-scale fluctuations (purple profile); (b) variation of mean skin friction (centres of gravity of PDFs in (a)) in regions of extreme large-scale fluctuations as a function of the condition,  $Area = 5 - 100\%$ , imposed on extreme large-scale fluctuations (5-100%); (c) variation of variance of PDFs in (a) subject to same conditions as (b); (d) PDFs of small-scale skin-friction fluctuations subject to same conditions as (a); (e) variation of variance of small-scale fluctuations subject to same conditions as (c).

substantially depresses the streamwise energy in the buffer layer. The streaks are evidently amplified by positive  $LS$  footprints. This type of amplification – or positive modulation – is also observed in canonical (uncontrolled) channel flow (see Agostini and Leschziner 2014; Agostini and Leschziner 2016a), but the effect may be accentuated by the fact that the locally elevated wall shear stress leads to locally non-optimum values of the wall-scaled actuation period  $T^+ = Tu_\tau^2/\nu$  (note the quadratic dependence on  $u_\tau$ ).

### 3.5.2 Characterising Skin-Friction Fluctuations in Large-Scale Footprints

In order to gain a more detailed, quantitative, view of the effects of the footprints on the skin-friction, conditional PDFs for the total skin-friction,  $Cf_{TT}$ , and small-scale skin-friction fluctuations,  $Cf_{SS}$ , were assembled in patches characterised by (i.e., conditioned on) prescribed limits of large-scale footprints. Figure 3.15(a) and (d) each shows three PDFs for  $Cf_{TT}$  and  $Cf_{SS}$ , respectively, two within regions conditioned on 5% positive and negative  $LS$  fluctuations and the third within the central 5% region in which the  $LS$  motions are weakest. All distributions are normalised by the mean skin-friction value of the unactuated flow, i.e. 1/0.7 of the actuated case. The vertical black lines indicate the centres of gravity of the respective PDFs – i.e., in the case of  $Cf_{TT}$  in Figure 3.15(a), the mean value of the skin friction is 0.7. Figure 3.15(b) and (c) show, respectively, the variations of the centers of gravity of the PDFs for the extreme positive and negative  $LS$  fluctuations and the variance of the PDFs as the value  $LS$  condition is progressively increased from 5% to 100% (identified by  $Area\%$ ), the latter representing the non-conditioned overall mean. Figure 3.15(e) pertains to the  $Cf_{SS}$  fluctuations and correspond to 3.15(c). A first conclusion emerging from the figure is that skin-

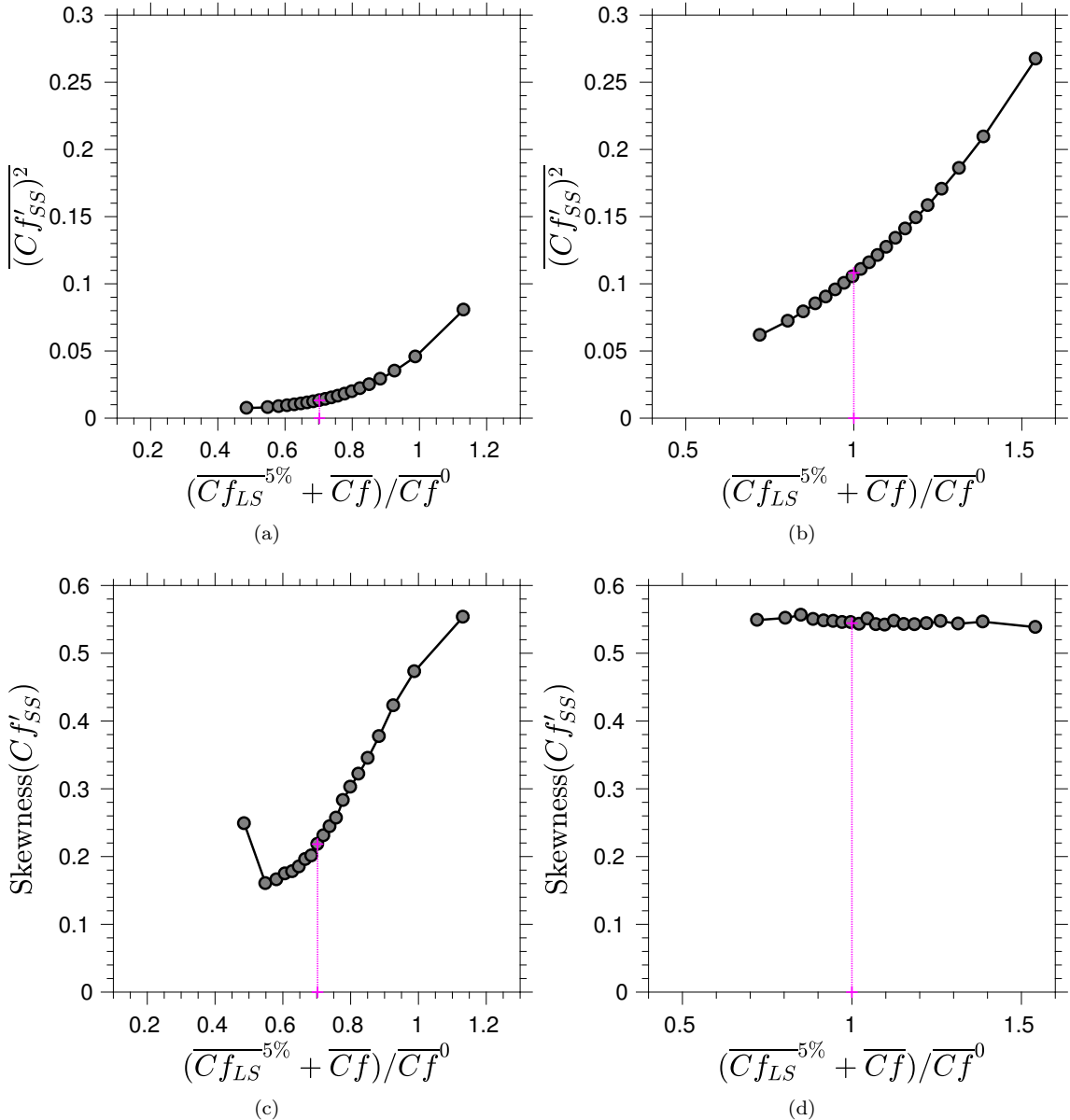


Figure 3.16: Asymmetric response of *SS* skin-friction fluctuations to the *LS* footprints: (a) variance for actuated flow; (b) variance for unactuated flow; (c) skewness for actuated flow; (d) skewness for unactuated flow. The circles indicate the centres of the 5% slivers of the *LS* PDF for the skin-friction fluctuations within which the *SS* PDFs have been determined. The vertical magenta lines indicate the average drag level, relative to the unactuated-flow value.

friction fluctuations are extremely high, especially within regions of high positive  $LS$  fluctuations. Thus, skin-friction fluctuations within regions of highest  $LS$  footprints exceed 100% of the overall average value. Moreover, the mean  $Cf_{TT}$  value within the extreme positive 5%  $LS$  fluctuations is about 30% higher than the average, while the standard deviation reaches 35% (the variance being 0.13). A second observation is that the variance of the PDFs, essentially representative of the intensity of the small-scale motions, differs greatly for positive and negative  $LS$  fluctuations, the variance associated with positive footprints being much larger. In other words, the modulation of the small-scale motions and skin-friction fluctuations is highly asymmetric. This is, thus, a quantitative confirmation of the qualitative observations previously made, by reference to Figure 3.14, and also Figure 3.12(d) – namely, that positive  $LS$  footprints cause (or are associated with) with a substantial amplification of small-scale activity, while negative footprints only cause weak attenuation of the  $SS$  fluctuations, which are already weak because of the actuation. Attention is drawn to the fact that the variance of the PDF for  $Cf_{SS}$ , Figure 3.15(b), is similar to that of the  $Cf_{TT}$  PDFs, thus justifying the earlier assertion that the shape of the PDFs of the total fluctuations is essentially representative of those for the  $SS$  fluctuations.

In Figure 3.15, it is demonstrated that increasing the  $LS$  condition value, i.e., moving towards the tail regions of the  $LS$  PDF where  $SS$  fluctuations are sampled, leads to a gradual convergence of the variance values of the PDFs for positive and negative  $LS$  fluctuations. This convergence culminates in a single value representing the mean state. To examine the properties of  $SS$  PDFs within the range of  $LS$  fluctuations more closely, the  $LS$  skin-friction PDF is divided into 5% sub-ranges or *slivers*. Within each sliver, the  $SS$  variance and skewness are determined. Figure 3.16 presents these results, comparing them to corresponding values for the unactuated flow at the same Reynolds number. The superscript 5% in the abscissa denotes the mean value of  $Cf_{LS}$  in the respective sliver, and the magenta lines indicate the overall mean skin friction value for both cases. The left-most value in all four figures pertains to the extreme negative tail of the  $LS$  PDF (condition  $-5\%$ ), while the right-most value corresponds to the extreme positive  $LS$  PDF condition ( $+5\%$ ).

Regarding the variance, the overall level in the actuated flow is significantly lower than in the canonical flow, reflecting the much lower intensity of small-scale turbulence, including streaks, in the buffer and viscous sublayers. In both cases, the variance increases substantially with increasing  $LS$  intensity. However, the rate of increase is much steeper in the actuated case: the variance rises sharply for increasing positive  $LS$  skin-friction fluctuations and declines modestly for negative  $LS$  fluctuations. This demonstrates that, in the actuated case, the response of small-scale turbulence to the  $LS$  motion is much more asymmetric with respect to the sign of the  $LS$  fluctuations, compared to the nearly linear variation in the canonical flow. An even more striking reflection of the asymmetric response to  $LS$  fluctuations emerges from the comparison of the skewness distributions. In the canonical case, the skewness is almost constant, while in the actuated case, it increases progressively with increasing  $LS$  intensity from a very low level at negative  $LS$  fluctuations, where turbulence is low, streaks are very weak, and turbulence is nearly Gaussian. The positive skewness at large positive  $LS$  fluctuations is well captured by the PDF in Figure 3.15 and is also consistent with the skewed features of the joint PDF in Figure 3.12(d). The increasingly positive skewness arises in combination with large-scale sweeping motions, which tend to transport high-intensity  $SS$  energy from the buffer layer towards the wall, favoring high positive  $SS$  fluctuations relative to negative fluctuations associated with ejections. Thus, the asymmetric response of the  $SS$  field to the  $LS$  fluctuation structures is expressed by both the width and shape of  $SS$  PDFs.

To summarise, the PDF of large-scale skin-friction fluctuations (Figure 3.6(a)) displays a significant asymmetry. A snapshot of the raw turbulent fluctuation field at  $y^+ \approx 3$  (Figure 3.6(c)) serves as a good approximation of skin friction. Notably, highly skewed small-scale patterns are observed in the high-velocity red zones, which correspond to near-wall streaks influenced by the Stokes strain. Applying Empirical Mode Decomposition (EMD) to this field allowed for the isolation of large-scale fluctuations, as shown in Figure 3.6(b). The highlighted areas in this Figure identify extreme  $+15\%$  and  $-15\%$  large-scale fluctuation events within the PDF of the large-scale motions on this plane. To analyse turbulence statistics (e.g., small-scale stresses) in relation to the large-scale motions, small-scale motions were sampled within the islands conveyed by Figures 3.6(b) and (c). Specifically, the large-scale PDF was divided into 5% bins, and these bins were sampled across all  $y^+$  planes where DNS data was available. In the following section, a novel and more general methodology for analysing statistical flow properties conditioned on large-scale skin-friction fluctuations will be introduced. This approach utilizes multivariate joint probability density functions, enabling the examination of any conditioning skin-friction signal value.

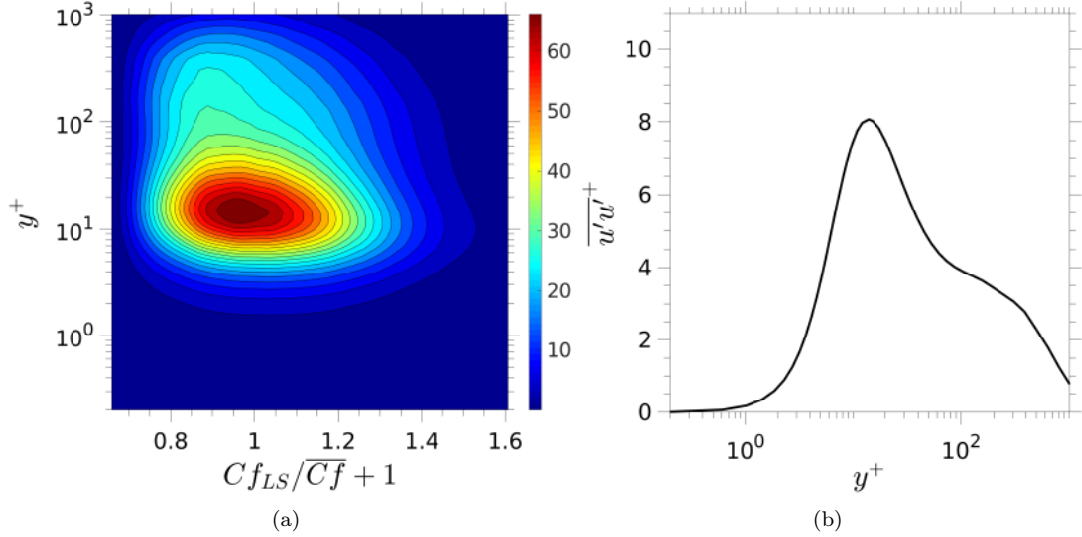


Figure 3.17: Properties of streamwise stress  $\bar{u}'u'^+$ : (a) map of stress derivative  $d\bar{u}'u'^+/dCf_{LS}$  across  $(Cf_{LS}, y^+)$  plane (equation 3.12); (b) wall-normal profile of the stress arising from integration of the field in map (a) with respect to  $Cf_{LS}$ .

## 3.6 The Multivariate Joint PDF Analysis

### 3.6.1 Leveraging Multivariate Joint PDF for In-depth Statistical and Conditional Analysis

The principal merit of this novel approach, based on multivariate joint PDFs, is that it allows a transparent identification of the mechanisms responsible for the observed response of the turbulent statistics to the large-scale motions. Here, only its key elements are summarised.

#### Estimating the conditional contribution to the total statistics

The general joint pdf  $P(X_1, \dots, X_n, Y)$  and  $P(X_1, \dots, X_n, Y)/P(Y)$ , the latter referred to as *conditional PDF*. The arguments  $X_i$  signify any flow variables of interest, such as velocity components or modal constituents derived via empirical mode decomposition. The argument  $Y$  denotes a distinct “conditioning variable” - statistics presented herein principally examine correlations between the  $X_i$  conditioned on specific states of  $Y$ . This facilitates targeted analysis of the relationship between the flow variables  $X_i$  and  $Y$ .

A standard condition imposed on the joint PDFs is,

$$\int_{-\infty}^{+\infty} \cdots \int_{-\infty}^{+\infty} P(X_1, \dots, X_n, Y) dX_1 \dots dX_n dY = 1. \quad (3.8)$$

The joint probability density functions can be used to derive quantities such as the mean value of any variable  $X_i$ ,

$$\bar{X}_i = \int_{-\infty}^{+\infty} \cdots \int_{-\infty}^{+\infty} X_i P(X_1, \dots, X_n, Y) dX_1 \dots dX_n dY, \quad (3.9)$$

the variance of fluctuations relative to the mean values,  $x'_i = X_i - \bar{X}_i$ , with  $\bar{x}'_i = 0$ ,

$$\begin{aligned} x'_i x'_j &= \overline{(X_i - \bar{X}_i)(X_j - \bar{X}_j)} \\ &= \bar{X}_i \bar{X}_j - \bar{X}_i \bar{X}_j, \end{aligned} \quad (3.10)$$

and distributions of the mean and variance across the conditioning variable  $Y$  - respectively,

$$\frac{d\bar{X}_i}{dY} = \int_{-\infty}^{+\infty} \cdots \int_{-\infty}^{+\infty} X_i P(X_1, \dots, X_n, Y) dX_1 \dots dX_n \quad (3.11)$$

$$\frac{d\bar{x}'_i x'_j}{dY} = \frac{d\bar{X}_i \bar{X}_j}{dY} - \frac{d\bar{X}_i}{dY} \frac{d\bar{X}_j}{dY} \quad (3.12)$$

These derivatives thus represent the contribution of the properties in question to their respective totals within a band of  $dY$ , and their integral with respect to  $Y$  then yields the property itself.

Figure 3.17 arises from the particular example,  $i = 1, j = 1, n = 1, X_1 = U^+$  in equation (3.11) and (3.12), and  $Y = Cf_{LS}$ , the large-scale skin-friction fluctuation – i.e. the local and instantaneous value associated with large-scale footprints. The distribution  $d\bar{u}' u'^+ / dCf_{LS}$  at any  $y^+$  location can be derived from equation 3.12 and the wall-normal profile of the streamwise stress  $\bar{u}' u'^+$  then arises upon integrating this field over  $Cf_{LS}$ . The former field is shown in Figure 3.17(a) and the latter profile is given in r.h.s plot.

### Highlighting the conditional response of any variable

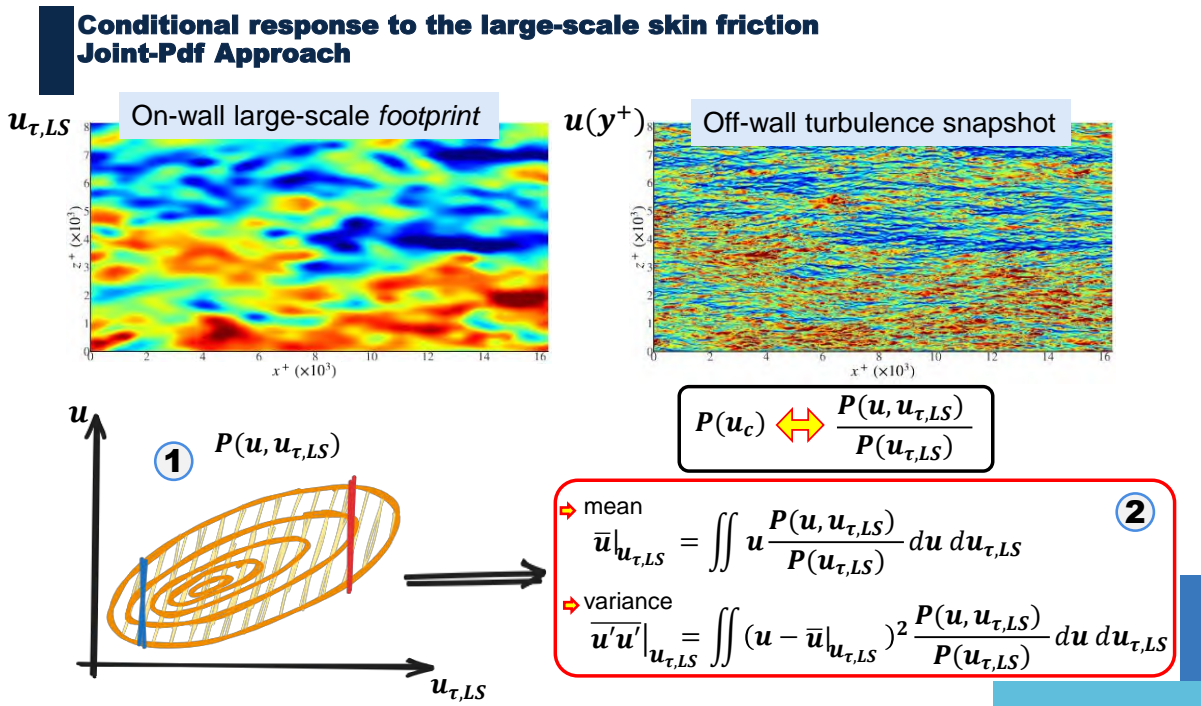


Figure 3.18: Illustration of the principles of conditional statistical analysis leveraging multivariate joint PDF.

A second set of informative statistical quantities are the conditional mean values and associated variances of  $X_i$ , conditioned on specific values of  $Y$ . These are calculated using the equations:

$$\bar{X}_i|_Y = \int_{-\infty}^{+\infty} \cdots \int_{-\infty}^{+\infty} X_i \frac{P(X_1, \dots, X_n, Y)}{P(Y)} dX_1 \dots dX_n \quad (3.13)$$

$$\begin{aligned} \bar{x}'_i x'_j |_Y &= \overline{(X_i - \bar{X}_i|_Y)(X_j - \bar{X}_j|_Y)} |_Y \\ &= \overline{X_i X_j}|_Y - \bar{X}_i|_Y \bar{X}_j|_Y \end{aligned} \quad (3.14)$$

The merit of the conditional mean and variance is illuminating the influence of large-scale fluctuations on the considered quantities  $X_i$ , without obscuring effects from low probability density levels in  $P(Y)$ .

Specifically,  $X_i$  represent instantaneous velocity components, while  $Y$  denotes the local, instantaneous skin friction driven by large-scale footprints,  $Cf_{LS}$ . In other words, variations in statistical velocity field properties (e.g. stresses and production rates) as a function of  $Cf_{LS}$  are examined. This relates the contributions of pertinent statistical properties to the sign and magnitude of skin-friction footprints. Since the actuated channel flow is statistically streamwise homogeneous, statistical properties only depend on wall-normal distance  $y$ . Thus, any property can be conveyed by contour maps in the  $y - Cf_{LS}$  plane, removing time lags between wall fluctuations and outer flow.

The joint probability density function (PDF) approach provides a more efficient and accurate estimation of conditional statistics compared to the classical method illustrated in Figure 3.13. To demonstrate the advantages of this alternative technique, the response of  $u(y^+)$  to large-scale footprints is investigated, following the same example as the classical approach. Figure 3.18 presents a visual representation of this methodology. For this example, the joint-PDF approach relies on the construction of a multivariate PDF, denoted as  $P(u, u_{\tau,LS})$ , which represents the joint probability distribution of the off-wall streamwise velocity,  $u(y^+)$ , and the large-scale skin friction velocity,  $u_{\tau,LS}$ . From this joint-PDF, the conditional statistics can be directly extracted without the need for a conditional velocity field,  $u_c$ .

The conditional mean,  $\bar{u}|u_{\tau,LS}$ , and conditional variance,  $\overline{u'u'}|u_{\tau,LS}$ , can be calculated using the following equations:

$$\bar{u}|u_{\tau,LS} = \iint u \frac{P(u, u_{\tau,LS})}{P(u_{\tau,LS})} dudu_{\tau,LS} \quad (3.15)$$

$$\overline{u'u'}|u_{\tau,LS} = \iint (u - \bar{u}|u_{\tau,LS})^2 \frac{P(u, u_{\tau,LS})}{P(u_{\tau,LS})} dudu_{\tau,LS} \quad (3.16)$$

Figure 3.18 provides an illustration of how the conditional mean and variance are determined from these equations for  $u(y^+)$  and  $u_{\tau,LS}$ . Compared to the classical approach shown in Figure 3.13, the joint-PDF method requires significantly fewer steps. The conditional statistics can be directly extracted from the joint-PDFs, eliminating the need for a conditional velocity field,  $u_c$ , as the conditional PDF,  $P(u_c)$ , can be directly estimated from the joint-PDF. The main advantage of the joint-PDF approach is that the conditional analysis can be performed for any single value of  $u_{\tau,LS}$ , rather than over bins as in the classical approach, this allows for a continuous variation of the conditional statistics over  $u_{\tau,LS}$  to be estimated. Furthermore, the higher-order statistics are more accurate, as they are estimated from conditional means determined from a single value of  $u_{\tau,LS}$ . In addition, the joint-PDF approach can be extended to multivariate PDFs, such as  $P(u, v, w, p, u_{\tau,LS})$ , which include additional variables like the wall-normal velocity ( $v$ ), spanwise velocity ( $w$ ), and pressure ( $p$ ). From these multivariate PDFs, a wide range of statistics can be constructed to any order, including terms such as the production term and skewness, among others.

The joint-PDF approach to conditional analysis offers a more efficient and precise method for investigating the relationship between large-scale structures and small-scale turbulence in turbulent flows. By directly extracting conditional statistics from joint-PDFs, this approach provides a continuous variation of the conditional statistics over  $u_{\tau,LS}$  and more accurate higher-order statistics. The extension to multivariate PDFs further enhances the versatility of this method, allowing for the construction of a wide range of statistics to gain deeper insights into the complex dynamics of turbulent flows, as it will be shown in following sections.

### 3.6.2 Relating Large-Scale Wall Events to Local Shear Strain Behaviours

The dependence of the mean-flow properties on the intensity of the large-scale footprints is conveyed by Figure 3.19. An important reason for examining these properties, in particular the strain rate, is that they are relevant, in conjunction with the Reynolds stresses, to the stress-production levels and also to the response of the small-scale turbulence levels near the wall to the footprints. Figure 3.19(a), (c) and (e) show, respectively, maps of the streamwise velocity, wall-normal velocity and strain rate, all three conditional on the large-scale skin-friction fluctuations  $Cf_{LS}$ . These maps arise from the application of the normalised PDFs, eq.(3.13), the aim being to avoid the obscuring influence of low probability density within the tails of the PDF in Figure 3.6(a), and they thus bring out the impact of the large-scale footprints relative to number of  $Cf_{LS}$  events (or probability density). The five full-line profiles in figures 3.19(b), 3.19(d) and 3.19(f) are sections through the corresponding contour maps at the five locations marked in Figure 3.6(a), the two locations on either side of the PDF median value bounding 10% and 1% of the extreme events, respectively. In addition, the dashed-line profiles represent the respective mean values across the entire  $Cf_{LS}$  range, the grey curve in

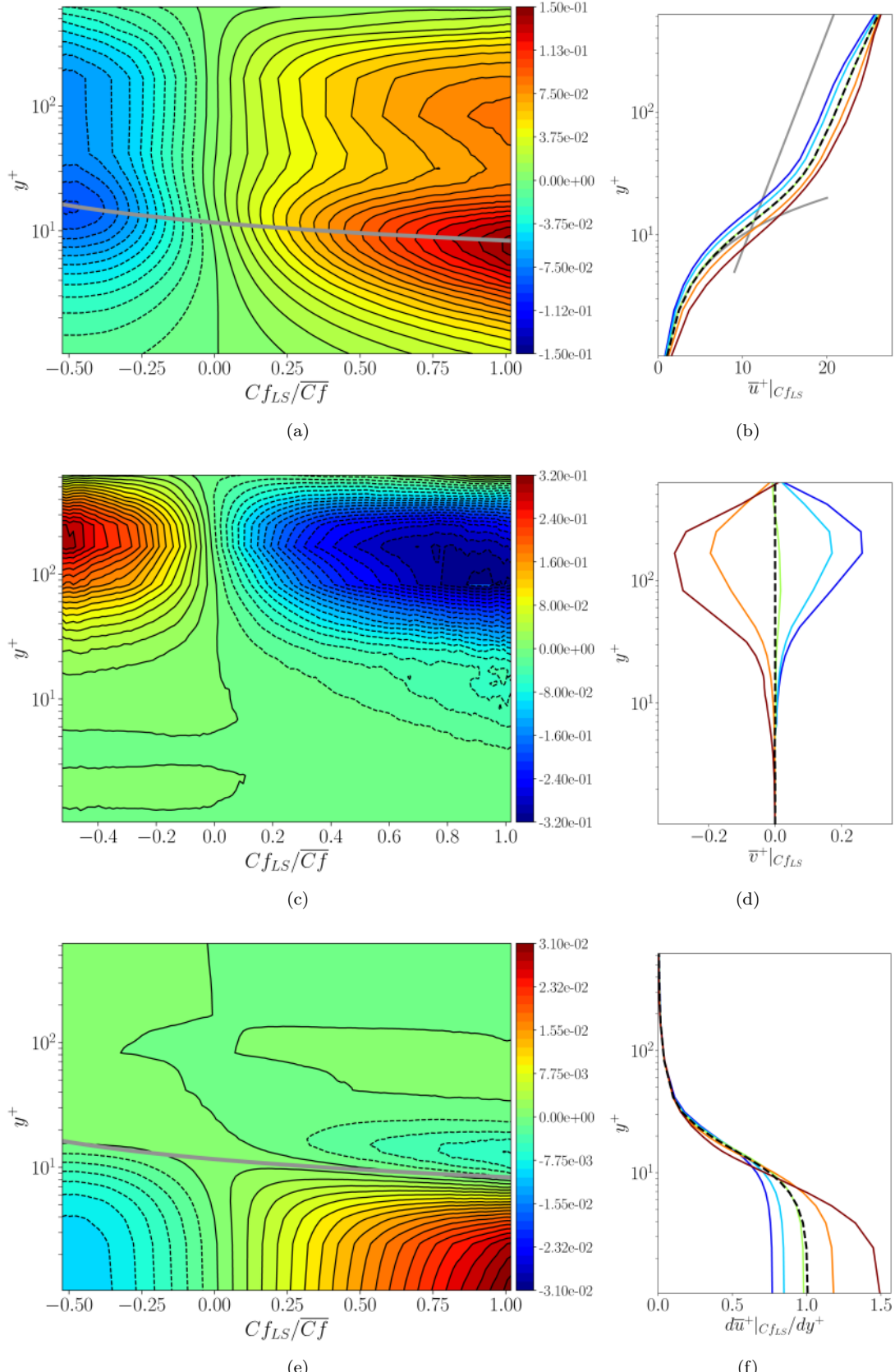


Figure 3.19: Velocity and strain fields conditional on large-scale skin-friction fluctuations: (a) mean streamwise velocity field relative to the average ( $\bar{u}^+|_{Cf_{LS}} - \bar{u}^+$ ); (b) velocity profiles at the five locations marked in the PDF in Figure 3.6(a); (c,d): as (a,b), respectively, but for the wall-normal velocity; (e,f) as (a,b), respectively, but for the streamwise shear strain rate ( $\bar{du}^+|_{Cf_{LS}}/dy - du^+/dy$ ). Dashed lines in (b), (d) and (f) are the respective mean profiles. Grey line and curve in (b) represent the canonical log-law and viscous-layer profile, respectively. Grey curve in (a) and (e) is the locus  $y_{LS}^+ \approx 12$ , with  $LS$  denoting scaling with large-scale friction velocity.

[3.19\(a\)](#) is the locus of  $y_{LS}^+ = 12$ , in which  $LS$  identifies scaling with the large-scale friction velocity, and the grey lines in [3.19\(b\)](#) identify the canonical log-law and the viscous-layer law, respectively. As regards the last item, attention is drawn to the fact that the mean-velocity profiles lying above the canonical log law is a well-known manifestation of the reduced drag level resulting from the actuation. The discontinuities in the slope of some of the profiles and contours in the outer region are due to the fact that the unsteady-flow data arising from the DNS were only saved at a relatively small number of wall-normal planes beyond  $y^+ \approx 80$ .

The results in Figure [3.19](#) reveal six features that deserve to be brought into focus:

- The velocity and strain fields respond asymmetrically to  $Cf_{LS}$ , and so do the thicknesses of the viscous sublayer, in consonance with the asymmetric PDF shown in Figure [3.6\(a\)](#).
- As the  $Cf_{LS}$  fluctuations increase, in the positive range, the velocity increases across the entire near-wall layer, but especially steeply around the buffer layer. Conversely, the velocity decreases throughout the layer for negative  $Cf_{LS}$  fluctuations, and again, especially around the buffer layer, as is indicated by the grey line in Figure [3.19\(a\)](#), which characterises the response of the viscous sublayer to the footprints. The fact that this line passes through the minimum and maximum contour values has no obvious physical relevance – except insofar as the wall-normal locations of the maximum increase in the streamwise velocity at positive  $Cf_{LS}$  values and its maximum decrease at negative  $Cf_{LS}$  values, as well as the variations in the thickness of the viscous sublayer and the location of maximum velocity curvature, are all driven in the same direction by the action of the conditional wall-normal motions shown in figures [3.19\(c\)](#) and [3.19\(d\)](#).
- Associated with the increase and decrease in the streamwise velocity are, respectively, large-scale downward and upward motions – i.e., large-scale sweeps and ejections – the latter being more intense than the former at the extreme levels of the large-scale footprints.
- For positive  $Cf_{LS}$  fluctuations, the strain increases steeply in the viscous sublayer, and decreases above  $y^+ \approx 12$ .
- For negative  $Cf_{LS}$  fluctuations, there is an increase in the strain, albeit weak, in the outer layer  $y^+ \approx 30 - 90$ .
- For negative  $Cf_{LS}$  fluctuations, the strain decreases in the viscous sublayer, but at a magnitude much lower than the increase for positive  $Cf_{LS}$  fluctuations. At the largest positive value of  $Cf_{LS}$ , the location of maximum curvature (the gradient of the strain profiles) moves markedly towards the wall, and this is consonant with the thinning of the viscous sublayer, as indicated by the grey line in Figure [3.19\(a\)](#).

The fact that the impact of the outer large scales on the strain in the buffer layer is rather weak might suggest that the distortions provoked by the large scales may not result in changes to the turbulent state in the buffer layer, the region in which the streaks reside and which is important to the drag. However, as will emerge below, in the examination of the strain-driven production rate, there is a strong increase in the shear stress in the buffer layer, for positive footprints, due to increased production rates of both the streamwise and shear stress, and hence an amplification of the streaks, associated with increased drag.

### 3.6.3 $Cf_{LS}$ -distribution of Stress Components

Figures [3.20\(a\)](#) and [3.20\(c\)](#) illustrate the  $Cf_{LS}$ -distribution rate of change of the streamwise stress ( $d\bar{u}'u'^+(y^+)/dCf_{LS}$ ) and the shear stress ( $-d\bar{u}'v'^+(y^+)/dCf_{LS}$ ), respectively, derived from eq. [\(3.12\)](#). These maps enable an assessment of the variation in stress levels across the  $Cf_{LS}$  range and the boundary layer. The black profiles on the right-hand side represent the statistical averages of the stresses across the boundary layer, obtained by integrating the corresponding left-hand-side maps over the  $Cf_{LS}$  range. The solid red and blue profiles denote partially integrated stress levels over the segments to the right and left of the median of the  $Cf_{LS}$  PDF in Figure [3.6\(a\)](#), corresponding to the positive and negative  $Cf_{LS}$  subranges. The dashed red and blue lines represent partial stresses arising from the integration over the extreme positive and negative 10% tails of the  $Cf_{LS}$  PDF.

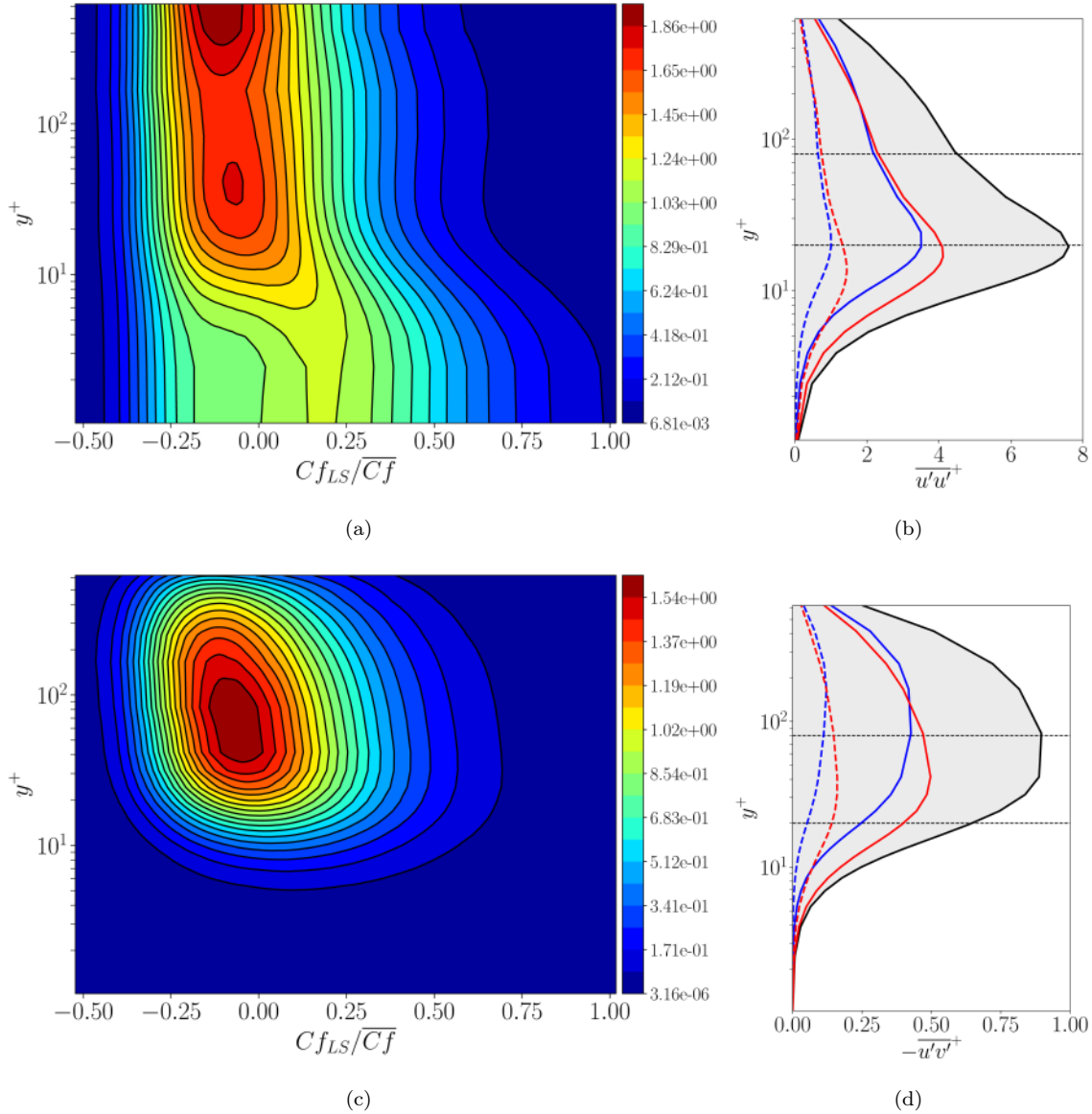


Figure 3.20: Response of the stresses to the large-scale skin-friction: (a) maps of  $Cf_{LS}$ -dependent rate of increase in the streamwise stress ( $d\overline{u'u'}^+/dCf_{LS}$ ); (b) profile of the streamwise stress ( $Cf_{LS}$ -wise integral of field (a)); (c) and (d) correspond to (a) and (b), respectively, but for the shear stress ( $-d\overline{u'v'}^+/dCf_{LS}$ ). Solid red and blue profiles in (b) and (d): partial integrals of the respective maps across  $Cf_{LS}$  sub-ranges to the right (positive  $Cf_{LS}$ ) and left (negative  $Cf_{LS}$ ) of the median of the  $Cf_{LS}$  PDF, respectively. Dashed red and blue lines: partial integrals over the extreme ±10% tails of the  $Cf_{LS}$  PDF, respectively.

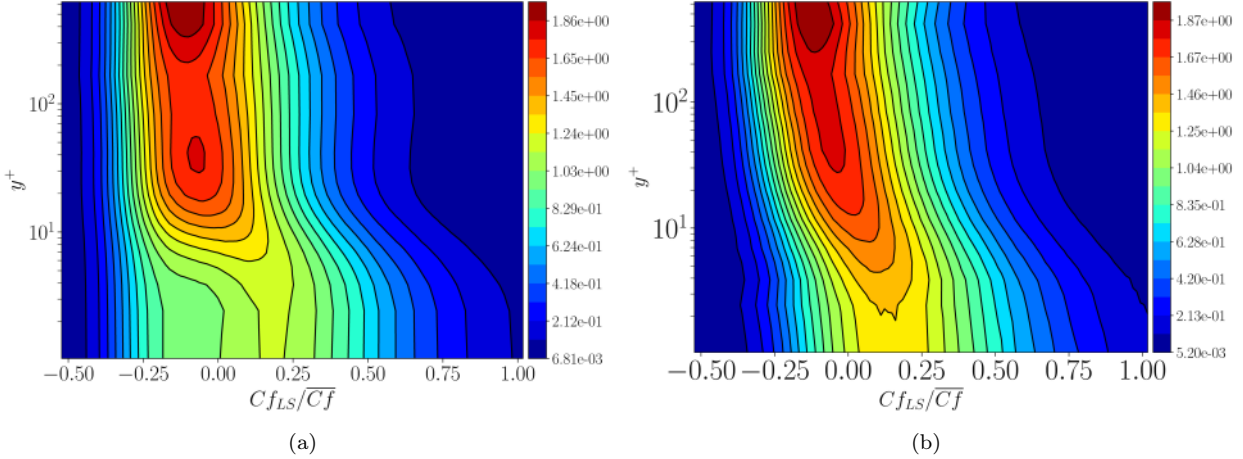


Figure 3.21: Normalised fields of stresses: (a) map of  $Cf_{LS}$ -dependent rate of change of streamwise stress normalised by streamwise stress  $(d\overline{u'u^+}(y^+)/dCf_{LS}) / (\overline{u'u^+}(y^+))$ ; (b) as (a) but for the shear stress  $(d\overline{u'v^+}(y^+)/dCf_{LS}) / (\overline{u'v^+}(y^+))$ .

As anticipated, the maps indicate that the majority of the stress contributions originate from the region surrounding the mean and median of the  $Cf_{LS}$  PDF, where the probability density is highest. However, the asymmetric behaviour on either side of  $Cf_{LS} = 0$  is of particular interest. Large positive  $Cf_{LS}$  values, associated with large-scale sweeping motions, lead to a preferential elevation of the streamwise and shear stresses compared to negative fluctuations. Notably, the increase in shear stress and, to a lesser extent, streamwise stress occurs in the buffer layer, indicating a strengthening of the streaks for positive  $Cf_{LS}$  fluctuations and an associated increase in drag. The disparity in stress responses to positive and negative footprints is particularly evident when focusing on the partial-stress profiles pertaining to the extreme  $\pm 10\%$  tails of the  $Cf_{LS}$  PDF. This behaviour aligns with the frequently observed “modulation” of near-wall turbulence by large-scale footprints. The dashed partial-stress profiles in the buffer region provide a clear connection to the images in Figure 3.6(c), which illustrate a pronounced strengthening of the inclined streaky structure within patches of highly positive  $Cf_{LS}$  levels.

The lower stress levels near the wall for negative  $Cf_{LS}$  are likely influenced by the lower shear strain shown in Figure 3.19(f). However, above  $y^+ \approx 12$ , the  $Cf_{LS}$ -conditional shear strain exhibits weak sensitivity to  $Cf_{LS}$ , indicating that the substantial differences in stress contributions for the positive and negative  $Cf_{LS}$  subranges at these  $y^+$  locations cannot be attributed to the strain rate. It is noteworthy that the strain rate in Figure 3.19(f) for  $C_f \approx 0.7$  (dark-red curve) is lower than that for negative  $Cf_{LS}$  values, although it must be acknowledged that, at this extreme positive  $Cf_{LS}$  value and beyond, the conditional stresses contribute minimally to the partial stress integrals for the positive  $Cf_{LS}$  subrange in Figure 3.20 (red curves).

The map and profiles related to the streamwise stress (Figures 3.20(a) and 3.20(b)) demonstrate that this stress is preferentially elevated around the buffer layer, where the streaks reside. The occurrence of maximum streamwise stress at  $y^+ \approx 20$ , rather than 12, reflects the turbulence-damping action of the spanwise forcing, which increases the viscous sublayer thickness for a fixed bulk Reynolds number, as implied by the elevated profiles relative to the log-law in Figure 3.19(b).

The maps given in figures 3.21(a) and 3.21(b) replot the information in figures 3.20(a) and 3.20(c), respectively, in the form  $(d\overline{u'u^+}(y^+)/dCf_{LS}) / (\overline{u'u^+}(y^+))$  and  $(d\overline{u'v^+}(y^+)/dCf_{LS}) / (\overline{u'v^+}(y^+))$ . They are intended to illuminate the relative contribution of the rate of increase of the stresses when normalised by the stress itself at any location  $y^+$ . The rationale of this presentation is that it accentuates the  $Cf_{LS}$ -driven rate of change of the stresses in regions of relatively low stress levels, but that are nevertheless important for the drag variation, especially in the viscous sublayer where the  $Cf_{LS}$  shear strain varies by a substantial margin. Here again, a strong asymmetry comes to the fore, and it is especially noteworthy that the relative impact of large positive  $Cf_{LS}$  levels is very pronounced in the case of the shear stress in the viscous sublayer where the strain rise is correspondingly high. This observation may therefore be taken

to indicate that large-scale positive footprints and associated sweeping motions are especially effective in degrading the drag-reduction effectiveness in the near-wall layer.

Figure 3.22 presents maps of the streamwise, shear, and wall-normal stress fields obtained by applying eqs. (3.13) and (3.14). These maps highlight regions where the stresses are elevated by the large-scale motion, without the obscuring effects of low  $Cf_{LS}$  probability density levels, which are associated with extreme events. The profiles on the right-hand-side figures represent sections through the maps at the five locations shown in the PDF in Figure 3.6(a). The inclusion of wall-normal stress results is intended to support the discussion in the following section on the shear stress production rate, which is the product of the wall-normal stress and the strain rate.

The results in Figure 3.22 are particularly relevant to the amplification of near-wall turbulence by the modulating action of positive large-scale footprints. They indicate a strong amplification of all stresses, particularly the shear stress, by positive footprints, with the most significant increase occurring in the buffer layer. Additionally, a weak amplification of the shear and wall-normal stress is observed in the outer region, around  $y^+ > 100$ , induced by negative large-scale footprints. This response implies a negative correlation between outer large-scale velocity fluctuations and skin-friction fluctuations. The negative correlation between the wall-normal stress and  $Cf_{LS}$  at large negative levels of the latter, evident in Figure 3.22(f), is intriguing. One plausible explanation for this behaviour is the presence of large-scale ejections that compensate for large-scale sweeps at positive  $Cf_{LS}$  values. The strength of such ejections is likely to increase with distance from the wall. However, this increase does not coincide with a correspondingly substantial rise in the streamwise stress in the outer region. Consequently, the aforementioned argument remains open to further investigation. A more pertinent observation regarding the impact of large-scale footprints on drag is the substantial elevation of the wall-normal stress,  $\bar{v}'v'$ , in the near-wall region for positive  $Cf_{LS}$  fluctuations. This increase plays a crucial role in elevating the near-wall shear stress through the process of generation, as explored in the subsequent subsection.

Figures 3.23(a) and (b) serve to accentuates the asymmetric response of the stresses to  $Cf_{LS}$  by way of examining the behaviour of the streamwise turbulent stress across the location  $y^+ = 20$  in figures 3.20(a) and 3.22(a), respective – i.e. the location at which this stress reaches its peak value. The blue profile in 3.20(a) is the  $Cf_{LS}$ -wise integral of the red curve, which shows  $(\bar{u}'\bar{u}')^+ / dCf_{LS}$ . Figure 3.23(b) is a section through the conditional streamwise-stress field in Figure 3.22(a), again at  $y^+ = 20$ . It is important to point out here that the  $Cf_{LS}$ -PDF median value is identified by the dashed vertical green line (see Figure 3.6(a)). Note also that the blue curve reaches a value  $\bar{u}'\bar{u}'^+|_{Cf_{LS}} \approx 6.5$ , which is the peak value shown in Figure 3.20(b). As is evident from Figure 3.23 the response to  $Cf_{LS}$  is strikingly asymmetric, with large positive  $Cf_{LS}$  values resulting in a strong rise in the conditional streamwise stress, Figure 3.23(b), reaching a value of approximately 12 at  $Cf_{LS}/\bar{C}f \approx 1$ . Correspondingly, the proportion of the streamwise itself associated with positive  $Cf_{LS}$  values is approximately 65% of the total.

### 3.6.4 $Cf_{LS}$ -distribution of Stress production

Figure 3.22 reveals intriguing features in the stress distributions, the origins of which can be elucidated by examining the shear-induced production of the streamwise normal stress and the shear stress. Figures 3.24 and 3.25 present maps of the  $Cf_{LS}$ -conditional productions, obtained by applying eqs. (3.13) and (3.14). For each stress, two maps and corresponding profiles are provided, displaying the same data. However, the production shown in the second rows of Figures 3.24 and 3.25 is pre-multiplied by  $y^+$  to highlight the response of the productions in the outer region, where Figures 3.22(b) and 3.22(d) show an outer increase in the streamwise and shear stresses for negative  $Cf_{LS}$  fluctuations.

The production of these stresses is governed by the wall-normal stress or the shear stress multiplied by the shear strain. Figure 3.19 indicates that large strain fluctuations predominantly occur in the viscous sublayer rather than above it. However, both the wall-normal and shear stresses exhibit high values not only in the viscous sublayer but also in the region above it, due to a mechanism discussed below. Therefore, the productions, particularly that of the shear stress, are elevated across a major proportion of the near-wall layer, including the buffer region, as evident from the profiles in Figures 3.22 and 3.24. The high levels of streamwise and shear stress productions at large positive  $Cf_{LS}$  fluctuations, in turn, give rise to correspondingly high stress levels in the buffer layer.

A crucial factor in the elevation of the shear stress and, subsequently, the streamwise stress in the buffer layer for positive  $Cf_{LS}$  values is the substantial increase in the wall-normal stress in this region (Figure 3.22(f)). This stress is not caused by production but by energy redistribution, driven by the pressure-strain

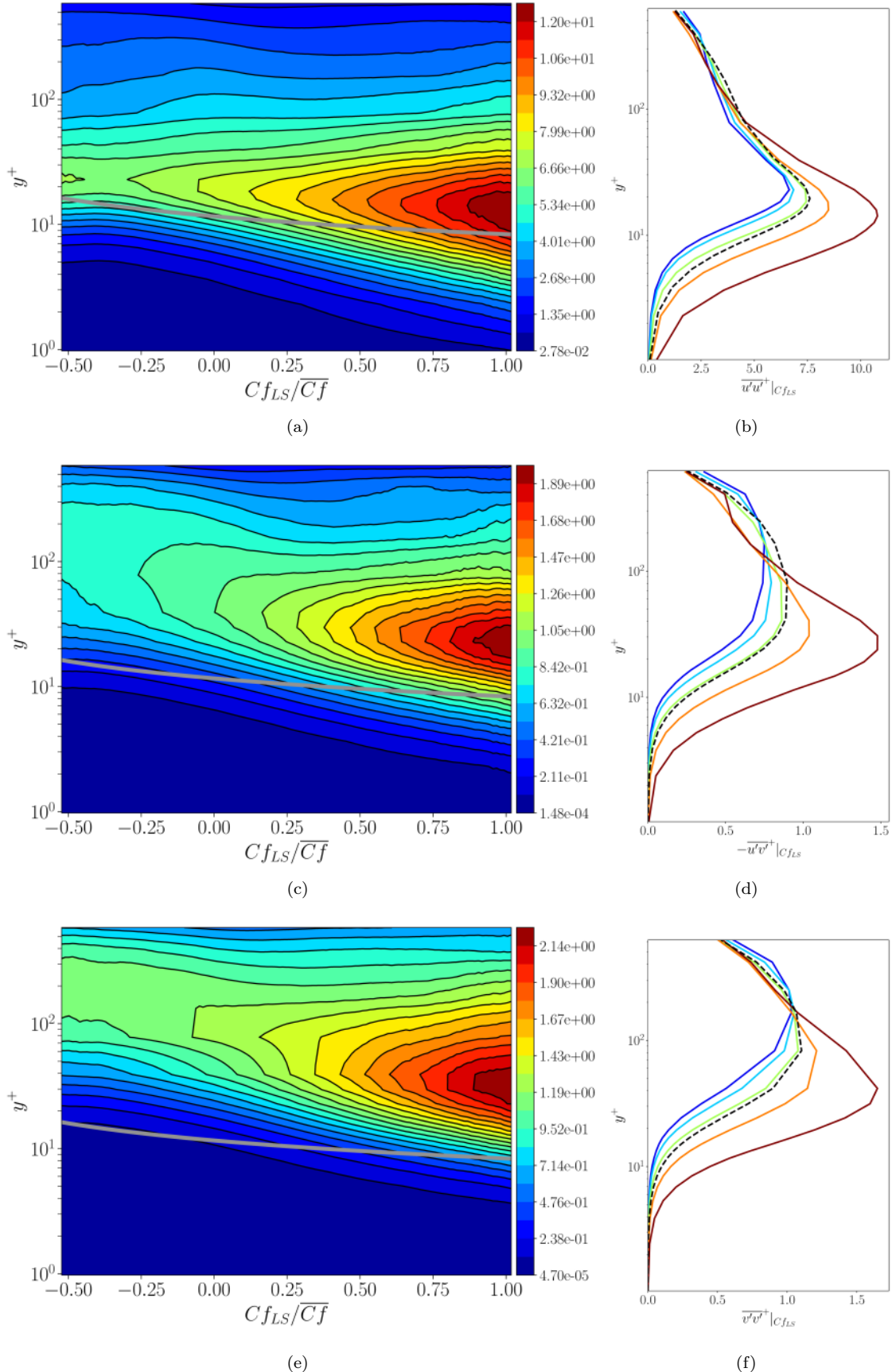


Figure 3.22: Conditional stress fields: (a) map of streamwise stress conditional on  $C_{fLS}$  (see eq. (4.4); (b) profiles of conditional streamwise stress at locations marked in the PDF of Figure 3.6(a); (c,e) and (d,f) as (a) and (b), respectively, for the shear stress and wall-normal stress; dashed profiles in (b), (d), (f) represent averages. Grey curve is the locus  $y_{LS}^+ \approx 12$ , with  $LS$  denoting scaling with large-scale friction velocity.

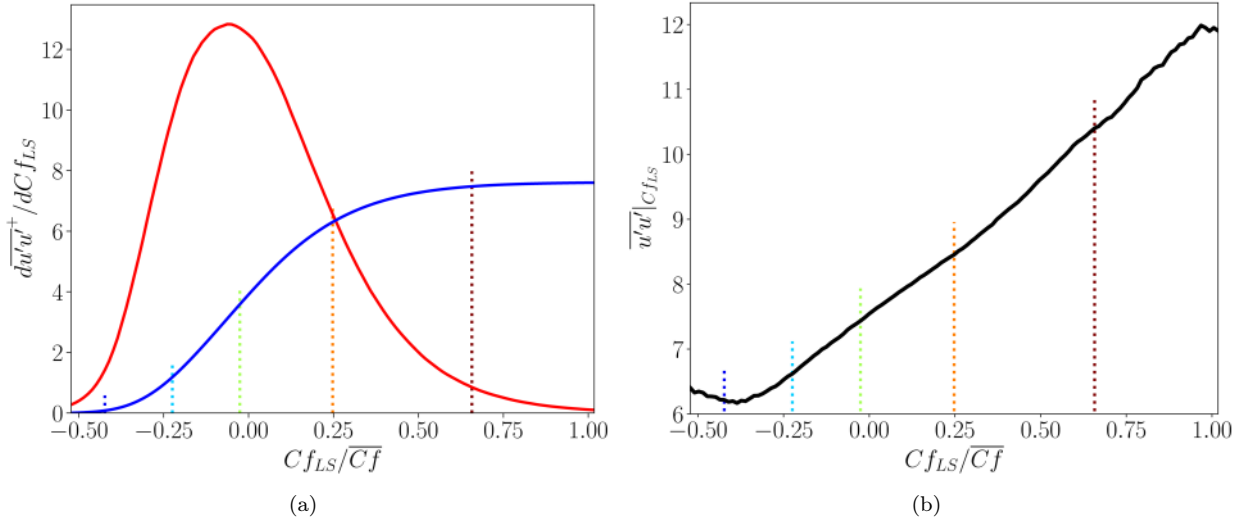


Figure 3.23: Properties of streamwise stress at  $y^+ = 20$ ; (a) variation of  $(\overline{u'u'})^+ / dCf_{LS}$  (red line) and its  $Cf_{LS}$ -wise integral  $\overline{u'u'}$  (blue line); (b) conditional streamwise stress  $\overline{u'u'}|_{Cf_{LS}}$ . The vertical straight lines correspond to those in the  $Cf_{LS}$  PDF, Figure 3.6(a).

interaction process, from the streamwise stress to the wall-normal and spanwise components. The observation that the spanwise stress component (not shown here) is also substantially elevated for positive  $Cf_{LS}$  values supports this conclusion. Thus, the mechanism driving the stresses in the buffer layer and the layer just above it, within  $y^+ \approx 50 - 70$ , is a cycle involving the production of the streamwise-normal stress by the shear stress, the elevation of the wall-normal stress by energy transfer from the streamwise stress, and the production of the shear stress by the wall-normal stress, with the latter feeding the production of the streamwise-normal stress.

Both sets of stress-production profiles demonstrate a highly asymmetrical response to  $Cf_{LS}$  fluctuations, with negative fluctuations resulting in a modest decrease in production within the buffer layer. The slight rise in production in the outer region gives rise to the increase in streamwise and shear stresses in this region, as observed in Figures 3.22(b) and 3.22(d).

Finally, it is worthwhile to observe that the increase in streamwise stress and its production for large positive  $Cf_{LS}$  fluctuations is associated with stronger streaky structures within the patches surrounded by the black boundaries in Figure 3.6(c) – bringing into focus the “modulation”. Conversely, low levels of production and stresses for negative  $Cf_{LS}$  fluctuations are associated with indistinct small-scale structures within the patches defined by the grey boundaries.

### 3.6.5 Small-scale and Large-scale Properties

The forgoing discussion focused on the response of the full turbulence field to large-scale fluctuations, with particular emphasis on the layer closest to the wall. The principal observation made therein was that positive large-scale fluctuations had a disproportionate large effect on the near-wall stresses and their production rates, both being amplified predominantly in the buffer layer. As shown in Figure 3.4(b), the energy in the near-wall region is dominated by the motions that are associated with small scales – i.e., broadly with the streaks that reside in the region  $y^+ \approx 20$  and are separated by a spanwise distance  $\delta z^+ \approx 100$ . Interest in the question of how these small scales respond to the large-scale fluctuations is rooted in the fact that this interaction is specifically associated with what is conventionally understood to be “modulation” – i.e., the amplification or attenuation of near-wall scales that are far removed from the scales of the large-scale motions. This is the subject of the present section.

Figure 3.26 provides the small-scale-stress equivalent to the total-stress results shown in Figure 3.22. Here again, the dominance of the large-scales motions is the most striking feature. The amplification of the small scales is observed to rise strongly in response to intensely positive large-scale fluctuations and to occur around

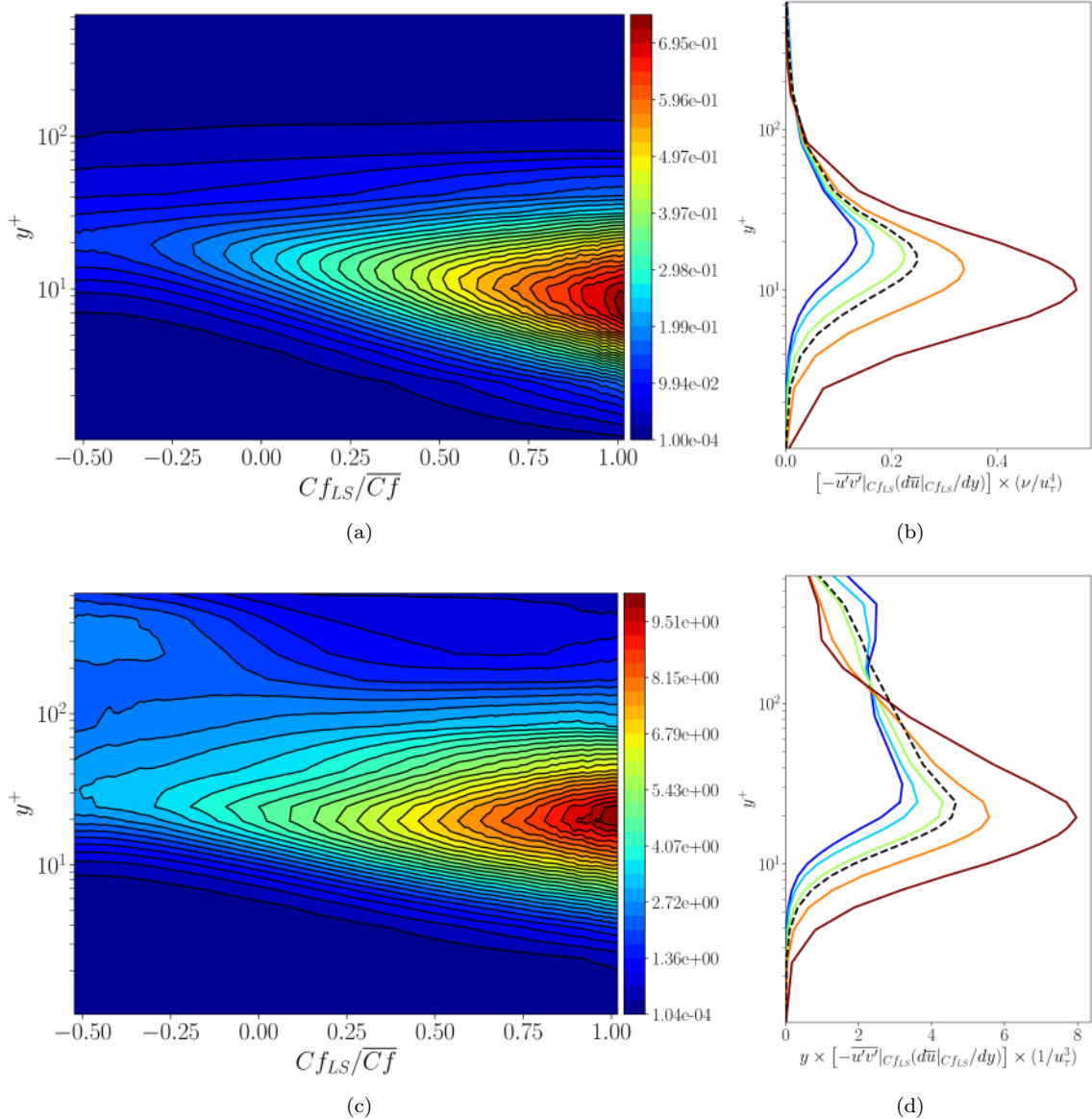


Figure 3.24: Production of streamwise stress: (a) map of production conditional on  $C f_{LS}$ ; (b) profiles of conditional production at the locations marked in the PDF in Figure 3.6(a); (c,d) as (a,b), respectively, but premultiplied by  $y^+$ . The dashed profiles in (b,d) represent averages.

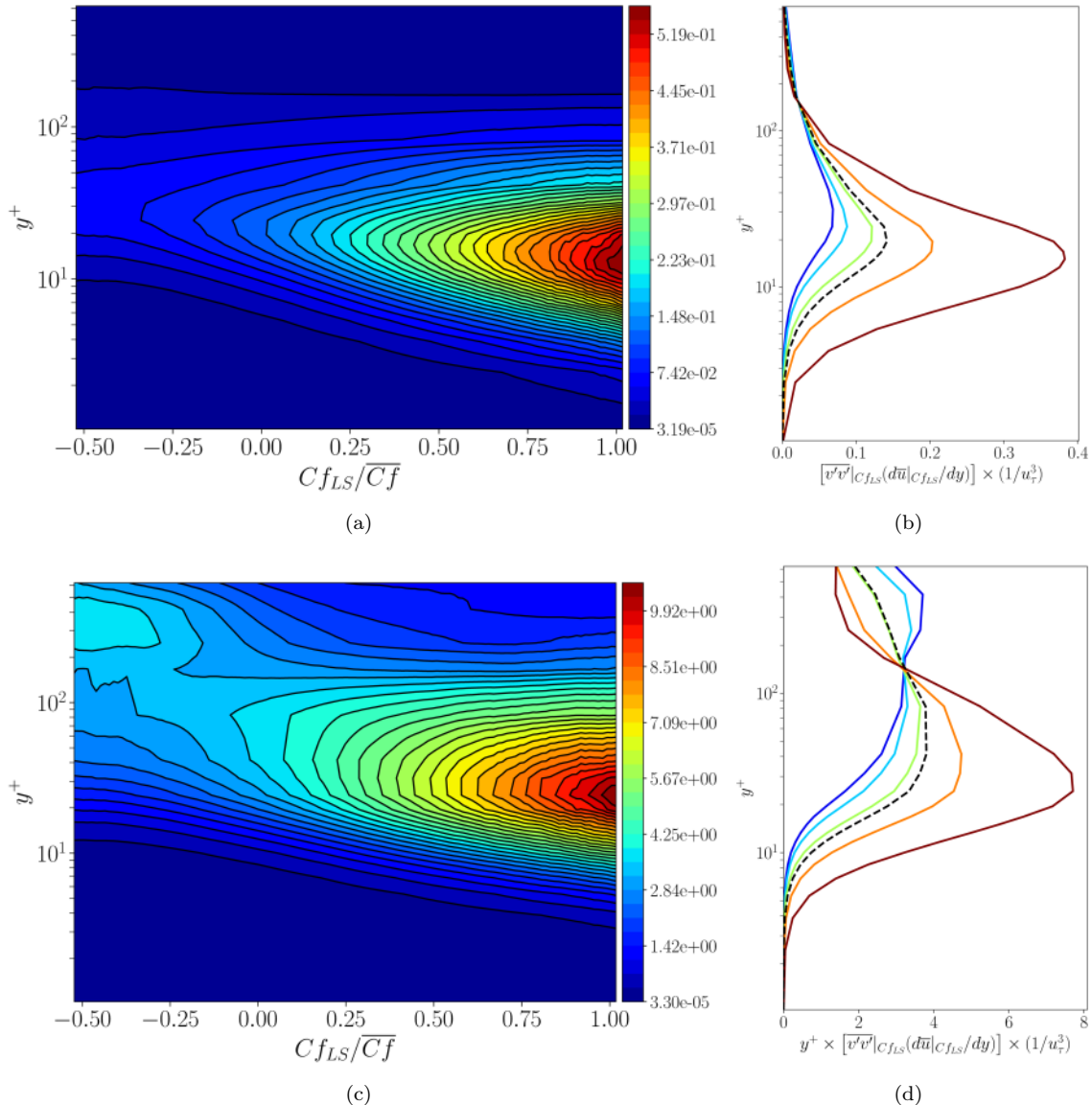


Figure 3.25: Production of shear stress: (a) map of production conditional on  $Cf_{LS}$ ; (b) profiles of conditional production at the locations marked in the PDF in Figure 3.6(a); (c,d) as (a,b), respectively, but pre-multiplied by  $y^+$ . The dashed profiles in (b,d) represent averages.

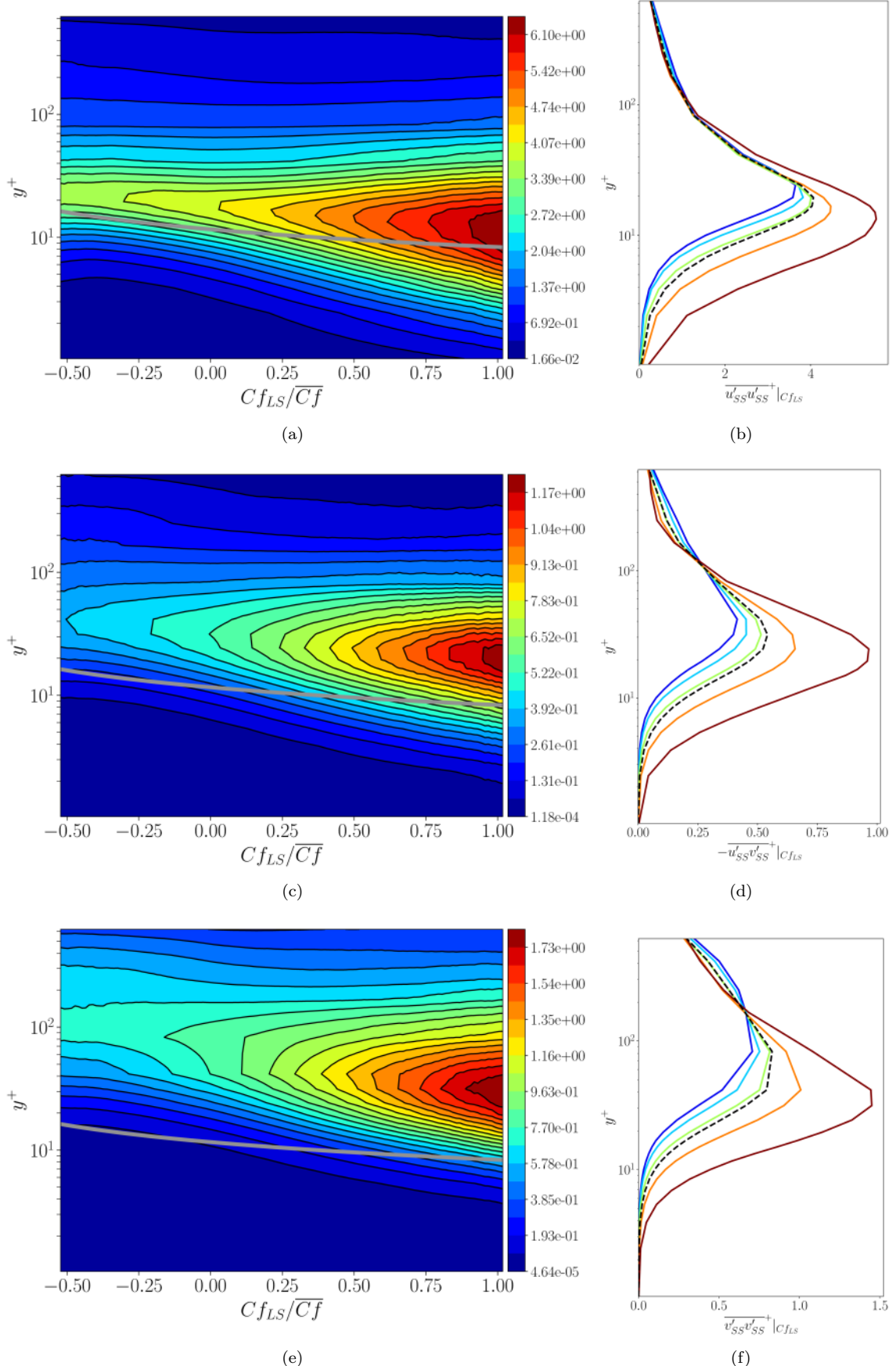


Figure 3.26: Conditional small-scale stress fields: (a) map of streamwise stress conditional on  $Cf_{LS}$  (see eq. (3.14)); (b) profiles of conditional streamwise stress at locations marked in the PDF of Figure 3.6(a). Dashed profile identifies the mean distribution; (c,e) and (d,f) as (a) and (b), respectively, for the shear stress and wall-normal stress. The dashed profiles in (b), (d), (f) represent averages.

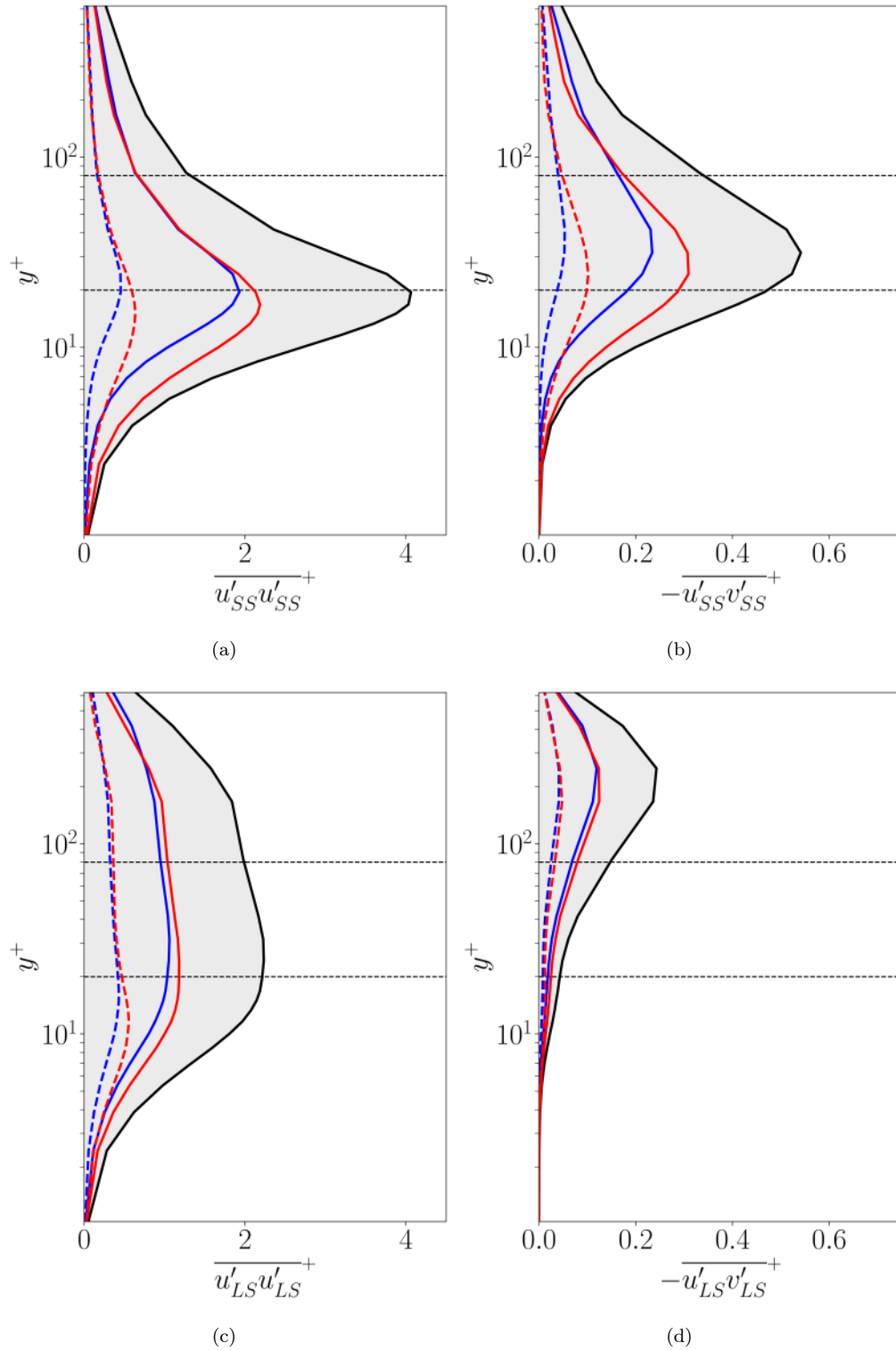


Figure 3.27: Profiles of stress components; (a) small-scale streamwise stress; (b) small-scale shear stress; (c) large-scale streamwise stress; (d) large-scale shear stress. Solid blue/red lines: contributions arising from the left/right of the median of the  $Cf_{LS}$  PDF, respectively; dashed blue/red lines: contributions arising from partial integration across extreme  $\pm 10\%$  tails of the  $Cf_{LS}$  PDF, respectively; black lines: total level (sum of solid blue and red profiles).

the buffer layer. In contrast, the attenuation provoked by negative large-scale fluctuations are quite modest, accentuating the arguments around the asymmetric effects of the large-scale fluctuations. It is instructive to emphasise here, as done in relation to the total stresses, that these results arise from the normalised PDF in equation (3.14), so that the profiles shown in Figure 3.26 are not actual contributions to, or are parts of, the relevant stresses. Rather, the profiles in Figure 3.26 represent the intensity of the stresses generated within specific portions of  $Cf_{LS}$  PDF, normalised by the local  $Cf_{LS}$  probability. Thus, large values derived at the tails of the PDF of (especially at 1% event level) contribute only modestly to the actual stress levels.

Figure 5.9 shows profiles for the small-scale [(a),(b)] and large-scale [(c),(d)] streamwise and shear stress stresses. In each plot, the black profile represents the contribution to the total stress, the red and blue solid profile arise from an integration over the positive and negative  $Cf_{LS}$  sub-ranges, and the dashed profiles are analogous to the solid profiles, but represent contributions from the  $\pm 10\%$  tails of the  $Cf_{LS}$  PDF, respectively. A comparison of Figures 3.27(a),(b) with Figures 3.20(b),(d) shows that the general behaviour of the small-scale stresses follows that of the total stresses, especially close to the wall, where the total stresses are dominated by the small-scale components. As with the total stresses, the small-scale contributions associated with positive footprints are markedly higher than those associated with negative footprints. This is especially so for the shear stress. For both stresses, the disparity increases substantially close to the wall, just below the mean position of the buffer,  $y^+ \approx 20$ . It is noted here, however, that the actual location of the buffer layer is a function of  $Cf_{LS}$ . As will be shown by results to follow, the nominal position of the buffer layer varies between  $y^+ \approx 22$ , for extreme negative footprints, and  $y^+ \approx 11$  for extreme positive footprints. This is why the peaks of the red and blue dashed profiles are at different wall-normal locations.

The large-scale-stress profiles, given in Figures 3.27(c) and (d), imply that the large-scale contributions are driven by mechanisms that are significantly different from those governing the corresponding small-scale profiles. The streamwise stress is broadly uniform over a large portion of the near-wall layer, right down to the viscous sublayer – a behaviour that is consistent with the concept of footprinting, whereby the large-scale streamwise fluctuations are highly correlated in the  $y$  direction. This is also observed in the spectrum in Figure 3.4(a) and the red profile in Figure 3.4(b), the latter identical to the black line in Figure 3.27(c). The peak of the sum of small-scale and large-scale profiles (EMD modes [1+2] and [4+5+residual], respectively) is around 6, compared to the maximum total streamwise stress of around 7.5 (see Figure 3.4(b)). The difference of around 1.5 accounts for the intermediate EMD scales as well as inter-scale interactions that give rise to mixed correlations of the form  $\overline{u'_{SS}u'_{LS}}^+$  etc (see Figure 3.10). In contrast to the streamwise component, the shear stress associated with the large-scale motions is only elevated in the outer portion of the near-wall layer, thus implying that the large-scale motions are dynamically only weakly active in and below the buffer layer. A further noteworthy difference between the profiles for the large-scale and small-scale stresses is that the disparity between contributions arising from positive and negative footprints are negligible or very modest. This is entirely as expected, because the large-scale stresses are derived from either half of the  $Cf_{LS}$  PDF for the large-scale footprints, in the case of the solid profiles, and from identically areas in the tails of this PDF, in the case of the dashed profiles.

While the profiles for the small-scale stresses in figures 3.27(a),(b) show that the positive footprints generate contributions that are significantly larger than negative ones, this does not, in itself, provide unambiguous evidence for an asymmetric amplification vs. attenuation process – although this issue has been considered by reference to Figure 3.26. Further evidence is provided, however, in Figure 3.28, which shows variations of the wall-normal location of maximum streamwise energy (Figure 3.28(a)) and the level of this maximum energy (Figure 3.28(b)) across the  $Cf_{LS}$  range. The red curves pertain to the actuated case, and these are compared to the corresponding blue variations for the canonical case, which is the subject of the study by Agostini and Leschziner 2019b. The rather noisy behaviour at the extreme ends of the  $Cf_{LS}$  range arises from a paucity of data underpinning the statistics. As noted already, the location of maximum streamwise stress declines from  $y^+ \approx 22.5$  to 13, the mean value being approximately 19 at  $Cf_{LS} = 0$ . Concurrently, the streamwise small-scale energy rises from  $\overline{u'_{SS}u'_{SS}}^+|_{Cf_{LS}} \approx 3.7$  to 6.7, the mean being approximately 4. For the canonical case (the Reynolds number of which is 15% higher), the blue variations indicate a similar qualitative behaviour, but at different quantitative levels.

In Figure 3.28(c), the data displayed in Figures 3.28(a),(b) are recast in a manner that reveals additional characteristics which are of interest to the drag-reduction behaviour. Two curves are shown for the actuated, one normalised with the baseline friction velocity (magenta line) and the other with the actual value (red line). The former scaling is relevant, because the bulk Reynolds number is the same for both flows. It is

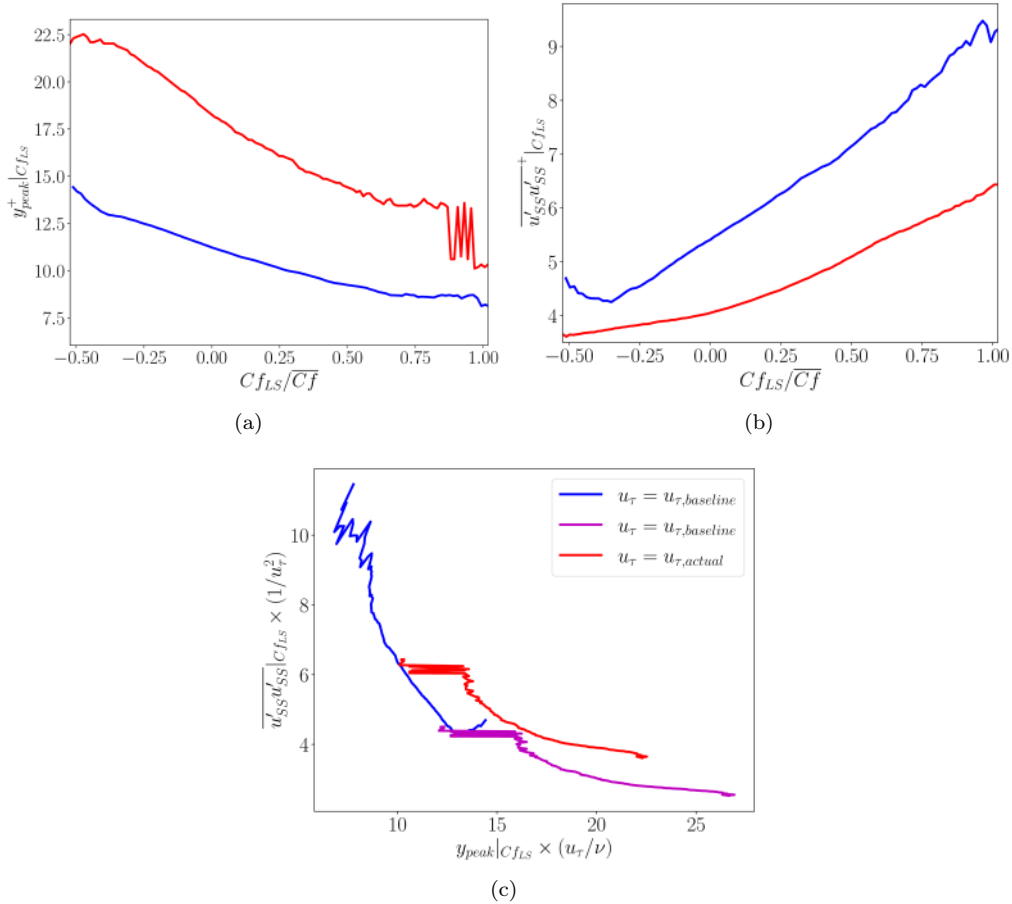


Figure 3.28: Variations of buffer-layer properties across the range of  $Cf_{LS}$ ; (a) wall-normal location of the nominal centre of the buffer layer, defined as the line of maximum streamwise energy of the small scales; (b) the magnitude of the maximum streamwise small-scale energy along the loci in (a); (c) the magnitude of the maximum streamwise small-scale energy in (b) as a function of the wall-normal distance  $y^+$  of the loci in (a). The red and magenta curves pertain to the actuated case, and blue curves to the canonical case examined in Agostini and Leschziner 2019b. The  $u_\tau$  scaling is indicated in (c)

instructive to point out here that the left hand-side of the curves are associated with positive  $Cf_{LS}$  values, while the right-hand sides characterise negative fluctuations. As observed already, the general trend, for both the canonical and actuated flows, is for the small-scale stress to increase and the viscous layer to decrease with increasingly positive skin-friction fluctuations, while the reverse occurs for increasingly negative values. However, the quantitative behaviour shows clear differences. First, the level of the stress is substantially lower, irrespective of the wall scaling, which goes hand-in-hand with the substantially thicker viscous layer. Second, the variation of the stress for the actuated flow is distinctly more non-linear: the initially steep rise in the stress for positive  $Cf_{LS}$  levels declines at a decreasing rate for negative  $Cf_{LS}$  values and appears to asymptote towards a constant level at which the streaks, which are already materially weakened by the actuation, are relatively insensitive to the large-scale motions. In explicit terms: the strong amplification of small-scale energy by positive large-scale fluctuations is not balanced by its attenuation at negative large-scale fluctuations, which clearly has adverse implications to the drag-reduction process.

Although it is reasonable to conjecture that the dominance of the high near-wall turbulence intensity associated with asymmetric processes discussed herein is responsible for the degradation in the drag-reduction effectiveness of the actuation, there is another pertinent mechanism that deserved to be discussed – namely the dependence of the wall-scaled actuation period  $T_{LS}^+ = Tu_{\tau,LS}^2/\nu$ . It is well established that  $T^+$  values higher than the near-optimum level of 100 (based on the friction velocity of the non-actuated case) tend to decrease the drag-reduction margin. In the present case,  $T_{LS}^+$  reaches 150, relative to the actual mean period  $T^+ = 70$  (the value 100 is for base-line, non-actuated case). One consequence of the significant increase in  $T^+$  above the near-optimum value is that the unsteady Stokes layer begins to penetrate through the buffer layer, thus increasing the near-wall turbulence level by extra strain-induced turbulence production. This process is likely to be exacerbated by the substantial thinning of the viscous sublayer at large  $Cf_{LS}$  values. An additional mechanism, but one that is arguably related to that above, has been proposed in Touber and Leschziner 2012; Blesbois et al. 2013; Agostini, Touber, and Leschziner 2015 and largely discussed in chapter 2. The key argument is that  $T^+$  (more precisely, one half of this actuation period) should be below the streak-generation time scale – i.e. the scale that dictates the re-generation of the streaks following their weakening or disruption by the optimum oscillatory period. If the actuation period is unduly high, the streamwise shear strain at the wall is able to regenerate the turbulent streaks. The asymmetric footprinting strongly favours high levels of  $T^+$ , and this can reasonably be expected to degrade the drag-reduction effectiveness by the action of highly positive  $Cf_{LS}$  values.

### 3.6.6 Assessing Direct and Indirect Impact of Outer-Flow Structures on Skin Friction

The examination of the average effect of small and large-scale structures on skin friction was conducted in section 3.4 using FIK analysis (refer to eq.(3.4)). This study underscored both the direct and indirect roles of each family of scales in skin friction fluctuations. The indirect contribution, resulting from the modulation of SS, was exposed by cross terms, particularly the term  $\bar{v}_{SS}u_{LS}$ . It is proposed that the subsequent step should utilise the multivariate joint PDF. This method is anticipated to facilitate tracking the evolution of these structures in relation to  $Cf_{LS}$ , potentially offering additional insight into the ways in which LS modulates the character of the small scale and impairs the control's effectiveness. Equations (3.11)–(3.14) now allow the manner in which the turbulent shear stress contributes to  $Cf$  to be studied. In fact, the EMD-derived modes of the total stress allows the contribution of the small-scale and large-scale contributions to be separately quantified, and the spatial origin of these contributions to be clarified. This is done, collectively, in Figure 3.29. The top row, (a), (b) and (c). arise from the application of equation (3.14) to the fields  $\left(1 - \frac{y^+}{Re_\tau}\right)(-\bar{uv}^+)$ ,  $\left(1 - \frac{y^+}{Re_\tau}\right)(-\bar{ussvss}^+)$  and  $\left(1 - \frac{y^+}{Re_\tau}\right)(-\bar{ulsrvls}^+)$ , respectively. The purpose of using the  $Cf_{LS}$ -conditional fields, as done in previous results, is to highlight, or accentuate, the origin of the contributions to the quantity being considered (in this case, the above pre-multiplied total, SS and LS shear stresses), without the obscuring influence of the variation of the PDF of  $Cf_{LS}$  – in particular, its low values at the PDF tails. Figure 3.29(d) shows distributions of the  $y$ -wise integrals of the  $Cf_{LS}$ -wise gradients of the above pre-multiplied shear stresses, as derived from equation (3.12). These distributions clarify the actual contributions of the shear stresses to the skin friction across the  $Cf_{LS}$  range, the blue and red areas pertaining to the small-scale and large-scale contributions, respectively, relative to the  $Cf_{LS}$  distribution of pre-multiplied total shear stress, represented by the black curve. Finally, the columns of the right-hand side of Figure 3.29(d) show the integrals across  $Cf_{LS}$  of the red and blue areas under the left-hand-side curves, representing the SS and LS contributions to the turbulent skin friction, as well as the integral under

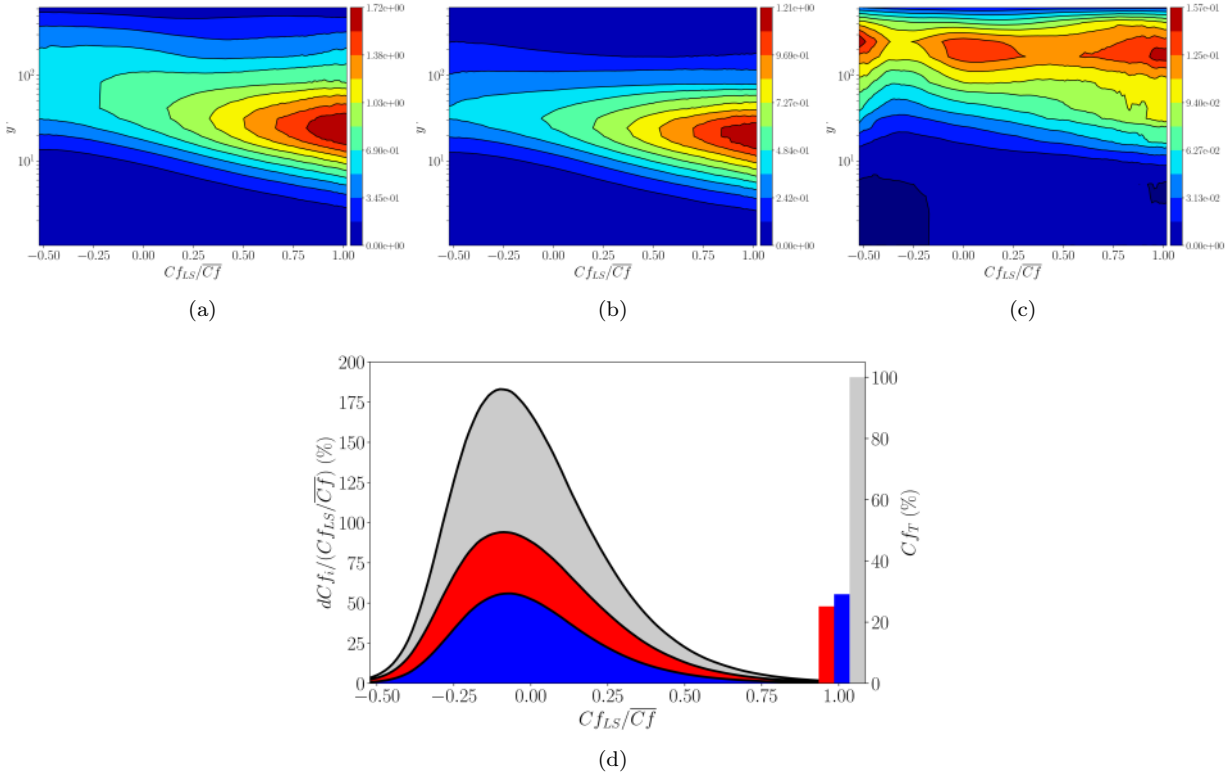


Figure 3.29: Contributions to the skin friction via the FIK relationship, equation (4.7): (a) map of  $\left(1 - \frac{y^+}{Re_\tau}\right) \left(-\overline{u'v'}^+|_{C_{fLS}}\right)$ ; (b) as (a) but for small-scale stress contribution; (c) as (a) but for large-scale stress contribution; (d)  $C_{fLS}$ -wise gradients of  $\left(1 - \frac{y^+}{Re_\tau}\right) \left(-\overline{u'v'}^+\right)$  in which the shear stress is either the total level (upper black curve), or the large-scale component (red area under lower curve), or the small-scale component (blue area under the middle curve); column on the right-hand-side of the figure represent the corresponding small-scale (blue) and large-scale (red) contributions to the turbulent skin friction  $C_f T$  (grey)

the black curve, the last being identically 100% – i.e. the total turbulent skin-friction portion – as must be the case. The fact that the blue and red columns do not sum up to 100% is indicative of the magnitude of the contributions arising from the intermediate EMD scales, as well as mixed scales – i.e. correlations between fluctuations at the large, small and intermediate scales.

The fields in Figure 3.29(a), (b) and (c) convey three main messages: (i) small-scale contributions arise primarily from positive large-scale fluctuations, generating high levels of stress in the buffer layer; (ii) large-scale contributions arise from the outer layer,  $y^+ \approx 180$ , across the entire range of  $C_{fLS}$  fluctuations; and (iii) the effect of the total shear stress to the skin friction is highly asymmetric and strongly dominated by contributions associated with positive large-scale fluctuations – hence, entirely consistent with earlier observations.

In terms of the contribution of different scales, it is remarkable that the outer large scale contribute, on their own, approximately 25% to the total skin friction – remarkable, because the friction Reynolds number is low, at 875, based on the true mean wall shear stress. Clearly, as the Reynolds number increases, this contribution is likely to rise substantially. The significant indirect effect of the large scales also deserved to be noted. This indirect effect is what is understood to be the modulating effect, and it is clearly the case, as already observed in Figure 3.26, that this modulation occurs primarily by the action of positive footprints generating enhanced small-scale motions in the buffer layer. Here again, this effect is likely to rise with the Reynolds number. Finally, it is remarked the contribution of mixed terms is quite large, of order 30%, and this reflects the lack of scale separation at the present relatively low Reynolds number, as implied by the overlapping regions in Figure 3.4(b).

### 3.7 Reynolds-Number Impact on Drag Reduction: Summary

The aim of this study, presented in this chapter, has been to illuminate and quantify the influence of outer large-scale structures, populating a portion of the log-law layer around  $y^+ \approx 180$ , on the buffer and viscous sublayers in which a transverse oscillatory Stokes strain is applied as a means of reducing the friction drag. To this end, large-scale and small-scale fluctuations have been separated by applying a data-driven filtering method (EMD) over planes parallel to the wall at different wall-normal locations, followed by the application of 5%-binned pdfs followed by the use of the new multiple-variable joint PDF method to quantify the characteristics of wall-normal variations of turbulence properties when conditional on the large-scale skin-friction footprints. These properties include the Reynolds stresses, their large-scale and small-scale parts, the production of the streamwise and shear stresses, and the characteristics of the buffer layer. This combination of methods offers a practical, flexible and accurate approach to performing conditional analyses. The purpose of this analysis is to identify how positive and negative large-scale fluctuations affect the conditions in different wall-normal regions, especially in the buffer layer whose wall-normal position varies greatly with the sign and magnitude of the footprints, and in which the turbulence intensity, associated with the streak strength, is also very sensitive to the large-scale footprints.

The major conclusions derived from the analysis may be summarised as follows:

- The most striking observation seen in maps of the total stresses, as well as their small-scale components, is the strong asymmetry in the effect of the large scales on the turbulence activity within the buffer layer – i.e. the intensity of the modulation – with positive large-scale footprints provoking a substantial amplification of the turbulence energy and the shear stress, while negative fluctuations cause a modest attenuation in the near-wall layer and a slight increase in the outer layer. The weak modulation that occurs at negative footprints is due to a combination of the relatively low intensity of the negative large-scale footprints and the non-linearity in the modulation, with the decline in turbulence in the buffer layer following a lower slope than the rate of increase for positive footprints. The observation that the slope of the  $Cf_{LS}$ -wise variation changes around  $Cf_{LS} = 0$  in the actuated case suggests that the streak response to the large-scale motions is not compatible with a linear modulation process observed in the baseline flow.
- The increase in activity within the buffer layer is consistent with the observed increase in the strength of the streaks in wall patches in which the large-scale skin friction is positive and high. Conversely, the streaks are barely distinguishable in patches in which the large-scale skin friction is negative. This asymmetry gives rise to the conjecture that the turbulence amplification plays an important role in the progressive decline in the drag-reduction level at increasing Reynolds number. One aspect of the asymmetry is that the  $Cf_{LS}$ -wise variations of the maximum small-scale streamwise stress (Figure 3.28(b)) increases by around 53% for the strongest large-scale sweeps and reduces by up to 45% during ejections.
- The wall-normal position of the buffer layer, when identified by reference to the maximum streamwise energy generated by the streaks, varies greatly with the sign and magnitude of the footprints. At the extreme positive end of the  $Cf_{LS}$  range, the buffer layer is only 10.5 wall units away from the wall, relative to a mean value of 20 and a maximum value of 22.5 at the extreme negative end of the  $Cf_{LS}$  range. This major asymmetry in the wall-distance is also likely to detrimental to the drag-reduction margin. When compared with the baseline case, the thickness of the viscous layer for the actuated case changes by a larger margin over the  $Cf_{LS}$  range (Figure 3.28(a)). As the high drag-reduction margin hinges on the wall-motion-induced Stokes layer being confined within the viscous sublayer, it follows that the disproportionate thinning of the layer for large positive large-scale footprints must have an added negative impact on the drag-reduction effectiveness. Associated with this process is a large variation of the actuation period when scaled with the large-scale wall shear stress,  $T_{LS}^+$ , the limiting values of this parameter being 50 and 110 and asymmetrically positioned relative to the actual mean value of 70 (which corresponds to the nominal canonical-case value of 100).
- A possible supplementary mechanism prejudicial to the drag-reduction margins is that strongly positive large-scale skin-friction fluctuations cause a substantial increase – by up to a factor 2, in the present

case – of the wall-scaled actuation period, when the period is scaled with the local large-scale skin friction. Thus, the conditions on parts of wall are such that the real actuation period is substantially different from the optimum value.

- The intensification of the near-wall Reynolds stresses is driven by increased streamwise and shear-stress production in the buffer layer at positive  $Cf_{LS}$  and a correspondingly weak production in the outer layer at negative  $Cf_{LS}$ . Although there is a strong increase in the shear strain at positive  $Cf_{LS}$ , this increase is confined mainly to the viscous sublayer, while changes in the strain in the upper parts of the buffer layer and the layer above it are small. Hence, the production increments in the buffer layer do not appear to be driven, primarily, by changes in the shear strain. Rather, there is an increase in the wall-normal stress, which then feeds into the shear stress and streamwise-stress production rates.
- Although the characterisation of the dynamics of the large-scale motions was not part of the present study, the analysis revealed the existence of distinctive large-scale sweeps and ejections, the former concurrent with positive footprints and the latter with negative footprints. The sweeping motions are likely to be the cause for the steep rise in strain near the wall due to the blocking effect of the wall, and they may well be the reason for the wall-normal coherence of the large-scale fluctuations and hence for the presence of the large-scale footprints. Finally, the fundamental mechanistic differences between sweeps and ejections, especially in respect of their interaction with the wall, are likely to be the cause of the asymmetry of the PDF for  $Cf_{LS}$ .
- Consistent with the asymmetry highlighted above, there is also a strong asymmetry in the contribution of the small-scale shear-stress component to the mean skin friction, as derived from the FIK relationship. Again, the contribution of the shear stress is enhanced by the amplification of small-scale turbulence at large positive  $Cf_{LS}$  fluctuations. The FIK analysis also shows that the direct shear-stress contributions of large-scale fluctuations arise from the outer parts,  $y^+ \approx 180$ , where these scales are most pronounced. In contrast, the large-scale shear stress is low near the wall, notwithstanding the substantial level of large-scale streamwise stress associated with large-scale footprinting extending into the buffer and viscous sublayers.
- By analysing stresses and production terms in the outerflow, it is shown that LS ejections generate structures, which, counter intuitively, also actively contribute to the drag.
- The influence of the large scales on the small-scale buffer-layer turbulence aside, it is remarkable that, at the relatively low Reynolds number of the flow, the direct contribution of large-scale shear stress to the mean skin friction is around 25%. While this level is similar to that recorded for the baseline (canonical) case, it has to be borne in mind that the friction Reynolds number is 15% lower in the actuated flow, for the same bulk Reynolds number. As a consequence, the outer structures are weaker in the actuated flow. However, the small-scale structures are also weaker, on average, because of the actuation. Hence, the influence of the large-scale structure increases in relative terms. This heightens the expectation that the outer structures play a significant role in the decline of the drag-reduction margin as the Reynolds number increases.

This study has illuminated the influential role of large-scale outer structures on near-wall turbulence under transverse wall oscillation for drag reduction. A key observation was the asymmetric modulation of small-scale turbulence in the buffer layer, with substantial amplification under positive large-scale sweeps contrasting with mild attenuation under negative large-scale ejections. Additionally, positive large-scale fluctuations were found to drive viscous sublayer thinning, drawing the buffer layer closer to the wall, while negative fluctuations prompted the opposite response. Importantly, the wall actuation period scaled on the fluctuating local skin friction deviated most from its optimum value under high positive fluctuations. Taken together, these findings underscore the crucial role of asymmetric large-small scale interactions in governing the Reynolds number dependence of drag reduction by spanwise oscillatory motion. The insights from the conditional analysis have important implications for ongoing research into wall-turbulence dynamics and control strategies. Building on these results offers significant potential to further elucidate the physical mechanisms at play and explore

their influence on drag reduction performance. Due to computational constraints, it is not feasible to perform simulations at substantially higher Reynolds numbers within this study. Therefore, the forthcoming chapter will conduct an in-depth investigation into the influence of outer-flow structures on unactuated channel flow with increasing Reynolds numbers, ranging from a relatively moderate  $Re_\tau \approx 1000$  up to  $Re_\tau \approx 5200$ . Databases spanning this range of Reynolds numbers have been made available to the public by other research teams, acknowledging the extensive computational resources required for their generation.



## Chapter 4

# The Impact of Increasing Reynolds Numbers on Wall-Bounded Flow Dynamics

### 4.1 Introduction

Investigations dating back to the 1970s and 80s (Rao, Narasimha, and Narayanan 1971; Bandyopadhyay and Hussain 1984) have explored the properties of large-scale structures in the outer regions of near-wall shear layers and their connection to small-scale structures in the near-wall region. Recently, there has been a renewed interest in the fundamental mechanisms governing near-wall turbulence, following the discovery of an outer ‘secondary peak’ (or plateau) in turbulence energy and its pre-multiplied longitudinal energy spectrum at high Reynolds numbers, along with the growing recognition that the small-scale near-wall streaks, which govern skin friction, are significantly affected by the large-scale structures populating the outer layer, where the secondary energy maximum is observed. The ability to gain insight into these interactions has been greatly enhanced by advancements in experimental, data-processing, and numerical simulation techniques. This has led to a surge in activity since 2003/4, resulting in numerous papers addressing various structural aspects of, and related interactions in, near-wall turbulence (see e.g. Adrian, Meinhart, and Tomkins 2000; Ganapathisubramani, Longmire, and Marusic 2003; Del Álamo and Jiménez 2003; Jiménez, Del Álamo, and Flores 2004; Hoyas and Jiménez 2006; McKeon and Morrison 2007; Chung and McKeon 2010; Schlatter et al. 2010). In a remarkable series of studies spanning over a decade, Marusic, Mathis, Hutchins, and their collaborators (Marusic 2001; Hutchins and Marusic 2007b; Mathis et al. 2009; Mathis, Hutchins, and Marusic 2009; Marusic, Mathis, and Hutchins 2010b; Marusic, Mathis, and Hutchins 2010a; Marusic et al. 2010; Hutchins et al. 2011; Mathis et al. 2013) have investigated, primarily using hot-wire techniques, the response of near-wall streaks in the viscosity-affected sublayer to outer structures, typically present at a distance of 0.1-0.2 of the boundary-layer thickness from the wall. They demonstrate that the outer structures influence near-wall turbulent fluctuations through two mechanisms: “footprinting” and “modulation”, as previously mentioned (see Chapter 1). However, the statistical characterisation of the correlation between large-scale motion and modulation remains a contentious issue and has been the subject of several recent studies (see Mathis, Hutchins, and Marusic 2009; Mathis et al. 2009; Schlatter and örlü 2010; Bernardini and Pirozzoli 2011; Agostini, Leschziner, and Gaitonde 2016). Of particular relevance to the present study are the measurements and related analysis of footprinting and modulation by Mathis, Hutchins, and Marusic (2011) and Marusic, Mathis, and Hutchins (2010a), following from earlier work by Mathis, Hutchins, and Marusic (2009), that has led to the proposal of an empirical relationship which “predicts” the effects of the large-scale outer fluctuations on the small-scale near-wall motions:

$$u_p^+(y^+) = u^*(y^+) \{1 + \beta(y^+) u_{O,LS}^+(y_O^+, \theta_{LS})\} + \alpha(y^+) u_{O,LS}^+(y_O^+, \theta_{LS}) \quad (4.1)$$

This equation, in which (importantly) scaling is effected with the mean-friction velocity, contains two contributions, one including the coefficient  $\alpha$  and the other  $\beta$ , that express, respectively, the effects of footprinting and modulation by the outer motions  $u_{O,LS}^+(y_O^+)$  on the canonical field  $u^*(y^+)$  that would exist if there were

no large-scale structures, and  $\theta_{LS}$  is the angle reflecting the lag between the outer motions and their footprints. The empirical coefficients  $\alpha$  and  $\beta$  depend on the wall distances  $y^+$  and  $y_O^+$ , but are of order 0.7 and 0.04, respectively, outside the viscous sublayer, varying only modestly beyond  $y^+ \approx 20$ . The main concept underpinning eq. (4.1) is, therefore, that the near-wall intensity can be “predicted”, at any Reynolds number and irrespective of the intensity of the outer motion, by imparting empirical corrections to the universal field  $u^*(y^+)$  that involve the Reynolds-number-dependent outer motions. On the assumption that the outer field  $u_{O,LS}^+$  is known, the predictive capability of eq. (4.1) thus hinges on the knowledge of  $u^*(y^+)$ , the empirical coefficients  $\alpha$  and  $\beta$  and the lag angle  $\theta_{LS}$ .

Eq.(4.1) has two important implications that are open to question:

- (i) positive and negative large-scale fluctuations cause equally-weighted modifications to the small-scale fluctuations — i.e. the unperturbed field  $u^*$  is “*symmetrically*” altered;
- (ii) scaling of all quantities (and thus also coefficients  $\alpha$  and  $\beta$ ) with the mean-friction velocity implies linearity, in the sense that the Reynolds-number universality expressed by eq.(4.1) is not conditional on large-scale variations in the friction velocity induced by the LS motions or the energy of the outer structures.

In this chapter, the statistical properties of velocity fluctuations derived from DNS data for channel flow at  $Re_\tau \approx 1025$  are analysed to examine various aspects of the model in eq.(4.1). The same DNS database used in the previous chapter is reused here to investigate the velocity statistics. The focus is on assessing key assumptions and implications of eq.(4.1) through scrutiny of the fluctuating velocity field. This statistical approach provides new perspectives into the model’s representation of scale interactions and modulation effects. This statistical approach provides new perspectives into the model’s representation of scale interactions and modulation effects. Although this Reynolds number is relatively low – certainly in comparison with experimental configurations — the flow is appropriate to the aims pursued in this study. As is shown in Figure 4.1(b), the streamwise turbulent stress is clearly elevated at  $y^+ \approx 100 - 400$ , and there is an outer, albeit weak, maximum in turbulence-production-to-dissipation ratio,  $\mathcal{P}/\epsilon$ , around  $y^+ \approx 180$ , corresponding to  $y^+/h = 0.15$ . Significantly, Figure 4.1(c) shows that this region is not simply characterized by a hump in the turbulence energy, but that the anisotropy experiences a significant elevation in the same region, showing a behaviour qualitatively similar to that at  $y^+ \approx 12.5$ , and this provides an indication that the outer structures are akin to streaks, characterized by a preferential concentration of energy in the streamwise component. Finally, it will be shown in the discussion to follow that the pre-multiplied energy spectrum features a secondary outer (albeit weak) maximum that allows the outer scales to be separated from the inner ones.

As the present examination is restricted to a single Reynolds number, it cannot shed light on the issue of Reynolds-number independence of eq. (4.1). Rather, the study aims to identify whether the response of the small near-wall scales to low-velocity and high-velocity large-scale outer motions is symmetric, whether — consistent with a symmetric response — a unique unperturbed field  $u^*$  can be reconstructed from the DNS data and the coefficients provided by Mathis, Hutchins, and Marusic (2011) in eq. (4.1), and whether mean-friction scaling, or one based on the large-scales-modified local-friction velocity, is appropriate. .

## 4.2 Processing Methodology – Scale Separation using BEMD

The work of Marusic and his collaborators — eq. (4.1), in particular — is based on the processing of temporal signals over large periods of time, recorded at specific spatial wall-normal locations, over a range of wall-normal distances. This is not possible to replicate with the DNS data available in the present work, simply because the duration of the simulation is too short to enable a valid statistical representation of the effects of the outer structures. Instead, attention is focused on full-volume snapshots at a number of time levels. A representative (raw)  $x - z$  snapshot at  $y^+ \approx 13.5$  is given in Figure 4.2(a). This shows contours of streamwise-velocity fluctuations. The plot conveys a clear view of both the small-scale streaks, which are at maximum strength at the wall-normal location chosen, and of the footprints of large-scale outer structures, which typically have a length  $x^+ = \mathcal{O}(5 \times 10^3)$  or 5 channel half-heights for the present Reynolds number.

Given snapshots of the form shown in Figure 4.2(a), the footprints need to be separated from the small-scale motions. The BEMD method is used to separate the large-scale and small-scale motions from the raw snapshot data. As outlined previously, EMD decomposes signals into Intrinsic Mode Functions representing different characteristic scales based purely on the local scales within the data itself, without requiring

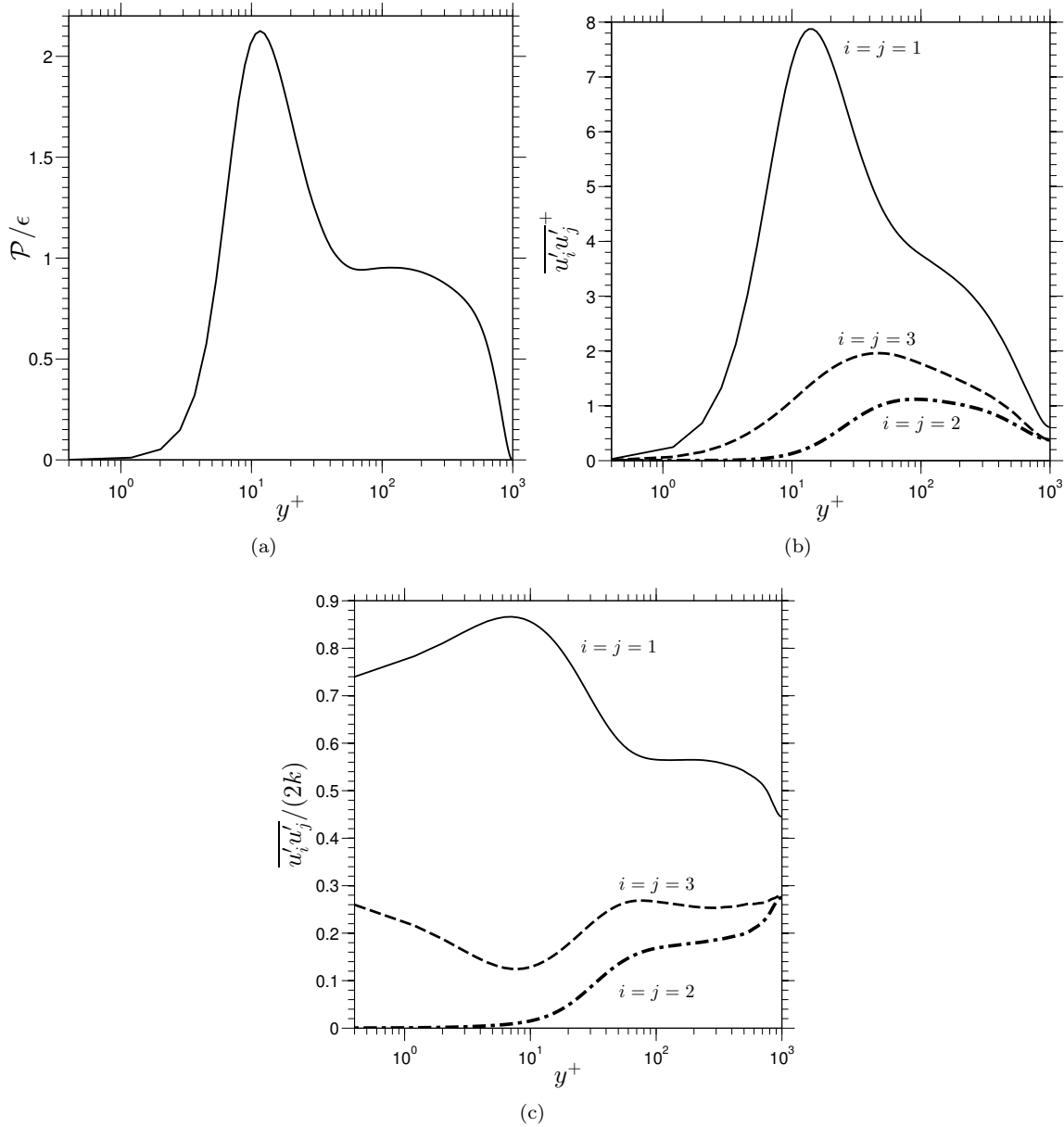


Figure 4.1: Statistical evidence of large-scale outer structures: (a) ratio of turbulence-energy production to dissipation; (b) normal Reynolds stresses; (c) anisotropy of the normal Reynolds stresses.

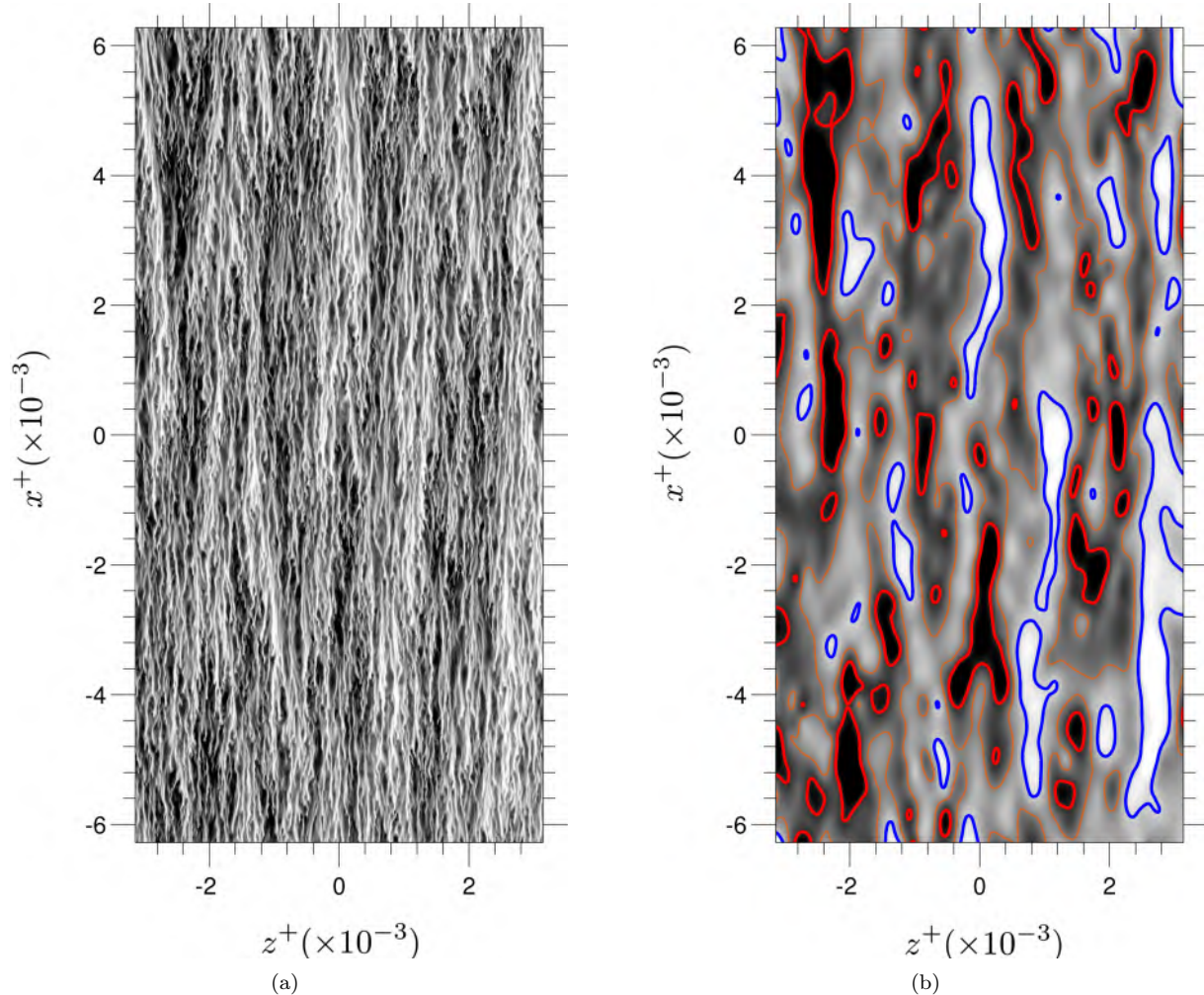


Figure 4.2: Snapshot of the streamwise-velocity fluctuations at  $y^+ \approx 13$ : (a) complete signal; (b) large-scale velocity fluctuations; islands with red/blue boundaries identify positive/negative fluctuations within the extreme 10% bands (tails) of the PDF of the large-scale fluctuations (see Figure 4.3(b) and related description).

predetermined functional elements. Applying EMD to the velocity snapshot data leads to a set of modes ordered by decreasing frequency and increasing scale. The first three modes are considered to represent the small scales, while the last mode captures the large-scale motions. This scale separation is justified through examination of the mode-specific energy spectra, correlation maps, and energy profiles presented earlier (see Chapter 3.3 for more details). The EMD approach provides an effective data-driven isolation of the key small- and large-scale fluctuations from the velocity snapshots for analysis as conveyed by Figure 4.2(a) and (b) in which the application of the EMD to the raw field leads to the large-scale streamwise-velocity fluctuations (Figure 4.2(b)), in which the islands surrounded by the line contours are areas within which the large-scale motions exceed a certain limit defined and discussed below. Typically, the large-scale velocity fluctuations within these islands are around 15–20% of the mean velocity (at  $y^+ \approx 13$ ). Analogous large-scale fields may be obtained for the spanwise- and wall-normal-velocity components.

In order to extract statistical data pertinent to the interactions between the large outer and small inner scales, and thus to eq. (4.1), 1-d PDFs and 2-d joint PDFs of SS velocity fluctuations have been assembled, conditional on regions of high-velocity, low-velocity and near-zero LS footprints. Regions of high-velocity and low-velocity LS motions are defined here as those which fall into the lowest and highest 10% bands of the PDF of the entire LS field, while regions which are, essentially, devoid of LS footprints are defined as those which fall into the central 10% of the PDF. This is illustrated in Figure 4.3. The PDF in Figure 4.3(a) gives the distribution of all LS motions contained in Figure 4.2(b), while the two PDFs in Figure 4.3(b) relate, respectively, to the top 10% (in terms of area) of positive (red) and negative (blue) LS fluctuations in the complete PDF of Figure 4.3(a). These correspond, respectively, to the red and blue islands in Figure 4.2(b), and LS fluctuations therein are of order 20% and 15%, respectively, of the mean velocity in the same plane. It needs to be emphasized that there is no fundamentally profound reason for the present focus on 10% bands within the LS PDF. This is a choice that reflect the wish to bring out as clearly as is possible differences in the effects of positive and negative LS fluctuations on the SS motion. An analysis based on extended bands (up to 40%) in no way changes, qualitatively, the conclusions presented herein. With the extreme 10% regions so identified, PDFs are then constructed of the SS motions within the blue and red regions, so to enable an examination of the effects of the footprints on the SS motions. A feature of the PDF in Figure 4.3(a), which will be relevant to the discussion to follow, is that it is only weakly asymmetric, with extreme positive fluctuations slightly more prevalent than extreme negative ones. This weak asymmetry (relative to the principal axes) also applies to the  $(u - v)$  joint PDF at the same wall-normal location, shown in Figure 4.3(c) and assembled with  $v_{LS}^+$  determined from the application of the EMD to the wall-normal component. The near-symmetry of the PDF in Figure 4.3(c) will later serve as a background against which to contrast corresponding PDFs for the SS motions, which display a much higher degree of asymmetry.

## 4.3 Examination of Small-Scale Response to Outer-flow structures

### 4.3.1 Asymmetry in Large-Scale Positive and Negative Influences: A Detailed Investigation

Most results presented herein are probability density functions (PDFs) at  $y^+ \approx 13.5$ , with velocity fluctuations scaled by the mean friction velocity. As such, they pertain to the “linear” model of Hutchins et al. (2011) (eq. (4.1)), which also employs mean-friction scaling.

Some basic arguments are first conveyed by means of 1-d PDFs of the form  $pdf(u^+)$ . Figures 4.4(a) - (c) give, respectively, PDFs of the total  $u$ -fluctuation field, of the SS-fluctuation field – i.e. with the LS motions subtracted from those of Figure 4.4(a), and of the SS fluctuations normalised, for reasons explained below, with the absolute LS velocity as follows:

$$u_{SS/LS}^+ = u_{SS}^+ \times \frac{\langle U_{1,LS} \rangle_{x,z,t}}{u_{1,LS} + \langle U_{1,LS} \rangle_{x,z,t}} \quad (4.2)$$

where  $\langle U_{1,LS} \rangle_{x,z,t}$  is the average streamwise velocity at  $y^+ \approx 13.5$ . Each plot contains three PDFs, relating to the lowest, middle and highest 10% bands, respectively, in the PDF of the large-scale motions shown in Figure 4.3(a). Unless stated explicitly otherwise, normalisation is performed with the mean-friction velocity.

This first comparison brings to light substantial differences in the manner in which the positive and negative LS motions affect the SS fluctuations. Importantly, this *asymmetric* response is not associated with the superposition of the LS motions onto the SS fluctuations — an effect that is included in Figure 4.4(a), but

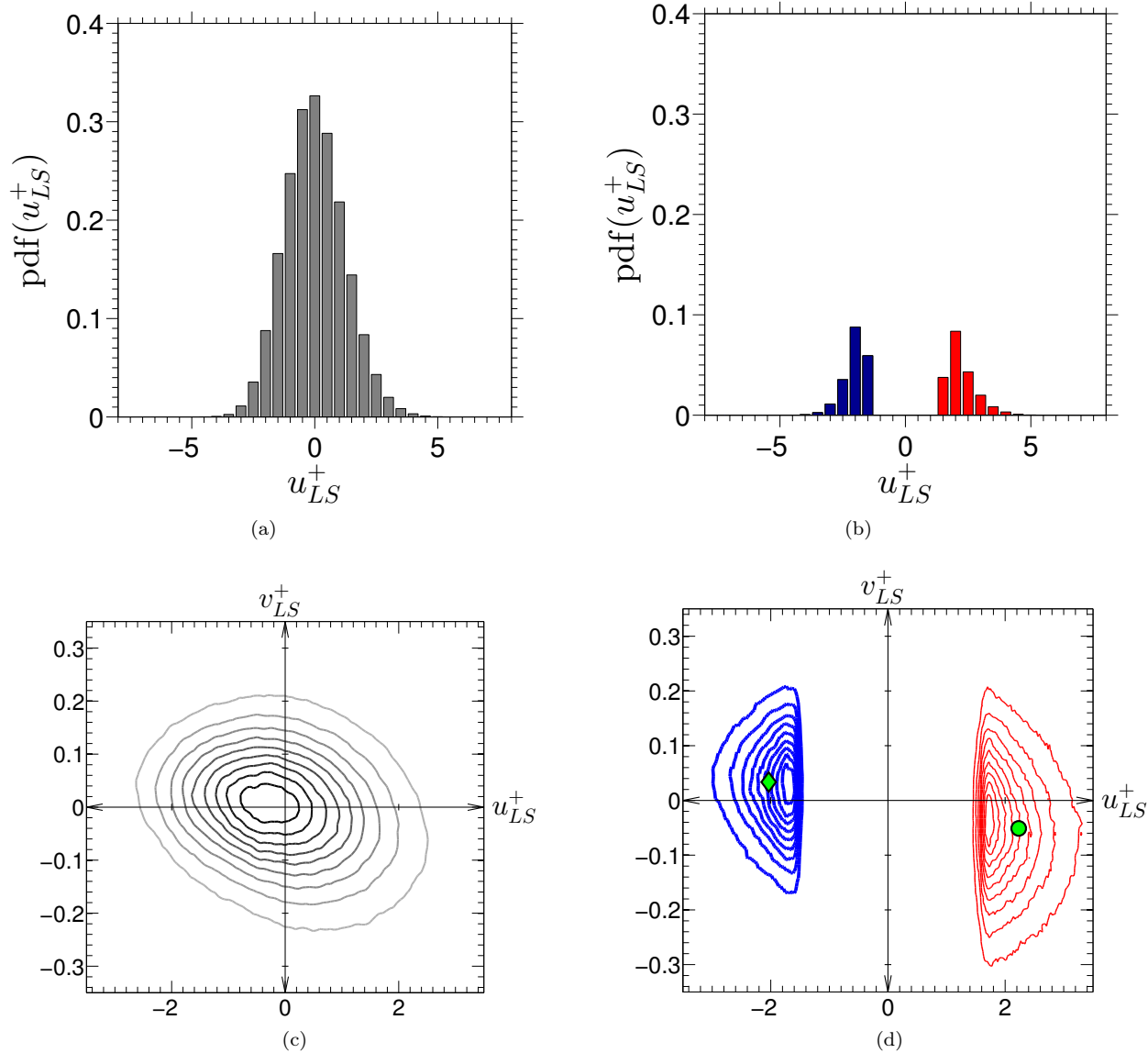


Figure 4.3: PDFs of large-scale  $u$ -velocity fluctuations (EMD mode 4) at  $y^+ \approx 13.5$ : (a) the whole 1-d PDF; (b) partial PDFs for the 10% lowest and highest velocity fluctuations for which the statistics of SS motions are studied; (c) joint 2-d ( $u - v$ ) PDF of large-scale velocity fluctuations equivalent to (a); (d) partial joint 2-d ( $u - v$ ) PDFs equivalent to (b). PDF contours identify 0.1-0.9 of the PDF height at constant increment 0.1.

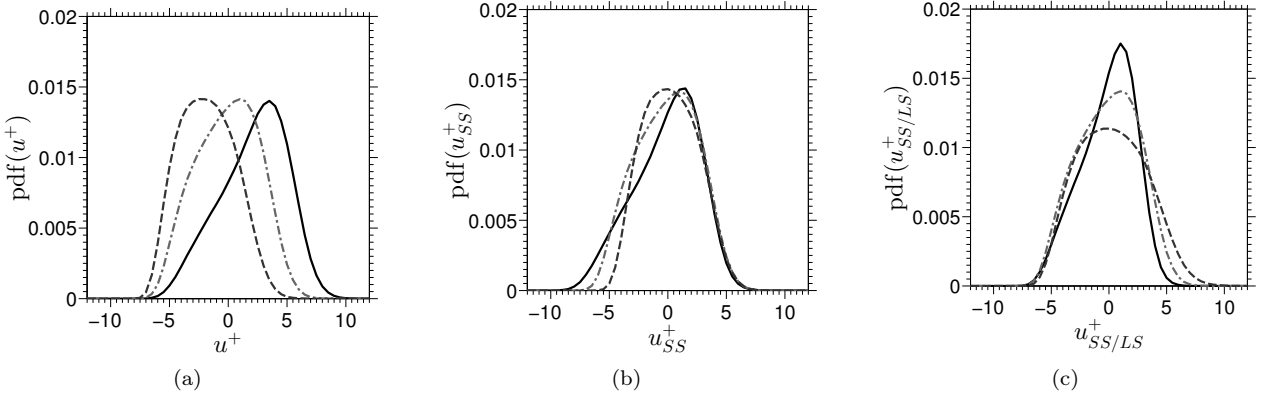


Figure 4.4: PDFs of  $u$ -velocity fluctuations at  $y^+ \approx 13.5$  pertaining to the bands of 10% extreme positive LS events (solid line), 10% minimum LS events (chain line) and 10% extreme negative events (dashed line); (a) total fluctuations; (b) SS fluctuations only; (c) SS fluctuations normalised with the LS velocity, eq. (4.2).

is excluded from 4.4(b). When the LS motion is removed, the SS PDF associated with negative LS fluctuations is close to Gaussian, while that associated with positive LS fluctuations is skewed, the latter characterized by a predominance of relatively weak positive fluctuations and relatively strong negative fluctuations. The removal of the LS motions corresponds, essentially, to the shift implied by the  $\alpha$ -related term in eq. (4.1), which reflects the assumption of a superposition process. Here, however,  $\alpha = 1$  (by implication), because the LS information is available, and so used, on the same plane as the SS field, rather than at  $y_O^+$ . The rationale of normalising the SS fluctuations with the absolute LS velocity, as done in Figure 4.4(c), is rooted in the observation that the velocity ratio in eq. (4.2) agrees closely with the normalised friction velocity  $u_\tau/u_{\tau,LS}$ , the latter evaluated by applying the EMD scale-decomposition to the plane  $y^+ \approx 3$  and restricting attention to the 10% extreme bands of the LS fluctuations. The implication of Figure 4.4(c) is, therefore, that the SS fluctuations neither scale universally with  $u_\tau$  nor with  $u_{\tau,LS}$  when these fluctuations are determined or considered at a fixed  $y^+$  location. The fact that the modulation of the SS fluctuations differs markedly for positive and negative LS fluctuations, in contrast to the implication of eq. (4.1), will be argued below to reflect the impact of splatting associated with sweeps. As a consequence, the modulation is not simply representable in terms of the streamwise LS fluctuations alone.

In eq. (4.1),  $u^*$  is assumed to be the canonical signal that would have been recorded in the absence of LS effects. In the present context of spatial statistics, it is reasonable to suppose that equivalent conditions prevail in areas to which the central portion of the LS PDF in Figure 4.3(a) relates. Figure 4.4 shows, by chain lines, the 1-d PDFs of the SS motions that relate to the central 10% band in the LS PDF. As might be expected, the SS fluctuation field in this central band has features intermediate between those within the two extreme areas of the LS PDF of Figure 4.3. However, this does not suffice, on its own, to judge this field as being free from *any* LS influences. The interpretation of the  $u^*$  field as either being or not being “universal” is one aspect of an examination of the validity of Mathis et al’s model by reference to  $(u-v)$  joint PDFs, considered next.

Figure 4.5 shows PDFs of the entire  $(u-v)$ -fluctuation field, of the total fluctuations in the blue and red areas of Figure 4.2, of the SS fluctuations in the blue and red areas, and of the SS fluctuations scaled by the LS velocity, in accordance with eq. (4.2), with  $v_{SS/LS}^+$  (and later also  $w_{SS/LS}^+$ ) obtained upon replacing  $u_{SS}^+$  by  $v_{SS}^+$  (or  $w_{SS}^+$ ). The circular and diamond-shaped symbols represent the centres of gravity of the PDFs in question. The collapse of the centres of gravity in Figure 4.5(c) points to the validity of the superposition component associated with  $\alpha$  in eq. (4.1). There is, furthermore, clear evidence that positive LS perturbations cause considerably stronger modulation of the SS motions than negative perturbations. Once scaled by the LS velocity, Figure 4.5(d), the SS fluctuations display fair universality in quadrant 2, associated with ejections, but substantial departures from universality in quadrant 4. That these drastic differences are not associated with a bias in the LS motions is demonstrated in Figure 4.3(c), which shows the near-symmetric PDF of the complete field of LS motions.

Figure 4.6 shows  $(u-w)$  joint PDFs, which correspond to the  $(u-v)$  PDFs in Figure 4.5. These suggest

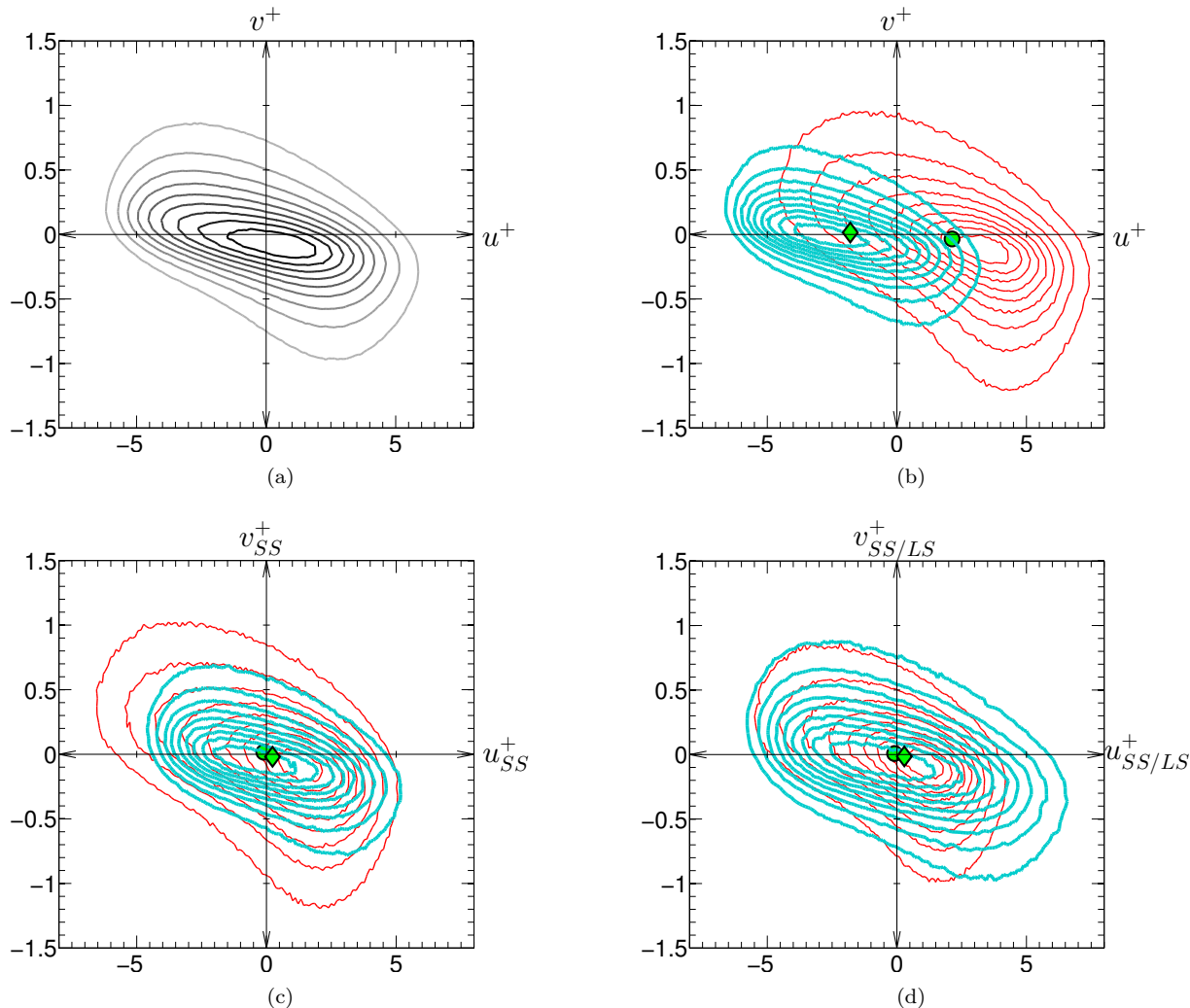


Figure 4.5: Joint  $(u-v)$  PDFs at  $y^+ \approx 13.5$  of (a) total fluctuation field; (b) total fluctuations in blue and red regions in Figure 4.2(b), respectively; (c) SS fluctuations; (d) SS fluctuations normalised by LS fluctuations. Red contours :  $+10\%$  LS fluctuations, blue contours  $-10\%$  LS fluctuations. PDF contours identify 0.1-0.9 of the PDF height at constant increment 0.1, subject to total PDF volume normalised to 1.

that the skewed shape of the PDF in Figure 4.4, associated with positive LS motions, is driven by sweeps which transport relatively weak SS fluctuations from beyond the buffer layer downwards. In contrast, SS ejections are weaker, more numerous and more normally distributed, thus unaffected by the bias caused by sweeps. In common with the  $(u - v)$  PDFs, the centres of gravity of the  $(u - w)$  PDFs collapse upon the removal of the LS motion. Similarly, the SS motions scaled by the LS velocity collapse for negative LS motions, but not for positive ones.

The conclusion thus emerging, so far, from the above discussion is that modulation is not a “symmetric” process, in the sense of positive and negative LS motions having the same weight on the SS field, and that the lack of symmetry is caused by major differences in the effects of sweeps and ejections on the SS structure. In particular, the  $(u - w)$  joint PDFs bring to light that sweeping motions go hand in hand with strong spanwise fluctuations in quadrants 1 and 4, which are characteristic of splatting. This process, and its effects on the SS motions, is not accounted for in eq. (4.1) and cannot be captured by the model.

### 4.3.2 Universal SS motions — the $u^*$ field

If, despite the above incompatibility, the model is to be retained, it is possible to determine (or rather estimate) the values for  $\alpha$  and  $\beta$  that secure the best possible compliance with the present data. To this end, eq. (4.1) is re-cast as follows:

$$u^* = \frac{u^+ - \alpha u_{O,LS}^+}{1 + \beta u_{O,LS}^+} \quad (4.3)$$

Given values  $\alpha$  and  $\beta$ , the question is whether the SS PDFs, conditional on the  $\pm 10\%$  extrema of the LS motion, can be made to collapse, such a collapse being interpretable as representing the field  $u^*$ . An *ambiguity* that arises with this process relates to the interpretation of  $v^*$  and  $w^*$ . In the absence of a credible alternative, the assumption is made here that  $v^* = v_{SS}^+$  and  $w^* = w_{SS}^+$ , respectively. A possible variation is to use eq. (4.3), with the numerator replaced by  $v_{SS}^+$  and  $w_{SS}^+$  to obtain  $v^*$  and  $w^*$ , respectively. However, this variation has only marginal effects on the results to follow.

As shown in Figure 4.7, use of  $\beta = 0.04$ ,  $\alpha = 0.7$ , with  $u_{O,LS}$  taken from  $y_O^+ \approx 150$ , subject to  $\theta_{LS} = 12.5^\circ$ , results in a fair correspondence in the  $u$ -wise widths of the PDFs, but in significant differences in their shape, especially in quadrant 4. Thus, although Figure 4.7 suggests that the amplitude, or intensity, of the  $u^*$ -fluctuations is fairly insensitive to whether the LS motions are positive or negative, supporting Mathis et al’s model (with the particular empirical constant  $\beta$  used), the PDFs in Figure 4.7 show that  $u^*$ -field is not, in fact, universal, because the PDF of the SS fluctuations subjected to positive LS fluctuations is skewed and distorted (see also Figure 4.4(b)). Moreover, if the joint  $(u^* - v^*)$  PDFs are projected onto the  $u^*$  axis, to yield corresponding 1-d PDFs, the shape of the latter are quite similar to that shown in Figure 4.4(c). This distortion is, again, a consequence of the sweeping motions – an effect that does not fall neatly under the heading “footprinting” and amplitude “modulation”, and which cannot be represented purely by reference to the outer LS motions  $u_{O,LS}^+$ .

### 4.3.3 Towards a More Comprehensive Predictive Description of Near-Wall Turbulence Universality

In view of the above discussion, the question may be posed as to whether another, purely phenomenological, model can be derived that provides an improved representation of the interaction between the LS structures and the near-wall SS structures, via an improved description of the  $u^*$  field. Such a model is proposed below.

Assuming the LS footprints are available at the near-wall location  $y^+$  under consideration, the following relationships are proposed to apply, so as to represent the dependence of the SS fluctuations,  $u_{i,SS}^+$  ( $i = 1, 2, 3$ ), on the LS motions,  $u_{LS}^+$ , at one and the same plane:

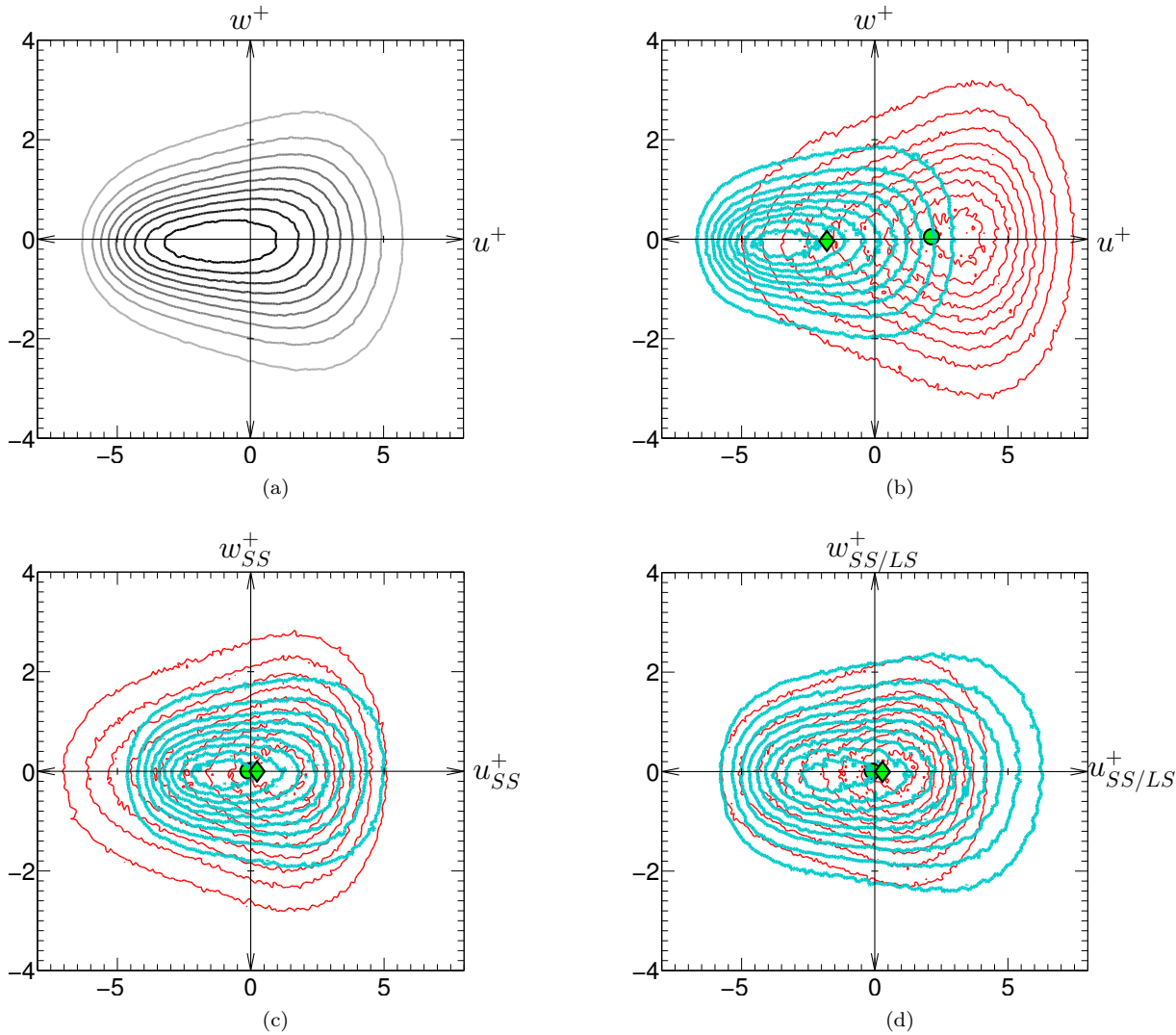


Figure 4.6: Joint  $(u - w)$  PDFs at  $y^+ \approx 13.5$  of (a) total fluctuation field; (b) total fluctuations in blue and red regions, respectively in Figure 4.2(b); (c) SS fluctuations; (d) SS fluctuations normalised by LS fluctuations. Contours levels: see caption of Fig. 4.5.

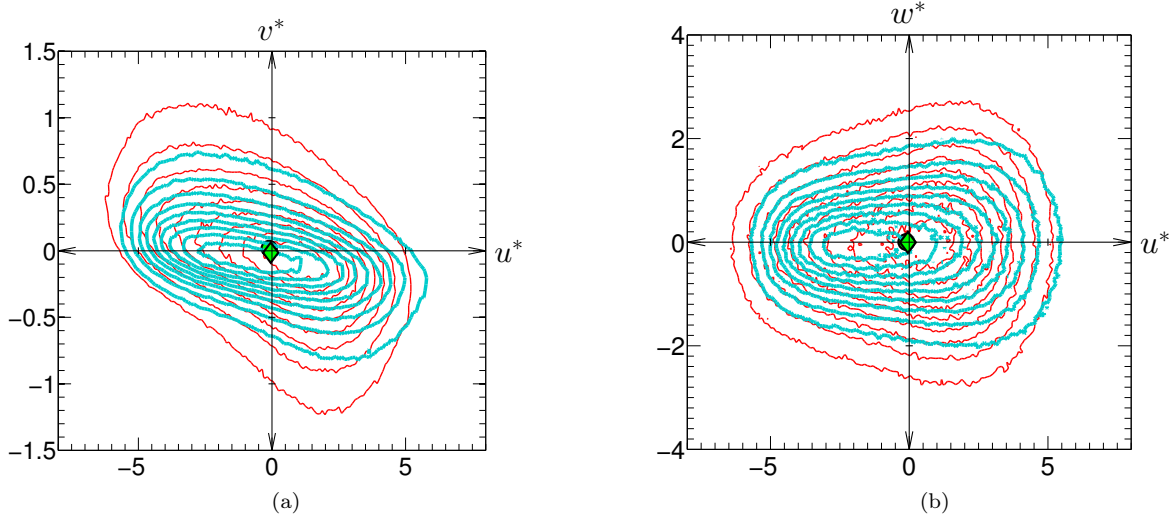


Figure 4.7: Joint PDFs: (a)  $u^* - v^*$ ; (b)  $u^* - w^*$ , both derived from eq. (4.3) at  $y^+ \approx 13.5$ , with  $\beta = 0.04$  and  $\alpha = 0.7$ . Contours levels: see caption of Fig. 4.5.

$$u_{i,SS}^+ = \frac{U_i - (u_{i,LS} + \langle U_{i,LS} \rangle_{x,z,t})}{u_\tau} \quad (4.4)$$

$$u_{i,SS/LS}^+ = u_{i,SS}^+ \times \frac{ < U_{1,LS} >_{x,z,t} }{ u_{1,LS} + < U_{1,LS} >_{x,z,t} } \quad (4.5)$$

$$u_i^* = u_{i,SS/LS}^+ f(U_{1,LS}, \chi_i) \quad (4.6)$$

where

$$f(U_{1,LS}, \chi_i) = 1 + \chi_i \times \frac{u_{1,LS}}{\zeta_{U_{1,LS} > x_{z,t}}}, \quad \chi_i = 1 \text{ if } i = 1 \text{ and } u_{1,SS}^+ > 0, \text{ otherwise } \chi_i = 0.$$

In the above equations, it is important to distinguish between the LS fluctuation  $u_{i,LS}$ , the plane-parallel average of which is zero, and the absolute LS velocity,  $U_{i,LS}$ , and its finite plane-parallel average,  $\langle U_{1,LS} \rangle_{x,z,t}$ .

The fidelity of this model is investigated in Figures 4.8 and 4.10. First, Figure 4.8 provides a qualitative view of the  $u^*$ -field predicted by eq. (4.6) in comparison with the complete (raw) field at  $y^+ \approx 13.5$  and the field of the LS motions. The only important point that this figure conveys is that the  $u^*$ -field shows no evidence of the LS motions. What this figure cannot show, however, is the presence or absence of modulation and any asymmetry therein. Such information is conveyed by Figures 4.9 and 4.10 which show, respectively,  $(u - v)$  and  $(u - w)$  joint PDFs for  $y^+ \approx 13.5$ , both derived from eq. (4.6). Each figure compares three alternative proposals: in Figures 4.9(a) and 4.10(a) are shown PDFs obtained directly from the DNS data in the 10% central portion of the LS PDF of Figure 4.2(a), where the SS motions should be least altered by the LS motions; in Figures 4.9(b) and 4.10(b) PDFs arising from eq. (4.3) (i.e. Mathis et al's model are reproduced; in Figures 4.9(c) and 4.10(c) are shown PDFs obtained with the present proposal, with the LS fluctuations taken from the same level as that to which the PDF applies.

The present model is observed to provide a much improved level of collapse to that achieved with Mathis et al's model when the LS motions are taken from the same level at which the SS PDFs are considered. When the LS motions are taken from  $y^+ \approx 180$ , the level of collapse is slightly degraded. Apart from reducing the distortions in the  $u^*$ -field that arise from the different effects of the positive and negative LS fluctuations, the model also provides a creditable representation of the  $w^*$ -field.

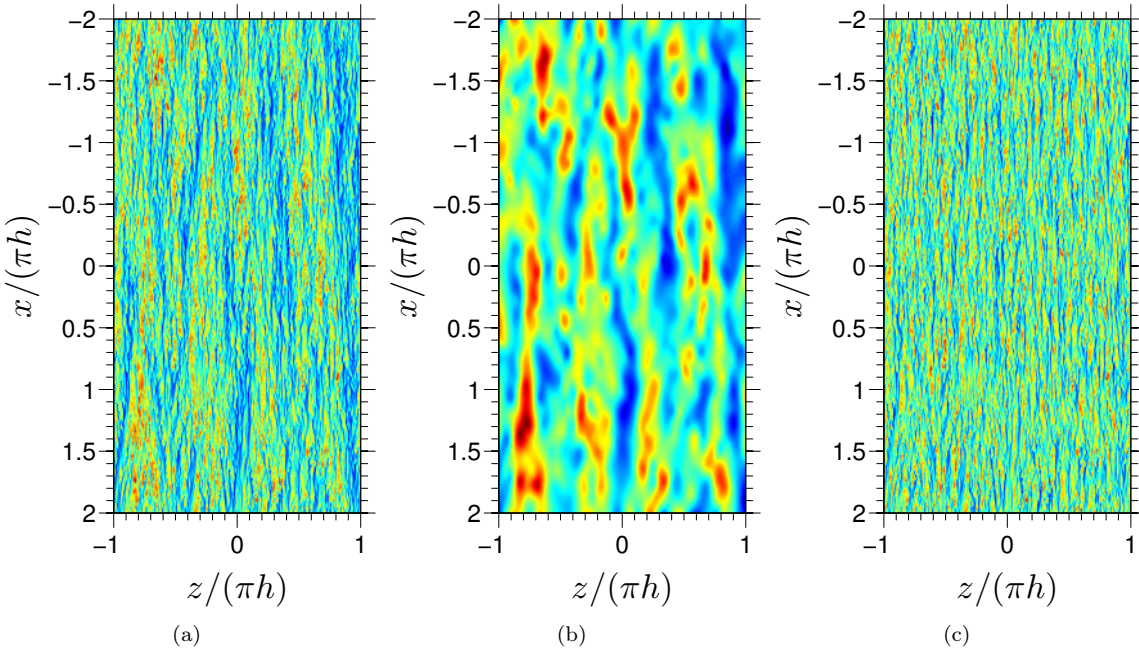


Figure 4.8: Snapshot of streamwise-velocity fluctuations at  $y^+ \approx 13.5$ ; (a) complete signal; (b) large-scale Motions; (c)  $u^*$ -field derived from eq. (4.6)

#### 4.4 Similarities with a Low Reynolds Number Compressible Boundary Layer

The data forming the basis of the present analysis originate from a DNS study for a boundary layer at  $M = 2.3$  in the free stream. The numerical scheme used in the DNS code is a sixth-order compact difference approach, combined with 8<sup>th</sup> order Pade-type filtering (see Poggie 2015; Poggie and Leger 2015, for details). Time integration is accomplished with an implicit approximately factored method. The simulation covered a streamwise domain  $L_x = 100\delta_0$ , where  $\delta_0$  is the upstream boundary layer thickness, corresponding to  $Re_{\delta_0} = 15000$ . The wall-normal and spanwise box dimensions were  $L_y, L_z = 5\delta_0$ . This box was covered by a mesh of  $1.1 \times 10^{10}$  nodes, for which the internodal distances, scaled by wall conditions at  $x/\delta_0 = 100$ , are  $\Delta x^+ = 6$ ,  $y_{wall}^+ = 0.5$ ,  $\Delta z^+ = 5$ . A database was assembled by collecting data for 35000 time levels over a period  $\Delta t^+ = 1862$  at one spanwise plane located at  $x/\delta_0 = 100$ . At this plane, the conditions are characterised by  $Re_\theta = 2000$ ,  $Re_\tau \approx 570$ . Statistics to follow thus arise from time- and spanwise-averaging of the data at one streamwise plane. Figure 4.11 shows wall-normal distributions of the mean velocity and the Reynolds-stress components at the above location, all scaled with the density-weighted friction velocity  $u_\tau$ . The mean velocity is seen to feature a rather short log-law region, due to the modest Reynolds number and the presence of the outer wake region beyond  $y^+ \approx 300$ . The peak of the streamwise stress occurs at  $y^+ \approx 13$ , at which the near-wall streaks are also observed to be most strongly pronounced. Within the layer  $y^+ \approx 150 - 200$ , a distinctive elevation in the streamwise stress is observed, giving rise to an inflection point at  $y^+ \approx 100$  and indicating the presence of energetic large-scale motions. In contrast, Marusic et al's correlation  $y^+ \approx 3.9\sqrt{Re_\tau}$ , yields  $y^+ \approx 93$  as an estimate of the location at which the energetic outer structures reside. However, this correlation was devised by reference to data at much higher Reynolds-number values, and is thus likely to be inaccurate at the present value.

A map of pre-multiplied energy spectra for the streamwise velocity component, showing the dependence of the energy density as a function of spanwise wave length and wall-normal distance, is provided in Figure 4.11(c). As expected, the maps indicate that the most energetic region is around  $y^+ \approx 13$ , as the near-wall streaks are conventionally associated with the magnitude of the streamwise fluctuations, it follows that the streaks are most pronounced at this wall-normal location. As regards the energy contained within the outer structures, the map indicates a diagonally stretched region of elevated energy density, extending to  $y^+ \approx 150$  over the wave-length range  $\lambda_z^+ = 300 - 500$  (i.e. roughly one boundary-layer thickness). In fact, the spectra

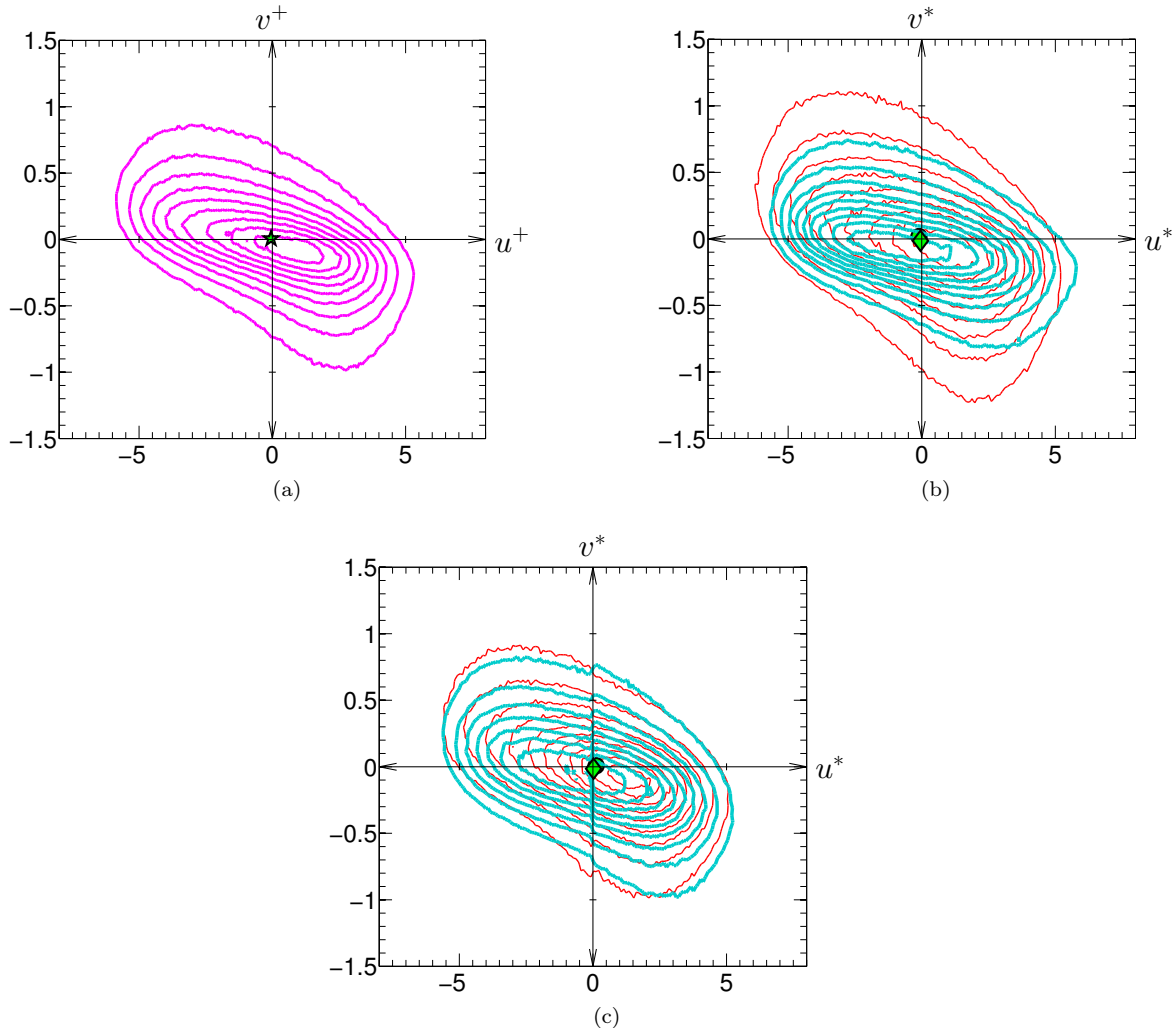


Figure 4.9: Joint  $u^* - v^*$  PDFs at  $y^+ \approx 13.5$ : (a) from 10% middle band of LS PDF; (b) Mathis et al's Mathis, Hutchins, and Marusic (2011) model (eq. (4.3)); (c) present model with LS motion taken at  $y^+ \approx 13.5$ .

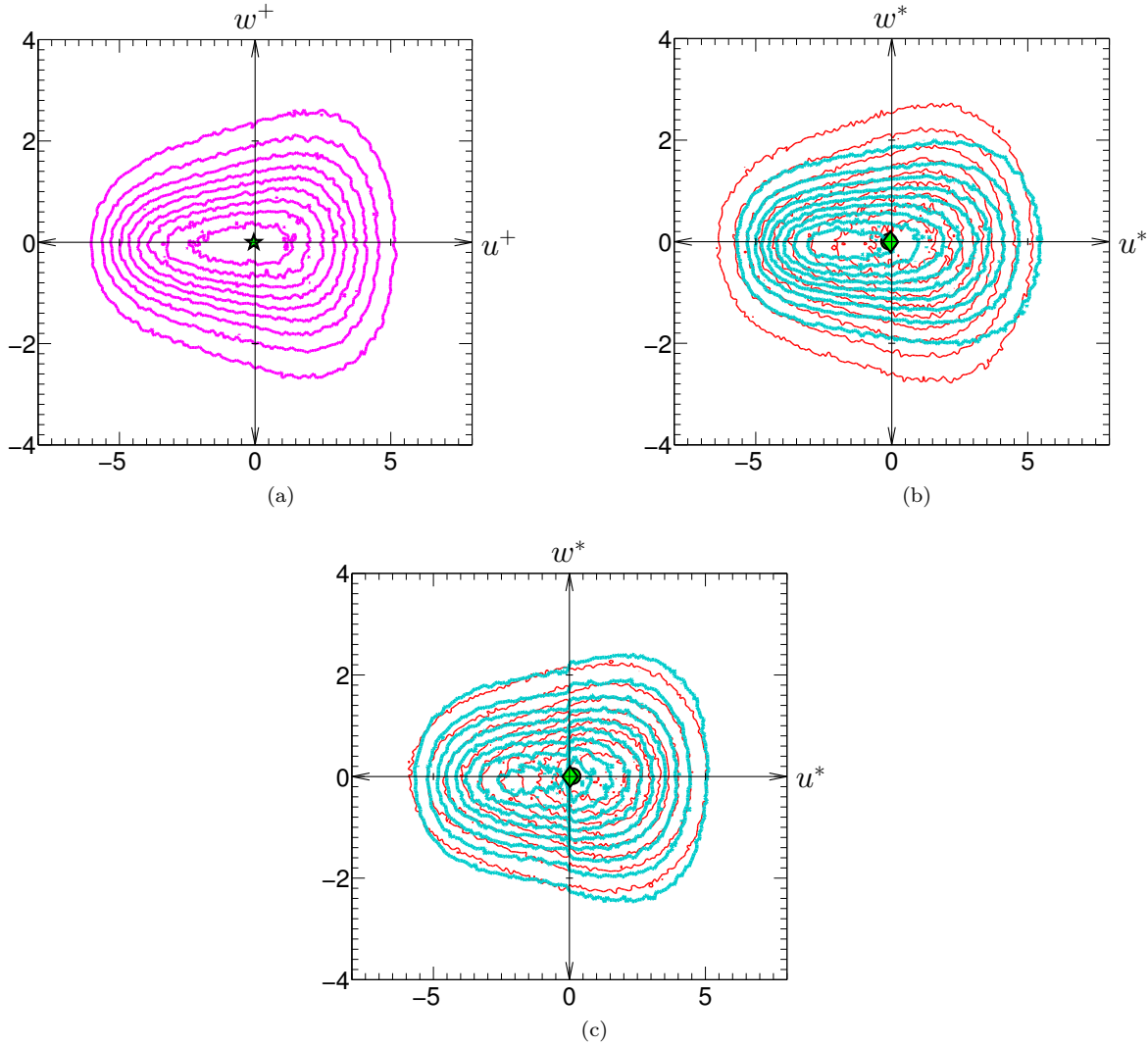


Figure 4.10: Joint  $u^* - w^*$  PDFs at  $y^+ \approx 13.5$ : (a) from 10% middle band in LS PDF; (b) Mathis et al's modelMathis, Hutchins, and Marusic (2011) (eq. (4.1)); (c) present model with LS motion taken at  $y^+ \approx 13.5$ .

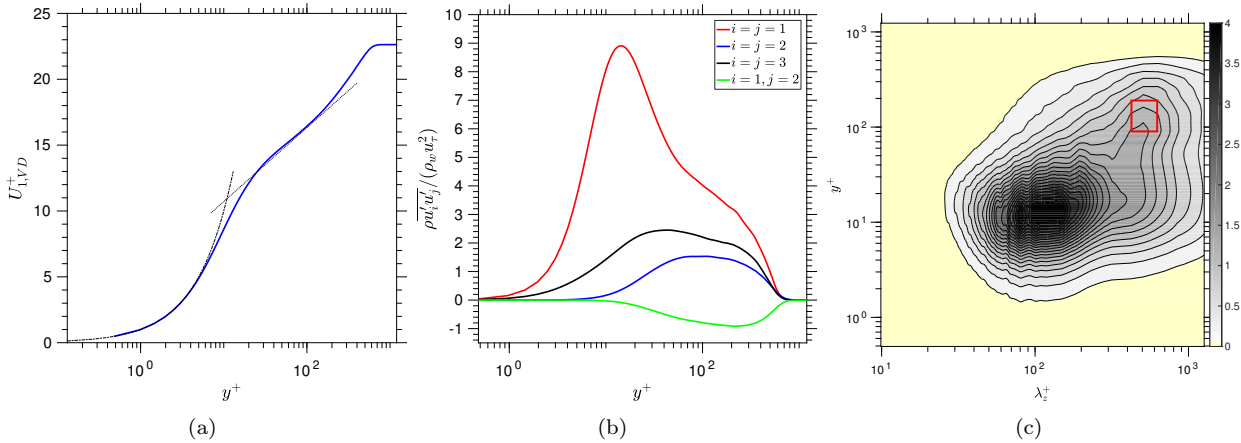


Figure 4.11: Mean-flow properties of the present boundary layer at the streamwise location  $Re_\theta = 2000$ ,  $Re_\tau \approx 570$ ; (a) Van-Driest scaled mean-velocity profile; (b) profiles of Reynolds-stress components, and (c) premultiplied power spectra  $\Phi_{uu}^+(y^+, \lambda_z^+)$  showing energy distribution by scale in the wall-normal direction produced by the streamwise velocity fluctuations

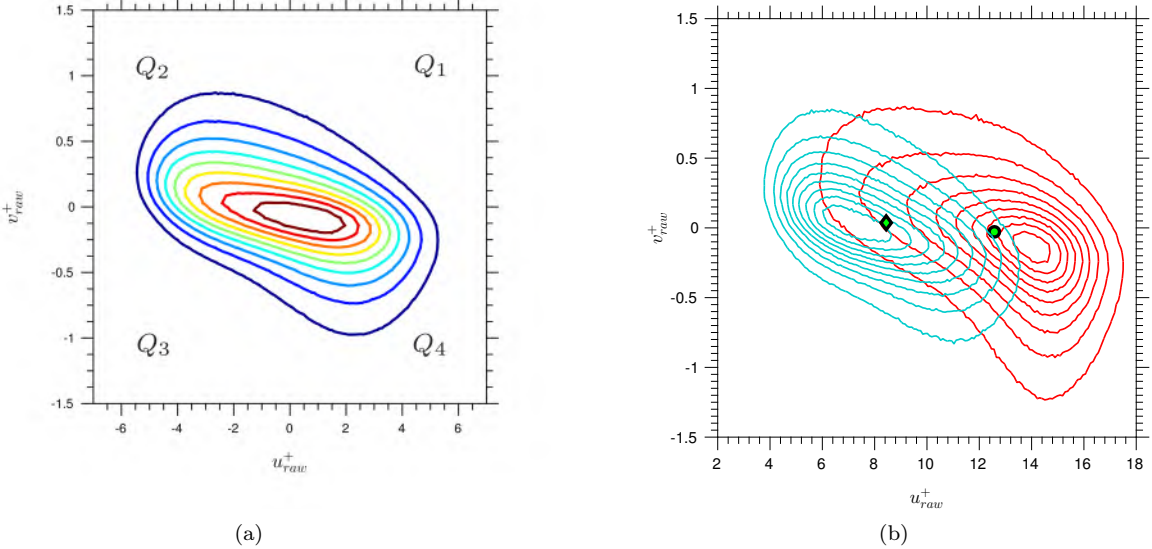


Figure 4.12: (a) Joint ( $u - v$ ) PDFs for the raw (total) fluctuations field at  $y^+ \approx 13$ , contours identify 0.1 - 0.9 of the PDF height at constant increment 0.1, subject to total PDF volume normalised to 1. (b) Joint PDFs of fluctuations sampled in footprints corresponding to  $\pm 10\%$  of slow and fast events of the large-scale motions.

hint at a weak local maximum at around  $y^+ \approx 100$ , suggesting the presence of distinct outer structures — or “super-streaks” – in the outer portion of the log-law layer. These features are entirely consistent with variation of the streamwise Reynolds stress in Figure 4.11(b). However, at this stage, neither map provides compelling evidence that the outer large-scale motions give rise to footprints in the lower layer and modify that layer’s structure.

In pursuit of the objective of illuminating the interactions between the large-scale and small-scale motions, it is instructive to conditionally sample the small-scale fluctuations separately within low- and high-velocity footprints. Here, the output of the sampling process is in the form of joint PDFs for the conditionally-sampled small-scale motions within the footprints.

In Figures 4.12(a) and (b) is plotted the ( $u - v$ ) joint PDFs for the raw signal. The r.h.s plot focus on fluctuations sampled in footprints corresponding to  $\pm 10\%$  of slow and fast events of the large-scale motions. The displacement of the gravity point corresponding to the magnitude of the large-scale motions. Figure 4.13 shows ( $u - v$ ) and ( $u - w$ ) Joint PDFs of the small-scale fluctuation field within high-speed and low-speed footprints. Both PDFs show very similar features to the ones observed in incompressible channel flow at higher Reynolds number. In particular, only the  $u - v$  PDF pertaining to the high-speed footprints features the strongly asymmetric contours, associated with sweeping events. The implication is, therefore, that high-speed and low-speed footprints have an unequal effect on the fluctuations field and thus the small-scale motions, suggesting an asymmetric modulation. Large spanwise fluctuations are predominantly present within the high-speed footprints in quadrants  $Q_1$  and  $Q_4$  – again, consistent with sweep events and thus splatting. This latter can be clearly seen in Figure 4.13(a), in which the joint-pdf takes a “pear”-shape during large-scale sweeps.

One of the main objectives was to examine whether the footprint and modulation of near-wall movements by large external structures, observed at high Reynolds numbers, were also present in flows with low Reynolds numbers. The results show that the boundary layer, although it is at a low Reynolds number and is compressible, shares many characteristics with those observed in higher Reynolds number incompressible plane channel flows. Thus,

- In the external flow, there are distinctive large-scale movements, albeit considerably weaker than in our previous studies, that produce high- and low-speed footprints on the lower part of the boundary layer.
- The intensity of small-scale movements is enhanced by high-speed footprints.

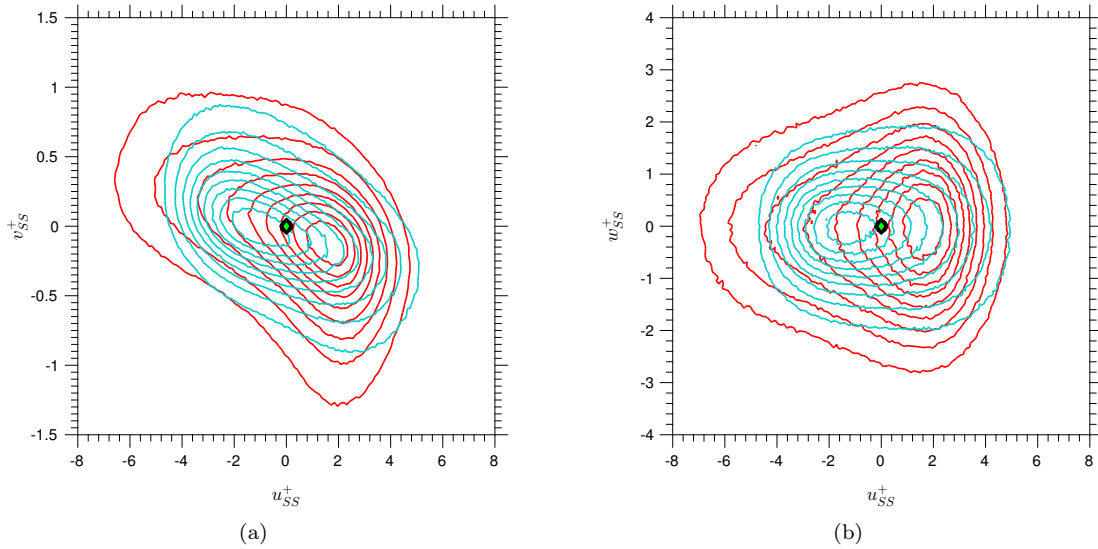


Figure 4.13: Joint PDFs at  $y^+ \approx 13$  for: (a)  $(u - v)$  and (b)  $(u - w)$  small-scale fluctuations sampled in footprints corresponding to  $\pm 10\%$  of slow and fast events of the large-scale motions

- The amplification and attenuation (reflecting a modulation of the small-scale signals) are asymmetric. The asymmetry is associated with splatting caused by large-scale sweeping events.

## 4.5 Scale Modulation: Model Limitations and Alternatives

The present study aimed to investigate the effects of large-scale motions in the log-law region on the small-scale streaks in the viscosity-affected near-wall layer. Particular emphasis was placed on examining the validity of the concepts underpinning the predictive model proposed by Mathis, Hutchins, and Marusic (2011), which expresses these effects through superposition- and modulation-related terms acting on a “universal” small-scale field, assumed to be unaffected by the large-scale motions.

In contrast to the analysis of time-signals at specific wall-normal locations, as performed in the experiments upon which the predictive model was based, the current approach employs spatial statistics, primarily 1-d and 2-d PDFs. Results obtained with scaling based on the mean-friction velocity, as in Mathis, Hutchins, and Marusic (2011), reveal significant differences in the response of the small-scale motions to negative and positive large-scale outer fluctuations. This indicates that the response of the small-scale motions is not “symmetric”, in the sense of the  $\beta$ -term used in the model of Mathis *et al.*, which represents modulation. In reality, the small-scale streaks are modified in three distinct ways: by superposition, by modulation, and by distortions of the small-scale field caused by the differential influence of sweeps (“**splatting**”) and ejections (“**anti-splatting**”). The third process is revealed by distinctive distortions in both the  $(u - v)$  and  $(u - w)$  joint PDFs. The PDFs presented herein, along with others at lower  $y^+$  values not included, suggest that the differential influence of the sweeps and ejections of the large-scale motions extends down to the lower levels of the viscous sublayer ( $y^+ \approx 3$ ). Notably, the pear-shaped  $(u - w)$  joint PDFs indicate the presence of “**splatting**” associated with sweeps, which is argued to be the cause of the asymmetry in the modulation of the streamwise small-scale fluctuations.

An alternative, purely phenomenological predictive model is proposed to explain the “universal” velocity fluctuations, which are considered to be uninfluenced by the large-scale motions. This model encapsulates the principles of superposition, modulation, and splatting-induced distortions, as represented by eq. (4.4), eq. (4.5), and eq. (4.6), respectively. Through these equations, the model determines the “universal” small-scale field without the need for the empirical coefficient  $\beta$ . It is noteworthy that Mathis *et al.*’s predictive model, built on a 1D signal, inherently lacked the capability to identify splatting. In this context, the  $\beta$  factor serves to rectify the effects associated with splatting. Qualitative and quantitative results presented herein indicate that this model provides a modestly better representation of the “universal” field, relative to Mathis *et al.*’s model. The results of this investigation are summarised in Figure 4.14, which presents a

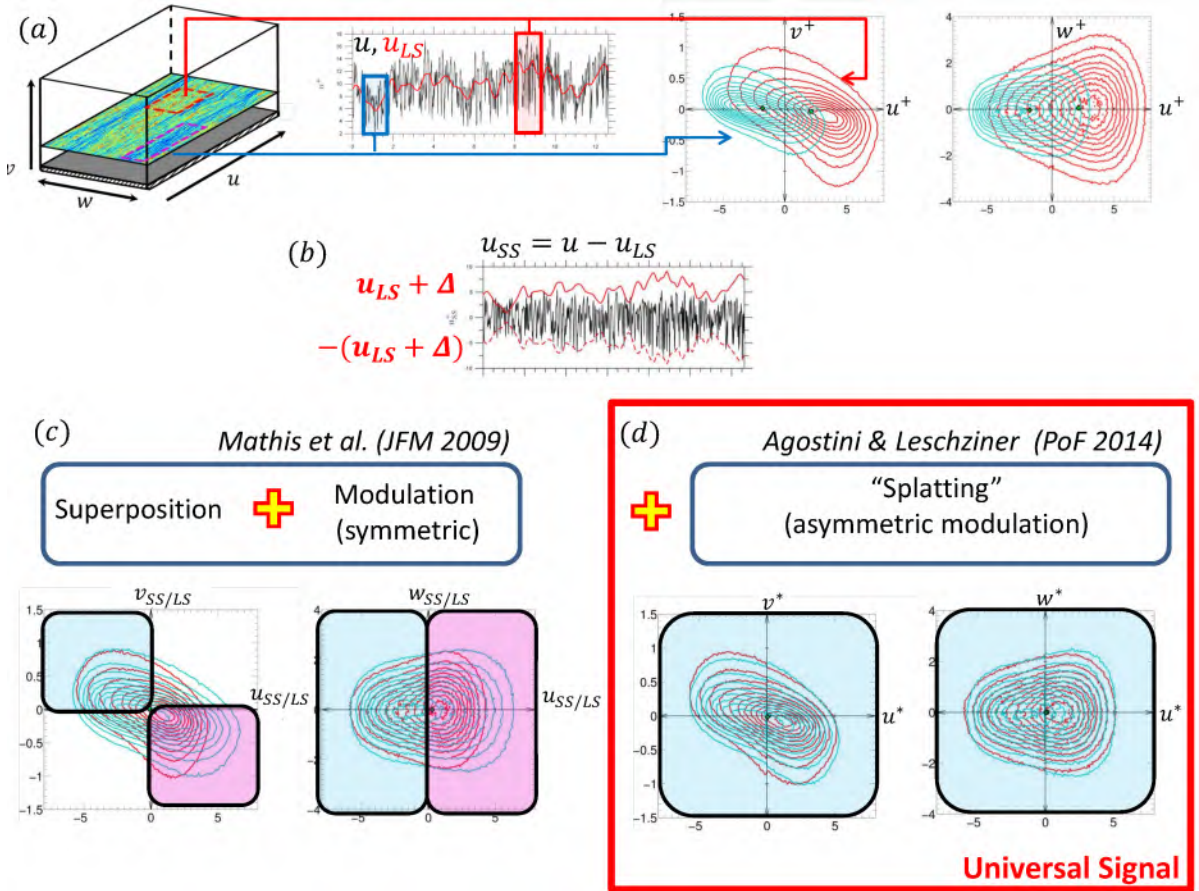


Figure 4.14: Conceptual schematic of the effects of large-scale fluctuations on streaks: Superposition, modulation and splatting

conceptual representation of the impact of large-scale motion on near-wall turbulence. The figure illustrates the results of statistics conditioned on extreme events, demonstrating the importance of considering the effects of splatting in addition to superposition and modulation in the construction of a universal signal. The study's results highlight the complex interactions between large-scale motion and near-wall turbulence, and suggest that traditional approaches employing only superposition and modulation may be inadequate for accurately predicting turbulent behaviour. Specifically, the findings indicate that the effects of splatting play a major role in modulating the intensity of near-wall turbulence.

## 4.6 Large-Scale Vortices vs Streak Modulation: Routes to Enhanced Drag

The quantification of the modulation has been the subject of several proposals. The classical approach, proposed by Mathis, Hutchins, and Marusic (2011), involves the evaluation the envelope of the small-scale signal,  $\text{Env}(u_{SS})$ , obtained by low-pass filtering  $u_{SS}^2$ , and determining its correlation with the large-scale signal through the correlation coefficient  $\overline{u_{LS}\text{Env}(u_{SS})}/\left(\sqrt{\overline{u_{LS}u_{LS}}}\sqrt{\overline{\text{Env}(u_{SS})^2}}\right)$ , with the envelope determined by means of the Hilbert transform. Among a number of interesting observations arising from the modulation correlation is that the correlation is positive below  $y^+ \approx 180$ , while it is negative beyond this distance. This sign reversal is observed to be only weakly dependent on the Reynolds number, as shown by Mathis, Hutchins, and Marusic (2009). There is, as yet, no consensus on the origin of this sign switch, alternative interpretations having been proposed by Jacobi and McKeon (2013) and Baars et al. (2015) and Zhang and Chernyshenko (2016). Agostini, Leschziner, and Gaitonde (2016) have shown that the envelope of positive small-scale fluctuation is significantly different from that of negative fluctuations, due to the skew-

ness of the PDF of the small-scale motions, related to the “splatting”/“anti-splatting” phenomena. Hence, in reality, there are two correlations coefficients. However, both feature a change in sign at  $y^+ \approx 100 - 200$ . It is arguable that the lack of insight into the details of the scale-interaction processes, in general, and the correlation behaviour, in particular, is due to insufficiently searching scrutiny of available DNS data – a gap the following analysis aims to fill.

The corner stone of the model eq. (4.1) is a “universal” small-scale signal, unaffected by large-scale motions (and thus Reynolds number), which is then modified (or corrected) by functional coefficients that vary with  $y^+$  and premultiply the Reynolds-number-dependent large-scale outer fluctuations in the log-law region. This relationship reflects the assumption that the modulation of the streamwise turbulence energy is symmetric with respect of the sign of the large-scale motions. Previous results show, however, that the assumption of symmetry is not correct, especially not in the presence of drag-reducing actuation, and that the physical interactions at play are more complicated than those represented by the prediction formula.

The correlation coefficient and the predictive equation eq.(4.1), while informative, does not provide tangible statements on the impact of modulation on the skin friction. To go beyond this rather limited framework, more extensive statistical analyses are required, exploiting full-volume fields. Such analyses have been already shown in previous chapter, in the context of skin-friction reduction by means of oscillatory spanwise wall motion. These studies have led, among others, to the quantification of the contribution of different scales to the skin friction and of the dependence of the variance of the small-scale skin friction fluctuations to the intensity and sign of the footprints, the latter shown to be exceptionally sensitive when the actuation causes the drag to reduce substantially through a drastic weakening of the near-wall streaks.

The present study represents a significant extension of the analysis performed in Chapter 3, focusing on the canonical channel flow. A wide range of statistical algorithms is applied to extensive data sets, with the primary objective of investigating the interaction between large and small scales, particularly the processes driving the modulation of the small scales by the large scales. This is accomplished through the derivation and manipulation of joint and conditional probability density functions (PDFs), from which the dependence of small-scale streamwise and shear stresses on large-scale fluctuations is extracted. Another major aspect of the study is the quantification of the contributions of different scales to the skin friction and the dependence of these contributions on the sign and magnitude of the large-scale wall-shear footprints.

In this section, a concerted effort is made to distinctly separate small-scale and large-scale motions, preventing any mixing of their content. Figure 4.15 presents the results of the BEMD method, displaying the pre-multiplied spanwise spectrum for the channel flow under investigation. Similar to the process employed for separating scales in the actuated flow, the spectrum is decomposed into three sub-ranges and reconstructed from six EMD modes:

- The *small-scale* (SS) sub-range, situated at the short-wavelength end, is composed of modes 1 and 2.
- The *large-scale* (LS) sub-range, positioned at the large-wavelength end, consists of modes 4, 5, and 6.
- The *intermediate-scale* (AE) sub-range is solely comprised of mode 3.

The original full spectrum can be reconstructed by summing the modal spectra and incorporating additional terms representing interactions between modes, as will be elucidated by the mode-specific normal and shear stress profiles. This multi-range decomposition ensures distinct small and large scale ranges without spectral overlap. It is acknowledged that the attribution of modes into “large scales” and “small scales” is somewhat subjective, similar to the conventional approach of imposing spectral Fourier filters to separate the scales. The present attribution is based on extensive experience by the author in applying the EMD to various flows, as reported and justified in Agostini and Leschziner (2014), Agostini and Leschziner (2017), and Agostini and Leschziner (2018). An inherent limitation of the present study is rooted from the relatively low Reynolds number of the investigated flow, which results in a somewhat ambiguous separation between large and small scales, as represented by the intermediate-scale sub-range. Despite this constraint, it is observed that the small-scale (SS) range is confined to spanwise wavelengths of approximately 200 wall units ( $\lambda_z^+ \approx 200$ ), while the large-scale (LS) subrange commences at spanwise wavelengths of around 800 wall units ( $\lambda_z^+ \approx 800$ ). Notably, the LS subrange encompasses the outer energetic maximum located at a wall-normal distance of roughly 200 wall units and a spanwise wavelength of approximately 1000 wall units ( $y^+ \approx 200$ ,  $\lambda_z^+ \approx 1000$ ). This outer energetic maximum is conventionally associated with the outer large scales that give rise to the characteristic plateau in the streamwise-energy profile.

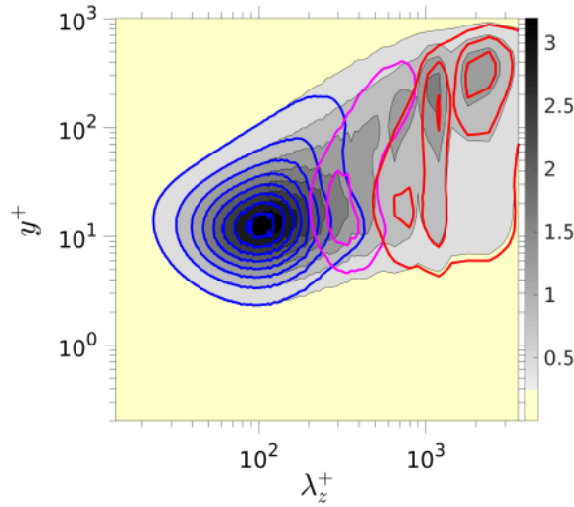


Figure 4.15: Premultiplied spanwise spectral maps for the streamwise turbulent fluctuations: grey contours represent the total field; blue, magenta and red iso-lines represent, respectively, sub-spectra for small-scale (SS), intermediate-scale (AE) and large-scale (LS) fluctuations.

## 4.7 Analysing Scale Contributions to Turbulent Stress

With the mode-decomposition effected, various statistical properties can be obtained to identify the contribution of modes to the turbulent stresses, the interactions between modes and the effect of different scales on the skin friction. These statistics were here derived from full-volume velocity fields at 150 time levels, separated by intervals of  $\Delta t u_\tau^2 / \nu = 50$ .

The approach taken here, is the same approach defined in Section 3.6, is to derive all statistical quantities of interest, at any wall-normal location,  $y^+$ , from two variants of joint PDFs of the form  $P(X_1, \dots, X_n, Y)$  and  $P(X_1, \dots, X_n, Y)/P(Y)$ , the latter referred to as *conditional PDF*.

In all statistics to follow,  $Y$  is  $Cf_{LS}$ , the PDF of which is shown in Figure 4.16. Its asymmetric shape indicates that positive large-scale velocity fluctuations, induced by large-scale motions, are fewer in number, but more intense than negative fluctuations, which are more numerous, but weaker in intensity. The coloured tails in the PDF define the regions of extreme 1.5% positive or negative events. Some statistics to follow focus specifically on these extreme tail regions, involving the integration of eq. (3.12) over the coloured tails only, in order to clarify the limiting states of  $Cf_{LS}$ -conditional correlations.

The map in Figure 4.17(a), derived from  $P(U^+, Cf_{LS})$  provides information, at any  $y^+$  location, about the rate of the contribution of  $\overline{u' u'}^+$  with  $Cf_{LS}$  to the total streamwise stress. Because the PDF is subject to the constraint expressed by eq. (3.8), it is not possible to gain a clear view of the variation of  $\overline{u' u'}^+$  at any condition  $Cf_{LS}$  relative to the mean level at this condition. This limitation can be circumvented by using the conditional PDF  $P(X_1, \dots, X_n, Y)/P(Y)$ . This then yields conditional mean values,  $\overline{X_i|Y}$ , and corresponding conditional variance values,  $\overline{x'_i x'_j|Y}$ , respectively, from equations (3.13) and (3.14).

For the same example considered above in Figures 4.17(a) and (b), the map of the conditional variation of the streamwise-velocity fluctuations,  $(\overline{u' u'}^+|Cf_{LS})$ , is shown in Figure 4.17(c). This brings to light the fact, obscured in Figure 4.17(a), that positive large-scale skin-friction fluctuations go hand-in-hand with an amplification of the streamwise stress in the buffer layer, associated predominantly with small-scale fluctuations, while at extreme negative skin-friction fluctuations, there is a weaker rise in the normal stress around  $y^+ \approx 300$ , indicative of the increasing prominence of outer large-scale motions. An enhanced view of the above features is given in Figure 4.17(d) by the blue and red profiles that represent, respectively, the average of the conditional streamwise stresses obtained by integrating eq. (3.14) over the blue and red 1.5% tails in Figure 4.16.

A major objective of this paper is to examine the contribution of different scales, and their interactions, to the skin friction. To this end, two previously established methods are exploited. Both are given below in two non-dimensional forms: one using outer scales and the other inner scales. The first is the the FIK relationship

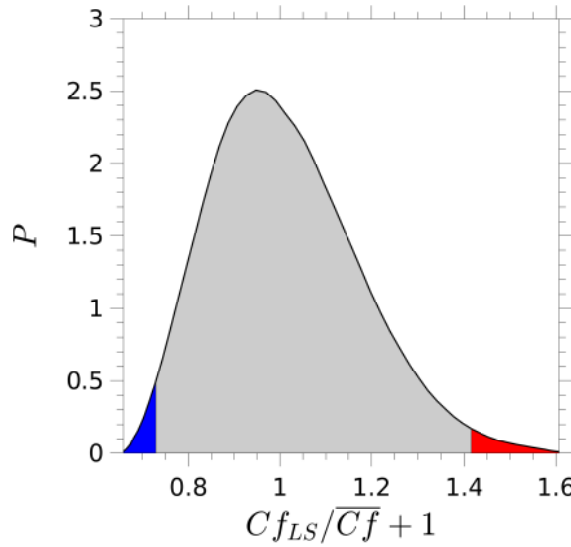


Figure 4.16: PDF of large-scale skin-friction fluctuations; the blue and red regions represent areas of 1.5% extreme negative and positive events, respectively.

(already used in section 3.4), derived upon integrating repeatedly the one-dimensional streamwise-momentum equation for fully-developed channel flow:

$$\begin{aligned} Cf &= \frac{6}{Re} + \int_0^1 6 \left(1 - \frac{y}{h}\right) \left(\frac{-\bar{u}'v'}{U_b^2}\right) d\left(\frac{y}{h}\right) \\ &= \frac{6}{Re} + \int_0^{Re_\tau} \underbrace{\frac{6Re_\tau}{Re^2} \left(1 - \frac{y^+}{Re_\tau}\right) \left(-\bar{u}'v'^+\right)}_{Cf_{FIK}^+} dy^+ \end{aligned} \quad (4.7)$$

in which the first term, containing the bulk Reynolds number, accounts for the laminar contribution.  $Re = \frac{U_b h}{\nu}$  is the bulk Reynolds number and  $h$  is the channel half-height.

An alternative relationship, proposed by Renard and Deck (2016) (referred to below by the acronym RD), arises from energy-conservation considerations, specifically the energy that is fed into the flow to cover the viscous dissipation and the turbulence-energy generation, represented by the two respective additive terms in,

$$\begin{aligned} Cf &= \int_0^\delta \left[ \frac{2\nu}{U_\infty^3} \left( \frac{\partial \bar{U}}{\partial y} \right)^2 + \frac{-2\bar{u}'v'}{U_\infty^3} \frac{\partial \bar{U}}{\partial y} \right] dy \\ &= \int_0^{Re_\tau} \left[ \underbrace{Cf \sqrt{\frac{Cf}{2}} \left( \frac{\partial \bar{U}^+}{\partial y^+} \right)^2}_{Cf_a^+} + \underbrace{Cf \sqrt{\frac{Cf}{2}} \left( -\bar{u}'v'^+ \frac{\partial \bar{U}^+}{\partial y^+} \right)}_{Cf_b^+} \right] dy^+ \end{aligned} \quad (4.8)$$

The integrand groups designated  $Cf_{FIK}^+$  in equation (4.7) and  $Cf_a^+$  and  $Cf_b^+$  in equation (4.8) will be used in the analysis performed in sections 4.10.1 and 4.10.2, respectively.

The two alternative expressions for the skin friction, equations 4.7 and 4.8, do not merely arise from physically different principles, but more importantly from the perspective of the present work, they allow different phenomena and interactions to be illuminated, as will emerge in Sections 4.10.1 and 4.10.2.

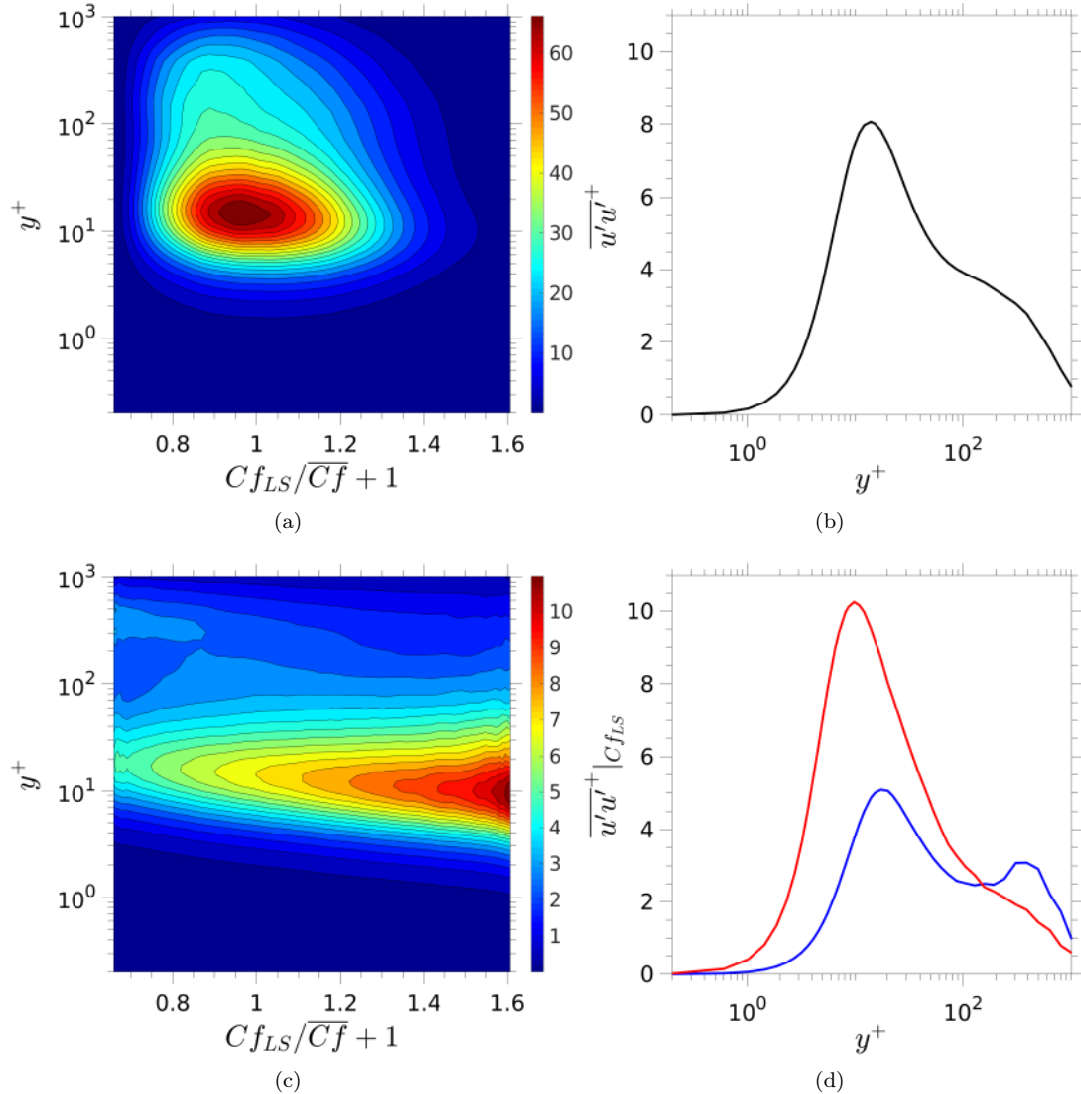


Figure 4.17: Properties of streamwise stress  $\bar{u}'\bar{u}'^+$  and  $\bar{u}'\bar{u}'^+|_{Cf_{LS}}$ : (a) map of stress derivative  $d\bar{u}'\bar{u}'^+/dCf_{LS}$  across  $(Cf_{LS}, y^+)$  plane (eq. (3.12)); (b) wall-normal profile of the stress arising from integration of the field in map (a) with respect to  $Cf_{LS}$ . (c) map of stress derivative  $\bar{u}'\bar{u}'^+|_{Cf_{LS}}$  across  $(Cf_{LS}, y^+)$  plane (eq. (3.14)); (d) wall-normal profiles of the conditional conditional streamwise stresses obtained by integrating eq. (3.14) over the blue and red 1.5% tails in Figure 4.16.

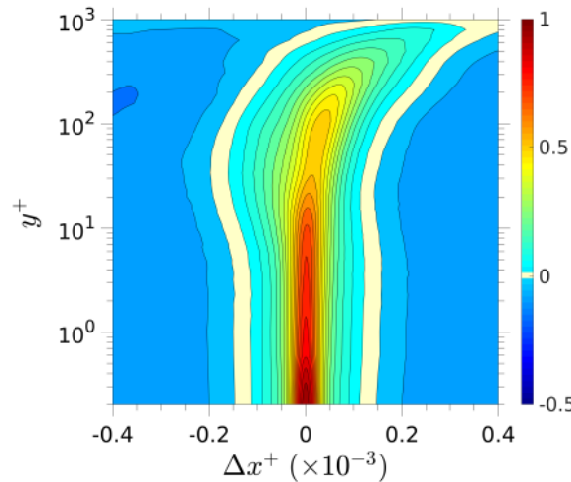


Figure 4.18: Map of two-point correlation between  $Cf_{LS}$  and  $u_{LS}(y^+)$  in the  $(y^+, \Delta x)$  plane, with  $y = 0$  the reference point.

## 4.8 Characteristics of Large-Scale Motions

Characteristics of the large-scale field are conveyed here in two ways. First, the level of wall-normal correlation is illustrated in Figure 4.18. This provides a map of the two-point correlation between  $Cf_{LS}$  and  $u_{LS}(y^+)$ , with the two-points separated by  $y^+$  and the streamwise increment  $\Delta x$ , where  $Cf_{LS}$  is defined from the streamwise velocity fluctuation at  $y^+ \approx 0.2$ . The inclusion of  $\Delta x$  allows the lag in the correlation to be clarified, especially of the locus of maximum correlation.

The plot shows, in agreement with previous observations, that the large-scale motions are highly correlated across the entire near-wall layer, with the streamwise lag in the maximum correlation level increasing with  $y^+$ . The lag at  $y^+ \approx 200$  is approximately 750 wall units, and this translates to an average angle across this layer of approximately  $15^\circ$ .

The set of plots in Figure 4.19 provides an alternative view of the wall-normal correlation of the large-scale motions. It shows, in Figure 4.19(a) the wall-normal variation of the *increment* between the mean velocity sampled conditionally on  $Cf_{LS}$  and its average across  $Cf_{LS}$  at the relevant  $y^+$  location – i.e.  $\overline{U'}^+|_{Cf_{LS}} = \overline{U^+}|_{Cf_{LS}} - \overline{U^+}$ . This increment can be determined from the  $(U^+, Cf_{LS})$  PDF using eq. (3.13) at each wall-normal location, namely:

The map of  $\overline{U'}^+|_{Cf_{LS}}(y^+)$ , shown in Figure 4.19(a), demonstrates that negative/positive large-scale skin-friction fluctuations – generally referred to a “footprints” – are strongly correlated with negative/positive large-scale velocity fluctuations, respectively, across a large section of the wall layer. As  $\overline{U'}^+|_{Cf_{LS}}$  tends to zero very close to the wall, the contour level declines rapidly below  $y^+ < 5$ . Figure 4.19(b) accentuates the wall-normal correlation by showing conditional mean-velocity profiles (blue and red lines) sampled across the extreme  $\pm 1.5\%$  tails in Figure 4.16, relative to the profile at  $Cf_{LS} = 0$  (magenta line), which is close to the  $Cf_{LS}$ -averaged overall mean velocity. A distinctive feature of the profiles, which will be the subject of the discussion of the modulation to follow below, is that the *increment* in the gradient of the conditional velocity profiles, relative to the overall mean, switches sign either from negative in the buffer layer to positive in the outer region, or vice-versa, beyond  $y^+ \approx 150$ . The importance of this switch relates to a corresponding switch in shear-induced generation of fluctuations, as will become clear below.

Figure 4.20, provides a view of the direct contribution of the outer large scales to the streamwise-normal and the shear stresses. The maps in Figures 4.20(a) and (b) were obtained from the joint PDF  $P(U_{LS}, V_{LS}, Cf_{LS})$ . Figures 4.20(c) and 4.20(d) show the scale-wise contributions (SS, LS and AE) to the streamwise stress and shear stress, respectively. Importantly, the plots includes not only the primary (diagonal) components ([SS,SS]; [LS,LS]; [AE,AE]) but also the mixed-scale contributions that may be interpreted as signifying the modulation by any one larger- scale signal of a smaller-scale signal – e.g.  $\overline{u_{LS}v_{AE}}$  may be interpreted as the large-scale motion modulating the intermediate-scale motion. The large-scale contributions in Figures 4.20(c) and 4.20(d) are given by the blue lines, and these have been obtained by integrating the maps 4.20(a) and (b), respectively, across  $Cf_{LS}$ .

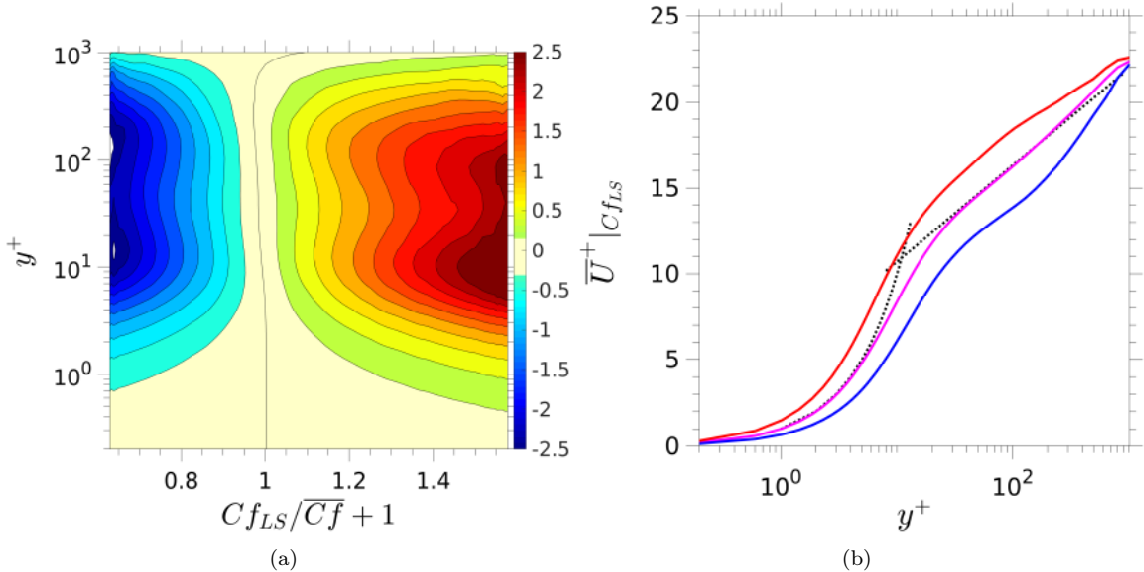


Figure 4.19: Conditional mean-velocity: (a) map of the conditional increment in the mean velocities ( $\bar{U}'^+|_{C f_{LS}} = \bar{U}^+|_{C f_{LS}} - \bar{U}^+$ ); (b) profiles of conditional mean velocity of  $\bar{U}^+|_{C f_{LS}}$  determined over the extreme  $\pm 1.5\%$  events of the tails of the PDF in Figure 4.16 and around the condition  $C f_{LS} = 0$  events, conveyed by the red, blue and magenta lines, respectively.

The contribution of the large-scale motions to the streamwise stress is fairly uniform within the range  $y^+ \approx 10 - 500$ , but features a weak maximum around  $y^+ \approx 300$ , i.e. markedly higher than the value  $3.9\sqrt{Re_\tau}$  ( $\approx 125$ , for  $Re_\tau \approx 1000$ ) proposed by Marusic, Mathis, and Hutchins (2010a) as the location at which the large-scale structures primarily reside. The origin of this discrepancy is not obvious. It is noted that the present Reynolds number is significantly lower than the values of the flows upon which the empirical correlation is based. Thus, the intensity of the outer motions is lower here, and the outer maximum in  $\bar{u}_{LS}u_{LS}^+$  is clearly quite tenuous. However, the corresponding maximum in  $-\bar{u}_{LS}\bar{v}_{LS}^+$  is more prominent, and this supports the observation that the  $y^+$  value that best defines the position of the large-scale structures is significantly higher than  $3.9\sqrt{Re_\tau}$ , at least at the present Reynolds number. The uniformity in the level of  $\bar{u}_{LS}u_{LS}^+$  is consistent with the footprinting concept, reflected by the relatively high level of energy density across the layer  $y^+ \approx 10 - 500$  in the high-wave-length range of the spectral map in Figure 4.15. As seen from the map in Figure 4.20(a), the large-scale streamwise stress arises from contributions originating primarily from negative large-scale-velocity events – around  $C f_{LS} / \bar{C f} + 1 = 0.85$ , in particular, close to the maximum of the skewed  $C f_{LS}$  PDF shown in Figure 4.16. In the outer part,  $y^+ > 100$ , the increase towards the maximum at  $y^+ \approx 300$ , coincide with the peak in large-scale shear stress, Figure 4.20(b), also around  $C f_{LS} = 0.85$ , and this is clearly the origin of the maximum in the large-scale (blue) shear-stress profile in Figure 4.20(d). This peak, coupled with the exceptionally high mean-velocity gradient – the blue profile in Figure 4.19(b) – suggests that the outer peak values in both stresses are due to elevation shear-induced production. Although the large-scale shear stress is low in the buffer region, it appears that it is high enough, especially in the bulges visible around  $y^+ \approx 10 - 20$  at  $C f_{LS} / \bar{C f} \approx -0.2$  and  $0.3$ , to combine with the very high shear strain in the buffer layer to induce, by production, the elevated normal stress around  $y^+ \approx 20$ . The peak large-scale stresses are of the order of 20-30% of the respective total maxima – although, as might be expected, the local proportion is considerably larger in the outer region, around  $y^+ \approx 300 - 500$ .

The effect of the shear stress on the skin friction can be quantified by means of the FIK and RD relationships, eqs. (4.7) and (4.8), respectively, and this will be shown below in the context of a discussion of other contributions to the skin friction. Suffice it to say here that the FIK relationship yields a large-scale contribution to the total skin friction of 24%, which may be claimed to be remarkably high, considering the low value of the Reynolds number of the flow being examined.

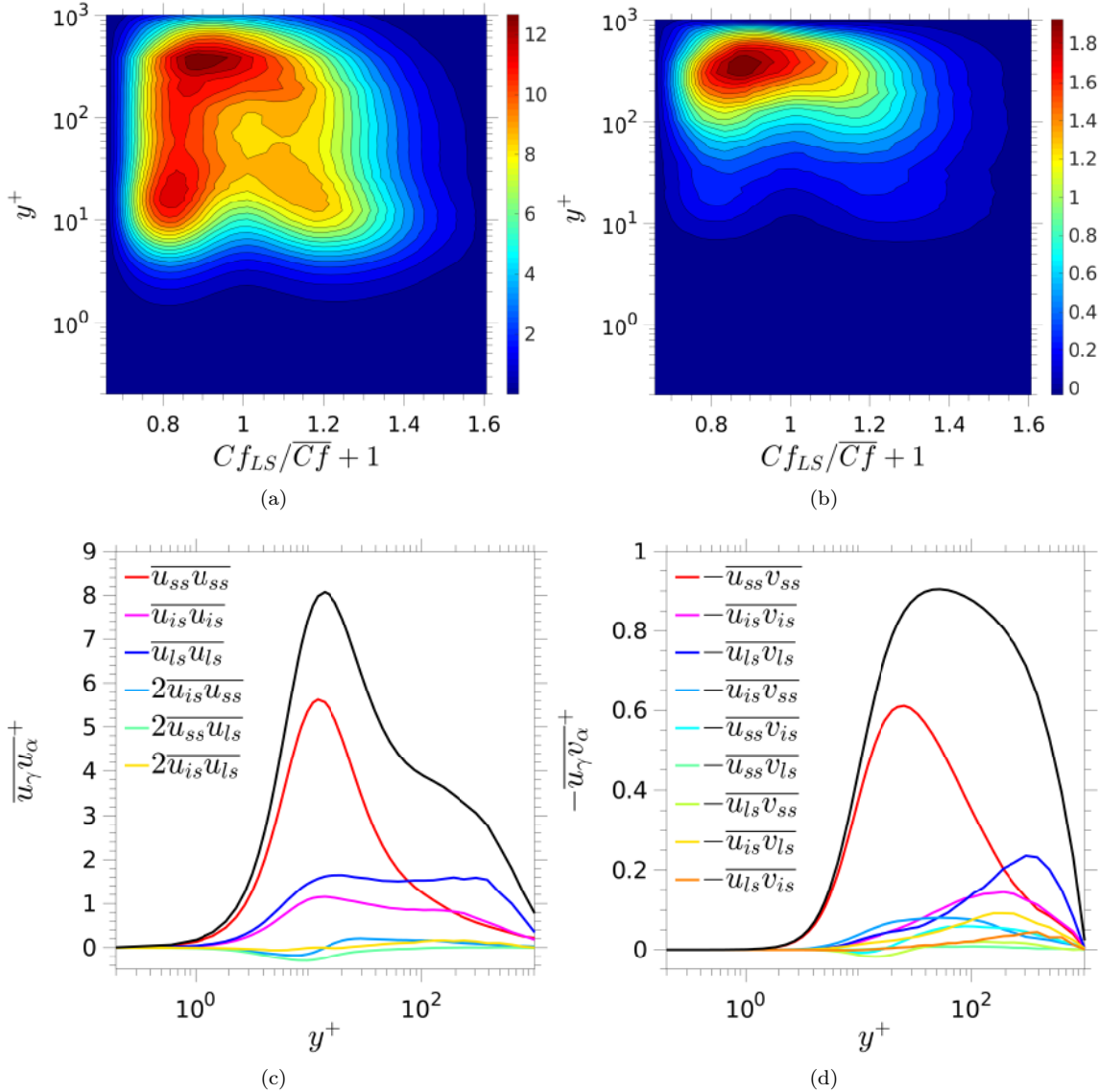


Figure 4.20: Contribution of large-scale turbulent stresses to the respective total levels: (a) map of  $Cf_{LS}$ -wise gradient of large-scale streamwise stress,  $\frac{du_{LS}u_{LS}}{dCf_{LS}}^+$ ; (b) map of  $Cf_{LS}$ -wise gradient of large-scale shear stress— $\frac{du_{LS}v_{LS}}{dCf_{LS}}^+$ ; (c) wall-normal profiles of scale-wise contributions to streamwise stress; (d) wall-normal profiles of scale-wise contributions to shear stress.

## 4.9 Impact of Large Scales on Small Scales

It is well established that the correlation between the intensity of small-scale motion and large-scale motions is positive close to the wall, but changes sign at some position beyond the buffer layer (Mathis, Hutchins, and Marusic 2011; Guala, Metzger, and McKeon 2011; Ganapathisubramani et al. 2012; Jacobi and McKeon 2013; Talluru et al. 2014; Duvvuri and McKeon 2015; Agostini, Leschziner, and Gaitonde 2016; Choi, Xu, and Sung 2002; Zhang and Chernyshenko 2016; Hwang and Sung 2017, among others). Various physical arguments have been advanced in efforts to explain this reversal, one is based on the concept that a traverse across the flow, on any wall-normal line along which the correlation is evaluated, crosses large-scale structures that are inclined roughly at 13–18° relative to the wall. Another explanation is based on the concept that large-scale convective motions, associated with sweeps and ejections, shift the profile of small-scale streamwise stress, which features a maximum in the buffer layer, normal to the wall. Thus, depending upon whether a location is above or below the maximum, the effect of either sweeps or ejections on the incremental change in the streamwise energy at that location will be of opposite sign. However, this explanation can only apply to a reversal at a location around the buffer layer, while the reversal occurs at  $y^+ > 100$ . Here, a different interpretation is advanced, based on an examination of the production of small-scale fluctuations.

The first issue examined below is the correlation between the small-scale and large-scale fluctuations,  $u_{SS}$  and  $u_{LS}$ , respectively. This can be deduced from the set of plots in Figure 4.21. The map of the conditional small-scale energy  $\overline{u_{SS}u_{SS}}^+|_{Cf_{LS}}$  is plotted in Figure 4.21(a). As expected, the contours bring to light the fact that  $\overline{u_{SS}u_{SS}}^+$  reaches a maximum in vicinity of  $y^+ \approx 12$ , and that its magnitude strengthens as  $Cf_{LS}$  and the velocity gradient increase near the wall. Conversely,  $\overline{u_{SS}u_{SS}}^-$  declines towards a minimum as  $Cf_{LS}$  and the near-wall velocity gradient reduce. The level of energy amplification and attenuation – conventionally understood to be the “modulation” – is accentuated in Figure 4.21(b), which shows three profiles of  $\overline{u_{SS}u_{SS}}^+$  for the extreme ±1.5% of  $Cf_{LS}$  (red and blue profiles, respectively), relative to the profile around  $Cf_{LS} = 0$  (magenta line).

The sensitivity of the small-scale fluctuations to the footprints, shown in Figure 4.21, also translates to a corresponding sensitivity of the small-scale skin-friction fluctuations. This is shown in Figure 4.22 in the form of the standard deviation of the conditional small-scale skin-friction fluctuations as a function of  $Cf_{LS}$ . Unsurprisingly, the intensity of the small-scale fluctuations varies substantially, with positive footprints causing a strong increase, while negative footprints result in a more modest decline, but this asymmetry is due to the fact that negative  $Cf_{LS}$  footprints are weaker than positive ones. The close to linear variation, consistent with the map in Figure 4.21(a), implies that the small-scale turbulence responds rapidly to changes in the large-scale fluctuation. The relationship between  $u_{SS}$  and  $Cf_{LS}$  in the outer region is difficult to recognise from the map of  $\overline{u_{SS}u_{SS}}^+|_{Cf_{LS}}$ , because the magnitude of the velocity fluctuations produced within the streaky buffer layer is at least ten times higher than the fluctuations associated with small-scales structures in the outer flow. This is readily recognised from the red profile for  $\overline{u_{SS}u_{SS}}^+$  in Figure 4.20(c). In order to overcome this limitation, attention is focused in Figures 4.21(c) and 4.21(d) on the increment ( $\overline{u_{SS}u_{SS}}^+|_{Cf_{LS}} - \overline{u_{SS}u_{SS}}^+|_{Cf_{LS}=0}$ ) and its normalised value ( $\overline{u_{SS}u_{SS}}^+|_{Cf_{LS}} - \overline{u_{SS}u_{SS}}^+|_{Cf_{LS}=0}) / (\overline{u_{SS}u_{SS}}^+|_{Cf_{LS}=0})$ , respectively. The former conveys the fact the negative and positive  $Cf_{LS}$  fluctuations go hand-in-hand with, respectively, an attenuation and amplification of small-scale motions around the buffer layer – i.e., the correlation is positive. However, the map in Figure 4.21(d) shows a reversal in correlation at approximately  $y^+ \approx 150$ , confirming earlier observations in studies noted at the beginning of this section.

An explanation for the above reversal in correlation, alternative to previous proposals, is suggested by the results in Figure 4.23. This shows, first, in Figure 4.23(a), the wall-normal gradient  $d\overline{U'}^+|_{Cf_{LS}}/dy^+$  of the fields in Figure 4.19(a) – i.e. the gradient of the incremental velocity, conditional on the large-scale skin-friction value. Purely for reasons of greater clarity, attention is restricted in this map to the range  $y^+ \approx 80 - 1000$ . There is, self-evidently, a close similarity between this map and the map in figure 4.21(d). Corresponding to the variations in the gradient in Figure 4.23(a) are variations in the production rate of the streamwise energy. Three different, conditional, forms of the production are shown in Figures 4.23, 4.23(c) and 4.23(d). The first is of the total production; the second is the production induced by the small-scale motion; and the third is the production associated with the large-scale motions. All three are pre-multiplied by  $y^+$ , so as to compensate for the optical distortion, due to compression, that is caused by the logarithmic scale of  $y^+$ .

In the map of the production rate, Figure 4.23, there are two regions within which maxima in the production are observed: one is close to the wall, driven by the increasing near-wall shear strain that accompanies the

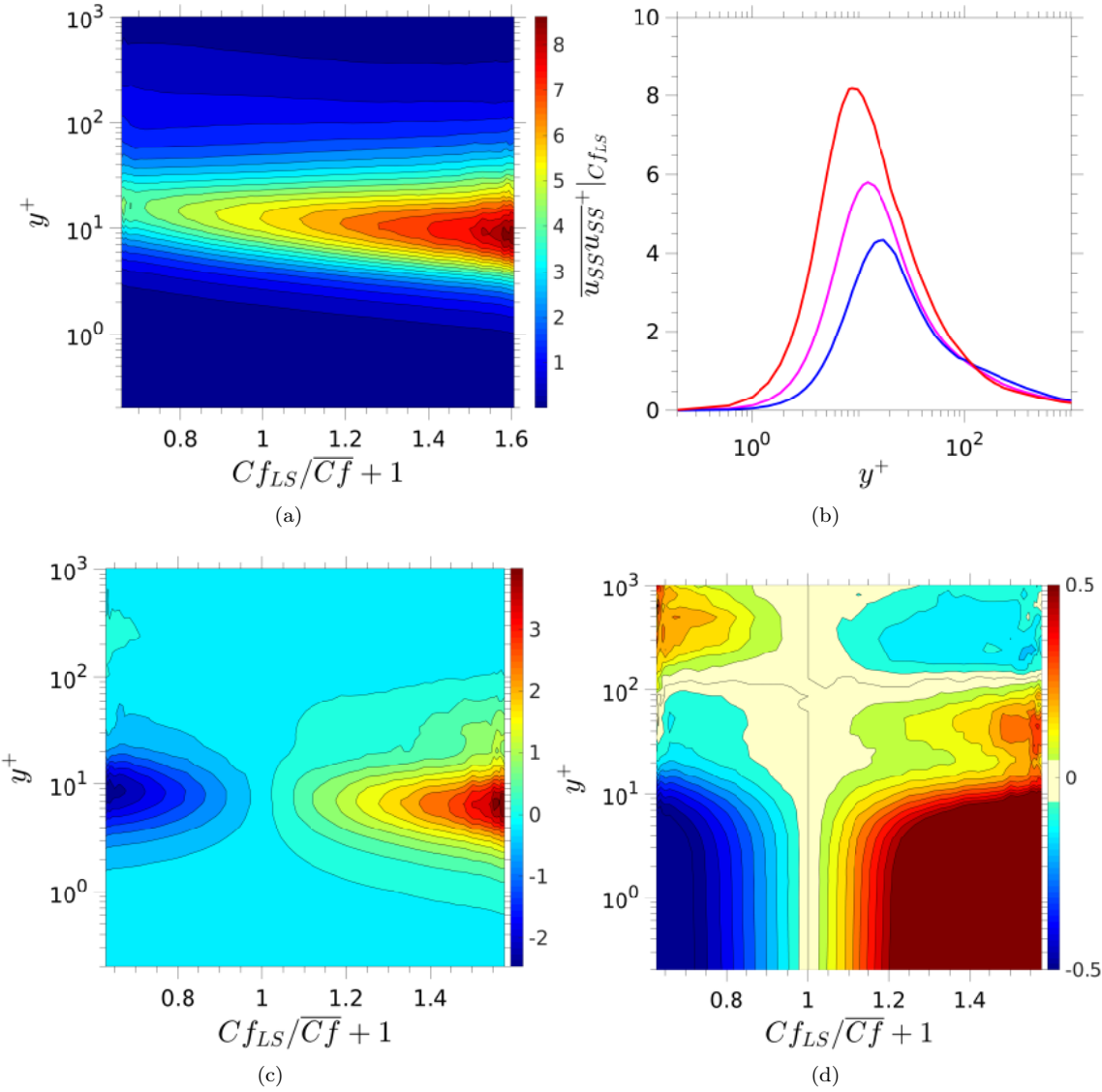


Figure 4.21: Correlation of small-scale and large-scale motions: (a) map of conditional streamwise small-scale stress  $\overline{u_{SS}u_{SS}^+}|_{Cf_{LS}}$ ; (b) profiles of conditional streamwise small-scale stress  $\overline{u_{SS}u_{SS}^+}|_{Cf_{LS}}$  averaged over the 1.5% lowest, highest and weakest  $Cf_{LS}$  events, conveyed by the blue, red and magenta lines, respectively; (c) map of increment of conditional streamwise small-scale stress  $\overline{u_{SS}u_{SS}^+}|_{Cf_{LS}} - \overline{u_{SS}u_{SS}^+}|_{Cf_{LS}=0}$ ; (d) map of normalised increment of conditional streamwise small-scale stress  $(\overline{u_{SS}u_{SS}^+}|_{Cf_{LS}} - \overline{u_{SS}u_{SS}^+}|_{Cf_{LS}=0}) / (\overline{u_{SS}u_{SS}^+}|_{Cf_{LS}=0}) - 1$ .

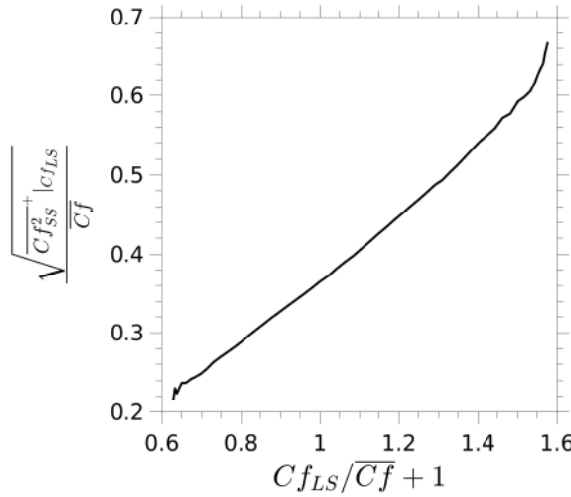


Figure 4.22: Standard deviation of small-scale skin-friction fluctuations conditional on large-scale skin-friction fluctuations.

increased  $Cf_{LS}$  level, and a second outer maximum, induced by the elevated strain in the negative range of  $Cf_{LS}$ . This connection is thus consistent with the observation that the level of small-scale energy in the inner region is positively correlated with large-scale fluctuations, while the outer small-scale energy is negatively correlated with the outer large-scale fluctuations. Although the map in Figure 4.23 shows the production of the total streamwise stress, involving the total shear stress, it is pointed out that this total is dominated, near the wall, by the small-scale component, while in the outer region, the total combines similar levels of small-scale and large-scale components. This argument is given weight by the maps in Figures 4.23(c) and 4.23(d), showing the production rates by the small-scale and large-scale shear stresses, respectively. The former highlights the fact that the production rate of the small-scale streamwise stress is concentrated in the buffer layer, and driven by positive large-scale fluctuations, while the large-scale production predominates in the outer part of the flow and is driven by negative large-scale motions. These causal connections are also consistent with the previous discussion on the implications of the results shown in Figure 4.21.

As observed earlier in Figure 4.20(d), the large-scale shear-stress contribution reaches its maximum at  $y^+ \approx 300$ . This contribution arises primarily in association with negative skin-friction fluctuations, which are positively correlated with large-scale velocity fluctuations throughout the log layer. As the turbulent shear stress is the principal driver of the skin friction, especially when its level is high in the outer layer, it is instructive to examine the conditions at  $y^+ \approx 300$  in greater detail. This is done in Figure 4.24, which compares, by way of joint PDFs  $P(u^+, v^+, Cf_{LS})$  (top row),  $P(u_{LS}^+, v_{LS}^+, Cf_{LS})$  (middle row) and  $P(u_{SS}^+, v_{SS}^+, Cf_{LS})$  (bottom row) the variations of the total, large-scale and small-scale velocity fluctuations at  $y^+ \approx 300$  as functions of the large-scale skin-friction fluctuations  $Cf_{LS}$ . In addition, the right-most plots included in the three rows are joint PDFs  $P(u^+, v^+)$ ,  $P(u_{LS}^+, v_{LS}^+)$  and  $P(u_{SS}^+, v_{SS}^+)$ , respectively, derived from  $P(u^+, v^+, Cf_{LS})$  and analogous PDFs for the large-scale and small-scale fluctuations. The red and blue PDF contours are conditional on events within, respectively, the extreme positive and negative 5% tails of the  $Cf_{LS}$  PDF (Figure 4.16), thus characterising the state of the stress field at the extreme positive and negative footprints.

The PDFs in the top and middle rows, Figures 4.24(a), (b), (d), (e), contain magenta lines, which identify the average values of the respective fluctuations across the  $Cf_{LS}$  range – e.g.,  $\bar{U}'^+|_{Cf_{LS}}$  and  $\bar{V}'^+|_{Cf_{LS}}$  in Figures 4.24(a) and (b). The shape of these PDFs in the upper two rows, accentuated by the magenta loci, allows the observation that negative  $Cf_{LS}$  values are associated preferentially with negative  $\bar{U}'^+|_{Cf_{LS}}$  and positive  $\bar{V}'^+|_{Cf_{LS}}$  values, i.e. ejections, while positive  $Cf_{LS}$  values are accompanied preferentially by sweeping motions. This conclusion is further supported by the joint PDFs for the velocity fluctuations in Figures 4.24(c) and (f). The red PDFs are clearly associated with large-scale sweeps, while the blue ones are associated with ejections. For large positive  $Cf_{LS}$  values, and hence also large positive  $u_{LS}^+$  levels in the outer region, the intensity of fluctuations is relatively low, while the reverse is observed for large negative  $Cf_{LS}$  values. This is in accord with the large-scale shear-stress map in Figures 4.20(b) and also with the associated

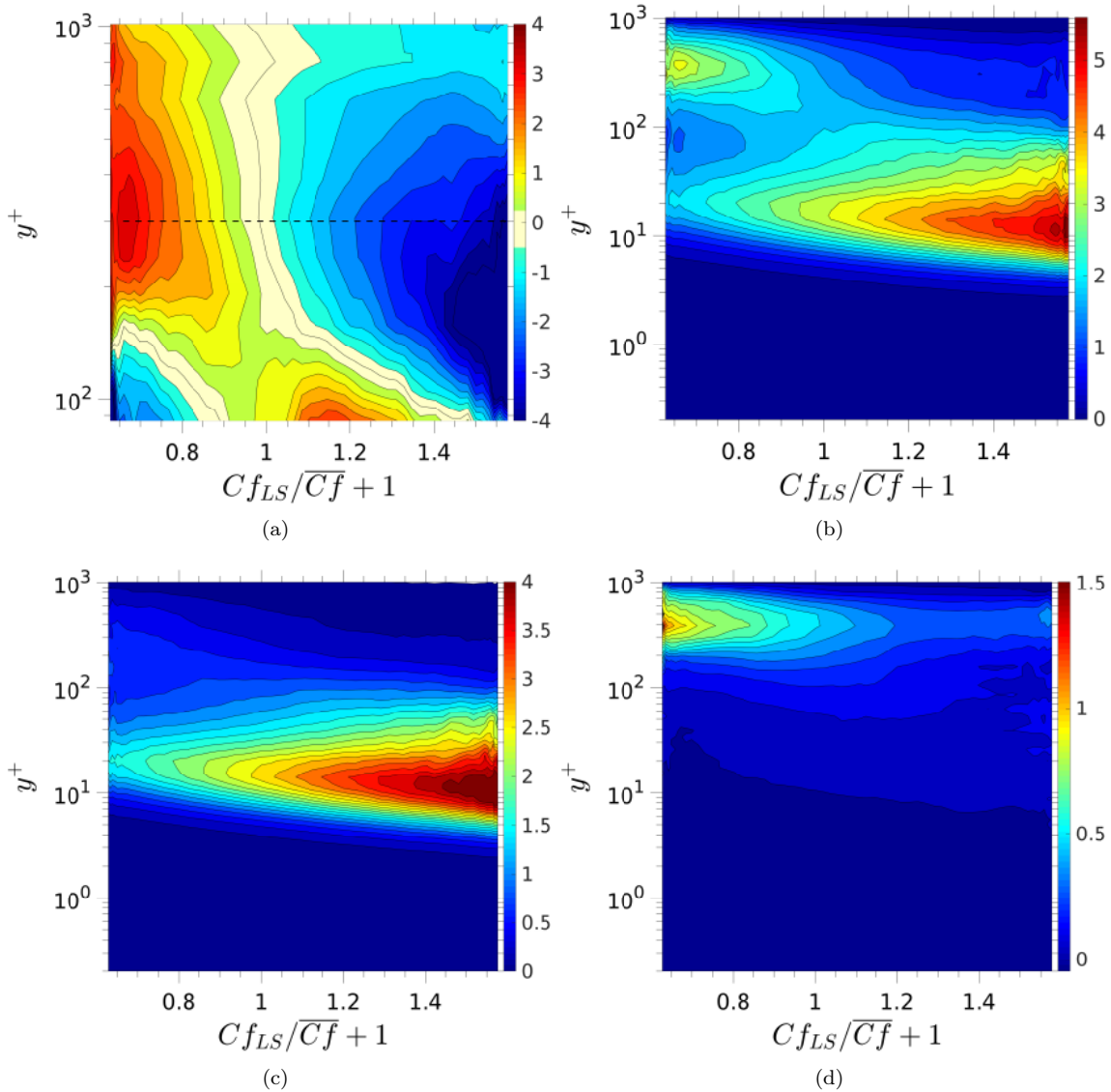


Figure 4.23: Alternative forms of the conditional production rates of the streamwise stress: (a) wall-normal gradient of the incremental large-scale velocity profile, conditional on  $Cf_{LS}$ ,  $\frac{d(\bar{U}'^+|_{Cf_{LS}} - \bar{U}'^+|_{Cf_{LS}=0})}{dy^+}$ , (b) Production driven by the total shear stress,  $y^+ \times -\bar{u}'v'^+ \frac{d\bar{U}^+}{dy^+}|_{Cf_{LS}}$ , (c) Production driven by the small-scale shear stress,  $y^+ \times -\bar{u}_{SS}v_{SS} + \frac{d\bar{U}^+}{dy^+}|_{Cf_{LS}}$  and (d) Production driven by the large-scale shear stress,  $y^+ \times -\bar{u}_{LS}v_{LS} + \frac{d\bar{U}^+}{dy^+}|_{Cf_{LS}}$

production-rate map in Figure 4.23(d). The implications of the PDFs is that there exist large-scale vortical motions in the cross-flow, associated with the ejections and sweeps, and this is entirely consistent with the behaviour of large-scale velocity field shown in Figure 4.19. The fact that the above features are broadly common to both the total and large-scale fluctuations is not surprising, as the large-scale motions exert a dominant influence on the total field at the wall-normal location considered ( $y^+ \approx 300$ ). An exception to this commonality of features relates to the marked differences in the shape of the joint velocity PDFs in Figures 4.24(c) and (f). The far more elongated shape in the latter PDFs signifies that the structures captured by these PDFs are elongated and thus characterised by a relatively low ratio  $\overline{v_{LS}^{+2}}/\overline{u_{LS}^{+2}}$ . Indeed, the ratio of the largest to the smallest eigenvalues of the large-scale-stress matrix was found to be around 10. Consistently, an examination of the Reynolds-stress field within the stress-invariant map (not included here) revealed a distinct trend towards one-component turbulence at the location considered.

PDFs for the small-scale velocity fluctuations, corresponding to those discussed above for the large-scale fluctuations and obtained from  $P(u_{SS}^+, v_{SS}^+, Cf_{LS})$ , are shown in Figures 4.24(g), (h) and (i). The plots reveal that negative large-scale fluctuations are associated with a modest increase in the level of small-scale intensity, implying a negative correlation between large-scale and small-scale fluctuations. This increase is consistent with the maps in Figures 4.21(c) and 4.23(c), the former showing a weak maximum and the latter featuring a weak ridge of elevated production of small-scale intensity around  $y^+ \approx 300$  for negative  $Cf_{LS}$  values. It is also consistent with the conditional profiles of small-scale streamwise stress shown in Figure 4.21(c), which indicates a reversal in the sign, at  $y^+ \approx 150$ , of the difference between the streamwise stress levels conditional on the extreme 1.5% positive and negative  $Cf_{LS}$  tails, respectively.

## 4.10 Scale Contributions to Skin Friction: Insights from FIK and RD Analyses

The present section discusses physical interactions which contribute to the skin friction. This subject is pursued by reference to equations 4.7 and 4.8, both of which link distributions of statistical properties across the boundary layer to the skin friction, the former derived from the  $y$ -wise integrated one-dimensional momentum equation, while the latter arises from the energy principle. The present EMD scale-decomposition method allows, in both cases, the contribution of different scales to the skin friction, as well as the contribution of terms conditional on  $Cf_{LS}$ , to be examined. This is the approach taken below in separate sub-sections relating, respectively, to the FIK and RD identities.

### 4.10.1 Analysis of the FIK Relationship

Attention is directed first to the FIK identity eq.4.7. In order to identify scale-specific contributions to  $Cf$ , the respective shear-stress fragments ( $\overline{u_\gamma v_\alpha}^+$ ) are injected into eq. (4.7). The wall-normal distributions of the constituent integrands in the FIK associated with the various fragments are shown in Figure 4.25(a) and 4.25(b). The only difference between the two figures is that the latter is pre-multiplied by  $y^+$ . While this scaling shifts the maxima towards larger  $y^+$  values, the advantage is that the areas under the respective curves represent faithfully the contribution of the fragments to the integrand  $Cf_{FIK}^+$ . The respective contributions to the total  $Cf$  thus arises from integrating these distributions over  $y^+$ , and the result is shown by the pie-chart given in Figure 4.25(c), the grey segment representing the laminar contribution. The most dominant terms, at 28% and 24%, are associated with small-scales and large-scales motions, respectively. The processes thus responsible for the major part of  $Cf$  are small-scale fluctuations, mainly in the buffer layer, and the large-scale structures, in the outer flow. The sum of the cross-terms contributes almost 30% to the total. Of these, the cross-terms  $\overline{u_{SS} v_{LS}}^+$  and  $\overline{u_{LS} v_{SS}}^+$  make a weak contribution at around 3%. The implication is that the explicit modulation of the small-scale motions by the large-scale fluctuations does not have a significant impact on the skin friction. In contrast, as shown in Figure 4.21, the magnitude of the small-scale fluctuations varies significantly with  $Cf_{LS}$ , the implication being that the contribution of the modulation is embedded in the characteristics of the small-scale fluctuations. In fact, it is arguable, in light of the discussion in Section 4.9, that the use of the term *modulation* is questionable, at least when interpreted as a direct wave-like interference between the large-scale and small-scale motions. In reality, the evidence presented in Section 4.9 suggests that the large-scale structures modify “locally” the velocity gradient and  $u_\tau$ , thus driving the variations of small-scale fluctuations by changes to the shear-induced production of the shear stress and turbulence energy. The adverb “locally” is intended to imply that the timescale associated

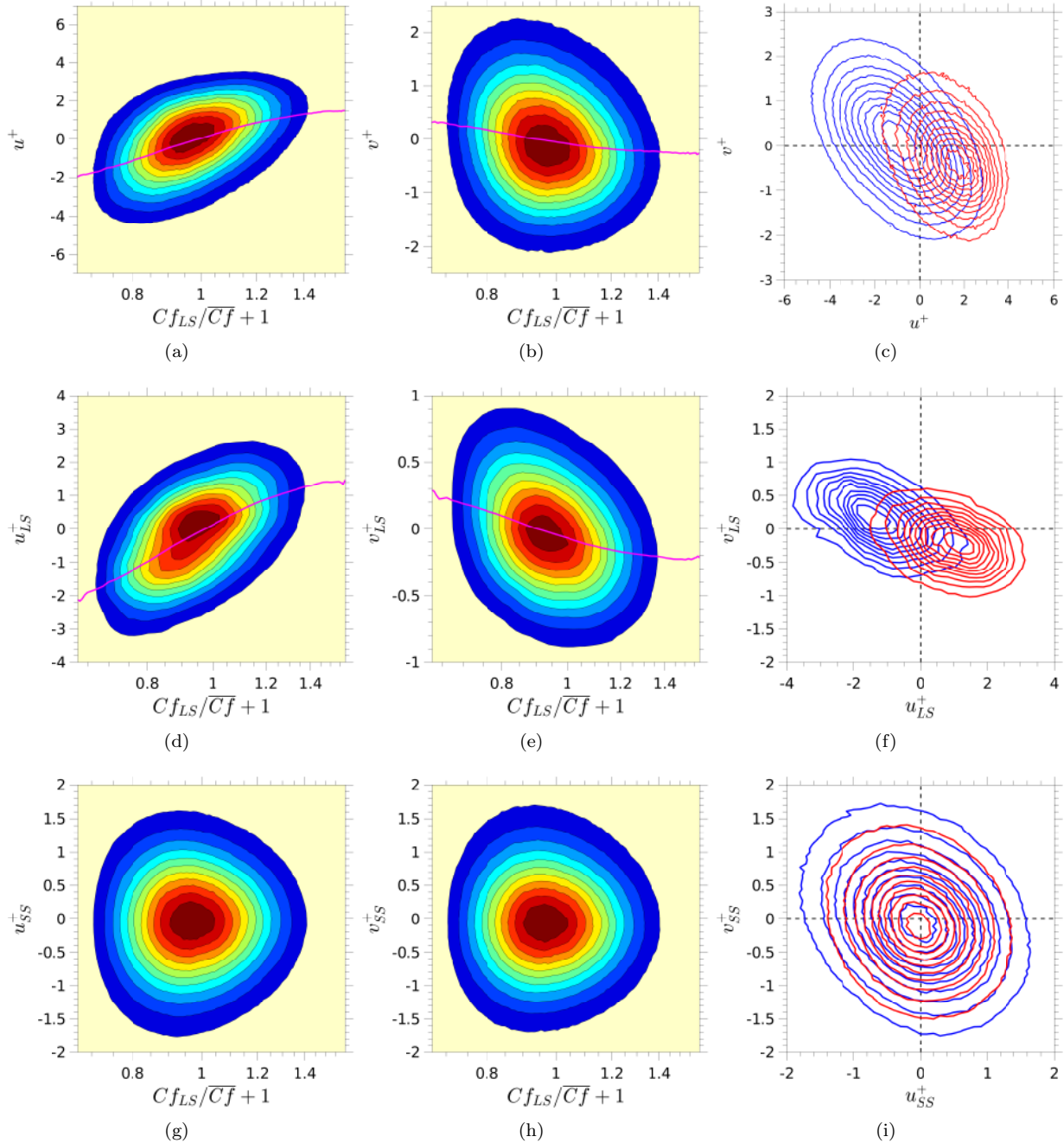


Figure 4.24: PDFs of turbulent-velocity fluctuations at  $y^+ \approx 300$ : (a) joint PDF  $P(u^+, Cf_{LS})$ ; (b) joint PDF  $P(v^+, Cf_{LS})$ ; (c) joint PDFs  $P(u^+, v^+)$  derived from joint PDF  $P(u^+, v^+, Cf_{LS})$  at the extreme positive and negative 5% of the  $Cf_{LS}$  tails; magenta lines in (a) and (b) are loci of the conditional averages  $\bar{U}'^+|_{Cf_{LS}}$  and  $\bar{V}'^+|_{Cf_{LS}}$ , respectively; (d)(g), (e)(h) and (f)(i) correspond to (a),(b) and (c), respectively, but pertain to the large scale and small-scale fluctuations, respectively.

with large-scale fluctuations and the regions affected by these fluctuations is much longer than the timescale dictating changes in the small scales.

In order to examine the distribution of the skin friction conditional on  $Cf_{LS}$  – i.e. the degree to which the friction is induced by contributions that vary with the sign and intensity of the large-scale fluctuations – a map of  $\frac{d\bar{w}v'^+}{dCf_{LS}}(Cf_{LS}, y^+)$  is derived from the joint pdfs  $P(u^+, v^+, Cf_{LS})$ , by using eq. (3.11) at each wall-normal location, and then by injecting the map obtained into the FIK decomposition eq. (4.7). Figure 4.26(a) presents the former map. The coloured lines represent the contributions identified in the caption – i.e.,  $\frac{dCf_{\alpha}}{dCf_{LS}}$ . The results shown in Figure 4.26 indicates that, while the skin friction is materially affected by all scales for both positive and negative large-scale footprints, there is a bias towards contributions from negative large-scale fluctuations in the outer region, above  $y^+ \approx 100$ . This is conforms to several results discussed earlier on the dominance of the large-scale stresses in association with negative  $Cf_{LS}$  values. In contrast, the main contribution at positive large-scale fluctuations originate preferentially from the buffer layer, due to the amplification of small-scale fluctuations by the footprints. However, large-scale motions also make a major contribution at large positive footprints, and this is consistent with the map in Figure 4.20(b), which features a bulge in the large-scale shear stress at large positive  $Cf_{LS}$  values. Hence, intense negative and, to a lesser extent, positive large-scale motions, which are correlated with  $Cf_{LS}$ -values, make significant contributions to the skin friction . Negative large-scale fluctuations tend to diminish the intensity of small-scale motions in the buffer layer, as shown in Figure 4.21(a), giving added weight to the large-scale turbulent motions occurring in the outer region.

#### 4.10.2 Analysis of the RD Relationship

Attention is directed next to the examination of various contributions to the alternative skin-friction relation given by eq. (4.8). Results are presented for the integrands in this latter, denoted by  $Cf_a^+$  and  $Cf_b^+$ , which represent the local viscous dissipation and turbulence production, respectively, and also for the total skin friction  $Cf$ , i.e. the sum of the  $y$ -wise integrals of  $Cf_a^+$  and  $Cf_b^+$ . First, Figure 4.27(a) gives, by way of the green and grey lines, respectively, the wall-normal distributions of  $Cf_a^+$  and  $Cf_b^+$ . As the profiles are plotted against  $\log y^+$ , they have been premultiplied, as before, by  $y^+$  so that the areas below the curves give a visually correct representation of their contribution to  $Cf$ . In the viscous sublayer, the turbulent production is close to zero, while the viscous term is close to constant, hence rising close to linearly in Figure 4.27(a) to a maximum around  $y^+ \approx 7$ , after which it drops rapidly to close to zero in the log-law region. The variation of the gradient  $y^+ \times \frac{dCf_a^+}{dCf_{LS}}$  across  $Cf_{LS}$ , shown in Figure 4.27(c), indicates a slight bias towards negative values of  $Cf_{LS}$ , and this reflects the fact that the viscous sublayer thickens (in absolute terms) when the negative large-scale footprints reduce the near-wall velocity and  $u_\tau$ . The turbulent production rises sharply from close to zero at the upper end of the viscous sublayer to reach a maximum in the buffer layer, but the pre-multiplication shifts this maximum to around  $y^+ \approx 20$ , after which the production then drops steeply to settle to a near-linear decline in the range  $80 < y^+ < 400$ . Because the large scales at  $y^+ \approx 300$  give rise to an increase in production, as shown in Figure 4.23, it is reasonable to expect a weak second maximum in Figure 4.27(a). However, no such maximum is present, and this must reflect the weakness of the outer large-scale production at the present low Reynolds number. On the other hand, Figure 4.27(d) showing  $y^+ \times \frac{dCf_b^+}{dCf_{LS}}$  across  $Cf_{LS}$  reveals, in accord with previous considerations (e.g. Figures 4.20) the presence of a weak outer maximum at  $y^+ \approx 300$ ,  $Cf_{LS}/\bar{Cf} \approx -0.15$ . It thus appears that the absence of an outer maximum in Figure 4.27(a) is simply due to the low level of the  $Cf_{LS}$ -wise integral in the outer part of the field in Figure 4.27(d). As previously shown by Renard and Deck (2016), an outer maximum does appear when the influence of the outer structures rises with increasing Reynolds number.

Figure 4.27(b) shows the contribution of the viscous and turbulent term (i.e. their integrals over  $y^+$  to  $Cf$ , the overall value being identical to that of the FIK identity. This split – 44% and 56%, arising from the viscous and turbulent fragment, respectively – will obviously shift progressively towards higher contributions of the turbulent fragment as the Reynolds number increases. As done in the FIK analysis, Section 4.10.1, it is possible to identify, here too, the production-related contribution of different fragments of the shear stress to  $Cf_b^+$  and hence to  $Cf$ . This is done in Figure 4.28(a), which shows the 9 fragments also considered in the FIK analysis. Integrating these with respect to  $y^+$  then gives the segments shown in Figure 4.28(b), which signify the respective contributions to  $Cf$ , alongside the contribution of the viscous term, represented by the green segment. It is important to point out that, as is the case with the stress fragments of Figure 4.25, the sum of all fragments in Figure 4.27 yields the total given by the black curve. The figure shows that the

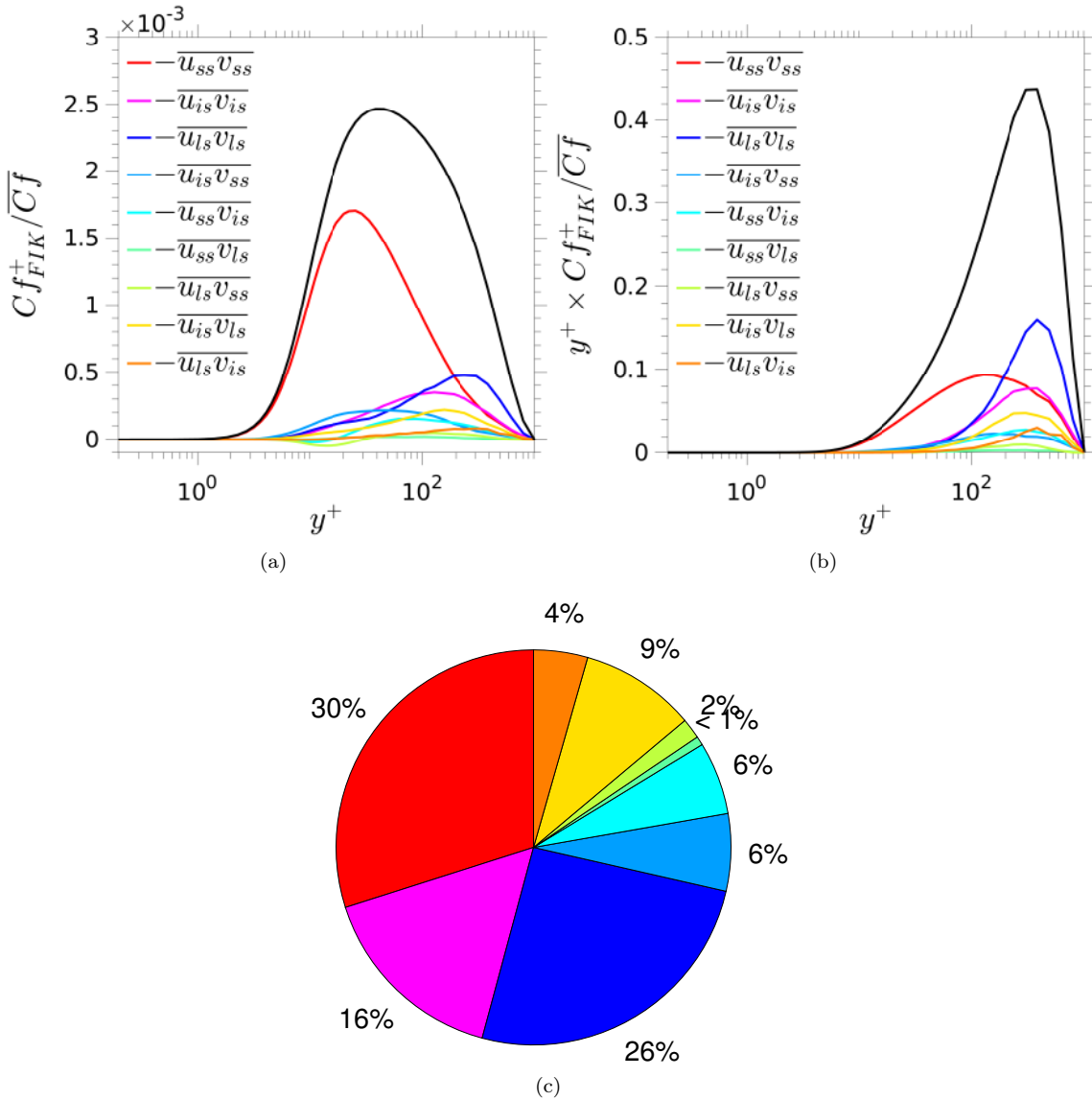


Figure 4.25: Contribution of different scales to the skin friction via the FIK identity: (a) contribution of different shear-stress fragments to the integrand in the FIK identity; (b) same as (a), but premultiplied by  $y^+$ ; (c) contributions of different scales to  $Cf$ ; the grey segment represents the viscous part, i.e. the leading term in eq. (4.7).

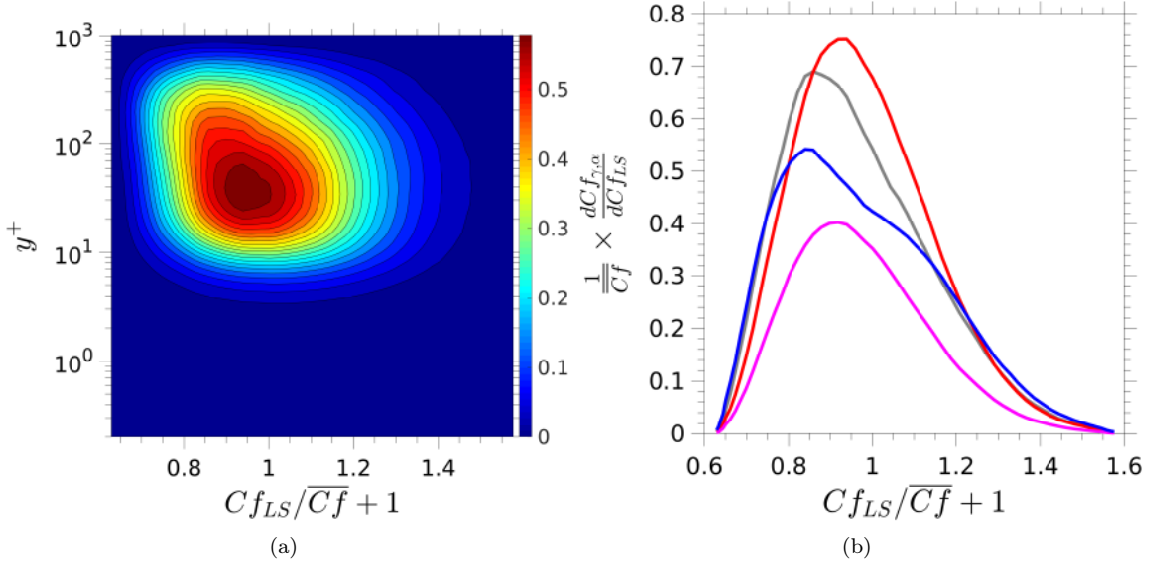


Figure 4.26: Conditional contributions to the skin friction via the FIK identity: (a) Wall-normal distribution of the  $Cf_{LS}$ -wise gradient of skin friction,  $\frac{dCf_{FIK}}{dCf_{LS}}$ ; (b) wall-normal-integrated  $Cf_{LS}$ -wise gradients of contributions of different scales, associated with  $\overline{u_\gamma u_\alpha}$ , to  $Cf$  (i.e. the  $y^+$ -integral of the field in map (a)); colours of lines correspond to the those in Figure 4.25, except for the grey line, which represents the sum of all mixed-scale terms.

bulk of  $Cf_b^+$  is due to the small scales  $-$ , namely 30% of the total. The distribution of its pre-multiplied gradient  $y^+ \times \frac{dCf_{b,ss}^+}{dCf_{LS}}$ , shown in Figure 4.28(c) reveals a bias towards negative footprints in the outer region, and this is consistent with the enhanced small-scale production indicated by the wedge-shaped, light-blue, region around  $y^+ \approx 300$ ,  $Cf_{LS}/\bar{C}f < -0.1$  in Figure 4.23(c). In contrast, the contribution of the large scales is relatively low, at 8%, and the map of  $y^+ \times \frac{dCf_{b,LS}^+}{dCf_{LS}}$  conveys the fact that this term is associated primarily with negative footprints, a feature entirely consistent with earlier results – e.g. Figures 4.23 and (d).

Figure 4.29 finally conveys the contribution of the small-scale, large-scale and intermediate-scale contributions to the skin friction. This figure is this analogous to Figure 4.26(b) pertaining to the FIK relationship. Here again, there is a clear bias of the large-scale contribution towards negative values of the fluctuations and thus  $Cf_{LS}$ , but the relative contributions of the small and large scales differ greatly from those derived from the FIK identity. The differences between the results of the FIK and RD relationships – exemplified most starkly by the juxtaposition of Figures 4.28(b) and Figure 4.25(c) – are perplexing at first sight. In particular, the contribution to  $Cf$  of the large scales arising from the RD analysis is only 8% relative to 24% derived from the FIK analysis. However, it needs to be recognised that the two relationship express very different physical processes. One important difference relates to the viscous contributions. In the FIK relationship, this contribution is insignificant, as it expresses the skin friction of a laminar channel flow at the given Reynolds number. In contrast, the viscous term in the RD relationship is almost 10 times larger, as it reflects the consequences of the severe steepening of the velocity gradient at the wall by the turbulent shear stress above the viscous sublayer on the viscous dissipation, thus almost halving the contribution of the turbulent part of the RD relationship. In addition, the large-scale footprints in the viscous layer cause significant variations in the near-wall shear strain, and this indirect effect also increases the weight of the viscous contribution at the expense of the turbulent one. If attention is restricted to the turbulent contributions of the FIK and RD relationships then the proportion associated with the large scales amount to 23% and 15%, respectively. This difference is still large, but both figures demonstrate the importance of the large scales to the skin friction.

A second important point of difference lies in the nature of the turbulence processes represented by the turbulence-related fragments in the two relationships. Within the RD framework, the turbulent contributions characterise the energy generated by the specific turbulent shear-stress fragments in combination with the

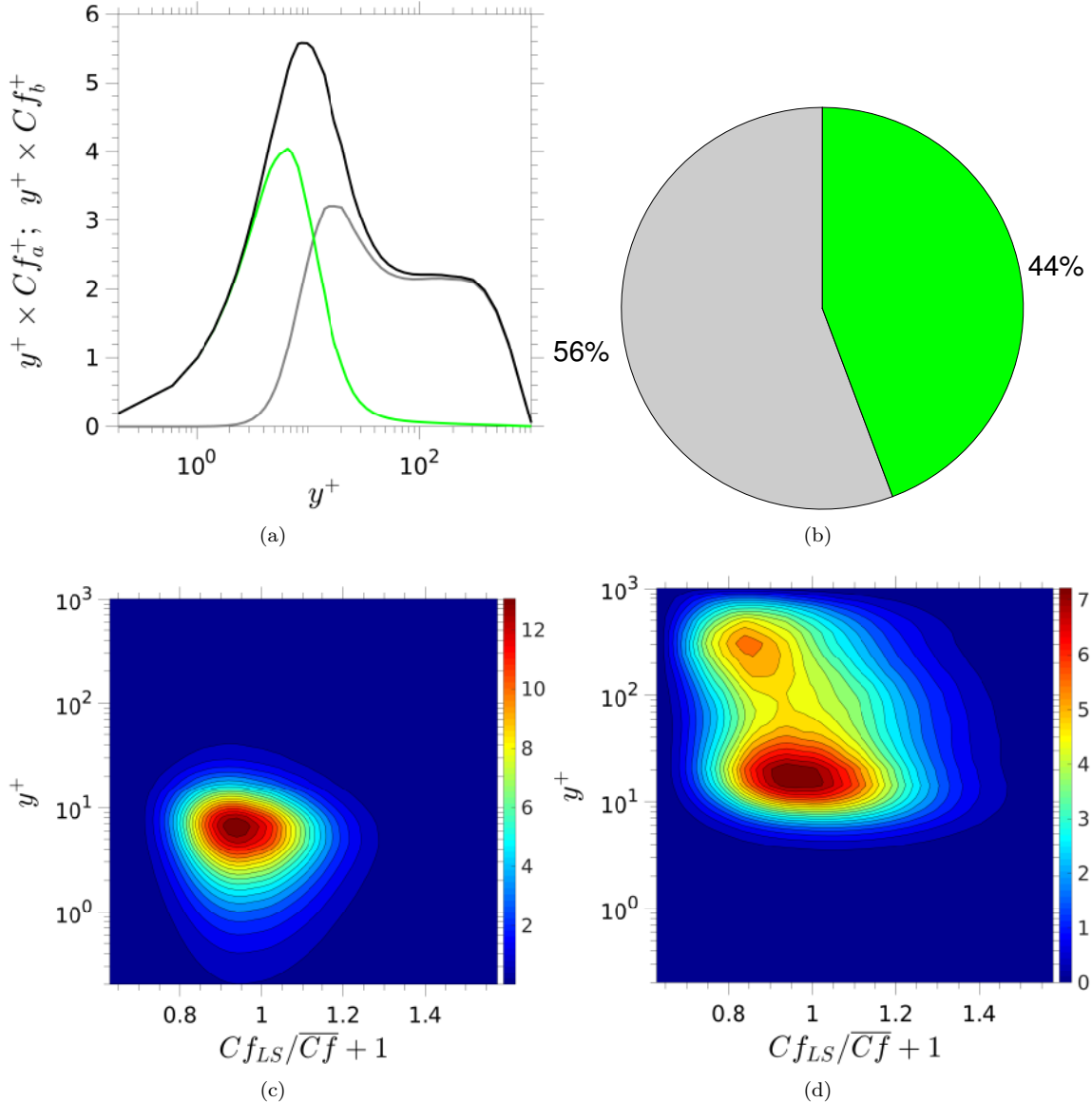


Figure 4.27: Contributions of viscous and turbulent terms to the skin friction as derived from the RD relationship; (a) wall-normal profiles of pre-multiplied integrands  $Cf_a^+$  (green line) and  $Cf_b^+$  (grey line) in eq. (4.8), the black line represents the sum of both fragments; (b) contribution of viscous and turbulent terms to the skin friction (i.e. integrals of  $Cf_a^+$  and  $Cf_b^+$ ; (c) map of  $y^+ \times \frac{dCf_a^+}{dCf_{LS}}$ , (d) map of  $y^+ \times \frac{dCf_b^+}{dCf_{LS}}$ .

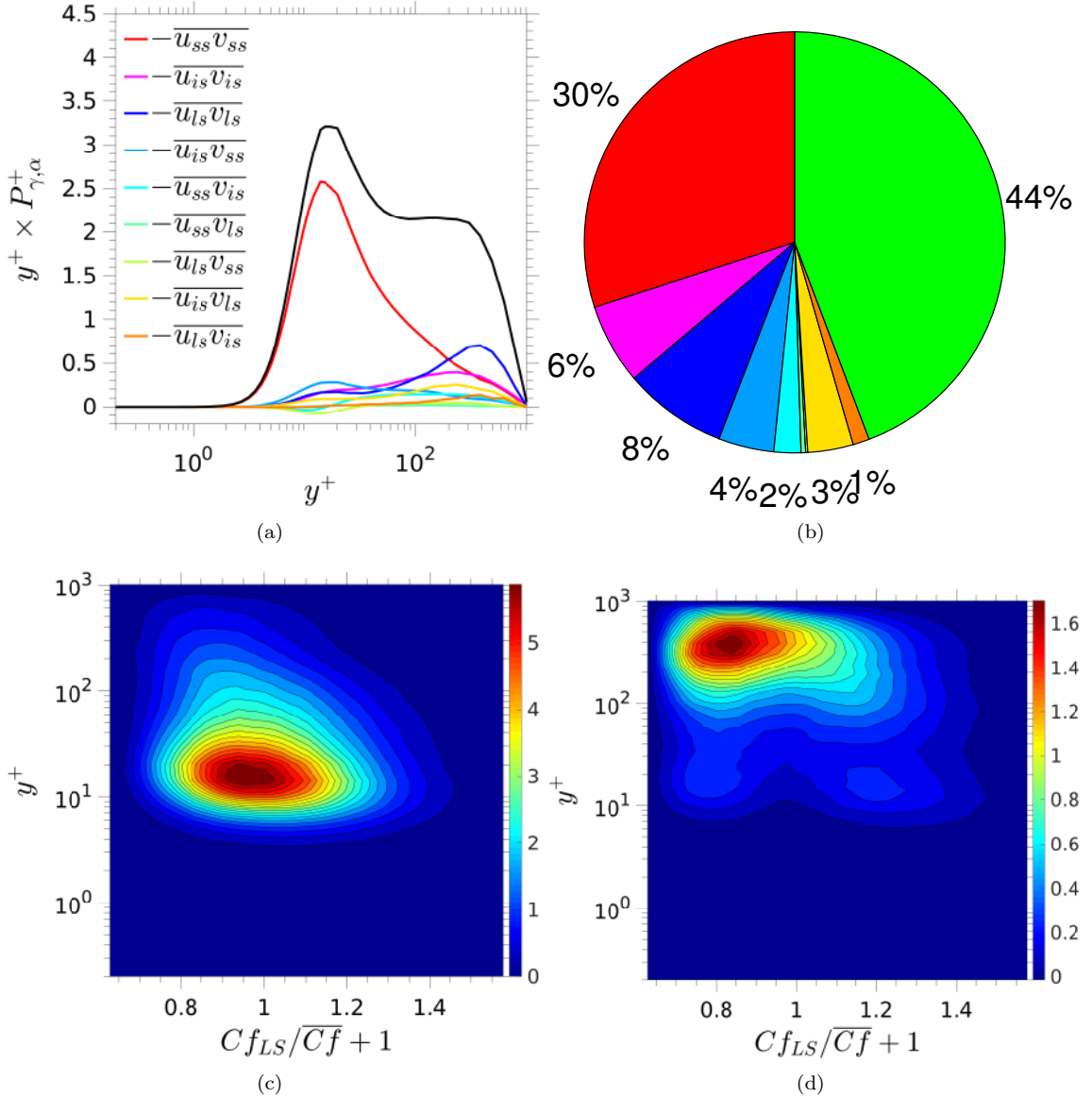


Figure 4.28: Contributions of scale-related turbulent shear-stress fragments to the skin friction via the RD relationship; (a) wall-normal profiles of scale-specific pre-multiplied production contributions to the integrand  $Cf_b^+$  in equation (4.8), the black line represents the sum of all contributions; (b) contribution of fragments to the skin friction, segment colours corresponds to those of curves in (a), except for the large green segment which represents the viscous contribution, as in figure 14(b); (c) map of  $y^+ \times \frac{dCf_{b,ss}^+}{dCf_{LS}^+}$  associated with the small-scale shear-stress fragment; (d) map of  $y^+ \times \frac{dCf_{b,LS}^+}{dCf_{LS}^+}$  associated with the large-scale shear-stress fragment.

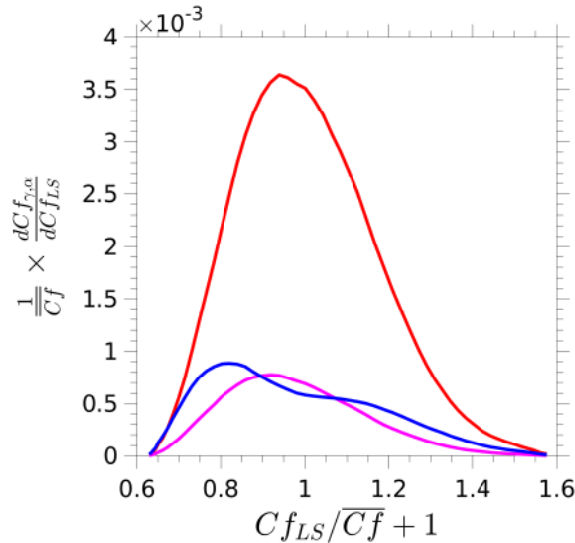


Figure 4.29: Contributions of wall-normal-integrated  $Cf_{LS}$ -wise gradients of different fragments, associated with  $\overline{u_\gamma u_\alpha}$ , to the skin friction via the RD relationship; red line: small-scale contribution; blue line: large-scale contribution; magenta line: intermediate scale contribution; the red and blue lines arise, respectively, from the  $y$ -wise integration of maps (c) and (d) in Figure 4.26.

shear strain. In the case of the large-scale motions, the associated structures are elongated and characterised by substantial streamwise fluctuations and only modest cross-flow fluctuations. The relatively modest shear stress associated with these structures thus gives rise, in combination with the relatively low strain in the outer region, to relatively modest production. This is illustrated in Figure 4.23(d), and Figure 4.28(d) also shows that the production by the large-scale structures is largely confined to layer above  $y^+ > 100$ . In the FIK identity, the contribution of the shear stress below  $y^+ \approx 100$  is also modest, but its importance to  $Cf$  above this distance is substantially enhanced by the much lower weight of the small-scale contributions of the small-scale motions returned by the FIK identity. The much higher level RD relationship yields is due to the intense shear-strain favours the production above and within the buffer layer, as conveyed by Figure 4.28(c). In the FIK relationship, the small-scale contribution to the integrand in the layer remote from the wall is rather low, as shown in Figure 4.25(b), and this enhances the weight of the large-scale contribution.

Ultimately, it is impossible to reconcile the FIK and RD described scale-related contributions, and to untangle the direct production-related contribution of the large-scale motion from its indirect effects via footprinting within the RD framework. A statement that can be made is that the FIK analysis gives a more direct, force-derived, and thus more meaningful, quantification of the contribution of the large scales to the skin friction.

## 4.11 Final Thoughts on The Reynolds Number Effects

The goal of this study was to illuminate the mechanisms by which the large outer scales in the energy-plateau region of a wall-bounded shear layer affect the small-scale turbulence field, in general, and the wall friction statistics, in particular. This was approached by means of a rational scale-separation technique and a rigorous extraction of relevant statistical properties from joint and conditional probability-density functions. Particular attention was devoted to identifying the dependence of the small-scale streamwise energy, shear stress and skin-friction variance on the intensity of large-scale skin-friction fluctuations – i.e., the footprints of the large-scale structures on the modulation of the small-scale field. A second major objective was to quantify the contribution of different scales to the skin friction.

The study has yielded a number statistical interactions that reinforce previous observations, but also revealed new mechanisms or explained more fully the former. The main conclusions may be summarised as follows, supported by the schematic given in Figure 4.30:

- The well established change in the sign of the correlation linking the large-scale motion with the small-

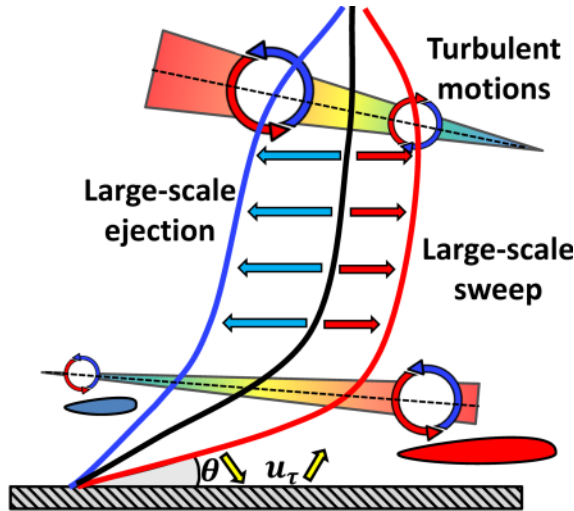


Figure 4.30: Conceptual schematic of the effects of large-scale fluctuations on the strain rate and consequent amplification/attenuation of near-wall and outer-layer turbulence

scale motion at  $y^+ \approx 100$  is due to a reversal of shear-induced production rates. With reference to Figure 4.30, positive large-scale fluctuations, associated with positive large-scale skin fluctuations, cause an increase of shear strain and shear production in the buffer layer, thus increasing small-scale activity. Concurrently, the shear strain in the outer region is reduced, resulting in a decline in the small-scale activity in the outer region. The reverse occurs in the presence of negative large-scale fluctuations. The variations in the velocity field are caused by large-scale sweeps and ejections, the former increasing the near-wall strain and the latter decreasing it.

- The wide-spread use of the term “modulation” suggests a direct interaction between the large-scale and small-scale fluctuations. However, in reality, the interaction is indirect, occurring via shear-strain increase and decrease in the buffer layer and consequent variations in turbulence production.
- The reversal of the shear gradient in the outer region also affects the intensity of the large-scale motions by shear-induced production. Thus, negative large-scale velocity fluctuations cause an increase in the outer production and hence a rise in the large-scale turbulence intensity. In other words, the increase in the large-scale outer motions goes hand-in-hand with a decrease in turbulence in the buffer layer.
- Small-scale turbulence in the buffer layer – i.e., the streak strength and the shear stress – rises close to linearly with the intensity of positive large-scale fluctuations in the velocity close to the wall and in the skin friction. The large-scale skin-friction fluctuations vary between -40% to +60% relative to the mean value, causing variations in the standard deviation of the small-scale skin friction to vary between 25% and 65% of the mean friction factor, the asymmetry relative to the mean value reflecting the skewness of the PDF of the large-scale skin-friction. These levels of fluctuations are remarkably large in view of the relatively low Reynolds number of the flow considered, and bring to light starkly the magnitude of the “modulation”.
- A quantification of the contributions of different scales to the skin friction via the FIK identity shows that the large-scale motions contribute 24% of the drag, a level almost as high as the small-scale motions. Mixed-scale contributions arising from correlations between the large-scale and small-scale motions to shear-stress fragments are small, implying that direct “modulation”, used in the strict sense of the term, is small. Rather, the effect of the large scales on the small scale is indirect, as already noted, and this gives rise to an intensification of the small-scale contribution to the skin friction.
- The alternative quantification via the RD identity suggests that the contribution of the large scales to the skin friction is much lower, at 8% (or 15% of the total turbulent part). However, this method partitions the roles of the different scales by virtue of their contribution to energy production, and it also characterises the influence of the viscous contribution by shear-strain driven dissipation in the near-wall layer. This method of portioning is very different from the FIK method, yielding a viscous

contribution which is almost as high as the turbulent contribution, relative to only 5% resulting from the FIK decomposition. The fact that the small-scale contribution to the drag is, proportionately, much larger than that arising from the FIK identity reflects that turbulence production by shear in the upper part of the buffer layer is the dominant contributor, relative to the modest generation in the outer region, and this suggests that the amplification of the small-scale intensity in the buffer layer by the action of the outer structures is of substantial importance, but not reflected explicitly by the contribution of the outer structures to the skin friction. Hence, the conclusion, based on heuristic arguments, is that the FIK identity gives a more realistic representation of the contribution of the large-scale structures to the skin friction.

In this chapter, scale separation combined to conditional statistics have been used in order to elucidate mechanisms by which large, outer-layer scales interact with, and impact, small scales and skin friction. A key finding is that “modulation” occurs indirectly through changes in local shear production rates induced by large-scale sweeps and ejections, rather than direct scale interactions. Despite this indirect effect, large scales still contribute substantially to overall skin friction. Positive large fluctuations amplify buffer layer shear and small scales, whilst negative large fluctuations have the opposite effect but increase outer large motions. The FIK identity suggests almost equal friction contributions from small and large scales, while RD points to a lower but still significant large scale role. Overall, results demonstrate that large scales significantly impact small scales and drive friction variations mainly through localised unsteady strain rate changes that alter shear production rates. This supports a quasi-steady conceptual model for scale interactions. The quasi-steady conceptual model, which was first introduce by Chernyshenko, Marusic, and Mathis (2012), refers to the idea that large-scale motions affect small-scales indirectly by altering the local strain rates and turbulence production in a quasi-steady manner, rather than through direct large-small scale interactions. Its validity and its limitation are investigated in the next chapter.

## Chapter 5

# Near-Wall Turbulence at High Reynolds: A Search for Universality

### 5.1 Interactions Between Outer and Near-Wall Turbulent Scales. How Do They Talk?

Numerous experimental and computational studies over the past two decades, including investigations presented in previous chapters, have invalidated the notion that the local turbulent state in the near-wall region is independent of large-scale structures in the outer layer, even at moderate Reynolds numbers. These studies have demonstrated a clear connection between large-scale motions in the log layer and perturbations to the small-scale motions and skin friction in the near-wall region, referred to as large-scale modulation or footprinting. This phenomenon has significant implications for skin friction prediction and control. Elucidating the underlying mechanisms of scale interaction has thus become a major research focus, driven by its relevance to skin friction. The present study continues this effort to further elucidate the modulation process at higher Reynolds numbers ( $Re_\tau \approx 5200$ ) using an alternative scale decomposition technique necessitated by the wider range of scales present.

As previously described, the perturbation caused by footprinting — apart from the large-scale motions constituting the process itself — is in the form of an amplification and an attenuation of the small-scale motions in harmony with positive and negative large-scale fluctuations, respectively — a phenomenon referred to as “amplitude modulation”. The intensity of the modulation is observed to go hand-in-hand with the intensity of the large-scale outer structures and their footprints, the latter two rising with the Reynolds number (Mathis et al. 2009). In addition, a few recent studies (Ganapathisubramani et al. 2012; Baars et al. 2015; Pathikonda and Christensen 2019; Iacobello, Ridolfi, and Scarsoglio 2021), discussed later, have provided evidence of “frequency modulation” — i.e., the increase and reduction in the time scale of the near-wall turbulence.

Alongside a general wish to record and understand the above interactions, interest in them is driven by three specific questions:

- (i) What fundamental mechanisms drive the modulation process?
- (ii) Is the near-wall turbulence — and, more specifically, its small-scale part — universal if scaled with the large-scale skin-friction, rather than with the average value?
- (iii) Do the interactions have consequences to the effectiveness of control schemes designed to reduce the skin friction?

Question (ii) can also be recast as follows:

- (iv) Does near-wall turbulence satisfy the quasi-steady hypothesis, wherein the small-scale turbulence responds (almost) instantaneously and linearly to the large-scale perturbations?

Statistical properties pertaining to the amplitude-modulation process have been reported, discussed and dissected in many recent papers. Experimental studies, the large majority performed with single hot-wire

probes in boundary layers (– e.g., Mathis et al. 2009; Schlatter and örlü 2010; Duvvuri and McKeon 2015; Pathikonda and Christensen 2019, pp. –) cover a wide range of Reynolds numbers, extending to  $Re_\tau \approx 19000$ . While all provide valuable insight into many aspects of the modulation process, none addresses specifically the questions posed above, simply because of the restricted nature and volume of the data that could be extracted experimentally. In contrast, computational studies. Among them Chung and McKeon (2010), Bernardini and Pirozzoli (2011), Eitel-Amor, Örlü, and Schlatter (2014), Agostini et al. (2017), Dogan et al. (2019), and Andreolloi et al. (2021), mostly employ DNS and, although restricted to much lower Reynolds numbers, give access to full-volume realisations that allow the above questions to be addressed. This route has been taken by Agostini and Leschziner (2019a) and Chernyshenko (2021), the latter specifically in support of formulating their quasi-steady (and quasi-homogeneous) theory pertaining to question (ii) and (iv) posed above.

A variety of aspects of the above large-scale/small-scale interactions have been investigated in previous chapter by analysing the DNS data for channel flow at  $Re_\tau \approx 1025$ , a value for which the interactions are relatively weak, however. The BEMD was employed to separate the turbulence spectrum across many full-volume DNS realisations into small, medium and large-scale modes. This allowed to construct small-scale statistics, conditional on large-scale skin-friction footprints, so as to infer the mechanisms by which small-scale amplification by positive footprints dominate asymmetrically over small-scale attenuation by negative footprints, thus explaining the progressive rise in the perturbations of the near-wall layer by footprinting.

Of particular relevance to question (i) in the above list on the mechanisms responsible for the amplitude modulation are the recent studies by the author and his collaborator (Agostini and Leschziner 2019b; Agostini and Leschziner 2019a; Agostini and Leschziner 2021), the last, for which results are conveyed by Chapter 4, focusing specifically on the effects of modulation on the drag-reduction effectiveness achieved by imposing oscillatory spanwise wall motion in channel flow at  $Re_\tau \approx 1025$ . It was shown that the mechanisms of amplification and attenuation are, essentially, the same in both the canonical and actuated cases, the principal element being the increase and decrease in near-wall turbulence generation provoked, respectively, by corresponding increase and decrease in the strain rate of the large scales close to the wall. However, the effects are more pronounced in the low-drag actuated flow, in which the modulation due to negative and positive large-scale fluctuations are substantially asymmetric, implying the origin of the decline in drag-reduction effectiveness as the Reynolds number increases (Gatti and Quadrio 2016; Ricco, Skote, and Leschziner 2021; Chung and Hurst 2014; Marusic et al. 2021).

In contrast to amplitude modulation, frequency modulation has received far less attention. This rarity has provided strong impetus for one major element of the present study wherein a statistical analysis of the second-order structure function is proposed as a basic for illuminating the modulation of the length scale of the near-wall turbulence by the footprints. To the authors' knowledge, there are only four studies that focus on this type of interaction for canonical flows – namely those by Ganapathisubramani et al. (2012), Baars et al. (2015), Pathikonda and Christensen (2019) and Iacobello, Ridolfi, and Scarsoglio (2021), the first three of which are based purely on processing experimental data, while the fourth involves both experimental and computational elements.

Ganapathisubramani et al. (2012) examined the frequency modulation, alongside amplitude modulation, in the near-wall region of a boundary layer at  $Re_\tau = 14150$  (database obtained by Nickels et al. (2005)). They did so by counting the number of maxima and minima in the recorded small-scale signals and analysing conditional small-scale spectra, observing that frequency modulation is relatively weak, confined to  $y^+ < 100$  and being positively correlated with the intensity of the large-scale motions. A limitation of the study, acknowledged explicitly therein, is that the results were observed to be sensitive to the width of the bins used to separate samples of the large-scale motions as a basis of the conditional characterisation of the modulation.

Baars et al. (2015) analysed hot-wire signals of the streamwise velocity in the same boundary layer that considered by Ganapathisubramani et al. (2012) but chose to use wavelet transforms so as to extract the amplitude and frequency modulation simultaneously. The method decomposes the small-small energy in the joint time-frequency space, allowing the derivation of the time-varying small-scale spectrum that provides temporal information on the instantaneous amplitude and frequency, thus yielding correlations and the time shifts between large-scale motions and amplitude and frequency variations in the small scales. In essence, these results confirmed the conclusions derived by Ganapathisubramani et al. (2012), including the observation that frequency modulation is weaker than amplitude modulation. However, significant uncertainties arise from the sizeable sensitivity of the frequency modulation to the choice of the wavelet shapes forming the basis of the analysis.

Pathikonda and Christensen (2019) analysed the streamwise and wall-normal velocity fields in a boundary layer in a water channel at  $Re_\tau \approx 1400$ , derived from time-resolved PIV. Similar to the approach of Baars et al. (2015), amplitude and frequency variations and related correlation coefficients were extracted from wavelet spectra for both streamwise and wall-normal components, supplemented by a spatio-temporal analysis to determine spatial- and temporal-lag characteristics pertaining to the large and conditioned small scale data. In respect of amplitude modulation, the correlation maps for the streamwise components were found to be entirely consistent with earlier observations, in addition to which the modulation of the wall-normal component was shown to be broadly similar to that of the streamwise component. On the other hand, and consistent with observations by Baars et al. (2015), frequency modulation was found to be modest, decaying to an insignificant level for  $y^+ > 100$ . Additionally, anomalous features were observed in respect of the wall-normal modulation, probably reflecting experimental or processing limitations.

Iacobello, Ridolfi, and Scarsoglio (2021) applied the so-called Natural Visibility Graph (NVG) approach, developed by Lacasa et al. (2008), to the boundary layer at  $Re_\tau \approx 14750$ , previously examined in Ganapathisubramani et al. (2012) and Baars et al. (2015), and to the channel flow of at  $Re_\tau \approx 5200$  ([lee2014direct](#)). The principle of this method is to count how many times a point (a "node") in the discretised signal can be linked to other discrete points by a straight line without crossing any part of the signal itself and staying above the signal. Regardless of whether the set of points belong to a discretised temporal or spatial signal, it is readily appreciated that the shorter the wavelength is the fewer connections there are, while the reverse applies to longer wavelengths. The number of connections between any one node to its neighbours is defined as the "degree of centrality" (DoC). As part of their study, Iacobello, Ridolfi, and Scarsoglio (2021) investigated the validity of the quasi-steady hypothesis by relating the velocity-fluctuations signals at  $y^+ \approx 10$  to the large-scale streamwise velocity derived from Fourier-based filtering. To this end, they estimated the DoC for various signal subsets conditioned on bins of large-scale skin-friction values. They showed that the distribution of the DoC for the streamwise signal complies with the quasi-steady scaling laws, which link the wave length and frequency of the near-wall fluctuations to the large-scale motions, thus supporting the hypothesis, but only in respect of the streamwise statistics. When this approach is applied to the spanwise and wall-normal velocity components, scaling laws are returned which are not compatible with those implied by the hypothesis. Limitations of the method include increasing uncertainties of the DoC at large wavelength and the non-transparent connection between the DoC formalism and the continuous power spectra for of the signals being processed.

In contrast to previous studies on frequency modulation, the present study proposes a methodology distinguished by its clear and transparent formalism, which relies on processing continuous statistical quantities, such as joint PDFs and the structure function. This approach does not require any discrete representation or binning beyond that imposed by the discrete DNS solution at  $Re_\tau \approx 5200$ . A unique aspect of the present framework is the utilisation of an auto-encoder algorithm to separate full-volume DNS realisations into large-scale and small-scale motions. This approach is preferred over the BEMD previously employed at lower Reynolds numbers, as the resource requirements of EMD become untenable due to the extremely large DNS data set and the expansive solution domain needed to capture the wide spectrum of scales at higher Reynolds numbers.

The present study focuses on four specific aspects:

1. The manner in which the decoder-encoder model is employed to separate scales over full-volume DNS realisations.
2. The method by which insightful conditional statistics are derived from the separated fields.
3. How the statistics obtained in (2) provide insight into the mechanisms by which large scales affect turbulent stresses, including small-scale portions, in terms of both amplitude and length-scale (or wavelength) modulation, which is distinct from frequency modulation.
4. How the decomposition in (1) allows for testing the quasi-steady hypothesis with respect to both amplitude and length-scale modulation, i.e., the proposition that turbulence fields are universal when scaled with the instantaneous and local large-scale wall shear stress.

The study aims to shed light on the complex interactions between large and small scales in turbulent channel flow at a high Reynolds number ( $Re_\tau \approx 5200$ ), utilising advanced statistical techniques and a novel auto-encoder algorithm for scale separation. By examining conditional statistics and testing the quasi-steady

hypothesis, the study seeks to provide a deeper understanding of the mechanisms underlying scale modulation and their impact on turbulent stresses.

## 5.2 How do Auto-encoders learn to identify large-scale structures?

As noted earlier, the EMD becomes untenable at the present Reynolds number, to which must be added some limitations regarding the possibly incomplete capture of large-scale motions the size of which is comparable with the computational box size. Thus, an alternative data-driven methodology, referred to as “Auto-Encoder” (AE), has been adopted herein to separate the large-scale from small-scale motions.

The exploitation of AE technology in fluid mechanics is relatively recent, and it has been applied successfully as an aid to flow prediction and the analysis of turbulence physics (Mohan et al. 2023; Maulik, Lusch, and Balaprakash 2021). However, it is not the purpose of this paper to provide a review of the various strands of AE applications; interested readers may wish to refer to a broad description and discussion in Agostini (2020) of AE techniques as pertinent to fluid dynamics. An AE is an unsupervised machine-learning (ML) algorithm that is trained to reconstruct a representation of its inputs from a data set that is highly reduced in volume and detail relative to the full input. As illustrated in Figure 5.1, an AE has three parts: an encoder, a bottleneck (latent space), and a decoder. Depending on how its architecture is defined, an AE can serve different purposes, functioning as denoiser (Vincent et al. 2010), anomaly detector (Zhou and Paffenroth 2017), and estimators (Guastoni et al. 2021), for example. In the present study, the goal is to use the AE’s ability to efficiently learn the most important features associated with large-scale outer-flow structures in a pre-defined portion of the flow and to extract them from the fields in other parts of the flow. The AE is thus used as an outer-flow-structure filter that yields a lower-order representation of raw fluctuation field. To do so, raw streamwise velocity fields at the wall-normal location  $y^+ \approx 3.9\sqrt{Re_\tau} \approx 280$ , a location at which the structures are especially well defined according to Mathis, Hutchins, and Marusic (2009), are fed to the AE. The fields consist of randomly chosen subsets with size  $1280 \times 1280$  data items, each being  $1/48^{th}$  of the total data items in the plane. Subsets from seven DNS snapshots are used for this training, and subsets from three other snapshots are used for validation. A validation set is required to ensure that the features learned by the AE correspond to a valid statistical description of the external-flow structures. This means that not only the noise will be filtered out, but that also any singular events produced by the structures are removed, which is a distinctive benefit of the AE over other methods such as FFT- or EMD-based methodologies. The main advantage is that the AE, once trained, is able to identify information reflecting the true impact of external flow structures at any wall-normal location, and extract them faithfully in isolation from spurious disturbances having spectral length-scale features similar to the true LS scales, which is not possible with low-pass filtering, wherein all information of a given length-scale spectrum is conserved whatever its source.

To force the AE to learn the most important features, the information passing through the AE is drastically reduced by using a relatively narrow bottleneck. The information between the input and the bottleneck is progressively reduced by using several convolutional layers, helping the AE to gradually define which features are the most important by minimising the absolute value of the reconstruction error ( $J = \sum_{i=1,j=1}^{1280,1280} (\text{output}(x_i, z_j) - \text{input}(x_i, z_j))^2$ ), so-called Mean Squared Error (MSE), steering the AE towards reconstructing the most energetic scales, which correspond to large-scale motions in this case AE can be regarded as a generalisation of the POD (Plaut 2018; Murata, Fukami, and Fukagata 2020). Both encoder and decoder have six convolution layers. Each layer contains two activation maps, and each is followed by a down-sampling layer for the encoder, or is preceded by an up-sampling layer for the decoder, the function ‘exponential linear unit’ (elu) (Clevert, Unterthiner, and Hochreiter 2015) is used as the activation function. To avoid over-fitting, a Gaussian-noise layer and batch-normalisation layers are added to the AE’s architecture during the training. The present AE architecture leads to a dramatic reduction in information: input images are compressed by a factor  $1/2048$ , from a size of  $1280 \times 1280$  data points to  $20 \times 20 \times 2$  points in the latent space (Bottleneck). Thus, only 0.05% of the original information is available to the decoder for constructing a reduced-order version of the original input that preserves the energetic LS structures present in the original.

Initially, the AE is trained to learn only the features associated with the outer-flow structures – i.e., the data used for training are streamwise-velocity-fluctuation fields at the wall-normal location  $y^+ \approx 280$ . By reducing the amount of information passing through the AE’s bottleneck, the AE must learn the most significant features of the input so that the output image is as close as possible to the input image. The level of closeness is defined by the absolute value of the reconstruction error  $J$ . Once the training (learning)

is achieved – here done by feeding in sub-domains of size  $1280 \times 1280$  wall units, chosen randomly from seven DNS 2D fields at  $y^+ \approx 280$  – the AE will only use the “library” of features learned at  $y^+ \approx 280$ , from the streamwise velocity fields, for reconstructing all velocity components of the flow at any wall-normal plane. In this way, the large-scale motions associated with the outer-flow structures are extracted by the AE from the raw data at each and every wall-normal location. The outcome of the above process is illustrated — arguably verified, if only in a qualitative sense — in two ways. First, Figures 5.2 and 5.3, show fields decomposition, spectra and streamwise energy profiles for the large-scale and small-scale motions respectively. Second, Figure 5.4 compares the AE-generated decomposition with the more conventional empirical-model decomposition (BEMD) applied in previous studies of channel flow at  $Re_\tau \approx 1025$ . Figure 5.2 shows sub-domains of streamwise-fluctuations fields across the wall-normal planes  $y^+ \approx 280$  and  $y^+ \approx 12$  on the left-hand side and right-hand side, respectively, both covering the sub-domain  $x^+ \times z^+ \approx 16000 \times 8000$ , corresponding to  $1/8$  and  $1/6$  of the total computational-box dimensions, respectively. The plots, from top to bottom, are for the full streamwise-fluctuations fields, the large-scale motions and the residual small-scale fields. Specific feature that deserve to be underlined are, first, the strong dominance of the large-scale component at the outer location; second, the presence of large-scale footprints in the near-wall layer; third, the fine-grained small-scale features in the near-wall layer; and fourth the influence of the large-scale footprints on the intensity of the small-scale structures in the near-wall layer.

Figure 5.3 demonstrates the scale-separation process by way of pre-multiplied energy-density spectra, in the  $y^+ - \lambda_z^+$  (spanwise wavelength) plane for – top to bottom rows – the streamwise, wall-normal and spanwise components, respectively. The red contours identify the large scales, while the blue contours pertain to the small scales, the sum of the two being identified by the black contours. The corresponding energy profiles in the wall-normal direction are given in the middle column, while the plots on the right-hand-side plots show the spectra with the energy density normalised by the total-energy profiles given in the middle column. The purpose of including the last set of plots is to bring out more clearly the proportion of large-scale and small-scale energy density in regions in which the magnitude of the energy is low. The plots convey a well-defined scale separation, with the large scales confined to wavelength values  $\lambda_z^+ > 800$ , which compares to  $\lambda_z^+ \approx 100$  at which the streamwise energy density peaks at  $y^+ \approx 13$ . The normalised spectra for the streamwise fluctuations also bring out prominently the penetration of the large-scale energy right down to the wall. This penetration, as well as the high level of large-scale energy, relative to the respective total levels, is further brought out in the energy-profile plots. An interesting observation is the exceptionally high anisotropy in the large-scale stress components, implied by the precipitous decline in the wall-normal stress towards the wall. One facet of this behaviour is that small-scale structures tend to be more isotropic than large-scale eddies. Another aspect arises from the large-scale/small-scale analysis reported in previous chapter for channel flow at  $Re_\tau \approx 1025$ , which strongly suggests that footprinting is closely associated with large-scale sweeps, ejection and quasi-steady streamwise vortices. Specifically, sweeps result in “splattering” due to inviscid wall blocking and the enhanced transfer of energy from the wall-normal component to the wall-parallel directions.

Next, Figure 5.4 provides some comparisons between the AE- and BEMD-derived decompositions. Here, it needs to be reiterated that the BEMD is too resource-intensive to be used across the entire solution domain. For this reason, the comparisons shown in Figure 5.4 restrict themselves to two partial  $y$ -planes of size  $x^+ \times z^+ = 16000 \times 8000$  containing  $1280 \times 1280$  data points within one DNS realisation. The BEMD is a purely data-driven method, wherein the LS filter characteristics are defined directly from the snapshot. Hence, if the snapshot is not large enough to capture the full length-scale range of the structures populating the flow, the LS filter will be slightly different from one subset to another, which is one further resource-related limitation of the use of the BEMD for the present Reynolds number. In agreement with earlier studies, the BEMD is used to decompose the spectrum into 5 modes and residual, each encapsulating a narrow range of length scales. Also, as done before, the upper two modes (strictly mode 4 and above) are defined as representing the large-scale portion of the spectrum. In Figure 5.4, the two images in the top row show the raw data at  $y^+ \approx 280$  and  $12$ , respectively, while the second and third rows convey the decomposition returned by the AE and BEMD, respectively. While this visual representation is essentially qualitative in nature, it demonstrates strong similarities of the large scales LS derived from both methods. The raw field at  $y^+ \approx 12$ , Figure 5.4(b), shows clearly the modulation of the small-scale motions by the outer-flow structures, and Figures 5.4(d) and 5.4(f) convey qualitatively the fact this modulation is correlated with the the large scales extracted by using either the AE or the BEMD. It is important to recall here that the AE is only trained at  $y^+ \approx 280$ . While both reconstructions at  $y^+ \approx 12$  are very similar, the AE-based decomposition seems to provide LS structures that are more continuously correlated in the streamwise direction, which

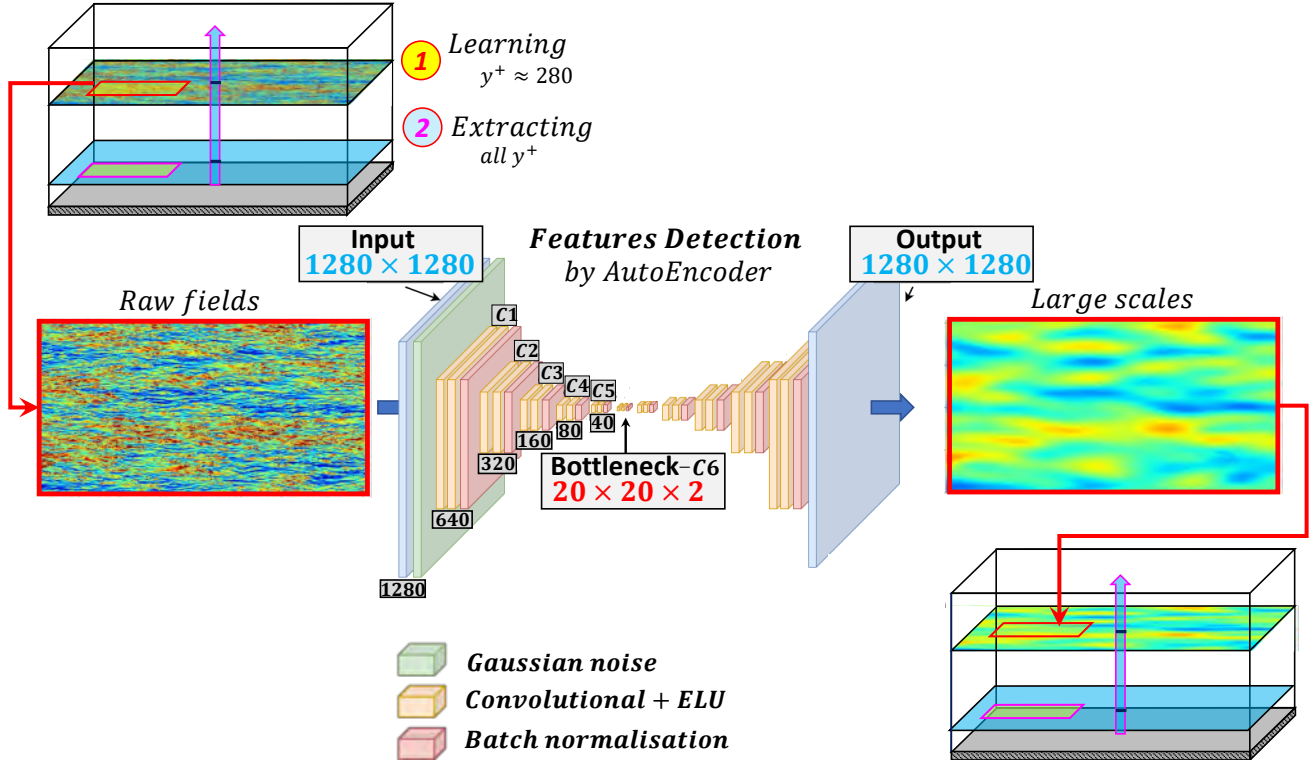


Figure 5.1: Schematic representation of the process of extracting the large-scale motions by using a multi-layer Auto-Encoder. Patches on the plane  $y^+ \approx 280$  are  $8 \times 6$  sub-domains (in  $x$  and  $z$  directions, respectively) of size  $\Delta x^+ \approx 1280$  and  $\Delta z^+ = 1280$  used for the learning process.

complies better with the expectation of streamwise-coherent LS regions.

## 5.3 Statistical characterisation

### 5.3.1 Amplitude modulation

As in the previous studies, the key aspect of the present statistical-processing method is to derive all statistical quantities from the general joint PDF  $P(u, v, w, Cf_{LS})$ , where  $Cf_{LS}$ , representing the unsteady and locally varying skin friction induced by the footprints of the large-scale motions. The different conditional values are determined using equations (3.13) and (3.14), approach detailed in section 3.6. The merit of these conditional values is that they bring into focus the influence of large-scale fluctuations on the quantities considered at large positive and negative  $Cf_{LS}$  values without the obscuring influence, or weighting, of the low-density levels in  $P(Cf_{LS})$ . Other statistics can then be derived from the above two, an example being the conditional production rates derived from products of the second moments and the conditional strain rate – e.g.,  $[-\bar{u}'v'dU/dy] |_{Cf_{LS}}$  shown in Figure 5.11. Any of these statistical properties can then be conveyed by respective fields in  $y^+ - Cf_{LS}$  plane, because of the  $x, z$ -wise homogeneity of the statistical properties, subject to the lag between the large-scale  $Cf_{LS}$  fluctuations and the large-scale velocity fluctuations  $u_{LS}$  at any  $y^+$  value being removed.

### 5.3.2 Length-Scale Modulation

The second-order structure function is proposed herein as a basis for investigating length-scale modulation. Given the fields of velocity  $u(x, z)$  across any  $y$ -plane, and the large-scale skin-friction  $Cf_{LS}(x, z)$ , the latter being wall footprint of the outer-large scale structures shifted forwards in streamwise direction by  $\Delta x = \Delta y \tan \theta$ , with  $\theta \approx 15^\circ$ , the starting point is the derivation of the PDFs from the DNS data set in

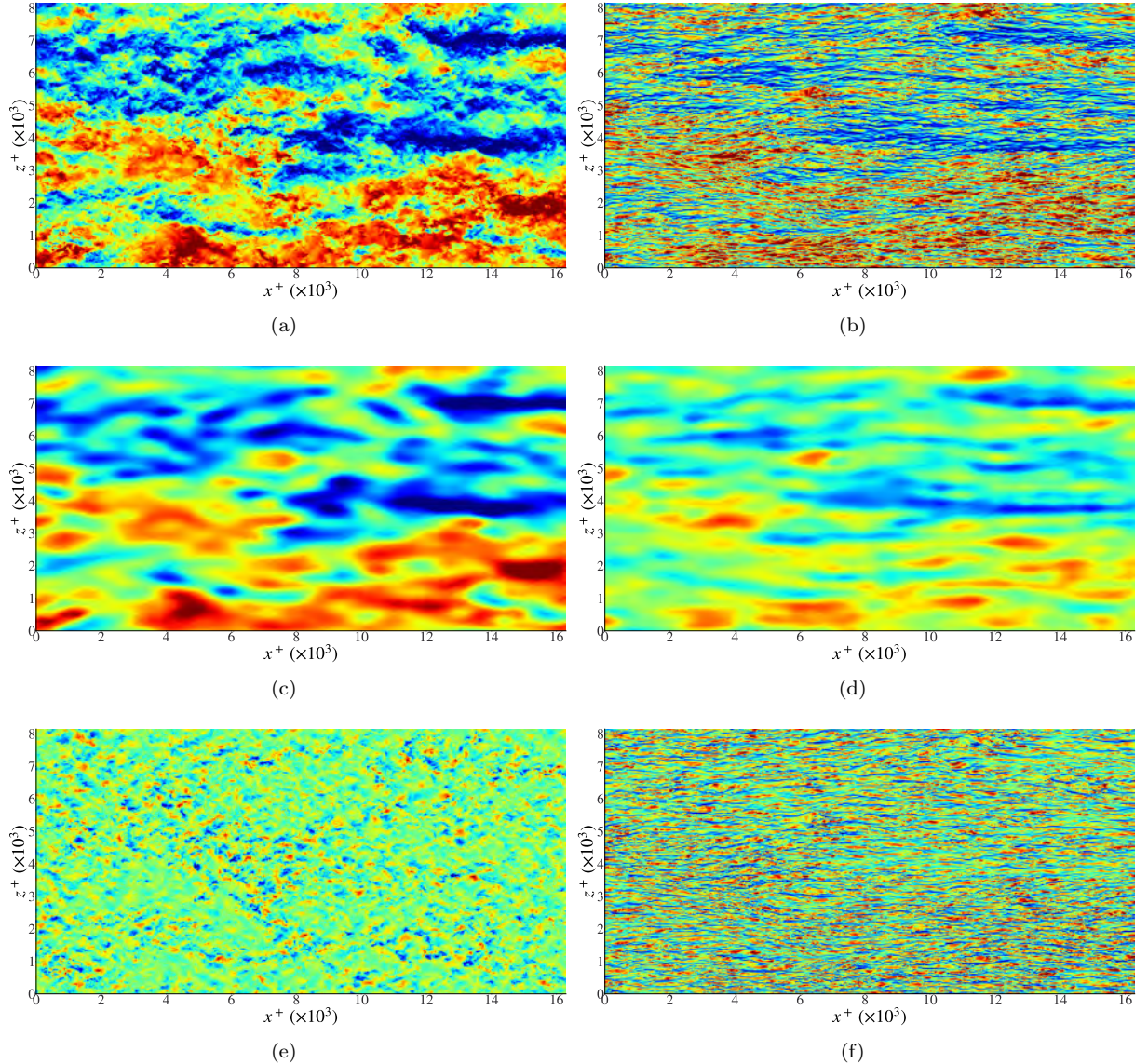


Figure 5.2: Illustration of scale decomposition using the approach shown in Fig. 5.1 at two wall-normal locations over a portion of the  $x - z$  DNS box (1/8th in streamwise direction and 1/6th in streamwise direction); (a),(c),(e):  $y^+ \approx 280$ ; (b),(d),(f):  $y^+ \approx 13$ ; (a),(b): full streamwise-fluctuations fields (input to the auto-encoder); (c),(d): large-scale fluctuations fields (output of the auto-encoder); (e),(f): small-scale fluctuations (total minus large-scale fluctuations).

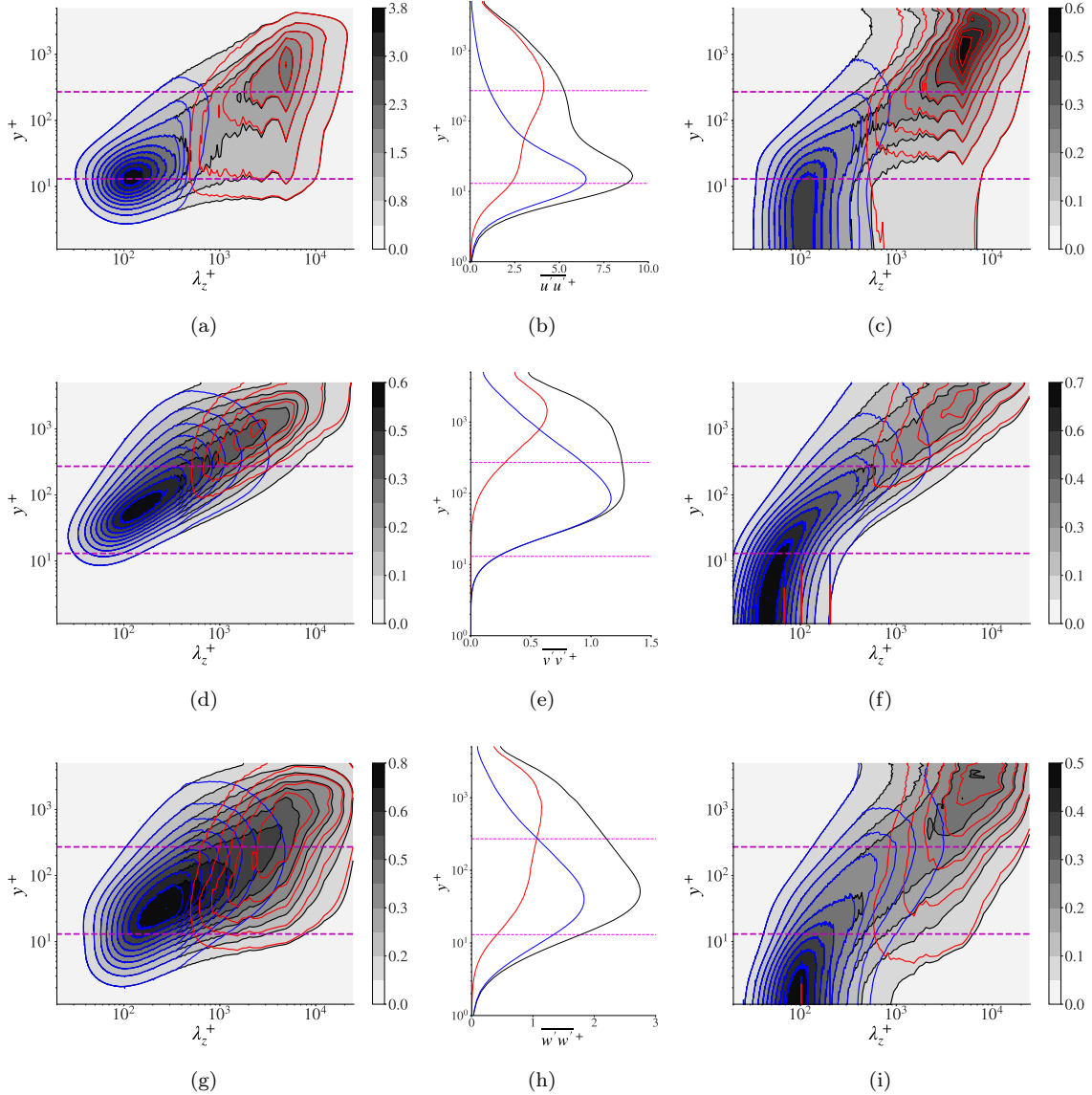


Figure 5.3: Statistical properties of small-scale and large-scale fluctuations in (a),(b),(c) streamwise, (d),(e),(f) wall-normal and (g),(h),(i) spanwise directions, respectively; (a),(d),(g): premultiplied power spectra – black contours identify total fluctuations, red contours large-scale fluctuations, blue contours small-scale fluctuations; (b),(e),(h): corresponding streamwise-energy profiles (colour code same as in LHS column); (c),(f),(i): premultiplied power spectra normalised by the total energy (black) profiles in the middle column.

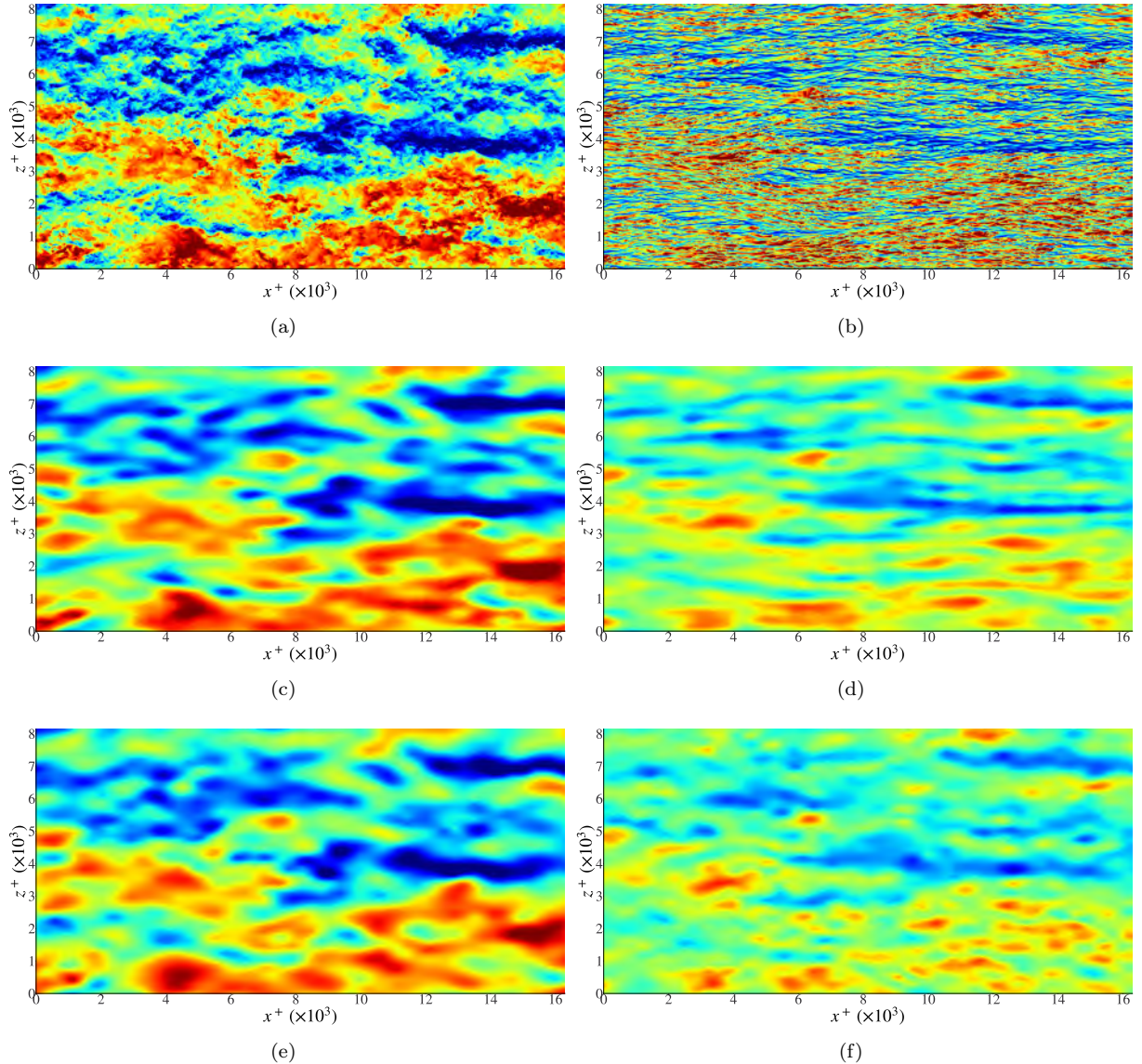


Figure 5.4: Extraction of large-scale fluctuations at  $y^+ \approx 280$  (left column) and  $y^+ \approx 12$  (right column) using Auto-Encoder (c,d) and bi dimensional empirical mode decomposition (e,f).

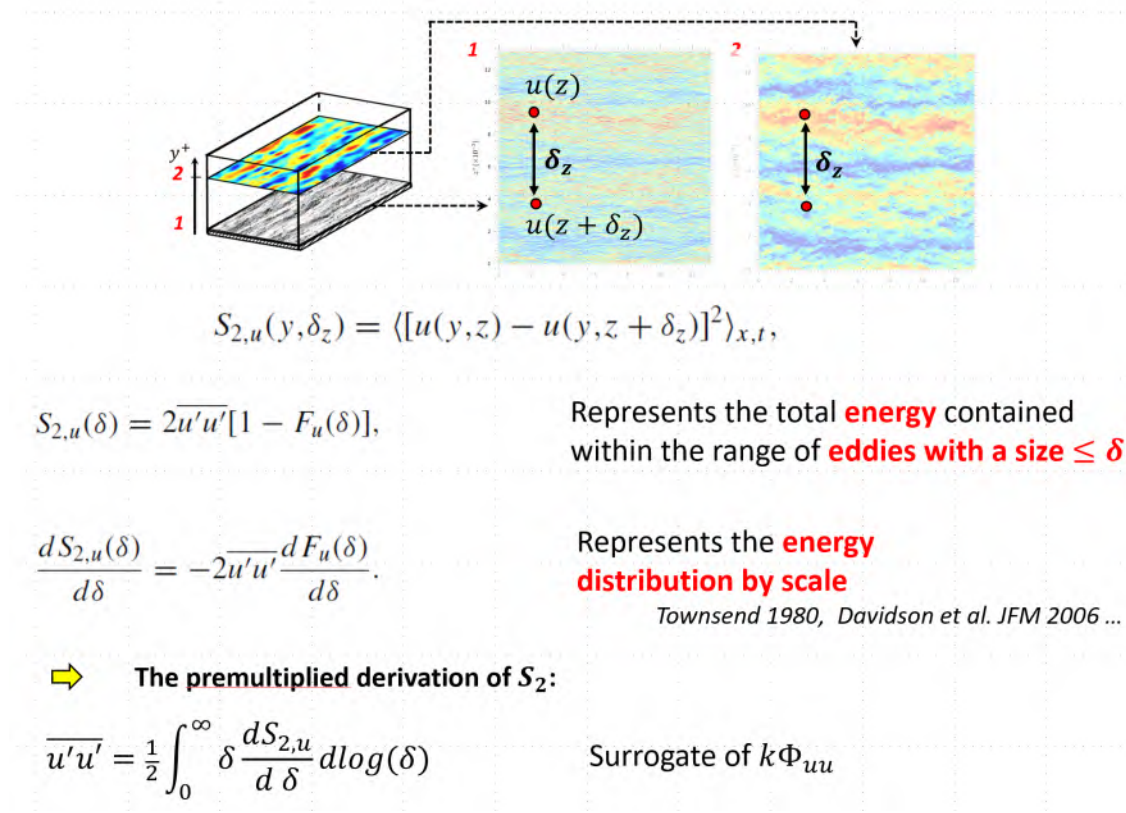


Figure 5.5: Estimating the scale-wise energy distribution from the 2<sup>nd</sup> order structure function.

which  $s_{u,\delta z} = u(x, z + \delta z) - u(x, z)$  is the instantaneous difference between velocity fluctuations separated by a given (i.e. chosen) value  $\delta z$  (the subscript  $y$  is omitted henceforth), as illustrated in Figure 5.5.

The  $n^{th}$  order structure function ( $S^n$ ) for a given  $\delta z$  can be derived from:

$$S_u^n(\delta z) = \langle |u(x, z + \delta z) - u(x, z)|^n \rangle = \int s_{u,\delta z}^n P(s_{u,\delta z}) ds_{u,\delta z} \quad (5.1)$$

The representation of the structure function via its PDF is important in the context of, and is consistent with, the strategy of using the multi-variable joint PDF strategy, as expressed by eq. (3.13).

Here, the focus is on the second-order structure function, or rather its incremental derivative with respect to  $\delta z$ , used as the surrogate of the scale-wise distribution of the energy. As demonstrated by Davidson, Nickels, and Krogstad (2006) and Agostini and Leschziner (2017), there is a close connection between the energy spectra and the derivative of the structure function, as is exemplified by Figures 5.6(a) and 5.6(b) for the total streamwise-fluctuation field. The preference for the structure function is rooted in the fact that it is a purely data-driven method, the results of which do not depend upon a projection basis and on how the hyper parameters are tuned, as is the case for FFT (window size, window function ... ) and wavelet-based analyses (see De Moortel, Munday, and Hood (2004)). Moreover, as the conditional statistics are derived from the *joint pdf* of the structure function, the conditional wavelength can be determined without any specific constraints on the length of the input signal, as this latter can continuously vary with the value of  $Cf_{LS}$ . Another advantage of the structure function is that it allows the contribution of the largest scales resolved by the DNS to be represented much more accurately than via the spectra, which suffer from limitation imposed by the FFT when the sample of scales is sparse and the domain size limited. As will emerge below, length-scale shifts in this derivative will be used to identify length-scale modulation conditional on  $Cf_{LS}$ .

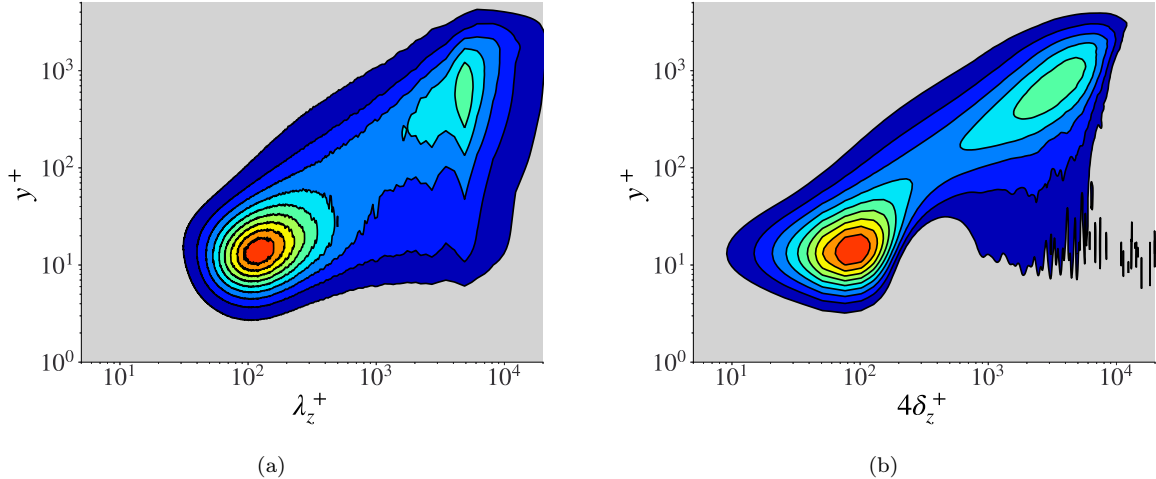


Figure 5.6: Equivalence between (a) premultiplied energy spectra and (b) premultiplied derivative of second-order structure function. Both maps consolidate the full data set for the streamwise fluctuations.

By using the multi-variable PDF approach, the variation of the structure function and its derivative conditional on  $Cf_{LS}$  can be investigated in the same sense as previously undertaken in relation to amplitude modulation, by way of:

$$S_u^n(\delta z) = \iint s_{u,\delta z}^n P(s_{u,\delta z}, Cf_{LS}) ds_{u,\delta z} dCf_{LS} \quad (5.2)$$

$$S_u^n(\delta z)|_{Cf_{LS}} = \int s_{u,\delta z}^n \frac{P(s_{u,\delta z}, Cf_{LS})}{P(Cf_{LS})} ds_{u,\delta z} \quad (5.3)$$

With the joint PDF,  $P(s_{u,\delta z}, Cf_{LS})$ , derived separately for each and every computational  $y$  place and for a set of values  $\delta z$ , the second-order structure function conditional on  $Cf_{LS}$  can be derived using equation (5.3) with  $n = 2$ . Alongside, the conditional structure function  $S_u^2(\delta z)|_{Cf_{LS}}$ , its premultiplied derivative  $\delta z \frac{dS_u^2(\delta z)}{d\delta z}|_{Cf_{LS}}$  can be computed at every wall-normal location. It is this derivative on which attention focuses primarily. Again, the reason is that the variation of this variable across  $\delta z$  is closely connected to the energy-density spectrum  $\Phi_{uu}(\lambda_z)$ , with  $\lambda_z$  connected to the separation  $\delta z$ , as it will be discussed at length in the next chapter (see Agostini and Leschziner 2017, for more details).

A limitation posed by equations (5.2) and (5.3) arises from the fact that the separation  $\delta z$  causes the two fluctuations  $u(x, z)$  and  $u(x, z + \delta z)$  to be located at different values of  $Cf_{LS}$ . However, in practice the spatial variation of  $Cf_{LS}$  is modest within the range of  $\delta z$  of interest and of thus of little effect on the contribution of the difference  $u(x, z + \delta z) - u(x, z)$  to the  $P(s_{u,\delta z}, Cf_{LS})$  distributions. Tests with excluding samples of this difference when the variation in  $Cf_{LS}$  exceeds prescribed limits have been performed by using a limiter  $W$  given by equation (5.4), where only samples satisfying the relation  $W > \alpha$  were retained, as expressed by equation (5.5):

$$W = \frac{2 \times Cf_{LS}(x, z + \delta z) \times Cf_{LS}(x, z)}{(Cf_{LS}(x, z + \delta z))^2 + (Cf_{LS}(x, z))^2} \quad (5.4)$$

$$Cf_{LS} \leftarrow \frac{Cf_{LS}(x, z + \delta z) + Cf_{LS}(x, z)}{2} |_{W > \alpha} \quad (5.5)$$

Use of different values of  $\alpha$ , ranging from 0 to 0.995, was observed to have insignificant consequences to the interpretation of the results.

A feature of the above conditional statistics that hinders an unambiguous interpretation of the modulation process is that field of  $u_{LS}$  is different at different  $y^+$  locations. The objective here is, however, to examine statistics that are conditional on a single reference field. This reference field is chosen to be  $Cf_{LS}$ . This allows questions to be asked about the validity of the quasi-steady concept which hypothesizes that scaling the wall-normal small-scale turbulence properties with the local large-scale wall shear stress  $\tau_{w,LS}$  results in identical

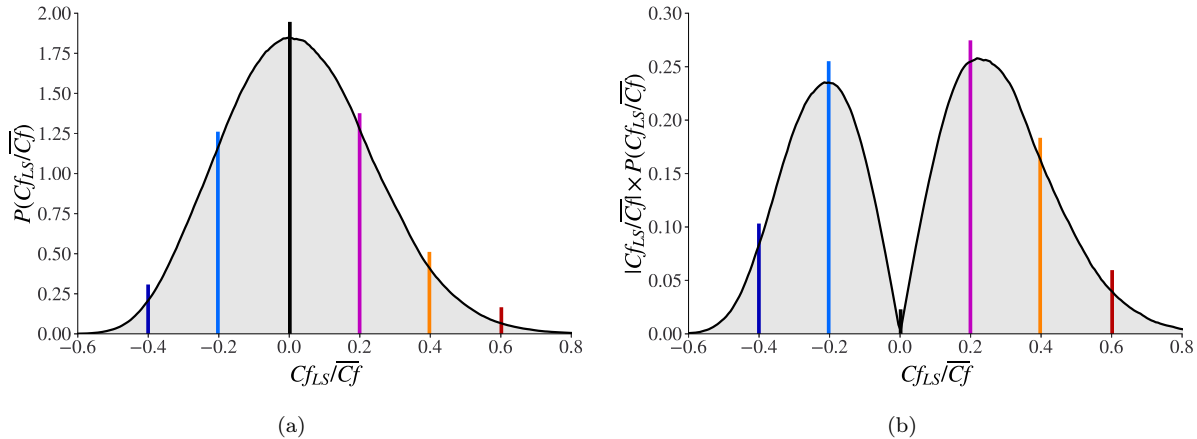


Figure 5.7: PDF of the large-scale skin-friction fluctuations; (a) *pdf* with specific  $Cf_{LS}$  at which profiles of statistical properties are given in figures to follow; (b) PDF premultiplied by  $|Cf_{LS}/\overline{Cf}|$  to accentuate the positive skewness.

statistics, i.e. statistics that do not vary with  $Cf_{LS}$ . However, a question that needs to be addressed is whether the condition  $Cf_{LS}$  is equivalent to the condition  $u_{LS}(y^+)$ . This equivalence is substantially favoured by the fact that large-scale fluctuations are highly correlated in  $y^+$ , subject to a spatial streamwise lag, as is discussed by Hutchins and Marusic (2007a) and several other studies. This has also been found to be the case in the present data set. Hence, here, the assumption has been invoked that  $u_{LS}$  is represented by  $Cf_{LS}$ , subject to the spatial lag  $\Delta x^+ = \Delta y^+ \tan(\theta)$ , with the angle arising from the two-point correlation maps. A consequence of this lag, and thus the gradient in  $u_{LS}$ , is a degree of ambiguity as regards the derivative of  $S(\delta z)$ , which is conditional of  $u_{LS}$  – or rather its  $Cf_{LS}$  equivalent. This is a problem similar to that discussed earlier in relation to spanwise variations in  $u_{LS}$ . However, the lag between two neighbouring  $y^+$  planes is small and the effect on the statistics is thus negligible.

### 5.3.3 Quasi-steady hypothesis

One objective of the study presented in this chapter is to investigate whether the quasi-steady hypothesis (QSH) applies in respect of amplitude as well as length-scale modulation. In essence, the QSH states that: **the small-scale turbulence statistics, when normalised by the local and instantaneous large-scale friction velocity, are universal – i.e., independent of the large-scale fluctuations.** Such a behaviour implies that the turbulence state adjusts itself rapidly to perturbations provoked by the large-scale motion, or that the time scale governing small-scale mechanisms is much shorter than the time scale of the large-scale motions.

In light of the foregoing argument, the QSH may be investigated upon a renormalisation of all statistical properties by reference to the local friction velocity:

$$\overline{X_i}^{+,LS}_{|Cf_{LS}} = \overline{X_i}^+_{|Cf_{LS}} \times u_\tau / u_{\tau,LS} \quad (5.6)$$

$$\overline{x'_i x'_j}^{+,LS}_{|Cf_{LS}} = \overline{x'_i x'_j}^+_{|Cf_{LS}} \times (u_\tau / u_{\tau,LS})^2 \quad (5.7)$$

$$y_{LS}^+ = y^+ \times u_{\tau,LS} / u_\tau \quad (5.8)$$

Thus, when any of the properties is displayed as a map in the  $y_{LS}^+ - Cf_{LS}$  maps, homogeneity in the contours along the  $Cf_{LS}$  axis can be taken to signify the validity of the QSH.

## 5.4 Amplitude Modulation

The present study investigates the modulation of turbulence in a high Reynolds number channel flow, building upon the understanding gained from previous chapters, which showed that modulation is provoked by large-scale-induced fluctuations in turbulence production. These production fluctuations are associated with concurrent streamwise strain and shear stress fluctuations accompanying large-scale ejections, sweeps, and quasi-streamwise vortices. The current flow not only has a significantly higher Reynolds number but also employs a different large-scale/small-scale decomposition strategy compared to the BEMD approach used previously.

The most evident manifestation of modulation is the amplification and attenuation of the streamwise energy, although the spanwise and wall-normal components also provide clear evidence of modulation. The response of the streamwise energy is conveyed in four ways:

- Figures 5.8(a) and 5.8(b) show contour plots and profiles for the total (small-scale + large-scale components), respectively.
- Figures 5.8(c) and 5.8(d) examine the validity of the quasi-steady hypothesis by rescaling the results from Figures 5.8(a) and 5.8(b) using the local skin friction ( $u_{\tau,LS}$ ) according to equations (5.6)-(5.8).
- Figures 5.9(a) and 5.9(b) pertain to the response of the small-scale energy component only to the large scales.
- Figures 5.9(c) and 5.9(d), corresponding to Figures 5.8(c) and 5.8(d) in the referential of the local friction velocity, expose the validity of the quasi-steady hypothesis for the small-scale energy only.

The profiles are given at six values of  $Cf_{LS}$  marked in the PDF  $P(Cf_{LS})$  shown in Figure 5.7. The PDF exhibits positive skewness, implying a tendency for large positive footprints to dominate over large negative ones, a feature also observed, albeit more pronounced, at  $Re_{\tau} \approx 1025$ .

Figures 5.8(a) and 5.8(b) reveal strong amplification and somewhat more moderate attenuation of the streamwise energy in the buffer layer for positive and negative footprints, respectively. In contrast, the energy in the outer layer is negatively correlated with the footprints. These features are well-known and have been reported in previous studies for other flows, reflecting fluctuations in strain-induced turbulence generation. Figures 5.8(c) and 5.8(d) suggest that the quasi-steady hypothesis holds for the streamwise energy, but only in the viscosity-affected layer, up to  $y^+ \approx 80$ , within which the time scale of the small-scale motions is substantially shorter than that of the footprints, in qualitative agreement with previous observations for  $Re_{\tau} \approx 1025$ .

With attention redirected to the results for the small-scale energy, in Figure 5.9, it is observed first that the amplification and attenuation levels in the buffer layer are very similar to those of the total energy, Figure 5.8, signifying the strong dominance of the small-scale energy component at the wall. However, in the outer region, the large scales dominate, and the sensitivity of the small-scale turbulence to the large scales is low. Again, in anticipation of what is to follow, it is remarked here that the behaviour both in the inner and outer layers is driven by conditional shear-strain fluctuations which are of opposite sign in the inner and outer layers for any given  $Cf_{LS}$  value.

The generative mechanism which is responsible for the modulation shown in Figure 5.8 is clarified by way of the shear-stress profiles in Figure 5.10 in conjunction with the streamwise-energy production in Figure 5.11. The latter profiles are shown in two ways: the default form in 5.11(a) and the  $y^+$ -premultiplied form in 5.11(b). The latter profiles accentuate the sensitivity in the outer layer in which actual production fluctuations are rather weak, but nevertheless clearly present. The shear-stress profiles demonstrate that the modulation of this stress follows closely that of the streamwise energy. The fact that the production also follows the same trends is due to the perturbations in the conditional shear strain being aligned with those of the shear stress: the near-wall strain steepens for positive  $Cf_{LS}$  and weakens for negative values, the reverse occurring in the outer layer. These strain fluctuations go hand-in-hand with large-scale sweeps, for positive  $Cf_{LS}$  values, and ejections for negative values. While profiles of the shear-stress production are not included herein, it is noted that these too follow similar trends as the streamwise-stress production, because the wall-normal stress is also modulated in a manner analogous to that of the other stress components. This includes the spanwise stress, profiles of which are given in Figure 5.12. While the production of this stress is zero, of course, the pressure-strain-interaction mechanism transfers energy from the streamwise to the spanwise stress component, thus causing a rise and fall in the near-wall stress alongside corresponding variations in the streamwise stress. The

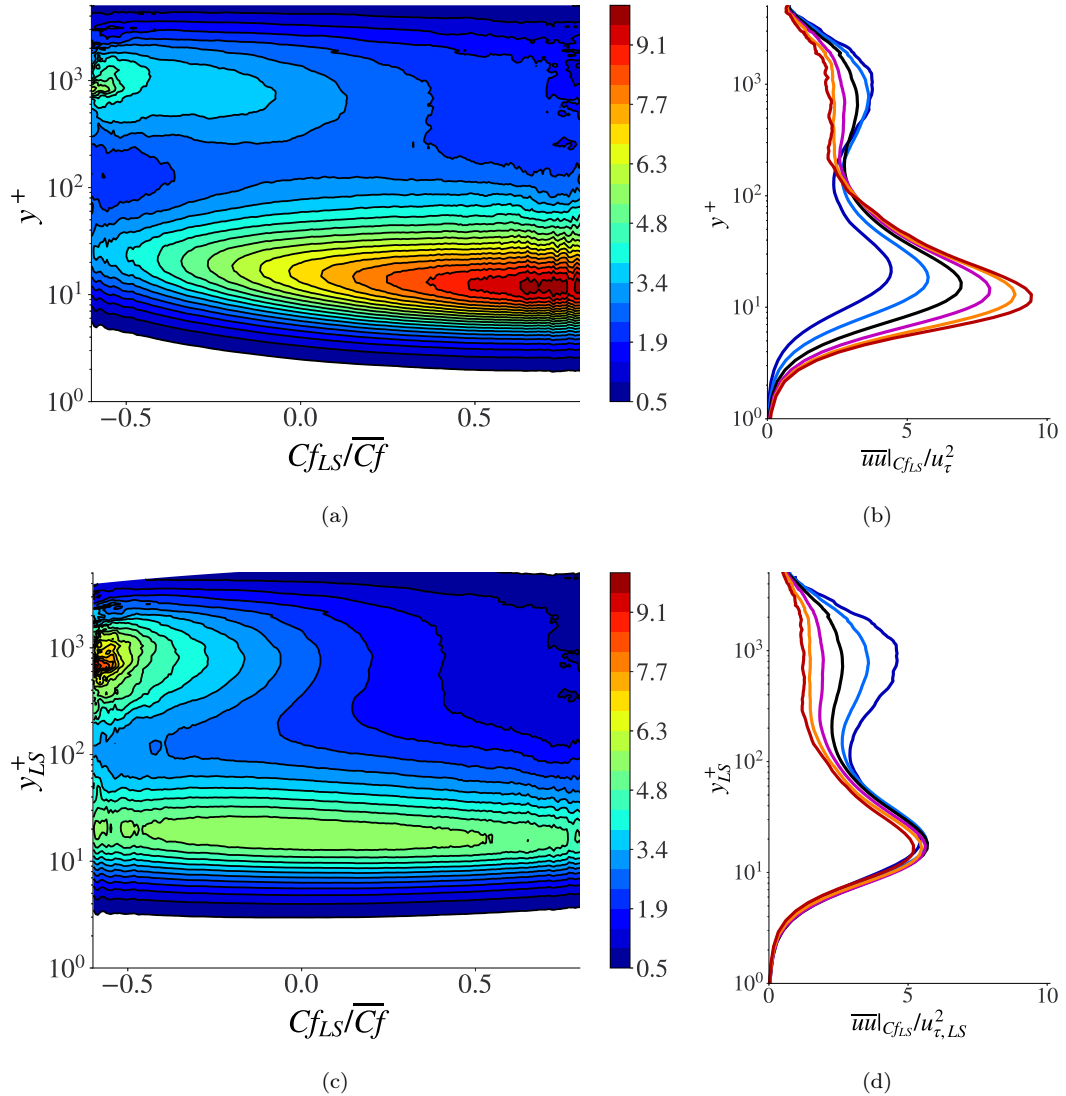


Figure 5.8: Conditional response of the streamwise energy to the large-scale skin friction  $Cf_{LS}$ ; (a) contours of conditional energy; (b) Profiles of conditional energy at locations marked on the inserted PDF; (c) contours in (a) re-scaled according to eqs.(5.6)-(5.8); (d) profiles in (b) re-scaled according to eqs. (5.6)-(5.8).

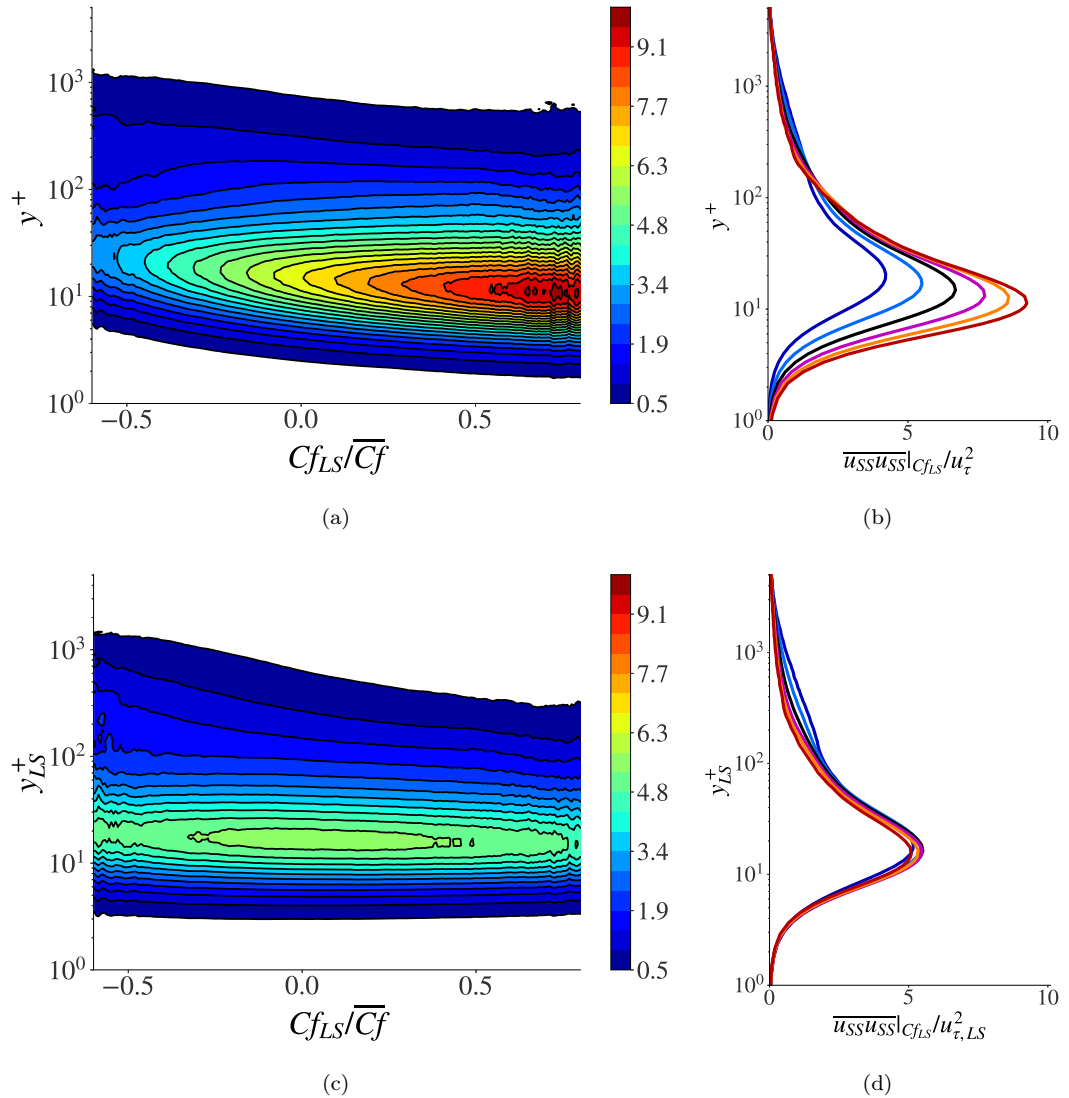


Figure 5.9: Conditional response of the small-scale component of the streamwise energy to the large-scale skin friction  $C_{f,LS}$ ; (a): contours of conditional energy; (b) profiles of conditional energy at locations marked on the inserted pdf; (c) contours in (a) re-scaled according to eqs. (5.6)-(5.8); (d) profiles in (b) re-scaled according to eqs. (5.6)-(5.8).

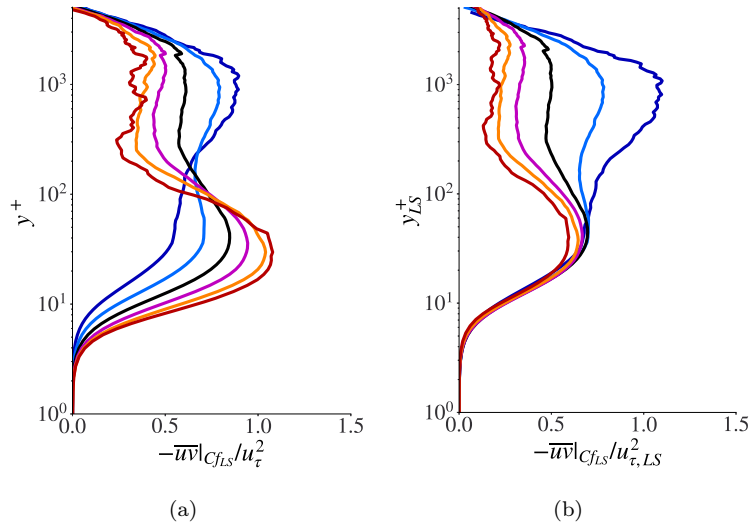


Figure 5.10: Conditional response of the shear-stress energy to the large-scale skin friction  $Cf_{LS}$ ; (a) Profiles of conditional stress at locations marked in Figure 5.7; (b) profiles in (a) re-scaled according to eqs. (5.6)-(5.8).

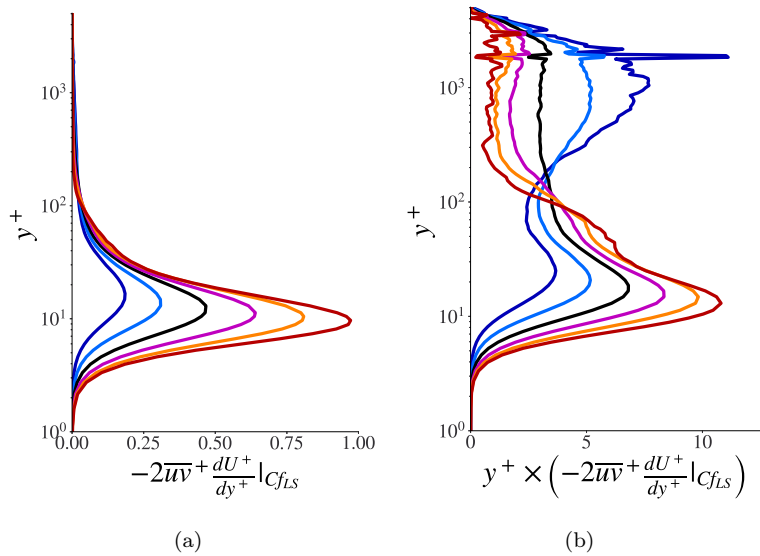


Figure 5.11: Conditional response of the production of the streamwise energy component to the large-scale skin friction: (a) profiles of conditional production at locations marked in Figure 5.7; (b) profiles in (a) premultiplied by  $y^+$ .

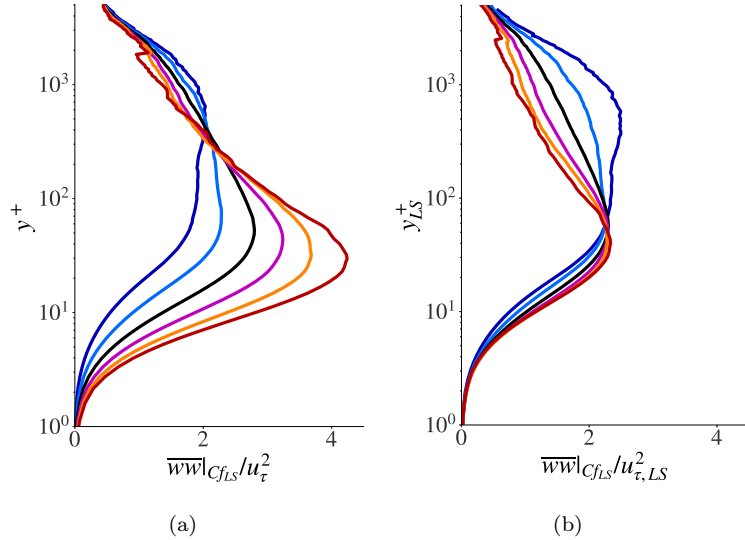


Figure 5.12: Conditional response of the spanwise energy to the large-scale skin friction  $Cf_{LS}$ ; (a): profiles of conditional stress at locations marked in Figure 5.7; (b): profiles in (a) re-scaled according to eqs. (5.6)-(5.8).

shear stress is seen to comply with the quasi-steady hypothesis, albeit over a reduced wall distance relative to the streamwise stress. Adherence of the spanwise stress with the quasi-steady hypothesis is markedly worse, however, and this departure has also been observed for channel flow at  $Re_\tau \approx 1025$  (see Agostini and Leschziner 2019a). In that chapter, the author discuss in some detail (see Figures 5.7 and 5.8 in that paper) the role of wall “splatting” provoked by large-scale sweeps on the near-wall behaviour of the spanwise stress. In particular, sweep-induced splatting causes a substantial strengthening of the spanwise fluctuations close to the wall, which partially decouples this stress from the processes governing the streamwise fluctuations and thus also from the associated universal scaling with the large-scale streamwise wall shear stress. A possible contributory reason for the indifferent behaviour shown in Figure 5.12(b) is a time lag between the elevation of the turbulence intensity by production and the transfer of some of that energy to the spanwise stress, thus likely to weaken the universality of the scaling of this stress with the large-scale wall shear stress.

## 5.5 Length-Scale Modulation

Figure 5.13 shows six maps of the premultiplied derivative of the second-order structure function in the  $\delta z^+ - y^+$  plane at the 6 conditional values of  $Cf_{LS}$  shown in the PDF of Figure 5.7. Attention is first drawn the choice of the abscissa:  $4\delta z^+$ . The choice of this multiplier is rooted in the correspondence between the derivative of the structure function and the spectra, an equivalence shown in Figure 5.6 and discussed by Agostini and Leschziner (2017). In the latter, the abscissa is conventionally the wave length  $\lambda_z^+$ . Multiplying  $\delta z^+$  by 4 is observed to shift the peak in the map at  $y^+ \approx 12$  and  $Cf_{LS} = 0$  to the value to  $4\delta z^+ \approx 100$ , corresponding to  $\lambda_z^+ \approx 100$  – i.e., the accepted level of the spanwise separation distance between streaks as derived from two-point correlations.

There are three observations that can now be made by reference to Figure 5.13. First, as  $Cf_{LS}$  increases, there is a progressive shift of the maximum towards the wall. This process and the mechanisms responsible have been discussed in detail in Chapter 4. In essence, large positive  $Cf_{LS}$  levels cause a steepening of the strain close to the wall, thus generating increased small-scale turbulence and thinning the viscous sublayer. More interesting in the present context is that the increase in  $Cf_{LS}$  is also accompanied by a progressive reduction in the length-scale maximum from  $4\delta z^+ \approx 100$  to around 65, which may be interpreted as indicating the length-scale modulation. The third feature deserved to be highlighted is the progressive widening of the scale spectra around the buffer layer for increasing  $Cf_{LS}$ . This widening appears to be due primarily to a shift of the range of short length scales towards lower values, a process especially noticeable when tracking the left-most edge of the spectra at  $y^+ \approx 10$ . In contrast, the longer scales around the buffer layer, at

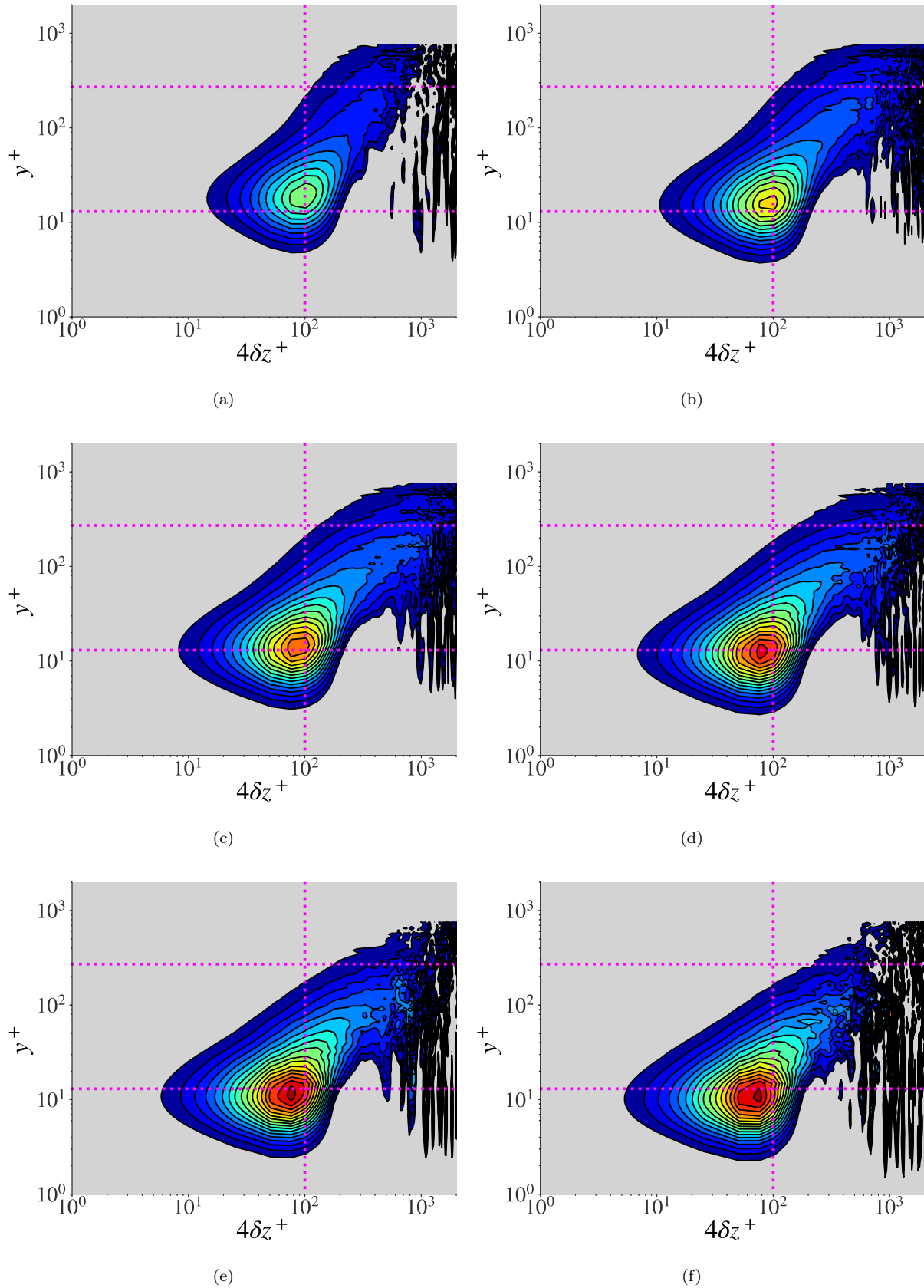


Figure 5.13: Maps of  $\delta z \frac{dS_u^2(\delta z)}{d\delta z}|_{Cf_{LS}}^+$  in the  $y^+ - \delta z^+$  plane conditional on the six  $Cf_{LS}$  shown in Figure 5.7; (a)-(f) arranged in order of rising  $Cf_{LS}$  values.

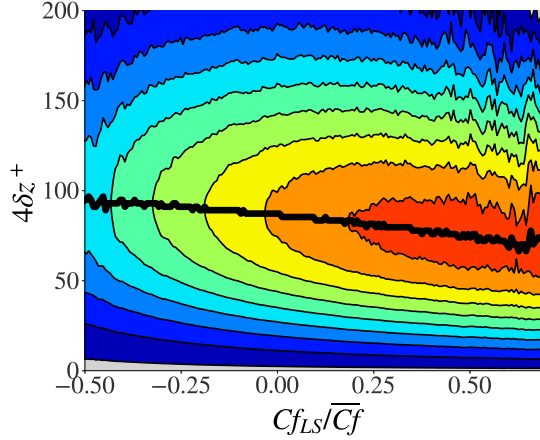


Figure 5.14: Map of  $\delta z \frac{dS_u^2(\delta z)}{d\delta z}|_{Cf_{LS}}^+$  in the  $\delta z^+ - Cf_{LS}^+$  plane at  $y^+ \approx 13$ . The black line is the locus of maximum conditional value of the premultiplied derivative, demonstrating the reduction in wavelength with  $Cf_{LS}$ .

$4\delta z^+ \approx 200$ , experience no discernible shift (the downward-pointing tongues at  $4\delta z^+ > 1000$  signify the footprinting process). The increased predominance of small scales with increasing  $Cf_{LS}$  will be revisited later in the context of discussing the applicability of the QSH to the length-scale modulation.

The length-scale reduction is well brought out in Figure 5.14, which shows contours of the premultiplied gradient of the second-order structure function in the  $Cf_{LS}-\delta z^+$  plane, derived by taking, for each value of  $Cf_{LS}$  (many more than included in Figure 5.13),  $\delta z^+$ -wise cuts at levels  $y^+$  at which the peaks of the derivative arise. The black line is thus the locus of the peak of the gradient across the  $Cf_{LS}$  range. This corresponds almost identically to the location  $y^+ \approx 13$ , scaled with the mean wall shear stress. As seen, the length scale for the location of the peak value in  $\delta z \frac{dS_u^2(\delta z)}{d\delta z}|_{Cf_{LS}}^+$  reduces from around 100 at high negative large-scale fluctuations to around 65 at the highest large-scale fluctuations.

To examine whether the QSH applies to the length-scale modulation, a map of contours of the wave length corresponding to the maximum value of the derivative of the structure function at different  $y^+$  values and conditional on  $Cf_{LS}$  is derived. This is shown in Figure 5.15(a). The map demonstrates that the wave length of the maximum derivative location at any given  $y^+$  is decreasing, as already observed by reference to Figures 5.13 and 5.14. For example, at  $y^+ \approx 13$ , the wave length in Figure 5.15(a) is seen to decline from 100 (green shade) to around 70 (dark blue shade), which is clearly consistent with the black line in Figure 5.14. Next, the map in Figure 5.15(a) is re-scaled with the wall-normal distance and the wave length normalised with the large-scale wall shear stress, in accordance with equation (5.8) and  $\delta z^{+,LS} = \delta z^+ \times u_{\tau,LS}/u_\tau$ . This yields the map given in Figure 5.15(b), which permits two major observations to be made. First, the contours are broadly horizontal in the positive range of  $Cf_{LS}$ , implying that the QSH applies to frequency modulations of the fluctuations within the near-wall layer,  $y^+ < 40$ . Second, the hypothesis is not satisfied for negative large-scale fluctuations. As the length-scale modulation is here considered within the confines of the near-wall layer, up to  $y^+$  of approximately 40, the lack of adherence of length-scale fluctuations with the QSH at negative  $Cf_{LS}$  is inconsistent with the behaviour observed in respect of the amplitude modulation. Similar observations can be made in respect of the maps shown in Figure 5.16 for the structure function  $S_w^2$  – i.e., those pertaining to the spanwise fluctuations, which also show a limited correspondence to the quasi-steady hypothesis.

It can be argued that there is no compelling reason for why amplitude and length-scale modulation should strictly go hand-in-hand. A possible, albeit somewhat tentative, interpretation of the behaviour in Figures 5.15 and 5.16 starts from the observation that the width of the spectra of scales in Figure 5.13 is narrowing at negative  $Cf_{LS}$  and broadening for positive  $Cf_{LS}$ . As observed earlier, by reference to Figure 5.14, the predominant feature of the broadening spectrum to  $Cf_{LS}$  is a shift of the length-scale range towards lower values. It is recalled that the conditional energy and shear strain increase for positive  $Cf_{LS}$  and decrease for negative values, with the conditional strain and the velocity itself following suit. It is reasonable

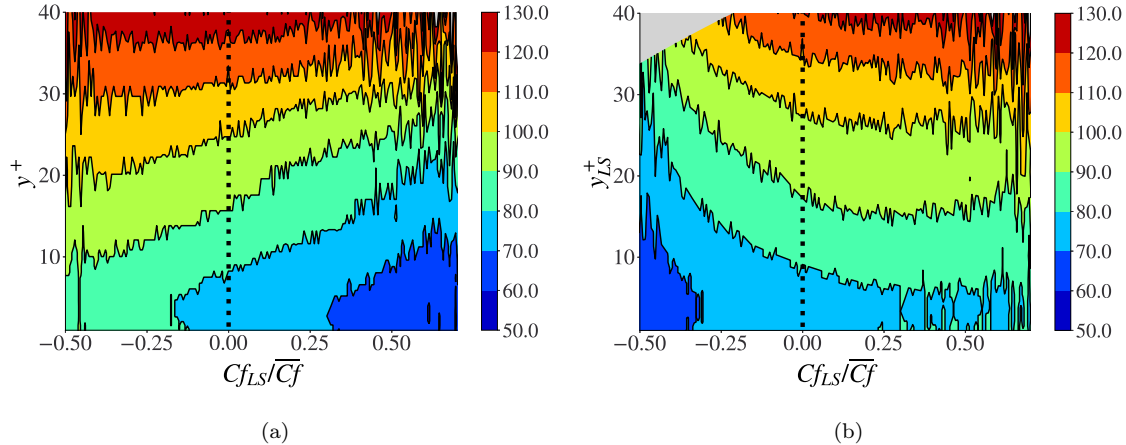


Figure 5.15: Maps of conditional  $4\delta z^+|_{Cf_{LS}}$  in the  $y^+ - Cf_{LS}$  plane derived from  $\delta z \frac{dS_u^2(\delta z)}{d\delta z}|_{Cf_{LS}}^+$  (for streamwise fluctuations); (a) nominal field scaled with mean wall shear stress; (b) field in (a) rescaled with large-scale wall shear stress (eq. (5.8)) to demonstrate adherence to the quasi-steady hypothesis.

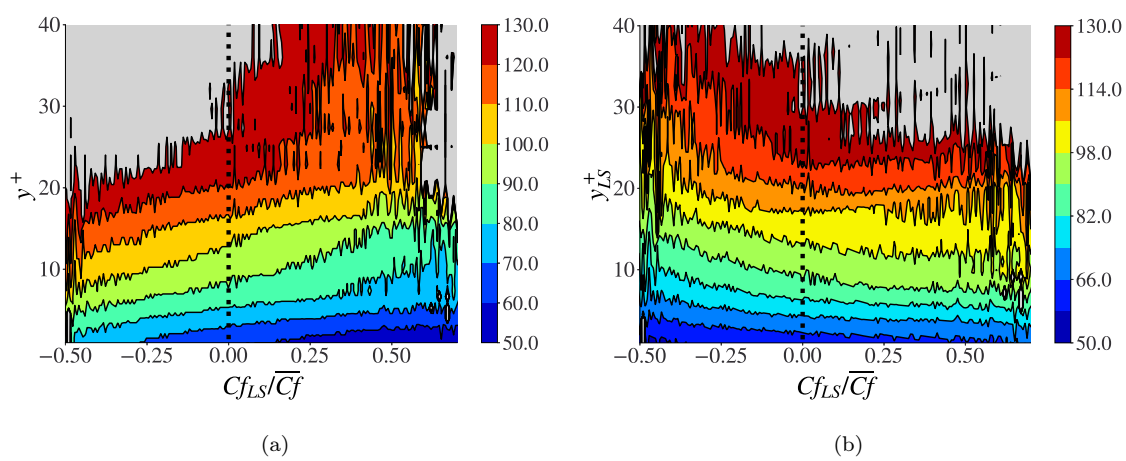


Figure 5.16: Maps of conditional  $4\delta z^+|_{Cf_{LS}}$  in the  $y^+ - Cf_{LS}$  plane derived from  $\delta z \frac{dS_w^2(\delta z)}{d\delta z}|_{Cf_{LS}}^+$  (for spanwise fluctuations); (a) nominal field scaled with mean wall shear stress; (b) field in (a) rescaled with large-scale wall shear stress (eq. (5.8)) to demonstrate adherence to the quasi-steady hypothesis.

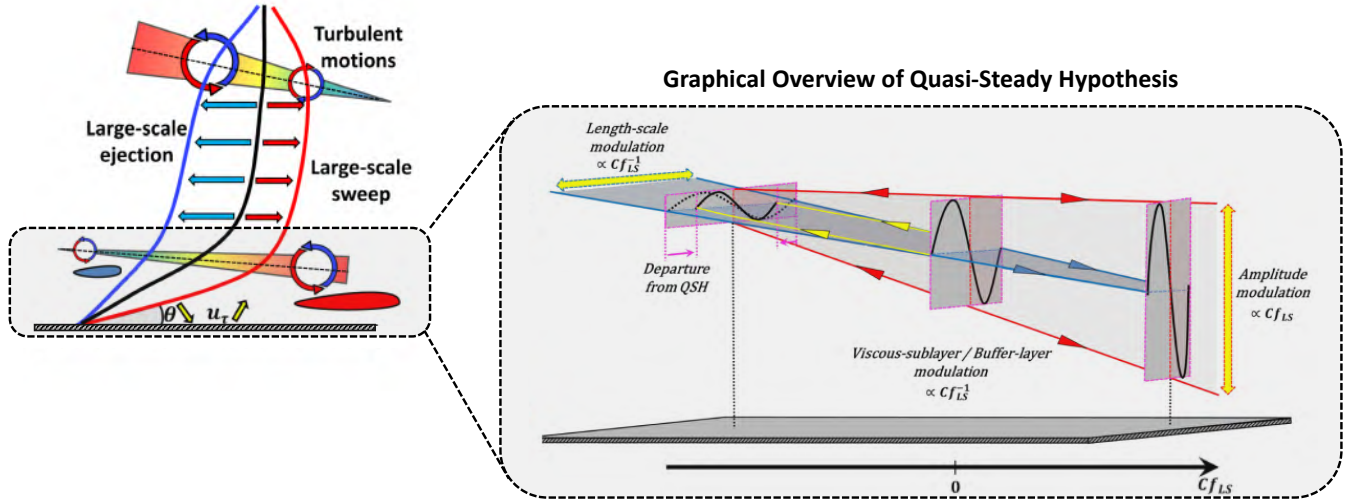


Figure 5.17: Conceptual representation of the effects of large-scale fluctuations on the strain rate and consequent amplification/attenuation of near-wall and outer-layer turbulence, in r.h.s plot the modulation of the near-wall turbulence induced by outer large-scale motions as predicted by the Quasi-Steady Hypothesis. Modulation closely in portion with  $Cf_{LS}$  indicates adherence to QSH and represented by straight diverging red and converging blue lines. Departure of length-scale modulation from QSH for negative  $Cf_{LS}$  indicated by curved yellow lines.

to argue, therefore, that the likely response of the spectra to this increase and decrease is the observed shift of the small-scale end of the scale spectra towards or away from low values, respectively. In fact, this shift has already been highlighted earlier when the spectra in Figure 5.13 were discussed. A shift towards smaller scales will favour the QSH, while a greater prevalence of larger scales will prejudice the hypothesis. Figure 5.15(a) indeed shows a continuous decline in the length scale across the entire range of  $Cf_{LS}$ . The fact is, however, that the large-scale shear stress in the negative  $Cf_{LS}$  range increases at a faster rate than the rate at which the length scale drops, which then results in the violation of the QSH in the left-hand-side part of Figure 5.15(b). Here, the objection might be raised that the same does not apply to the stress components (except perhaps  $wu^+$ ). However, it is reasonable to assume that velocity fluctuations are more closely tied to (and are more akin to) the shear velocity than is the length scale. Hence, it is not entirely surprising to observe differences in the level of adherence to the hypothesis for physically different types of statistical properties.

## 5.6 The Quasi-Steady Hypothesis: Extent of Applicability in Near-Wall Turbulence

This study combined a joint, multiple-variable joint-PDF methodology, with two entirely novel elements – a decoder-encoder-based scale-decomposition technique and the conditional derivative of the structure function — for the purpose of analysing the response of the near-wall layer in a turbulent channel flow at  $Re_\tau \approx 5200$  to energetic large-scale outer structures in the log-layer. The joint-PDF technique was previously exploited to reveal the mechanisms underpinning the observed amplitude modulation by large-scale footprinting in the boundary layer of a channel flow at  $Re_\tau \approx 1025$ . Here, amplitude modulation is re-examined, as one part of the study, for a channel flow at a much higher Reynolds number by processing full-volume DNS realisations generated by Lee and Moser (2015). The structure function, derived by sampling the DNS data conditionally on large-scale skin-friction footprints, is used to investigate the modulation of the length scale in the near-wall layer. The main conclusions can be summarised as follows:

- As is conveyed by the conceptual sketch in Figure 5.17, the overarching conclusion of the study is that the modulation of the energy around the buffer layer rises in proportion to the large-scale skin friction  $Cf_{LS}$ , while the length scale modulation declines at a similar rate.

- The amplitude modulation of the stresses follows, qualitatively, that observed previously for  $Re_\tau \approx 1025$ , but is more intense and more pronounced (see Agostini and Leschziner 2014; Agostini and Leschziner 2019a, for results at  $Re_\tau \approx 1025$  ).
- The conditional streamwise stress in the buffer layer varies within the range of approximately 70% of the mean over the range of the skin-friction footprints. Similar variations arise in the conditional shear stress and the spanwise energy. In all stress components, the levels are amplified for positive large-scale skin-friction fluctuations and are attenuated for negative ones. These variations are governed primarily by the response of the small-scale components to the footprints – i.e., sweeps and ejections produced by the outer large-scale structures.
- The response of the conditional stresses in the outer layer is negatively correlated with the footprints — i.e., their response is opposite to that of the near-wall stresses. In this layer, the large-sale components dominate over the small-scale ones, and thus the modulation is primarily a reflection of the role of the large-scale stresses.
- The generation rate of the streamwise energy varies in harmony with the stress components — i.e., the generation is positively correlated with the large-scale footprints in the buffer layer, while they are negatively correlated in the outer layer. This is entirely in accord with previous observations and strengthens the conclusion that the modulation is a consequence of the conditional production being driven by large-scale sweeps and ejections, the former provoking buffer-layer implication and the latter outer-layer amplification.
- Rescaling the conditional stresses, production and wall-normal distance with the large-scale wall shear stress is shown to support the quasi-steady hypothesis, but the validity of the hypothesis is confined to the near-wall layer,  $y^+ < 80$ . Adherence of the spanwise energy to the quasi-steady hypothesis is rather less good than that of the streamwise and shear-stress components, and this is attributed to distortions associated with sweep-induced "splatting" (flattening the structures) at the wall, and with the time lag between the production and the redistribution (pressure-strain) process.
- The modulation of the length scale is quantified primarily by way of the shift in the peak of the conditional derivative of the second-order structure function for the streamwise fluctuations in the buffer layer, at the location commensurate with that of the maximum energy density in the spectrum. This maximum is found to decrease progressively by about 40% across the range of the large-scale footprints. The shift in the maximum declines with increasing  $y^+$  when judged by reference to the peak at that  $y^+$  location. A qualitatively similar behaviour is observed in respect of the structure function for the spanwise fluctuations.
- Only a tentative interpretation of the length-scale modulation can be offered. This is based on the observation that the spectrum of scales widens with increasing  $Cf_{LS}$  values, thus increasing the content and contribution of smaller scales and hence also decreasing the length scale at the peak of the conditional derivative of the structure function.
- The conditional length scale is found to adhere to the quasi-steady hypothesis only for positive large-scale footprints. In the negative range, the friction velocity declines faster than the rate at which the length scale increases, so that the length scale, when rescaled with the friction velocity of the footprints, is not constant across the  $Cf_{LS}$  range (a limitation indicated schematically by the broken yellow lines in Figure 5.17). This is at variance with the behaviour observed in respect of the stresses, but there is no compelling physical reason to believe that both should go strictly hand-in-hand.

A combined approach of joint probability density function statistics and a novel decoder-encoder technique was utilised to analyse large-scale modulation of near-wall turbulence in a channel flow at  $Re_\tau \approx 5200$ . A key finding was buffer layer shear stresses exhibiting  $\approx 70\%$  variation across the footprint amplitude range. This large modulation arose from small-scales responding to sweeps and ejections that alter shear production. Rescaling stresses by the local large-scale friction velocity showed adherence to the quasi-steady hypothesis, whereby small-scale statistics become universal when normalised by the instantaneous wall shear stress due to large-scales. However, length scales quantified through the conditional structure function peak followed quasi-steady behaviour only for positive footprints, diverging for negative footprints. This divergence may originate from widening of scale spectra under negative footprints.

# Chapter 6

## Between Streaks and “Super Streaks”: the Attached Eddies

### 6.1 Introduction: Attached Eddies’ Paradigm

The Townsend-Perry Attached-Eddy Hypothesis (AEH) is a fundamental concept underpinning the statistical physics of sheared near-wall turbulence. A key aspect is that the energy-containing motions in the logarithmic region are generated by coherent eddies with dimensions and energy scaling linearly with distance from the wall. The logarithm region defined by regions 1 and 2 in Figure 6.2(a) is thus populated by self-similar eddies.

Figure 6.1 graphically presents this conceptual model, illustrating four distinct attached eddies labelled as  $e_1$  through  $e_4$ . Here,  $e_1$  is the smallest, and  $e_4$  is the largest. Close to the wall, all eddies interact with and influence the local flow. However, as one moves further from the surface, the impact of the smaller attached eddies gradually decreases (Townsend 1980). This introduces the concept of eddy “attachment”, which does not suggest a physical anchoring to the surface. Instead, it indicates that the features of an eddy are shaped by the wall, as the latter instigates a blocking effect that enhances wall-parallel velocity fluctuations and reduces wall-normal disturbances (Townsend 1980).

Statistical self-similarity represents a fundamental characteristic of attached eddies, implying that across the spectrum of existing scales, their relative geometry and energy content maintain consistent scaling. Given that the energy of an eddy scales in accordance with its size, normalising energy by wall distance and the wavelength results in superimposed energy profiles (as illustrated in Figure 6.1), thereby validating the self-similarity of these structures (Townsend 1980).

When the premultiplied power spectra are plotted against the wall-distance ( $y$ ) and the spanwise wavelength ( $\lambda$ ), they form a triangular domain. This formation is attributed to the fact that, when moving away from the wall, scales shorter than the wall-normal location cease to exert influence on the flow. Since the lower limit of integration is determined by  $y$ , it follows that the wavelength domain of energetic scales shortens with increasing distance from the wall. As result, the variance, defined as the integral of the premultiplied spectra, demonstrates a logarithmic decline with the escalating distance from the wall (see eq.(6.1)).

Townsend’s conceptual hypothesis provided the basis for Perry and Chong’s 1982 hierarchical attached eddy model, proposing wall turbulence consists of geometrically self-similar eddies spanning viscous to outer scales (Perry and Chong 1982), with doubling size between hierarchies, as illustrated in Figure 6.1.

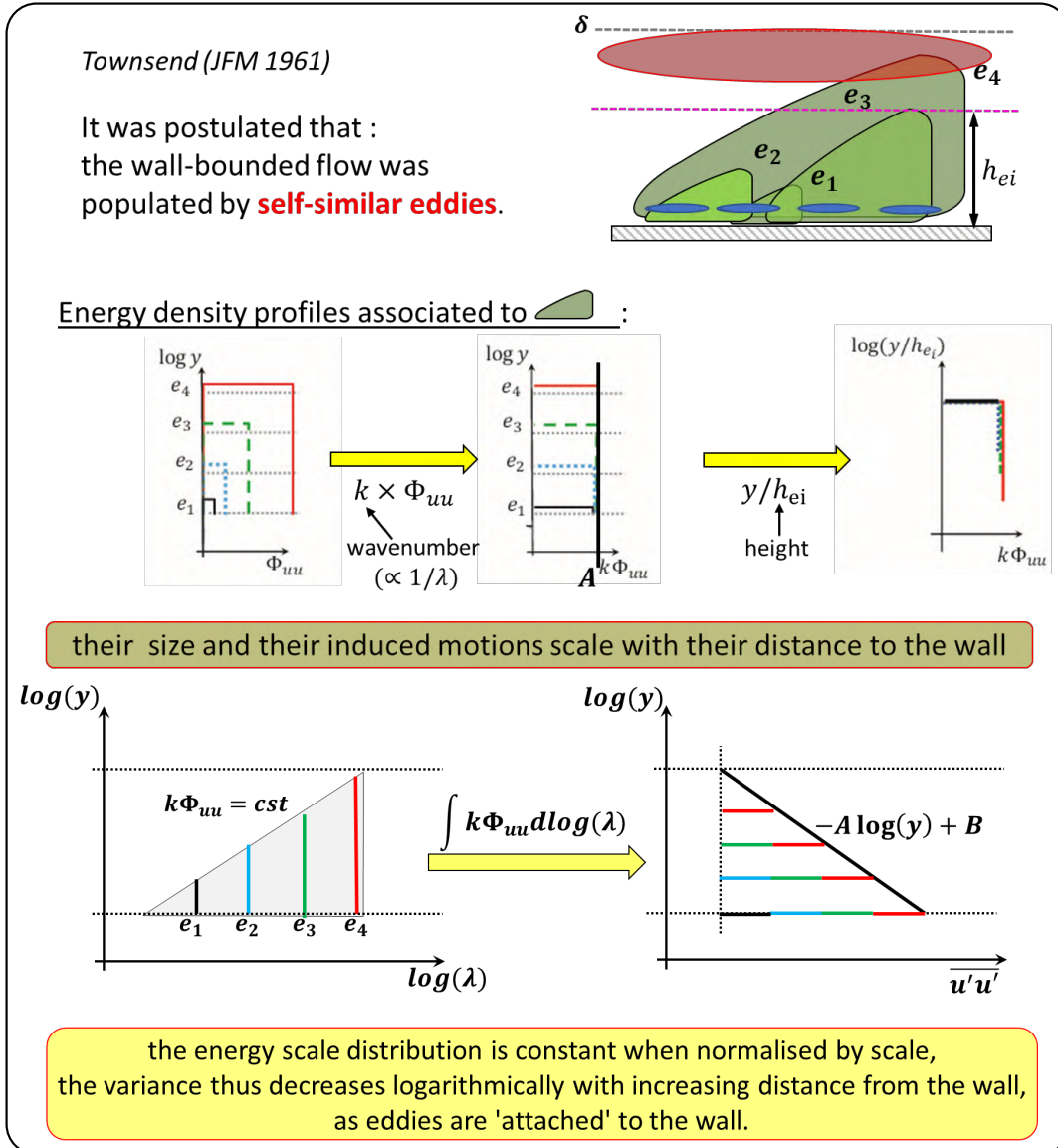


Figure 6.1: Conceptual view of Attached Eddies Hypothesis, illustration of self-similarity (size and induced motions scale with distance to the wall) and implications.

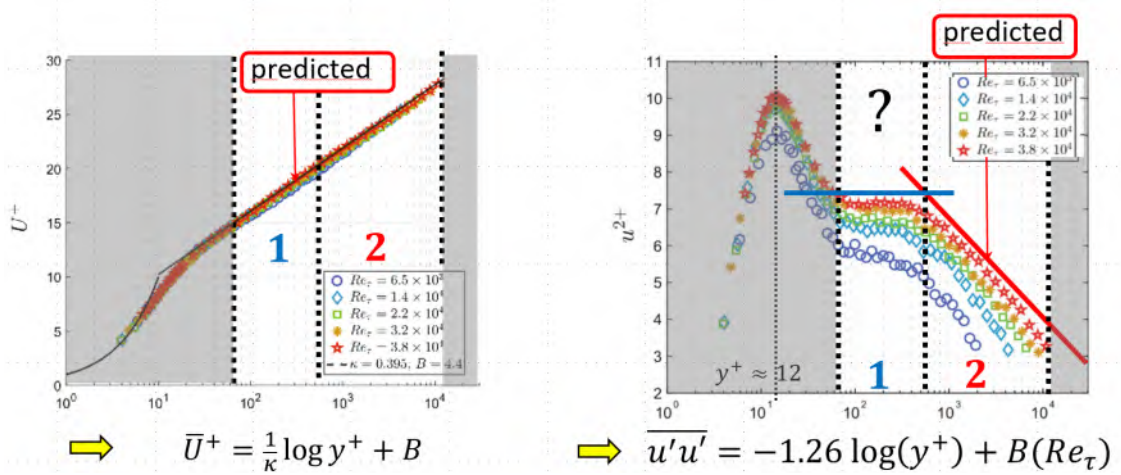


Figure 6.2: Wall-normal distribution of: (a) the mean streamwise velocity and (b) streamwise stress obtained from experimental data in Turbulent Pipe flow (exp. CICloPe) Fiorini et al. (2017), for  $Re_\tau$  between  $6.5 \times 10^3$  to  $3.8 \times 10^4$ .

To resume, the attached eddy hypothesis continues to serve as a fundamental framework for statistically understanding the physics of near-wall turbulence, particularly in relation to the two characteristics outlined above :

- **Self-similarity** - In the Attached Eddy Hypothesis, “self-similarity” refers to the principle that eddies, or turbulent structures, maintain a uniform relative geometry and energy scaling across various scales. This concept suggests that larger eddies are statistically equivalent to their smaller counterparts, but magnified in size. When normalised by wavelength and wall-distance, energy profiles superimpose due to this scale invariance, thus demonstrating self-similarity.
- **Logarithmic variance decrease** - Within the logarithmic layer, the energy spectra adhere to the law  $\Phi_{uu}(k_x) \propto k_x^{-1}$ ,  $\Phi_{ww}(k_x) \propto k_x^{-1}$ , indicating that a constant value is assumed by the pre-multiplied spectra (Perry, Henbest, and Chong 1986; Perry and Marusic 1995; Nickels et al. 2005). When the premultiplied power spectra are integrated over wavelengths, the linear wall-distance dependence of the lower integration limit results in a logarithmic decay of the streamwise and spanwise turbulence-energy components,  $u'u'$  and  $w'w'$  respectively, towards the edge of the velocity log layer. This is substantiated by Figure 6.2, which depicts the streamwise stress derived from experimental data in turbulent pipe flow for  $Re_\tau$  in the range of  $6.5 \times 10^3$  to  $3.8 \times 10^4$  (Fiorini et al. 2017). The plot unambiguously demonstrates a logarithmic decay of streamwise turbulence energy within Region 2, and this log layer lengthens in the wall-normal direction as the Reynolds number increases.

Wall-bounded flow close to the wall is typically divided into three regions: the viscous sublayer, the buffer layer, and the logarithmic layer. The AEH, as introduced by Townsend and Perry, suppose that the attached eddies are primarily located within this logarithmic layer. However, within the logarithmic layer, two distinct behaviours are displayed by the wall-normal distribution of the streamwise velocity variance: a plateau in the first part, identified as Region 1, and a logarithmic decrease in the latter part, referred to as Region 2, consistent with the predictions of the AEH. The existence of a plateau in Region 1 is not consistent with the AEH. This discrepancy has led numerous studies to suggest that attached eddies populate only Region 2 of the logarithmic layer. There are however two important questions that remain unanswered: why does the AEH not apply to region 1, and what is the cause of the plateau observed in this region 2?

## 6.2 Introduction: The Application and Limitations of the Attached Eddy Hypothesis

Since the AEH is founded on the concept of self-similarity, a natural approach to elucidate its applicability and limitations involves investigating the energy’s scale-distribution, and thus show its  $k_x^{-1}$  varia-

tion. As the presence of this latter is not easily identifiable, at least in one-dimensional spectra at moderate Reynolds-number values, Davidson et al. (2006) proposed that the second-order structure function  $S_{2,u}(\delta_x) = \langle [u(x + \delta_x) - u(x)]^2 \rangle$  should provide a more sensitive indicator of the validity of the AEH. They show that the behaviour is consistent with a logarithmic rise of  $S_{2,u}(\delta_x)$  up to the integral length scale, beyond which the structure function tends to a constant value. When the structure function is scaled with the squared of the shear velocity  $u_\tau^2$ , and  $\delta_x$  is scaled with  $y$ , the expectation is that it should display a universal behaviour, independent of the wall distance  $y$ , and this is indeed demonstrated for two particular boundary layers at momentum-thickness Reynolds-number values  $Re_\theta = 12600$  and  $37500$ , the latter corresponding to  $Re_\tau \approx 14000$  (Davidson, Nickels, and Krogstad 2006; Davidson et al. 2006). A focus on  $S_{2,u}(\delta_x)$ , as a diagnostic indicator of wall-normal eddy organisation and the AEH, was most recently advocated by Silva et al. (2015) and Chung et al. (2015), the former analysing the structure of boundary layers at  $Re_\tau$  up to approximately  $10^6$ , and the latter aimed primarily at reconciling significant differences between high-Reynolds-number boundary-layer and pipe-flow data in respect of the  $k_x^{-1}$  region in the associated spectra. In common with most studies examining aspects of the AEH, de Silva *et al.* concentrate their attention on the outer portion of the respective boundary layers, beyond the position of the plateau (or second maximum) in the wall-normal variation of the streamwise turbulence-energy component, where the second-order structure function varies logarithmically with the two-point separation and where the variations collapse if this separation is normalised by the wall distance (corresponding to region 2 in Figure 6.2). Based on theoretical considerations by Woodcock and Marusic (2015), who provide theoretical support and rigorous model for the AEH, de Silva *et al.* also extend their investigation to higher-order structure functions and demonstrate a logarithmic-scaling behaviour for these functions at sufficiently high Reynolds-number values and a separation distance larger than the wall distance.

Townsend's and Perry's original interpretation was that the AEH applies to the entire velocity log-law region – i.e to both regions 1 & 2 shown in Figure 6.2. Studies consistent with this view are those of Davidson *et al.* (Davidson, Nickels, and Krogstad 2006; Davidson et al. 2006) and Hwang (2015). The former discusses the logarithmic behaviour of the structure function within the range  $100 < y^+ < 200$ , in relation to the  $k_x^{-1}$  behaviour that is observed by Nickels et al. (2005) to apply in the boundary layer at  $Re_\theta = 37500$  over a similar  $y^+$  range. Analysing the implications of a sequence of minimal-channel simulations, each used to isolate the characteristics of a narrow size ranges of eddies, Hwang (2015) argues that the entire log-law layer is populated, as suggested by Jiménez and Hoyas (2008) and Marusic et al. (2013), by a hierarchical set of self-similar and self-sustaining attached eddies, in line with the original AEH. However, the above interpretation appears at odds with results derived from experimental data for high-Reynolds-number pipe flow (Hultmark et al. 2013; Rosenberg et al. 2013; Fiorini et al. 2017, see region 1 in Figure 6.2) and also DNS data for channel flow at  $Re_\tau \approx 4200$  (Lozano-Durán and Jiménez 2014a; Lozano-Durán and Jiménez 2014b), which show that the logarithmic variation of  $\overline{u'u'}^+$  does not apply across the intermediate portion of the velocity log-law layer – referred to as the “meso-layer” henceforth – which separates the layer below  $y^+ \approx 100$  from the outer region lying beyond  $y \approx 0.5\delta$  (around  $y^+ = 2000$  in the channel flow considered herein). The reason is that the streamwise fluctuation-energy profile is increasingly affected, as the Reynolds number exceeds  $Re_\tau \approx 1000$ , by contributions arising from energetic outer structures having streamwise and spanwise length scales of order  $5 - 10\delta$  and  $0.5 - 1\delta$ , respectively (Kim and Adrian 1999; Del Álamo and Jiménez 2003; Hutchins and Marusic 2007b). The wall-normal variation of the streamwise energy associated with these structures is fairly flat (Marusic, Mathis, and Hutchins 2010a; Fiorini et al. 2017), increases with  $Re_\tau$ , and its (weak) maximum is reported by (Mathis, Hutchins, and Marusic 2009) to follow the location  $y \approx 3.9\sqrt{Re_\tau}$  (corresponding to around  $0.05\delta$ ). Importantly, the energy remains elevated well beyond this location, as well across the entire near-wall region including meso-layer and, indeed, the viscosity-affected sublayer, causing substantial friction footprints on the wall; in other words, the energetic outer large-scale motions are highly correlated in the wall-normal direction. As a consequence, the energy profile no longer scales with  $u_\tau$  and the logarithmic variation of  $\overline{u'u'}^+$  in the velocity log-law region is lost or becomes highly indistinct, at least at  $Re_\tau < 5000$ . As observed by Vassilicos et al. (2015), this behaviour is incompatible with the AEH, and this led them to propose a new spectral range of the form  $E_{uu} = Cu_\tau^2\delta(k_x\delta)^{-m}$  for the intermediate range, allowing them to “predict” the rise in  $\overline{u'u'}^+$  due to the outer scales.

Measurements at  $Re_\tau > 7000$  display a tendency for  $\overline{u'u'}^+$  to re-establish a logarithmic-decay variation well beyond the meso-layer of the velocity log-law and also well beyond the position of maximum large-scale energy — although with a slope different from that applicable within the velocity log-law layer at much lower Reynolds-number values (Hutchins et al. 2009; Hultmark et al. 2012; Hultmark et al. 2013; Rosenberg

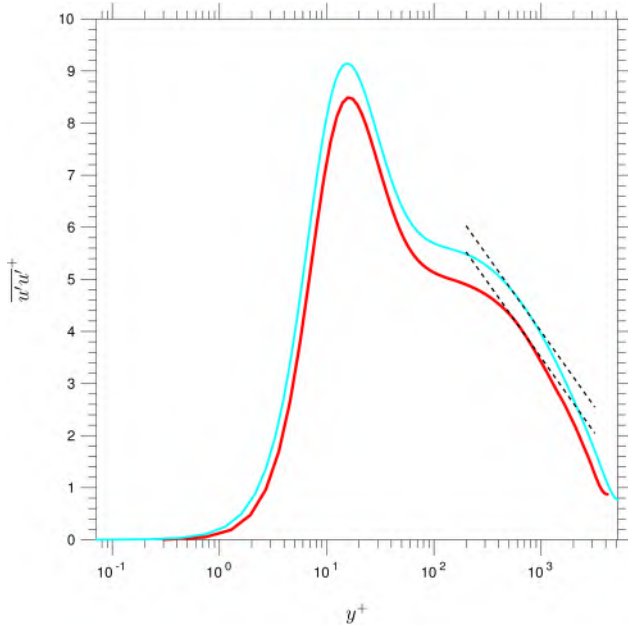


Figure 6.3: Wall-normal distribution of the streamwise stress at  $Re_\tau \approx 4200$  (red line) and  $Re_\tau \approx 5200$  from Lee and Moser (2015). The dashed lines represents the variation  $\overline{u'w'}^+ = -1.26 \log y^+ + B$ , with  $B = 12.2$  and  $12.7$  for  $Re_\tau \approx 4200$  and  $Re_\tau \approx 5200$ , respectively.

et al. 2013). This has led to a proposition that the AEH should only apply in the extreme outer layer of the velocity log-law region, on the grounds that “*determining the extend of the logarithmic layer from  $U^+$  alone is difficult because of the slow departure from any log law*” (Smits, McKeon, and Marusic 2011).

The evident controversy on the subject of the AEH — in particular, the wall-normal range to which it applies — motivated the present study to examine the statistical properties of a channel flow at  $Re_\tau \approx 4200$ . This value is substantially lower than that achieved in experiments, but is arguably high enough to undertake a searching study by post-processing the highly resolved data that yield well-converged statistics (which is easily accessible at that time). The DNS data were obtained with a spectral code by Lozano-Durán and Jiménez (2014a), according to well established quality criteria, over a domain  $L_x = 2\pi h$ ,  $L_z = \pi h$ , with a grid containing  $3072 \times 3072 \times 1081$  nodes and cell dimensions  $\Delta x^+ = 12.8$ ,  $\Delta z^+ = 6.4$ ,  $\Delta y_{max}^+ = 10.7$ . Downloaded data consisted of full-volume snapshot at 40 time levels, corresponding to 15 turnovers of the global eddies. While the motivation for the present study is rooted in, and emphasis is placed on, the AEH, the analysis extends, more broadly, to an examination of the statistical properties of, and scaling laws pertaining to, different scale sub-ranges within the spectrum of turbulent fluctuations across the near-wall layer. Observations derived from this latter part turn out to be highly pertinent to the discussion on the validity of the AEH in the meso-layer.

### 6.3 Statistical Properties of Eddy-length-scale Sub-ranges

Figure 6.3 shows profiles of the streamwise turbulence energy for  $Re_\tau \approx 4200$  and 5200. The latter originates from DNS study by Lee and Moser (2015) for a channel flow performed over a box of  $L_x = 8\pi h$ ,  $L_z = 3\pi h$  — i.e. much larger than that exploited in the present study. Attention focuses here on what is termed the “meso-layer”, divided into two portions: the “plateau” region, covering  $y^+ \approx 80 - 500$ , and the outer layer, extending to around  $y^+ \approx 2000$  — i.e., roughly  $0.5h$  in the present flow (corresponding to regions 1 & 2 in Figure 6.2), respectively. The outer portion of the meso-layer, beyond the region in which the streamwise energy features an inflection region or a (second) maximum, is populated with very large scale motions (VLSMs), and it is this layer that has been the focus of attention in studies of Vassilicos et al. (2015), Marusic et al. (2013), Hultmark et al. (2013) and Rosenberg et al. (2013), at  $Re_\tau > 7000$ , who show that the streamwise energy displays a logarithmic-decay variation at the same slope as that in Figures 6.2 and 6.3. The variation of the energy in the outer layer,  $500 < y^+ < 1000$ , suggests a log-like decay, especially at the high Reynolds value,

and the slope of this decay is given in Figure 6.3. Whether a logarithmic-decay law within the meso-layer is supported by other statistical properties will be examined below.

A property consistent with the log-variation of  $\overline{u'u'}^+$  and with the AEH is the presence of a region of constant value in the pre-multiplied spectra  $k_x \Phi_{uu}$ , where  $x$  is assumed statistically homogeneous. If this region is bounded by  $\lambda_{x,min}^+ = Cy^+$  and  $\lambda_{x,max}^+ = cst$ , the log relationship emerges from:

$$\begin{aligned}\overline{u'u'}^+(y^+) &= \int_{\lambda_{x,min}^+}^{\lambda_{x,max}^+} k_x \phi_{uu}(y^+, \lambda_x^+) d \log(\lambda_x^+) \\ &= \int_{Cy^+}^{cst} A d \log(\lambda_x^+) \\ &= -A \log(y^+) + B\end{aligned}\quad (6.1)$$

If, on the other hand, the upper limit of integration is a line parallel to that defining the lower limit – i.e.  $\lambda_{x,max}^+ = Dy^+$  – then  $\overline{u'u'}^+(y^+) = cst$ . The significance of this distinction between the two variations in the upper limits of integration will transpire in Section 6.4. It is important to underline that, for the AEH to be valid, the equivalent of equation (6.1) must also apply in respect of the spanwise spectra, i.e.  $k_z \Phi_{uu}$  must also be constant within boundaries corresponding to those applicable to the streamwise spectra.

Figure 6.4 shows the pre-multiplied spectra for  $Re_\tau \approx 4200$ . Although there is an indication that the  $\lambda_x^+$  and  $\lambda_z^+$  locations at which the energy begins to rise steeply vary linearly with  $y^+$ , neither spectral maps features a well-defined constant-value plateau within the meso-layer, thus offering no obvious support for equation (6.1). A curious feature observed in Figure 6.4(b) is the oscillatory behaviour of the contours below and to the right of the red line, especially along the  $y^+ - \lambda_z^+$  locus of maximum energy density. Although relatively mild, this behaviour is indicative of a lack of convergence of the FFT – an artefact that encourages the alternative use of the second-order structure function as a primary diagnostic means, pursued in Section 6.4. The use of the structure function is also motivated by the fact that it is not affected by aliasing associated to the large-scale motion and thus leads to a better identification of the plateau region (see Davidson, Nickels, and Krogstad 2006). However, prior to this change in focus, the spectra, both those in Figure 6.4 and others pertaining to the spanwise and wall-normal fluctuations, are used to examine some statistical properties of turbulence within different spectral portions of the eddy scales. The main objective is to identify and separate sub-ranges of isotropic and anisotropic scales, the former characterizing the inertial subrange and associated with detached eddies (Jiménez 2011), and the latter – at larger scales – associated with attached eddies (Perry, Henbest, and Chong 1986; Högström, Hunt, and Smedman 2002; Davidson, Nickels, and Krogstad 2006). This identification is pursued below.

### 6.3.1 Inertial Range - Detached Eddies

In order to shed light on the characteristics of scale sub-ranges, some specific manipulations of the spectral maps are proposed herein. Figure 6.5 shows two ways of highlighting the region in which the scales are close to being isotropic. The first entails the use of compensated spectra  $\epsilon^{-2/3} k_x^{5/3} \Phi_{uu}$  and  $\epsilon^{-2/3} k_z^{5/3} \Phi_{uu}$ , which are shown figures 6.5(a) and 6.5(b), respectively, where  $\epsilon$  is a surrogate of rate of turbulence-energy dissipation, defined such as  $\epsilon = \overline{\omega_k} \overline{\omega_k} / 3$ . The red lines in the  $x$ -wise and  $z$ -wise maps are defined, respectively, by  $\lambda_x^+ = 3.5 \times y^+$  and  $\lambda_z^+ = 7 \times y^+ = 2 \times \lambda_x^+$ , while the blue lines describe, respectively, the variations  $\lambda_x^+ = 3.5 \times (y^+)^{1/3}$  and  $\lambda_z^+ = 7 \times (y^+)^{1/3} = 2 \times \lambda_x^+$ . The red and blue lines bound, approximately, plateau regions characteristic of near-isotropy.

The second route rests on the definition of the following “isotropy parameter”:

$$\gamma^{3c} \equiv \frac{3|\Phi_{uu}| |\Phi_{vv}| |\Phi_{ww}|}{|\Phi_{uu}|^3 + |\Phi_{vv}|^3 + |\Phi_{ww}|^3} \quad (6.2)$$

in which  $\Phi_{uu}$ ,  $\Phi_{vv}$  and  $\Phi_{ww}$  are the  $x$ -wise or  $z$ -wise spectra for the three components  $u$ ,  $v$  and  $w$ , respectively. This parameter tends to a maximum of 1 in the case of isotropy, declining to zero in the case of a two-component or a one-component state. The maps in figures 6.5(c) and 6.5(d) show (for greater visual impact) the square of  $\gamma^{3c}$  as functions of  $\lambda_x^+$  and  $\lambda_z^+$ , respectively. The fact that regions of high  $\gamma^{3c}$  are, again, bounded by the red and blue lines and broadly coincide with the near-plateau regions in the compensated spectra supports the proposition that these regions within the meso-layer characterize detached eddies.

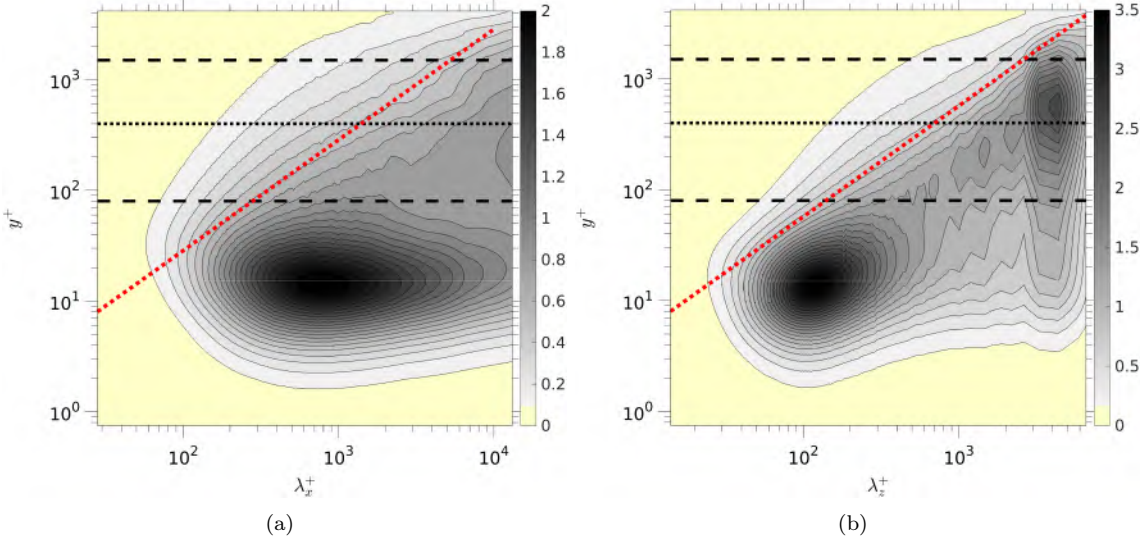


Figure 6.4: Pre-multiplied power spectrum of the streamwise fluctuations, in both streamwise (a) and spanwise direction (b); at  $Re_\tau \approx 4200$ . The dotted red lines show either the relation  $\lambda_x^+ = 3.5y^+$  or  $\lambda_z^+ = 7y^+ = 2\lambda_x^+$ .

### 6.3.2 Anisotropic Range – Attached Eddies and Large-Scale Motions

An analogous route to that taken in the previous sub-section to highlight isotropy by use of the parameter  $\gamma^{3c}$  is adopted here to identify region of elevated anisotropy. Thus, a parameter that identifies the dominance of the streamwise component over the two others is:

$$\gamma_u^{1c} \equiv \frac{3|\Phi_{uu}||\Phi_{uu}|}{|\Phi_{uu}|^2 + |\Phi_{vv}|^2 + |\Phi_{ww}|^2} \quad (6.3)$$

This parameter tends to 1 when the energy is increasingly contained in the  $\Phi_{uu}$  spectra, and diminishes when the anisotropic state departs from the one-component condition. Maps of  $(\gamma_u^{1c})^3$  in the  $x$  and  $z$  directions (the cubic exponent designed to accentuate gradients in the maps) are shown in Figures 6.6(a) and 6.6(b), respectively.

Both maps reveal that, within the meso-layer, the dominance of the streamwise component is confined to the larger scales beyond the boundaries identified by the red lines, and this is the attached-eddy region, as will be argued in Section 6.4. In fact, the most pronounced regions in Figure 6.6 pertain to scales which are the subject of many studies that deal with elongated large-scale structures in the outer part of the log-layer (Marusic 2001). Figure 6.6 also contains a  $y^+$ -wise profile of the normalised streamwise energy, and this provides confirmation of the existence of energetic structures in the outer layer around  $y^+ = 500$ . Reference to the  $(\gamma_u^{1c})^3$  distribution along the dotted black line at  $y^+ = 500$  clearly shows that this peak in streamwise energy is associated with structures having wavelengths of order  $\lambda_x^+ \gtrsim 8000$  and  $\lambda_z^+ \gtrsim 4000$ . The near-wall energy peak, at  $y^+ \approx 10$  is also clearly brought out in the  $(\gamma_u^{1c})^3$  maps, in which a maximum at  $\lambda_z^+ \approx 100$  is evidently indicative of the strong small-scale streaks in the buffer layer.

### 6.3.3 Anisotropic Range – Small-Scale Motions

The maps shown in Figures 6.5 and 6.6 contain small-scale ranges to the left of the blue lines  $\lambda^+ \propto (y^+)^{\frac{1}{3}}$  which neither comply with isotropy nor with one-component dominance. The scales in question are not far from the Kolmogorov range  $\lambda^+ \propto (y^+)^{\frac{1}{4}}$ . In order to identify the state of the turbulence in this range, a third parameter,  $\gamma_{ij}^{2c}$ , is defined as follows:

$$\gamma_{ij}^{2c} \equiv \frac{2|\Phi_{ii}||\Phi_{jj}|}{|\Phi_{uu}|^2 + |\Phi_{vv}|^2 + |\Phi_{ww}|^2} \quad (6.4)$$

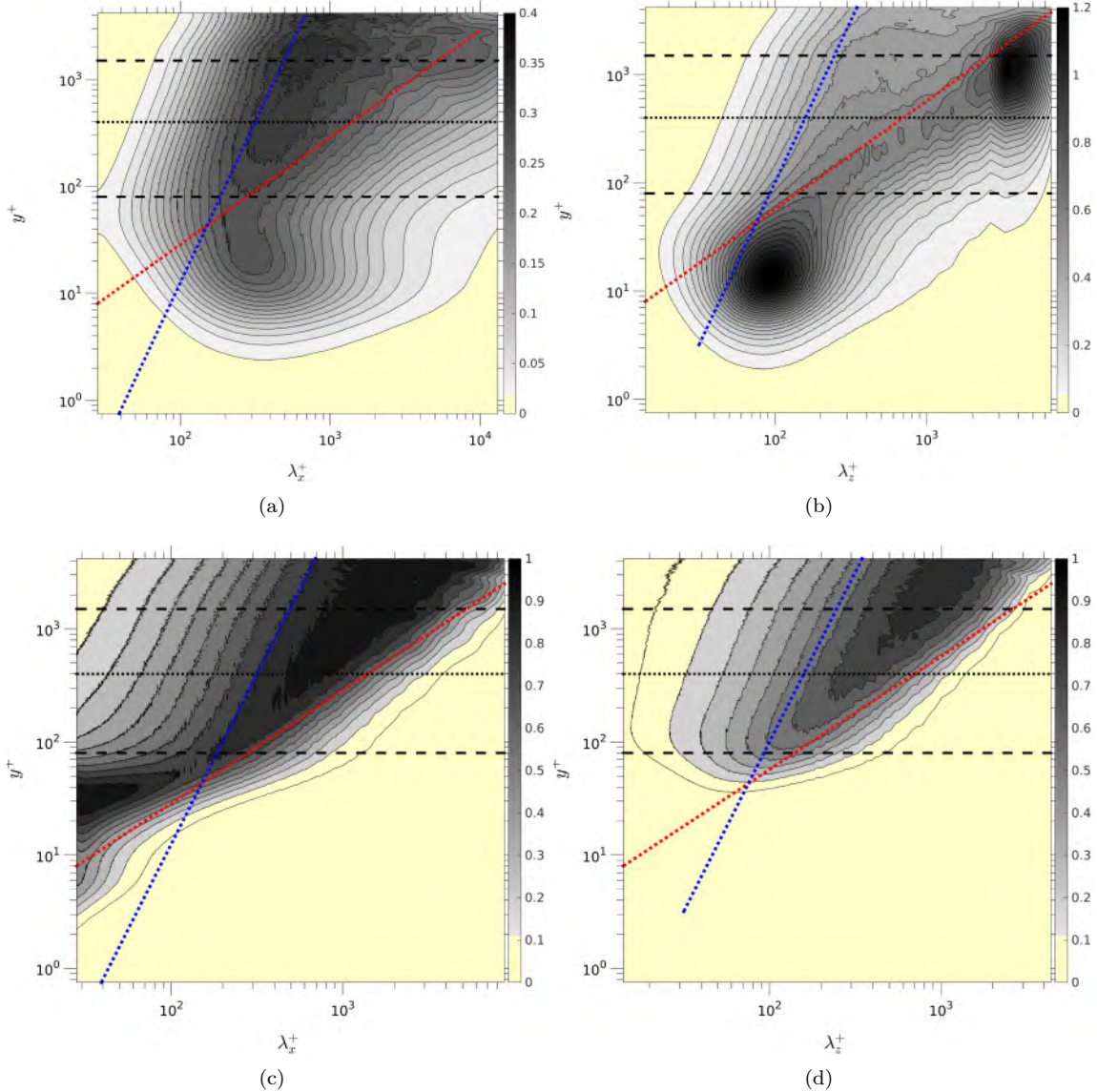


Figure 6.5: Characterisation of isotropy across eddy-size range: (a) compensated spectra  $\epsilon^{-2/3} k_x^{5/3} \Phi_{uu}$ , (b) compensated spectra  $\epsilon^{-2/3} k_z^{5/3} \Phi_{uu}$ , (c) and (d) maps of the square of the “isotropy parameter”  $(\gamma^{3c})^2$ , derived from the streamwise and spanwise spectral components. The red lines show either the relation  $\lambda_x^+ = 3.5y^+$  or  $\lambda_z^+ = 7y^+ = 2\lambda_x^+$  and the blue lines show either the relation  $\lambda_x^+ = 3.5(y^+)^{1/3}$  or  $\lambda_z^+ = 7(y^+)^{1/3} = 2\lambda_x^+$ .

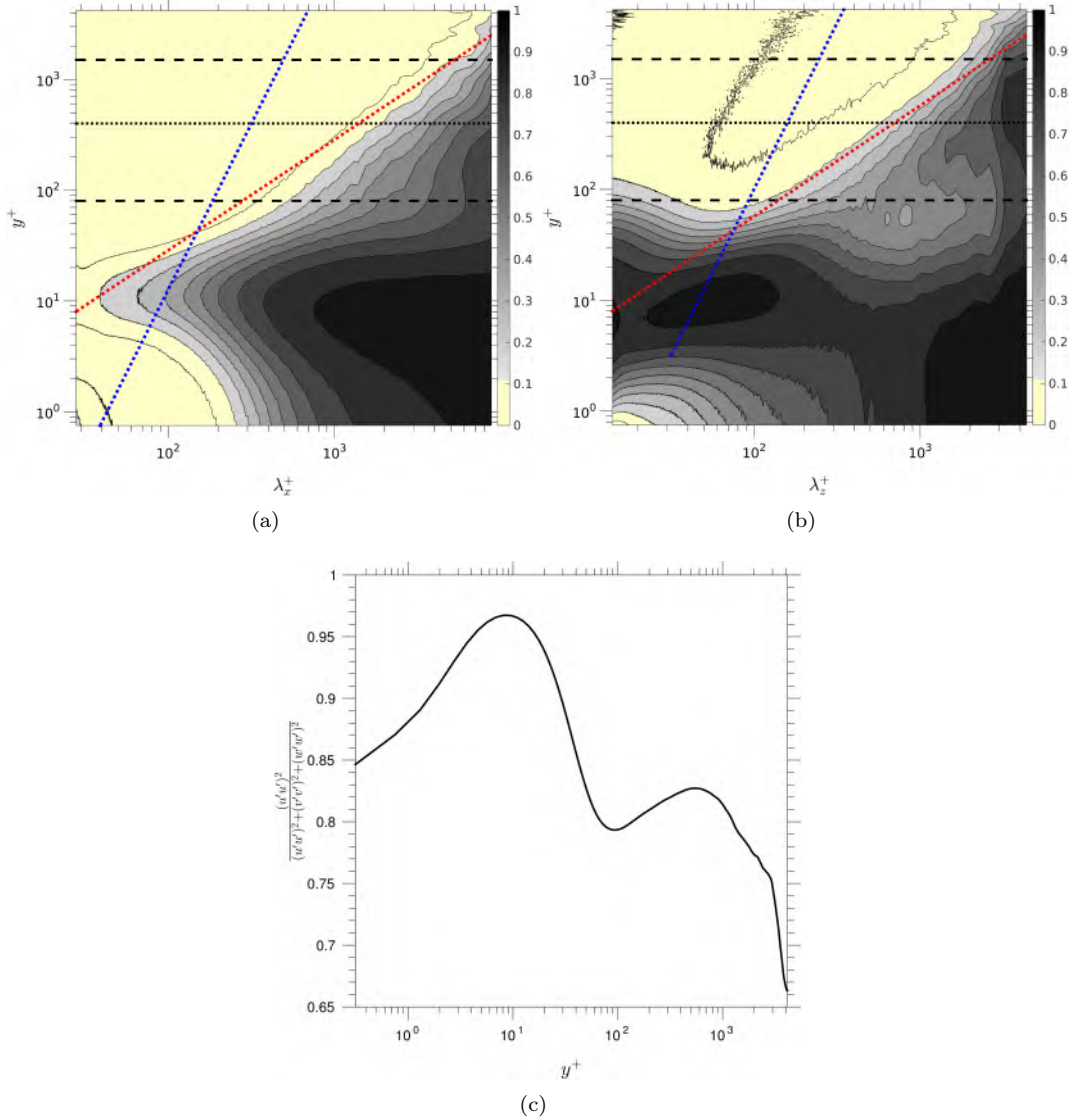


Figure 6.6: Characterisation of anisotropy due to dominance of streamwise energy  $\overline{u'u'}^+ >> \overline{v'v'}^+, \overline{w'w'}^+$ : (a) maps of  $(\gamma_u^{1c})^3$  in streamwise direction, (b) maps of  $(\gamma_u^{1c})^3$  in spanwise direction and (c) cross-spectrum average of  $\gamma_u^{1c}$ . Red and blue dotted lines: see caption of Figure 6.5.

This parameter identifies the dominance of two normal components,  $i \neq j$ , over the third, and thus highlights the range where the anisotropic turbulence is characteristic of two-component turbulence. Figure 6.7(a) shows a map of  $(\gamma_{vv}^{2c})^3$ , which brings into focus the region where the spectra of the wall-normal and spanwise components have similar energy level, both exceeding the streamwise component. The suggestion emerging from this map is that small-scale motions, of scales  $\lambda_x^+$  lower than  $3.5 \times (y^+)^{1/3}$ , are characterised by  $\overline{v'_{ss} v'_{ss}}^+ \approx \overline{w'_{ss} w'_{ss}}^+ > \overline{u'_{ss} u'_{ss}}^+$ . This rather unexpected result has motivated the isolation of these small scales from larger scales by means of a spatially two-dimensional version of the Empirical Mode Decomposition (see 3.3 for details on BEMD). The energetic properties of the small scales, shown in Figure 6.7(b), support the implication of Figure 6.7(a) to the extent that, above the buffer region, the wall-normal and spanwise small-scale energy components exceed the streamwise component. Attention is drawn to the  $\sqrt{y^+}$  scaling of the energy components in Figure 6.7(b), intended to bring to the fore the constancy of the scaled energy components, the magnitude of which thus varies as  $1/\sqrt{y^+}$ . The physical significance of the plateau region arising from the  $\sqrt{y^+}$  scaling is unclear, at present.

An interesting feature in the small-scale range emerges upon scaling the power spectrum as  $y\epsilon^{-1/3}k_x^{7/3}\Phi_{uu}$ . The use of  $k_x$  scaling reflects the fact that the energy level in the spectrum tends to vary with  $k_x^{-7/3}$  in anisotropic turbulence. When the  $y$ -scaling is added to the compensated spectrum, the resulting map, shown in Figure 6.7(c), features an elongated plateau within the meso-layer, just to the left of the blue line  $\lambda_x^+ = 3.5 \times (y^+)^{1/3}$ . The implication is that the contribution of small-scale energy to the total energy declines inversely with  $y^+$ .

### 6.3.4 Summary of Sub-Ranges

Based on considerations so far, it is possible to identify distinct regions within the spectral map in which the structures possess different characteristics. Such a map is proposed in Figure 6.8.

Within the meso-layer, of primary interest herein, there are three major regions:

- **Region “A”**, associated with (very) small scales, is characterised by a dominance of the wall-normal and spanwise component over the streamwise fluctuations.
- **Region “B”** is characterised by a trend towards isotropy. This is, essentially, indicative of the inertial sub-range, where the eddies are presumed to be “detached”.
- **Region “C”** is characterised by a high level of anisotropy in the scales, with the streamwise component dominating and the streamwise and spanwise components larger than the wall-normal component. This region is associated to the attached eddies and with large-scale motion. It is emphasized here that this region extends across the entire meso-layer. While the associated condition  $\Phi_{uu} \propto k^{-1}$  is not clearly present in Figure 6.4, an examination of the structure function, to follow, will support the interpretation of this region being associated with attached eddies.

## 6.4 The Attached Eddy Hypothesis

### 6.4.1 Structure-Function Analysis

In the absence of a clear region of  $\Phi_{uu} \propto k^{-1}$ , conventionally associated with the Townsend-Perry AEH, attention is directed towards the second-order structure function  $S_{2,u}(y, \delta)$  as a potentially superior indicator of the validity of the AEH. This is a route previously advocated by Davidson, Nickels, and Krogstad (2006). Its rationale is based on the observation that there is a close correspondence between the pre-multiplied spectra and the derivative of the second-order structure function, as shown in the previous Chapter (Chap. 5). In particular, Davidson *et al.* argue that, since the two are effectively Fourier-transform pairs, the structure function should exhibit a real space analogue of the  $k^{-1}$  spectrum, shown to manifest itself by a constant value of the pre-multiplied derivative of the structure function. This correspondence is pursued and exploited below.

In channel flow, with homogeneous directions  $x$  and  $z$ , the relevant second-order structure functions are:

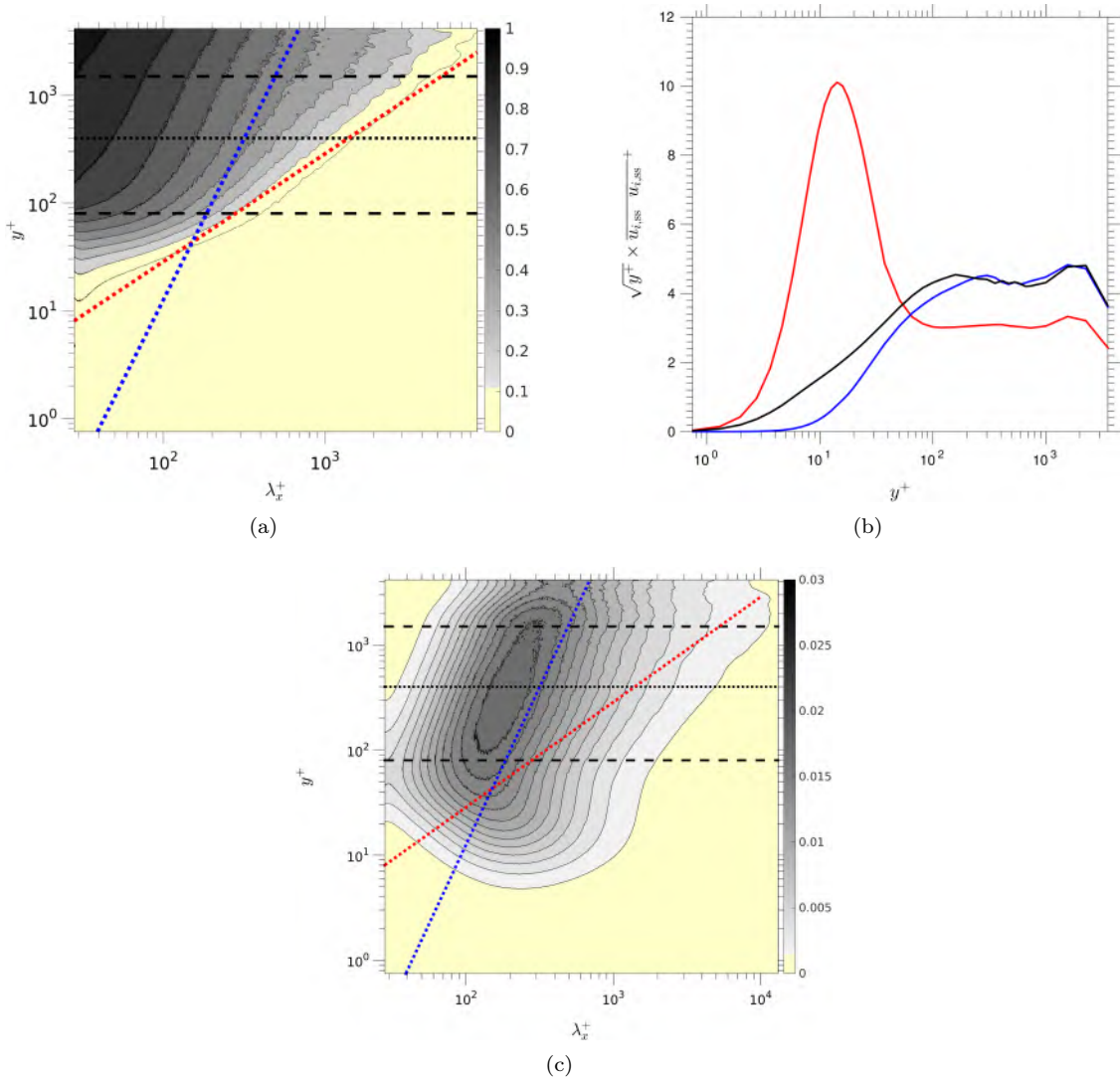


Figure 6.7: Characterisation of anisotropy of small-scale motions due to dominance of cross-flow energy components: (a) map of  $(\gamma_{vw}^{2c})^3$ , (b) streamwise stress associated with small-scale motions, normalised by  $\sqrt{y^+}$ : streamwise stress (red line), wall-normal stress (black line) & spanwise stress (blue line), and (c) compensated power spectra  $y\epsilon^{-1/3}k_x^{7/3}\Phi_{uu}$ . Red and blue dotted lines: see caption of Figure 6.5.

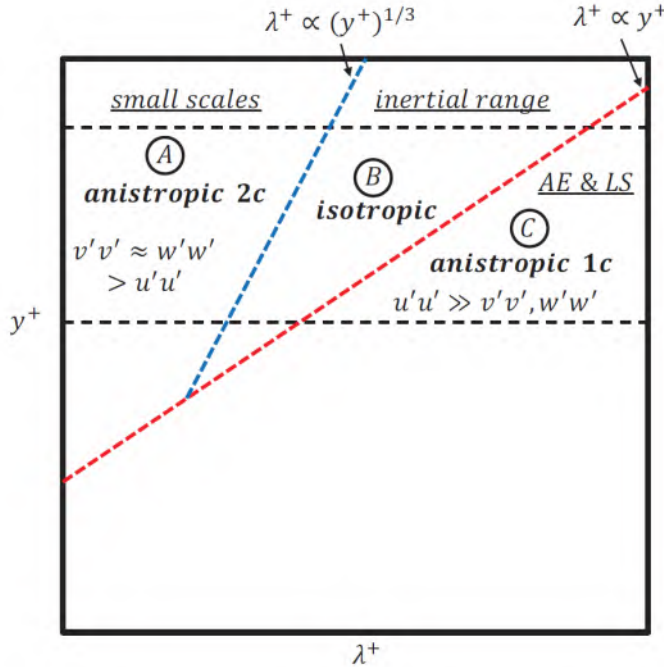


Figure 6.8: Sub-ranges in spectral map having distinct turbulence characteristics (1c: dominance of streamwise component; 2c: dominance of cross-flow components).

$$\begin{aligned} S_{2,u}(y, \delta_x) &= \left\langle [u(y, x) - u(y, x + \delta_x)]^2 \right\rangle_{z,t} \\ S_{2,u}(y, \delta_z) &= \left\langle [u(y, z) - u(y, z + \delta_z)]^2 \right\rangle_{x,t} \end{aligned} \quad (6.5)$$

with the subscripts at the end identifying the averaging directions.

The structure function essentially represents the total energy contained within the range of eddies with size less or equal to  $\delta$  (either  $\delta_x$  or  $\delta_z$ ). The contribution from eddies larger than  $\delta$  is negligibly small, because  $u(y, x) \approx u(y, x + \delta)$ . When  $\delta = L$ , the largest distance across which there is a correlation between motions at  $x$  and  $x + \delta$ , i.e. with the motions uncorrelated,  $S_{2,u}(L)$  reaches a maximum equal to twice the streamwise turbulence energy. At the other extreme,  $\delta = 0$ ,  $S_{2,u}(0) = 0$ , and the correlation reaches a maximum.

Figure 5.5 brings into focus the relationship between the second-order structure function and the energy scale distribution. The energy contribution associated with eddies of a length  $\delta$  is represented by the pre-multiplied derivative of the structure function (PMDS2),  $\delta \times \frac{dS_{2,u}(\delta)}{d\delta}$  (Davidson, Nickels, and Krogstad 2006). Though equivalent, this is not identical to the pre-multiplied power spectra ( $k\Phi_{uu}$ ). Given a constant PMDS2 level, which aligns with a  $k^{-1}$  variation of the spectrum as suggested by Davidson *et al.*, a logarithmic variation of  $S_{2,u}(\delta/y)$  is immediately yielded upon integration, resulting in a logarithmic dependence  $\overline{u'u'}^+(\delta/y)$  for  $\delta = L$ . In summary, the following consistent relationships are observed: (1) the  $k^{-1}$  spectrum, (2) a constant PMDS2 level, (3) the logarithmic variation of  $\overline{u'u'}$ , and (4) the attached eddy hypothesis. When Figures 6.9(c) and 6.9(d) are compared to Figure 6.4, a clear resemblance can be discerned between the pre-multiplied spectrum and PMDS2, as anticipated given these mutual consistencies.

It is important to note that the abscissa scaling in the  $x$ -wise and  $z$ -wise maps of Figure 6.9 has been selected as  $8\delta_x$  and  $4\delta_z$ , respectively. The introduction of these multipliers, 8 and 4, results in a range of values in Figure 6.9 that align closely with those presented in Figure 6.4. While this may initially appear to be an arbitrary decision, a rational basis for it does exist, as detailed by Agostini and Leschziner (2017) in Appendix A.

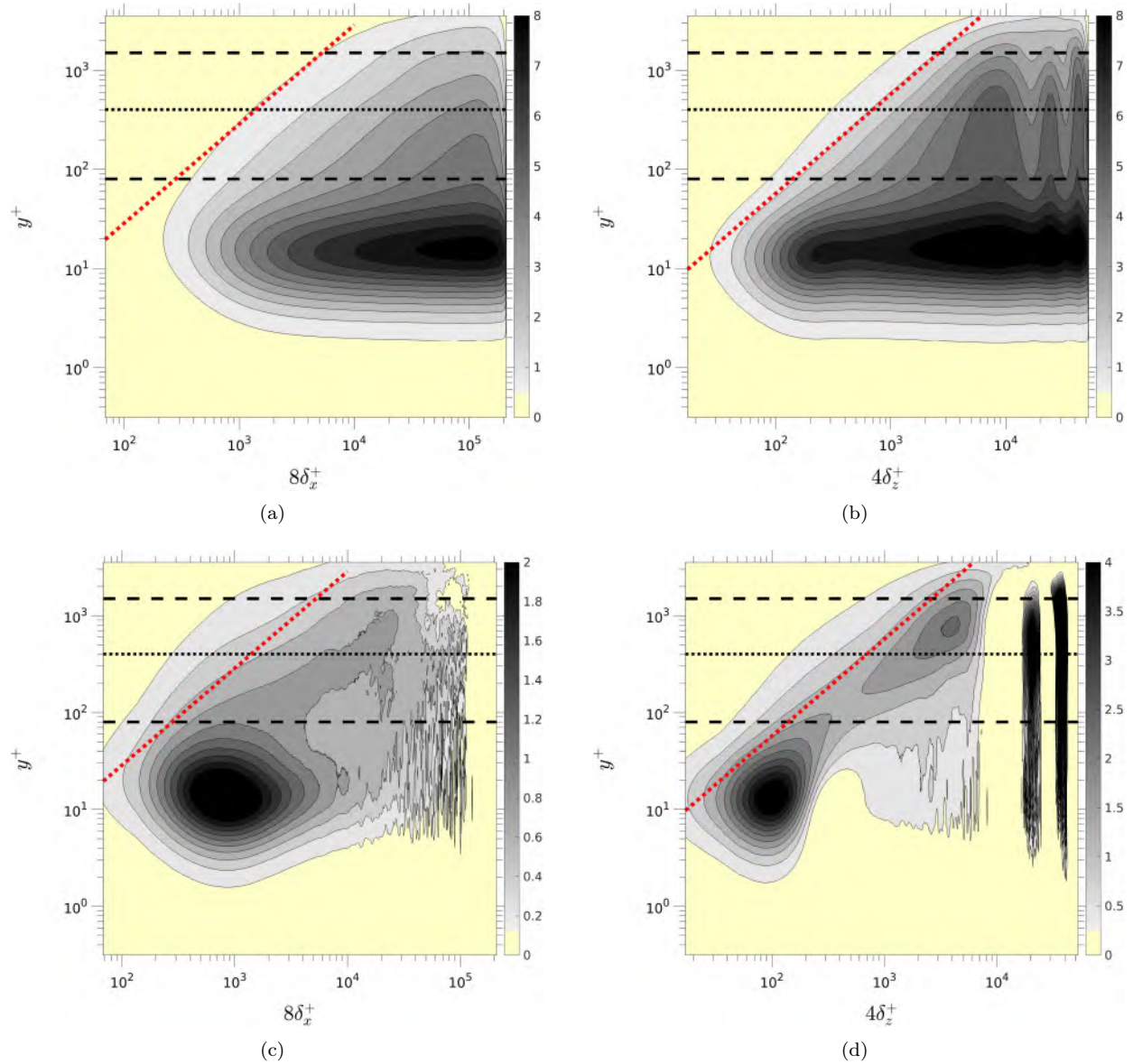


Figure 6.9: Maps of the second-order structure function and its pre-multiplied derivatives: (a)  $S_{2,u}(\delta_x)/2$ ; (b)  $S_{2,u}(\delta_z)/2$ ; (c)  $\delta_x(dS_{2,u}/d\delta_x)$ ; (d)  $\delta_z(dS_{2,u}/d\delta_z)$ . Red and blue dotted lines: see caption of Figure 6.5.

Figures 6.9(c) and (d) convey the PMDS2 maps ( $\delta_x dS_{2,u} / d\delta_x$  and  $\delta_z dS_{2,u} / d\delta_z$ , respectively), revealing several features that are either absent or not clearly identified from the spectra:

- Firstly, the resolution range in terms of  $\delta_x$  surpasses that offered by  $\lambda_x$ . This is simply a result of the more stringent constraints placed on the post-processing obtained by the spectra.
- Secondly, and related to the first point, these Figures indicate the existence of a spanwise spatial quasi-periodicity in the very large scales at the extreme right of the map. This feature is not captured by the spectra, and a pronounced wall-normal coherence is also suggested.

However, in view of the rather small box size (especially  $\pi h$  in the spanwise direction), the question might be posed as to whether the oscillatory behaviour seen in Figure 6.9(b) and the associated bands in Figure 6.9(d) are physically significant. The oscillatory behaviour is seen to occur at  $\delta z^+ \approx 5000$  (i.e.  $\approx h$ ) and 10 000. The former value is substantially smaller than the spanwise domain size  $L_z^+ = 13000$ . There is reason, therefore, to suppose that this feature is physically significant, reflecting the spanwise quasi-periodicity of large-scale motions and their footprints, observed in previous chapters to be separated by a distance of order  $h$ .

Third, the seemingly ‘‘noisy’’ portions present in these maps at low  $y^+$  and intermediate  $\delta$  values is argued to constitute a physical feature and reflects the fact that medium-scale motions are strongly correlated across the near-wall layer, and are present on top of earlier mentioned large-scale footprints associated with outer large-scale motions in the upper portion of the meso-layer.

#### 6.4.2 The Regime of Attached Eddies

Following Townsend (1980) and Davidson et al. (2006), among others, the PMDS2 may be used to shed light on the validity of the AEH. The relevant test is whether  $\delta dS_{2,u} / d\delta = cst$ .

In section 6.3.4, it was proposed that the meso-layer may be divided into three different domains – A, B and C in Figure 6.8. These are associated, respectively, with spectra of the form  $\phi_{uu} \sim \epsilon^{1/3} k_x^{-7/3}$ ,  $\phi_{uu} \sim \epsilon^{2/3} k_x^{-5/3}$  and  $\phi_{uu} \sim k_x^{-1}$ , the last indicative of the AEH. As argued by Pope (2001), a power-law spectrum  $\Phi(\omega) \approx C_1 \omega^{-p}$  can be related to the second-order structure function  $S_p(\delta) \approx C_2 \delta^q$  with  $p = q + 1$ , valid only under the condition that  $p > 1$ . In accordance with the AEH,  $p = 1$ , in which case  $S^2(\delta) \approx C_3 \log(\delta) + B$  (Davidson, Nickels, and Krogstad 2006; Davidson et al. 2006). The implications for subregions are therefore:

- region A:  $\delta_x dS_{2,u} / d\delta_x \sim \epsilon^{1/3} \delta_x^{4/3}$
- region B:  $\delta_x dS_{2,u} / d\delta_x \sim \epsilon^{2/3} \delta_x^{2/3}$
- region C:  $\delta_x dS_{2,u} / d\delta_x = cst$

Figure 6.10(a) shows a map of  $\delta_x \frac{dS_{2,u}}{d\delta_x}$  compensated by  $\epsilon^{-1/3} \delta_x^{-4/3}$ . As expected, on the basis of the above statements on the spectra, there is a ‘‘plateau’’ in region A, bounded by the blue line. Figure 6.10(b) relates to the isotropic state through the augmentation by  $\epsilon^{-2/3} \delta_x^{-2/3}$ , along with a normalised version thereof in Figure 6.10(c), in which the levels at any  $y$ -value are normalised by the maximum at that level. Both maps bring to light the plateau in region B in the meso-layer, bounded by the blue and red lines. This region is narrow in the lower part of the layer, but broadens as  $y$  increases – i.e. the inertial range becomes wider in the outer portion of the log-layer. These features concur with those in the map in Figure 6.6 showing the parameter  $(\gamma^{3c})^2$  (see equation 6.2). The PMDS2 maps shown in Figure 6.9(c) and (d) – especially the latter – include an oblique band to the right of, and parallel to, the red line, i.e. region C, in which the condition  $\delta_x dS_{2,u} / d\delta_x = cst$  is met, at least approximately. Although this provides some support for the validity of the AEH in the meso-layer, the absence of a well-defined plateau is counter-indicative. Further support is sought, therefore, from an examination of joint PDFs pursued below. Implicit in this route being taken is the assumption that the processes in the spectral range C dominates over those in ranges A and B, assumed to make sub-ordinate contributions to cross-scale-averaged PDFs.

In an effort to shed light on any statistical bias in the motions within the meso-layer, and thus possibly draw inferences on the ‘‘shape’’ of the coherent structures, attention is directed first towards the skewness of the PDFs in the meso-layer. Figure 6.11(a) shows the wall-normal distributions of skewness of the streamwise

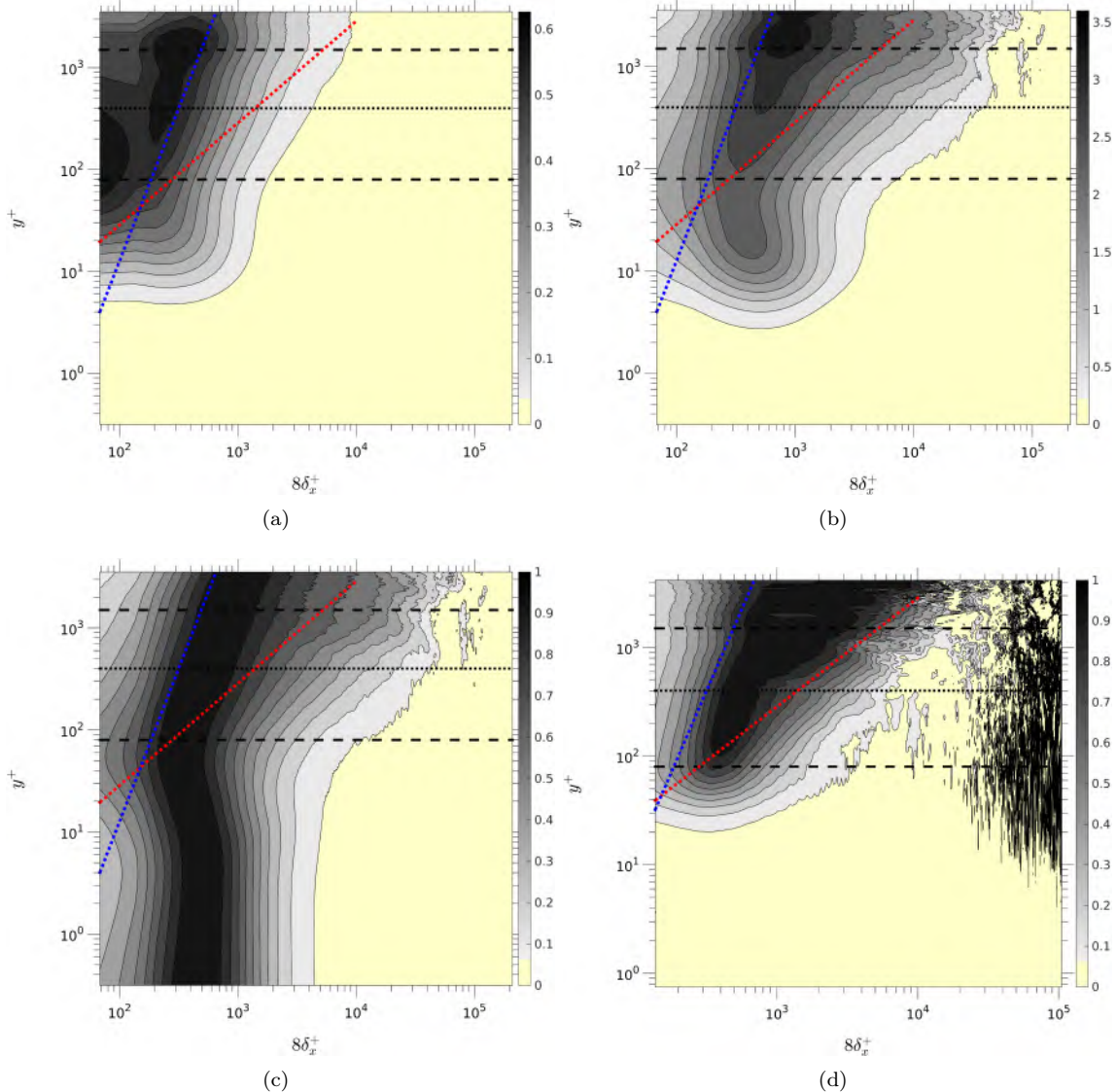


Figure 6.10: Turbulence state, premultiplied derivative of the structure function compensated by : (a)  $\epsilon^{-1/3}\delta_x^{-4/3}$ , (b)  $\epsilon^{-2/3}\delta_x^{-2/3}$ ; (c) the compensated  $\delta_x \frac{dS_{2,u}}{d\delta_x}$  defined for the isotropic case is divided by the maximum value at each  $y$ -location and (d) istropic parameter  $(\gamma^{3c})^2$ . Red and blue dotted lines: see caption of Figure 6.5.

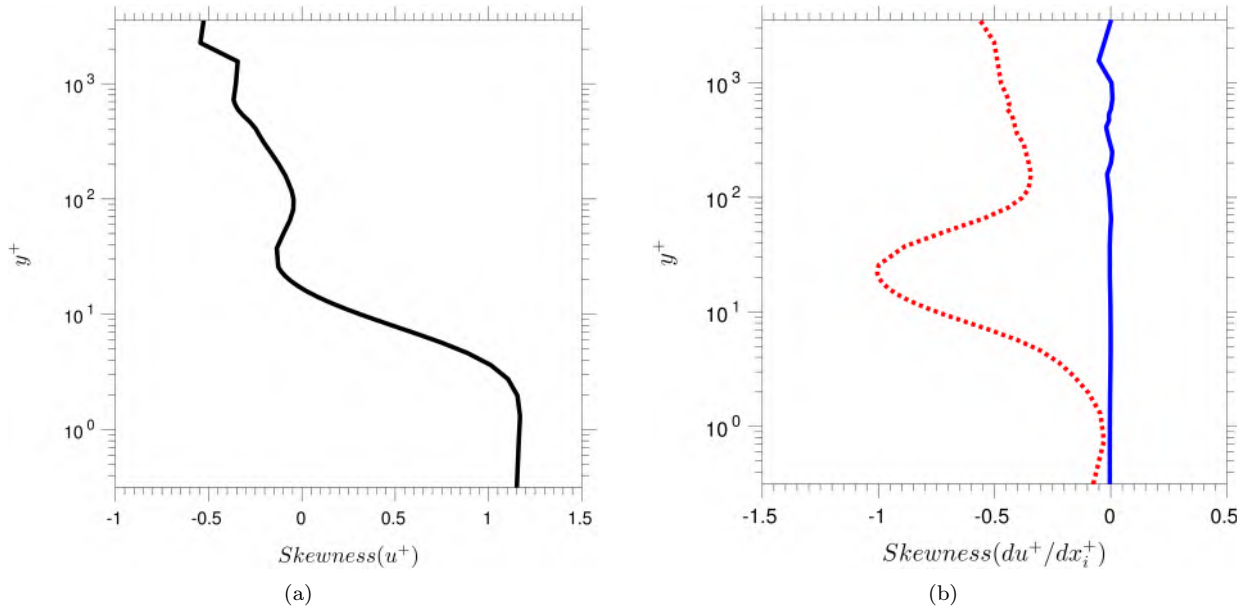


Figure 6.11: Wall-normal distribution of: (a) the skewness of the streamwise velocity, (b) the skewness of the streamwise and spanwise derivative of the streamwise velocity, identified by the red and blue lines, respectively.

fluctuations and their streamwise derivative. The inclusion of the latter, in combination with the former, may be argued to allow observations to be made on a streamwise bias in the length scales, which then leads to statements on the shape of the coherent structures. Both figures bring to light a substantial asymmetry in the streamwise fluctuations: few large negative events occurring in combination with many weak positive events. This also suggests asymmetric structural properties of the coherent motions, an issue pursued next by reference to joint PDFs of the streamwise fluctuations and their derivatives.

Figures 6.12(a) and 6.12(b) show the joint PDFs of  $u^+$  and  $du^+/dx^+$ , and  $u^+$  and  $du^+/dz^+$ , respectively, at  $y^+ = 600$ , approximately the middle of the meso-layer. The conclusions apply across the entire meso-layer, as the skewness of the velocity fluctuations and derivatives is fairly uniform. Three major features are observed in Figure 6.12(a): first, consistent with the skewness in Figure 6.11(a), an asymmetry exists in  $u^+$ ; second, weak positive  $u^+$  combines with highly negative  $du^+/dx^+$ , implying small positive fluctuation length scales; third, strong negative  $u^+$  occurs with low positive  $du^+/dx^+$ , suggesting larger length scales; fourth,  $|du^+/dx^+|$  is larger for negative fluctuations, consistent with Figure 6.11(b) skewness. This indicates a bias - fewer but more intense acceleration events versus more prevalent but weaker decelerations.

In Figure 6.12(b), the  $du^+/dz^+$  contours are symmetric, agreeing with the zero-skewness in Figure 6.11(b). In contrast to Figure 6.12(a), large spanwise gradients combine with negative  $u^+$ , while small gradients occur with positive fluctuations. Interpreting gradient/fluctuation combinations as indicative of length scales, the spanwise length scale tends to be larger for positive fluctuations and smaller for negative ones.

In summary, the joint PDFs reveal asymmetric streamwise fluctuations and gradients, but symmetric spanwise gradients. The fluctuation-gradient combinations provide information on anisotropic length scale biases - streamwise accelerations are intense yet fewer, while spanwise length scale associates with fluctuation sign.

The skewness distributions, and the length scales inferred, qualitatively, from the joint PDFs in Figure 6.12 and the ratio between  $\lambda$  and  $\delta$  previously argued, suggest the form of “coherent structures” conveyed conceptually in Figure 6.13. This structure, symmetric in the spanwise direction and tail-like in the streamwise direction, arguably provides support for the AEH. In particular, it is consistent with the sequence of several generations of attached eddies, as indicated in the sketch.

The PMDS2 maps, conveyed by Figures 6.9(c) and (d), offer supplementary evidence in support of the AEH. These plots are replicated in 6.14 and 6.15, in which two primary regions are highlighted: a larger blue

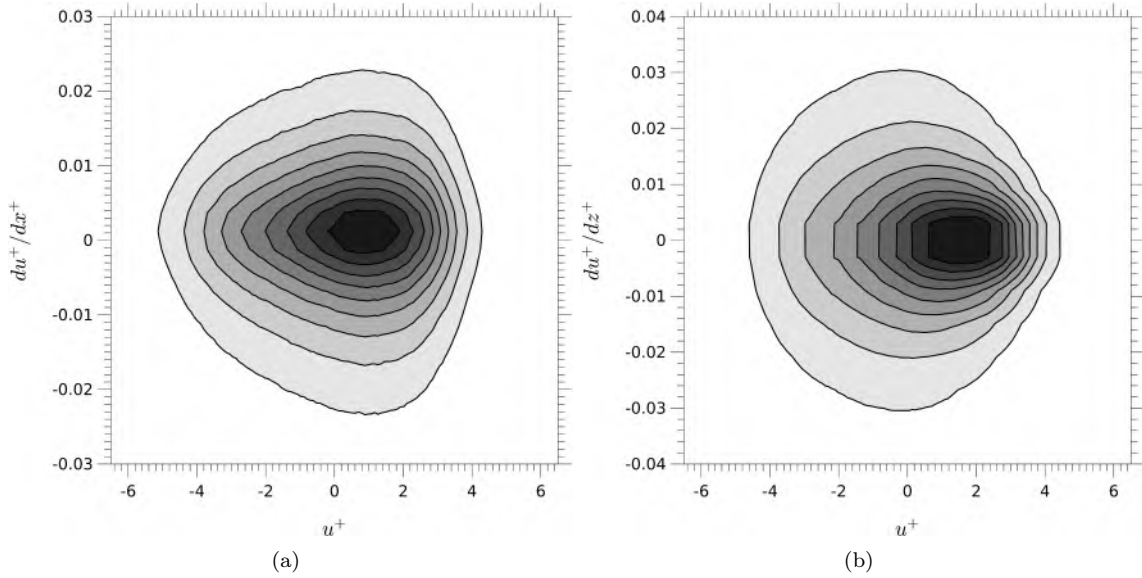


Figure 6.12: Joint PDFs between the streamwise velocity and its derivative at  $y^+ \approx 600$ : (a)  $u^+ - du^+ / dx^+$  and (b)  $u^+ - du^+ / dz^+$ . PDF contours identify 0.1–0.9 of the PDF height at constant increment 0.1, subject to total PDF volume normalised to 1.

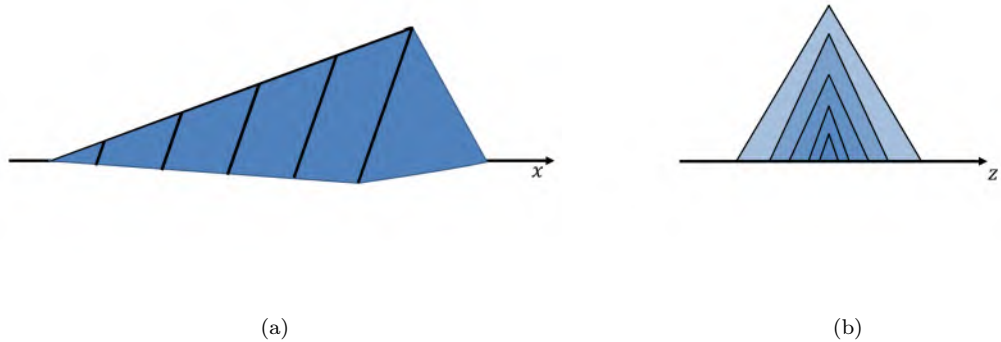


Figure 6.13: Conceptual sketch of the “form” of the coherent structures associated with attached eddies.

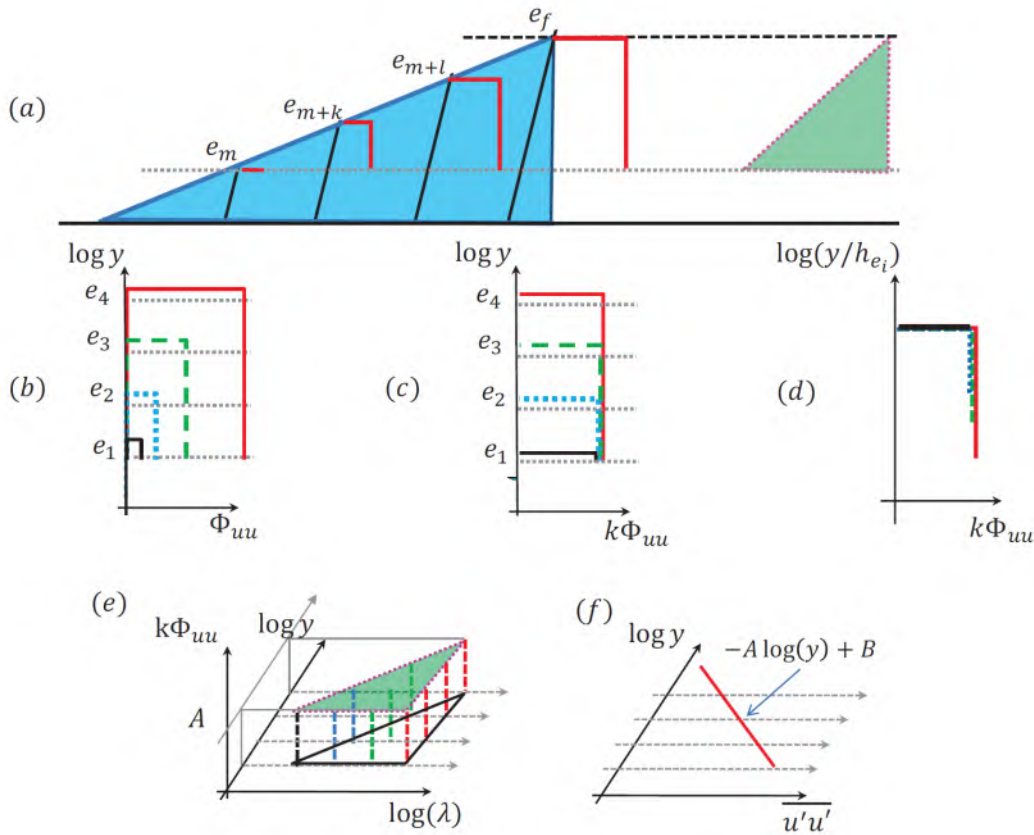


Figure 6.14: Conceptual representation of self-similarity through the meso-layer associated with AEH ( $e_m$ ,  $e_{m+k}$ , etc. represent hierarchical attached eddies): (a) Maps of PMDS2 with  $\delta$  taken in streamwise and spanwise direction, respectively. Conceptual velocity-fluctuations profile associated with (b) idealised representation of AEH and (c) extended interpretation of AEH.

triangle and a more restricted red trapezoid.

Assuming a “flawless” plateau within the triangular region of the PMDS2 and its corresponding pre-multiplied spectra, the implications for the AEH would align with the schematic representation in 6.15. Here,  $e_i$  signifies the modelled attached eddies. Hypothetical variations of these eddies’ energy contributions ( $\overline{u'u'}$ ) in relation to  $y$ , along with their scaled fluctuations – determined by the eddy height ( $h$ ) and wavelength ( $\lambda$ ) – are shown alongside the conceptual attached-eddy sketch. The collapse in the scaled uniform profiles reflects the linear dependence of the eddy height on  $y$  and the implied constancy of  $k\Phi_{uu}$  in the pre-multiplied spectra. This is then fully consistent with the AEH, and also with the logarithmic variation of  $\overline{u'u'}$  as per equation (6.1).

Contrary to expectations, Figure 6.14 reveals an absence of a clear triangular region. However, an approximately constant level is discernible within the red trapezoidal region. This confined plateau implies that the logarithmic variation in equation (6.1) pertains solely to the upper region of the meso-layer (Region 2), as indicated above the dotted line in Figures 6.9(c) and (d). Below that line, the linear variation of the parallel boundaries of the trapezoid, when transcribed to the pre-multiplied spectra, implies a constant level of  $\overline{u'u'}^+$ , broadly in line with the variations shown in Figure 6.3. The interpretation derived from the confined plateau within the trapezoidal region is illustrated in Figure 6.15. This interpretation deviates substantially from the conventional AEH representation in Figure 6.14, but does imply a self-similar set of partial profiles when scaling with  $h$  and  $\lambda$ . This leads to the plausible argument that, despite the lack of a clearly demarcated triangular plateau, the plateau within the trapezoidal region in Figures 6.9(c) and (d) is fundamentally in accordance with the AEH.

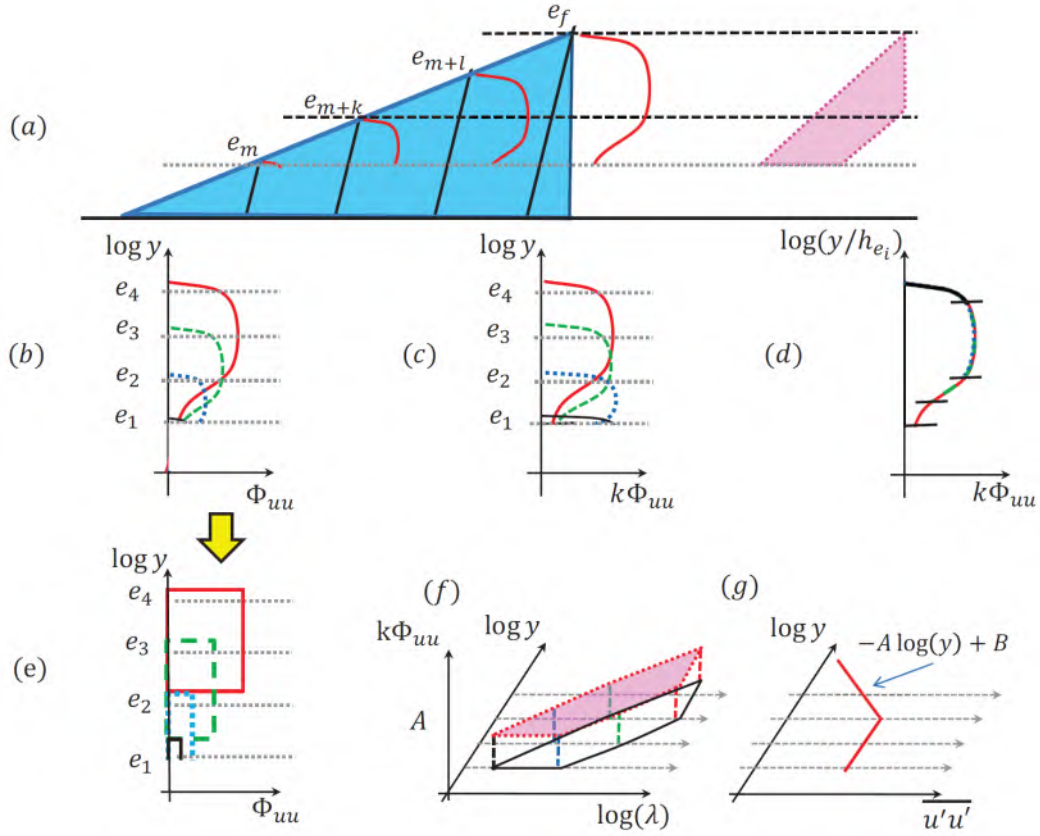


Figure 6.15: Conceptual representation of the modified Attached Eddy Hypothesis pertaining to the trapezoidal plateau region in the spectrum or PMDS2 map: (a,b) hierarchy of attached eddies  $e_m$ ,  $e_{m+k}$ , etc.; (c) eddy energy density normalised by  $\lambda$ ; (d) eddy size normalised by  $h_{ei}$ ; (e) idealized representation of the energy density profiles in sketch (b); (f) normalised eddies in the trapezoidal plateau region; (g) resulting logarithmic and constant portions in profile of streamwise turbulence energy.

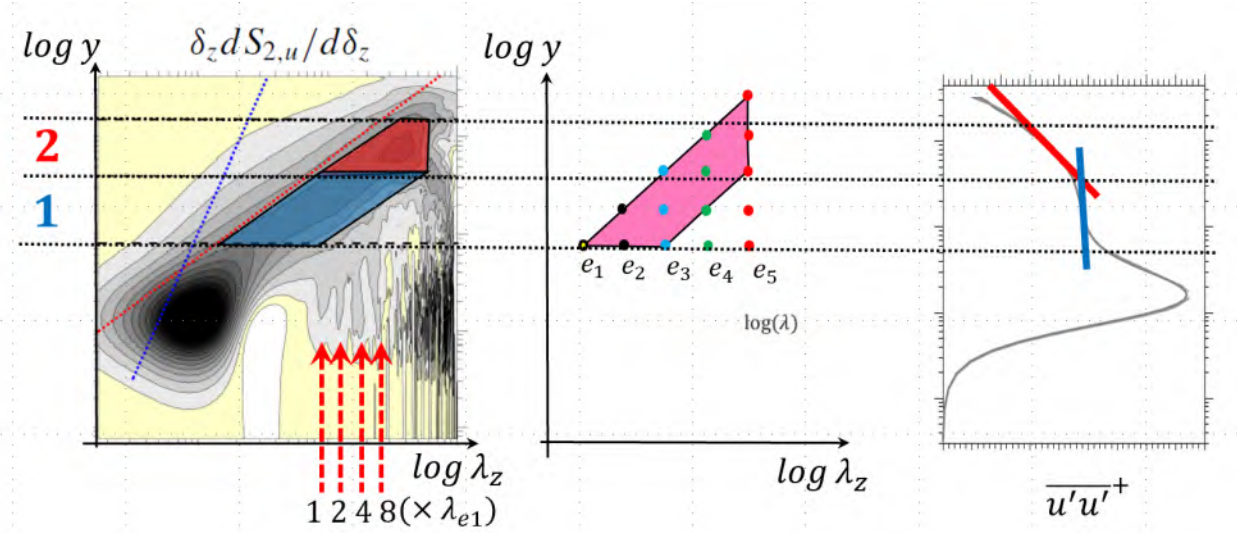


Figure 6.16: Consistency of the modified AEH with turbulence statistics shown through the plateau regions in the PMDS2 and corresponding stress profile behaviour.

The detailed analysis of the pre-multiplied density spectra map (PMDS2) in the wall-normal/wavelength space has revealed several important features that support the association between the attached eddy hypothesis (AEH) and the turbulence statistics in the meso-layer of the high Reynolds number channel flow. The meso-layer, spanning approximately  $150 \leq y^+ \leq 2000$ , is of particular interest as it encompasses the logarithmic region of the mean velocity profile and is populated by a hierarchy of attached eddies, as proposed by the AEH.

One of the most striking observations in the PMDS2 map is the presence of a trapezoidal plateau region, denoted as region “C” in Figure 6.16. This plateau is characterised by a nearly constant level of PMDS2, indicating a self-similar behaviour of the energy-containing scales within this region. The trapezoidal shape of the plateau has important implications for the wall-normal distribution of the streamwise turbulence intensity,  $\overline{u'u'}^+(y^+)$ . Integrating the PMDS2 along the wavelength axis within the plateau region leads to a constant value of  $\overline{u'u'}^+$ , as indicated by the vertical blue line in the accompanying profile. Beyond the upper boundary of the trapezoidal plateau, the PMDS2 level remains constant with increasing wall-normal distance, while the lower boundary continues to increase. This results in a logarithmic decay of  $\overline{u'u'}^+$  in the outer portion of the meso-layer, as conveyed by the red line in the profile.

The direct correspondence between the geometry of the plateau in the PMDS2 map and the behaviour of the streamwise turbulence intensity profile provides compelling evidence for the validity of the AEH in the meso-layer. The self-similar nature of the energy-containing scales within the trapezoidal plateau is consistent with the concept of attached eddies, which are proposed to exhibit a hierarchical structure and maintain a constant energy level when scaled with their respective length scales.

To further support these findings, the analysis was repeated over a restricted time interval of the DNS data, spanning approximately two global eddy-turnover periods. This approach aimed to minimize the influence of the strengthening large-scale motions in the outer region of the log-layer on the statistics. The resulting PMDS2 map, shown in Figure 6.16, reveals additional features that corroborate the AEH. In particular, the presence of four “fingers” in the sublayer, emanating from the meso-layer above, suggests the footprinting of attached eddies onto the near-wall region. The equidistant spacing of these fingers in logarithmic units indicates a sequential doubling of the eddy size, which aligns with the hierarchical structure proposed by Perry, Henbest, and Chong (1986).

The comprehensive analysis of the PMDS2 map in the wall-normal/wavelength space has provided strong evidence for the applicability of the attached eddy hypothesis in the meso-layer of high Reynolds number turbulent channel flow. The self-similar behaviour of the energy-containing scales within the trapezoidal plateau region, the logarithmic decay of the streamwise turbulence intensity in the outer meso-layer, and the footprinting of attached eddies in the sublayer all support the existence of a hierarchy of attached eddies that play a important role in the dynamics of wall-bounded turbulent flows.

## 6.5 Towards an Improved Attached Eddies Representation: An Extended Model

The availability of DNS data for channel flow at the credibly high friction Reynolds number of 4200 has provided an unique opportunity for exploring open questions on structural and spectral properties of near-wall turbulence in streamwise and spanwise direction. The examination has been undertaken by reference to maps of properties in the spectral/wall-normal space, the former being either the wave length, in the case of spectra, or the separation distance, in the case of the structure function. A first objective has been to examine the properties of turbulence across the spectral range from small-scale motions to the largest resolved motions. To this aim, new anisotropy parameters were defined, and maps of these parameters were examined, alongside pre-multiplied, compensated spectra and the pre-multiplied derivative of the second-order structure function, the latter shown to be closely related to the former. Primary emphasis was put on the meso-layer - essentially, the log-law layer spanning the range  $80 < y^+ < 2000$ .

A first important result derived from the above is a map in wall-normal-distance/wave-length space in which three major sub-ranges were identified within the meso-layer:

- (A) a sub-range at low wavelength (small-scale eddies) in which turbulence is anisotropic, characterised by a dominance of wall-normal and spanwise energy components over the streamwise component and the spectrum  $\Phi_{uu} \propto k_x^{-7/3}$ ;

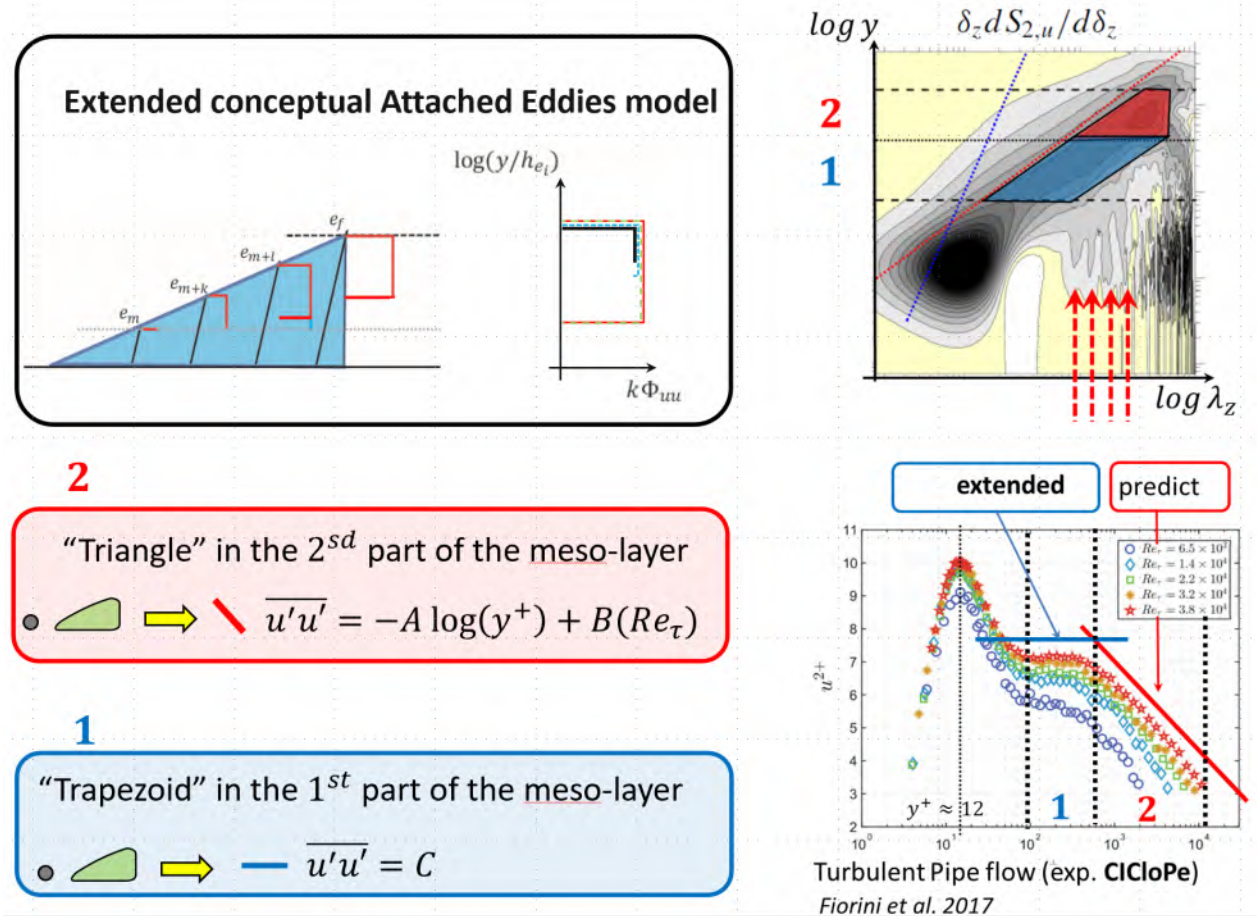


Figure 6.17: Revised attached eddies hypothesis: prediction of the plateau and logarithm decay.

- (B) a central range, which conforms to the conventional view of close to isotropic turbulence in which  $\Phi_{uu} \propto k_x^{-5/3}$ ;
- (C) a sub-range at high wave length in which the streamwise energy component dominates and in which the spectrum complies with a variation not far from  $\Phi_{uu} \propto k^{-1}$ .

The first result, (A), is rather counter-intuitive, as the expectation is that turbulence in the smallest range of eddies should be close to isotropic. Importantly, the sub-range (C) is not merely confined to the highest wavelength, but extends, in lower parts of the log-law meso-layer, well into the range of low wavelengths.

The above investigation, and its results, formed the background against which the second major objective was pursued – namely, to examine whether the attached-eddy hypothesis (AEH) is valid within the meso-layer. To this end, attention focused primarily on the pre-multiplied derivative of the second-order structure function (PMDS2), in preference to the premultiplied spectrum. This preference is based on the observation that the two are closely related, while the latter is a more promising foundation for examining the validity of the AEH – in particular, because the latter brings to light, much more clearly than the former, the “plateau” region with which the AEH is associated. This examination was further aided by the inclusion of one-dimensional PDFs for the streamwise-velocity fluctuations and their streamwise derivative, both displaying significant levels of negative skewness in the meso-layer, and of joined PDFs between the streamwise fluctuations and their streamwise or spanwise derivatives.

A conclusion derived from the PDFs is that the coherent structures in the meso-layer feature a “shape” that is characterised by a broad and short head and a narrow long tail, consistent with existence of a hierarchical structure of attached eddies. Consideration of the PMDS2 in wall-normal/spanwise-separation space, brought to light a trapezoidal region, contained within the sub-region (C) in the wall-normal/wave-length map, in which the PMDS2 level is close to being constant. Based on conceptual arguments, closely connected

to the conventional concept of self-similarity of the scaled energy of attached eddies in a triangular plateau region, the present observations of an approximate plateau in the trapezoidal region led to the conclusion that self-similarity – and hence, the AEH – also applies across the entire meso-layer. An interesting implication of the trapezoidal shape is that the upper part of the meso-layer is consistent with a logarithmic decay of the streamwise energy, while the lower part of the meso-layer is consistent with a constant level of energy – a behaviour broadly consistent with the directly computed (or measured)  $y$ -wise profile of the streamwise energy.

Retaining the conceptual framework of hierarchically stacked, geometrically self-similar attached eddies, a revision to their energy distribution enables consistency with the observed turbulence statistics. In this way, as shown in Figure 6.17, a subtle adjustment to the original AEH model, wherein attached eddy energy concentrates nearer the edge, aligns theory with experimental data. The conceptual model is largely unchanged, but by slightly modifying the eddy energy wall-normal profile - specifically, concentrating energy production in the upper portion of attached eddies - the AEH can be reconciled with statistics in the first part of the meso-layer. This synthesis demonstrates the flexibility of revised/extended Townsend's AEH in accommodating details of real flows.

## Chapter 7

# Towards a Unified Picture of Wall-Bounded Turbulence: Eddy Characteristics, Interactions, and Impact.

Turbulent boundary layers, ubiquitous in both engineered systems and natural environments, are populated by a wide range of coherent structures, each contributing substantially to turbulence dynamics. As illustrated in Figure 7.1, where a conceptually simplified representation of channel flow dynamics is proposed, depicted as a “puzzle” where each piece symbolises a distinct eddy family – streaks, attached eddies, and super-streaks – and the connecting segments represent the influential interactions between them and the mixing momentum. Gaining a comprehensive understanding of channel flow dynamics requires not only an in-depth study of individual “puzzle pieces”, but also an appreciation for their interconnections. Despite a substantial research effort involving high-accuracy simulations and experiments, gaps in our understanding persist. To address this, the research detailed herein is focused on elucidating the structures and mechanisms that underpin wall-bounded turbulence and related phenomena, such as skin friction. This includes a meticulous examination of large-scale motions, near-wall streaks, and attached eddies, leveraging high-fidelity simulations. Specific focus is given to the exploration of interactions between eddies and the subsequent activity near the wall. This effort is driven by the need to determine how wall turbulence self-sustains through synergistic interactions of its fundamental components. The in-depth investigations provide valuable insights aiding the assembling of this complex puzzle, by characterising structural families in wall-bounded flows and shedding light on their connections and impact on momentum mixing. In summary, this work seeks to deepen comprehension of wall-bounded turbulence’s multifaceted dynamics. Gaining insight into eddy characteristics and interactions is critical for enhancing predictive models and developing more effective control strategies.

The research presented in this manuscript offers new insights into the dynamics of both actuated and canonical wall-bounded turbulent flows. Leveraging high-fidelity simulation databases and applying statistical methods combined with data-driven algorithms, the work unravels the essential structural features, physics and interactions that govern these ubiquitous and complex flows:

- Chapter 2 investigates the mechanisms enabling drag reduction through imposed oscillatory spanwise wall motion. The analysis reveals how the unsteady Stokes layer disrupts near-wall streaks, influential vortical structures known to contribute to skin-friction generation. Drag reduction was found to involve complex transient interactions, with velocity skewness introducing asymmetry between streak suppression and recovery within the actuation cycle. Localised regions of high near-wall skewness were shown to play a crucial role in periodic drag oscillations by prolonging low drag phases. During these prolonged phases, rapid directional changes in the Stokes strain in the upper viscous sublayer prevent streak regeneration against the typical streak amplification timescale. These observations provide new physical insight into the multifaceted dynamics that enable overall time-averaged drag reduction. A notable finding is that oft-cited turbulence dissipation increases do not directly drive the process, as previously thought. Instead, drag decreases closely tie to inhibited production and amplification of streaks. As the Stokes layer weakens and rapidly changes direction, the formation of this latter is

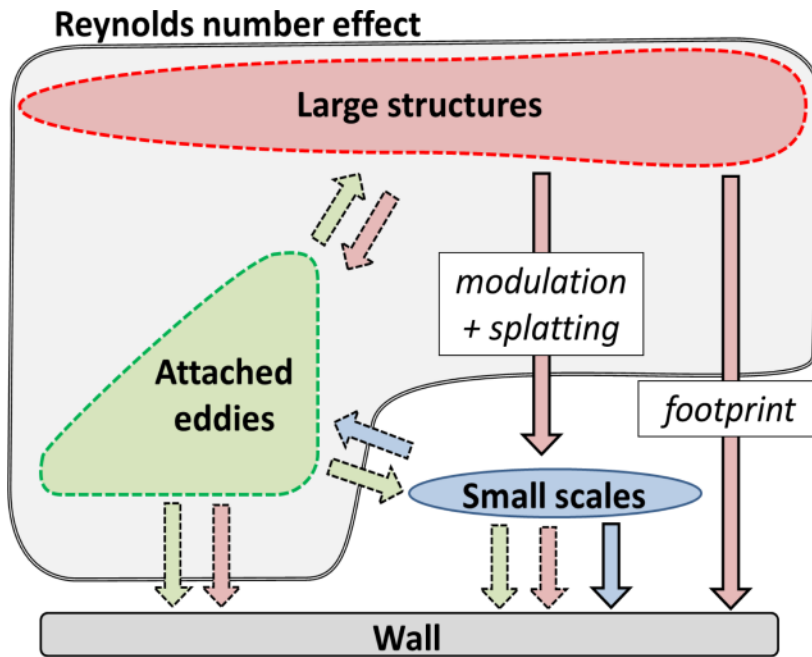


Figure 7.1: Conceptual organisation of the near-wall Turbulence dynamics.

disrupted. With further research building on these investigations on streak manipulation, Stokes strain effects, and skewness-induced asymmetry, there are promising opportunities to refine oscillatory control approaches and achieve greater, more robust drag reduction. The research significantly advances comprehension of the intricacies of how spanwise wall forcing interacts with coherent near-wall turbulence dynamics to induce a lowered drag state. The insights gained constitute an important foundation for ongoing efforts seeking to extend the efficacy of oscillatory drag-reduction strategies.

- Chapter 3 explores why drag-reduction efficiency declines with increasing Reynolds number. At higher Reynolds numbers, large-scale outer flow structures become more influential and can interfere with the control strategy. To study this, the flow field was separated into large-scale, small-scale and intermediate-scale motions using bi-dimensional empirical mode decomposition (BEMD). This allowed conditioned statistics to be derived that analysed how actuated small-scales respond to large-scale motions. The conditioned analysis revealed asymmetric modulation - positive large-scale fluctuations substantially amplify small-scales while negative fluctuations cause only mild attenuation. Positive fluctuations were also found to thin the viscous sublayer and draw the buffer layer containing streaks closer to the wall, strengthening the mixing momentum closer to the wall, while negative large-scale fluctuations did the opposite. When scaled by the fluctuating local skin friction, the actuation period was found to deviate significantly from its optimal value  $T^+ \approx 100$  under extreme positive fluctuations. This helps explain the reduced control effectiveness at higher Reynolds numbers. Multivariate joint PDF analysis was performed to relate flow statistics like stresses and production to the large-scale skin friction. This facilitated an in-depth study of scale interactions. Using the FIK identity, contributions of different scales to skin friction were quantified, showing large-scales directly contributed 26% to the total skin friction, for a channel flow at relatively low Reynolds number. To summarise, the results presented in this chapter demonstrate that the asymmetric response of near-wall turbulence to positive and negative large-scale motions, coupled with the thinning of the viscous sublayer under positive fluctuations, plays a key role in the Reynolds number dependence of drag reduction by spanwise wall oscillations.
- Chapter 4 further investigates the effects of increasing Reynolds number on canonical channel flow dynamics. An in-depth statistical analysis is conducted that exposes new insights into the purported “modulation” of near-wall turbulence by large-scale outer structures. The results seem to demonstrate that modulation does not occur through “direct” interactions from large to small scales. Rather, the influence of large scales is “indirect”, occurring through localised changes in shear strain that alter near-

wall turbulence intensity. Specifically, positive large-scale fluctuations, associated to sweep motions, are found to induce significant increases in local shear-strain rates. This enhances near-wall turbulence production, amplifying small-scale motions. In contrast, negative large-scale fluctuations prompt more modest attenuation. This modulation asymmetry is tied to the unsteady strain environment generated by large-scale sweeps and ejections. The analysis also clearly shows that large scales still substantially contribute to overall skin friction. This is quantitatively exposed by applying integral analysis methods to turbulence contributions from different scales. Large scales are found to directly account for over an important portion of total skin friction even at relative moderate Reynolds numbers. To conclude, results presented in this Chapter provides significant new perspective on the nature of scale interactions in wall-bounded turbulence. The findings contradict the notion of “direct” modulation while confirming large scales still impart major influence through more indirect means. Ongoing research can leverage these insights to further advance comprehension of multi-scale couplings inherent in turbulent flows.

- Chapter 5 demonstrates that within a canonical boundary layer flow, the characteristics of small-scale structures in the near-wall region exhibit a quasi-steady response. The “quasi-stationary” hypothesis proposes near-wall turbulence rapidly reacts to changes imposed by much larger, energetic outer structures. This assumes small scales instantly adjust due to the order of magnitude scale difference. A critical means of validating the hypothesis is examining whether small-scale statistics collapse to universality when scaled by the spatially varying large scale friction velocity,  $u_{\tau LS}$ . This was first examined in channel flow at  $Re_\tau \approx 4200$  and then at  $Re_\tau = 5200$ . Mean velocity, second-order moments, production term and PDFs were analysed. Results showed the quasi-steady hypothesis held for both amplitude and length-scale modulation of near-wall structures. The validity depends on the investigated quantity and small-scale spectrum range. As illustrated in Figure 5.17, small-scale energy increases linearly as  $Cf_{LS}$  strengthens, while their lengthscales decline. This aligns with quasi-steady hypothesis. As  $Cf_{LS}$  weakens, the structures expand as expected. However, negative  $Cf_{LS}$  produced smaller lengthscale growth than fully quasi-steady hypothesis would predict. A potential source of this deviation is large-scale negative fluctuation-induced outer flow mixing momentum interfering with the hypothesis accuracy.
- Finally, Chapter 6 critically re-examines the attached eddy hypothesis originally proposed by Townsend. Detailed analysis of structure functions and spectra suggests several refinements to better capture the hierarchy of eddy scales and inherent anisotropy. Investigations presented in this chapter provide an in-depth examination of the statistical properties of eddy length-scale sub-ranges. The Empirical Mode Decomposition method is leveraged to achieve scale separation in channel flows for analysis. The insights gained inform the development of an enhanced attached eddy framework. While retaining the essence of Townsend’s original conceptual model, which is the flow is populated of self-similar eddies shape by the presence of the wall, a critical refinement is introduced regarding the wall-normal energy distribution within attached eddies. In contrast to the constant distribution assumed initially, the revised model hypothesizes lower energy production near the wall, peaking higher within eddies. This nuanced representation of energy distribution significantly enriches the model’s predictive capabilities. It not only allows predicting the logarithmic decrease in the boundary layer’s outer region, as in the original model, but also captures the meso-layer plateau. Given the improved depiction of energy partitioning within turbulent structures, the potential of the revised attached eddy model to enhance turbulence model accuracy is substantial. This could enable major advancements in comprehending and controlling turbulent flows.

This manuscript makes significant contributions to furthering the understanding of the intricate flow physics and structural interactions underpinning wall-bounded turbulence and skin friction. Through rigorous computational analyses, the research provides novel insights into the multifaceted phenomena inherent to these complex flows, benefiting ongoing research efforts in this area. Wall turbulence is characterised by interactions between various coherent structures. Using conceptual representations, this research identifies and focuses on three distinct eddy families that collectively sustain wall turbulence: near-wall streaks, attached eddies, and large-scale motions. Despite extensive prior work, the precise characteristics and interactions of these eddies are not fully understood. The investigations presented scrutinise each eddy type to illuminate their distinct features and behaviours. Particular emphasis is placed on elucidating the interactions between these eddies and resultant impacts on skin friction. For actuated flows, phase-averaged analysis reveals the mechanisms by which oscillatory wall motions disrupt near-wall streaks to reduce drag. Furthermore, statistical evaluations demonstrate modulation of near-wall eddies by outer scales does not arise from direct

interactions. Rather, it occurs through localised unsteady strain rate changes imposed by large scales that alter near-wall production. Findings also show small scales exhibit a quasi-steady response, adapting rapidly to local conditions imposed by large scales. In summary, these focused studies significantly advance understanding of the intricate multi-scale dynamics in wall turbulence. The insights gained contribute to an integrated picture of how diverse coherent structures interact within the flow. Fully explaining the complexity of wall turbulence will require ongoing efforts to elucidate eddy characteristics and interconnection. Improved understanding will be crucial for refining predictive models and developing effective control strategies.

# Chapter 8

## Research Horizons

### 8.1 Rationale and Purpose Behind my Research Activities

Fluid dynamics is a fundamental discipline that underpins a wide range of natural phenomena and engineered systems. It governs the circulation of the Earth's atmosphere and oceans, shaping our climate and weather patterns. In meteorology, fluid dynamics plays a pivotal role in forecasting weather events and unravelling the complexities of extreme phenomena such as tornadoes and hurricanes. Fluid dynamics provides valuable insights into cardiovascular blood flow, facilitating the diagnosis and treatment of heart disease within the medical field. From an engineering perspective, the principles of fluid dynamics are indispensable for the design and operation of pumps, turbines, vehicles, ships, and many other applications. Aerodynamics and hydrodynamics form the foundation of efficient air and water transportation. Fluid dynamics plays a crucial role in the energy sector, particularly in the development of wind turbines, hydroelectric plants, and other power generation technologies. It is a fundamental aspect of our daily lives, driving advancements in system performance and efficiency, enabling the prediction of natural events, and catalysing the emergence of groundbreaking technologies.

My research focuses on the study of wall-bounded flows, with particular emphasis on the turbulent structures that populate these flows and determine the performance of industrial equipment and the prediction of environmental flows. The presence of these structures leads to increased mixing momentum and high friction drag, which can exceed laminar levels by a factor of 10 to 100, depending on the Reynolds number. Friction has a significant impact on the effectiveness of devices in many applications, especially in the context of self-propelling bodies and duct/pipe flows. As climate change is a growing concern, there is an urgent need to reduce transport emissions, of which friction is a major component. Although reducing mixing momentum can effectively mitigate drag, enhancing it typically provides benefits in terms of heat transfer. Therefore, achieving an optimal design for heat exchangers requires a delicate balance between drag and heat transfer. Improving their capacity is a critical challenge in achieving efficient and cost-effective energy transfer across a wide range of engineering systems.

Driven by the urgent need to address climate change, my research activities focus on improving efficiency and minimising pollution in a wide range of applications. These include fluid transport, vehicle efficiency and advances in heat exchange, all of which are critical in a wide range of industrial settings and in the design and development of novel technologies for harnessing green energy.

Heat exchangers are the “unsung heroes” of countless engineering systems, playing a major role in determining overall system efficiency and performance. In the transportation sector, heat exchangers are integral components in vehicles, aircraft, and ships, where they are employed for engine cooling, thermal load management, and ensuring optimal operating conditions. Even a slight improvement in heat exchanger efficiency can lead to significant fuel savings and reduced emissions, contributing to a greener and more sustainable transportation industry. Beyond transportation, heat exchangers are also crucial in the harvesting of green energy, such as solar and geothermal power. In solar thermal systems, heat exchangers are used to transfer heat from solar collectors to working fluids, which can then be used for power generation or space heating. Similarly, in geothermal systems, heat exchangers facilitate the transfer of heat from the Earth's interior to working fluids, enabling the production of clean, renewable energy. Enhancing the efficiency of heat exchangers in these applications can greatly increase the viability and cost-effectiveness of green energy solutions, accelerating the transition towards a low-carbon future and cut our dependence to fossil energy sources. In

this context, developing new control strategies and designs for heat exchangers could be a game-changer for a wide spectrum of applications, it is not only critical for the performance of numerous engineering systems but also could hold the key to unlocking the full potential of green energy technologies. Within this context, the ultimate ambition of my research is to **deepen our understanding of wall-bounded turbulence**. In doing so, I aim to develop reduced-order models that will facilitate more accurate predictions and the design of robust control strategies. The expected outcomes of this research include significant **improvements in energy transfer efficiency**. More specifically, by deepening our fundamental understanding of wall-bounded turbulence and **introducing innovative control approaches**, this work is expected to contribute to the development of cleaner and more optimised technologies for power generation, transport, heat exchange and green energy harvesting. My ambition, by focusing my research efforts on advancing heat exchanger design and control, is to contribute to the development of cleaner, more efficient, and more sustainable solutions across a broad range of industries, ultimately wishing to help to combat climate change and build a more resilient future.

## 8.2 The novelty and originality of my research contributions

### 8.2.1 Momentum and thermal boundary layers.

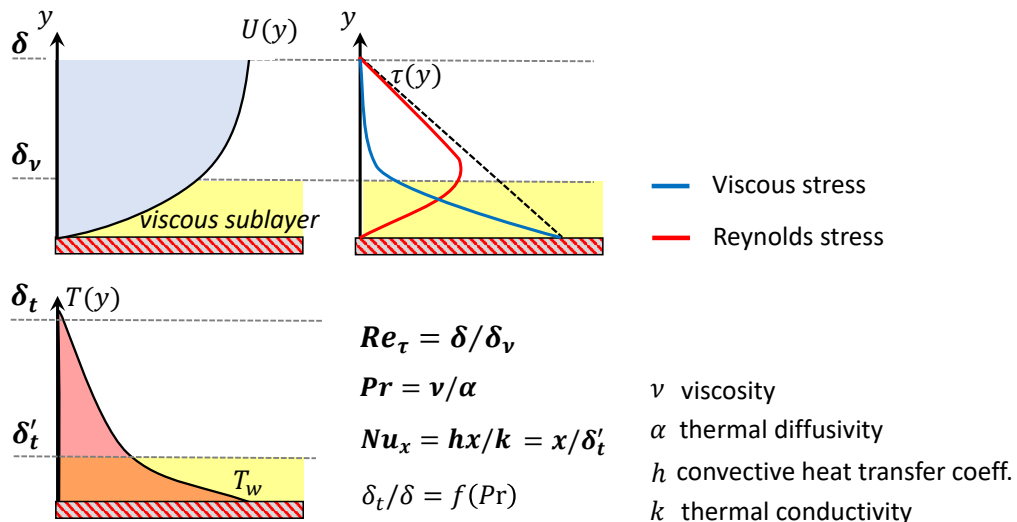


Figure 8.1: Conceptual representation of a momentum and thermal boundary layers.

Although emphatically chaotic, flow produced by this shear layer has some coherent structural components that are of major influence on the **mixing-momentum process** and consequently to the **drag** and **heat exchange**. The stronger the shear layer is, richer and more complex is the dynamics. A conceptual representation of a boundary layer over a flat plate is conveyed in Figure 8.1. When the gradient is relatively weak, only the viscous stress is in play. However, when the Reynolds number increases ( $Re_L = U_\infty L/\nu$ ), the shear strain strengthens leading to the apparition of structures producing Reynolds stress, the flow departs from a laminar state to become turbulent. As previously mentioned, high mixing momentum leads to high skin friction, which strongly weakens the operational effectiveness of a large amount of device and process. Therefore, reducing drag is a challenge to tackle in priority for many industrial, for both to be more competitive and to reduce their carbon footprint. However, for some processes the heat transfer is also the priority, for enhancing heat transfer, for these applications increasing mixing momentum at wall may be necessary. When a wall is at a temperature  $T_w$ , different from the temperature of the free stream,  $T_\infty$ , a thermal boundary layer is also present, with a thickness,  $\delta_t$ , different from the momentum boundary layer thickness,  $\delta$ . The turbulent thermal boundary layer has also an inner and outer regions. In the viscous sublayer, the turbulent mixing weakens drastically and conductive motions dominate (as illustrated in Figure 8.1). Because turbulent mixing is ineffective in the viscous sublayer, the latter is known to contribute to a substantial fraction of the thermal resistance of a turbulent boundary layer. The buffer layer, just above the viscous sublayer, is the region where the Reynolds stress contributes the most, the heat transport is mainly

driven by the turbulent mixing. Away from the wall, mixing motions gradually weaken until they ultimately vanish, defining the thickness of both thermal and momentum boundary layer. At first, it might seem that the Prandtl number ( $Pr$  defined in Figure 8.1) is not associated to the heat transfer as  $\delta_t$  and  $\delta$  are similar, but it first describes the flow behaviour in the first part of the wall-bounded flow, where molecular viscosity and thermal conductivity still control the transport of heat and momentum (so driving heat transfer and skin friction). As the turbulent momentum mixing within the wall-bounded region enhances, the **thinner** the boundary layer becomes, offering **less resistance to heat flow but increasing the drag**. Thus, for heat exchangers, a balance need to be found between drag-induced losses and the heat transfer. To improve heat exchange, convection must be enhanced. The ratio of convective to conductive heat transfer across a boundary is defined by the Nusselt number (see definition of  $Nu_x$  in Figure 8.1). By using the Reynolds-Colburn analogy **colburn\_method\_1964**, for a canonical turbulent boundary layer, the heat transfer can closely be related to shear stress on the wall by the semi-empirical equation (8.1).

$$Nu = \frac{Re \ Pr \ Cf/2}{1 + 12.7 \left( Pr^{2/3} - 1 \right) \sqrt{Cf/2}} \quad (8.1)$$

One objective is to predict the heat transfer under actuation and to characterise the influence of the Reynolds number when the control is directed towards the near wall structures. The aim is to extend the equation (8.1) to account for the effects of actuation and the presence of external flow structures with increasing Reynolds number. This extended model aims to incorporate the control and flow dependencies into the prediction of heat transfer. Evaluation of the model in different flow regimes will elucidate the coupled response of heat transfer to forcing and intrinsic turbulence. By improving our understanding of the underlying mechanisms, the model can enable the development of optimised control strategies and precise control of heat transfer. Overall, this work aims to improve our predictive capabilities by developing a comprehensive framework that encompasses the parameters governing convective heat transfer in wall-bounded turbulence.

### 8.2.2 An introduction to near-wall turbulence dynamics

Despite its intrinsically disordered nature, wall-bounded turbulence contains coherent structures that substantially impact momentum transfer and transport. These organised flow features are central to the dynamics driving skin friction and convective heat transfer at the wall. First, it is well established, both from simulations and experiments, that the highly-sheared viscosity-affected near-wall layer is characterised by a quasi-organised streaky structure – collectively referred to as “**streaks**” – formed by a spanwise, quasi-regular, elongated, high- and low-velocity regions and depend on the viscous scales ( $\delta_\nu$ ). They can be directly visualised from the streamwise velocity field conveyed by left-hand side snapshot in Figure 8.2(a)). The plot shows a velocity field for a channel flow at  $Re_\tau \approx 4200$  at a wall-normal location  $y^+ = y u_\tau / \nu \approx 12$ , where streaks are the most energetic, and indeed the plot reveals numerous small-scale structures, of order of the streaks ( $\lambda_x^+ \approx 10^3$  &  $\lambda_z^+ \approx 10^2$ ) and smaller. The streaks are associated with quasi-streamwise vortices that cause a “lift-up” of low-velocity fluid and a “draw-down” of high-speed fluid. A conceptual representation of eddies populating a wall-bounded flow and their dynamic are sketched in Figure 8.2(b), the streaks are represented by the grey ovals, the lift up and draw-down motions by the grey arrows. As these turbulent structures occur during transition from laminar to turbulent conditions, in which case the spectrum of their scales is very narrow, modest resources are required for investigating them, therefore, their nature is fairly well understood. Unlike, fully turbulent flows at high Reynolds numbers, these pose far greater challenges, as a new family of much larger eddies emerges. Indeed computations and measurements have shown that there exists a particular set of large-scale structures (often referenced as “super streaks”) that are most pronounced in the middle of the near-wall layer. These remain coherent throughout the boundary layer. In contrast to the streaks, the super streaks scale with the thickness of the boundary layer  $\delta$  and the outer mean velocity. The right-hand side plot in Figure 8.2(a), showing the streamwise velocity field taken away from the wall, brings into light the presence of these eddies which are much larger than the streaks seen on l.h.s snapshot ( $\lambda_x^+ \approx 5 - 8Re_\tau$  &  $\lambda_z^+ \approx Re_\tau$ ). Visual inspection of the two velocity fields shown in Figure 8.2(a) highlights the strong correlation of the long-wavelength fluctuations between these two wall-normal locations, demonstrating a footprinting phenomenon of the outer-flow structures on the wall. Furthermore, these figures show that the magnitude and frequency of the streaks depend on the motions of the outer flow, increasing during the large-scale sweeps, while decreasing during the large-scale ejections. These phenomena are summarised in the conceptual representation given in Figure 8.2(b): super streaks are represented by the coloured ovals,

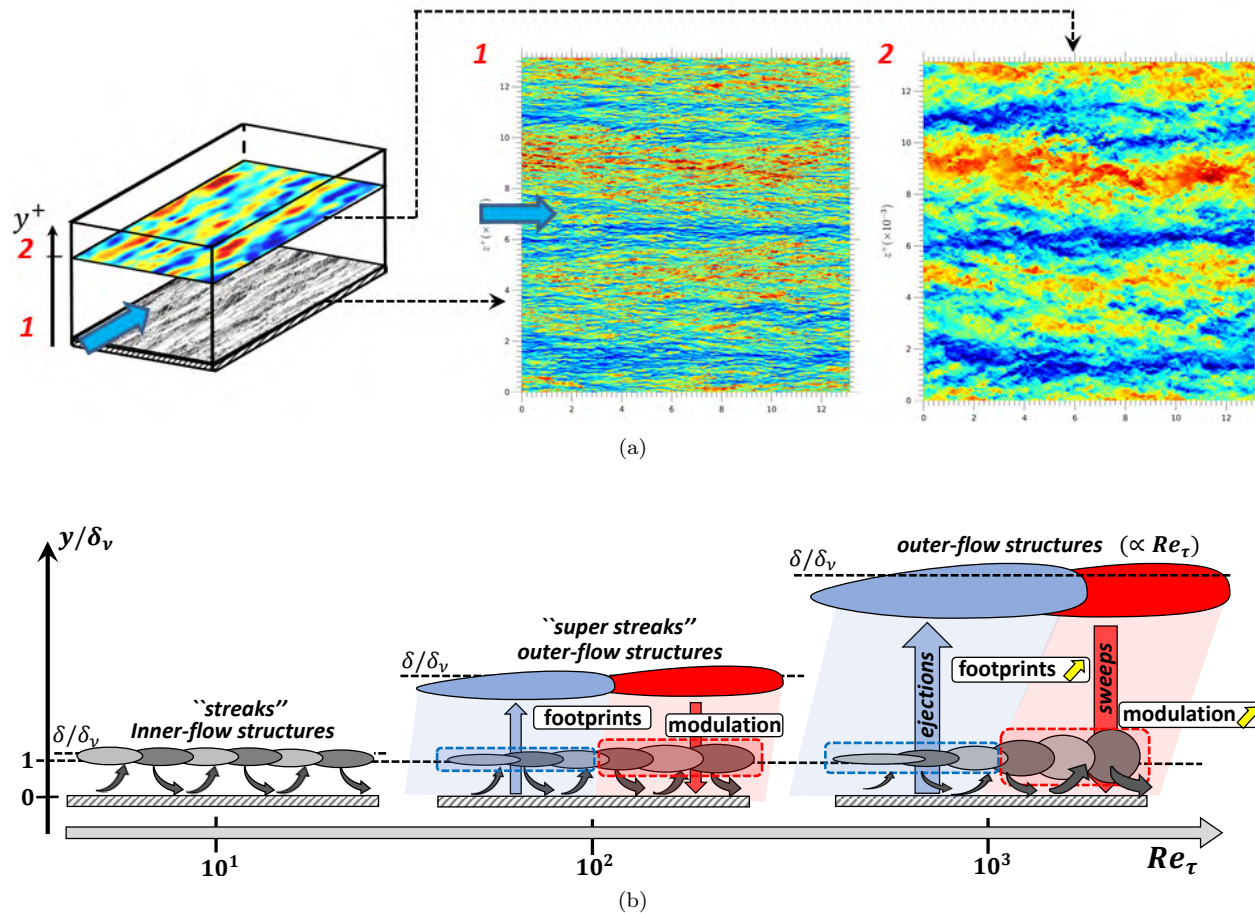


Figure 8.2: (a) Streamwise velocity fields for a channel flow at  $Re_\tau \approx 4200$  at two wall-normal location: (1)  $y^+ \approx 12$  and (2)  $y^+ \approx 260$ , (b) Schematic representation of wall-bounded flow as the Reynolds increases.

the vertical arrows show the footprint: ejection and sweep, in blue and red respectively. The response of the streaks to the outer-flow structures are represented, showing that the magnitude and the frequency vary depending of the footprint magnitude, and their contribution to the boundary-layer dynamics increase as the Reynolds number rises. Essentially, as the Reynolds number increases, the outer motions become progressively stronger and so does their influence on the near-wall structures. The outer structures, altered directly the near-wall turbulence by an effect referenced as “footprint” and indirectly by strengthen the streaks, phenomenon called “modulation”. The quantification of this latter has been the subject of several proposals. The classical approach, proposed by Marusic and his collaborators (Marusic, Mathis, and Hutchins 2010b; Mathis, Hutchins, and Marusic 2011), involves the evaluation of the envelope of the small-scale signal, and determining its correlation with the large-scale signal. A tangible outcome of the studies is **an empirical relationship** that permits the statistics of the near-wall turbulence to be “predicted” ( $u_p$ ), at any Reynolds number, from a “universal” small-scale signal  $u^*$ , unaffected by large-scale outer-flow structures  $u_{O,LS}$  and thus Reynolds number, the empirical relationship it is given by :

$$u_p^+ = u^* \underbrace{[1 + \beta u_{O,LS}^+(y_O^+, \theta_{LS})]}_{\text{modulation}} + \underbrace{\alpha u_{O,LS}^+(y_O^+, \theta_{LS})}_{\text{superposition}}, \quad (8.2)$$

$\beta$  and  $\alpha$  being empirical parameters.

This empirical relationship suffers from shortcomings and gaps in several aspects. For example, this relation assumes that streak modulation is symmetric, but recent studies have shown that this assumption is invalid. Indeed, when the footprint strengthens, the streaks are splatted” in the spanwise direction. Figure 8.3 provides a conceptual representation of the effect of outer-flow structures on small-scale structures populating a canonical boundary layer. Large-scale ejections and sweeps locally shift the velocity near the wall, proportionally modifying the magnitude of the streaks (as given by equation (8.2)). However, as illustrated in Figure 8.3, there is also a phenomenon of splatting” that occurs during large-scale sweeps, which strengthens as the magnitude of the sweeps increases. This phenomenon is not predicted by the current form of the empirical relationship given in eq. (8.2). The inability to accurately predict the reaction of the streaks means that the mixing momentum causing drag and heat transfer cannot be predicted correctly either, and this inaccuracy worsens as the Reynolds number increases. It is worth mentioning that the impact of splatting on wall-bounded flow is already clearly visible at relatively low Reynolds numbers ( $Re_\tau \approx 1000$ ), for which external flow structures start to become relevant.

Further analyses are needed to understand how near-wall structures are affected by outer flow features and to develop robust predictive models, not just for canonical flows but also when external actuation is applied, which is one of my objectives. To address these challenges, my research aims to combine turbulence knowledge and fluid dynamics approaches with machine learning techniques. By bringing together these fields, we can more effectively extract key information from immense datasets to identify important flow characteristics. This will enable the development of accurate predictive models that include control effects and Reynolds number dependencies. By leveraging the power of machine learning, we can uncover hidden patterns and relationships within the data that may not be easily discernible through traditional analysis methods. This approach will allow us to build more comprehensive and robust models that can accurately capture the complex interactions between near-wall structures, outer flow features, and external actuation across a wide range of Reynolds numbers. Ultimately, this research will contribute to a deeper understanding of wall-bounded turbulence and provide valuable insights for the design of effective flow control strategies and the optimisation of engineering systems.

### 8.2.3 Harnessing the power of machine learning for unravelling the complexities of near-wall turbulence

Nowadays, experimental and numerical simulations progressively provide an unprecedented volume of extremely detailed data, which need to be examined and interpreted. There is therefore an increasing urgency of refined investigative tools for appropriate statistical analyses and data mining. Machine-learning (ML) algorithms offer a new path for investigating high-dimensional, nonlinear problems, such as near-wall turbulence. The development of ML methods, associated with the abundance of data and combined with solid background in turbulence, offers an unique opportunity for achieving major breakthrough in terms of advances in wall-bounded flows and their control. The identification of the phenomena driving the flows dynamics remains one of the major challenges of physics and engineering today. This complexity has traditionally been

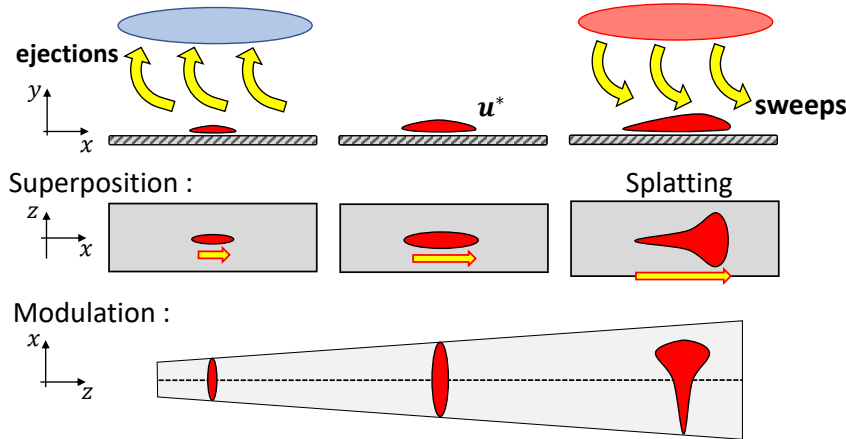


Figure 8.3: Conceptual representation of the effects of the outer- flow structures on the inner structures for a baseline flow.

addressed by statistical turbulence models, but these are proven to have only limited generality, even in the case models are based on the most elaborate transport equations for the second moments of the turbulent fluctuations. The recent developments of Machine Learning methods for the modelling of large-scale problems and their control prove to be a promising way forward. Moreover, thanks to recent advances in metrology, and the drastic reduction in computational costs, both the number and the size of database have undergone substantial growth in fluid mechanics. This abundance of data poses new challenges for the postprocessing that requires appropriate tools. Thankfully, many techniques have been developed by the Machine Learning (ML) community that are readily applicable to spatiotemporal fluid data, and are sustained by the recent advances in hardware (development of GPU/TPU platforms), algorithms and open-source libraries. By definition, ML is the field of study that gives computers the ability to learn without being explicitly programmed (Samuel 1959). Machine Learning algorithms are categorised as *supervised*, *semi-supervised* and *unsupervised* learning (see Figure. 8.4 and the recent review of Brunton, Noack, and Koumoutsakos (2019)). The task of supervised learning is to learn a function that maps input to output based on labelled examples. On the other hand, unsupervised learning consists in learning unknown patterns in a set of data without *a priori* information. Finally, semi-supervised learning operate on a large amount of unlabelled data, or with corrective information from the environment, for training a small amount of labelled data. In my research, Machine Learning algorithms will not aim to replace knowledge from physics (evolution laws for instance) with data, but rather to use models, physical insights and data in synergy. After years of in-depth analysis of boundary layer dynamics in compressible and incompressible regimes, and my recent studies using Machine Learning algorithms, I believe that significant progress in understanding near wall flows and their control can only be achieved by making the best use of a solid background in turbulence and new approaches offered by Machine Learning.

#### 8.2.4 Machine learning: switch of paradigm

In a “classical” approach, the first step for determining an predictive model or optimal control law is to fully understand the dynamics, then model and finally optimise. However, for the vast majority of flow configuration, this “sequential” approach is untenable. Indeed, as flows are highly dimensional, strongly nonlinear and multi-scale, the first two phases required major effort, this is especially true for wall-bounded flows. Moreover, this “model-driven approach” has two major drawbacks: (i) it is difficult to interact in real time as the model is often complex, (ii) the dynamical model can not be easily generalisable.

As illustrated in Figure 8.5, Machine Learning is an iterative process between data-driven modelling and control strategy optimisation. At a given level of understanding, a prediction model is determined from data, then an optimisation strategy is evaluated. This deepens understanding and improves the prediction model. Data-driven algorithms efficiently unravel mechanisms driving flow dynamics and identify optimal control laws. The approach relies on three main pillars: “Big” Data (obtained by Numerical simulations or/and experiments) – Low-dimensional dynamical model – Control strategies First, high-fidelity numerical

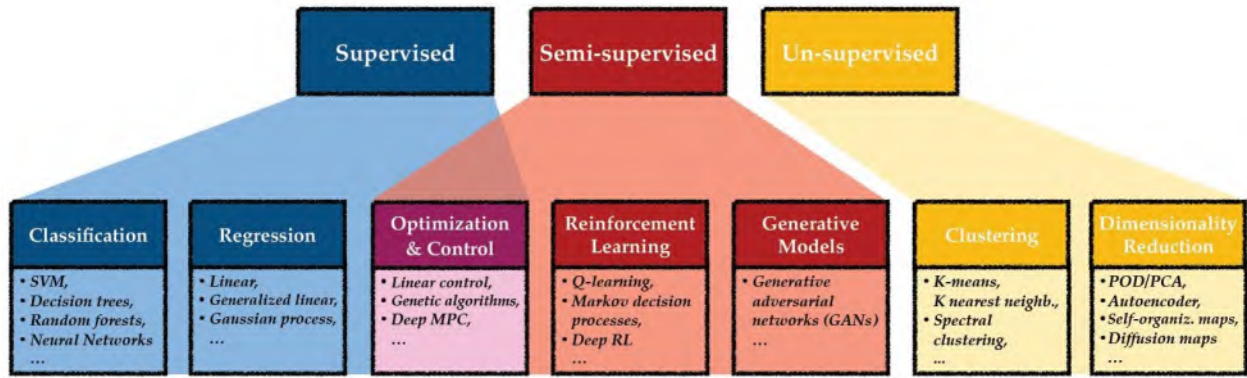


Figure 8.4: Organisational overview of various Machine Learning methods (after Brunton, Noack, and Koumoutsakos (2019)).

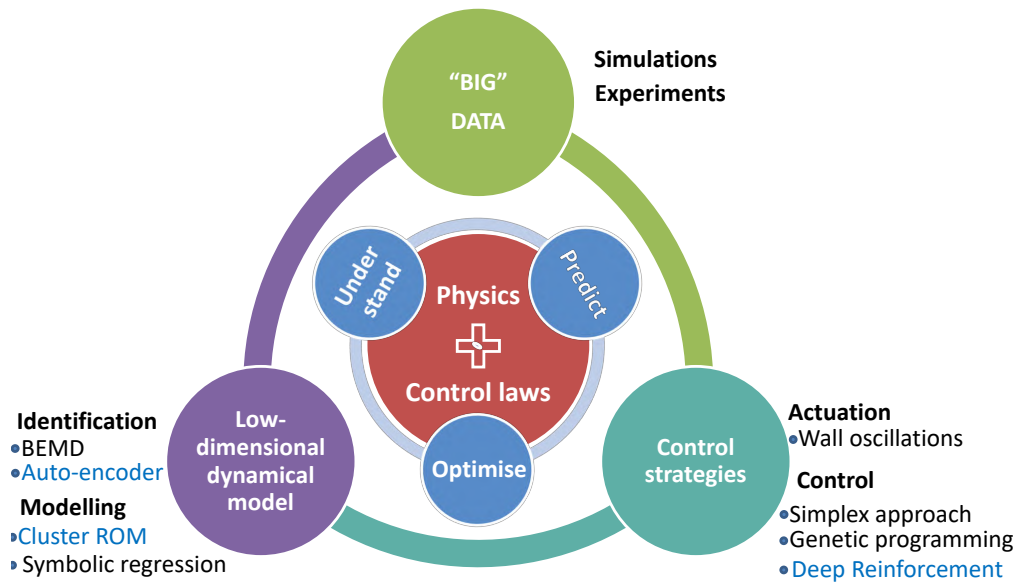


Figure 8.5: Machine learning control : switch of paradigm.

simulation or experiments data provides insights into the flow physics. Next, main features of the dynamics are extracted into low-dimensional models. Finally, these models enable designing and testing control strategies. The process repeats in a virtuous circle, progressively refining the models and controls through new data. This data-driven framework couples modelling and optimisation to rapidly advance knowledge and performance.

### - Data-driven reduced order modelling

A common approach to reduced order modelling is to determine a compact coordinate system in which the dynamics are effectively represented. Figure 8.6 illustrates the process of transforming high-dimensional experimental or simulation data into a lower-dimensional latent space for simplified tracking and modelling. This process can be divided into several key steps:

1. The first step is to acquire extensive data that encompass the evolution of the flow field, providing a comprehensive representation of the flow dynamics across various conditions and time scales.
2. An encoder is then used to identify the dominant flow features and project them into a compact latent space. Coding techniques from fluid dynamics or machine learning, such as Fast Fourier Transform (FFT), Proper Orthogonal Decomposition (POD) or autoencoders, are used to extract the key dynamics and represent them in a reduced-dimensional space.
3. Within this reduced-order space, models are developed to predict the evolution of the flow. Methods from fluid dynamics can provide interpretable models with reasonable accuracy. Machine learning techniques, such as neural networks, can offer higher model performance, albeit with reduced interpretability and generalisability. The choice of method involves weighing these trade-offs based on the specific modelling goals and requirements.
4. As flow conditions change, the accuracy of the reduced-order models may decrease due to drift. To address this issue, the encoder can be retrained to identify new dominant flow features that emerge under the changed conditions. Alternatively, direct field measurements can be used to correct model deviations from reality and ensure that the reduced-order models remain accurate and reliable.
5. Finally, the decoder reconstructs the full flow fields from the latent space, closing the loop and enabling the visualisation and analysis of the predicted flow dynamics.

The objective of my research is to introduce a framework that synergistically combines fluid dynamics and machine learning techniques to extract the underlying physics and predict flow dynamics without the need for exhaustive simulations or experiments. By innovatively integrating methods such as FFT, POD, autoencoders, and neural networks, I aim to develop data-driven reduced-order models that capture the essential flow features and dynamics while minimising computational complexity. This framework will not only advance our understanding of complex flow phenomena but also facilitate the development of effective flow control strategies. By leveraging the strengths of both fluid dynamics and machine learning, this research seeks to push the boundaries of reduced-order modelling and provide powerful tools for analysing, predicting, and manipulating flow dynamics in a wide range of applications.

### - Inner-flow structures and control

As previously mentioned, “**streaks**” – formed by a spanwise, quasi-regular, elongated, high- and low-velocity regions, are associated with quasi-streamwise vortices that cause a lift up of low-velocity fluid and a draw-down of high-speed fluid, thus important momentum mixing. Their development therefore leads to a strong drag increase, for decades the aerodynamic community has been investigating a wide range of passive and active control strategies to remove these structures.

There are very few control options that are demonstrably effective at reducing friction drag over large surfaces, and it must be acknowledged that all involve formidable engineering challenges. Passive devices, such as riblets and super-hydrophobic surfaces, either offer modest drag-reduction margins and degrade rapidly, or are only realisable in very special circumstances - e.g. in liquids. Active methods, most of the time involve wall-based actuation. At low Reynolds number, all target the processes in the viscosity-affected near-wall layer, and all are designed to disrupt the near-wall streaky structure and associated regeneration mechanism that sustains the streaks and vortical motions. Leaving aside rather tentative attempts to use synthetic jets, active dimples/pimples and plasma actuators, mostly applied locally and at very low Reynolds number, one

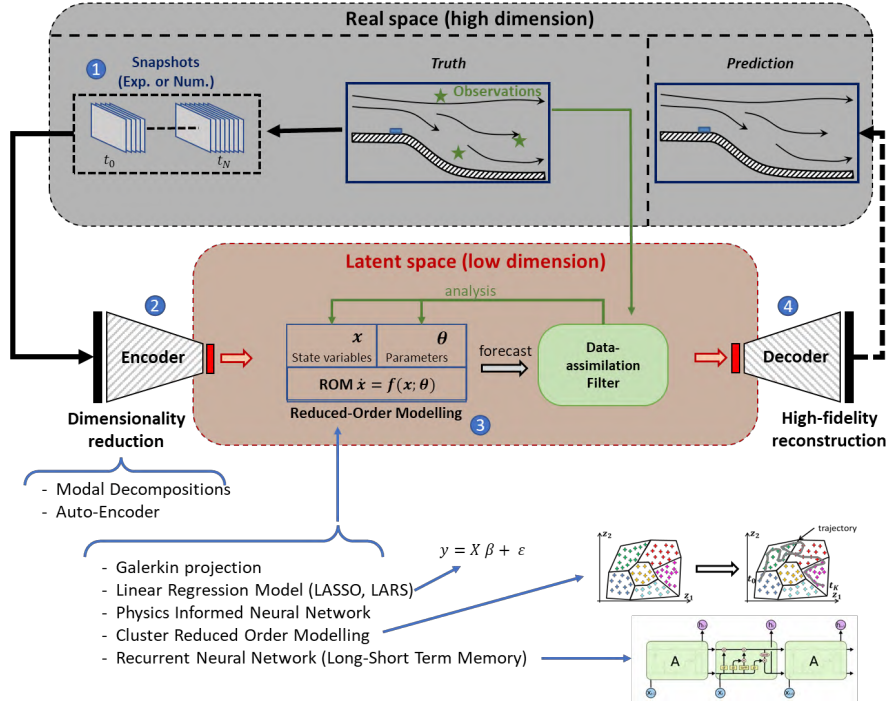


Figure 8.6: General framework for building a data-driven low-dimensional dynamical system

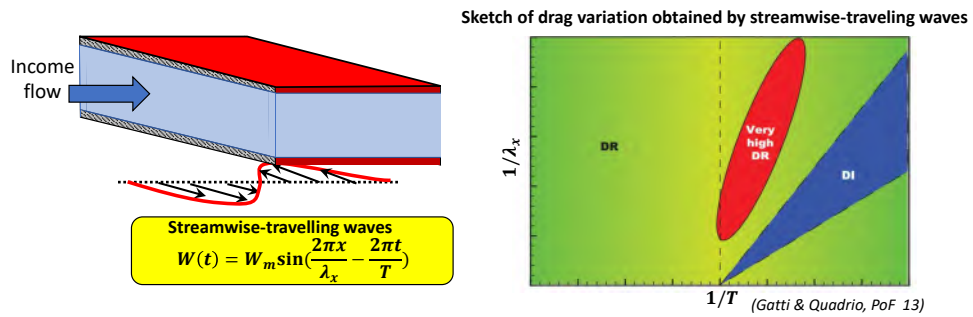


Figure 8.7: Left-hand side plot: schematic of the system for turbulent channel flow with travelling-wave actuation. Right-hand side plot: map of the drag variation in the plane spanned by  $\lambda_x-T$ , DR: Drag reduction and DI: Drag increase. (Gatti and Quadrio (2013)).

of tenable approach – at least in a laboratory setting (Auteri et al. (2010) and Marusic et al. (2021)) – is to impart unsteady transverse shear onto the thin viscous sublayer by oscillatory wall motion. The oscillatory flow patterns that are most effective involve streamwise waves of spanwise motion, where the spanwise velocity of the wall is  $W = W_m \sin(2\pi x/\lambda_x - 2\pi t/T)$ <sup>1</sup>. (Gatti and Quadrio 2013) performed an extensive study at  $Re_\tau \approx 200$  investigating a large combination of set of parameters  $\lambda_x$  and  $T$  and their effect on the drag. The map of the drag variation in the plane spanned by  $\lambda_x - T$  is shown in Figure 8.7. With a careful choice of actuation parameters, gross drag-reduction level in excess of 45% has been demonstrated in direct numerical simulations of low Reynolds number channel flows ( $Re_\tau \approx 200$ ) Quadrio and Ricco (2004) and Quadrio, Ricco, and Viotti (2009). These studies show that the drag can be also substantially enhanced, depending on the choice of actuation parameters (see Figure 8.7). It is established that for wall-scaled oscillation periods  $T^+ \approx 100$  drag is substantially reduced, while  $T^+ \gtrsim 200$  leads to a substantial drag increase. The exact mechanism by which such oscillations control the drag is complex and the subject of many studies (e.g. Ricco et al. (2012) and Agostini, Touber, and Leschziner (2015)). Essentially, the oscillations set up an unsteady Stokes layer close the wall that weakens or enhance the turbulent streaks in the viscous sublayer and the quasi streamwise vortices, thus reducing or enhancing turbulent momentum exchange close to the wall. An intensification of the near-wall turbulence can be expected to enhance the heat transfer, and a question is whether it is possible to substantially increase the heat transfer at only modest penalty of increased drag.

More recent studies (Agostini and Leschziner 2019b; Agostini and Leschziner 2021) have shown that the outer motions strongly altered the streaks behaviours when wall oscillations is applied, indeed in region where the large-scale footprints strengthen by the large-scale sweep motions, streaks rapidly reappear and drag quickly increases. There is a strong asymmetry from the streaks response between negative and positive large-scale motions, -i.e. the modulation does not linearly depend on large-scale motion (as illustrated in Figure 8.3 for a baseline flow), the empirical relation given by eq.8.2 can no longer be applied.

### 8.3 Active research activities

My current research activities are centred around three main projects, each focusing on different aspects of wall-bounded flows and heat transfer:

- The first project investigates the control of small-scale structures on drag and heat transfer, and how the efficiency of this control changes as the Reynolds number increases. This project aims to understand the fundamental mechanisms of how small-scale structures affect drag and heat transfer, and to develop effective control strategies that can be adapted to different flow conditions. The investigation of the small-scale structure characteristics at different Reynolds numbers will provide insight into how their dynamics and interactions with the flow evolve as the flow becomes more turbulent. This knowledge is essential for designing control strategies that remain effective over a wide range of flow conditions.
- The second project involves predicting and modelling the evolution of wall-bounded flow dynamics as the Reynolds number increases (see section 8.3.1). The objective is to develop accurate and efficient low-order dynamical models that can capture the non-linear multi-scale dynamics of wall-bounded flows at high Reynolds numbers, which is essential for designing and optimising flow control strategies. These low-order models are designed to reduce the computational complexity of simulating high Reynolds number flows while still capturing the essential flow features and dynamics. More efficient and effective control strategies that can be applied to real-world systems should be able to be introduced by incorporating these models into flow control algorithms.
- The third project focuses on exploiting secondary flow instabilities to create and control large structures that improve heat transfer with minimum energetic input perturbation (see section 8.3.2). It explores the potential of using secondary flow instabilities, such as those induced by surface roughness or geometric features, to generate large-scale structures that can enhance mixing and heat transfer between the wall-bounded and outer flow regions. By carefully designing surface features or introducing specific perturbations, we can trigger secondary flow instabilities that give rise to coherent large-scale structures. These structures can significantly enhance mixing and heat transfer by promoting the transport of heat and momentum across different flow regions. The project focuses on identifying the optimal perturbations that can produce the desired large-scale structures maximising the efficiency of the heat-transfer enhancement with a minimal cost.

---

<sup>1</sup>The control parameters are represented in red.

The assumption that controlling small-scale structures can enhance heat transfer at the wall where temperature gradients are steepest, and that controlling large-scale structures can promote mixing between the wall-bounded and outer flow regions where the temperature difference is greatest, suggests that these two control strategies can be implemented without mutual interference. A multi-scale control strategy can significantly enhance heat transfer by operating on different timescales and affecting different flow regions. This can be achieved by simultaneously controlling small-scale structures near the wall and large-scale structures in the outer flow region, thus optimizing heat transfer across the entire flow domain. In addition, controlling large-scale movements can help predict their local effects on small-scale structures, allowing small-scale control to be adapted for optimal performance. This adaptive control approach can further improve the effectiveness and robustness of the multi-scale control strategy, making it suitable for a wide range of flow conditions and applications.

### 8.3.1 Project: Influence of Near-Wall Turbulence on Heat Transfer & Modelling the Influence of Reynolds Number

In contrast with many scientific fields, fluid mechanics is in the enviable position of having a first principle equation, the Navier-Stokes (NS) equations, to describe flows. In principle, the flow motions can be perfectly predicted by solving these equations. However, for wall-bounded flows, solving the NS equations rapidly proves to be too computationally expensive, as the flow becomes increasingly complex as the Reynolds number increases. The reason for such flow complexity relies on the fact that for any viscous fluid in motion relative to a solid, the velocity decreases to zero at the wall inducing a shear layer. This latter creates chaotic turbulent structures within a wide spectrum of length and time scales. Indeed, eddies populating the flow cover a range bounded by the Kolmogorov length, at one end, and multiples of the boundary-layer thickness, at the other. The stronger the shear layer is, richer and more complex is the dynamics. This is all more true since as the Reynolds number increases new families of outer-flow structures are produced and enrich the flow dynamics, which renders the study of near-wall turbulence extremely fascinating and challenging.

Streamwise velocity fields in the inner and outer regions of a channel flow at a relatively moderate Reynolds number ( $Re_\tau \approx 4200$ ) are shown in Figure 8.2(a). A visual inspection clearly brings into focus the complexity of this flow, highlighting the fact that the dynamics is highly dimensional, multi-scale, and strongly non-linear. When direct numerical simulation (DNS) is applied to such flow conditions, it is easy to demonstrate that the consequence of the aforementioned increase in scale disparity is that the numerical grid required to resolve all scales must increase in proportion to  $Re_\tau^3$ . As a result, **simulations at high Reynolds numbers rapidly become untenable**. The largest  $Re_\tau$  simulated by DNS is around 5 200 (Lee and Moser (2015)), which is relatively low compared to industrial applications and atmospheric boundary layers where the orders of magnitude of  $Re_\tau$  exceed 100 000. It is thus essential to have ***surrogate models*** that reduce the complexity of the problem, leading to solutions at a lower computational cost. These models are needed to provide **conceptual frameworks that are interpretable, improve physical understanding, predict flow dynamics, and facilitate the design of control strategies**. Numerical and experimental studies tend to show that outer structures drive the variations in wall-bounded flows as the Reynolds number increases. Both the size and magnitude of these structures increase with the Reynolds number. Without a sufficiently detailed understanding of how the outer-flow structures directly and indirectly alter the mixing momentum, accurate flow prediction at high Reynolds numbers will not be possible, and most control strategies are fated to remain sub-optimal or even ineffective, as they are designed at low Reynolds numbers. Therefore, in order to design active and passive control strategies capable of significantly reducing drag or improving heat transfer for practical flows, it is essential to first improve our understanding of wall turbulence, focusing on skin friction and heat transfer. In addition, it is essential to characterise their variation with increasing Reynolds number by considering the effects of large external flow structures. This understanding will form the basis for the development of robust and effective control strategies that can be applied to a wide range of industrial applications and atmospheric boundary layers where Reynolds numbers are significantly higher than those currently achievable by direct numerical simulation.

In this framework, the objectives of my current research are as follows:

1. To deepen our understanding of how the mixing momentum generated by the inner structures drives the drag and, more specifically, the heat transfer. This objective aims to elucidate the complex interaction between the near-wall turbulent structures and the resulting mixing momentum, which has significant implications for both drag and heat transfer properties. By shedding the light on the underlying physical mechanisms, valuable insights can be gained about the fundamental principles governing these processes and more accurate predictive models can be developed. This work is part of the ANR Inference.
2. To characterise the effect of control on drag and, more specifically, on heat transfer when streaks are manipulated by wall oscillations. This work is currently in progress with the ANR SOLAIRE project, with the supervision of PhD student Lou Guerin and in collaboration with the Promes laboratory. By investigating the response of near-wall streaks to wall oscillations, we aim to quantify the impact of this control strategy on drag reduction and heat transfer enhancement. This research will provide valuable insights into the effectiveness of wall oscillations as a flow control technique and guide the development of optimised control parameters for specific applications.
3. To provide a more accurate model capable of predicting the effect of external flow structures on near-wall turbulence, particularly on the mixing momentum, and to define an estimator of the near-wall flow fluctuations from outer-flow sensors. These investigations will be performed within the framework of the ANR Inference project. By developing advanced models that capture the influence of outer-flow structures on near-wall turbulence, we aim to improve the predictive capabilities of flow simulations and enable the estimation of near-wall flow fluctuations based on outer-flow measurements. This research will contribute to a more comprehensive understanding of the multi-scale interactions in wall-bounded turbulence and facilitate the development of efficient flow control strategies.
4. To gain a deeper understanding of the effects of external flow structures on controlled near-wall turbulence and to be able to model them. These investigations will be carried out within the ANR Inference project. By studying the way external flow structures interact with actively controlled near-wall turbulence, we aim to unravel the complex dynamics and develop robust models that capture these interactions. This research will provide valuable insights into the effectiveness of flow control strategies in the presence of external flow structures and guide the design of adaptive control algorithms that can account for these effects.

This project is inherently **interdisciplinary**, with both fundamental scientific and practical engineering significance. It combines and advances the cutting edge of several advanced scientific concepts and capabilities; as such, it has the potential for substantial academic impact in broader contexts, regardless of ultimate practical use. First, the exploitation of advanced DNS for combined drag and heat-transfer optimisation, subject to a combination of active control strategies using wall oscillations, is novel and is likely to advance DNS into a new flow-control direction of interest to the flow-physics community. Second, the adaptation of machine learning (ML) to optimise thermo-fluids systems is in its early infancy; the application of this emerging technology for modelling, predicting, and optimising drag and heat transfer in the manner proposed has many unique aspects. The research outputs are expected to help model, predict, and control heated wall-bounded flows, paving the way for more efficient and sustainable engineering systems across a wide range of applications, from aerospace and automotive industries to energy production and environmental management.

The project is structured around three questions (in Figure 8.8) :

1. How skin friction and heat transfer are related and driven by wall-bounded structures?
2. What are the effects of outer-flow large-scale structures on wall-bounded flow?
3. Modelling of the Reynolds number effects on the turbulent boundary layer?

#### **Q1 - How skin friction and heat transfer are related and driven by wall-bounded structures?**

##### **⇒ Canonical turbulent boundary layer-**

For turbulent boundary layer at low Reynolds number, the small scales generate vortical motions, promoting momentum mixing and, consequently, an increase in drag. One of the first task is to investigate the **correlation between the drag and the convective heat transfer**, and this for different ratio between the

Outer-flow structures effects ( Reynolds number)		
open-ended questions	$Re_\tau \approx 200$	$Re_\tau \approx 1000 \rightarrow 5200$
	<p><b>Q1 – How skin friction and heat transfer are related and driven by wall-bounded structures?</b></p>	<p><b>Q2 – What are the effects of outer-flow large-scale structures on wall-bounded flow:</b> → Streaks → Skin friction → Heat transfer</p>
Achievements	<ul style="list-style-type: none"> <li>⇒ Relation between drag and convective heat transfer.</li> <li>⇒ How effective is spanwise wall motion in increasing or decreasing the heat transfer?</li> <li>⇒ Map of <math>Nu</math> variation depending on control parameters &amp; identified set of parameters for maximising <math>Nu</math>.</li> </ul>	<ul style="list-style-type: none"> <li>⇒ Predict the effects of outer-flow structure on drag and heat transfer for both canonical and actuated flows.</li> <li>⇒ Revise the empirical relationship:  <math display="block">u_p^+ = u^* [1 + \beta u_{O,LS}^+(y_O^+, \theta_{LS})] + \alpha u_{O,LS}^+(y_O^+, \theta_{LS})</math> </li> <li>⇒ Introduce a relation for the <math>Nu</math> taking under consideration the effect of large-scale motions</li> </ul>
		<p><b>Q3 – Modelling of the <math>Re</math> effects on the turbulent boundary layer.</b></p>

Figure 8.8: Open questions and milestones

thermal and momentum diffusivity, to highlight the role of the thickness of thermal boundary layer to promote or prevent heat transfer. Efforts to optimise the heat transfer efficiency will benefit from an in-depth fundamental understanding of how turbulent structures present in wall-bounded turbulent flows relate to heat transfer.

#### ⇒ Actuated turbulent boundary layer

The second part of this work aims to explore the use of oscillatory spanwise wall motion to alter convective heat transfer in turbulent boundary layers. Spanwise wall oscillations have been extensively investigated within the aerodynamics community for reducing friction drag over large surface areas and have proven to be effective extremely effective, at least for relatively low Reynolds number. However, the potential to leverage this actuation strategy for enhancing heat transfer remains largely uninvestigated. The objective is to create a coarse map of the heat transfer response to oscillatory wall motion across a range of forcing parameters, similar to the drag variation map shown in Figure 8.7. This latter demonstrates that drag can be increased or decreased using different parameter combinations. It is expected that heat transfer enhancements may occur alongside drag increase, but the primary factor is determining the achievable heat-transfer gains and their associated drag penalties. Passive heat transfer enhancement techniques often result in significant pressure drop, which can be detrimental to the performance of the complete system. In contrast, if properly designed, active flow control using transverse wall oscillations could significantly enhance convective heat transfer over large areas, limiting the drag penalty. To develop effective actuation strategies, it is essential to understand the fundamental dynamics that relate oscillatory wall motion to heat transfer performance. This understanding will enable the identification of optimal forcing parameters that maximise heat transfer enhancement while minimising drag penalties. The design of active control strategies for enhancing heat transfer over large areas will be one of the major achievements of this work, as it has the potential to “revolutionise” heat exchanger design and improve the efficiency of various thermal systems. By leveraging the knowledge gained from the aerodynamics community and applying it to the field of heat transfer, this research aims to bridge the gap between these two domains and unlock new possibilities for optimising convective heat transfer in turbulent boundary layers.

#### Q2 - What are the effects of outer-flow large-scale structures on wall-bounded flow?

The prediction of wall-bounded turbulence dynamics as Reynolds number increases has been an active research area over the past two decades. A pioneering contribution was made by Marusic and colleagues, who introduced a model to predict near-wall turbulence by measuring outer-flow structures (Mathis et al. 2009; Marusic, Mathis, and Hutchins 2010b). This model, known as the predictive inner-outer (PIO) model, uses a mathematical framework to relate the large-scale motions in the outer region of the boundary layer

to the small-scale fluctuations in the near-wall region. As discussed in section 4, this predictive model has limitations, such as the assumption of a symmetric amplitude modulation coefficient and the need for a priori knowledge of the near-wall velocity statistics for setting the value of empirical coefficients . We aim to address these limitations using machine learning algorithms, which can potentially provide interpretable laws to better understand the underlying mechanisms and enable generalisation to other flows. Previous analyses have mainly focused on the momentum field, with limited attention given to the thermal boundary layer. There is currently a lack of assessment of the impact of external flow structures on the thermal boundary layer, which is mandatory for understanding and predicting heat transfer in wall-bounded flows as the the Reynolds strengthens. Extending predictive modelling to include temperature fluctuations, so that heat transfer predictions can be made from measurements of outer-flow structures alone, is one of our main objectives. By leveraging machine learning algorithms, we aim to shed the light on the characteristics of the connections between outer-flow events and near-wall thermal variations. This will involve developing novel algorithms and techniques to extract “meaningful” patterns and identify their connections, which can then be used to build robust predictive models. It is an open challenge to elucidate how convective-heat transfer at the wall responds to external turbulence forcing across a large range of scales, and our research aims to provide new insights and solutions to this problem.

The first step for investigating how the different families of turbulent structures contribute to the drag and heat transfer, is to separate the families from each others. To do so, we propose an data-driven methodology referred to as “**Auto-Encoder**” (AE) and described in section 5.2.

An autoencoder (AE) is an unsupervised machine learning algorithm that is trained to reconstruct its inputs from a highly reduced dataset. As illustrated in Figure 5.1, an AE consists of an encoder, decoder, and bottleneck. The encoder compresses the input into a low-dimensional latent space, and the decoder then reconstructs the original input using the compressed information. The algorithm learns and exploits any structure or correlations in the data when forcing it through the bottleneck. By reducing the latent space dimension, the AE must identify the most efficient representation to compress the data without losing critical information. Dimensionality reduction acts as information filtering, with the bottleneck limiting the “information flow”. The low-dimensional representation of flow dynamics within latent space can then be leveraged to identify a low-dimensional dynamical system. Section 5.2 details how autoencoders can be used to extract the effects of external flow structures. The training data consists of streamwise velocity fields at the wall-normal location where large-scale motions are most energetic. By restricting the bottleneck, the AE learns only the most prominent features necessary to reconstruct the input. The reconstruction error guides the model to focus on energetic large-scale fluctuations. Once trained, the AE can effectively filter full velocity fields at any wall distance, extracting the large-scale components using its learned feature “library”. This allows for the isolation of the large-scale fluctuations driven by external structures across wall-normal locations. In summary, the AE is trained on energetic large scales and then serves as an extractor to identify these structures from velocity fields based on their learned signatures.

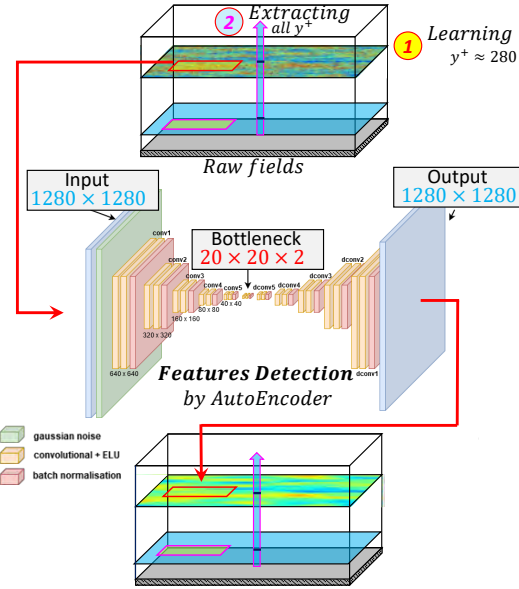


Figure 8.9: Schematic representation of the process of extracting the large-scale motions by using a multi-layer Auto-Encoder (Agostini and Leschziner 2022) .

Once the large-scale structures are separated from the rest of the flow, it becomes possible to determine their influence on near-wall turbulence, drag, and heat transfer. To achieve this, we intend to employ an approach based on *symbolic regression*, a machine learning algorithm capable of learning to model input data with analytic expressions. Unlike traditional regression methods, such as linear or polynomial regression, symbolic regression does not assume a predefined functional form for the relationship between the input variables and the output. Instead, it searches a space of mathematical expressions to find the one that best fits the data, allowing for the discovery of potentially complex and non-linear relationships that might be difficult

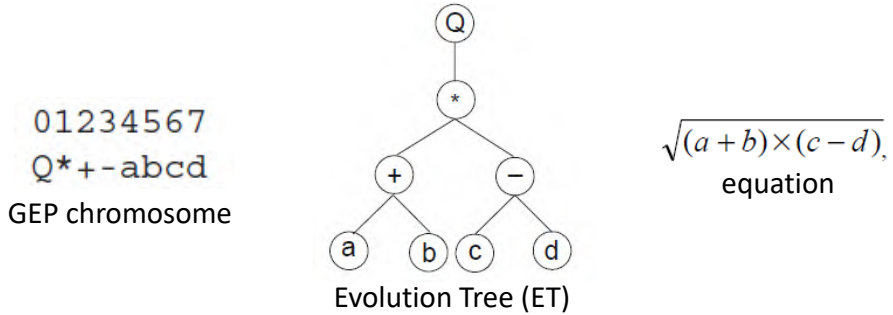


Figure 8.10: GEP representation of the expression  $\sqrt{(a+b) \times (c-d)}$ . The genotype (left side) is made of  $\{Q, *, -, +, a, b, c, d\}$  where “Q” represents the square root function. The phenotype corresponds to the expression tree represented in the middle plot. Figure adapted from Wikipedia.

to identify using traditional methods. The motivation behind using symbolic regression lies in the fact that the resulting mathematical expression is concise, interpretable, and generalises better to out-of-distribution training data, such as higher Reynolds numbers or higher wall temperatures. Interpretability is a significant advantage of symbolic regression, as the resulting expressions can be easily understood and analysed by domain experts, providing valuable insights into the underlying physical mechanisms.

For this research programme, we will employ a specific implementation of symbolic regression called *Gene Expression Programming (GEP)*, an *evolutionary algorithm* introduced by Ferreira (2001). GEP is a purely data-driven method that has been introduced into computer programming to solve complex optimisation problems, closely related to Genetic Programming (GP, see Koza (1994)), which has been widely used in the literature to determine control laws (Li et al. 2018). The philosophy behind GEP is to iteratively improve a population of candidate solutions through a process similar to the survival of the fittest. Like any evolutionary process, GEP relies on selection operators and random changes to the genome through mutation and crossover, making it a non-deterministic algorithm. The underlying concept is to allow the algorithm to freely choose the best possible representation model by providing it only with a dictionary of unknowns and/or mathematical operations, enabling the discovery of novel and potentially unexpected mathematical relationships that may be otherwise undetected by traditional methods. The resulting outputs of GEP are symbolic expressions that correspond to mathematical equations, providing complementary information about the dynamic process and serving as surrogate models for predicting flows. Surrogate models are computationally efficient approximations of complex systems that can be used to explore a wide range of design parameters and operating conditions without the need for expensive simulations or experiments. By using GEP-derived expressions as surrogate models, we can rapidly evaluate the performance of different flow control strategies and optimise them for specific objectives, such as drag reduction or heat transfer enhancement.

GEP presents itself as a promising approach for defining physics-based models that capture the complex interactions between large-scale structures and near-wall turbulence, drag, and heat transfer. By harnessing the power of GEP, we aim to unveil the underlying mathematical relationships that govern the influence of large-scale structures on flow dynamics, enabling us to develop interpretable and generalisable models that can accurately predict the behaviour of turbulent flows over a wide range of Reynolds numbers and wall temperatures. Furthermore, these models will provide insights that contribute to a deeper understanding of the fundamental mechanisms at work, paving the way for the development of more effective flow control strategies and the optimisation of heat transfer in a vast range of engineering applications. Through this research programme, we aim to bridge the gap between data-driven methods and traditional physics-based approaches, ultimately advancing the state of the art in turbulence modelling and heat transfer improvement. By combining the power of evolutionary algorithms with the interpretability of mathematical expressions, we can leverage the vast amounts of available flow data to uncover new physical insights and develop more accurate and efficient models for a wide range of applications. This approach has the potential to significantly advance the field of turbulence modelling and heat transfer optimisation, enabling the development of novel flow control strategies and the design of more efficient and sustainable engineering system.

To illustrate how GEP can be applied to wall-bounded flows to unveil the impact of outer-flow structures on the near-wall region, we will describe the GEP process in more detail. Figure 8.10 illustrates the GEP

representation of a given algebraic expression. Each individual, in this case a mathematical expression (for instance  $\sqrt{(a + b) \times (c - d)}$ ), can be represented as a tree (see middle plot, where “Q” represents the square root function), in which each internal node corresponds to an operator and each leaf node corresponds to an operand. In the evolutionary terminology, the ensemble  $Q, *, -, +, a, b, c, d$  that is used to encode each individual corresponds to the *genotype*, and the evolution tree is the *phenotype* of the GEP individuals. This type of expression tree can be read recursively from left to right and from bottom to top. These trees can be easily manipulated to create better representations from one generation to the next until convergence is finally obtained (i.e., no significant change in the fitness function between two iterations). When applied to wall-bounded flow, by considering the genotype ensemble  $u^*, u^+ O, LS, \beta, \alpha, +, -, \times, /, T_w, TO, LS, Re_\tau, Pr$ , GEP should lead to an accurate relationship for predicting near-wall turbulence. This physics-informed formulation focuses the search and accelerates convergence to robust, interpretable models. The goal is to represent additional mechanisms like splatting and discover accurate predictive laws that outperform existing relationships (such as the one provided by eq.8.2). GEP’s symbolic regression evolves the model structure along with parameters, avoiding predefined forms. The obtained concise expressions offer insight into how outer-flow structures alter near-wall statistics and properties such as skin friction and heat transfer. This data-driven GEP approach can uncover novel physical relationships. The ultimate goal is to predict the response of friction and heat transfer under the influence of external flow structures for both canonical and actuated turbulent boundary layers. Previous work has shown that the response of small-scale near-wall structures to large-scale fluctuations differs between canonical and actuated cases; specifically, near-wall streaks strengthen much more intensely with increasing footprint magnitude under actuation compared to the canonical case Agostini and Leschziner (2021). This is a challenging task, as simulations must be performed at higher Reynolds numbers (at least  $Re_\tau \approx 1000$ ) for influential external structures to develop sufficiently. High-fidelity simulations coupled with innovative machine learning techniques offer a promising approach to derive such predictive models. Our aim is to unveil the underlying mathematical relationships that govern the influence of large-scale structures on flow dynamics, enabling us to develop interpretable and generalisable models that can accurately predict the behaviour of turbulent flows, especially the drag and heat transfer, over a wide range of Reynolds numbers and wall temperatures.

### Q3 - Modelling of the Reynolds number effects on the turbulent boundary layer?

Previous research has primarily focused on the inner region of the boundary layer, attempting to elucidate the mechanisms that characterise how small-scale near-wall structures respond to external large-scale motions. The ultimate goal is to determine how measurements of external flow events can be used to predict the evolution of drag and convective heat transfer. However, to provide predictive capabilities across the boundary layer as the Reynolds number increases, attention needs to shift to the outer region. Efforts should focus on modelling the large-scale super streaks that populate the boundary layer, as their influence increases with the Reynolds number, and their dynamics remain poorly understood. To deepen our knowledge, the present work aims to formulate a low-dimensional dynamical model, including Reynolds number effects, to represent the essential physics governing these influential outer coherent motions. The aim is to create a unified model that integrates both inner and outer turbulence mechanisms into a single model that is applicable to a wide range of operating conditions. This task requires extensive statistical analysis of high-fidelity simulation databases. The focus is on deriving accurate models that have clear physical interpretations and elucidate the fundamental flow physics underpinning wall-bounded turbulent flows.

The development of the low-dimensional dynamical model will be based on an extension of the framework introduced in Section 8.2.4. The first step in this process is to identify a more relevant coordinate system in which the dynamics of the system can be represented in a simpler but more effective way. To achieve this, we intend to employ Auto-Encoder technology Agostini (2020) or a variant such as the Variational Auto-Encoder (Eivazi et al. 2022). These methods will enable us to determine an optimal embedding space that captures the essential flow physics. Subsequently, the elements of the model’s skeleton within the reduced coordinate system will be determined by efficiently clustering the embedded data into similar groups, with each cluster representing an ensemble of related flow states. By combining the low-dimensional representation of the data and a clustering algorithm (e.g., k-means), a coarse-grained description of the data will be defined, resulting in a “skeleton” of the low-dimensional space. To establish the interactions between these skeletal elements, the relationships between cluster transitions can be determined by applying symbolic regression methods (Li et al. 2018) or the Cluster Reduced-Order Model (CROM) method (Kaiser et al. 2014). Although modelling the more complex turbulent channel flow represents a greater challenge, we have successfully

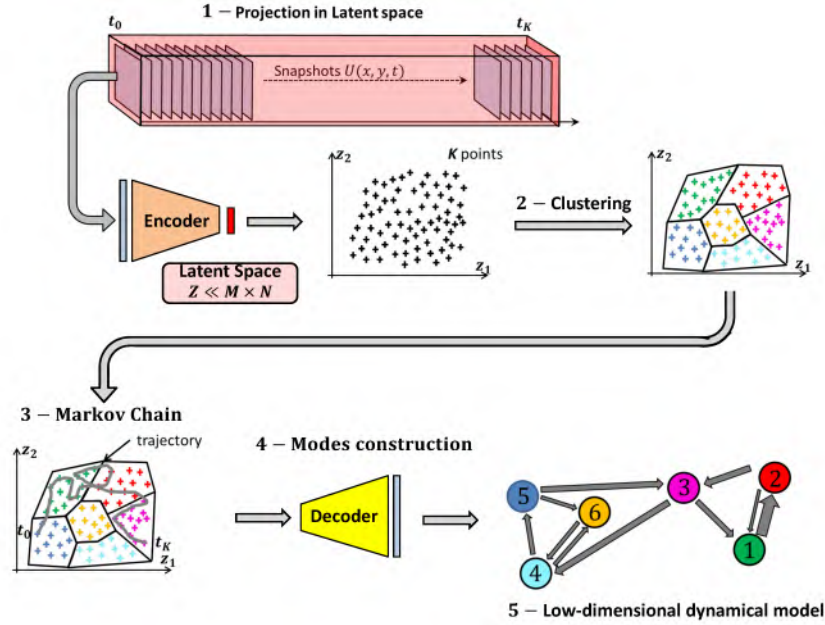


Figure 8.11: Reduced-order modelling framework that combines: dimensionality reduction by Auto-Encoders (step 1), clustering of the low-dimensional data (step 2), low-dimensional dynamical modelling of the encoded data (step 3), and decoded data (steps 4 and 5).

used a similar approach for modelling flow behind a cylinder (Agostini 2020), which we intend to apply here. Figure 8.11 illustrates the process of developing the low-dimensional dynamical model. Stacked flow snapshots serve as inputs to the Auto-Encoder, which identifies a low-dimensional projection subspace via the encoder layer. The embedded data is then efficiently clustered using the k-means algorithm, providing a skeleton of key flow states. A probabilistic Markov chain is employed to describe the transition probabilities between clusters. Finally, the decoder layer is used to reconstruct a low-order dynamical representation of the data in the original space. This integrated approach distils the turbulence into a compact model that elucidates the underlying physics and provides a simplified dynamical description, offering novel insights into the fundamental mechanisms sustaining wall-bounded turbulent flows.

The objectives of this research are twofold. First, we will highlight how small-scale structures drive drag and heat transfer in the absence of outer-flow structures. The results obtained will allow us to determine how the outer-flow structures modify the streaks and provide relationships for predicting drag and heat transfer. Once a low-order dynamical model of outer-flow structures is defined, synthetic super streaks can be built, and by using these relationships, we will be able to model the evolution of wall-bounded flows with the effect of Reynolds number. The main challenge lies in modelling the outer-flow structures, especially in defining a model that can predict the effect of the Reynolds number. It is relatively well known from numerical simulations and experiments that outer flow structures become larger and stronger as the Reynolds number increases; however, their nature does not seem to change. Therefore, one of the expectations is that the model developed from data for  $Re_\tau = 500$  to  $Re_\tau = 5200$  can be easily extended to higher Reynolds numbers by retaining some sort of “homothety”. Identifying the perfect model that is both accurate and robust is an extremely challenging task, and there is a high risk of failure. However, even a step in its direction will be considered a success, and the chances of developing a model that performs relatively well are reasonably high. As George E. P. Box famously stated, “All models are wrong, but some are useful”.

### 8.3.2 Project : Enhancing Convective heat Transfer by active control of secondary-flow instabilities

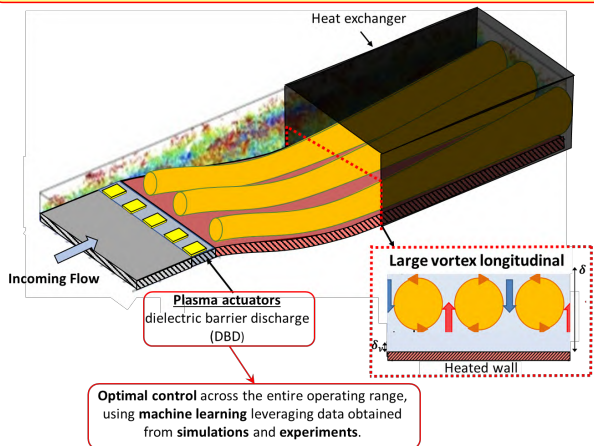
A collaborative research programme with IUSTI and Safran Aircraft Engines aims to explore the efficacy of controlling near-wall turbulence using optimised active devices. These devices will be designed to generate significant, meandering streamwise vortices by capitalising on the naturally occurring secondary flow instabilities that manifest over concave surfaces. The characteristics of these vortices will be modulated using plasma actuators, with the primary objective of maximising heat transfer capacity while minimising the associated drag penalty.

Enhancing the performance of heat exchangers is a critical technological challenge that is essential for improving efficiency and cost-effectiveness in systems where heat transfer plays a fundamental role. With the rapid global increase in energy consumption in recent decades, there is a growing demand for innovative concepts, methodologies, and designs to optimise heat transfer processes. This research programme seeks to address this need by investigating novel active control strategies for near-wall turbulence in heated boundary layers.

The scientific challenges to be addressed include understanding the physical mechanisms behind how generating streamwise vortical structures can boost heat transfer without increasing drag, and developing robust models to predict the effects of different control parameters, such as actuator geometry and excitation frequency, on the flow and heat transfer characteristics. By coupling advanced numerical simulations and experiments with machine learning techniques, the project aims to design new strategies for improving the efficiency of heat exchangers by manipulating the development of eddies at the interface between the wall and the fluid.

#### Dynamic Enhancement of Heat Transfers:

- The control is adjustably modified in response to external conditions, with an aim to optimise the efficiency of thermal exchanges.
- A 'boost in the heat exchange coefficient' is generated to accommodate extreme scenarios within the operational range



- **Exploitation of Görtler instabilities:** These instabilities, naturally present in flows, are easily controllable with very slight disturbances, allowing an intensification of convective heat transfer.
- **Strategically placed plasma controllers:** Installed upstream of the heat exchange area, they facilitate the creation of longitudinal vortices.
- **Adaptability of control:** The plasma controllers provide extensive versatility in determining the type of disturbance to implement (such as amplitude, wavelength, frequency) and can be conveniently fine-tuned 'on the fly'.
- **Optimisation of vortex mobility:** Plasma control can be designed to facilitate the spanwise movement of vortices, guaranteeing a more homogeneous and effective heat extraction.

Figure 8.12: Left: Illustrative concept of an optimised heat exchanger, leveraging active control techniques for the enhancement of heat transfer. Right : Structure of the research program. The program combines numerical simulations and experiments in a data-driven perspective. The modelling of near-wall flows and the development of control strategies are based on Machine Learning.

Designing heat exchangers for engines is challenging due to the need to accommodate a wide range of operating conditions, including rare extreme ambient temperature events. These events, such as the 'extremely hot day' specification, occur less than five times in the lifetime of an aircraft engine but still dictate the sizing of the heat exchanger. The oversized system resulting from this will have excess thermal margin under typical conditions, leading to an increase in weight and pressure drop, which in turn results in a specific consumption and fuel burn penalty. To address this challenge, advanced control strategies need to be developed that can adaptively optimize the performance of the heat exchanger across a wide range of operating conditions. This will ensure efficient operation while minimizing the impact on system weight and pressure drop.

This research programme aims to explore the relatively unexplored field of active control of near-wall turbulence in a heated boundary layer, combining advanced numerical simulations, experiments, and machine learning techniques. The project seeks to advance fundamental knowledge of controlling turbulent thermo-fluid systems at high Reynolds numbers, an area of ongoing exploration in the scientific community that holds great promise for future advancements in heat transfer enhancement and energy efficiency. The successful outcomes of this research have the potential to enable significant improvements in the energy efficiency of heat exchangers across various industrial applications, leading to the development of more efficient and sustainable engineering systems.

To achieve these goals, several scientific challenges must be addressed:

- Investigate whether convective heat transfer can be significantly enhanced without incurring a substantial drag penalty by generating streamwise vortical structures in turbulent wall-bounded flows. A comprehensive understanding of the underlying physical mechanisms governing the interaction between these vortical structures and the near-wall turbulence is crucial to characterise their impact on heat transfer and drag. This will require a detailed analysis of the flow behaviour in the wall-bounded region, where viscosity and thermal conductivity control the transport of momentum and heat, driving both skin friction and heat transfer. As turbulent mixing momentum within this region increases, the boundary layer becomes thinner, offering less resistance to heat flow but simultaneously increasing drag.
- Develop robust models that capture the relationship between different control parameters (such as actuator geometry and excitation, wavelength, and transverse velocity of vortical structures) and their influence on heat transfer and drag. These models will be essential for predicting the performance of the controlled system and optimising the control strategies for maximum effectiveness.
- Optimise control strategies by integrating observations from experiments and numerical simulations, along with machine learning capabilities. This approach will leverage the strengths of each method, combining the high fidelity of numerical simulations, the realism of experimental data, and the pattern recognition and optimization capabilities of machine learning algorithms to develop control strategies that are both effective and robust.
- Generalise the results obtained to a wide range of operating conditions (Reynolds, Mach, and Prandtl numbers) to enable multi-parameter control strategies suitable for the diverse conditions relevant to aerospace applications. This will ensure that the developed control strategies are applicable not only to a specific set of conditions but can be adapted to the varying requirements encountered in real-world aerospace systems.

The ultimate goal of this research programme is to build a sufficient fundamental understanding of the active control of near-wall turbulence in heated boundary layers to enable the rational design of effective control systems for improving heat exchangers at relatively high Reynolds numbers, while also accounting for compressibility effects. By addressing the scientific challenges outlined above and leveraging the expertise of the partnering institutions, this project has the potential to make significant contributions to the field of heat transfer enhancement and to drive the development of more efficient and adaptable heat exchangers for a wide range of industrial applications, with particular relevance to the aerospace sector.

The fundamental challenge facing the design of heat exchangers installed within engine is the need to accommodate a wide range of operating conditions. These include infrequent extreme ambient temperature events, such as the “extremely hot day” specification. Although rare, typically occurring less than five times in the lifetime of an aircraft engine, such conditions dictate the sizing of the heat exchanger. The resulting oversized system will have excess thermal margin under typical conditions, with associated weight increase and pressure drop, resulting in a specific consumption and fuel burn penalty.

This project aims to explore the relatively unexplored field of active control of near-wall turbulence in a heated boundary layer. It combines advanced numerical simulations, experiments and machine learning techniques. Advances in this area could lead to significant improvements in the energy efficiency of heat exchangers for various industrial applications. In addition to its technological interest, this project aims to advance fundamental knowledge of the control of turbulent thermo-fluid systems at high Reynolds numbers, an area that is currently being explored.

The scientific challenges to address are:

- Understand how generating streamwise vortical structures could boost heat transfer without increasing drag, including the physical mechanisms involved.
- Develop robust models of how different control parameters (actuator geometry and excitation, wavelength, transverse velocity of vortical structures, etc) influence heat transfer and drag.
- Optimise control strategies by integrating observations from experiments and numerical simulations, along with machine learning capabilities.
- Generalise the results obtained to a wide range of operating conditions (Reynolds, Mach and Prandtl numbers) to enable multi-parameter control strategies suitable for the wide range of conditions relevant to aerospace applications.

The goal is to build sufficient fundamental understanding to enable the rational design of effective control systems for improving heat exchangers at relatively high Reynolds numbers, accounting for compressibility effects.

Flow manipulation strategies can be categorised into two distinct groups. The first encompasses techniques aiming to modify the primary flow, while the second group is based on either the introduction or the leveraging of secondary flows. When feasible, it is more desirable to utilise flow instabilities for flow control, as secondary flow movement naturally expands from a minor disturbance. A broad range of methodologies has been examined to enhance heat transfer over a plate. These studies indicate that, irrespective of the type of turbulators employed, the devices demonstrating the highest efficiency are those that encourage counter-rotating secondary flows (Jacobi and Shah 1995; Fiebig 1995). The passive generation of longitudinal vortices has been proven to be notably effective at boosting heat transfer. This is because by escalating the mixing momentum near the wall, the longitudinal vortices instigate the boundary layer to become turbulent (Jacobi and Shah 1995; Méndez, Shadloo, and Hadjadj 2020). In instances where the boundary layer is already turbulent, a boost in mixing momentum coupled with a thinning of the boundary layer due to downwelling, leads to an increase in convective heat transfer. However, this advantage is partially neutralised by upwelling, leading to a spanwise variation in both heat transfer and drag. This variation in temperature across the span results in significant stresses being imparted on the structure. To overcome this limitation, the idea is to apply unsteady flow control strategies using periodic excitation that exploits natural flow instability phenomena. One innovative aspect of this research proposal is leveraging flow instabilities to generate large streamwise vortices with very weak perturbations. The benefits are: (i) they are easier to control, and (ii) more cost-effective. Unsteady flow control via periodic excitation harnessing natural flow instabilities has the potential to overcome efficiency barriers.

The study focuses on flow over a concave wall, shown in Figure 8.12. The wall's curvature induces centrifugal force that lead to secondary flow instabilities, -i.e. the formation of coherent flow vortices known as Görtler vortices. The primary objective is to understand the effect of these structures on heat transfer in turbulent wall-bound flow. Subsequently, a control law will be designed using plasma actuators to provide an optimal control strategy that maximises heat transfer with minimum drag penalty. The project relies on numerical simulations and experiments supported by Machine Learning (ML) techniques in an integrated manner. The ML algorithms include dimensionality reduction, low-dimensional dynamical modelling and optimal control law design, and are organised in 4 distinct steps:

**⇒ 1 Unveil the physics.** The effect of streamwise vortex structures will be investigated. These structures, characterised by a wide range of spanwise wavelengths and varying degrees of streamwise coherence, are generated by a body force. It should be noted, however, that these do not necessarily reflect practical control strategies. The fundamental objective is to elucidate the correlation between drag and heat transfer associated with unsteady streamwise vortices. To achieve this, statistical algorithms, data-driven decomposition and machine learning algorithms such as the autoencoder will be used.

The primary goal is to develop a low-order dynamical model and to identify those vortical structures that have the most substantial impact on the mixing of momentum, drag, and heat transfer. Given the inherent complexity of wall-bounded flows, it is essential that machine learning algorithms are directed by our comprehension of the phenomena that drive the dynamics (Agostini and Leschziner 2014; Silva et al. 2020). The knowledge gained from this fundamental step will play an important role in the next two steps.

⇒ **2 Flow prediction.** This step consists of two independent parts, with different goals:

- **Designing a robust estimator.** Experiments that investigate wall-bounded turbulent flows face significant challenges when it comes to directly measuring the quantities of interest, such as heat transfer and skin friction drag. To overcome this limitation, a promising approach involves leveraging databases from numerical simulations and experiments to develop algorithms that can estimate these variables from direct measurements. One methodology for improving accuracy is to use genetic programming. This follows an evolutionary principle where an initial population of models is progressively refined through selection and reproduction operations. Li et al. (2018) demonstrated the effectiveness of this technique in producing linear estimators. Additionally, integrating real-time data assimilation to update model parameters could potentially improve robustness against noise and small flow configuration changes. Combining simulations, experiments, and machine learning methods provides the capability to infer hard-to-measure quantities and construct reliable reduced-order models. This advances our understanding of wall turbulence dynamics and interactions that control heat transfer and drag.
- **Improving RANS/LES closures.** One of the major difficulty of the RANS modelling is to reproduce the impact of secondary flows (development and breakdown of the longitudinal streaks). Unsteady RANS models can be improved with ML algorithms by developing corrective terms of a baseline model with deep neural network (Ling, Kurzawski, and Templeton 2016; Cherroud et al. 2022) or genetic programming (Weatheritt and Sandberg 2016).

⇒ **3 Design realistic control strategies.** The primary aim is to conduct investigations into various “realistic” control strategies employing plasma actuators. Here, “realistic” indicates that the control devices are viable for experimental implementation. Initially, numerical simulations involving plasma actuators will be executed using the Pprime in-house code Oracle3D. The central objective is to recreate turbulent structures, as identified in the first step, which enhance heat exchange between the wall and the working fluid, using diverse forcing strategies. Notably, it is only through the insights obtained from preceding steps that it will be feasible to narrow down the range of control-parameter possibilities. This in turn will enable machine learning algorithms to more rapidly converge towards a robust solution.

⇒ **4 Determine optimal control strategies.**

In the previous tasks, the objective is to determine from numerical simulations the characteristics that coherent structures must have to improve heat transfer. Additionally, these tasks aim to propose methods to detect these structures from experimental measurements. In these initial tasks, efforts focused on the identification, modelling and estimation of coherent structures. Leveraging this knowledge optimization investigations will be undertaken to identify the most effective control law.

To limit complexity and mitigate risks, this task will be divided into two steps:

- Initially, a parametric study will be conducted to evaluate the influence of different plasma actuator parameters on heat transfer and drag. Although the likelihood of identifying an optimal control law is limited through manual tuning, this study will map the parameter space and impacts on near-wall turbulence to prepare for Deep Reinforcement Learning (DRL). Wind tunnel experiments at IUSTI are well-suited for efficiently scanning parameters including voltage, frequency and actuator arrangement. The most promising settings found to manipulate near-wall dynamics will subsequently undergo in-depth analysis using numerical simulation. Simulations provide detailed access to generated coherent structures and heating effects on secondary vortices and heat transfer. The parametric study has two aims:
  1. To make a broad but coarse exploration of the control parameter domain in order to restrict it for DRL. Thus, with the search domain being more limited, this will allow the DRL to limit its exploration phase and focus more on exploitation in order to converge more quickly towards a robust solution.
  2. To improve the understanding of the physics of controlled flows. This will refine the prediction and estimation models developed in previous WPs. Above all, it will facilitate the design of relevant cost and reward functions, by incorporating physical knowledge into them. With cost and reward functions based on physics, DRL will be more effective at finding the optimal control law.

- Subsequently, DRL will be applied to autonomously search for the best control law to maximize heat transfer while minimizing pressure losses. DRL is a reinforcement learning technique based on deep neural networks in which an agent interacts with its environment by taking actions and receiving rewards. Its goal is to determine the optimal actions that maximize its long-term rewards. Different variants of DRL will be tested, by varying the neural network architecture, learning and exploration algorithms, and the definition of rewards. The objective is to determine the most effective approach to quickly find an optimal control law, even with limited compute time. Ultimately, DRL should achieve performance difficult to attain with a conventional method. Implementation of DRL algorithms will be done by the postdoctoral researcher and continue until the end of their funding.

## 8.4 global objectives: Piecing together the puzzle of multi-scale interactions in turbulent boundary layers for predictive modelling and control.

The main goal of my current research is to deepen our fundamental knowledge of the complex interactions between different scales of turbulent structures populating boundary layers and their influence on drag and convective heat transfer. One important objective is to unveil the complex interactions between near-wall turbulence and large-scale coherent motions, and to elucidate their combined effect on heat transfer and drag over a wide range of Reynolds numbers. By combining insights from high-fidelity numerical simulations, advanced experimental techniques, and data-driven analysis, this research seeks to provide a comprehensive characterisation of the multi-scale dynamics governing momentum and thermal transport in wall-bounded flows. Base on this knowledge, the aim is to design a multi-scale active control strategies leveraging the wall-bounded flow dynamic complexity that can optimise heat transfer enhancement while minimising associated drag penalties, paving the way for more efficient and sustainable engineering systems :

- On one hand a particular attention is paid to the control of small-scale structures to enhance mixing in the immediate vicinity of the wall, where the temperature gradient is steepest. Near-wall turbulence can be manipulated through techniques such as oscillatory wall motion to generate beneficial vortices that intensify thermal mixing within this critical region. The challenge is to develop control strategies that enhance heat transfer while minimizing any associated increase in drag. It is important to investigate how the effectiveness of these strategies changes as the Reynolds number increases.
- On the other hand, we also investigate the exploitation of secondary flow instabilities, such as Görtler vortices, to generate large-scale structures that promote mixing between the inner and outer boundary layer regions, where temperature difference is the most significant. By selectively promoting these instabilities, we aim to improve heat transfer throughout the boundary layer, and also we aim to characterise how these large-scale structures and their effect on heat transfer vary with increasing Reynolds number.

The development of predictive models that accurately capture the dynamics of wall-bounded flows and their response to active flow control across a wide range of Reynolds numbers is a prominent aspect of this research. By adopting and enhancing the concept of predicting near-wall turbulence from outer-flow measurements, as introduced by Marusic, Mathis, and Hutchins (2010b), we aim to construct reduced-order models that can reliably predict flow behaviour and heat transfer characteristics at both low and high Reynolds numbers. These models will serve as powerful tools for optimising system performance and designing effective control strategies that remain robust and efficient as the flow conditions may vary.

The ultimate goal of this multifaceted research programme is to advance our understanding of the intricate interactions between different scales of motion in turbulent boundary layers, and their influence on heat transfer and drag across a wide range of Reynolds numbers. By combining state-of-the-art numerical simulations, cutting-edge experimental techniques, and advanced data analysis methods, we seek to unravel the complex dynamics governing momentum and thermal transport in wall-bounded flows. A comprehensive characterisation of these multi-scale interactions will guide the development of novel, multi-scale active flow control strategies that synergistically manipulate both small-scale near-wall turbulence and large-scale coherent motions. These strategies aim to optimise heat transfer enhancement while minimising associated drag

penalties, ensuring robust performance across diverse operating conditions. Furthermore, by leveraging the predictive capabilities of data-driven models, this research will pave the way for adaptive control techniques that can dynamically adjust to changes in Reynolds number and flow configuration. The knowledge gained and the innovative control approaches developed will have far-reaching implications for the design and optimisation of heat exchangers, thermal management systems, and other engineering applications. Ultimately, this transformative research programme will contribute to a more sustainable and energy-efficient future by enabling the development of high-performance, environmentally friendly technologies that can efficiently harness the complex nature of turbulent flows.



# Bibliography

- Adrian, R. J., C. D..S. Meinhart, and C. D. Tomkins (2000). “Vortex organization in the outer region of the turbulent boundary layer”. In: *Journal of Fluid Mechanics* 422, pp. 1–53.
- Agostini, L. (June 2020). “Exploration and prediction of fluid dynamical systems using auto-encoder technology”. In: *Physics of Fluids* 32.6, p. 067103. ISSN: 1070-6631.
- Agostini, L. and M. Leschziner (2014). “On the influence of outer large-scale structures on near-wall turbulence in channel flow”. In: *Physics of Fluids* 26.7, p. 075107.
- (Apr. 2016a). “On the validity of the quasi-steady-turbulence hypothesis in representing the effects of large scales on small scales in boundary layers”. en. In: *Physics of Fluids* 28.4, p. 045102. ISSN: 1070-6631, 1089-7666.
- (2016b). “Predicting the response of small-scale near-wall turbulence to large-scale outer motions”. In: *Physics of Fluids* 28.1.
- (Jan. 2017). “{Spectral analysis of near-wall turbulence in channel flow at  $\text{Retau} = 4200$  with emphasis on the attached-eddy hypothesis}”. In: *Phys. Rev. Fluids* 2.1. Publisher: American Physical Society, p. 014603.
- (2018). “The Impact of Footprints of Large-Scale Outer Structures on the Near-Wall Layer in the Presence of Drag-Reducing Spanwise Wall Motion”. In: *Flow, Turbulence and Combustion*. Publisher: Springer Netherlands, pp. 1–25.
- (2019a). “On the departure of near-wall turbulence from the quasi-steady state”. In: *Journal of Fluid Mechanics* 871. Publisher: Cambridge University Press.
- (July 2019b). “The connection between the spectrum of turbulent scales and the skin-friction statistics in channel flow at”. en. In: *Journal of Fluid Mechanics* 871. Publisher: Cambridge University Press, pp. 22–51. ISSN: 0022-1120, 1469-7645.
- (2021). “Statistical analysis of outer large-scale/inner-layer interactions in channel flow subjected to oscillatory drag-reducing wall motion using a multiple-variable joint-probability-density function methodology”. In: *Journal of Fluid Mechanics* 923. Publisher: Cambridge University Press.
- (Nov. 2022). “Auto-encoder-assisted analysis of amplitude and wavelength modulation of near-wall turbulence by outer large-scale structures in channel flow at friction Reynolds number of 5200”. In: *Physics of Fluids* 34.11, p. 115142. ISSN: 1070-6631.
- Agostini, L., M. Leschziner, and D. Gaitonde (2016). “Skewness-induced asymmetric modulation of small-scale turbulence by large-scale structures”. In: *Physics of Fluids* 28.1, p. 015110.
- Agostini, L., E. Touber, and M. Leschziner (2014). “Spanwise oscillatory wall motion in channel flow: drag-reduction mechanisms inferred from DNS-predicted phase-wise property variations at  $\text{Retau}=1000$ ”. In: *Journal of Fluid Mechanics* 743. Publisher: Cambridge University Press, pp. 606–635.
- Agostini, L, E Touber, and M. Leschziner (2015). “The turbulence vorticity as a window to the physics of friction-drag reduction by oscillatory wall motion”. In: *International Journal of Heat and Fluid Flow* 51, pp. 3–15.
- Agostini, L. et al. (2017). “Multi-scale interactions in a compressible boundary layer”. In: *Journal of Turbulence* 18.8. Publisher: Taylor & Francis, pp. 760–780.
- Andreolli, A et al. (2021). “Effects of sweeps and ejections on amplitude modulation in a turbulent channel flow”. In: *arXiv preprint arXiv:2109.09486*.
- Auteri, F. et al. (Nov. 2010). “Experimental assessment of drag reduction by traveling waves in a turbulent pipe flow”. In: *Physics of Fluids* 22.11, p. 115103. ISSN: 1070-6631.
- Baars, WJ et al. (2015). “Wavelet analysis of wall turbulence to study large-scale modulation of small scales”. In: *Experiments in Fluids* 56.10, pp. 1–15.

- Baars, Woutijn J., Nicholas Hutchins, and Ivan Marusic (Sept. 2016). "Spectral stochastic estimation of high-Reynolds-number wall-bounded turbulence for a refined inner-outer interaction model". In: *Physical Review Fluids* 1.5. Publisher: American Physical Society, p. 054406.
- Bandyopadhyay, Promode R and AKMF Hussain (1984). "The coupling between scales in shear flows". In: *Physics of Fluids* 27.9, pp. 2221–2228.
- Bernardini, Matteo and Sergio Pirozzoli (2011). "Inner/outer layer interactions in turbulent boundary layers: a refined measure for the large-scale amplitude modulation mechanism". In: *Physics of Fluids* 23.6, p. 061701.
- Bissonnette, L. R. and G. L. Mellor (Apr. 1974). "Experiments on the behaviour of an axisymmetric turbulent boundary layer with a sudden circumferential strain". en. In: *Journal of Fluid Mechanics* 63.2. Publisher: Cambridge University Press, pp. 369–413. ISSN: 1469-7645, 0022-1120.
- Blesbois, O. et al. (2013). "Pattern prediction by linear analysis of turbulent flow with drag reduction by wall oscillation". In: *Journal of Fluid Mechanics* 724, pp. 607–641.
- Bookstein, F.L. (June 1989). "Principal warps: thin-plate splines and the decomposition of deformations". In: *IEEE Transactions on Pattern Analysis and Machine Intelligence* 11.6, pp. 567–585.
- Bradshaw, P and NS Pontikos (1985). "Measurements in the turbulent boundary layer on an 'infinite' swept wing". In: *Journal of Fluid Mechanics* 159, pp. 105–130.
- Brunton, Steven L, Bernd R Noack, and Petros Koumoutsakos (2019). "Machine learning for fluid mechanics". In: *Annual Review of Fluid Mechanics* 52. Publisher: Annual Reviews.
- Chernyshenko, Sergei (2021). "Extension of QSQH theory of scale interaction in near-wall turbulence to all velocity components". In: *Journal of Fluid Mechanics* 916. Publisher: Cambridge University Press, A52.
- Chernyshenko, S.I., I. Marusic, and R. Mathis (2012). "Quasi-steady description of modulation effects in wall turbulence". In: *arXiv:1203.3714 [physics]*.
- Cherroud, S. et al. (2022). "Sparse Bayesian Learning of Explicit Algebraic Reynolds-Stress models for turbulent separated flows". In: *International Journal of Heat and Fluid Flow* 98. Publisher: Elsevier, p. 109047.
- Choi, J.I., C.X. Xu, and H.J. Sung (2002). "Drag reduction by spanwise wall oscillation in wall-bounded turbulent flows". In: *AIAA journal* 40.5, pp. 842–850.
- Choi, K. S. (2002). "Near-wall structure of turbulent boundary layer with spanwise-wall oscillation". In: *Physics of Fluids* 14, p. 2530.
- Chung, D and BJ McKeon (2010). "Large-eddy simulation of large-scale structures in long channel flow". In: *Journal of Fluid Mechanics* 661, pp. 341–364.
- Chung, Daniel et al. (2015). "On the universality of inertial energy in the log layer of turbulent boundary layer and pipe flows". In: *Experiments in Fluids* 56.7, pp. 1–10.
- Chung, Y. M. and E. Hurst (2014). "Turbulent drag reduction at high Reynolds numbers". In: *Fluid-Structure-Sound Interactions and Control*. Ed. by Y. Zhou et al. Springer-Verlag, pp. 95–99.
- Clevert, Djork-Arné, Thomas Unterthiner, and Sepp Hochreiter (2015). "Fast and accurate deep network learning by exponential linear units (elus)". In: *arXiv preprint arXiv:1511.07289*.
- Cormier, M., D. Gatti, and B. Frohnäpfel (2016). "Interaction between inner and outer layer in drag-reduced turbulent flows". In: *PAMM* 16.1. Publisher: Wiley Online Library, pp. 633–634.
- Davidson, P. A. (2003). *Turbulence:an introduction for scientists and engineers*. Oxford university press.
- Davidson, PA, TB Nickels, and P-Å Krogstad (2006). "The logarithmic structure function law in wall-layer turbulence". In: *Journal of Fluid Mechanics* 550, pp. 51–60.
- Davidson, PA et al. (2006). "A refined interpretation of the logarithmic structure function law in wall layer turbulence". In: *Physics of Fluids* 18.6, p. 5112.
- De Moortel, Ineke, SA Munday, and Alan William Hood (2004). "Wavelet analysis: the effect of varying basic wavelet parameters". In: *Solar Physics* 222.2. Publisher: Springer, pp. 203–228.
- Del Álamo, J.C and J. Jiménez (2003). "Spectra of the very large anisotropic scales in turbulent channels". In: *Physics of Fluids* 15.6, p. L41.
- Di Cicca, G. M. et al. (2002). "Particle image velocimetry investigation of a turbulent boundary layer manipulated by spanwise wall oscillations". In: *Journal of Fluid Mechanics* 467, pp. 41–56.
- Dogan, E. et al. (2019). "Quantification of amplitude modulation in wall-bounded turbulence". In: *Fluid Dynamics Research* 51.1. Publisher: IOP Publishing, p. 011408.
- Duvvuri, Subrahmanyam and Beverley J McKeon (2015). "Triadic scale interactions in a turbulent boundary layer". In: *Journal of Fluid Mechanics* 767, R4.

- Etel-Amor, G., R. Örlü, and P. Schlatter (2014). "Simulation and validation of a spatially evolving turbulent boundary layer up to  $Re_{\eta} = 8300$ ". In: *International Journal of Heat and Fluid Flow* 47. Publisher: Elsevier, pp. 57–69.
- Eivazi, Hamidreza et al. (2022). "Towards extraction of orthogonal and parsimonious non-linear modes from turbulent flows". In: *Expert Systems with Applications* 202. Publisher: Elsevier, p. 117038.
- Ferreira, C (2001). "Gene Expression Programming: a New Adaptive Algorithm for Solving Problems". In: *ArXiv Computer Science e-prints*.
- Fiebig, Martin (1995). "Embedded vortices in internal flow: heat transfer and pressure loss enhancement". In: *International Journal of Heat and Fluid Flow* 16.5. Publisher: Elsevier, pp. 376–388.
- Fiorini, T. et al. (2017). "Turbulent Pipe Flow Near-Wall Statistics". In: *Progress in Turbulence VII*. Ed. by Ramis Örlü et al. Springer International Publishing, pp. 89–94.
- Fishpool, G. M. and M. A. Leschziner (2009). "Stability bounds for explicit fractional-step schemes for the Navier –Stokes equations at high Reynolds number". In: *Computers & Fluids* 38.6, pp. 1289–1298.
- Flandrin, P., G. Rilling, and P. Goncalves (2004). "Empirical mode decomposition as a filter bank". In: *Signal Processing Letters, IEEE* 11.2, pp. 112–114.
- Fukagata, Koji, Kaoru Iwamoto, and Nobuhide Kasagi (Oct. 2002). "Contribution of Reynolds stress distribution to the skin friction in wall-bounded flows". In: *Physics of Fluids* 14.11, pp. L73–L76. ISSN: 1070-6631.
- Furuya, Yoshimasa, Ikuo Nakamura, and Hidekazu Kawachi (1966). "The experiment on the skewed boundary layer on a rotating body". In: *Bulletin of JSME* 9.36. Publisher: The Japan Society of Mechanical Engineers, pp. 702–710.
- Ganapathisubramani, B et al. (2012). "Amplitude and frequency modulation in wall turbulence". In: *Journal of Fluid Mechanics* 712, pp. 61–91.
- Ganapathisubramani, Bharathram, Ellen K Longmire, and Ivan Marusic (2003). "Characteristics of vortex packets in turbulent boundary layers". In: *Journal of Fluid Mechanics* 478, pp. 35–46.
- Gatti, Davide and Maurizio Quadrio (Dec. 2013). "Performance losses of drag-reducing spanwise forcing at moderate values of the Reynolds number". en. In: *Physics of Fluids* 25.12, p. 125109. ISSN: 1070-6631, 1089-7666.
- (Sept. 2016). "Reynolds-number dependence of turbulent skin-friction drag reduction induced by spanwise forcing". en. In: *Journal of Fluid Mechanics* 802, pp. 553–582. ISSN: 0022-1120, 1469-7645.
- Giovanetti, Matteo de, Yongyun Hwang, and Haecheon Choi (Dec. 2016). "Skin-friction generation by attached eddies in turbulent channel flow". en. In: *Journal of Fluid Mechanics* 808, pp. 511–538. ISSN: 0022-1120, 1469-7645.
- Guala, M., M. Metzger, and B.J. McKeon (2011). "Interactions within the turbulent boundary layer at high Reynolds number". In: *Journal of Fluid Mechanics* 666. Publisher: Cambridge University Press, pp. 573–604.
- Guastoni, Luca et al. (2021). "Convolutional-network models to predict wall-bounded turbulence from wall quantities". In: *Journal of Fluid Mechanics* 928. Publisher: Cambridge University Press.
- Hoyas, S. and J. Jiménez (2006). "Scaling of the velocity fluctuations in turbulent channels up to  $Re = 2003$ ". In: *Physics of fluids* 18, p. 011702.
- (Oct. 2008). "Reynolds number effects on the Reynolds-stress budgets in turbulent channels". In: *Physics of Fluids* 20.10, p. 101511.
- Huang, N. E. et al. (1998). "The empirical mode decomposition and the Hilbert spectrum for nonlinear and non-stationary time series analysis". In: *Proceedings of the Royal Society of London. Series A: Mathematical, Physical and Engineering Sciences* 454.1971, pp. 903–995.
- Hultmark, Marcus et al. (2012). "Turbulent pipe flow at extreme Reynolds numbers". In: *Physical review letters* 108.9, p. 094501.
- Hultmark, Marcus et al. (2013). "Logarithmic scaling of turbulence in smooth-and rough-wall pipe flow". In: *Journal of Fluid Mechanics* 728, pp. 376–395.
- Hurst, Edward, Qiang Yang, and Yongmann M Chung (2014). "The effect of Reynolds number on turbulent drag reduction by streamwise travelling waves". In: *Journal of Fluid Mechanics* 759, pp. 28–55.
- Hutchins, N. and I. Marusic (2007a). "Large-scale influences in near-wall turbulence". In: *Philosophical Transactions of the Royal Society of London A: Mathematical, Physical and Engineering Sciences* 365.1852. Publisher: The Royal Society, pp. 647–664.
- Hutchins, N. and Ivan Marusic (2007b). "Evidence of very long meandering features in the logarithmic region of turbulent boundary layers". In: *Journal of Fluid Mechanics* 579, p. 1.

- Hutchins, N et al. (2009). "Hot-wire spatial resolution issues in wall-bounded turbulence". In: *Journal of Fluid Mechanics* 635, pp. 103–136.
- Hutchins, N. et al. (2011). "Three-dimensional conditional structure of a high-Reynolds-number turbulent boundary layer". In: *Journal of Fluid Mechanics* 673, pp. 255–285.
- Hwang, J. and H.J. Sung (2017). "Influence of large-scale motions on the frictional drag in a turbulent boundary layer". In: *Journal of Fluid Mechanics* 829. Publisher: Cambridge University Press, pp. 751–779.
- Hwang, Y. (2015). "Statistical structure of self-sustaining attached eddies in turbulent channel flow". In: *Journal of Fluid Mechanics* 767, pp. 254–289.
- Högström, U, JCR Hunt, and A.S Smedman (2002). "Theory and measurements for turbulence spectra and variances in the atmospheric neutral surface layer". In: *Boundary-Layer Meteorology* 103.1, pp. 101–124.
- Iacobello, Giovanni, Luca Ridolfi, and Stefania Scarsoglio (2021). "Large-to-small scale frequency modulation analysis in wall-bounded turbulence via visibility networks". In: *Journal of Fluid Mechanics* 918. Publisher: Cambridge University Press.
- Jacobi, A. M. and R. K. Shah (1995). "Heat transfer surface enhancement through the use of longitudinal vortices: a review of recent progress". In: *Experimental Thermal and Fluid Science* 11.3. Publisher: Elsevier, pp. 295–309.
- Jacobi, I and BJ McKeon (2013). "Phase relationships between large and small scales in the turbulent boundary layer". In: *Experiments in fluids* 54.3, pp. 1–13.
- Jiménez, J. (2013). "Near-wall turbulence". In: *Physics of Fluids* 25.10, p. 101302.
- Jiménez, J., J. C. Del Álamo, and O. Flores (2004). "The large-scale dynamics of near-wall turbulence". In: *Journal of Fluid Mechanics* 505.1, pp. 179–199.
- Jiménez, J. and S. Hoyas (2008). "Turbulent fluctuations above the buffer layer of wall-bounded flows". In: *Journal of Fluid Mechanics* 611, pp. 215–236.
- Jiménez, Javier (2011). "Cascades in wall-bounded turbulence". In: *Annual Review of Fluid Mechanics* 44.1, p. 27.
- Jiménez, Javier and Alfredo Pinelli (1999). "The autonomous cycle of near-wall turbulence". In: *Journal of Fluid Mechanics* 389.1, pp. 335–359.
- Kaiser, Eurika et al. (2014). "Cluster-based reduced-order modelling of a mixing layer". In: *Journal of Fluid Mechanics* 754. Publisher: Cambridge University Press, pp. 365–414.
- Kim, K. C. and R. J. Adrian (1999). "Very large-scale motion in the outer layer". In: *Phys. Fluids* 11, pp. 417–422.
- Koza, John R (1994). "Genetic programming as a means for programming computers by natural selection". In: *Statistics and computing* 4.2. Publisher: Springer, pp. 87–112.
- Lacasa, Lucas et al. (2008). "From time series to complex networks: The visibility graph". In: *Proceedings of the National Academy of Sciences* 105.13. Publisher: National Acad Sciences, pp. 4972–4975.
- Lardeau, S. and M. A. Leschziner (July 2013). "The streamwise drag-reduction response of a boundary layer subjected to a sudden imposition of transverse oscillatory wall motion". In: *Physics of Fluids* 25.7, pp. 075109–17.
- Lee, M. and R. D. Moser (July 2015). "Direct numerical simulation of turbulent channel flow up to  $\text{Re}_{\tau} \approx 5200$ ". In: *Journal of Fluid Mechanics* 774, pp. 395–415. ISSN: 1469-7645.
- Li, R. et al. (2018). "Linear Genetic Programming Control for strongly nonlinear dynamics with frequency crosstalk". In: *Arch. Mech.* 70.6, pp. 505–534.
- Ling, Julia, Andrew Kurzawski, and Jeremy Templeton (2016). "Reynolds averaged turbulence modelling using deep neural networks with embedded invariance". In: *Journal of Fluid Mechanics* 807. Publisher: Cambridge University Press, pp. 155–166.
- Lohmann, R. P. (Sept. 1976). "The Response of a Developed Turbulent Boundary Layer to Local Transverse Surface Motion". In: *Journal of Fluids Engineering* 98.3, pp. 354–363. ISSN: 0098-2202.
- Lozano-Durán, A. and J. Jiménez (2014a). "Effect of the computational domain on direct simulations of turbulent channels up to  $\text{Re}_{\tau} = 4200$ ". In: *Physics of Fluids* 26.1. Publisher: AIP Publishing, p. 011702.
- (2014b). "Time-resolved evolution of coherent structures in turbulent channels: characterization of eddies and cascades". In: *Journal of Fluid Mechanics* 759, pp. 432–471.
- Lozano-Durán, Adrián, H. Jane Bae, and Miguel P. Encinar (Jan. 2020). "Causality of energy-containing eddies in wall turbulence". en. In: *Journal of Fluid Mechanics* 882. Publisher: Cambridge University Press, A2. ISSN: 0022-1120, 1469-7645.

- Luchini, P (1996). "Reducing the turbulent skin friction". In: *ECCOMAS conference on numerical methods in engineering*, pp. 465–470.
- Marusic, I. (2001). "On the role of large-scale structures in wall turbulence". In: *Physics of fluids* 13, p. 735.
- Marusic, I., R. Mathis, and N. Hutchins (2010a). "High Reynolds number effects in wall turbulence". In: *International Journal of Heat and Fluid Flow* 31.3, pp. 418–428.
- (2010b). "Predictive model for wall-bounded turbulent flow". In: *Science* 329.5988, pp. 193–196.
- Marusic, I. et al. (2010). "Wall-bounded turbulent flows at high Reynolds numbers: Recent advances and key issues". In: *Physics of Fluids* 22, p. 065103.
- Marusic, Ivan et al. (2013). "On the logarithmic region in wall turbulence". In: *Journal of Fluid Mechanics* 716, R3.
- Marusic, Ivan et al. (Oct. 2021). "An energy-efficient pathway to turbulent drag reduction". en. In: *Nature Communications* 12.1. Number: 1 Publisher: Nature Publishing Group, p. 5805. ISSN: 2041-1723.
- Mathis, R., N. Hutchins, and I. Marusic (2009). "Large-scale amplitude modulation of the small-scale structures in turbulent boundary layers". In: *Journal of Fluid Mechanics* 628, pp. 311–337.
- (2011). "A predictive inner –outer model for streamwise turbulence statistics in wall-bounded flows". In: *Journal of Fluid Mechanics* 681, pp. 537 –566.
- Mathis, R. et al. (2009). "Comparison of large-scale amplitude modulation in turbulent boundary layers, pipes, and channel flows". In: *Physics of Fluids* 21.11, p. 111703.
- Mathis, R. et al. (2013). "Estimating wall-shear-stress fluctuations given an outer region input". In: *Journal of Fluid Mechanics* 715, pp. 163–180.
- Mathis, Romain et al. (2011). "The relationship between the velocity skewness and the amplitude modulation of the small scale by the large scale in turbulent boundary layers". In: *Physics of Fluids* 23.12, p. 121702.
- Maulik, Romit, Bethany Lusch, and Prasanna Balaprakash (Mar. 2021). "Reduced-order modeling of advection-dominated systems with recurrent neural networks and convolutional autoencoders". In: *Physics of Fluids* 33.3, p. 037106. ISSN: 1070-6631.
- McKeon, BJ and JF Morrison (2007). "Asymptotic scaling in turbulent pipe flow". In: *Philosophical Transactions of the Royal Society A: Mathematical, Physical and Engineering Sciences* 365.1852, pp. 771–787.
- Mohan, Arvind T. et al. (Jan. 2023). "Embedding hard physical constraints in neural network coarse-graining of three-dimensional turbulence". In: *Physical Review Fluids* 8.1. Publisher: American Physical Society, p. 014604.
- Moser, R. D., J. Kim, and N. N. Mansour (1999). "Direct numerical simulation of turbulent channel flow up to  $\text{Re}_{\tau} = 590$ ". In: *Physics of Fluids* 11.4, pp. 943 –945.
- Murata, Takaaki, Kai Fukami, and Koji Fukagata (2020). "Nonlinear mode decomposition with convolutional neural networks for fluid dynamics". In: *Journal of Fluid Mechanics* 882. Publisher: Cambridge University Press.
- Méndez, M, Mostafa Safdari Shadloo, and A Hadjadj (2020). "Heat-transfer analysis of a transitional boundary layer over a concave surface with Görtler vortices by means of direct numerical simulations". In: *Physics of Fluids* 32.7. Publisher: AIP Publishing LLC, p. 074111.
- Nickels, TB et al. (2005). "Evidence of the  $k^{-1}$  law in a high-Reynolds-number turbulent boundary layer". In: *Physical review letters* 95.7. Publisher: APS, p. 074501.
- Nunes, J.C. et al. (2003). "Image analysis by bidimensional empirical mode decomposition". In: *Image and vision computing* 21.12, pp. 1019–1026.
- Pathikonda, Gokul and Kenneth T Christensen (2019). "Investigation of inner-outer interactions in a turbulent boundary layer using high-speed particle image velocimetry". In: *Physical Review Fluids* 4.3. Publisher: APS, p. 034607.
- Perry, AE and MS Chong (1982). "On the mechanism of wall turbulence". In: *Journal of Fluid Mechanics* 119, pp. 173–217.
- Perry, AE, S Henbest, and MS Chong (1986). "A theoretical and experimental study of wall turbulence". In: *Journal of Fluid Mechanics* 165. Publisher: Cambridge Univ Press, pp. 163 –199.
- Perry, AE and I. Marusic (1995). "A wall-wake model for the turbulence structure of boundary layers. Part 1. Extension of the attached eddy hypothesis". In: *Journal of Fluid Mechanics* 298, pp. 361–388.
- Plaut, Elad (2018). "From principal subspaces to principal components with linear autoencoders". In: *arXiv:1804.10253*.
- Poggie, J. (2015). "Compressible Turbulent Boundary Layer Simulations: Resolution Effects and Turbulence Modeling". In: *53rd AIAA Aerospace Sciences Meeting* 10.2514/6.2015-1983.
- Poggie, J and T Leger (2015). "Large-scale unsteadiness in a compressible, turbulent reattaching shear layer". In: *Experiments in Fluids* 56.11. Publisher: Springer, pp. 1–12.

- Pope, Stephen B (2001). *Turbulent flows*.
- Quadrio, M and P Ricco (2003). "Initial response of a turbulent channel flow to spanwise oscillation of the walls". In: *Journal of Turbulence* 4.7.
- Quadrio, M. and P. Ricco (2004). "Critical assessment of turbulent drag reduction through spanwise wall oscillations". In: *Journal of Fluid Mechanics* 521, pp. 251–271.
- Quadrio, M., P. Ricco, and C. Viotti (2009). "Streamwise-travelling waves of spanwise wall velocity for turbulent drag reduction". In: *Journal of Fluid Mechanics* 627, pp. 161–178.
- Rao, K Narahari, R Narasimha, and MA Narayanan (1971). "The ‘bursting’phenomenon in a turbulent boundary layer". In: *Journal of Fluid Mechanics* 48.02, pp. 339–352.
- Renard, N. and S. Deck (2016). "A theoretical decomposition of mean skin friction generation into physical phenomena across the boundary layer". In: *Journal of Fluid Mechanics* 790. Publisher: Cambridge University Press, pp. 339–367.
- Rhie, C. M. and W. L. Chow (1983). "Numerical study of the turbulent flow past an airfoil with trailing edge separation". In: *AIAA Journal* 21.11.
- Ricco, P. (2004). "Modification of near-wall turbulence due to spanwise wall oscillations". In: *Journal of Turbulence* 5.24.
- Ricco, P. and M. Quadrio (2008). "Wall-oscillation conditions for drag reduction in turbulent channel flow". In: *International Journal of Heat and Fluid Flow* 29.4, pp. 891–902.
- Ricco, P. et al. (2012). "Changes in turbulent dissipation in a channel flow with oscillating walls". In: *Journal of Fluid Mechanics* 700.1, pp. 1–28.
- Ricco, Pierre, Martin Skote, and Michael A Leschziner (2021). "A review of turbulent skin-friction drag reduction by near-wall transverse forcing". In: *Progress in Aerospace Sciences* 123. Publisher: Elsevier, p. 100713.
- Rosenberg, BJ et al. (2013). "Turbulence spectra in smooth-and rough-wall pipe flow at extreme Reynolds numbers". In: *Journal of Fluid Mechanics* 731, pp. 46–63.
- Samuel, Arthur L (1959). "Some studies in machine learning using the game of checkers". In: *IBM Journal of research and development* 3.3. Publisher: IBM, pp. 210–229.
- Schlatter, P. et al. (June 2010). "Simulations of spatially evolving turbulent boundary layers up to". In: *International Journal of Heat and Fluid Flow* 31.3, pp. 251–261.
- Schlatter, Philipp and Ramis örlü (2010). "Quantifying the interaction between large and small scales in wall-bounded turbulent flows: A note of caution". In: *Physics of Fluids* 22.5, p. 051704.
- Silva, CM de et al. (2015). "Scaling of second-and higher-order structure functions in turbulent boundary layers". In: *Journal of Fluid Mechanics* 769, pp. 654–686.
- Silva, CM de et al. (2020). "Periodicity of large-scale coherence in turbulent boundary layers". In: *International Journal of Heat and Fluid Flow* 83. Publisher: Elsevier, p. 108575.
- Skote, M. (2011). "Turbulent boundary layer flow subject to streamwise oscillation of spanwise wall-velocity". In: *Physics of Fluids* 23, p. 081703.
- (Dec. 2012). "Temporal and spatial transients in turbulent boundary layer flow over an oscillating wall". In: *International Journal of Heat and Fluid Flow* 38, pp. 1–12. ISSN: 0142-727X.
- (2013). "Comparison between spatial and temporal wall oscillations in turbulent boundary layer flows". In: *Journal of Fluid Mechanics* 730, pp. 273–294.
- Smits, Alexander J, Beverley J McKeon, and Ivan Marusic (2011). "High-Reynolds number wall turbulence". In: *Annual Review of Fluid Mechanics* 43, pp. 353–375.
- Talluru, KM et al. (2014). "Amplitude modulation of all three velocity components in turbulent boundary layers". In: *Journal of Fluid Mechanics* 746, R1.
- Temmerman, L. et al. (2003). "Investigation of wall-function approximations and subgrid-scale models in large eddy simulation of separated flow in a channel with streamwise periodic constrictions". In: *International Journal of Heat and Fluid Flow* 24.2, pp. 157–180.
- Touber, E. and M. Leschziner (2012). "Near-wall streak modification by spanwise oscillatory wall motion and drag-reduction mechanisms". In: *Journal of Fluid Mechanics* 693, pp. 150–200.
- Townsend, Albert A (1980). *The structure of turbulent shear flow*. Cambridge university press.
- Vassilicos, JC et al. (2015). "The streamwise turbulence intensity in the intermediate layer of turbulent pipe flow". In: *Journal of Fluid Mechanics* 774, pp. 324–341.
- Vincent, Pascal et al. (2010). "Stacked denoising autoencoders: Learning useful representations in a deep network with a local denoising criterion." In: *Journal of machine learning research* 11.12.

- Weatheritt, J. and R. Sandberg (2016). "A novel evolutionary algorithm applied to algebraic modifications of the RANS stress-strain relationship". In: *Journal of Computational Physics* 325. Publisher: Elsevier, pp. 22–37.
- Woodcock, JD and I Marusic (2015). "The statistical behaviour of attached eddies". In: *Physics of Fluids (1994-present)* 27.1, p. 015104.
- Wu, Z. and N.E. Huang (2004). "A study of the characteristics of white noise using the empirical mode decomposition method". In: *Proceedings of the Royal Society of London A: Mathematical, Physical and Engineering Sciences*. Vol. 460. The Royal Society, pp. 1597–1611.
- Xu, C.-X. and W.-X. Huang (2005). "Transient response of Reynolds stress transport to spanwise wall oscillation in a turbulent channel flow". In: *Physics of Fluids* 17, p. 018101.
- Xu, Jin et al. (2007). "Turbulent drag reduction by constant near-wall forcing". In: *Journal of Fluid Mechanics* 582, pp. 79–101.
- Zhang, Chi and Sergei I. Chernyshenko (May 2016). "Quasisteady quasihomogeneous description of the scale interactions in near-wall turbulence". en. In: *Physical Review Fluids* 1.1. ISSN: 2469-990X.
- Zhou, Chong and Randy C Paffenroth (2017). "Anomaly detection with robust deep autoencoders". In: *Proceedings of the 23rd ACM SIGKDD international conference on knowledge discovery and data mining*, pp. 665–674.